Nominally volatile-free mantle minerals: a reservoir for water and fluorine in the Kaapvaal Craton

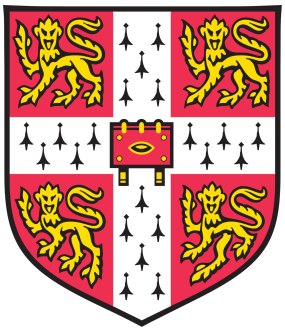

Charlotte Gabrielle Jackson

Department of Earth Sciences
University of Cambridge

This dissertation is submitted for the degree of
Doctor of Philosophy

Jesus College

April 2020

Declaration

This thesis is the result of my own work and includes nothing which is the outcome of work done in collaboration except where specifically indicated in the text.

It is not substantially the same as any that I have submitted, or, is being concurrently submitted for a degree or diploma or other qualification at the University of Cambridge or any other University or similar institution. I further state that no substantial part of my thesis has already been submitted, or, is being concurrently submitted for any such degree, diploma or other qualification at the University of Cambridge or any other University or similar institution.

The total length does not exceed the 275 numbered page limit for the Degree Committee of Earth Sciences, including 225 pages of text, appendices, illustrations and bibliography.

Charlotte Gabrielle Jackson
April 2020

Nominally volatile-free mantle minerals: a reservoir for water and fluorine in the Kaapvaal Craton

The extent to which Earth's sub-cratonic lithospheric mantle acts as a major repository for volatile elements is poorly constrained. This study presents the first systematic investigation into water, fluorine and chlorine storage in nominally volatile-free mantle minerals from sub-cratonic mantle. Full petrologic and chemical characterisation (using EPMA, LA-ICP-MS, SIMS, FTIR, SEM, EBSD) of nineteen mantle xenoliths from the interior (Bultfontein, South Africa) and margin (Mothae, Lesotho) of the Kaapvaal craton has placed important constraints on the capacity of olivine and pyroxenes to store volatiles. Cryptically metasomatised olivine is found to be a major host of fluorine (up to 196 ppm). A new incorporation mechanism involving triple coupling of F, OH and Ti in olivine is recognised: Ti^{4+} in an octahedral site is charge balanced by F^{-} in an oxygen site and OH^{-} in a neighbouring tetrahedral vacancy. This triple coupling limits the independent diffusion of each element and hence preserves metasomatic enrichment on timescales of millions to billions of years.

Four different types of metasomatism have been recognised in the Kaapvaal xenolith suites, each with different controls on the storage of volatile elements in olivine and pyroxenes. Proto-kimberlite metasomatism is found to flux the largest amount of volatile elements into the sub-cratonic lithospheric mantle. This has important implications for the pre-conditioning of the mantle prior to the host kimberlite eruption, because assimilation of volatile-rich mantle wall-rock contributes volatile species to kimberlite magmas and drives their ascent through hundreds of kilometres of lithosphere to the surface.

The Kaapvaal craton has previously been considered as dry compared to the Slave and Siberian cratons but this new dataset includes water concentrations of clinopyroxene and orthopyroxene that are as high as those in the published literature. Olivine F concentrations are some of the highest recorded in global lithospheric mantle and provide evidence that F input at subduction zones is recycled through the convecting mantle, transported into the cratonic mantle by small-fraction melts and stored in both NVFMMs and new metasomatic phases. A metasomatic front at 120 km depth coincides with high concentrations of volatiles and corresponds to seismic mid-lithospheric discontinuities and has important implications for craton stability.

"That’ll do Donkey, that’ll do"

Acknowledgements

Firstly I'd like to thank my supervisor Sally Gibson, who has been extremely encouraging, supportive and understanding for the last four years. Sally's course on kimberlites and small-fraction melts during my undergraduate degree absolutely caught my interest and sparked the desire to apply for a PhD so that I could learn more about these fascinating volcanic and chemical systems. I have had incredible support throughout the Department of Earth Sciences and have really valued the network of support from fellow PhD students, Post Docs, Academic staff and support staff. I owe special thanks to Jason Day, Iris Buisman and Guilio Lampronti whose technical support has been invaluable. Similarly, I am extremely grateful to Cristina Talavera Rodriguez (University of Edinburgh) and Peter Tollan (University of Bern) for assistance with SIMS and FTIR, respectively, as well as fruitful discussions!

I'd like to thank NERC for sponsoring my studentship and Jesus College, British Geological Survey and the committee of the 11th International Kimberlite Conference for funding towards conferences and workshops. I'm particularly grateful for the experience to attend the 11IKC in Gaborone, Botswana. To be able to see kimberlite outcrops in the field and visit diamond mines is an experience I will never forget. The opportunity to attend the 11IKC at the end of my first year introduced me to a fantastic community including other PhD students who I really enjoyed seeing at subsequent conferences and discussing our research on the same level.

I owe special thanks to my wonderful office mates, especially Euan Mutch, Victoria Honour, Nick Barber and Carrie Soderman who have supplied a constant stream of chat and laughter over the past 3 years. I've been lucky enough to be surrounded by wonderful friends, a big thanks to to Claire Nichols, Jenny Woods, Katy Relph, Laura Rogers, Julia Woitischek, Ellie Aris and Jack Ellis for always being there through the best and worst times.

It wouldn't be right to finish without mention of rowing. Jesus College Boat Club and Cambridge University Women's Boat Club have provided a source of release, friendship and utmost joy without which I would not have enjoyed my time in Cambridge half as much. Rowing has the ability to bring people together, the crews have formed my family away from home and I will always associate my time at Cambridge with you all - special mentions to Jesus W1 of 2016-18 and Blondie+ 2019 with whom I have formed some of my best memories.

Finally I want to thank my Mum, Dad and brother Henry, who have been absolute pillars of support until now and I know they always will be. Thank you for everything!

Nominally volatile-free mantle minerals: a reservoir for water and fluorine in the Kaapvaal Craton

The sub-cratonic lithospheric mantle is an important but poorly constrained reservoir for volatiles in the solid Earth. Water, fluorine and chlorine are all fluxed into the convecting mantle at subduction zones, and while most water and chlorine is released into the mantle wedge and recycled via arc volcanic systems a significant amount of fluorine is retained in the subducting slab and recycled into the convecting mantle. The thick lithospheric lid (200-250 km) of cratons requires that melting in the underlying asthenosphere only occurs in particularly hot or volatile-rich conditions. Small-fraction melts and fluids that infiltrate cratons are extremely volatile-rich but do not transport heat (McKenzie, 1989) and rarely reach Earth's surface, instead they percolate through the sub-cratonic lithospheric mantle and freeze in the cool conditions (Sleep, 2009). This ancient and long-lived reservoir has the ability to store significant amounts of water and fluorine for billions of years. This is evidenced in mantle xenoliths from kimberlites that contain significant quantities of volatile-rich metasomatic phases such as phlogopite, amphibole and carbonate. The presence of metasomes in the mantle composed of concentrations of these volatile-rich phases is proposed to be the origin of seismic mid-lithospheric discontinuities observed in cratons worldwide, but the estimated abundance of phlogopite and amphibole required to produce the 6-7% decrease in seismic velocity is, however, vastly different to the quantities of these phases observed in natural xenoliths.

Metasomatic melts and fluids not only precipitate new phases but also interact with the pre-existing mantle minerals, namely olivine, orthopyroxene, clinopyroxene, garnet and spinel. Experiments have shown that these nominally volatile-free mantle minerals (NVFMM) have the capacity to host non-negligible quantities of water and fluorine. When this is considered alongside their overwhelming abundance in the SCLM, the potential of NVFMM to contribute to the volatile budget of the mantle is huge. This study investigates the storage of water, fluorine and chlorine in olivine, orthopyroxene and clinopyroxene from variably metasomatised mantle xenoliths from two Late Cretaceous kimberlites in the Kaapvaal Craton: Bultfontein and Mothae, at the craton interior and margin, respectively. Nineteen xenoliths have been analysed that cover a depth range of 70-170 km and represent four different types of metasomatism including: carbonatite-, proto-kimberlite- and siliceous fluid-metasomatism. In this systematic study the major-, trace- and volatile-element concentrations of NVFMMs are used to investigate the controls on volatile transport and storage in the Kaapvaal craton. The results suggest that NVFMMs are an under-estimated store of water and fluorine in the SCLM.

Olivine is found to be a significant host of water (up to 120 ppmw) and fluorine (up to 196 ppm) in the Kaapvaal craton, following melt-rock reaction with volatile-rich metasomatic agents, while orthopyroxene and clinopyroxene contain significantly more water than olivine (up to 300 and 400 ppmw, respectively) but are a less important store of fluorine (< 50 ppm). Each metasomatic agent recognised in the Bultfontein and Mothae xenoliths has a different control on the volatile concentration of the NVFMMs during melt-rock reaction. Shallow carbonatite metasomatism and melt fertilisation by the addition of clinopyroxene and garnet at the base of the lithosphere are both found to be ineffective carriers of volatiles to the NVFMM, whereas proto-kimberlite melts and hydrous siliceous fluids both introduce significant amounts of water

and fluorine into the mantle wall-rock. The latter two styles of metasomatism can increase the localised bulk F concentrations by a factor of five compared to the mean bulk peridotite F concentration. Between Group II (130-110 Ma) and Group I (90-80 Ma) kimberlite activity there was a change in the style of metasomatism to dominantly silicate-carbonate (kimberlite) melt metasomatism. This change is proposed to have increased the bulk H_2O concentration of the Kaapvaal SCLM (hosted in NVFMM) from 40 to 55 ppmw, and the bulk F concentration from 21 to 37 ppm. An increase of this magnitude over a 20-50 Ma period has implications for the stability of the craton by decreasing the viscosity of the volatile-enriched regions. Models that predict the origin of mid-lithospheric discontinuities do not yet account for metasomatic enrichment and hydration of NVFMM but the results here suggest they could have an important role. If the water and fluorine-rich nature of olivine, orthopyroxene and clinopyroxene in and around metasomes, and at the metasomatic front (~40 kbar), are considered then the required abundance of hydrous metasomatic phases (phlogopite, amphibole) is reduced and could reflect more accurately the observations from natural xenoliths.

Three of the mantle xenoliths from Bultfontein show evidence of metasomatism by proto-kimberlite (silicate-carbonate) melts. In one of these, a spectacular branching clinopyroxene and phlogopite vein cuts through a deformed dunite protolith. The melt-rock reaction of the proto-kimberlite melt and pre-existing mantle olivine is preserved in Ni and Cr zoning within large olivine porphyroclasts. The preservation of Ni and Cr disequilibrium captures the process of subsolidus re-equilibration in the act. Diffusion modelling has been used to define the timing of metasomatism prior to Ni and Cr reaching their closure temperature during the eruption of the host kimberlite. This has showed that the metasomatism by proto-kimberlite melts occurred within 500,000 years of the eruption of the Bultfontein kimberlite at 84 (± 0.9) Ma (Kramers *et al.*, 1983). Pre-conditioning of the mantle by proto-kimberlite melts that freeze in the craton is an important precursory process that aids final kimberlite ascent, this study shows for the first time that this pre-conditioning enriches the mantle in water, fluorine and chlorine. The volatile enriched mantle wall-rock is assimilated into the host kimberlite during ascent and contributes to the overall volatile-rich nature of the kimberlite magma itself. This addition of extra volatiles is important to propel the host kimberlite to the surface before it can freeze in the cool cratonic lithosphere.

The main findings of this study that (i) different metasomatic agents have the ability to increase mantle wall-rock volatile contents by diffusive exchange of water and fluorine during melt-rock reaction and; (ii) olivine is a major host of both water and fluorine if it has interacted with a proto-kimberlite melt or siliceous fluid, imply that the sub-cratonic lithospheric mantle is a major reservoir for water and fluorine in the Earth. Billions of years of melt infiltration at the base of the lithosphere has fluxed volatile elements into the craton during effective recycling. Volatile enrichment in NVFMM should be accounted for in global volatile cycles, in the consideration of craton stability, to explain the anomalous seismic mid-lithospheric discontinuities and in kimberlite ascent dynamics.

Table of contents

Nomenclature **xix**

1 Introduction **1**

1.1 Volatile cycles in the solid Earth 1

1.2 Sub-cratonic lithospheric mantle 3

1.3 Volatile re-mobilisation in the sub-cratonic lithospheric mantle 5

1.4 Nominally volatile-free mantle minerals 9

1.5 Kaapvaal Craton 11

1.5.1 Previous work investigating H_2O storage in NVFMMs in the Kaapvaal craton . . 13

1.6 Geological setting: Bultfontein and Mothae kimberlites 14

1.7 Thesis outline 15

2 Petrography of Bultfontein and Mothae peridotites **17**

2.1 Introduction 17

2.2 Bultfontein 18

2.2.1 Spinel harzburgite 20

2.2.2 Phlogopite lherzolite 21

2.2.3 Wehrlite 21

2.2.4 Dunite 22

2.2.5 Garnet harzburgite 22

2.3 Mothae 22

2.3.1 Spinel-harzburgite 23

2.3.2 Garnet harzburgite 23

2.3.3 Garnet lherzolite 24

2.4 Detailed classification of lithological groups 24

2.5 Summary 25

3 Mineral chemistry **27**

3.1 Major- and minor- element chemistry 27

3.1.1 Olivine 27

3.1.2 Orthopyroxene . . . 32
3.1.3 Clinopyroxene . . . 33
3.1.4 Garnet . . . 34
3.1.5 Phlogopite . . . 36
3.2 Trace-element chemistry . . . 39
3.2.1 Olivine . . . 39
3.2.2 Orthopyroxene . . . 39
3.2.3 Clinopyroxene . . . 39
3.2.4 Garnet . . . 40
3.3 Bulk rock chemistry . . . 42
3.4 Assessment of major-element equilibrium . . . 45
3.5 Classification of lithological groups . . . 46
3.5.1 Principal component analysis . . . 49
3.6 Summary . . . 50

4 Thermobarometry 51
4.1 Introduction . . . 51
4.2 Thermometers . . . 51
4.2.1 Two-pyroxene thermometer . . . 51
4.2.2 Fe-Mg orthopyroxene-garnet thermometer . . . 52
4.2.3 Single phase thermometers . . . 53
4.3 Barometers . . . 54
4.3.1 Al-exchange in orthopyroxene and garnet barometer . . . 54
4.3.2 Single orthopyroxene barometer . . . 56
4.4 *PT* estimates of the Bultfontein and Mothae xenoliths . . . 56
4.5 Perturbed conductive geotherm . . . 61
4.6 Final *PT* estimates . . . 63

5 Xenolith history: melt depletion and metasomatism 65
5.1 Chapter outline . . . 65
5.2 Introduction . . . 65
5.3 Evidence for melt depletion . . . 67
5.4 Metasomatic agents in the sub-cratonic mantle . . . 72

5.5 Equilibrium melts . . . 74
5.5.1 Published mineral-melt partition coefficients . . . 75
5.5.2 Lattice strain model . . . 75
5.5.3 Melts in equilibrium with clinopyroxene . . . 78
5.6 Carbonatite melt metasomatism . . . 80
5.7 Proto-kimberlite (silico-carbonatite melt) metasomatism . . . 81
5.8 Hydrous siliceous fluid metasomatism . . . 83
5.9 Melt re-fertilisation . . . 88
5.10 Kaapvaal database . . . 90
5.11 Conclusions . . . 92

6 Constraining the timescales of proto-kimberlite metasomatism: a case study of BD3067 93
6.1 Introduction . . . 93
6.2 Petrographic description . . . 94
6.3 Mineral chemistry . . . 94
6.3.1 Clinopyroxene . . . 94
6.3.2 Olivine . . . 94
6.3.3 Sulfides . . . 99
6.3.4 Zircon . . . 100
6.4 Crystallographic orientation and Ni heterogeneity in olivine . . . 100
6.5 Disequilibrium in olivine . . . 101
6.5.1 Subsolidus re-equilibration of olivine and clinopyroxene . . . 103
6.5.2 Late-stage crystallisation of accessory phases . . . 105
6.5.3 Olivine diffusion anisotropy . . . 106
6.6 Timing of kimberlite metasomatism . . . 108
6.6.1 Zircon dating . . . 108
6.6.2 Diffusion modelling . . . 108
6.7 Xenolith history . . . 110
6.8 Metasomatism preceding kimberlite eruption . . . 111
6.9 Conclusions . . . 112

7 Volatile storage in NVFMMs 113
7.1 Introduction . . . 113

7.2 Secondary ion mass spectrometry: Concentration of H_2O, F and Cl in NVFMMs 113
7.2.1 Olivine 114
7.2.2 Orthopyroxene 116
7.2.3 Clinopyroxene 117
7.2.4 Bulk rock 119
7.3 Fourier transform infrared spectroscopy: Position of absorbance bands in OH-stretching region 120
7.3.1 Olivine 122
7.3.2 Orthopyroxene 127
7.4 Summary 129

8 Incorporation of H_2O and F within and between NVFMMs 131
8.1 Introduction 131
8.2 Incorporation mechanisms of H and F in NVFMMs 132
8.2.1 Olivine 132
8.2.2 Orthopyroxene 135
8.3 Volatile partitioning 137
8.3.1 $D_{H_2O}^{cpx-opx}$ 137
8.3.2 $D_F^{cpx-opx}$ 140
8.3.3 D_F^{ol-pxn} 142
8.4 Subsolidus re-equilibration in NVFMMs 143
8.5 Implications of Ti-H-F coupling to diffusion rates 149
8.6 Volatile enrichment in mantle olivines 150
8.7 Summary 151

9 Controls on volatile storage in the SCLM 153
9.1 Introduction 153
9.2 Spatial controls on volatile concentration 154
9.3 Metasomatic controls on volatiles in NVFMM 157
9.3.1 Volatile contents in metasomatic agents 157
9.3.2 Metasomatic indicators and volatiles 159
9.3.3 Volatile behaviour during melt-rock reaction by different metasomatic agents . . 161
9.4 The influence of metasomatism and oxygen fugacity 168

9.5 Implications 171

10 History of metasomatic enrichment in the Kaapvaal craton 173

10.1 Metasomatic history of the craton 173

10.1.1 Craton formation: melt depletion and hydrous fluid metasomatism 173

10.1.2 Metasomatism and magmatism 176

10.1.3 Cretaceous plume impingement: Group II kimberlite magmatism and fertilisation of the lithosphere 177

10.1.4 Lithospheric pre-conditioning: Group I kimberlite magmatism 177

10.2 Seismic anomalies 180

10.3 Reservoir capacity, implications for craton stability 181

10.4 Summary 184

11 Conclusions 187

11.1 Future Work 193

References 195

Appendix Analytical Techniques 217

A Scanning Electron Microscopy 217

B Electron Microprobe Analysis 217

C Laser Ablation - ICP-MS 217

D Secondary Ion Mass Spectrometry 219

E Fourier Transform Infrared Spectroscopy 220

Appendix Data Tables 223

Nomenclature

Acronyms / Abbreviations

chon	Chondrite
cpx	Clinopyroxene
gt	Garnet
HFSE	High-field-strength elements
HREE	Heavy rare earth element
MREE	Middle rare earth element
LILE	Large-ion-lithophile elements
LREE	Light rare earth element
NVFMM	Nominally volatile-free mantle mineral
ol	Olivine
opx	Orthopyroxene
PC1	Principal component 1
PCA	Principal component analysis
phl	Phlogopite
pm	Primitive mantle
REE	Rare earth element
SCLM	Sub-cratonic lithsopheric mantle

Chapter 1

Introduction

1.1 Volatile cycles in the solid Earth

Volatiles, such as hydrogen (H), sulfur (S), carbon (C), fluorine (F) and chlorine (Cl), are a crucial component for life on Earth and play critical roles in the chemical and physical processes at both Earth's surface and interior. The solid Earth is a significant host of volatile elements but its influence and capacity is poorly constrained. While most studies have focused on the storage of H and C in Earth's various reservoirs, the capacity to store halogens (F, Cl) is less well understood. Peslier *et al.* (2017) highlight the debate in the study of H and the wide ranging estimates of the mass of water in the Earth and its hydrosphere. Figure 1.1 compares three estimates of the mass of water in seven different reservoirs: (i) core; (ii) lower mantle; (iii) transition zone; (iv) upper mantle; (v) oceanic crust; (vi) continental crust; and (vii) hydrosphere. Peslier *et al.* (2017) calculate that the core hosts the greatest quantity of water (Figure 1.1a); this is in contrast to the estimates by Nestola & Smyth (2016) where the lower mantle is the main host of water (Figure 1.1b), and by Bodnar *et al.* (2013) where water is estimated to be more evenly spread between the different reservoirs (Figure 1.1c). The greatest difference between these three estimates is in the relative influence of the core and mantle, which may reflect the methods used in the calculation: Nestola & Smyth (2016) and Bodnar *et al.* (2013) use planetary accretion models, whereas Peslier *et al.* (2017) calculated the expected H concentration in the core using the results of experiments that determined the compatibility of H into molten iron. In this study, the focus is on the sub-cratonic lithospheric mantle, which is part of the rigid upper mantle. In the three models for water storage in the Earth in Figure 1.1 a, b and c, the upper mantle constitutes 0.6%, 1.2% and 3% of the total water content, respectively.

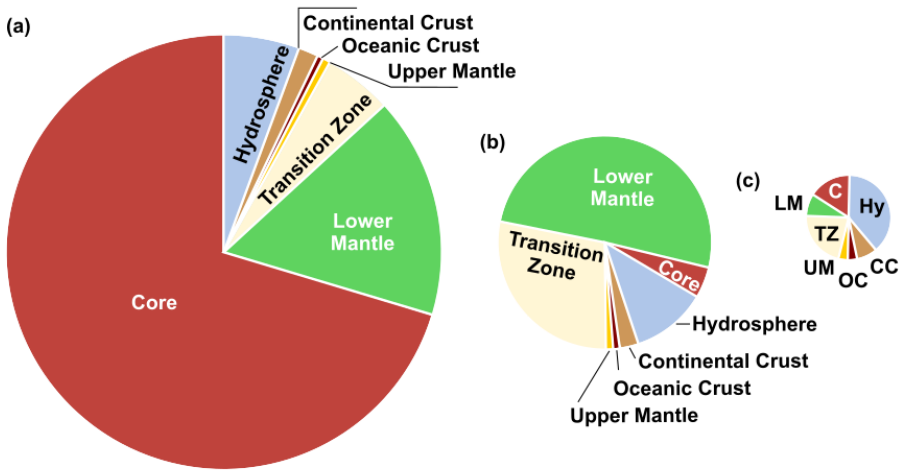

Figure 1.1 *The proportion (mass %) of the total mass of water stored in the Solid Earth according to three different estimates. The relative area of the circle is proportional to the total mass of water estimated in each model: (a) 24.7 × 10^{24} g H_2O, Peslier* et al. *(2017); (b) 12.1 × 10^{24} g H_2O, Nestola & Smyth (2016); and (c) 3.61 × 10^{24} g H_2O Bodnar* et al. *(2013). Figure modified from Peslier* et al. *(2017)*

The storage of volatiles within the mantle is not uniform. The estimates in Figure 1.1 segment the mantle into the lower mantle, transition zone and upper mantle, based on phase transitions of olivine, wadsleyite and ringwoodite and spinel to perovskite and magnesiowüstite (see Akaogi 2007). The mantle is also divided into the lithospheric mantle and the asthenosphere, based on thermal properties and strength (see Section 1.2), and there are further discrete chemical reservoirs within the mantle that have been recognised primarily by their isotopic composition. Each reservoir contributes to the overall heterogeneity in chemical composition in the mantle that can be recognised in magmas and mantle xenoliths at the Earth's surface. An example involving volatile elements is the primordial mantle signature in Ocean Island Basalts identified using noble gas isotope ratios (e.g. $^{3}He/^{4}He$, $^{40}Ar/^{36}Ar$, $^{20}Ne/^{22}Ne$). It is assumed that the mantle plumes, which cause melting beneath volcanic ocean islands, tap a primordial reservoir in the lower mantle that preserves the volatile signature of the early Earth (e.g. Woodhead *et al.* 2019) and can be used to estimate volatile budgets. Primordial He and Ne is dominant in the mantle, but significant fractions of H_2O, CO_2 and other noble gases (e.g. Ar, Xe) are derived from recycled material via subduction zones (Ballentine & Barfod, 2000; Ballentine & Holland, 2008; Halliday, 2013; Matsumoto *et al.*, 2001; Sarda *et al.*, 1999; Staudacher & Allègre, 1988), hence additional reservoirs (e.g. subducted sediment and oceanic lithosphere) in the mantle carry different signatures of recycled volatiles (e.g. Hanyu & Nakamura 2000; Hart & Staudigel 1989; Kogiso *et al.* 1997; Rapp *et al.* 2008; Ryan & Chauvel 2014; Stracke *et al.* 2005; Workman *et al.* 2004; Zindler & Hart 1986).

Subduction zones provide the primary flux of water, fluorine and chlorine from the Earth's surface into the mantle (Figure 1.2). Hydrothermal fluids are a crucial agent that enrich the slab in the halogens and H_2O via serpentinisation. Consequently, the oceanic crust, sediments and seawater in the subducting slab are all enriched in H_2O, F and Cl (Ito *et al.*, 1983; Kendrick *et al.*, 2012; Schilling *et al.*, 1978; Seyfried Jr & Ding, 1995; Straub & Layne, 2003b). During subduction two important serpentinite ($[Mg, Fe]_3[Si_2O_5][OH]_4$) breakdown reactions cause slab fluids to be released into the overlying mantle: (i) at shallow depths (< 70 km) lizardite breaks down to antigorite releasing fluids enriched in S, F and Cl (Debret *et al.*, 2014); and (ii) at depths of ~150 km the breakdown of antigorite releases H_2O-rich fluids (Debret *et al.*, 2013; Wunder & Schreyer, 1997). Eventually slab melting occurs, but the point at which the melting temperature is reached in the cold, down-going slab, is well beyond the fore arc (Bebout *et al.*, 1999; Plank & Kelley, 2001).

Multiple approaches have been used to estimate the flux of recycled F, Cl and H_2O through the mantle wedge including measuring: (i) concentrations in arc magmas (e.g. Straub & Layne 2003b); (ii) concentrations in variably serpentinised oceanic crust in ophiolite sequences (e.g. Debret *et al.* 2014); and (iii) the release of F, Cl and H_2O during serpentinite breakdown reactions via experiments (e.g. John *et al.* 2011). Most studies agree that almost all subducted Cl and a significant proportion of H_2O is released from the slab to the mantle wedge, whereas the majority of F is retained in the slab and transported to the deep, convecting mantle. Mass balance calculations suggest that only 4-6% of F (compared to > 77% Cl) is recycled through arc volcanism (Ryan & Chauvel, 2014; Straub & Layne, 2003a). Straub & Layne (2003a) propose that this disparity could be because most F is hosted in nominally volatile-free minerals and is, therefore, only liberated during slab melting at great depths and not susceptible to entrainment by slab fluids. Mass balance calculations indicate that the F released during the shallow reaction of lizardite to antigorite alone can account for the entire outflux of F from arc volcanoes (Debret *et al.*, 2014). As serpentinites represent only one reservoir of F in the subducting slab, this implies that there is significant

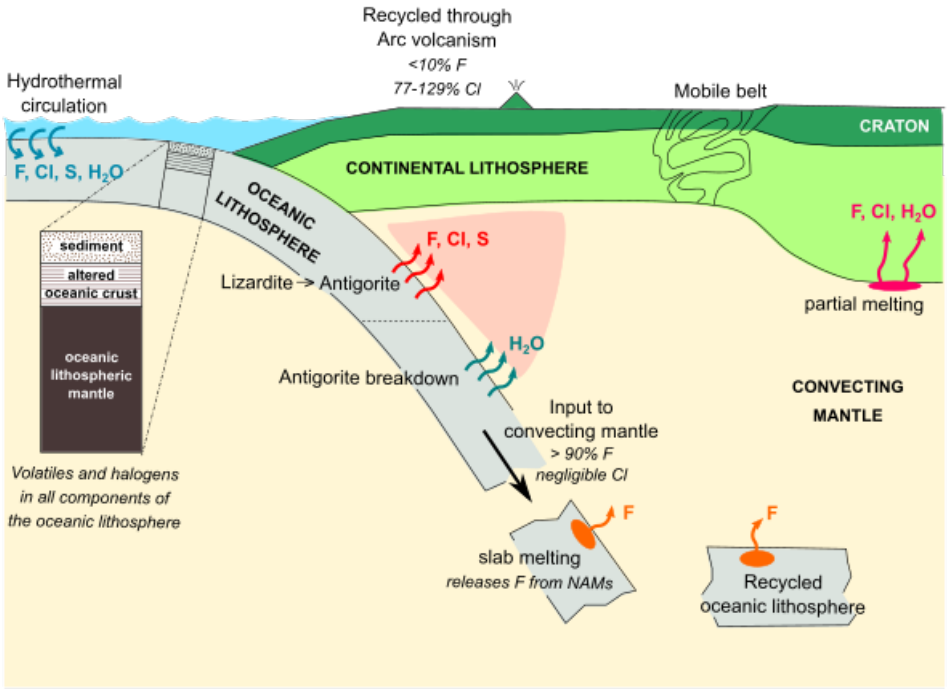

Figure 1.2 *Schematic illustration of the flux of H_2O and halogens (F, Cl) into the mantle via a subducting slab. These are recycled via the mantle wedge or into the convecting mantle. See text for description and key references.*

flux of F into the deeper mantle at subduction zones. Consequently, one can assume that the Earth's convecting mantle has been accumulating F for billions of years after the onset of plate tectonics, from deep slab melting and F release and in the form of recycled oceanic lithosphere that is physically remixed into the mantle and can be re-mobilised by partial melting. Melting occurs in particularly hot or volatile-rich mantle where either a perturbed geotherm intersects the dry-peridotite solidus, or the presence of volatile species (H_2O and CO_2) or halogens (F, Cl) reduce the solidus to intersect the unperturbed geotherm (e.g. Brey *et al.* 2009; Dasgupta & Hirschmann 2006; Hirschmann 2000), or in some cases a combination of the two.

1.2 Sub-cratonic lithospheric mantle

An important, long-lived, but poorly constrained reservoir for volatiles in the upper mantle is the sub-cratonic lithospheric mantle (SCLM). This underlies the crust and forms the lower lithosphere, which is the brittle outer layer of the Earth. The lithosphere can be defined in terms of the mechanical boundary layer (MBL) or the thermal boundary layer (TBL). The MBL is defined by the strength of peridotite, and the transition from a brittle to a ductile regime. The thermal boundary layer is defined by the change from a conductive to convective thermal regime, with a transitional zone between, at the top of the convecting mantle (Figure 1.3; Eaton *et al.* 2009; McKenzie & Bickle 1988).

Oceanic and continental lithosphere differ significantly in terms of their age, thickness and composition. The oceanic lithospheric mantle predominantly forms at mid-ocean ridges, it thickens over time and reaches a constant thickness at an age of approximately 70 Ma (Parsons & Sclater, 1977). Oceanic lithosphere is relatively uniform in composition globally (Warren, 2016). By comparison, the sub-continental

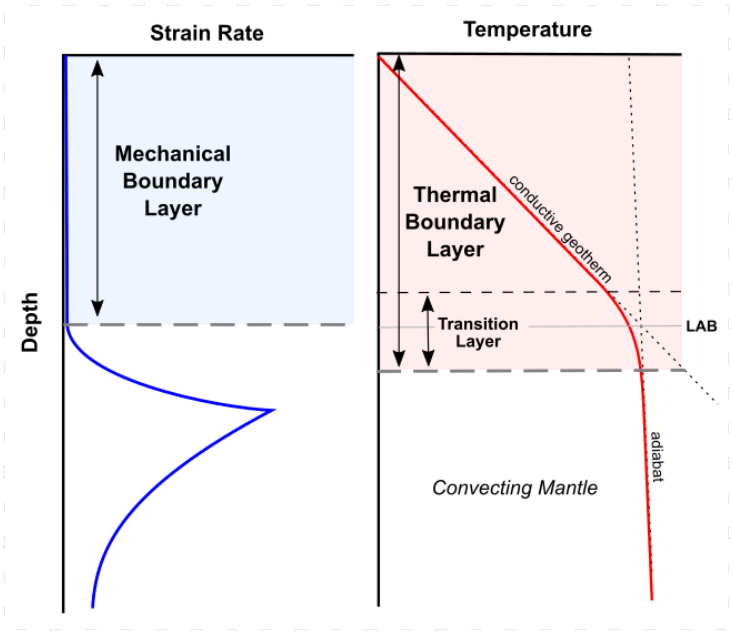

Figure 1.3 *The mechanical boundary layer defined by an increase in strain rate, moving from a brittle to ductile regime. The thermal boundary layer is defined as the region at the top of a convecting system where the geotherm deviates from the adiabat. The thermal transition zone identifies the region where the geotherm is intermediate between the conductive geotherm to the adiabat. In this definition, the Lithosphere-Asthenosphere-Boundary (LAB) marks the point where the conductive geotherm intersects the adiabat. Modified from McKenzie & Bickle (1988) and Eaton* et al. *(2009)*

lithospheric mantle is formed by various melt depletion and enrichment events at different tectonic settings and its thickness varies considerably (Figure 1.4). The continental lithosphere reaches its greatest thickness (> 200 km) beneath Archean cratons (e.g. Fishwick 2010; Priestley & McKenzie 2013; Priestley *et al.* 2006), which make up the ancient cores of continents. Cratons are, by definition, older than 2.5 Ga and have been largely unaffected by tectonic processes over this time. They have anomalously low heat flow, ~ 41 ± 12 mWm^{-2} (global average of archean cratons) compared to 55 ± 17 mWm^{-2} in Proterozoic terrane over 400 km from the craton margin (Nyblade & Pollack, 1993). Despite this, cratons show no observable gravity excess (Pollack & Chapman, 1977). Jordan (1975) first suggested that the long-term stability of cratons could be due to a positive buoyancy, created by the depletion of the sub-cratonic lithospheric mantle during melting events, which offsets the negative buoyancy imparted by the low temperatures. This is known as the isopycnic hypothesis and it forms the foundation behind most models of craton formation and evolution.

Three endmember models for craton formation exist: (i) plume accretion; (ii) subduction stacking; and (iii) shortening and thickening (Pearson & Wittig, 2008). In the plume accretion model, large scale melting occurs in the upper mantle where there is a thermal upwelling. Extraction of large volumes of melt leaves a depleted residue that builds up to form the cratonic root (e.g. Wyman & Kerrich 2002). The subduction stacking model suggests that the craton is built up by the tectonic stacking of oceanic lithosphere (e.g. Tappe *et al.* 2011), but given the dense eclogite component of oceanic lithosphere at high pressure, this scenario does not have long-term gravitational stability (Pearson & Wittig, 2008). Over the past few years, the third model of shortening during continental collision followed by gravitational thickening has gained traction in the community and has emerged as the preferred hypothesis (Aulbach *et al.*, 2017a; McKenzie & Priestley, 2016; Pearson & Wittig, 2008; Regier *et al.*, 2018; Scott *et al.*, 2019). In this model, inital

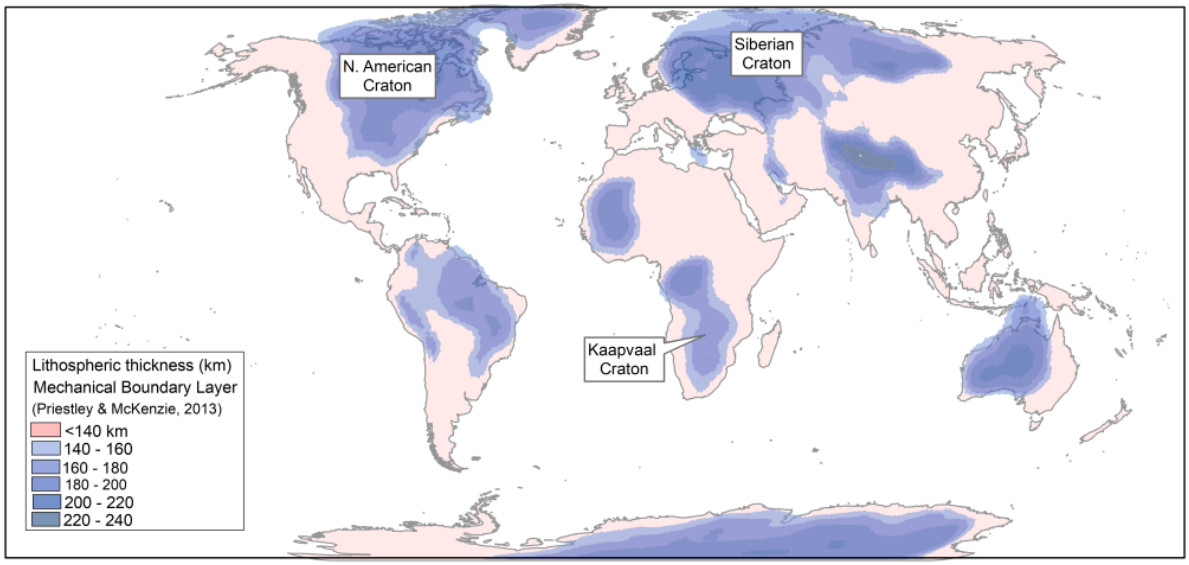

Figure 1.4 *Simplified map of lithospheric thickness, defined by the thickness of the mechanical boundary layer (Priestley & McKenzie, 2013). The Kaapvaal, North American and Siberian Cratons are marked for reference.*

melting occurs in a sub-arc (Pearson & Wittig, 2008; Regier *et al.*, 2018) or mid-ocean-ridge (Gibson *et al.*, 2008; Pearson & Wittig, 2014; Simon *et al.*, 2007) environment and produces a depleted mantle residue. During continental collision, multiple sources of depleted residue are accreted to form a low density body of heterogeneous lithosphere beneath the continent. The new lithospheric keel undergoes gravitational thickening to produce the observed cratonic root that extends down to depths of 200-250 km.

Cratons are long-lived archives of the oldest rocks and processes on Earth. Their conductive thermal regime means that heterogeneity in the sub-cratonic lithospheric mantle is not homogenised over time as it would be in the asthenosphere. As a result, mantle xenoliths from the sub-cratonic lithospheric mantle exhibit a wide range of different chemical compositions that reflect melt depletion and enrichment from fluid- or melt-rock reaction (i.e. metasomatic enrichment). Strongly alkaline silicate magmas, such as kimberlites and lamproites, carry fragments of the cratonic mantle to the surface that provide an unparalleled insight into the composition of the SCLM and the processes that have affected it throughout Earth's history. Studies of mantle xenoliths from kimberlites have provided key information to try and unravel the processes behind craton formation, melt depletion, lithospheric thinning, metasomatic enrichment, kimberlite dynamics and more.

1.3 Volatile re-mobilisation in the sub-cratonic lithospheric mantle

Partial melting

The thickness of the sub-cratonic lithosphere exceeds the depth where the mantle adiabat intersects the dry-peridotite solidus. In order for melting to occur beneath or within cratonic lithosphere, there must be a heat source, or the mantle must be abnormally volatile-rich. The latter factor produces very small-fraction melts and can occur in either the asthenosphere beneath the craton or, rarely, within the sub-cratonic lithosphere. One mechanism that directly requires and produces volatile species is redox melting of

peridotite, where a change in oxidation state produces H_2O or CO_2 which, in turn, lowers the peridotite solidus. Foley (2011) highlight two forms of redox melting: (i) hydrous redox melting; and (ii) carbonate redox melting. Hydrous redox melting occurs in more reducing conditions where methane is oxidised to form H_2O and C (Taylor, 1985). The H_2O released acts to depress the solidus and melting will occur if it intersects the geotherm (Green, 1973; Taylor & Green, 1988). Foley (2011) show that this condition can be reached where the water activity (aH_2O) increases from 0.35 to 0.85 following the oxidation of methane in the lower cratonic lithosphere. The carbonate redox melting mechanism involves the oxidation of carbon in a carbon-saturated (graphite or diamond-bearing) environment by fluids or melts, or the occurrence of redox gradients between adjacent blocks of recycled or accreted material (Foley, 2011; Green *et al.*, 1987). The base of the cratonic lithosphere is particularly susceptible to carbonate redox melting, as it contains abundant carbon in the form of diamond (Boyd & Gurney, 1986). Redox melting has also been proposed as a mechanism involved in the production of kimberlite parental magmas (e.g. Dasgupta & Hirschmann 2010; Foley 2011; Yaxley *et al.* 2017) and is undoubtedly an important process in re-mobilising volatile elements within the SCLM.

Small-fraction volatile-rich melts

Evidence for the re-mobilisation of volatiles in and below the sub-cratonic lithospheric mantle is manifested in the presence of kimberlites and lamproites at the surface. These are hybrid magmatic bodies that originate as small-fraction volatile-rich melts and assimilate mantle and crustal material during ascent. Kimberlites can be split into two primary groups based on studies of southern African occurrences: Group I and Group II kimberlites (Becker & Roex, 2006; Smith, 1983; Wagner, 1914). The latter are mica-rich and have been renamed carbonate-rich olivine lamproites by Pearson *et al.* (2019) based on their chemistry. The predominant melt source of lamproites is within the lithosphere, whereas the source of kimberlites is more likely to involve the asthenosphere (Smith, 1983). There are multiple hypotheses for the origin of archetypal Group I kimberlite magmas, which implicate different source regions and necessary volatile concentrations to drive ascent, to date no consensus has been reached. Isotope systematics (e.g. Sr, Nd, Pb and Hf) suggest that the primary melt originates in the asthenosphere by small-fraction melting either immediately beneath the lithospheric lid (Tappe *et al.*, 2018) or deeper, associated with subducted oceanic lithosphere (Nowell *et al.*, 2004; Pearson *et al.*, 2019) or even the transition zone (Tappe *et al.*, 2013). There is convincing evidence for lithospheric interaction during ascent, for example the following features summarised by Pearson *et al.* (2019): (i) the bulk Mg/Si ratio of kimberlites is inherited from cratonic lithosphere; (ii) the high variance in trace element composition requires the digestion of variably enriched lithospheric mantle; (iii) the unradiogenic Os isotope composition of kimberlites requires interaction with the lithospheric mantle (Araujo *et al.*, 2001); and (iv) there is a broad overlap between ocean island basalt isotope compositions and kimberlites with less evidence of assimilation (e.g. Nowell *et al.* 2004; Smith 1983). Additionally, Foley *et al.* (2019) argue that interaction of the kimberlite melt with an oxidised region in the mid-lithosphere is necessary to produce specific compositional variables such as high K_2O/Na_2O and a correlation between CaO and CO_2, although observations from the Udachnaya kimberlite (Siberian craton; Figure 1.4) suggest this could be a primary feature (Kamenetsky *et al.*, 2012, 2014). No experimental studies have been able to accurately reproduce the kimberlite compositions observed at the surface. Most experiments have investigated the role of H_2O or CO_2 (e.g. Dasgupta & Hirschmann 2006),

and occasionally both (Foley *et al.*, 2009; Wallace & Green, 1988) on the melting of dry peridotite but, despite there being evidence for F and Cl decreasing the solidus temperature of peridotite (Brey *et al.*, 2009), very few studies investigate the role of the halogens in kimberlite petrogenesis.

Traditionally parental kimberlite melts were considered to be hydrous, carbonated ultrabasic melts (e.g. Dawson 1971, 2012; Kopylova *et al.* 2007; Mitchell 2008; Roex *et al.* 2003), but over the last few years experimental and empirical evidence has accumulated that suggests the parental liquid to kimberlites is a carbonatite melt enriched in Ca, K and Na (e.g. Arndt *et al.* 2010; Brett *et al.* 2015; Golovin *et al.* 2019; Kamenetsky & Yaxley 2015; Kamenetsky *et al.* 2013; Keshav *et al.* 2005; Pilbeam *et al.* 2013), although this view is controversial (Foley *et al.*, 2019). Estimates of the H_2O and CO_2 concentrations of the parental kimberlite melt vary widely: e.g. from < 1% to 7% H_2O and 2-22% CO_2 (e.g. Kamenetsky *et al.* 2013; Kjarsgaard *et al.* 2009; Kopylova *et al.* 2007; Roex *et al.* 2003; Soltys *et al.* 2018). The halogen concentrations also vary: high F concentrations (>0.4 wt.%) have been analysed from the Roger kimberlite (Canada; Abersteiner *et al.* 2018) and the Udachnaya kimberlite (Siberia) is renowned for having high Cl concentrations (e.g. 6 wt.%; Förster *et al.* 2019; Gubanov *et al.* 2019; Kamenetsky *et al.* 2009, 2012). Recent studies on the Cl-rich Udachnaya kimberlite have raised a number of questions within the kimberlite community. This is considered a 'fresh' kimberlite, unlike most other localities which exhibit extensive serpentinisation, and has low H_2O contents (<1 wt.%) and high Na_2O concentrations (up to 6.2 wt.%), which are deemed to reflect the parental melt (Golovin *et al.*, 2019; Kamenetsky *et al.*, 2012, 2013). This has lead to the hypothesis that the 'archetypal' Na-poor, H_2O-rich kimberlite composition present worldwide is a secondary consequence of alteration and serpentinisation rather than a primary feature. Furthermore, chlorides are present in the groundmass of the Udachnaya kimberlite, which is considered to represent the lack of serpentinisation and hydrous alteration (Kamenetsky *et al.*, 2009, 2012). Chloride mineral preservation supports the hypothesis that the parental melt was Cl-rich and chlorides are a primary precipitating phase in kimberlites (Förster *et al.*, 2019; Kamenetsky *et al.*, 2004, 2009). Indeed, Broadley *et al.* (2018) suggest that the lower 30 km of the Siberian lithosphere has been extensively enriched in Cl during interaction with sea-water derived fluids released during subduction of altered oceanic crust. Additional experiments by Förster *et al.* (2019) found that melting of subducted sediments produces a Cl-rich melt that forms chlorides on reaction with mantle peridotite and can explain the presence of chlorides in the Udachnaya groundmass.

Udachnaya is the only Cl-rich kimberlite to have been identified to date, but fluid inclusions in diamonds from localitites worldwide provide additional evidence for halogens in the mantle. These contain high-density-fluids that form a compositional array between three endmember compositions: (i) saline (Na + K); (ii) high-Mg carbonatitic (Ca + Mg); and (iii) low-Mg carbonatitic to silicic (Gubanov *et al.*, 2019; Navon *et al.*, 1988; Shirey *et al.*, 2013; Tomlinson *et al.*, 2006; Weiss *et al.*, 2009). The saline fluids may play an important role in the formation of both the high-Mg and low-Mg carbonatitic melts during reaction with carbonated peridotite and eclogite, respectively (Weiss *et al.*, 2009). The high-mobility and reactivity of saline fluids involved in kimberlite evolution (Kamenetsky *et al.*, 2014) therefore has the potential to significantly chemically enrich the SCLM in recylced halogens.

Metasomatism

Kimberlite magmatism has varied through time, peaking in the Mesozoic, but an unequivocal lack of kimberlites from the Archean implies that the conditions for kimberlite magmatism were not reached until mantle volatile concentrations had increased following the onset of deep-subduction plate tectonics (Giuliani & Pearson, 2019; Heaman *et al.*, 2019). The low density, volatile-rich nature of kimberlites enables the suspension and transport of mantle xenoliths up to 50 kg in size. This xenolith cargo provides an exceptional insight into the composition of the cratonic lithosphere to depths in excess of 250 km. Depleted harzburgites typical of the cratonic mantle root are prevalent, but there is also a range of lithologies that reflect metasomatic enrichment by different agents (Nixon, 1973). Different melts and fluids impart a different signature on the mantle peridotite which can be identified using petrographic observations, major and trace element chemistry (Dawson *et al.*, 2001; Dawson, 2012).

Xenolith studies of kimberlites globally have revealed a wide array of metasomatic agents that enrich the sub-cratonic mantle to variable degrees. Two of the most important suites of metasomatised xenoliths in the Kaapvaal craton are the Mica-Amphibole-Rutile-Ilmenite-Diopside (MARID) suite (Dawson & Smith, 1977) and the Phlogopite-Ilmenite-Clinopyroxene (PIC) suite (Grégoire *et al.*, 2002), which both exhibit extreme metasomatism in their hydrous mineralogy (e.g. Figure 1.5) and LREE enrichment. The origin of the PIC suite is generally agreed to be related to kimberlite melt metasomatism, either as a product of the reaction between the melt and peridotite (Fitzpayne *et al.*, 2018b) or direct crystallisation of a kimberlite melt (Grégoire *et al.*, 2002). A consensus on the origin of the MARID assemblage has not been reached; it is debated as to whether this assemblage represents a magmatic cumulate or the product of a reaction (Banerjee *et al.*, 2018; Dawson & Smith, 1977; Fitzpayne *et al.*, 2018a; Grégoire *et al.*, 2002; Sweeney *et al.*, 1993), but it is generally agreed that the melt involved was carbonatitic rather than a pure silicate melt. Recent work by Fitzpayne *et al.* (2019) has identified a signature in MARID xenoliths from Kimberley that could be related to the short-term storage of recycled material in the lithosphere.

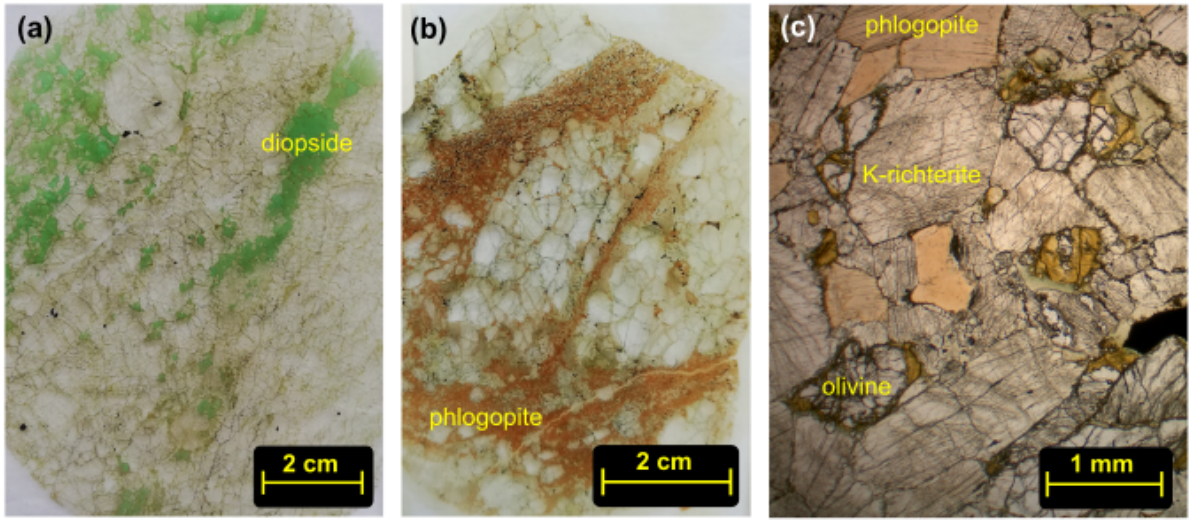

Figure 1.5 *Metasomatised mantle xenoliths from Bultfontein. All are from the Dawson collection donated to S. A. Gibson at the University of Cambridge. (a) BD3043, metasomatic Cr-diopside veins in a lherzolite; (b) BD3056, phlogopite veins in harzburgite; and (c) Micro-photograph showing K-richterite (amphibole) and phlogopite adjacent to serpentinised olivine.*

Melts and fluids of different compositions cause different reactions and variably enrich the mantle in both incompatible trace-elements and volatile elements. The volatile concentration of the metasomatic agent has a strong control on different features of the mantle peridotite, for example at high H_2O contents olivine is stable at the expense of garnet and the pyroxenes whereas the opposite is true at high CO_2 concentrations. Therefore, the CO_2/H_2O ratio of the metasomatic agent during melt-rock reaction strongly controls the modal mineralogy of the metasomatised peridotite. The contrasting effects of CO_2 and H_2O in the metasomatic agent can also impact on the behaviour of fluorine during metasomatism. The partitioning of F into olivine is strongly dependent on melt polymerisation (Guggino, 2012; Urann *et al.*, 2017) and while H_2O is highly soluble and known to depolymerise melts, CO_2 acts to polymerise melts by forming complexes with network modifying cations (i.e. Ca and Na; Mysen *et al.* 1982). Consequently, in order to investigate volatile storage in the SCLM, it is important to establish the composition of the different metasomatic agents in order to understand the mechanism(s) by which H_2O, F and Cl are mobilised through the craton.

1.4 Nominally volatile-free mantle minerals

Metasomatic phases, such as phlogopite and amphibole, are undoubtedly important hosts of H_2O, F and Cl in the sub-cratonic lithospheric mantle, but their low volumetric abundance overall (see Figure 1.6) limits their impact on the capacity of the SCLM as a reservoir for volatiles. By contrast, studies have shown that nominally volatile-free mantle minerals (NVFMMs), such as olivine, orthopyroxene, clinopyroxene and garnet, have the capacity to hold non-negligible quantities of H_2O and F in their crystal structure (e.g. Bell & Rossman 1992; Bromiley & Kohn 2007; Demouchy & Bolfan-Casanova 2016; Grützner *et al.* 2017; Hervig & Bell 2005; Peslier *et al.* 2017; Skogby 2006; Urann *et al.* 2017; Warren & Hauri 2014). The sheer abundance of the NVFMMs, which constitute > 95% of the SCLM, makes them a potentially important repository for H_2O and F in the Earth (Figure 1.6). This has important implications for craton stability because the presence of small amounts of H_2O influences both physical and chemical properties of NVFMMs, including viscosity (e.g. Hirth & Kohlstedf 2003; Karato 1990; Mackwell *et al.* 1985), melting temperature (e.g. Hirschmann 2000; Padrón-Navarta & Hermann 2017), electrical conductivity (e.g. Karato 1990; Li *et al.* 2017), and seismic wave velocity (e.g. Férot & Bolfan-Casanova 2012; Katayama *et al.* 2004; Wagner *et al.* 2008). Constraining the volatile content of NVFMMs in the cratonic mantle is, therefore, critical to understanding the buoyant nature and long-term stability of cratons.

In this thesis, in accordance with other studies (Demouchy & Bolfan-Casanova, 2016; Peslier, 2010; Peslier *et al.*, 2017), the term water is used to refer to a number of H-bearing species (H, OH, H_2, H_2O) and the concentrations in NVFMM are given as ppmw (ppm wt. H_2O). Hydrous phases are defined as those which incorporate water as OH^- (as a stoichiometric component), while NVFMM incorporate water as H^+ in trace amounts (< 0.1 wt.% H_2O). In reduced conditions there is evidence that olivine, pyroxenes and garnet can also incorporate water as H_2 (Yang *et al.*, 2016). In NVFMMs, H occurs as point defects by forming hydroxyl (OH^-) groups, or occasionally as an interstitial phase (Demouchy & Bolfan-Casanova, 2016). Fluorine is incorporated into both NVFMMs and hydrous minerals through the substitution of fluoride (F^-) for hydroxyl ions (OH^-), aided by their similar ionic radius and equal charge (Crépisson *et al.*, 2014; Hervig & Bell, 2005; Li *et al.*, 2017). Li *et al.* (2017) suggest that the similarity and close association in the crystal lattice implies that F should have similar effects on the properties of

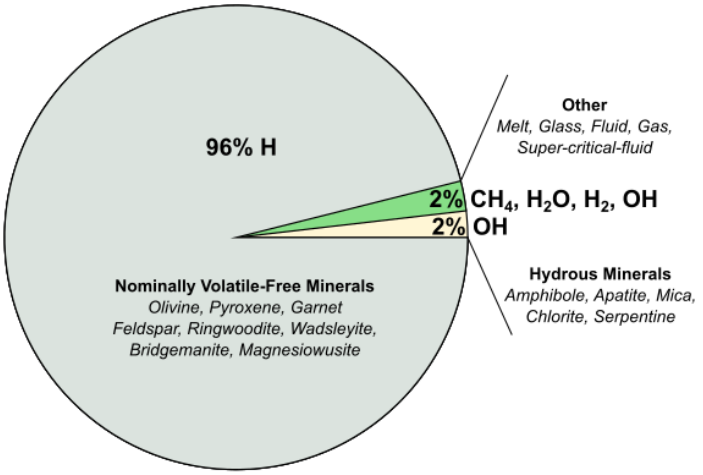

Figure 1.6 *Figure adapted from Peslier* et al. *(2017) showing the main hosts of water in the Earth's mantle and crust. The main host is the nominally volatile-free mantle minerals which incorporated 'water' as H. A small proportion of hydrous minerals host water as OH and 'water' is present as other H-bearing species in melts, fluids and gases. The size of the slice represents the rough proportion by volume of each phase.*

host minerals as H. An example where this is shown to be true is for electrical conductivity. Many studies have shown that the presence of hydrogen significantly enhances the electrical conductivity of mantle minerals, including olivine, enstatite and pyrope garnet (Dai & Karato, 2009; Karato, 1990; Li *et al.*, 2016; Poe *et al.*, 2010; Yang *et al.*, 2008; Zhang *et al.*, 2012). Li *et al.* (2017) presented the first evidence that F in phlogopite greatly enhances electrical conductivity and suggest this should be the same for F in NVFMMs. The effect of H_2O on other physical properties of NVFMM has important implications for craton stability. Firstly, the presence of H_2O and F lowers the solidus temperature of peridotite (Brey *et al.*, 2009; Gaetani & Grove, 1998; Hirschmann, 2000), hence reducing the strength of the mantle. Secondly the presence of H in the lattice of olivine is proportional to the strain rate, because it increases the number of vacancies and hence the self-diffusivity of Si (Kohlstedt, 2006). This has the effect of increasing the climb controlled creep or deformation and hence decreases the strength and viscosity (Hirth & Kohlstedf, 2003; Mackwell *et al.*, 1985). The combined effects can have major implications for craton stability over geological time and, while the effect of H_2O is relatively well-understood, more studies are required to investigate the effects of the halogens on physical properties of mantle minerals.

The H_2O concentration of olivine, pyroxene and garnet has historically been measured using Fourier Transform Infrared Spectroscopy (FTIR; e.g. Bell *et al.* 2003a; Libowitzky & Beran 1995; Stalder & Skogby 2003; Withers *et al.* 2012), but development in analytical techniques and the availability of standards over the past decade has established and improved the use of Secondary Ion Mass Spectrometry (SIMS) to measure H_2O in NVFMM (e.g. Hauri *et al.* 2006; Koga *et al.* 2003; Kumamoto *et al.* 2017; Mosenfelder & Rossman 2013a,b; Mosenfelder *et al.* 2011; Rossman 2006; Urann *et al.* 2017). Both techniques are now able to analyse H_2O down to detection limits of < 0.5 ppmw (Peslier *et al.*, 2017). The advantage of SIMS is that other elements, such as the halogens, can be analysed at the same time due to the full characterisation of orthopyroxene and clinopyroxene standards by Kumamoto *et al.* (2017). For this reason, SIMS is the primary method chosen to measure H_2O, F and Cl concentrations in this study.

Numerous studies have investigated H_2O contents in nominally volatile-free mantle minerals in a range of environments, including the sub-cratonic lithospheric mantle (e.g. Baptiste *et al.* 2012; Bell

& Rossman 1992; Demouchy & Bolfan-Casanova 2016; Doucet *et al.* 2014; Grant *et al.* 2007; Peslier 2010; Peslier *et al.* 2012, 2015; Schmädicke *et al.* 2013). Analyses of H_2O contents of NVFMM from the sub-continental mantle show a broad range. In one of the earliest studies of this kind Bell & Rossman (1992) measured the H_2O concentration in olivine, orthopyroxene, clinopyroxene and garnet from both off-craton and cratonic sub-continental mantle. The highest concentrations in all minerals were present in cratonic xenoliths, however there is also a great degree of variation in this setting. Garnet lherzolites from three different host kimberlites in the Kaapvaal craton exhibit a range of 17-79 ppmw H_2O in olivine and 210-460 ppmw in orthopyroxene. The Colorado Plateau sub-continental lithospheric mantle has relatively high H_2O concentrations in NVFMM (e.g. Marshall *et al.* 2018), Li *et al.* (2008) measure up to 45 ppmw in olivine, 402 ppmw in orthopyroxene and 957 ppmw in clinopyroxene. This is considered to be elevated, especially when compared to concentrations of San Carlos minerals (4, 82 and 178 ppmw in olivine, ortho- and clinopyroxene, respectively) analysed in the same study. Li *et al.* (2008) attribute the re-hydration in the Colorado Plateau to be associated with Cenozoic subduction. Demouchy & Bolfan-Casanova (2016) compared the storage of H in NVFMM from different continental settings and found, somewhat surprisingly, that there is no systematic difference between H_2O contents in a subduction setting than elsewhere. In fact, they found the highest H_2O concentrations in olivine from the cratonic lithosphere (up to 49 ppmw H_2O in peridotite nodules, and up to 194 ppmw in peridotite xenocrysts in kimberlite). They suggest that this is due to a strong pressure control on H_2O concentrations in olivine and the greater pressure of origin of cratonic xenoliths. Urann *et al.* (2017) also found that there is no systematic difference in F or Cl concentration in NVFMM from different tectonic settings. These studies, amongst others, have established that rather than tectonic setting being a controlling factor on volatile and halogen behaviour, smaller scale features are important, such as localised metasomatism (Peslier *et al.*, 2012), oxygen fugacity (Foley *et al.*, 1986; Tollan & Hermann, 2019), melt polymerisation (Guggino, 2012; Urann *et al.*, 2017) and mineral chemistry (e.g. Demouchy & Mackwell 2006; Stalder *et al.* 2005; Tollan *et al.* 2018; Urann *et al.* 2017).

Very few observations have been published to date of F and Cl concentrations in mantle minerals despite the fact that experimental work has shown that olivine and orthopyroxene alone are able to host the entire F budget of the upper mantle (Grützner *et al.*, 2017). Urann *et al.* (2017) and Gibson *et al.* (2020) present some of the first analyses of F and Cl in olivine, orthopyroxene and clinopyroxene from the sub-continental lithospheric mantle, however neither include samples from Archean cratonic lithospheric mantle. A handful of studies have analysed F concentrations in megacrysts from South African kimberlites (Beyer *et al.*, 2012; Hervig & Bell, 2005; Mosenfelder & Rossman, 2013a,b; Mosenfelder *et al.*, 2011), but the effect of contamination by the kimberlite host cannot be resolved. Nevertheless, Mosenfelder & Rossman (2013a,b) measured up to 17 ppm F in orthopyroxene and up to 29 ppm F in clinopyroxene megacrysts from the Gibeon (Namibia) and Premier (South Africa) kimberlites.

1.5 Kaapvaal Craton

The Kaapvaal Craton is a sub-region of the larger Kalahari Craton that extends across most of southern Africa, encompassing the north east of South Africa, southern Botswana, western Eswatini (formerly Swaziland) and western Lesotho (Figure 1.7). The Kaapvaal Craton formed between 3.5-2.6 Ma. Diamonds from the Kaapvaal Craton date back to 3.5 Ga (Richardson *et al.*, 1984), and their inclusions preserve

evidence of crustal recycling in the mantle above a low angle subducting slab (Smart *et al.*, 2016). The intial proto-continental shield stabilised at 3.1 Ga (De Wit *et al.*, 1992; Poujol *et al.*, 2003) followed by the closure of the final major subduction zone in the area at 2.9 Ga, bringing together the Witswatersrand block to the east and the Kimberley block to the west (Figure 1.7a). The Coleburg lineament marks the suture and the position of the paleosubduction zone (Pearson *et al.*, 1995b; Schmitz *et al.*, 2004; Shirey *et al.*, 2013). This was followed by the establishment of a thick lithospheric keel that achieved long-term stability by 2.6 Ga (De Wit *et al.*, 1992; Poujol *et al.*, 2003).

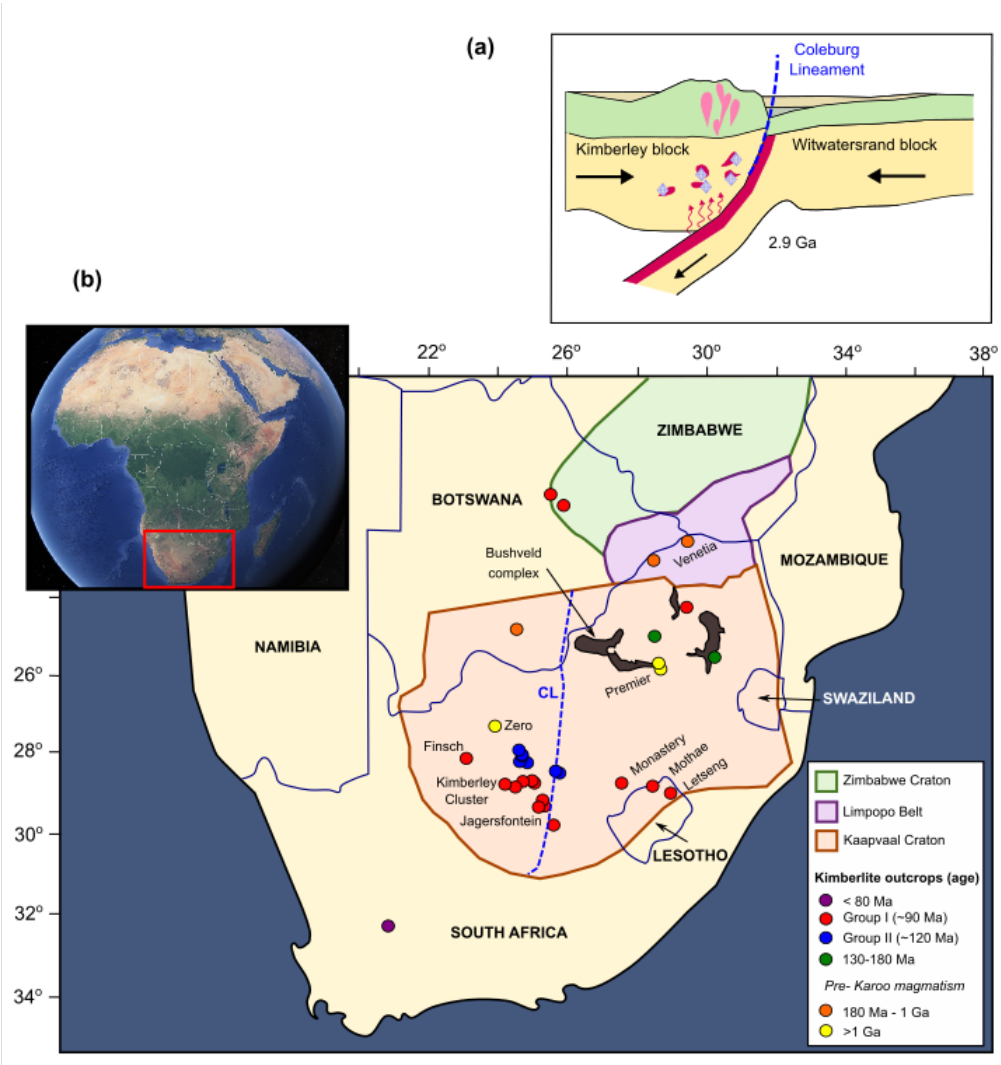

Figure 1.7 *(a) The collision of the Kimberley block and the Witswatersrand block along the Coleburg lineament (adapted from Shirey* et al. *2013) (b) The location of the Kaapvaal craton, Limpopo belt and southern edge of the Zimbabwe craton in southern Africa. A selection of kimberlites are marked and colour coded according to their age of emplacement. The Bushveld complex is shown in dark grey and labelled. The location of kimberlites were taken from Faure (2010) and the ages are from Griffin* et al. *(2014a).*

Two large magmatic events produced the Bushveld complex at 2.05-2.06 Ga in the north and the Karoo flood basalts which erupted through the eastern edge of the craton at ~ 180 Ma. Additionally, hundreds of kimberlites have been emplaced through the Kaapvaal craton (Faure, 2010). This has occurred in specific periods from 1700 Ma (1700, 1200, 500, 200 Ma and 50-130 Ma; Griffin *et al.* 2014a) and includes two extended periods of intense magmatism at 120-130 Ma (Group II) and the main 'bloom' at 90 ± 10 Ma (Group I). The abundant kimberlites in the Kaapvaal craton are a source of many mantle xenoliths that

provide an insight into the sub-cratonic lithospheric mantle, extending from the MOHO all the way down to the base of the lithosphere. Xenoliths from kimberlites have been used for the past half a century (Boyd, 1989; Dawson & Smith, 1977; Nixon, 1973) to shed light on the evolution of the Kaapvaal craton including its formation, major melting and enrichment events and more localised metasomatism, all of which will be discussed further within this study.

1.5.1 Previous work investigating H_2O storage in NVFMMs in the Kaapvaal craton

The Kaapvaal sub-cratonic lithospheric mantle has been the subject of a number of studies into the storage of water in olivine, orthopyroxene, clinopyroxene and garnet (e.g. Baptiste *et al.* 2012; Bell & Rossman 1992; Bell *et al.* 2004; Bonadiman *et al.* 2009; Demouchy & Bolfan-Casanova 2016; Grant *et al.* 2007; Ingrin & Grégoire 2010; Peslier 2010; Peslier *et al.* 2012, 2017). The highest H_2O contents in nominally anhydrous minerals have been found in the cratonic mantle, and indeed many of these in xenoliths and megacrysts from the Kaapvaal. There is a large range in measured water contents from different locations in the Kaapvaal which could reflect the evolution of the craton as a reservoir through time, or local variation due to melt depletion or metasomatic enrichment. Peslier *et al.* (2010, 2012) measure concentrations of 150-400 ppmw H_2O in clinopyroxene, 40-250 ppmw in orthopyroxene, 0-86 ppmw in olivine and 0-20 ppmw in garnet in peridotite xenoliths from multiple localities across the Kaapvaal craton. The highest H_2O concentration measured in olivine is 262 ppmw in a megacryst from Monastery (Bell *et al.*, 2004), which Grant *et al.* (2007) acknowledge must record magmatic or metasomatic enrichment. Particularly high H_2O concentrations were analysed by Bonadiman *et al.* (2009) in clinopyroxene from the craton containing 342-1012 ppmw H_2O and orthopyroxene 180-491 ppmw. In the same study Bonadiman *et al.* (2009) measured H_2O in pyroxenes from a sub-arc environment at much lower concentrations, where clinopyroxene had 140-528 ppmw H_2O and orthopyroxene 38-280 ppmw.

Ingrin & Grégoire (2010) record very low volatile concentrations (30-40 ppmw total H_2O) from the oldest kimberlite in the Kaapvaal craton (Premier) which erupted at 1150 Ma (Griffin *et al.*, 2014a), whereas the highest H_2O concentrations in NVFMM from the Kaapvaal craton are found in the Group I kimberlites that erupted $\sim$ 90 Ma. Within the multitude of Group I kimberlites, there are lateral variations over very short length scales. For example, Peslier *et al.* (2012) measured extremely low H_2O concentrations in NVFMM from Letseng, but very high H_2O concentrations in Liqhobong, which erupted at a similar time and only 15km apart in northern Lesotho. This variation on such a short length-scale is attributed to localised metasomatic enrichment by different agents that had contrasting ability to hydrate the mantle peridotite. Peslier *et al.* (2012) find convincing evidence for a link between metasomatism and water contents in the co-variance of H with Ti and Ca in garnet rims produced by melt-rock reaction. The presence of H zoning alongside Ti and Ca zoning proves the influence of a metasomatic agent as opposed to H loss during kimberlite ascent, the latter of which would exhibit isolated H zoning. Doucet *et al.* (2014) also observed strong correlations between water concentration and metasomatic indicators such as clinopyroxene and garnet modal abundance, bulk rock FeO and TiO_2 and LREE enrichment in clinopyroxene megacrysts from the Udachnaya kimberlite in the Siberian craton.

The H_2O concentration of olivine in the Kaapvaal craton seems to reach a maximum around 100 ppmw at $\sim$6 GPa before dramatically decreasing with increasing pressure to < 10 ppmw in the deepest xenoliths analysed from the Kaapvaal craton (Baptiste *et al.*, 2012; Grant *et al.*, 2007; Kurosawa *et al.*,

1997; Peslier *et al.*, 2010). A similar trend is not observed in pyroxene H_2O contents in the Kaapvaal (Demouchy & Bolfan-Casanova, 2016), or in olivine H_2O concentrations in the Siberian craton (Doucet *et al.*, 2014). The dry olivine at depths > 180 km in the Kaapvaal craton has been proposed to represent a crucial barrier to cratonic erosion and delamination by setting a high viscosity contrast between a highly viscous dry peridotite base and the relatively low viscosity asthenosphere (Peslier *et al.*, 2010). This hypothesis resides on the results of experimental work by Mackwell *et al.* (1985) which show that the viscosity of the mantle increases with decreasing H_2O content in olivine, and is critical for the long-term stability of the craton. Estimates suggest that to avoid cratonic root delamination a viscosity difference of 10 is required between the base of the lithosphere and the asthenosphere (O'Neill *et al.*, 2008; Sleep, 2003), this is surpassed if a dry olivine zone is present at the base of the lithosphere.

1.6 Geological setting: Bultfontein and Mothae kimberlites

This study aims to build on previous work by increasing the small existing dataset for H_2O concentrations in olivine, orthopyroxene and clinopyroxene from the Kaapvaal sub-cratonic lithospheric mantle, and present for the first time a systematic analysis of F and Cl storage in the region.

Mantle xenoliths from two Late Cretaceous kimberlites in the Kaapvaal Craton are the focus of this study: Bultfontein (Kimberley, South Africa) and Mothae (northern Lesotho). Both are Group I kimberlites that were emplaced during the main 'bloom' of activity. Many studies have dated the Bultfontein kimberlite and agree with the age of 84 ± 0.9 Ma initially determined by Kramers *et al.* (1983). Only one study has dated zircon from the Mothae kimberlite, at 87.1 Ma (Davis, 1977). Griffin *et al.* (2014a) dated other kimberlites from the Lesotho cluster and suggested that they all intruded within less than 10 Ma of each other (weighted mean 92.1 ± 1.5 Ma).

Different types of metasomatism have been identified in the Kaapvaal Craton including carbonatite metasomatism, silicate melt metasomatism, proto-kimberlite melt metasomatism and hydrous siliceous fluid metasomatism (e.g. Aulbach *et al.* 2017b; Bell *et al.* 2005; Fitzpayne *et al.* 2019; Gibson *et al.* 2008; Griffin *et al.* 1999a,b, 2009; Jackson & Gibson 2018; Jollands *et al.* 2018; Kamenetsky *et al.* 2013; Pilet *et al.* 2011; Simon *et al.* 2007; Wasch *et al.* 2009). Bultfontein and Mothae were chosen to represent the craton interior and the craton margin, respectively (Figure 1.7). They were emplaced either side of the Coleberg lineament and therefore the cratonic lithosphere sampled by the kimberlites may have experienced different histories. Metasomatism has been shown to vary significantly in style and extent in xenoliths from different pipes over very small length-scales. It has been shown that the Kimberley cluster, including Bultfontein, has sampled extensively metasomatised lithospheric mantle (e.g. Creighton *et al.* 2008; Dawson & Smith 1977; Fitzpayne *et al.* 2018b; Giuliani 2018; Giuliani *et al.* 2013a,b; Gurney *et al.* 1980). The effects of different styles of metasomatism will be investigated with respect to their influence on the transport and storage of H_2O, F and Cl in the SCLM. To do this, eleven xenoliths from Bultfontein and eight from Mothae, from the J.B. Dawson sollection based in the Sedgwick Museum at the University of Cambridge, have been chosen for this study.

1.7 Thesis outline

This thesis considers the role of nominally volatile-free minerals as a reservoir of H_2O, F and Cl the sub-cratonic lithospheric mantle, by evaluating the influx and removal of volatiles by metasomatic agents and magmatic bodies. To do this a systematic analysis of the petrology, major- and trace-element chemistry of mantle phases are combined with measurements of H_2O, F and Cl and crystallographic orientation to establish the mechanisms by which these important volatile elements are stored in peridotite.

In **Chapter 2** the petrography of nineteen mantle xenoliths from Bultfontein and Mothae are described and a broad classification is made based on the lithology and texture. The classification is refined in **Chapter 3** by the geochemical characterisation of individual components of each xenolith. Major-, minor- and trace-element concentrations of olivine, orthopyroxene, clinopyroxene, garnet and phlogopite are combined to build a chemical profile for each xenolith. Using the results of Chapters 2 and 3, five distinct types of peridotite are identified, each with a characteristic clinopyroxene and garnet trace element pattern. The equilibration pressure and temperature conditions of each xenolith are calculated using a variety of thermometers and barometers in **Chapter 4**.

Chapter 5 investigates the origin of each chemical signature within the suite of xenoliths from Bultfontein and Mothae. The role of melt depletion and metasomatism by four different metasomatic agents is inferred from the major- and trace-element concentrations as well as the modal mineralogy. One xenolith, with a spectacular metasomatic vein, is the focus of a case study into metasomatism by proto-kimberlite melts in **Chapter 6**, and the timing of proto-kimberlite metasomatism is established by diffusion modelling (Jackson & Gibson, 2018).

In **Chapter 7** the concentrations of H_2O, F and Cl (measured by Secondary Ion Mass Spectrometry) in olivine, orthopyroxene and clinopyroxene are presented. The partitioning behaviour of each element is investigated in **Chapter 8** using mineral separates from the same sample and the incorporation mechanisms of H_2O and F in olivine and orthopyroxene are explored using the results of Fourier Transform Infrared Spectroscopy alongside major-element chemistry. In **Chapter 9**, the external controls on water and halogen storage in NVFMM are considered by establishing the effects of pressure, temperature, oxygen fugacity and the composition of the metasomatic agent on the mobilisation and storage of H_2O and F in the Kaapvaal craton. Each style of metasomatism is found to have a strong, and different, control on H_2O and F concentrations in olivine, orthopyroxene and clinopyroxene. The capacity of the SCLM as a reservoir is, therefore, found to depend on the proportion of the craton that has been metasomatised by each different agent. An estimate of the metasomatic proportions in the Kaapvaal craton is made in **Chapter 10** and combined with the volume of the lithospheric keel to calculate the bulk H_2O and F concentrations in the SCLM. The timing of metasomatic events is reviewed with a focus on the relative timing of volatile enrichment or depletion during the history of the Kaapvaal craton. The results have major implications for craton stablility and kimberlite magma dynamics that are also discussed in Chapter 10.

Chapter 2

Petrography of Bultfontein and Mothae peridotites

2.1 Introduction

Nineteen peridotite xenoliths from two highly-diamondiferous kimberlites on the Kaapvaal Craton (Bultfontein and Mothae, at the craton interior and margin, respectively) were analysed in this study. The samples were initially selected from the J.B. Dawson collection donated to S. A Gibson at the University of Cambridge. The primary aim of this investigation is to assess the storage of volatiles in the nominally volatile-free minerals (olivine, orthopyroxene and clinopyroxene) in the sub-cratonic lithospheric mantle (SCLM), and the samples were chosen to avoid extensive modal metasomatism of phlogopite and amphibole. The xenoliths were chosen for their diversity in both lithology and texture in order to cover a large depth range throughout the SCLM. This is based on the knowledge that there are lithological boundaries in the lithosphere, such as between spinel- and garnet-bearing peridotites, and it is suggested that sheared peridotites originate from the base of the lithosphere while coarse, granular peridotites represent shallower levels (Griffin *et al.*, 1989; Mather *et al.*, 2011; Pearson *et al.*, 2003).

The lithologies are classified based on the International Union of Geological Sciences (IUGS) nomenclature (Bas & Streckeisen, 1991; Le Maitre *et al.*, 2004) for ultramafic rocks where dunite has >90% olivine, harzburgite has <5% clinopyroxene, wehrlite <5% orthopyroxene and the rest are lherzolites (Figure 2.1). The xenoliths in this study exhibit a limited range in clinopyroxene abundance; with the exception of the wehrlite from Bultfontein (BD3067) all samples contain less than 10% clinopyroxene, most less than 5% and hence are classified as harzburgites. There is a much wider spread in the modal abundance of olivine (51.6 - 91.8%) and orthopyroxene (0 - 38.8%).

The textural descriptions are based on the following nomenclature of Harte (1977):

Porphyroclast: Relatively large and strained mineral grain or aggregate of such grains that reflect the nature of the rock prior to deformation. They are surrounded by markedly smaller mineral grains (neoblasts).

Neoblast: Small grains that formed during re-crystallisation of original crystals. Neoblasts are usually olivine which re-crystallises in response to pressure.

Coarse texture: The rock lacks porphyroclasts, all minerals tend to be large. Grain boundaries can be straight, smoothly curved or irregular.

Porphyroclastic texture: Over 10% of olivine is present as porphyroclasts as opposed to neoblasts. The rock contains large porphyroclasts surrounded by abundant small neoblasts, hence there is generally a strong bimodal distribution of mineral size.

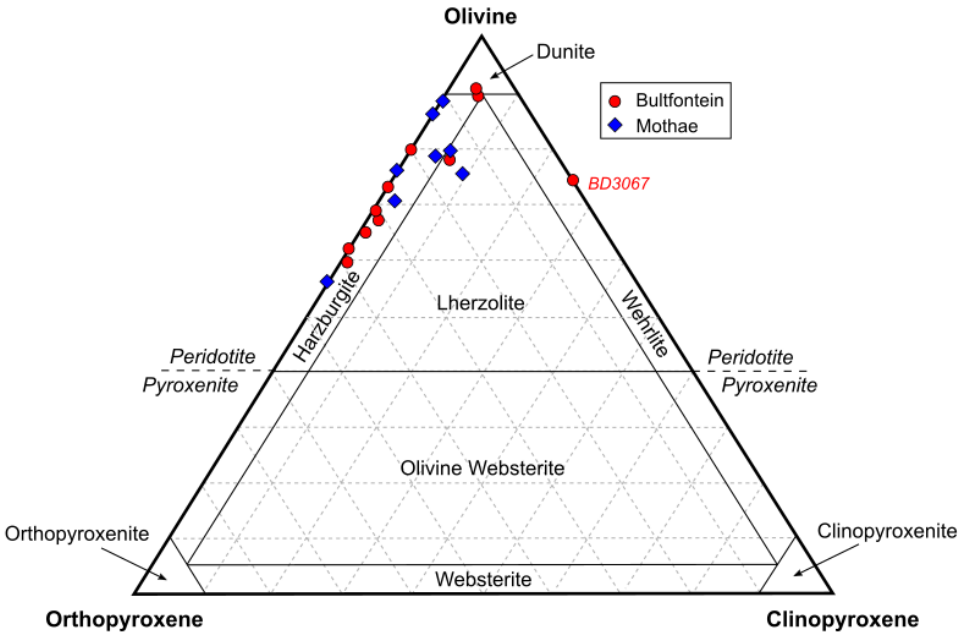

Figure 2.1 *Ternary diagram showing the classification of peridotites and pyroxenites based on IUGS nomenclature. The Bultfontein samples are marked in red circles, the Mothae samples are marked in blue diamonds.*

Mosaic porphyroclastic texture: Over 90% of olivine is present as neoblasts. Individual mineral grains are approximately equi-dimensional. The olivine neoblasts are small and have approximately polygonal shapes. Other phases (orthopyroxene, clinopyroxene, garnet) are still present as porphyroclasts.

Sheared texture: A direction of shear is evident in the shape and orientation of the minerals. Shearing is identified by elongation of minerals or visible laminations. This occurs within a porphyroclastic or mosaic porphyroclastic texture.

Granuloblastic: There is only a small range in grain size, and less than 5% porphyroclasts. A coarse rock can be granuloblastic, as can a mosaic rock if there are very few porphyroclasts.

The modal abundance of each phase was determined using ImageJ software on thin section and QEMSCAN images. Each phase was traced and the area was measured, this was then divided by the total area of the thin section to produce a modal proportion. This method is limited by the assumption that the thin section is representative of the whole mantle xenolith specimen. The lithology, mineral assemblage, modal abundances and texture of each xenolith studied from Bultfontein and Mothae are summarised in Table 2.1.

2.2 Bultfontein

Bultfontein is part of the Kimberley cluster and a well-known mantle xenolith location. It is especially notorious for the diversity of mantle lithologies. Eleven peridotite xenoliths (10-15 cm diameter) were studied from Bultfontein. These were chosen to be representative of the peridotite lithologies and textures present at this location (Figure 2.2). Two xenoliths, wehrlite (BD3067) and phlogopite-lherzolite (BD1141A), contain modal phlogopite in addition to the nominally volatile-free mantle minerals.

			Modal abundance					
Sample	**Lithology**	**Texture**	ol (%)	opx (%)	cpx (%)	gt (%)	sp (%)	phl (%)
Bultfontein						-	-	-
BD3670	Sp-Harzburgite	C	62.4	37.5	-	-	0.1	-
BD1141A	Phl-Sp-Gt-Lherzolite	Pc	68.2	13.3	5.8	0.1	2.5	10.2
BD3067	Wehrlite	Pc	68	0	23	-	-	9
BD1153	Dunite	Pc	91.8	6.1	1.8	-	0.3	-
BD1140	Gt harzburgite	Pc	80.2	5.1	4.2	10.5	-	-
BD1152	Gt harzburgite	C	63.4	29.6	1.1	5.9	-	-
BD1672	Gt harzburgite	MPc	61.2	31.5	1.3	6	-	-
BD1999	Gt harzburgite	C/Pc	55.7	36.8	1	5.4	-	1.2
BD3021	Gt harzburgite	SPc	67.4	29.7	-	2.9	-	-
BD3028	Gt harzburgite	C	67.9	25.5	-	6.6	-	-
BD3676	Gt harzburgite	C	75	18.6	-	6.4	-	-
Mothae								
BD2133	Sp-Harzburgite	C	75.6	24.3	-	-	0.1	-
BD2135	Sp-Harzburgite	C	70.5	27.1	1.8	-	0.6	-
BD2122	Gt harzburgite	Pc	85.5	12.8	0	1.6	-	-
BD2125	Gt harzburgite	C	51.6	38.8	0.2	9.2	-	0.2
BD2128	Gt harzburgite	SPc	74.5	15.9	3.5	6.1	-	-
BD2170	Gt harzburgite	MPc	86.2	11.1	-	2.7	-	-
BD2124	Gt lherzolite	C	71.7	13.4	5	9.9	-	-
BD2126	Gt lherzolite	C/Pc	66.9	13.6	8.1	11.5	-	-

Table 2.1 *Sample lithology, texture and modal abundance from Bultfontein and Mothae, where: C: coarse; Pc: porphyroclastic; MPc: mosaic porphyroclastic; SPc: sheared porphyroclastic.*

The remaining nine samples include one dunite (BD1153), spinel-harzburgite (BD3670) and seven garnet-harzburgites.

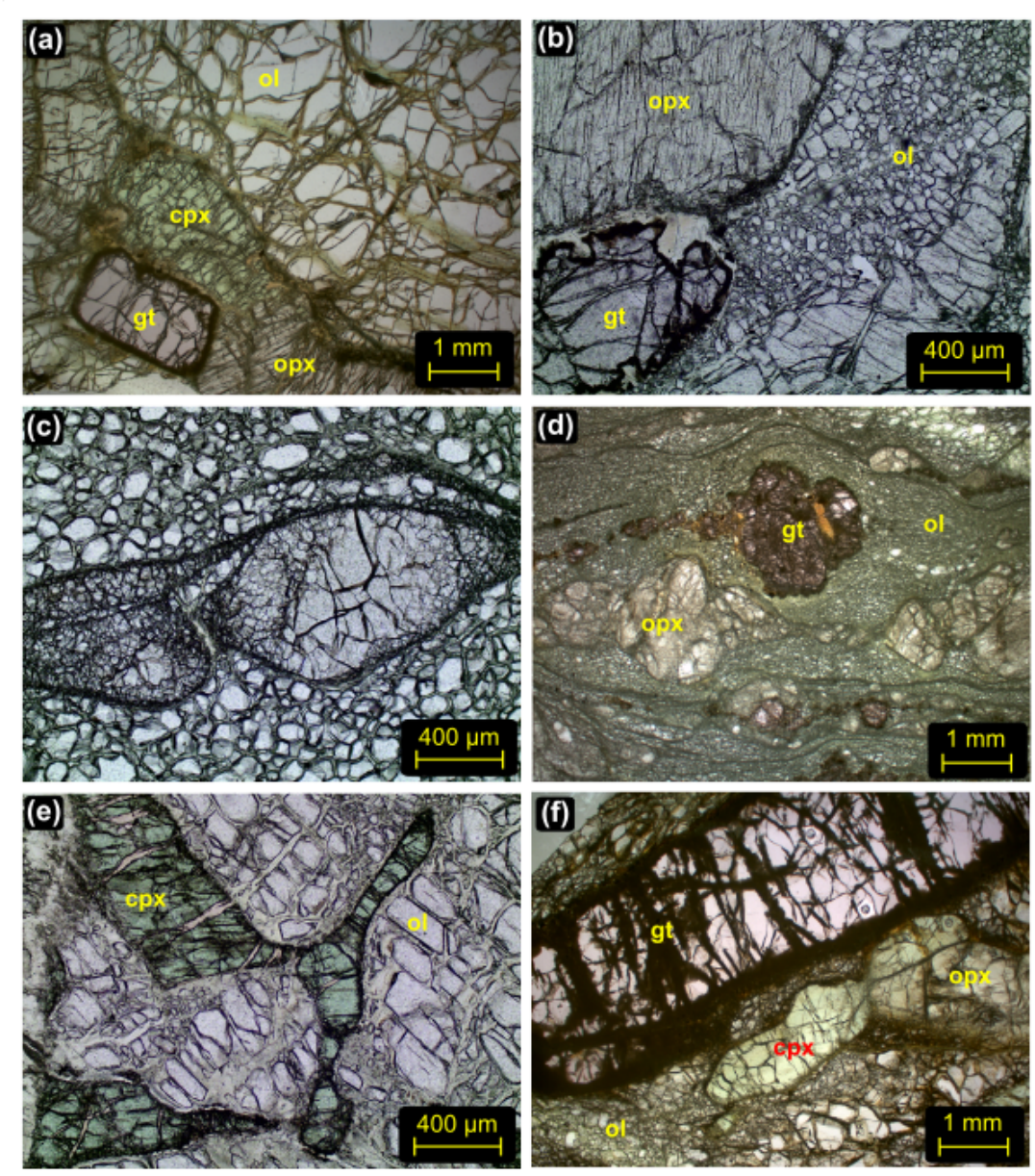

Figure 2.2 *Micro-photographs of textures in the Bultonfontein and Mothae xenoliths: (a) BD1152, coarse texture; (b) BD1672, porphyroclastic texture; (c,d) BD3021, sheared and mosaic texture; (e) BD1153, clinopyroxene following grain boundaries between olivine and orthopyroxene; (f) BD2128, Mothae sheared garnet harzburgite taken in plane polarised light, showing the elongate garnet.*

2.2.1 Spinel harzburgite

The spinel-harzburgite (BD3670) has a coarse, relatively granoblastic, texture with a grain size greater than 1 cm in diameter. It contains no clinopyroxene and only minor spinel (0.1%). The mineral assemblage is dominated by olivine (62.5%) and orthopyroxene which is present at a very high modal proportion (37.5%). The orthopyroxene is fresh, compared to the extensively serpentinised olivine, and preserves narrow exsolution lamellae of clinopyroxene.

2.2.2 Phlogopite lherzolite

One xenolith (BD1141A) contains >5% clinopyroxene and according to IUGS nomenclature is a lherzolite. The high modal abundance of phlogopite (10%) allows this to be classified further as a phlogopite-lherzolite. Olivine is the most abundant phase (68%), and there is a relative low modal proportion of orthopyroxene (13%). Garnet and spinel are both present, however their abundances are low. Garnet is particularly scarce (0.1%), and present exclusively as inclusions within large orthopyroxene grains. The presence of both garnet inclusions and isolated spinel grains could indicate an origin from close to the spinel-garnet transition zone in the lithosphere. Clinopyroxene occurs as large, bright emerald green, anhedral grains, often along grain boundaries of olivine and orthopyroxene. Additionally the clinopyroxene is commonly associated with phlogopite. The whole xenolith has a porphyroclastic texture, with a large proportion of the olivine recrystallised to neoblasts.

2.2.3 Wehrlite

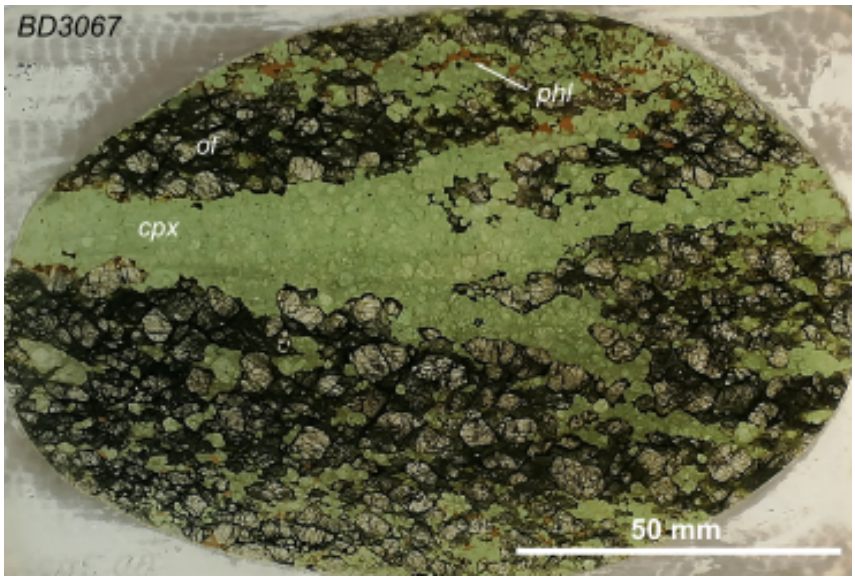

Figure 2.3 *BD3067 large thin section showing the branching clinopyroxene vein amongst olivine porphyroclasts and neoblasts, in addition to phlogopite.*

Bultfontein sample BD3067 contains abundant clinopyroxene, olivine and phlogopite i.e. is a wehrlite (Figure 2.3; Jackson & Gibson 2018). It is unique to this study because it contains a prominent vein within the hand specimen, whereas all other xenoliths have a relatively homogeneous distribution of phases throughout. Figure 2.3 shows the essentially mono-mineralogic vein of clinopyroxene with peripheral phlogopite which has crystallised where the clinopyroxene is more diffuse. The vein assemblage also includes a few large zircons and sulfides, both reaching up to 5 mm in size. There is no orthopyroxene in this xenolith and the clinopyroxene vein is surrounded by olivine. If it is assumed that all clinopyroxene has the same petrogenetic origin, then the host peridotite is a dunite (100% olivine). The olivine is extensively recrystallised but >10% exists as large porphyroclasts (up to 1 cm diameter), which produces a porphyroclastic texture. The clinopyroxene vein has a coarse texture with a relatively large crystal size. This xenolith is the subject of a case study of modal metasomatism presented in Chapter 6, and is described in greater detail there.

2.2.4 Dunite

Bultfontein xenolith BD1153 contains 92% olivine, a small amount of orthopyroxene (6%) and 2% clinopyroxene and is therefore a dunite. Garnet is absent and there is minor spinel. The olivine is extremely large (> 4 mm diameter) giving the xenolith a coarse texture. There is a small modal amount of clinopyroxene which is a very distinctive, emerald green colour and occurs along the grain boundaries of the olivine (Figure 2.2 e). The clinopyroxene in the dunite has a very similar appearance, in texture and colour, to the clinopyroxene in the phlogopite-lherzolite. These two xenoliths differ from others from Bultfontein examined in this study because the latter have much paler green clinopyroxene.

2.2.5 Garnet harzburgite

The seven Bultfontein garnet harzburgites span a wide range of mineral assemblages, proportions and textures. They can be divided into two categories: clinopyroxene-bearing and clinopyroxene-absent. The IUGS lithological definition of harzburgite requires that the rock has less than 5% clinopyroxene and in-fact all but one (BD1140) of the clinopyroxene-bearing garnet-harzburgite studied here have less than 2% clinopyroxene. The modal proportion of garnet varies from 3-11% with an average of 6%. Orthopyroxene is an abundant phase in all but two of the garnet harzburgites (BD1140 and BD3676), and the modal abundance of orthopyroxene is such that it can be used categorise the garnet-harzburgites further. Pearson *et al.* (2003) find that the average proportion of orthopyroxene in on-craton xenoliths (n = 210) is 20.8%, four of the clinopyroxene-bearing garnet-harzburgites contain significantly more orthopyroxene (30-37%) than this and are therefore considered to be orthopyroxene-rich. The orthopyroxene crystals themselves are particularly large and often form an interconnected network through the sections. All of the orthopyroxene-rich xenoliths (BD1152, BD1672, BD1999) also have very low clinopyroxene abundances (<2%). The clinopyroxene is small, pale green and irregular in shape and occurs as isolated crystals without any systematic association with another phase.

The textures of the garnet harzburgites span the whole range from coarse granoblastic to porphyroclastic and sheared mosaic porphyroclastic. The sheared garnet-harzburgite xenolith (BD3021) shows a fluidal texture with lenses of garnet and orthopyroxene grains that have been drawn out in the direction of shear. Both the orthopyroxene and garnet have both broken up in response to deformation. The olivine neoblasts (>90% of the olivine) in the garnet-harzburgites are exceptionally small and form bands around the remnant garnet and orthopyroxene. Another interesting texture between orthopyroxene and garnet can be seen in an orthopyroxene-rich garnet-harzburgite (BD1999; Figure 2.4). The large orthopyroxene crystals form an interconnected network through the xenolith and the garnet is present in smaller grains that exclusively share a grain boundary with the orthopyroxene. The cleavage in the orthopyroxene appears to be bent around the boundaries with garnet, as if the orthopyroxene has deformed to accomodate the garnet. This could be an indication of the sequence of crystallisation of the orthopyroxene and garnet.

2.3 Mothae

The Mothae kimberlite pipe is one of numerous that occur in northern Lesotho, including Letseng La Terae, Kao, Thaba Putsoa and Liqhobong. These Lesotho kimberlites are renowned for the presence of bouth

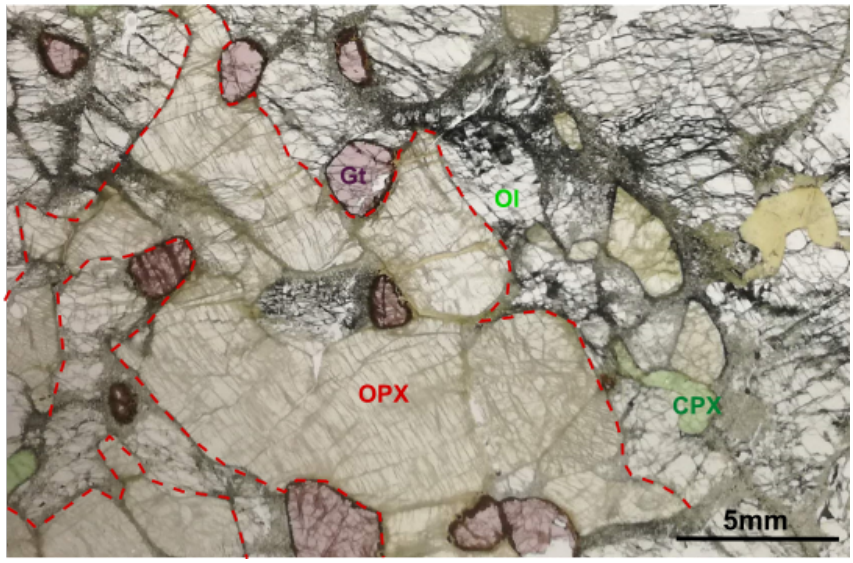

Figure 2.4 *Photograph of the thin section of sample BD1999 with the main phases labelled, including the interconnected orthopyroxene*

granular and sheared peridotites (Nixon, 1973). The Mothae subset of mantle xenolith samples (10-15 cm diameter) contains eight peridotites across three lithologies: spinel-harzburgite, garnet-harzburgite and garnet-lherzolite. None of the samples studied from Mothae contain any modal phlogopite.

2.3.1 Spinel-harzburgite

The Mothae harzburgites have a porphyroclastic texture, and include both clinopyroxene-absent and clinopyroxene-bearing xenoliths. They contain 70-75% olivine and 25-30% orthopyroxene. Spinel is a minor phase. In the clinopyroxene-bearing harzburgite (BD2135), clinopyroxene is still only a minor phase (<2%). A QEMSCAN of this thin section (Figure 2.5) highlights narrow zones of clinopyroxene, following the grain boundaries of large orthopyroxene porphyroclasts, that are not visible in thin section. This is prevalent through the section. This harzburgite has a mosaic porphyroclastic texture with very few olivine porphyroclasts but abundant large orthopyroxene porphyroclasts.

2.3.2 Garnet harzburgite

Four garnet harzburgites from Mothae were studied here. Three of these contain clinopyroxene, although in BD2170 this is only associated with the kelyphite rim of garnet and constitutes less than 0.1% of the section. The modal abundance of orthopyroxene varies in accordance with the categories identified in the Bultfontein garnet-harzburgites. One of the orthopyroxene-rich and clinopyroxene-poor samples (BD2125) contains 39% orthopyroxene which is the highest proportion in the whole Bultfontein and Mothae sample set. The other clinopyroxene-bearing garnet harzburgite (BD2128) contains slightly more clinopyroxene (4%) and less orthopyroxene (16%). It has a porphyroclastic texture and a small sense of shear is evident in the elongate nature of the garnets (10 mm long, 3 mm wide; Figure 2.2f).

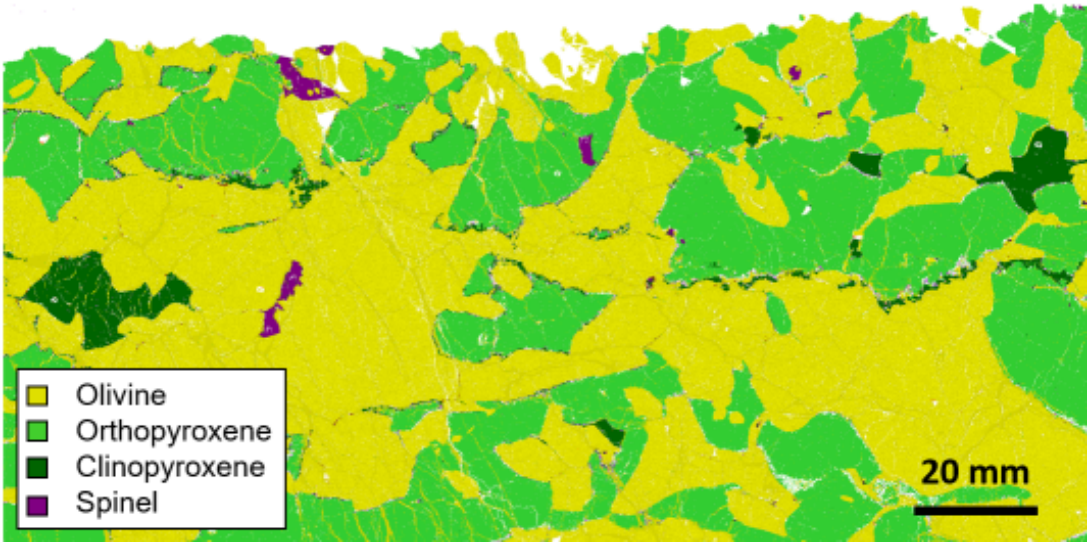

Figure 2.5 *QEMSCAN map of Mothae xenolith BD2135 (spinel-harzburgite) showing the prevalence of narrow zones of clinopyroxene along the orthopyroxene grain boundaries in addition to larger interstitial grains of clinopyroxene.*

2.3.3 Garnet lherzolite

Thin sections of only two of the Mothae xenoliths contain > 5% clinopyroxene and according to IUGS nomenclature are lherzolites. The lherzolites contain a high abundance of olivine, and much less orthopyroxene (14-16%) than the orthopyroxene-rich garnet-harzburgites. The clinopyroxene is small (<2 mm) and exists as isolated crystals. They are irregular in shape but do not obviously follow grain boundaries. In BD2126 some of the larger clinopyroxenes form equilibrated 120° grain boundaries with olivine and orthopyroxene. In both samples the garnet has kelyphite rims (spinel and pyroxene). In BD2124 the garnets are large (9 mm diameter) and less abundant than in BD2126, which has numerous small (2 mm diameter), rounded garnets. The garnet lherzolites are porphyroclastic edging towards a mosaic texture, the smaller olivine crystals are tabular. In BD2126 the olivine has recrystallised in narrow regions that are often associated with garnet.

2.4 Detailed classification of lithological groups

In addition to the IUGS lithological classification of ultramafic rocks described above, petrographic observations within each lithology have been used to subdivide these groups further. As alluded to in the previous sections, the presence/absence of clinopyroxene and the modal abundance of orthopyroxene are useful characteristics to define sub-groups. The chart in Figure 2.6 shows a more detailed method to classify the xenoliths beyond their overarching lithology. The samples are divided into garnet- or spinel-facies peridotite, by modal proportion of clinopyroxene (>5%, 5% > x > 0, none) and by the modal abundance of orthopyroxene. Using this method, groupings emerge such as the orthopyroxene-rich garnet-harzburgites (BD1152, BD1672, BD1999, BD2125). This classification will be referred to in later chapters.

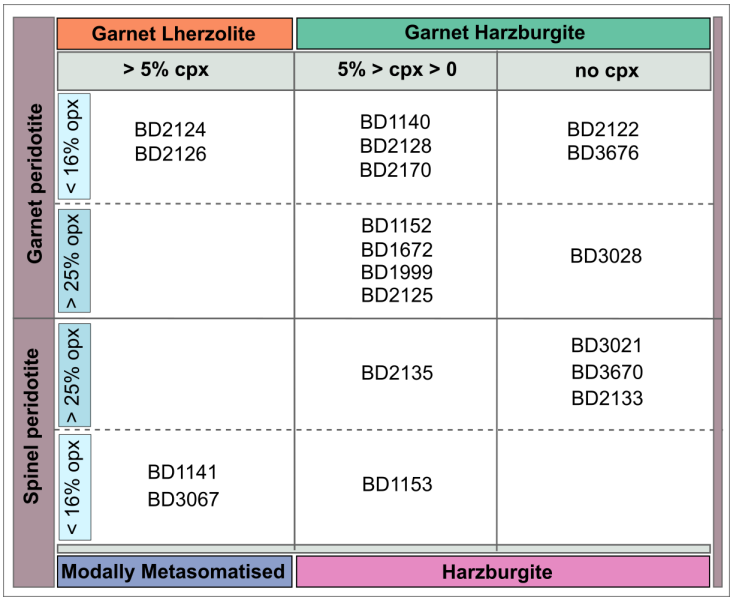

Figure 2.6 *Classification diagram, identifying groups within the sample set based on lithology, aluminous phase, modal abundance of clinopyroxene and orthopyroxene.*

2.5 Summary

The nineteen peridotite xenoliths hosted by the Bultfontein and Mothae kimberlites, represent six different lithologies and four different textures. The majority of xenoliths are garnet-harzburgites but the sample suite also includes spinel-facies peridotite, garnet-lherzolites from Mothae, and two modally metasomatised peridotite xenoliths from Bultfontein. In Chapter 3 the corresponding chemistry of the xenoliths is presented, and in later chapters the role of lithology and texture on the storage of water and fluorine will be investigated.

Chapter 3

Mineral chemistry

The major-, minor- and trace-element chemistry of all of the main phases present in each mantle xenolith studied from Bultfontein and Mothae was analysed in-situ in both thin sections, and mineral separates. All analytical techniques were implemented on the same grains to provide an internally consistent dataset. Tables 3.1 to 3.4 present the representative major-, minor- and trace-element geochemistry of the main phases in each xenolith. The full set of analyses are presented in the data tables in the appendices. These are discussed with reference to the lithological categories defined in Chapter 2 rather than by location.

3.1 Major- and minor- element chemistry

The major-element chemistry of olivine, orthopyroxene, clinopyroxene and garnet was determined using a Cameca SX100 electron probe microanalyser in the Department of Earth Sciences at the University of Cambridge. An accelerating voltage of 15 keV was used alongside a current of 10 or 20 nA. Appendix 1 describes the method in full with instrument setup and standard recovery.

3.1.1 Olivine

The olivine composition varies widely across all types of peridotite. FeO ranges from 5.2 - 11.5 wt.% and MgO 46.8 – 52.9 wt.% (Figure 3.1), such that Mg# ($MgO/(MgO+FeO)mol$) ranges from 88.1-94.7. The Mg# is generally high but fits within the scope of sub-cratonic lithospheric mantle (SCLM) olivine. The olivine in the Bultfontein wehrlite (BD3067) has a low Mg# (88.1) relative to all of the other Bultfontein and Mothae xenoliths which have Mg# greater than 90. Olivines in the spinel harzburgites and (spinel-)dunite have the highest Mg# (93.5-94.8). The olivine in the garnet-harzburgites exhibit a broad range in the concentration of all elements, there is no systematic difference between the clinopyroxene-bearing and clinopyroxene-absent harzburgites. The olivine in the garnet-lherzolites have lower Mg# (90-91) due to their high FeO (7.50 - 8.62 wt.%) contents. In all xenoliths except the Bultfontein wehrlite (BD3067), the NiO contents are towards the upper range of peridotitic olivine from the Kaapvaal craton (0.35 – 0.44 wt.%). In the Bultfontein wehrlite, the NiO contents are low (0.17 - 0.32 wt.%). Similarly, the olivine span a range of MnO contents (0.04 - 0.18 wt.%) contents that reflect the olivine composition in the SCLM. The Bultfontein wehrlite and Bultfontein phlogopite-lherzolite have the highest MnO contents (0.15-0.17 and 0.12 wt.%, respectively) but there is no systematic relationship between the MnO content and the other lithologies.

Table 3.1 *Average major and trace-element compositions of olivine in the Bultfontein and Mothae xenoliths*

Sample	BD1140	BD1141A	BD1152	BD1153	BD1672	BD1999	BD3021	BD3028	BD3670
Location	Bult	Bult	Bult	Bult	Bult	Bult	Bult	Bult	Bult
Lithology	gt-hz	phl-lz	gt-hz	dun	gt-hz	gt-hz	gt-hz	gt-hz	sp-hz
EPMA									
SiO_2	41.31	40.77	41.77	41.60	41.00	41.63	41.64	41.39	41.13
TiO_2	0.03	0.02	-	0.03	-	-	-	-	-
Al_2O_3	-	0.01	0.01	0.01	0.01		0.01	0.02	0.02
Cr_2O_3	-	-	0.03	0.04	-	-	0.01		0.05
FeO	8.01	8.75	7.94	5.21	8.01	7.32	7.30	6.13	7.83
MgO	50.53	49.36	50.73	52.93	50.24	51.12	51.26	52.18	50.70
MnO	0.10	0.12	0.09	0.10	0.11	0.10	0.10	0.09	0.11
NiO	0.41	0.39	0.45	0.36	0.44	0.45	0.42	0.37	0.39
CaO	0.02	0.02	0.02	0.04	0.03	0.03	0.04	0.02	0.05
Na_2O (wt.%)	-	-	-	-	-	-	-	-	-
Total	100.39	99.46	101.03	100.32	99.87	100.69	100.80	100.23	100.25
Mg#	91.8	91.0	91.9	94.8	91.8	92.6	92.6	93.8	92.0
LA-ICP-MS									
Li (ppm)	1.70	2.61	1.48	2.28	1.58	1.30	1.17	0.88	1.07
B	18.6	1.5	12.3	1.4	1.3	9.6	11.1	1.5	1.9
Na	25	90	44	114	64	65	86	86	45
Al	16.7	26.5	27.3	36.0	39.5	35.2	37.8	47.7	65.5
P	60	73	64	60	62	66	50	96	37
Ca	126	227	197	249	242	205	259	232	262
Sc	0.72	1.71	0.98	1.71	1.62	1.00	1.13	1.46	2.42
Ti	57	114	5	172	14	20	68	2	11
V	2.75	3.21	5.21	3.68	5.55	5.01	5.27	5.51	4.89
Cr	52	152	137	357	172	201	184	186	129
Mn	572	956	720	683	799	682	678	606	835
Co	132	146	150	121	155	142	138	127	147
Ni	3117	3126	3502	2952	3629	3402	3337	3035	3086
Cu	2.05	2.94	1.96	3.69	3.57	4.18	2.34	2.99	3.72
Zn	73	81	75	48	68	68	70	50	65
Ga	0.181	0.122	0.123	0.127	0.098	0.522	0.103	0.092	0.135
Y		0.010	0.032	0.001	0.005	-	0.063	0.002	0.004
Zr	0.160	0.297	0.113	0.167	0.112	0.098	0.285	0.070	0.024
Nb	0.676	0.362	0.472	0.109	0.176	0.518	0.177	0.488	0.010
Sn	0.427	0.400	0.392	0.374	0.415	0.416	0.325	0.382	0.391
Pb	0.013	0.014	0.015	0.006	0.000	0.013	0.018	0.007	0.017

Sample	BD3676	BD2122	BD2124	BD2125	BD2126	BD2128	BD2133	BD2135	BD2170
Location	Bult	Moth	Moth	Moth	Moth	Moth	Moth	Moth	Moth
Lithology	gt-hz	gt-hz	gt-lz	gt-hz	gt-lz	gt-lz	sp-hz	sp-hz	gt-hz
EPMA									
SiO_2	41.41	41.27	41.17	41.67	41.58	40.87	41.49	41.60	41.00
TiO_2	0.01	0.03	0.01	-	-	0.01	-	0.01	0.04
Al_2O_3	0.01	0.01	0.03	0.01	0.02	0.03	0.01	0.01	0.03
Cr_2O_3	0.05	0.03	0.04	0.04	0.01	0.04	0.04	-	0.08
FeO	6.30	9.15	8.62	6.96	7.50	7.73	6.42	5.74	8.38
MnO	0.07	0.10	0.11	0.10	0.11	0.09	0.10	0.08	0.11
MgO	51.78	49.60	49.86	51.81	50.98	50.23	52.03	52.33	50.02
NiO	0.39	0.44	0.41	0.45	0.42	0.40	0.41	0.41	0.39
CaO	0.02	0.03	0.06	0.03	0.04	0.06	0.03	0.02	0.06
Na_2O (wt.%)	-	0.01	0.05	0.02	0.02	-	-	-	0.05
Total	100.01	100.67	100.36	101.09	100.67	99.48	100.53	100.19	100.13
Mg#	93.6	90.6	91.2	93.0	92.4	92.1	93.5	94.2	91.4
LA-ICP-MS									
Li (ppm)	1.16	1.66	1.57	0.90	1.66	1.71	1.11	1.10	2.34
B	1.4	15.0	12.8	10.3	2.5	1.7	2.6	2.0	1.9
Na	78	80	137	190	75	151	42	10	287
Al	49.6	29.5	101.5	858.6	75.3	106.9	32.1	4.2	141.9
P	63	65	52	43	59	49	62	65	43
Ca	227	172	384	853	282	358	247	168	380
Sc	1.47	1.59	1.50	0.94	2.19	2.04	2.08	2.06	2.75
Ti	13	178	56	26	16	50	15	2	202
V	5.93	5.63	8.67	8.53	4.82	7.90	3.49	0.58	11.32
Cr	194	191	318	618	137	340	167	11	604
Mn	603	780	816	602	748	807	664	597	889
Co	132	140	138	102	137	146	135	123	145
Ni	3095	2991	3254	3203	3121	3259	3229	3182	3096
Cu	2.05	3.30	6.68	2.04	4.63	6.10	3.52	2.05	7.01
Zn	54	82	79	54	64	70	55	35	75
Ga	0.105	0.074	0.201	0.330	0.166	0.181	0.083	0.073	0.275
Y	0.002	0.029	-	-	0.003	0.005	0.004	0.005	0.012
Zr	0.113	0.422	-	0.184	0.012	0.083	0.350	0.004	0.146
Nb	0.310	0.103	0.044	0.238	0.014	0.089	0.784	0.002	0.027
Sn	0.384	0.370	0.417	0.336	0.411	0.396	0.433	0.393	0.402
Pb	0.017	0.024	0.011	0.182	0.003	0.015	0.003	0.007	0.015

Table 3.2 *Average major and trace-element compositions of orthopyroxene in the Bultfontein and Mothae xenoliths*

Sample	BD1140	BD1141A	BD1152	BD1153	BD1672	BD1999	BD3021	BD3028	BD3670
Location	Bult	Bult	Bult	Bult	Bult	Bult	Bult	Bult	Bult
Lithology	gt-hz	phl-lz	gt-hz	dun	gt-hz	gt-hz	gt-hz	gt-hz	sp-hz
EPMA									
SiO_2	57.92	57.80	58.21	58.60	57.84	58.55	58.15	58.66	56.28
TiO_2	0.03	0.06		0.15	0.01	0.02	0.07	0.01	
Al_2O_3	0.71	0.45	0.70	0.51	0.72	0.78	0.74	0.77	2.74
Cr_2O_3	0.22	0.39	0.26	0.49	0.28	0.33	0.36	0.30	0.88
FeO	4.92	5.23	4.81	3.31	4.81	4.19	4.43	3.66	4.35
MnO	0.02	0.15	0.02	0.06	0.13	0.02	0.12	0.05	0.11
MgO	35.57	34.86	35.20	36.28	35.31	35.78	35.59	36.28	34.37
NiO	0.08	0.12	0.11	0.11	0.12	0.11	0.12	0.11	0.08
CaO	0.24	0.43	0.45	0.47	0.51	0.42	0.49	0.36	0.94
Na_2O (wt.%)	0.06	0.15	0.08	0.17	0.11	0.12	0.12	0.12	0.03
Total	99.77	99.62	99.84	100.16	99.85	100.31	100.19	100.31	99.77
Mg#	92.8	92.2	92.9	95.1	92.9	93.8	93.5	94.6	93.4
LA-ICP-MS									
Li (ppm)	0.87	1.49	0.68	1.01	0.78	0.63	0.77	0.48	2.13
B	1.49	2.29	1.40	2.07	1.90	2.61	3.42	1.87	3.24
Na	413	1374	545	1515	814	926	1348	978	248
Al	3690	2361	3584	2643	4340	3860	4221	4200	12922
P	28	34	28	35	43	30	43	39	31
Ca	1485	2072	2620	2387	2500	2413	3052	2005	5895
Sc	2.05	3.06	2.12	2.66	2.76	2.27	3.57	2.28	12.35
Ti	182	347	19	798	71	63	385	11	2
V	35	25	42	23	44	41	44	43	68
Cr	1414	2744	1810	3377	2141	2205	2647	2091	6289
Mn	732	1050	812	704	858	711	753	673	802
Co	55	58	60	47	63	56	58	53	55
Ni	729	827	915	770	975	877	912	838	687
Cu	1.66	2.24	1.45	2.43	2.21	2.17	1.95	1.97	1.15
Zn	50	47	42	29	49	37	38	34	39
Ga	2.12	0.91	1.28	1.77	1.60	1.24	1.15	1.20	0.91
Y	0.030	0.075	0.005	0.070	0.016	0.009	0.101	0.013	0.004
Zr	0.263	0.662	0.146	0.594	0.284	0.218	1.108	0.278	0.011
Nb	0.116	0.147	0.169	0.193	0.092	0.175	0.477	0.444	0.018
Pb	0.003	0.011	0.004	0.024	0.005	0.013	0.042	0.036	0.004

Sample	BD3676	BD2122	BD2124	BD2125	BD2126	BD2128	BD2133	BD2135	BD2170
Location	Bult	Moth	Moth	Moth	Moth	Moth	Moth	Moth	Moth
Lithology	gt-hz	gt-hz	gt-lz	gt-hz	gt-lz	gt-lz	sp-hz	sp-hz	gt-hz
EPMA									
SiO_2	58.33	57.84	57.75	58.42	57.84	58.23	58.40	57.66	57.84
TiO_2	0.02	0.15	0.09	0.02	0.04	0.07	0.01	0.03	0.22
Al_2O_3	0.71	0.82	0.86	0.73	0.94	0.84	0.70	1.64	0.88
Cr_2O_3	0.36	0.45	0.31	0.32	0.25	0.33	0.36	0.51	0.50
FeO	4.45	5.44	5.07	4.15	5.49	4.30	3.94	3.75	5.12
MnO	0.02	-	0.14	0.09	0.14	0.15	0.12	0.09	0.12
MgO	35.54	35.25	34.70	36.00	34.55	35.77	36.46	36.26	34.64
NiO	0.11	0.11	0.12	0.12	0.12	0.11	0.10	0.08	0.13
CaO	0.44	0.46	0.93	0.51	1.08	0.70	0.38	0.35	0.97
Na_2O (wt.%)	0.10	0.15	0.19	0.10	0.19	0.15	0.06	0.05	0.27
Total	100.08	100.68	100.16	100.43	100.55	100.56	100.48	100.40	100.63
Mg#	93.4	92.0	92.4	93.9	91.8	93.7	94.3	94.5	92.3
LA-ICP-MS									
Li (ppm)	0.69	0.95	0.82	0.65	1.19	0.67	0.50	0.42	1.18
B	1.97	1.48	1.48	1.89	1.62	1.80	1.47	1.69	1.70
Na	802	1196	1399	797	1440	1222	382	350	2308
Al	3755	3945	4018	3870	4731	4401	3581	7862	4837
P	32	29	28	30	30	35	26	32	24
Ca	2648	2610	4183	2961	5952	4022	1854	2056	5787
Sc	2.40	4.10	3.07	2.39	3.17	2.76	3.03	8.73	4.67
Ti	71	746	433	72	207	218	65	154	1280
V	39	46	42	27	49	46	33	54	62
Cr	2448	2930	1884	2240	1684	2255	2472	3477	3737
Mn	775	927	735	735	903	737	735	685	941
Co	58	58	53	56	64	56	52	44	63
Ni	927	859	816	910	978	899	806	625	997
Cu	3.33	2.33	3.95	1.87	4.55	3.15	2.42	1.38	4.42
Zn	40	50	37	37	50	37	31	25	43
Ga	1.47	1.94	2.09	0.83	2.79	1.70	0.53	1.21	3.30
Y	0.011	0.122	0.057	0.011	0.058	0.035	0.014	0.322	0.153
Zr	0.365	1.170	0.128	0.284	0.077	0.253	0.335	0.233	0.493
Nb	0.487	0.229	0.068	0.150	0.065	0.451	0.286	0.032	0.049
Pb	0.023	0.010	0.004	0.019	-	0.032	0.010	0.027	0.007

Table 3.3 *Average major and trace-element compositions of clinopyroxene in the Bultfontein and Mothae xenoliths*

Sample	BD1140	BD1141A	BD1152	BD1153	BD1672	BD1999	BD3067	BD2124	BD2125	BD2126	BD2128	BD2135
Location	Bult	Bult	Bult	Bult	Bult	Bult	Bult	Moth	Moth	Moth	Moth	Moth
Lithology	gt-hz	phl-lz	gt-hz	dun	gt-hz	gt-hz	wehr	gt-lz	gt-hz	gt-lz	gt-lz	sp-hz
SiO_2	54.18	54.79	55.09	55.28	54.83	54.94	55.10	55.06	54.89	54.95	55.23	54.67
TiO_2	0.14	0.11	0.01	0.39	0.02	0.03	0.22	0.16	0.03	0.08	0.11	0.07
Al_2O_3	1.80	2.52	1.62	2.07	1.93	1.86	0.62	2.16	1.83	1.88	1.83	2.59
Cr_2O_3	1.54	1.78	1.43	3.88	1.55	2.15	0.93	1.20	1.62	0.92	1.24	1.66
FeO	2.50	2.38	2.14	1.63	2.32	2.07	2.89	2.84	1.84	3.15	2.82	1.19
MnO	-	0.09	0.07	0.05	0.09	0.10	0.08	0.11	0.08	0.11	0.11	0.05
MgO	16.30	15.37	17.02	16.05	16.69	16.34	16.46	17.93	16.86	18.60	18.48	16.10
NiO	-	-	-	-	0.10	0.09	-	0.09	-	0.12	0.11	-
CaO	21.62	20.29	20.82	17.81	19.87	19.83	22.01	17.80	20.30	17.78	18.00	21.61
Na_2O (wt.%)	1.08	2.13	1.35	2.86	1.64	1.84	1.18	1.59	1.51	1.29	1.40	1.46
Total	99.30	99.47	99.56	100.01	98.95	99.18	99.50	98.91	99.00	98.79	99.30	99.40
Mg#	92.1	92.0	93.4	94.6	92.8	93.4	91.0	91.8	94.2	91.3	92.1	96.0
Li (ppm)	na	na	0.52	0.90	0.63	na	na	na	na	0.94	na	0.18
Sc	23.05	21.51	13.70	25.83	16.89	15.74	47.76	15.53	13.20	12.59	12.85	53.93
Ti	652	609	38	2468	121	180	1126	960	151	458	676	388
V	377	351	274	228	301	297	351	240	190	190	196	204
Co	17.1	16.0	22.5	17.1	24.3	22.6	18.6	29.0	23.0	31.6	28.6	14.0
Ni	320	297	449	343	485	448	228	531	477	549	536	258
Sr	437	411	618	127	385	441	163	179	316	76	122	582
Y	1.95	1.80	0.22	3.23	0.34	0.27	4.32	1.72	0.43	1.20	1.19	14.21
Zr	41.1	38.3	6.7	45.4	9.4	11.0	105.5	4.3	14.4	1.8	3.1	17.5
Nb	1.15	0.74	0.50	0.73	0.45	0.59	0.43	0.59	0.39	0.26	0.30	0.16
La	15.16	14.45	4.71	2.03	4.27	4.55	2.51	2.41	4.55	1.77	1.32	88.74
Ce	54.6	52.5	27.0	8.1	19.9	22.2	12.0	10.4	20.8	6.0	5.3	252.0
Pr	7.14	6.83	5.35	1.37	3.44	4.08	2.17	1.62	3.63	0.83	0.89	30.27
Nd	26.66	25.61	23.94	7.48	17.48	22.01	11.29	7.57	16.83	3.74	4.64	113.45
Sm	3.60	3.22	2.36	2.06	3.06	3.22	2.99	1.37	2.86	0.83	1.18	15.87
Eu	0.782	0.733	0.361	0.654	0.612	0.560	0.946	0.397	0.726	0.239	0.334	3.510
Gd	1.72	1.66	0.68	1.55	0.98	0.79	2.45	0.90	1.26	0.58	0.84	9.01
Tb	0.168	0.162	0.034	0.191	0.062	0.043	0.299	0.099	0.094	0.067	0.079	0.852
Dy	0.654	0.611	0.082	1.090	0.128	0.087	1.431	0.480	0.278	0.316	0.364	3.640
Ho	0.081	0.080	0.008	0.138	0.016	0.012	0.205	0.073	0.023	0.053	0.046	0.562
Er	0.153	0.163	0.027	0.294	0.034	0.027	0.379	0.157	0.029	0.116	0.109	1.348
Tm	0.015	0.018	0.002	0.026	0.003	0.002	0.035	0.022	0.006	0.012	0.010	0.158
Yb	0.080	0.078	0.012	0.144	0.018	0.020	0.182	0.099	0.024	0.078	0.084	0.900
Lu	0.008	0.006	0.002	0.014	0.004	0.003	0.018	0.012	0.002	0.009	0.010	0.113
Hf	1.680	1.583	0.432	2.777	0.482	0.620	6.694	0.276	0.844	0.107	0.190	0.502
Ta	0.095	0.067	0.033	0.042	0.039	0.043	0.026	0.044	0.040	0.015	0.015	0.014
Pb	4.260	3.063	1.071	0.273	0.823	1.289	1.122	0.793	0.720	0.252	0.213	9.503

Table 3.4 *Average major and trace-element compositions of garnet in the Bultfontein and Mothae xenoliths*

Sample	BD1140	BD1152	BD1672	BD1999	BD3021	BD3028	BD3676	BD2124	BD2125	BD2126	BD2128	BD2170	BD2170
Location	Bult	Bult	Bult	Bult	Bult	Bult	Bult	Moth	Moth	Moth	Moth	Moth	Moth
Lithology	gt hz	gt hz	gt hz	gt hz	gt hz	gt hz	sp hz	gt lz	gt hz	gt lz	gt lz	gt hz	gt hz
SiO_2	42.28	42.28	42.37	42.21	42.36	42.30	42.90	41.81	42.20	42.40	42.85	41.79	
TiO_2	0.05		0.05	0.06	0.21	0.22	0.04	0.53	0.06	0.22	0.38	1.09	
Al_2O_3	21.91	20.46	20.33	19.12	19.39	19.39	21.36	19.52	19.59	20.80	19.74	16.26	
Cr_2O_3	2.27	4.19	4.33	5.90	5.40	5.50	3.51	4.31	5.55	3.18	4.48	7.96	
FeO	8.37	7.26	7.38	6.78	6.71	6.58	5.78	6.88	6.04	7.38	6.50	6.72	
MnO	0.42	0.34	0.37	0.36	0.32	0.30	0.26	0.30	0.30	0.27	0.29	0.32	
MgO	20.69	20.89	21.02	20.82	21.39	21.37	23.34	21.13	20.60	21.08	21.66	20.37	
CaO	4.68	5.35	5.08	5.53	5.03	5.15	3.53	4.64	5.41	4.73	5.12	5.96	
Na_2O (wt.%)								0.08	0.04	0.06	0.08	0.11	
Total	100.67	100.77	100.94	100.78	100.82	100.87	100.72	99.21	99.80	100.11	101.11	100.58	
pyrope	0.71	0.72	0.72	0.72	0.74	0.74	0.80	0.74	0.73	0.73	0.74	0.71	
grossular	0.12	0.13	0.13	0.14	0.12	0.13	0.09	0.12	0.14	0.12	0.13	0.15	
almandine	0.16	0.14	0.14	0.13	0.13	0.13	0.11	0.14	0.12	0.14	0.13	0.13	
spessartine	0.01	0.01	0.01	0.01	0.01	0.01	0.01	0.01	0.01	0.01	0.01	0.01	
Sc	87	102	108	114	107	79	81	85	79	80	85	101	141
Ti	290	86	314	399	1664	36	285	2739	337	1202	2098	5560	3405
V	130	222	226	232	216	177	189	240	162	220	230	292	360
Ni	22	48	59	56	58	50	52	72	38	72	69	81	77
Rb	-	0.880	-	-	2.327	-	-	0.008	-	0.007	0.014	0.023	0.092
Sr	0.96	0.85	0.96	0.94	9.09	1.53	0.84	0.43	0.57	0.33	0.45	1.65	0.87
Y	11.15	3.08	2.59	2.92	21.53	1.10	2.62	14.03	2.68	13.53	14.06	14.54	1.59
Zr	3.17	34.09	39.58	49.49	110.87	19.00	50.22	35.74	57.73	22.87	40.50	72.45	53.46
Nb	0.165	0.433	0.499	0.702	0.728	1.294	0.536	0.680	0.622	0.504	0.388	0.428	0.438
Ba	0.188	0.025	0.068	0.186	3.124	-	-	0.020	0.796	0.045	0.068		2.210
La	0.047	0.035	0.028	0.052	0.457	0.088	0.037	0.032	0.062	0.031	0.026	0.052	0.067
Ce	0.248	0.761	0.462	0.721	1.266	1.482	0.588	0.423	0.684	0.307	0.302	0.692	0.631
Pr	0.062	0.387	0.212	0.319	0.186	0.764	0.242	0.148	0.361	0.092	0.106	0.213	0.234
Nd	0.41	4.39	2.55	4.13	1.74	7.87	2.80	1.27	3.33	0.88	1.24	2.03	2.36
Sm	0.194	1.769	1.867	2.486	1.818	2.587	1.432	0.915	1.563	0.541	1.184	1.310	0.961
Eu	0.103	0.518	0.656	0.741	0.973	0.698	0.532	0.365	0.467	0.194	0.388	0.497	0.226
Gd	0.501	1.337	1.679	1.699	3.407	1.469	1.366	1.371	1.676	1.088	1.746	1.890	0.776
Tb	0.163	0.161	0.155	0.163	0.654	0.110	0.179	0.292	0.198	0.231	0.327	0.386	0.068
Dy	1.699	0.829	0.674	0.652	4.537	0.319	0.726	2.050	0.852	1.910	2.190	2.180	0.333
Ho	0.509	0.146	0.102	0.107	0.853	0.040	0.098	0.476	0.099	0.460	0.458	0.443	0.066
Er	1.813	0.396	0.279	0.328	2.001	0.169	0.289	1.518	0.186	1.433	1.305	1.074	0.143
Tm	0.323	0.066	0.046	0.057	0.236	0.042	0.058	0.225	0.024	0.245	0.221	0.165	0.027
Yb	2.542	0.563	0.452	0.496	1.382	0.471	0.604	1.801	0.172	1.800	1.509	1.008	0.300
Lu	0.422	0.103	0.085	0.093	0.184	0.106	0.117	0.245	0.040	0.287	0.224	0.149	0.067
Hf	0.083	0.878	0.599	0.840	1.843	0.427	0.886	0.702	0.895	0.486	0.912	1.470	1.090
Ta	0.005	0.029	0.034	0.045	0.039	0.100	0.051	0.092	0.050	0.049	0.034	0.044	0.021
Pb	0.063	0.061	0.046	0.034	0.082	-	0.036	-	0.057	0.068	0.039	-	-
Th	0.014	0.006	0.010	0.010	0.059	0.024	0.010	0.011	0.031	0.021	0.012	0.019	-
U	0.053	0.135	0.043	0.035	0.034	0.106	0.024	0.017	0.050	0.022	0.013	0.017	0.017

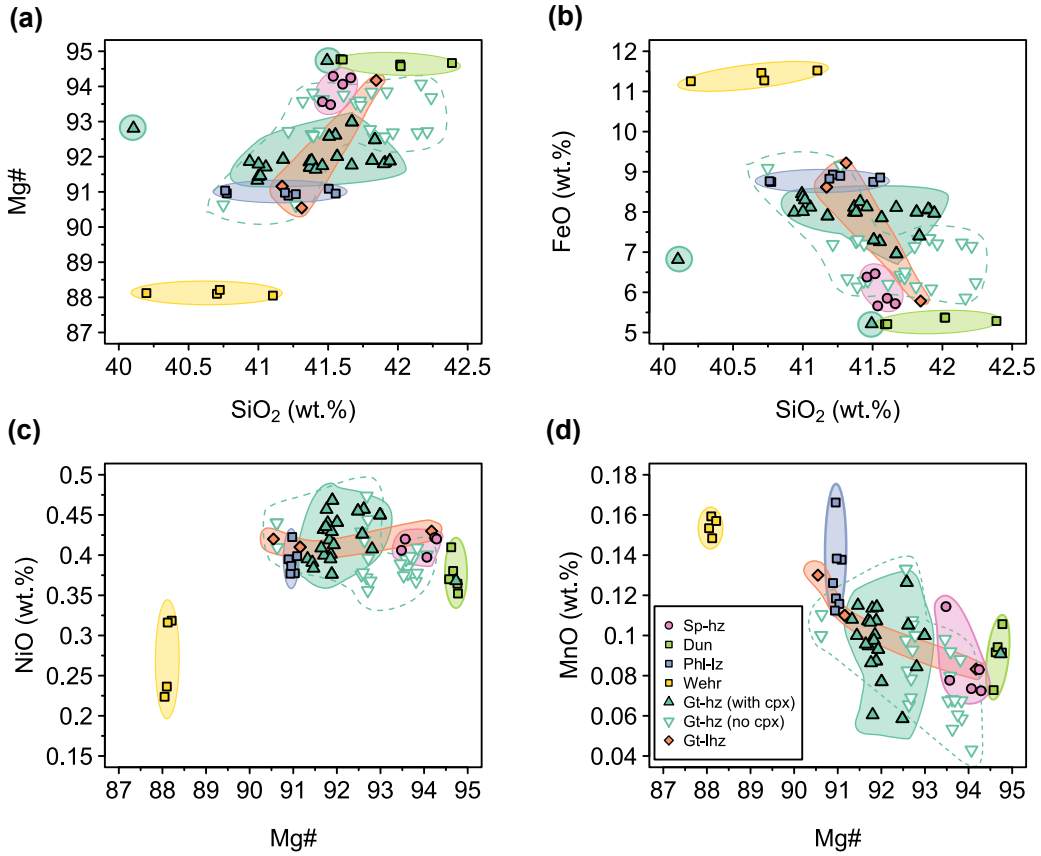

Figure 3.1 *Olivine major-element compositions in the Bultfontein and Mothae xenoliths divided by lithology*

3.1.2 Orthopyroxene

All orthopyroxenes in this study are enstatite, as demonstrated in the pyroxene ternary diagram in Figure 3.2. The variation in orthopyroxene FeO concentration (3.2 – 5.8 wt.%) is greater than that in MgO (34.1 – 36.6 wt.%). The Mg# of orthopyroxene (91.5 – 95.1) varies in correspondence with the co-existing olivine. There is a large range in the concentrations of minor elements for example Na_2O (0.03 – 0.29 wt.%), TiO_2 (0.01 – 0.23 wt.%), Cr_2O_3 (0.21 – 0.89 wt.%) and Al_2O_3 (0.5 – 2.8 wt.%). The CaO content of the orthopyroxene has a relatively bimodal distribution with no samples between 0.6-0.8 wt.% CaO (Figure 3.3).

The orthopyroxene compositions show a greater variation between the different xenolith lithologies than olivine. Orthopyroxene in the spinel harzburgites show a large variation in FeO (3.7 - 4.5 wt.%), Mg # (92.4 - 94.6), NiO (0.07 - 0.13 wt.%) and CaO (0.2 - 1.0 wt.%) relative to other lithologies (Figure 3.3). They extend to a more SiO_2-poor and Al_2O_3- and Al_2O_3-rich compoisitions compared to garnet-bearing peridotites. Again, orthopyroxene in the garnet-harzburgites show a wide range in concentration of all major-elements except Al_2O_3, and there is no systematic difference between the clinopyroxene-bearing and clinopyroxene-absent harzburgites. Orthopyroxene in the garnet-lherzolites plot towards the upper limit of MgO, FeO, CaO, NiO and Na_2O concentration, but have some of the lowest Cr_2O_3 contents (0.23 - 0.32 wt.%). There are three samples that have orthopyroxene with slightly anomalous compositions relative to the rest of the suite: (i) BD3670 (clinopyroxene-absent spinel-harzburgite) has high Al_2O_3 (2.8 wt.%) and Cr_2O_3 (0.9 wt.%) and low Na_2O (b.d.l) compared to the others; (ii) orthopyroxene in BD2170

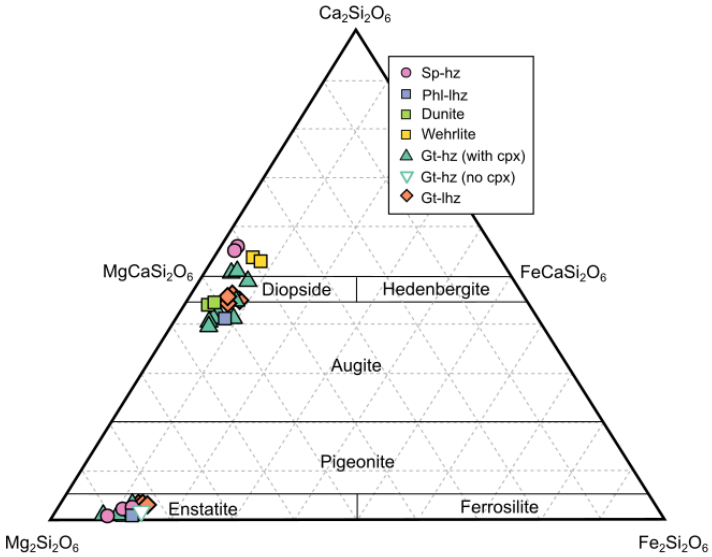

Figure 3.2 *Pyroxene ternary diagram showing the composition of both the clinopyroxene and orthopyroxene in the different lithologies present in the mantle peridotite xenoliths from Bultfontein and Mothae.*

(clinopyroxene-absent garnet-harzburgite) has much higher than average Na_2O (0.27 wt.%) and TiO_2 (0.22 wt.%) concentrations; and (iii) BD2135 (clinopyroxene-bearing spinel-harzburgite) has high Al_2O_3 (1.6 wt.%) concentrations. Orthopyroxene in the garnet-harzburgites define individual trends within the dataset, such as a positive correlation between Cr_2O_3 and Na_2O and Al_2O_3.

3.1.3 Clinopyroxene

The clinopyroxenes in the mantle xenoliths studied from Bultfontein and Mothae show only a small variation in their major-element composition (Figure 3.2). Clinopyroxene in the spinel-harzburgite and wehrlite have the most calcium rich composition (CaO = 22 wt.%; Figure 3.2). All other samples plot around the diopside-augite boundary. Similar variation in the Mg# is evident in the clinopyroxenes as the orthopyroxene and olivine. The clinopyroxene Mg# varies from 90.8 - 95.8, FeO from 1.2 – 3.2 wt.% and MgO 15.4 – 18.5 wt.% (Figure 3.4). The largest variation is observed in Al_2O_3 (0.50 – 2.60 wt.%), CaO (17.7 - 22.7 wt.%), TiO_2 (0.02 – 0.23 wt. %) and Cr_2O_3 (0.79 – 2.22 wt.%).

There is a strong positive correlation between Cr_2O_3 and Na_2O in the Bultfontein and Mothae clinopyroxenes (Figure 3.4e). Those in the garnet-lherzolites have the lowest Na and Cr concentrations while the phlogopite-lherzolite and dunite have the highest Na and Cr contents. The only anomalous clinopyroxene composition is the low Al_2O_3 in the Bultfontein wehrlite (BD3067; Figure 3.4f), otherwise the major-element concentrations of all other clinopyroxenes fall within a fairly continuous spectrum. Most of the clinopyroxenes in the Bultfontein and Mothae xenoliths are Cr-diopsides, defined by the statistical analysis of Stephens & Dawson (1977; Figure 3.5). The TiO_2 concentrations of all of the clinopyroxene (0 - 0.45 wt.%) fall within the range of Cr-diopside, however the Cr_2O_3 contents extend up to 4 wt.% in the dunite (BD1153) and gives them a bright emerald green colour in thin section (Figure 2.2e,f).

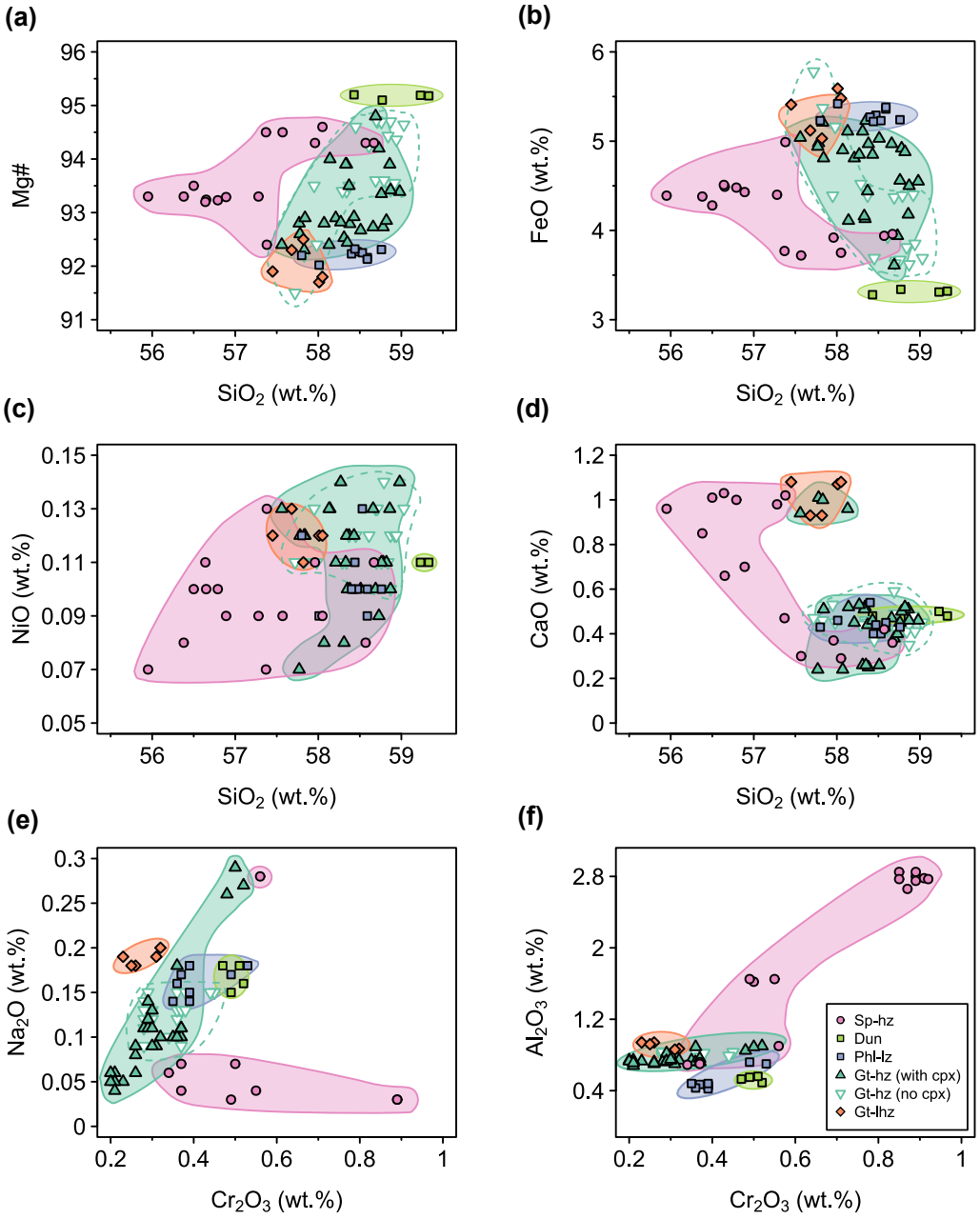

Figure 3.3 *Orthopyroxene major-element composition split by lithology*

3.1.4 Garnet

The garnet in all of the Bultfontein and Mothae xenoliths is Mg-rich and so plots close to the pyrope endmember on the garnet ternary diagram (Figure 3.6). The grossular component is < 15% and the almandine + spessartine component is also < 15% but marginally greater than the grossular component in all of the xenoliths. The Al_2O_3 content of the pyrope is fairly uniform (19 – 22 wt.%), as is the SiO_2 content (42-43 wt.%). There are, however, systematic differences in compositions of the garnet from clinopyroxene-bearing-harzburgites and -lherzolites, and the clinopyroxene-absent harzburgites. In the absence of clinopyroxene the garnets have higher MgO (23 wt. % compared to 21 wt.%), slightly lower

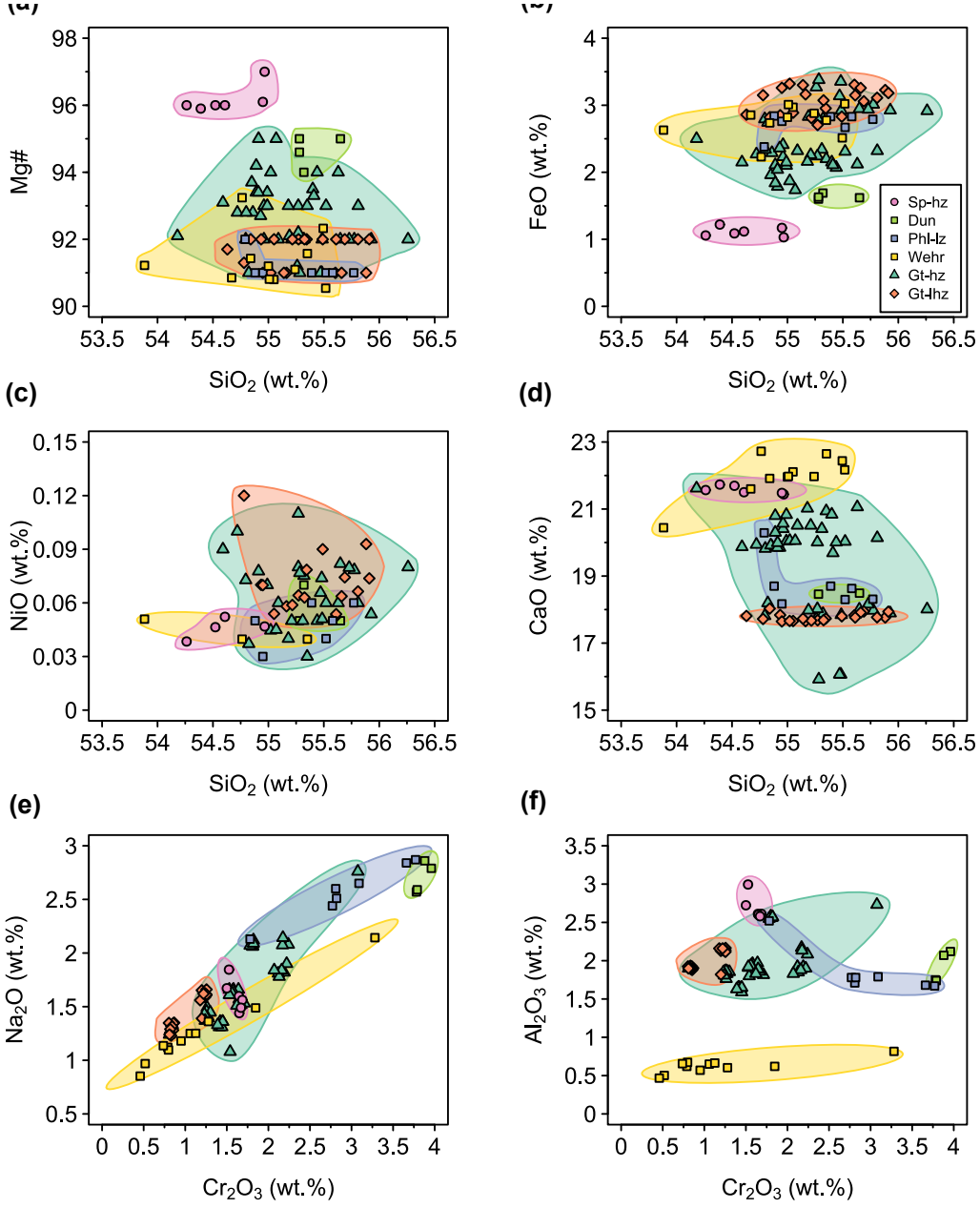

Figure 3.4 *Clinopyroxene major-element composition defined by lithology*

Cr_2O_3 on average (3.5 wt.% compared to a range of 2.3-8.0 wt.% and average 4.8 wt. %) and lower CaO (3.5 wt.% compared to 5.2 wt.%) contents.

There are strong positive correlations between SiO_2 and MgO, and between Cr_2O_3 and CaO in the garnet-harzburgites (Figure 3.7). The commonly used plot of CaO vs. Cr_2O_3 for mantle garnets has been split into regions of harzburgite (Hz), lherzolite (Lz) and wehrlite based on the definitions of Dawson & Stephens (1976) and Grütter *et al.* (2006). Most of the garnets from Bultfontein and Mothae peridotite xenoliths plot within the lherzolite field despite their modal mineralogy defining them as harzburgites, this is because they are in equilibrium with a small amount of clinopyroxene.

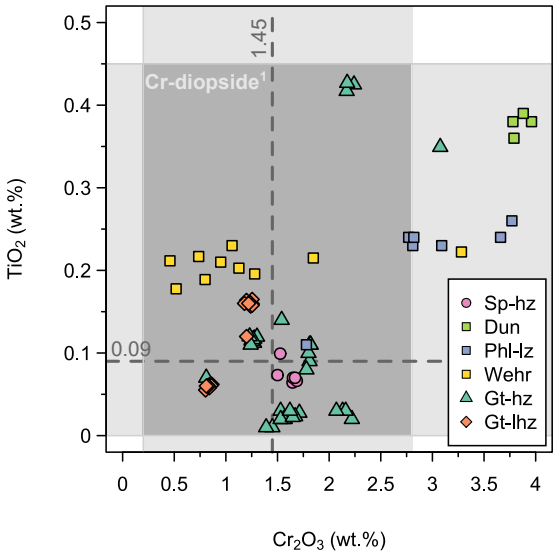

Figure 3.5 *Clinopyroxene Cr_2O_3 vs. TiO_2 composition defined by lithology and compared to the range of Cr_2O_3 and TiO_2 in Cr-diopside (Stephens & Dawson 1977). The dashed lines are the mean average Cr_2O_3 at 1.45 wt.% and TiO_2 at 0.09 wt.% within the range shown by the grey shaded regions.*

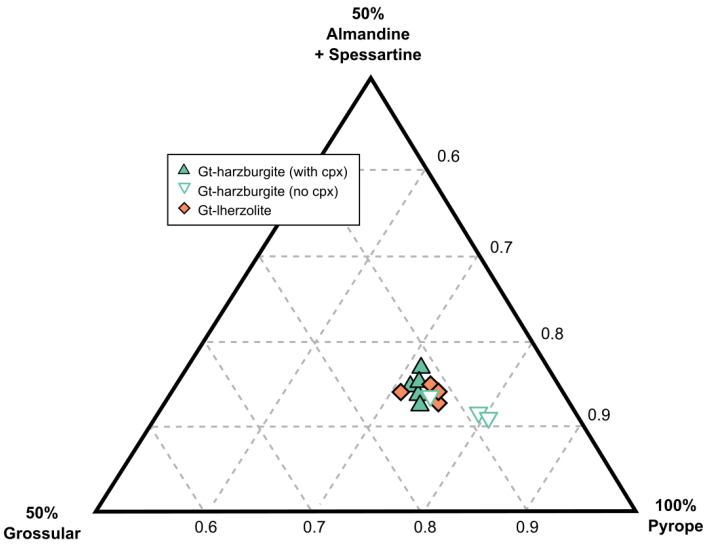

Figure 3.6 *Garnet ternary diagram showing the composition of garnet in all garnet-bearing lithologies in the Bultfontein and Mothae xenoliths.*

3.1.5 Phlogopite

Three xenoliths contain phlogopite, there is abundant phlogopite in the phlogopite-lherzolite (BD1141A, Bultfontein) and wehrlite (BD3067, Bultfontein) and very minor phlogopite in one of the orthopyroxene-rich garnet harzburgites (BD2125, Mothae). There is a wide degree of variation in phlogopite composition between all three xenoliths, with a wide range in Mg# from 91 to 96, TiO_2 from 0.1 to 1 wt.% and F content from 0.3 to 0.8 wt.% (Figure 3.8). There are two populations of phlogopite in the wehrlite sample, BD3067, which are highlighted by yellow ellipses' in Figure 3.8. The majority of phlogopite grains analysed from BD3067 have low Mg# (91-92), high KO, Al_2O_3, and F; whereas the minority

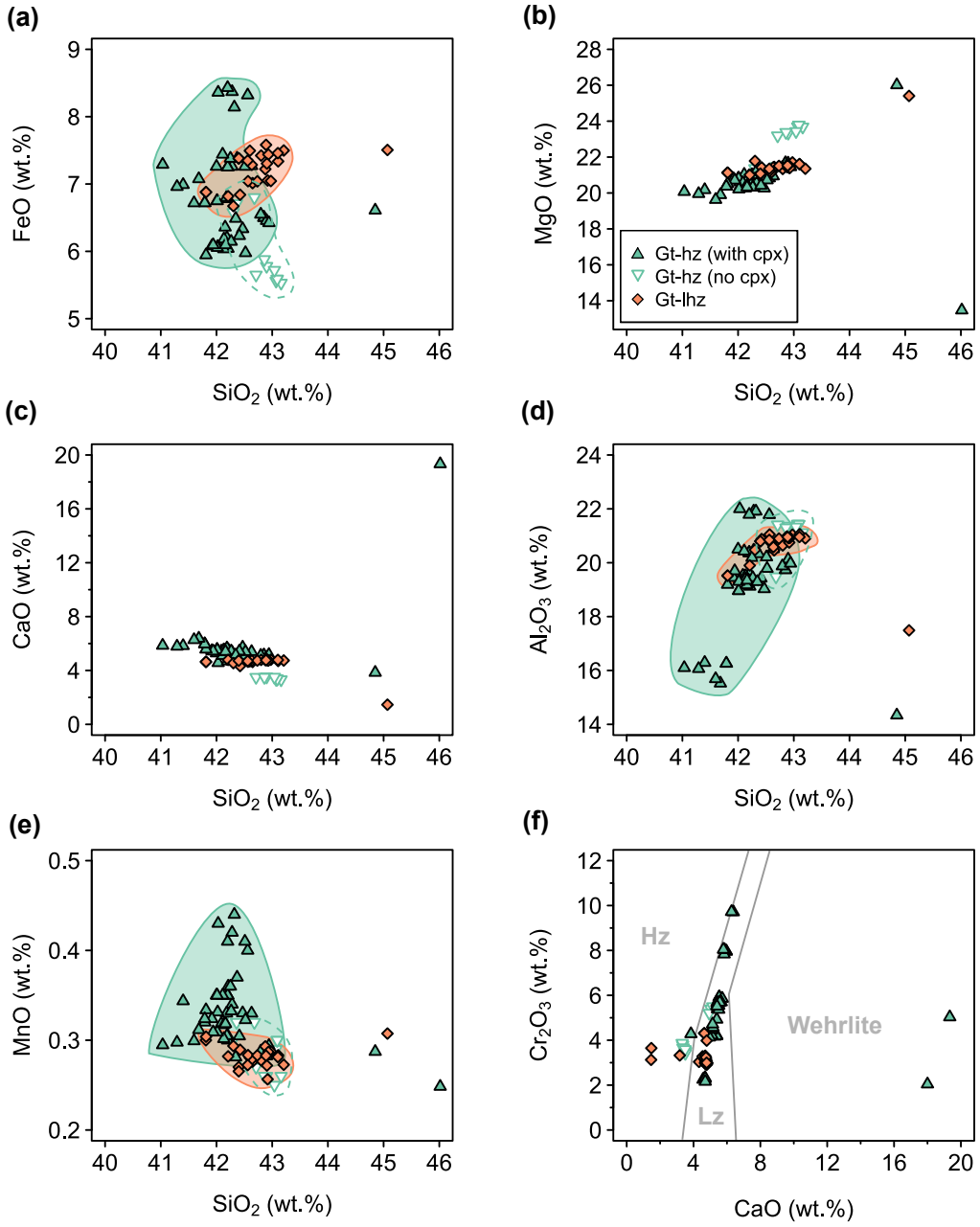

Figure 3.7 *Variations in garnet major-element compositions of garnets in the different lithologies present in the Bultfontein and Mothae xenolith suites. In (f) Hz: Harzburgite; Lz: lherzolite*

have very high Mg# (95-96) and much lower KO, Al_2O_3 and F concentrations. The phlogopite from BD1141A have an intermediate Mg# relative to the two populations in BD3067 but similar KO, Al_2O_3 and F concentrations to the lower Mg# phlogopite in BD3067. They have higher TiO_2, Na_2O and Cr_2O_3 concentrations, however. The phlogopite in BD1141A is much more uniform in composition than that in BD3067, and also homogeneous; core and rim analyses showed no variation in BD1141A. Only one phlogopite grain was able to be analysed from BD2125 (the point represents the average of 6 analyses on said grain). It has high Mg# similar to the second population in BD3067, but much higher KO, Al_2O_3 and Cr_2O_3 contents.

Sample	BD1141A	BD3067a	BD3067b	BD2125
Location	Bult	Bult	Bult	Moth
Lithology	phl-lz	wehr	wehr	gt-hz
SiO_2 (wt.%)	41.67	42.15	41.93	41.69
TiO_2	0.99	0.48	0.80	0.12
Al_2O_3	11.34	7.57	11.95	12.51
Cr_2O_3	0.48	0.10	0.18	0.84
FeO	3.19	2.65	4.15	2.44
MgO	24.78	31.46	25.13	25.20
MnO	0.02	0.07	0.06	-
NiO	-	0.06	0.11	-
CaO	0.06	0.10	0.05	0.06
Na_2O	0.21	0.14	0.13	0.07
K_2O	10.79	6.40	10.69	10.79
F	0.47	0.32	0.60	0.49
Cl	0.04	-	-	0.17
Total	94.01	91.50	95.70	94.42

Table 3.5 *Average major-element compositions of phlogopite in the Bultfontein and Mothae xenoliths*

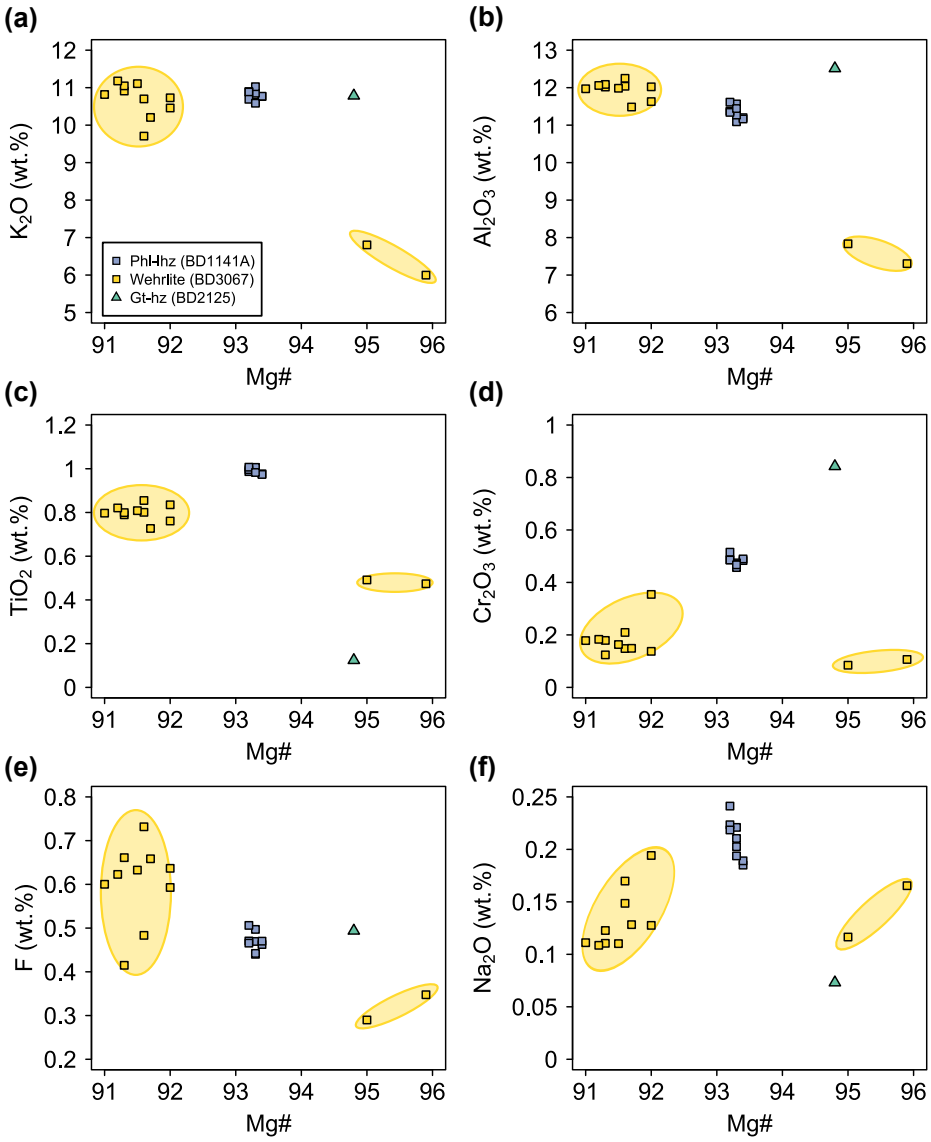

Figure 3.8 *Variations in phlogopite major-element compositions of garnets in the different lithologies present in the three phlogopite-bearing xenoliths from Bultfontein (BD1141A, BD3067) and Mothae (BD2125)*

3.2 Trace-element chemistry

The trace-element concentrations in olivine, orthopyroxene, clinopyroxene and garnet were analysed using an ESI UP193UC laser coupled to a Nexion 350D quadrupole inductively coupled mass spectrometer (LA-ICP-MS) in the Department of Earth Sciences at the University of Cambridge. A new San Carlos olivine internal standard was characterised during this research. The analytical setup, reproducibility and precision, and full list of elements analysed in each mineral are presented in Appendix 1. The rare earth elements (REE) were analysed in clinopyroxene and garnet but not in olivine or orthopyroxene.

3.2.1 Olivine

The trace-elements analysed in olivine are highly variable across the sample suite (Figure 3.9). There is an extremely large range in Al concentration (3.6 – 152 ppm) and Na concentration (1.5 – 358 ppm). The first-row transition metals show the most variation with Ti (0.6 – 183 ppm) and Cr (10 – 542 ppm) but V (0.53 – 11.3 ppm) and Cu (1.8 - 7.3 ppm) do not show such a large range in the xenolith suites. Li contents in olivine reach up to 3 ppm, and the high field strength element concentrations are low (Nb < 0.8 ppm; Zr < 0.36).

3.2.2 Orthopyroxene

The same elements were analysed in olivine and orthopyroxene. Orthopyroxene contains more Na than olivine (223 – 2471 ppm) but similar Li contents (0.4 – 2.4 ppm; Figure 3.10). There is more V in the orthopyroxene (22 – 70 ppm) but less Cu (1.1 – 4.6 ppm). Nb is similar to olivine (<0.82 ppm) but the Zr content is much higher (up to 1.61 ppm).

3.2.3 Clinopyroxene

The trace-element composition of clinopyroxenes in the Bultfontein and Mothae xenolith suites varies considerably and systematically. Most exhibit enrichment in the light rare earth elements (LREE) relative to primitive mantle (e.g. La, Ce; Figure 3.11). The most enriched clinopyroxene is in sample BD2135 (spinel-harzburgite), which has a La concentration of 74 ppm, followed by the clinopyroxene in the orthopyroxene-poor garnet-harzburgite (BD1140) and phlogopite-lherzolite (BD1141A) that both contain 15 ppm La. The rest of the xenoliths contain clinopyroxene with La in the range 1.3 to 5 ppm. The clinopyroxenes all have relatively high Sr concentrations (up to 590 ppm) and generally low Nb (< 1.2 ppm) and Ta (< 0.1 ppm).

A systematic variation is evident in the primitive-mantle-normalised incompatible trace-element patterns (Figure 3.11). Somewhat surprisingly, the least enriched samples are the garnet-lherzolites (Figure 3.11d) with less than 10 times primitive mantle enrichment in all elements. Some of the clinopyroxene in the garnet-harzburgites (Figure 3.11c) show an interesting pattern in the middle to heavy rare earth elements (MREE, HREE), where the HREE appear to plateau. This produces an unusual sinusoidal signature more commonly observed in garnet rather than clinopyroxenes. The HREE in the clinopyroxene in the garnet-harzburgites are the most depleted, more so than the clinopyroxene in the garnet-lherzolites.

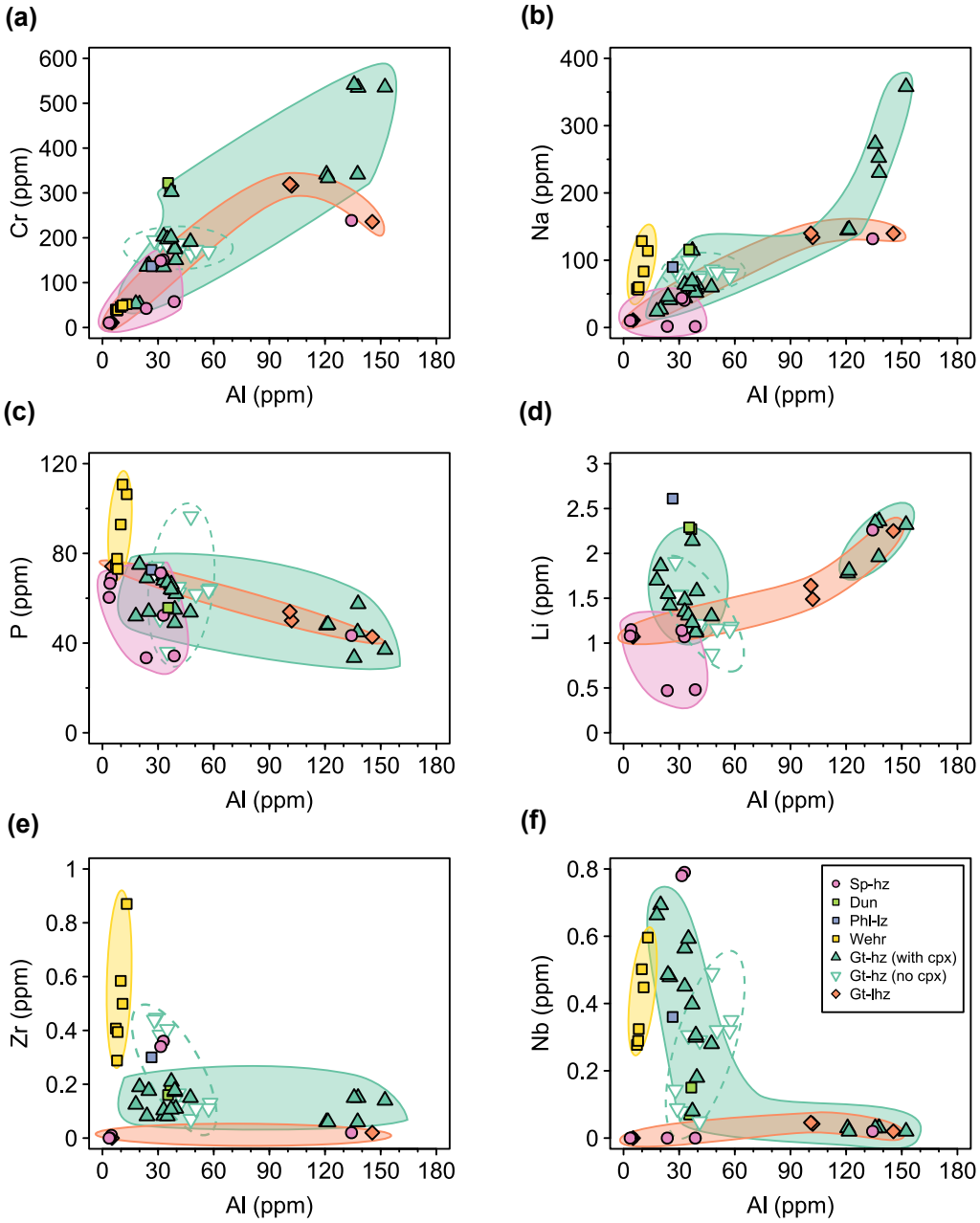

Figure 3.9 *Selected olivine trace-elements plotted against Al.*

The two phlogopite-bearing samples (BD1141A, BD3067) are grouped in Figure 3.11b. These have a very distinct clinopyroxene trace-element pattern when compared to the other lithologies, primarily due to the lack of a Zr anomaly and a positive Hf anomaly. This same pattern is also observed in the dunite, BD1153 (Figure 3.11a). All of the clinopyroxene in the Bultfontein and Mothae xenolith suites display negative anomalies for the high field strength elements (HFSE), i.e. Nb, Ta, Ti.

3.2.4 Garnet

Figure 3.12 shows the variation in chondrite normalised garnet REE signature within each lithology. The garnets in the garnet-lherzolites have a relatively conventional REE pattern in which the MREE and HREE

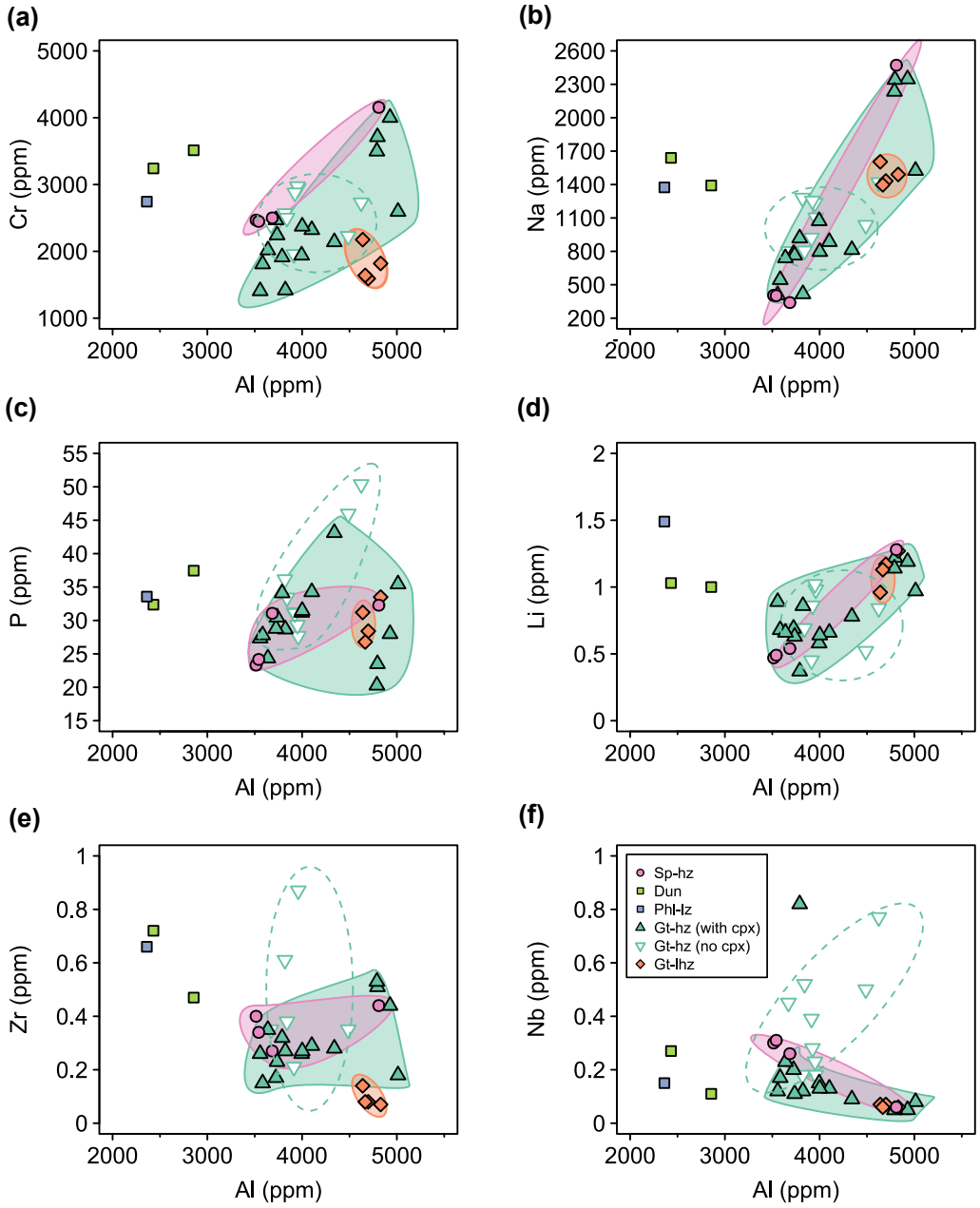

Figure 3.10 *Selected orthopyroxene trace-elements plotted against Al.*

are greater than the LREE, and plateau in the HREE. This reflects fact that the HREE are much more compatible in garnet than the LREE. Within the garnet-harzburgites five samples have garnets with a sinusoidal REE pattern with a relative depletion in the MREE and HREE. BD1140 (orthopyroxene-poor garnet-harzburgite) has a positive gradient in the REE signature, the level of enrichment increases with decreasing ionic radii so that the HREE have the highest concentrations. BD3021 (sheared garnet-harzburgite) has an unusual signature, the garnet is enriched in La and Ce, which are both incompatible elements in garnet. Finally, BD2170 is the only sample in which garnet displays a variety of normalised REE patterns; of the five crystals analysed two have a pattern similar to the garnet-lherzolites, two have a sinusoidal signature and one is intermediate (Figure 3.12c).

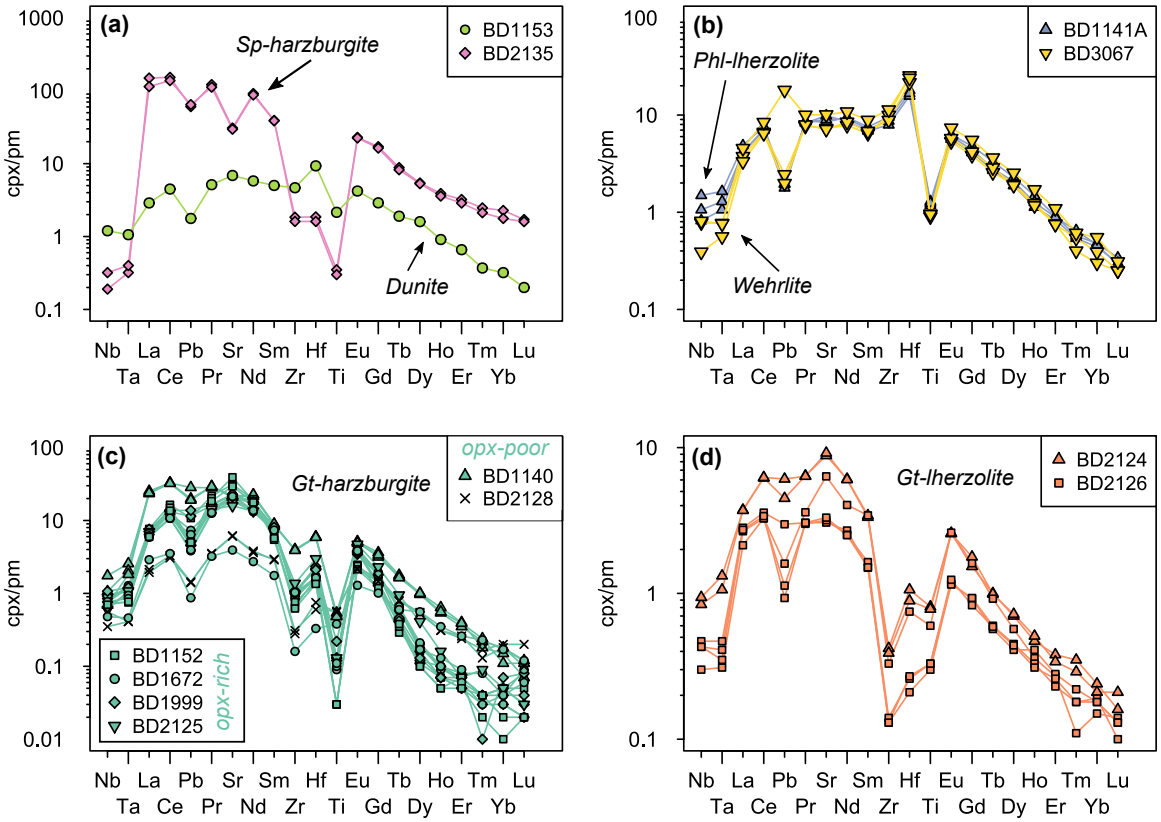

Figure 3.11 *Primitive mantle normalised (McDonough & Sun, 1995) incompatible trace-element plots for clinopyroxene from each lithology.*

3.3 Bulk rock chemistry

Bulk rock chemistry has not been measured directly because: (i) the serpentinisation of the xenoliths has altered this during and post-emplacement, and (ii) there are potential secondary effects associated with infiltration of the host kimberlite. Instead, the bulk rock major-, minor- and trace-element composition for each element (i) is calculated using the measured concentration in each phase (C_i^{min}), and the modal proportion (X^{min}) of each phase in the xenolith, according to Equation 3.1. For the most incompatible elements (e.g. the REE) the concentration in olivine and orthopyroxene was assumed to be negligible. For elements where concentrations in olivine and orthopyroxene were measured (e.g. Nb, Pb, Zr, Ti) they were included in the calculations.

$$C_i^{bulk} = X^{ol}C_i^{ol} + X^{opx}C_i^{opx} + X^{cpx}C_i^{cpx} + X^{gt}C_i^{gt} \tag{3.1}$$

The calculated bulk major and minor element contents are shown in Figure 3.13. The average bulk composition of the depleted MORB mantle (Workman & Hart, 2005) is plotted for reference as a depleted mantle residue, although the sub-cratonic mantle is considered an even more depleted residue (Pearson *et al.*, 1995a; Walter, 1998). The garnet-lherzolites have very similar bulk SiO_2 contents as the DMM reference, whereas many of the harzburgites exhibit significant Si-enrichment in the bulk rock

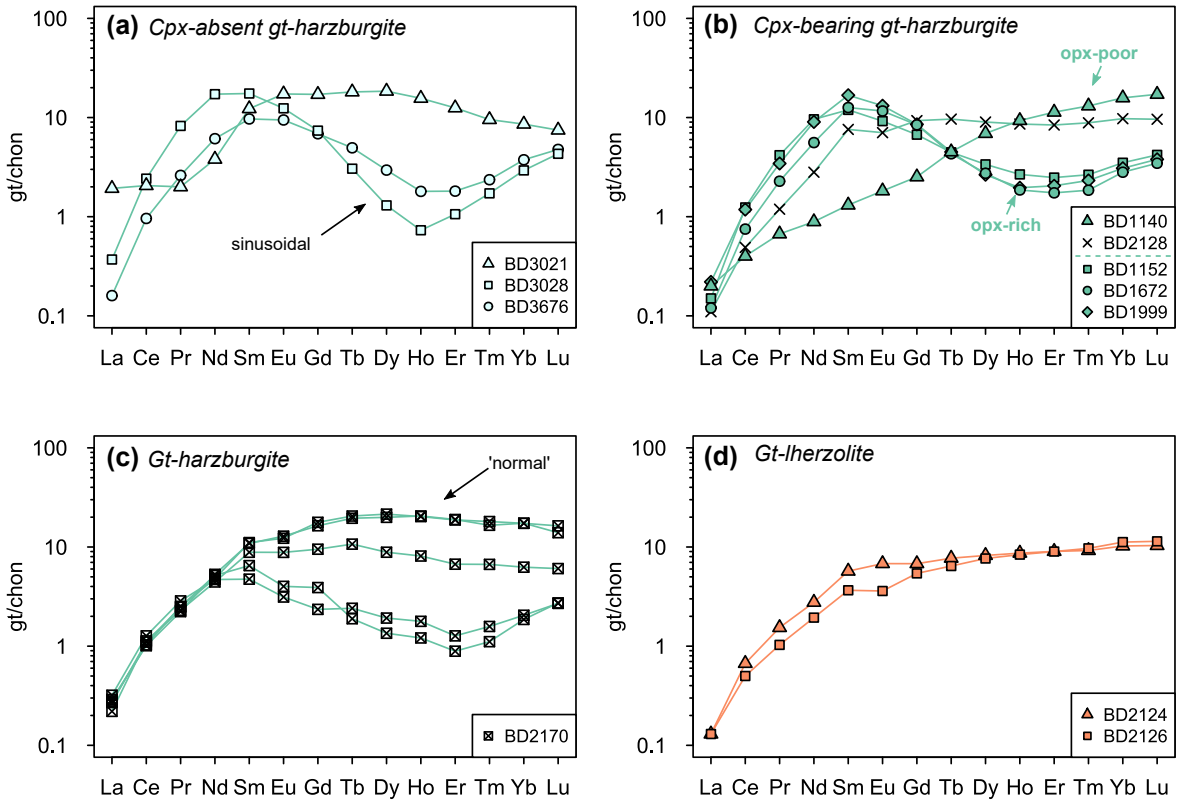

Figure 3.12 *Chondrite-normalised (McDonough & Sun, 1995) REE plots for garnet from each lithology.*

composition. This is primarily due to high modal abundance of orthopyroxene. In both the spinel- and garnet-harzburgites there are positive correlations between bulk-rock SiO_2, Al_2O_3 and Cr_2O_3; and negative correlations between bulk-rock SiO_2, MgO and NiO. This difference separates the preferential distribution of Al and Cr into garnet/spinel and the pyroxenes versus Mg and Ni into olivine. Hence as the proportion of olivine decreases, with increasing bulk SiO_2, the bulk MgO and NiO also decrease and vice versa for Al_2O_3 and Cr_2O_3.

The primitive mantle normalised bulk xenolith REE composition for each lithology is plotted in Figure 3.14. The garnet-lherzolites have the bulk composition most similar to the primitive mantle, evident in the flat trace-element pattern, albeit slightly depleted. The garnet-harzburgite, BD2128 also shows this flat trend, with a slight depletion in the LREE. The concentrations of LREE and HREE in orthopyroxene-poor garnet-harzburgite BD1140 are very close to primitive mantle but there is a slight depletion in the MREE, this could be due to the presence of another phase in which the MREE are more compatible. BD2135 (spinel-harzburgite) is enriched in the LREE but depleted in the HREE, and BD1153 (dunite) is depleted in all REE. Both are depleted in the HREE relative to the LREE, showing a negative gradient in Figure 3.14a. The unusual sinusoidal signature evident in the clinopyroxene and garnet in the orthopyroxene-rich garnet-harzburgites (Figure 3.14c) is superimposed on the bulk xenolith composition.

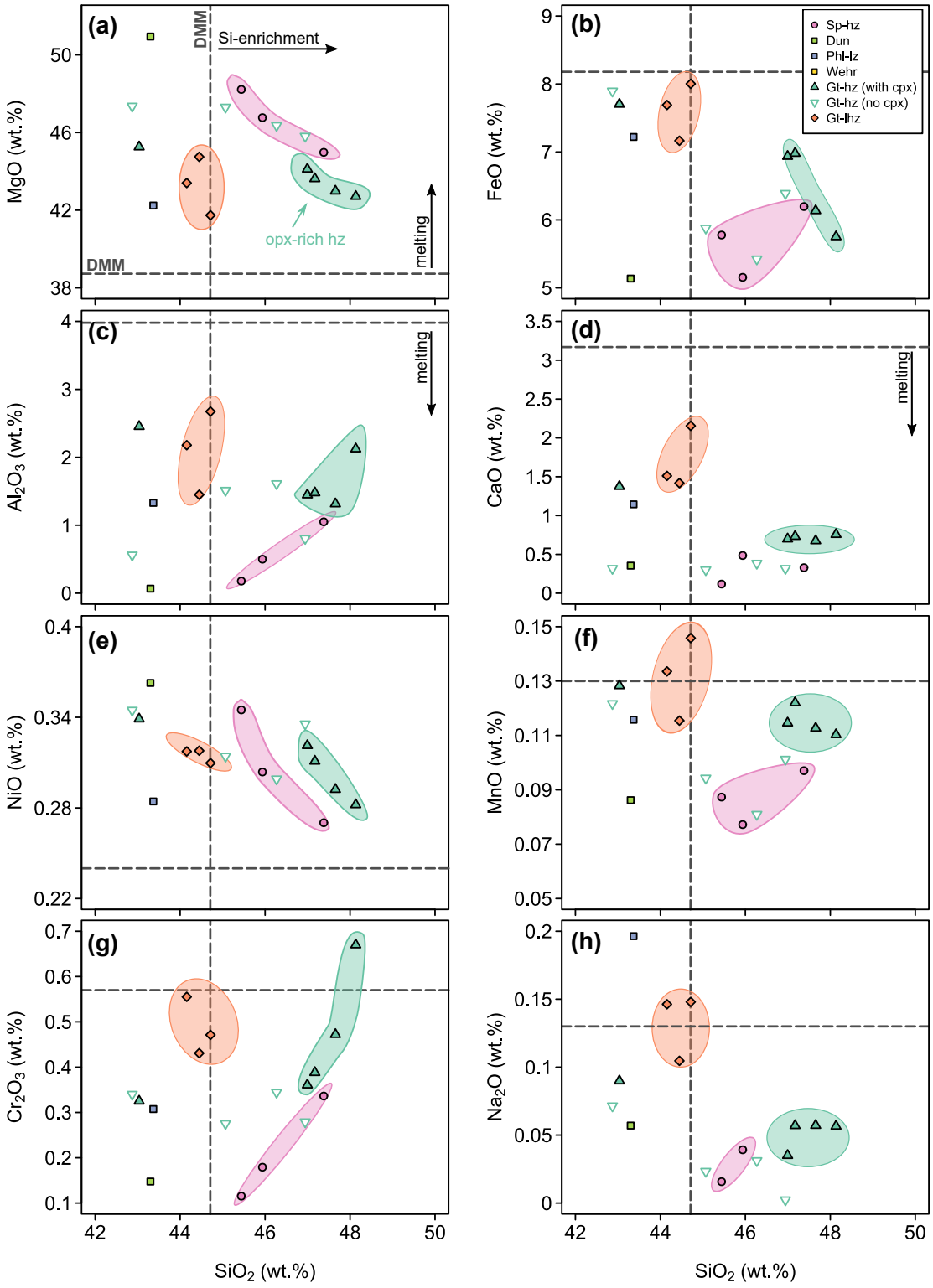

Figure 3.13 *Bulk major and minor element composition calculated according to Equation 3.1. Reference values for depleted MORB mantle (DMM) are marked as grey lines (Workman & Hart, 2005).*

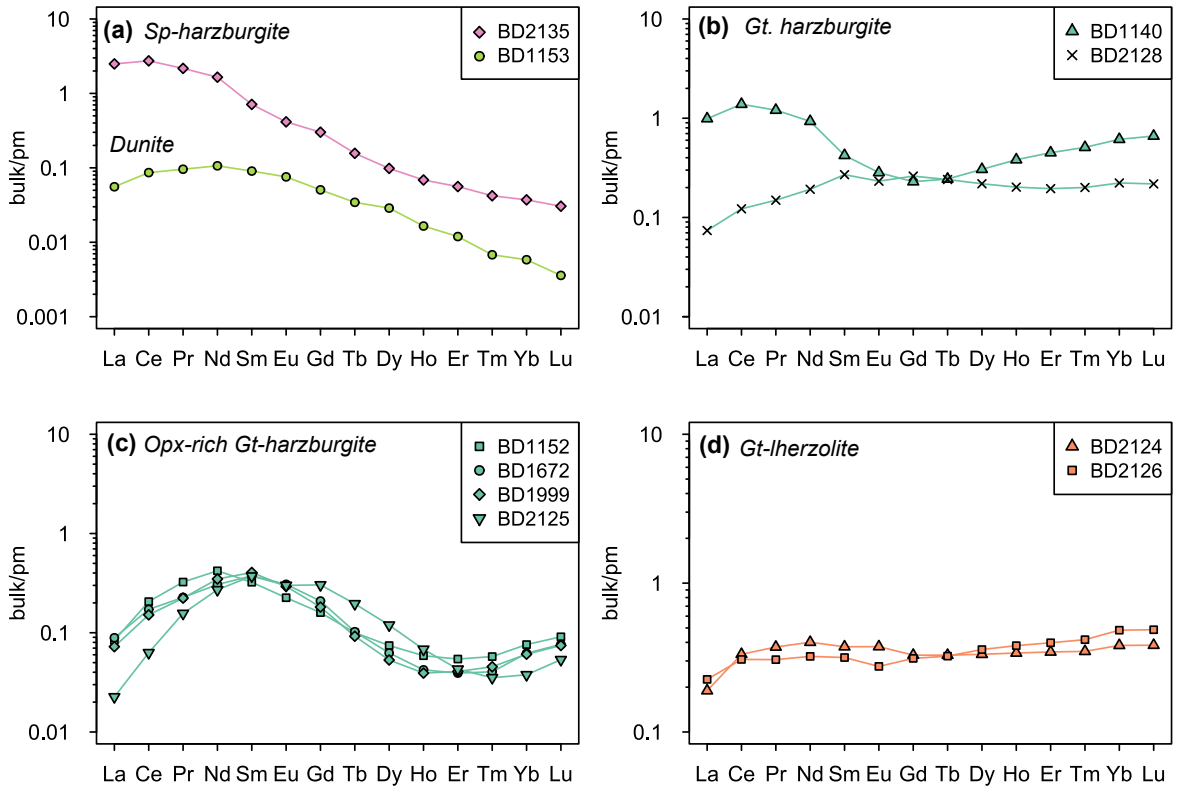

Figure 3.14 *Bulk REE composition calculated according to Equation 3.1 and normalised to primitive mantle.*

3.4 Assessment of major-element equilibrium

The major-element compositions of the olivine, orthopyroxene and clinopyroxene can be used to assess whether the phases are in chemical equilibrium. It is conventional to use the MgO and FeO contents, due to their fast diffusion rates and hence short re-equilibration timescales. The MgO-FeO equilibrium constant, K_D (Equation 3.2), between olivine and orthopyroxene is around 1, and slightly greater than 1 between olivine and clinopyroxene (Pearson *et al.*, 2003).

$$K_D = \frac{[MgO]_A.[FeO]_B}{[MgO]_B.[FeO]_A} = \frac{[MgO/FeO]_A}{[MgO/FeO]_B} \tag{3.2}$$

Figure 3.15 compares the MgO/FeO ratio between olivine and co-existing pyroxenes for each sample , the gradient reflecting the K_D equilibrium constant. This shows that the two pyroxenes in many samples have K_D equal to 1, however olivine has K_D closer to 1.1 with both pyroxenes in many samples. The samples that deviate significantly from these trends are assumed to have not fully equilibrated, these include the clinopyroxene of BD2135, BD1141A, BD3067 and BD2125 and the orthopyroxene of BD2128 and BD1141A.

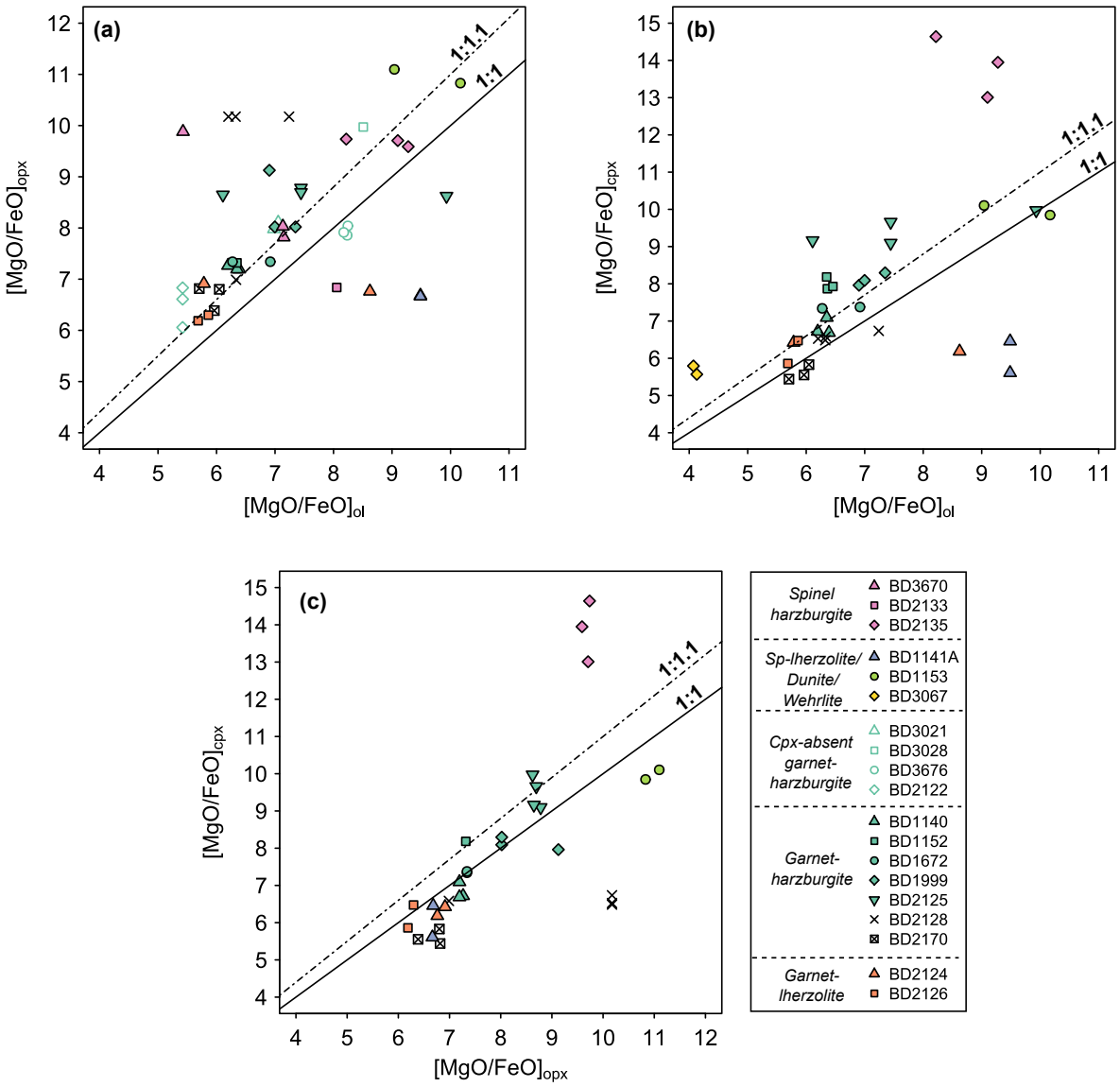

Figure 3.15 *MgO/FeO of olivine, orthopyroxene and clinopyroxene. Solid line is the 1:1 ratio and the dashed line is a 1:1.1 ratio. The ratio is the K_D value (Equation 3.2). Olivine and orthopyroxene should have a K_D equal to 1 whereas with clinopyroxene the K_D is slightly greater than 1 (Pearson* et al.*, 2003).*

3.5 Classification of lithological groups

In Chapter 2, Section 2.4, peridotite xenoliths from Bultfontein and Mothae were classified according to their modal mineralogy and petrography. The major- and trace-element chemistry has been presented according to lithology, but by using the combined petrographic and chemical observations it has been possible to identify five distinct groups of clinopyroxene-bearing peridotites (Table 3.6).

The first group (A) has the most enriched trace-element signature, this is a spinel-harzburgite (Figure 3.16a). The dunite (sample BD1153) has the same trace-element signature as the clinopyroxene in the modally-metasomatised phlogopite-lherzolite (BD1141A) and phlogopite-wehrlite (BD3067), these three samples form the second group (B) (Figure 3.16b). The orthopyroxene-rich (>30%) garnet-harzburgites (Group C) have an unusual concave HREE signature and enriched LREE in clinopyroxene (Figure 3.16c)

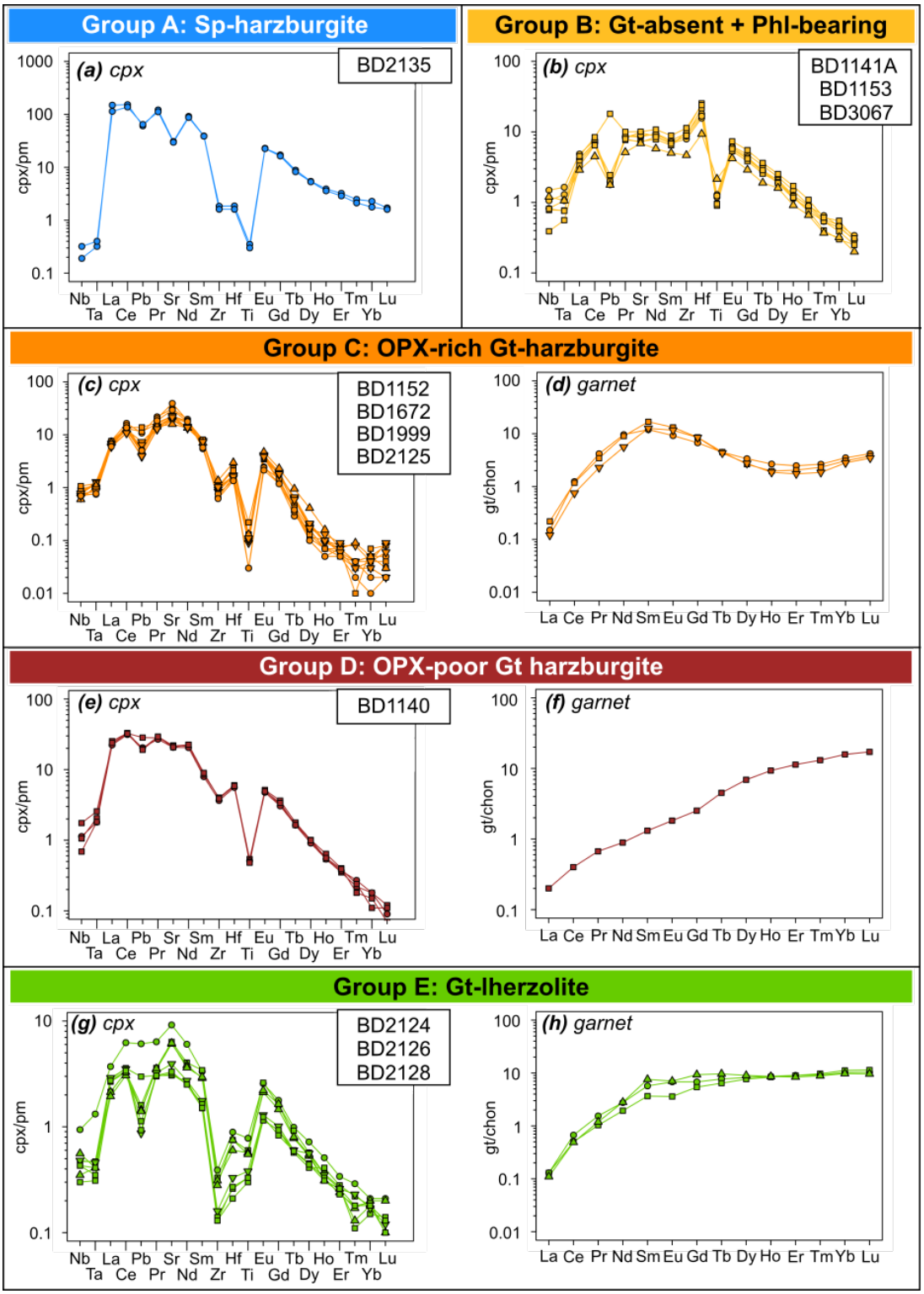

Figure 3.16 *Clinopyroxene signature of (a) spinel-harzburgites, Group A; (b) dunite and modally metasomatised peridotite, Group B; (c) Clinopyroxene and (d) garnet signatures of orthopyroxene-rich garnet-harzburgite, Group C; (e) Clinopyroxene and (f) garnet signatures of orthopyroxene-poor harzburgites, Group D; (g) Clinopyroxene and (h) garnet signatures of garnet-lherzolites, Group E*

Group	Lithology	Mineral Chemistry	Sample
A	Spinel-harzburgite	LREE enriched, large HFSE negative anomalies	BD2135
B	Dunite & modally metasomatised harzburgite	Minor HFSE anomalies, Hf-enriched clinopyroxene	BD1141A BD1153 BD3067
C	OPX-rich garnet-harzburgite	Sinusoidal garnet and clinopyroxene patterns	BD1152 BD1672 BD1999 BD2125
D	OPX-poor garnet-harzburgite	Positive gradient in garnet REE	BD1140
E	Garnet-lherzolite	Least enriched, HREE plateau in garnet	BD2124 BD2126 BD2128

Table 3.6 *Summary of the classification of clinopyroxene-bearing harzburgites and lherzolites*

and a sinusoidal REE signature in the garnet (Figure 3.16d) and bulk trace-element patterns, that sets them apart from the garnet-lherzolites and orthopyroxene-poor harzburgites. The clinopyroxene in sample BD1140 is very similar to the orthopyroxene-rich garnet-harzburgites but the garnet signature is very different (Figure 3.16e,f). The unique garnet signature, low modal proportion of orthopyroxene and higher modal proportion of clinopyroxene set BD1140 aside from the orthopyroxene-rich garnet-harzburgites to create it's own group (D). The other garnet-harzburgite that does not fit the overarching harzburgite trend is BD2128; the clinopyroxene, garnet and bulk composition all have the same trace-element signature as the garnet-lherzolites. As such, BD2128 will now be considered as a garnet-lherzolite based on mineral chemistry. This may reflect the high uncertainty in using thin sections to calculate the modal proportions of a whole xenolith, therefore assigning the lithological nomenclature is not always the most reliable. In this case, the mineral chemistry appears to be a better indicator of garnet-lherzolites, which make the fifth group (E) (Figure 3.16g,h).

The remaining samples are clinopyroxene-absent harzburgites and all but three of these (BD2122, BD2133, BD3670) contain abundant garnet. The composition of the garnet in these xenoliths varies with texture:

Sheared porphyroclastic *(BD3021)*: The garnets in this sample exhibit LREE enrichment relative to all other xenoliths studied from Bultfontein and Mothae (Figure 3.12a), which give an unusual sigmoidal pattern that differs to the HREE depleted sinusoidal pattern of the orthopyroxene-rich garnet-harzburgites.

Coarse *(BD3028/BD3676)*: The garnets in these xenoliths have a sinusoidal REE pattern, much like the orthopyroxene-rich garnet-harzburgites (Figure 3.12a). BD3028 contains a high modal proportion of orthopyroxene (26%), but BD3676 has an average amount of orthopyroxene (19%) for the cratonic mantle (20.8%; Pearson *et al.* 2003).

3.5.1 Principal component analysis

The five categories of clinopyroxene-bearing peridotite defined in Table 3.6 have been identified using geochemical and petrographic observations. This categorisation has been qualitative and based on trace-element patterns of clinopyroxene and garnet. To improve on this approach principal component analysis (PCA) was undertaken in order to investigate the specific features defining each category, in particular using the clinopyroxene chemistry as each group has a unique trace-element pattern.

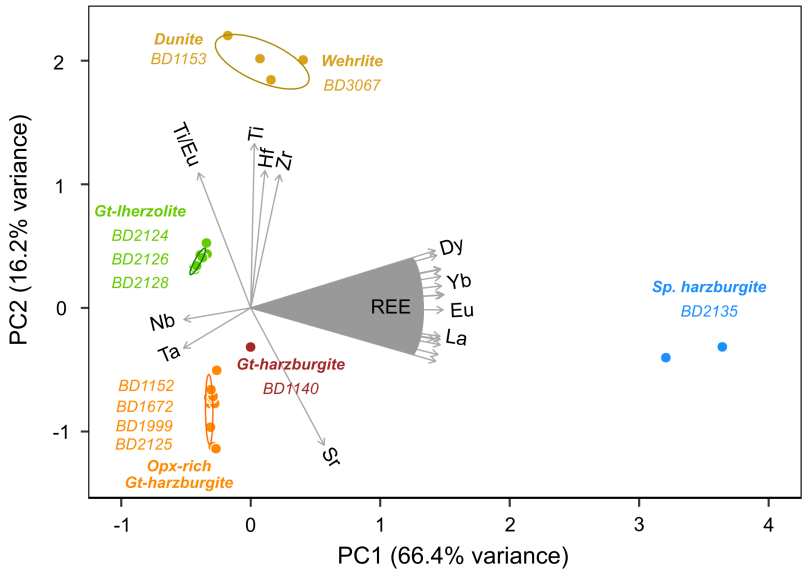

Figure 3.17 *Principal component analysis of the clinopyroxene in all clinopyroxene-bearing xenoliths. The first two principal components make up 82% of all variance. The components parallel to each axis give an indication of the nature of each component.*

The clinopyroxene incompatible trace-element concentrations were input into the PCA. Additionally the Ti/Eu ratio was included to add a measure of the Ti anomaly evident in all groups. This analysis divided the the Bultfontein and Mothae xenolith suites into the same groupings identified in Table 3.6 and therefore successfully highlighted the elements or ratios instrumental in defining each category. Figure 3.17 shows the groupings identified by Principal Component 1 (PC1), which accounts for 66% of the variance, and Principal Component 2 (PC2), accounting for 16% of the variance. By looking at the elements parallel to the axes, true variables can be assigned to each principal component. PC1 is related to the level of REE enrichment and, to some extent, the Nb and Ta concentrations. This principal component is dominated by the extreme REE enrichment in clinopyroxene from Group A (spinel-harzburgite). PC2 is controlled by the concentrations of Ti, Hf and Zr. There is a clear distinction between the shape of the primitive normalised pattern between these three elements in each group, for example Group E (garnet-lherzolite) has a small negative Ti anomaly but large Zr anomaly and the opposite is true for Group C (orthopyroxene-rich garnet-harzburgite). Sr also has some control on PC2, high Sr in the orthopyroxene-rich garnet-harzburgites gives these samples a negative factor for PC2 relative to the dunite and phlogopite-bearing peridotite.

Principal component analysis has statistically corroborated the subdivision of the clinopyroxene -bearing peridotites in this sample set into five categories. The significance of these groupings will be

discussed in later chapters and the subdivisions will be used in most of the subsequent plots and discussion within this thesis.

3.6 Summary

In this chapter, the major-, minor- and trace-element chemistry of each of the Bultfontein and Mothae peridotite xenoliths and their constituent minerals have been presented. While there is a wide range of mineral and bulk chemistry, it has been possible to identify trends and categorise five types of clinopyroxene-bearing peridotite in the sample suites. In some cases the chemical signature corresponds exclusively with specific petrographic features, for example the peridotite xenoliths with a sinusoidal garnet and bulk rock REE pattern also have very high modal abundance of orthopyroxene (30-38%). The different lithological and chemical categories described in this chapter reflect different processes in the SCLM, namely partial melting and metasomatism by melt:rock reaction. The melting and metasomatic history of each group of peridotite xenoliths will be discussed in Chapter 5.

Chapter 4

Thermobarometry

4.1 Introduction

In this chapter, the final equilibrium conditions of the nineteen xenoliths from Bultfontein and Mothae are calculated to investigate the role of pressure (P) and temperature (T) on the storage of volatile elements in nominally volatile-free mantle minerals (NVFMM). Previous studies have shown that pressure and temperature may control the partitioning of water and fluorine between orthopyroxene and clinopyroxene in the SCLM (e.g. Gibson *et al.* 2020).

The solubility of different elements and their partitioning between co-existing phases is often dependent on pressure and/or temperature. Empirical relationships between mineral compositions and pressure and temperature have been derived in numerous studies using experimental run-products, equilibrium constants and thermodynamic laws. These have been applied to mantle xenoliths to estimate their equilibration PT conditions. The most reliable geothermobarometers are based on the PT-dependence of partitioning of elements between two phases in a four phase lherzolite (Nimis & Grütter, 2010). They require a state of chemical equilibrium between the two phases and rely on iterative calculations for both pressure and temperature to obtain an accurate estimate. As seen in Chapter 2, the lithology of the Bultfontein and Mothae xenoliths is variable and the mineralogy does not always contain clinopyroxene or garnet. For the two- and three-phase assemblages single-phase geothermobarometry can be applied, albeit with greater uncertainty. In this chapter the relative merits of a number of thermometers and barometers are compared and applied to the Bultfontein and Mothae xenoliths.

4.2 Thermometers

4.2.1 Two-pyroxene thermometer

The two-pyroxene thermometer was first characterised by Wells (1977) based on the temperature dependence of the miscibility gap between diopside and enstatite, i.e. Mg partitioning in co-exisiting pyroxenes. The Wells (1977) two-pyroxene thermometer (Wells77; Equation 4.1) is still useful for spinel peridotites because it is independent of pressure.

$$T_{Wells77}^{Mg-cpx-opx}(K) = \frac{7341}{3.355 + 2.44(X_{Fe}^{opx} - lnK_d)} \tag{4.1}$$

where:

$$K_d = \frac{X^{cpx}_{Mg,M1} * X^{cpx}_{Mg,M2}}{X^{opx}_{Mg,M1} * X^{opx}_{Mg,M2}}$$

Brey & Köhler (1990) compared the temperature estimates calculated using the Wells (1977) thermometer to an experimental dataset and found that it reproduced temperatures at 900 °C well but underestimated those > 900 °C.

Finnerty & Boyd (1987) produced another formulation of the two-pyroxene thermometer which reproduced high temperatures (> 1100 °C) well but vastly underestimated low temperatures. This discrepancy was recognised by Brey & Köhler (1990) who improved on the initial two-pyroxene thermometer by accounting for minor elements, notably Na, present in natural systems. The resultant thermometer was able to reproduce experimental temperatures to within ± 16 °C. The Brey & Köhler (1990) two-pyroxene thermometer has been used as the standard in many mantle studies, however Taylor (1998) recognised that it overestimated the temperature for fertile peridotite by exaggerating the influence of Na. Taylor (1998) published a new version of the two-pyroxene thermometer that better accounts for Ca, Na, Cr and Ti in the activity of the enstatite component in clinopyroxene and orthopyroxene by using a three-site solid solution model, e.g. $(1 - Ca - Na).(1 - Al^{VI} - Cr - Ti).(1 - \frac{Al^{IV}}{2})^2$.

$$T^{cpx-opx}_{TA98}(K) = \frac{24.787 + 678P(GPa)}{15.67 + 14.37Ti^{cpx} + 3.69Fe^{cpx} - 3.25X_{ts} + (lnKd)^2} \tag{4.2}$$

where:

$$lnKd = ln[a(En)^{cpx}] - ln[a(En)^{cpx}]$$

$$X_{ts} = (Al + Cr + Na)^{cpx}$$

$$a(En) = (1 - Ca - Na).(1 - Al^{VI} - Cr - Ti).(1 - \frac{Al^{IV}}{2})^2$$

Taylor (1998) found that this thermometer reproduces the temperatures in two experimental datasets to an accuracy of ΔT = +6 °C with a precision of 1σ = 31 °C compared to ΔT = +81 °C and 1σ = 36 °C using the Brey & Köhler (1990) thermometer. Nimis & Grütter (2010) further compared the two thermometers and drew the conclusion that the TA98 two-pyroxene thermometer (Equation 4.2) produces the most accurate temperature estimates over the wide range of temperatures applicable to garnet peridotites.

4.2.2 Fe-Mg orthopyroxene-garnet thermometer

The two-pyroxene thermometers necessitate that both clinopyroxene and orthopyroxene are present and are fully equilibrated. If clinopyroxene is absent then an alternative is the Fe-Mg orthopyroxene-garnet thermometer (NG10; Nimis & Grütter 2010). The NG10 thermometer is based on the equilibrium of Fe-Mg exchange between orthopyroxene and garnet. Early thermometers based on orthopyroxene-garnet equilibria (e.g. Harley 1984; Lee & Ganguly 1988) produced systematic differences with two-pyroxene thermometers and were hence deemed inappropriate. Nimis & Grütter (2010) addressed this by a new 'natural' calibration that empirically fitted the orthopyroxene-garnet thermometer using mineral compositions from ultramafic rocks whose equilibration pressure and temperature conditions had already been calculated using the TA98 two-pyroxene thermometer (Taylor, 1998) and the NG85 Al-in-orthopyroxene barometer (Nickel & Green, 1985). The empirical calibration produces the following relationship:

$$T_{NG09}^{opx-gt}(K) = \frac{1215 + 17.4P + 1495(X_{Ca}^{gt} + X_{Mn}^{gt})}{lnK_{Fe-Mg}^{opx-gt} + 0.732} \tag{4.3}$$

where:

$$K_{Fe-Mg}^{opx-gt} = \frac{Fe^{gt} \times Mg^{opx}}{Mg^{gt} \times Fe^{opx}}$$

$$X_{Ca}^{gt} = \frac{Ca}{Ca+Mn+Mg+Fe}$$

$$X_{Mn}^{gt} = \frac{Mn}{Ca+Mn+Mg+Fe}$$

This approach produces very large uncertainties (e.g. 150 °C) relative to thermometers calibrated using experiments, but a better agreement with the two-pyroxene thermometers than the early experimentally calibrated versions of the same thermometer. Nimis & Grütter (2010) also recognise that the Fe-Mg orthopyroxene-garnet thermometer can underestimate temperature with depth if all Fe is treated as Fe^{2+} and hence will yield inaccurate temperature estimates in lithospheric sections where there are anomalous relationships between depth and oxidation state, e.g. at Kimberley (Creighton *et al.*, 2008).

4.2.3 Single phase thermometers

There are also single phase thermometers for orthopyroxene, clinopyroxene and olivine in mantle xenoliths. These are all based on the temperature dependent solubility of specific elements in each mineral phase. The solubility of Ca in orthopyroxene, Al in olivine and the enstatite component in clinopyroxene are all temperature dependent and have been calibrated experimentally to produce the following three single phase thermometers.

1. BKN90: Ca-in-orthopyroxene thermometer (Brey *et al.*, 1990)

$$T_{BKN90}^{Ca-in-opx}(K) = \frac{6425 + 26.4P}{-ln(Ca^{opx}) + 1.843} \tag{4.4}$$

2. NT00: Enstatite-in-clinopyroxene (Nimis & Taylor, 2000). All elements used in the parameterisation represent their concentration in clinopyroxene by atom per formula unit (a.p.f.u).

$$T_{NT00}^{En-in-cpx}(K) = \frac{23166 + 39.28P}{13.25 + 15.35Ti + 4.5Fe - 1.55(Al + Cr - Na) + [ln(En)]^2} \tag{4.5}$$

3. BS17: Al-in-olivine (Bussweiler *et al.*, 2017)

$$T_{BS17}^{Al-in-ol}(K) = \frac{11245 + 46P}{13.68 - ln(Al^{ol})} \tag{4.6}$$

These three thermometers are all calibrated for a four phase lherzolite assemblage that includes garnet. The BS17 thermometer is specifically calibrated for garnet peridotites only, whereas BKN90 and NT00 thermometers can be used (albeit with caution) for spinel peridotites. Witt-Eickschen & Seck (1991) formulated a thermometer (WS91) specifically for spinel peridotites based on the temperature dependence

of the solubility of Al and Cr in orthopyroxene. The relationship is derived from the BKN90 thermometer and simplified to the following relationship:

$$T_{WS91}^{Al-Cr-opx}(^{o}C) = 636.54 + 2088.21X_{Al,M1}^{opx} + 14527.32X_{Cr,M1}^{opx} \quad (4.7)$$

Like the original two pyroxene thermometer of Wells (1977), the Witt-Eickschen & Seck (1991) Al-Cr in orthopyroxene thermometer is independent of pressure, but there are strict compositional restraints. The WS91 thermometer is only appropriate if Al and Cr are linearly correlated within a small compositional range, shown in Figure 4.1. All of the orthopyroxenes from the two- or three-phase Bultfontein and Mothae xenoliths have X_{M1}^{Al} or X^{Cr} that plot outside this range.

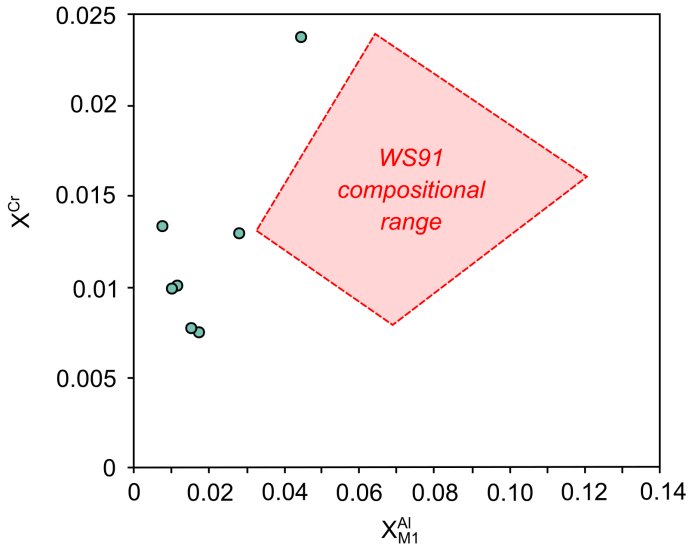

Figure 4.1 *The compositional range in Al and Cr content of orthopyroxene that is valid for the Witt-Eickschen & Seck (1991) orthopyroxene thermometer (shaded area). The xenoliths that are not appropriate for the TA98 two-pyroxene thermometer are plotted, none fall within the compositional range that deems the WS91 geothermometer appropriate.*

4.3 Barometers

4.3.1 Al-exchange in orthopyroxene and garnet barometer

The most reliable barometer for garnet peridotites is the Al-in-orthopyroxene barometer (Nimis & Grütter, 2010; Taylor, 1998). This is based on the pressure and temperature dependence of Al exchange between orthopyroxene and garnet (Brey *et al.*, 1990; Nickel & Green, 1985). The barometer uses the reaction between the Mg-tschermak component of orthopyroxene and pyrope garnet as follows:

$$Mg_2Si_2O_6 + MgAl_2SiO_6 = Mg_3Al_2Si_3O_{12} \quad (4.8)$$

Nickel & Green (1985), Brey *et al.* (1990) and Brey *et al.* (2008) have all used a thermodynamic approach to calibrate the Al-in-orthopyroxene barometer. Nimis & Grütter (2010) recommend the use of the Nickel & Green (1985) formulation (NG85) because it better reproduces the pressures of fertile peridotite up to 60 kbar whereas the Brey *et al.* (1990) formulation increasingly overestimates P > 50 kbar and produces a larger degree of scatter around the geotherm. The most recent version (Brey *et al.*, 2008) was found to produce results with low precision at moderate pressures and severe inconsistency with the graphite-diamond curve (Gibson *et al.*, 2008; Nimis & Grütter, 2010). Consequently, the pressures of garnet-bearing peridotite have been calculated using the NG85 Al-in-orthopyroxene barometer with an estimated error of ± 3 kbar (Equation 4.9).

$$\begin{aligned} P_{NG85}^{Al-opx-gt} = & \left(1/-[183.3+178.98X_{Al}^{M1}(1-X_{Al}^{M1})]\right) \\ & \times \Big(-RTln\Big[[(1-X_{gt}^{Ca})^3(X_{Al}^{gt})^2] \\ & \times [X_{Mg,Fe}^{M1}(X_{Mg,Fe}^{M2})^2 X_{Al}^{M1}]^{-1}\Big] \\ & -9000(X_{Ca}^{gt})^2 - 3400[2(X_{Ca}^{gt})^2 - X_{Mg}^{M1}X_{Cr}^{opx}] \\ & - X_{Ca}^{gt}X_{Cr}^{gt}(90853-52.1T) \\ & -7590X_{Fe}^{gt}X_{Ca}^{gt} + 5157X_{Mg}^{M1}X_{Fe}^{M1} + 6047 - 3.23T\Big) \end{aligned} \tag{4.9}$$

where the site distributions are calculated as follows:

$$X_{Al}^{M1} = (Al - Cr - 2Ti + Na)/2$$

$$X_{Mg,Fe}^{M1} = 1 - X_{Al}^{M1} - Cr - Ti$$

$$X_{Mg,Fe}^{M2} = 1 - Ca - Na - Mn$$

$$X_{Mg}^{M1} = [Mg/Mg + Fe]X_{Mg,Fe}^{M1}$$

$$X_{Ca}^{gt} = [Ca/(Ca + Mg + Fe + Mn)]^{gt}$$

$$X_{Al}^{gt} = [Al/(Al + Cr)]^{gt}$$

$$X_{Cr}^{gt} = [Cr/(Al + Cr)]^{gt}$$

M1 and M2 refer to the appropriate sites in orthopyroxene, unless otherwise stated. The expression for X_{Mg}^{M1} can be adjusted accordingly for X_{Fe}^{M1} and X_{Mg}^{M2}). As is true for X_{Fe}^{gt} from X_{Ca}^{gt}.

When used with the TA98 two-pyroxene thermometer, the NG85 barometer reproduces very accurate estimates of pressure in experimental datasets. Taylor (1998) proposed a correction to the NG85 barometer to account for Ti in the activity term for the Mg-tschermaks component, such that $X_{MgTs} = X_{Al}^{M1} = (Al - Cr + Ti + Na)/2$. Using this modification, Taylor (1998) found that the NG85 barometer reproduced pressures of the same experimental datasets with perfect accuracy ($\Delta + 0$ kbar) and precision of $1\sigma = 2.3$ kbar. Nimis & Grütter (2010) further recommend the use of the NG85 Al-in-orthopyroxene barometer

alongside the TA98 two-pyroxene thermometer based on the accuracy and precision of this barometer but also on the consistency of the carbon species present in garnet lherzolites with the graphite-diamond curve, and the reduced scatter it produces around the geotherm (Grütter, 2009).

Modifications to the NG85 barometer have been proposed by Carswell (1991) to account for Na in fertile xenoliths at the base of the cratonic lithosphere and by Taylor (1998), again for fertile xenoliths at P < 35 kbar. Based on the recommendation of Nimis & Grütter (2010), neither modification was applied to the NG85 barometer because the Carswell (1991) modification only affects highly sodic orthopyroxene and was found to yield unreasonably high pressures and the Taylor (1998) modification produced pressure estimates that were not consistent with the graphite-diamond curve.

4.3.2 Single orthopyroxene barometer

The only single phase barometer that can be used on both spinel and garnet peridotites is the MacGregor (1974) Al-in-orthopyroxene barometer (MC74) based on the solubility of Al_2O_3 in orthopyroxene (Equation 4.10).

$$P^{Al-opx}_{MC74}(kbar) = \frac{-T(lnK - 1.46) - 3736}{97.1} \tag{4.10}$$

where:

$$K = (Al_2O_3 wt.\%)/100$$

Taylor (1998) found this barometer to reproduce experimental pressures to an accuracy of $\Delta + 6$ kbar and precision of $1\sigma = 2.8$ kbar. The MC74 barometer reproduces well-matched estimates at low pressures, however above 40 kbar it has a tendency to overestimate pressure.

4.4 *PT* estimates of the Bultfontein and Mothae xenoliths

The preferred thermometer-barometer combination of TA98-NG85 requires two conditions to be met: (i) clinopyroxene-orthopyroxene equilibrium; and (ii) the presence of garnet. Mg-Fe equilibrium between the two pyroxenes was checked in Chapter 3. Major element equilibrium was deemed complete where K_D was equal to 1 (± 0.1; Pearson *et al.* 2003). Where the assemblage was equilibrated in the Bultfontein and Mothae xenoliths with a four-phase assemblage, the TA98 two pyroxene thermometer and NG85 Al-in-orthopyroxene barometer were used to calculate the equilibration pressure and temperature conditions of the xenoliths (as recommended by Nimis & Grütter 2010).

In order to estimate the final equilibration pressures and temperatures of the clinopyroxene-absent garnet harzburgites a number of approaches were taken. Firstly, the best thermo-barometer combination that does not require clinopyroxene was assessed. To do this, the equilibration pressures and temperatures were calculated using each thermometer with the NG85 preferred barometer for all garnet peridotites in the suite of Bultfontein and Mothae xenoliths. The results are shown in Table 4.1, and compared to the preferred TA98-NG85 estimates in Figure 4.2. While there is very good agreement at all temperatures between

	Thermometer/ Barometer	TA98 (cpx-opx)	NG85 (Al-in-opx-gt)	BK90 (cpx-opx)	NG85 (Al-in-opx-gt)	TA98 (cpx-opx)	MC74 (Al-in-opx)	NT00 (En-in-cpx)	MC74 (Al-in-opx)
Sample	**Mineral assemblage**	***T*** **(°C)**	***P*** **(kbar)**	***T*** **(°C)**	***P*** **(kbar)**	***T*** **(°C)**	***P*** **(kbar)**	***T*** **(°C)**	***P*** **(kbar)**
Mothae									
BD2122	ol+opx+cpx+gt	1001	46	1018	46.5	929	38.7	973	41.5
BD2124	ol+opx+cpx+gt	1241	51.2	1219	50.1	1231	57.3	1259	59
BD2125	ol+opx+cpx+gt	1057	44.2	1030	42.9	1036	47.2	1062	48.9
BD2126	ol+opx+cpx+gt	1273	50.6	1203	39.5	1284	59.7	1303	60.9
BD2128	ol+opx+cpx+gt	1260	51.2	1183	39.8	1265	58.9	1283	60
BD2133	ol+opx								
BD2135	ol+opx+cpx					770	21.3	790	22.4
BD2170	ol+opx+cpx+gt	1270	52.6	1243	51.5	1262	58.5	1286	60.1
Bultfontein									
BD1140	ol+opx+cpx+gt	859	35.5	858	35.5	805	32.3	848	35.1
BD1141A	ol+opx+cpx			1000	44.4	963	47	978	48.1
BD1152	ol+opx+cpx+gt	1016	43.8	1000	43	996	45.2	1013	46.4
BD1153	ol+opx+cpx					1004	49	1029	50.7
BD1672	ol+opx+cpx+gt	1052	44.1	1027	42.9	1028	46.9	1054	48.6
BD1999	ol+opx+cpx+gt	1009	42.9	972	36.9	980	43.8	1005	45.4
BD3021	ol+opx+gt			1043	49.4				
BD3028	ol+opx+gt			959	36				
BD3670	ol+opx								
BD3676	ol+opx+gt			954	37.7				

Table 4.1 *All PT estimates for the Bultfontein and Mothae xenoliths, using a range of two-mineral and single mineral thermometers and barometers.*

	Thermometer/ Barometer	BKN90 (Ca-in-opx)	MC74 (Al-in-opx)	BS17 (Al-in-ol)	NG85 (Al-in-opx-gt)	BKN90 (Ca-in-opx)	Geotherm fit (P = 0.0425T - 3)	BKN90 (Ca-in-opx)	P fixed at 20 kbar
Sample	**Mineral assemblage**	***T*** **(°C)**	***P*** **(kbar)**	***T*** **(°C)**	***P*** **(kbar)**	***T*** **(°C)**	***P*** **(kbar)**	***T*** **(°C)**	***P*** **(kbar)**
Mothae									
BD2122	ol+opx+cpx+gt	1005	43.6	1056	42.3	984	38.8		
BD2124	ol+opx+cpx+gt	1267	59.6	1173	47.5	1211	48.5		
BD2125	ol+opx+cpx+gt	1055	48.4	1037	42.1	1017	40.2		
BD2126	ol+opx+cpx+gt	1320	62	1292	51.5	1261	50.6		
BD2128	ol+opx+cpx+gt	1290	60.4	1265	51.0	1233	49.4		
BD2133	ol+opx	955	42.4			929	36.5	858	20
BD2135	ol+opx+cpx	905	29			939	36.9	866	20
BD2170	ol+opx+cpx+gt	1288	60.2	1284	51.1	1233	49.4		
Bultfontein									
BD1140	ol+opx+cpx+gt	860	35.9	1126	50.9	848	33.0		
BD1141A	ol+opx+cpx	1034	51.9	1016	47.0	974	38.4	892	20
BD1152	ol+opx+cpx+gt	1016	46.5	1050	45.0	981	38.7		
BD1153	ol+opx+cpx	1056	52.5			996	39.4	910	20
BD1672	ol+opx+cpx+gt	1052	48.5	1051	43.5	1014	40.1		
BD1999	ol+opx+cpx+gt	1012	45.9			980	38.6		
BD3021	ol+opx+gt	1025	45.4	1181	56.1	998	39.4		
BD3028	ol+opx+gt	993	43.7	1086	45.5	969	38.2		
BD3670	ol+opx	1108	33.1			1177	47.0	1042	20
BD3676	ol+opx+gt	970	41.6	1094	44.9	953	37.5		

Table 4.1 cont: *All PT estimates for the Bultfontein and Mothae xenoliths, using a range of two-mineral and single mineral thermometers and barometers.*

the BK90-NG85 and TA98-NG85, the pressure is underestimated in three samples. The BS17-NG85 combination has good agreement in all but one xenolith. The NG09-NG85 combination shows the poorest agreement with the TA98-NG85 combination.

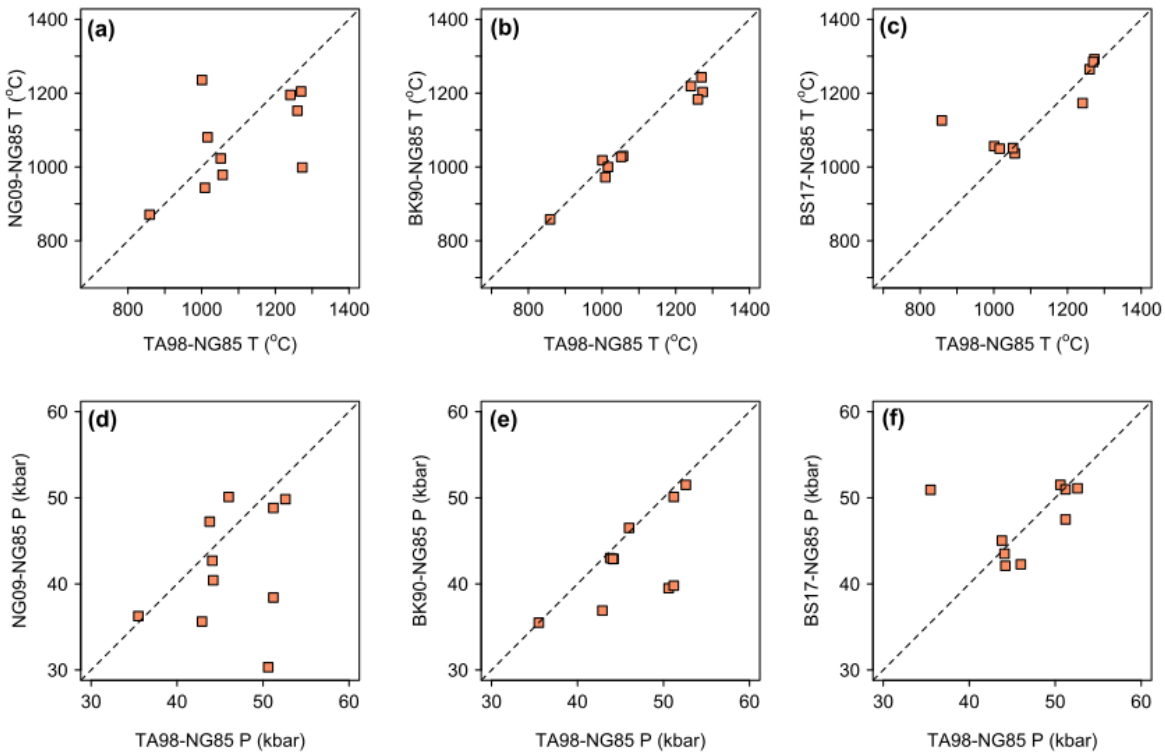

Figure 4.2 *Comparison of the equilibration PT estimates calculated using the preferred combination of the TA98 two-pyroxene thermometer (Taylor, 1998) and the NG85 Al-in-orthopyroxene barometer (Nickel & Green, 1985) with three different thermometers that are appropriate for clinopyroxene-absent assemblages: (a,d) NG09 - Fe-Mg orthopyroxene-garnet (Nimis & Grütter, 2010); (b,e) BK90 - Ca-in-orthopyroxene (Brey* et al.*, 2009); (c,f) BS17 - Al-in-olivine (Bussweiler* et al.*, 2017). All used in conjunction with the NG85 barometer.*

In the spinel peridotites there are three possible thermometers to use: the two-pyroxene thermometer (Wells77; TA98), the single orthopyroxene thermometer (BKN90) and the single clinopyroxene (NT00) thermometer. The Wells77 two-pyroxene thermometer is independent of pressure. When the temperature parameterisation is dependent on pressure there are three options:

1. MacGregor (1974) Al in orthopyroxene barometer (MC74, Equation 4.10)
2. Fit the temperature estimate to an approximation of the geotherm (i.e. $P = f(T)$)
3. Fix the pressure within the spinel stability field (20 kbar)

The combination of the MC74 barometer with the TA98 two-pyroxene, BK90 Ca-in-orthopyroxene and NT00 single clinopyroxene thermometers for all nineteen xenoliths are plotted against the Bultfontein geotherm (Mather *et al.*, 2011) in Figure 4.3. This geotherm approximates mantle potential temperature (T_p) at 1315 °C and estimates the surface heat flow to 43 mWm^{-2}. Mather *et al.* (2011) define the lithospheric thickness to represent the point at which the projection of the conductive geotherm (mechanical boundary layer) intersects the adiabat, and find the lithospheric thickness at Bultfontein to be 183 ± 30 km. Using Figure 4.3, it is apparent that the MC74 barometer vastly overestimates at pressures >40 kbar,

compared to those calculated using the TA98-NG85 combination, but the lower pressure estimates are similar. Three of the spinel peridotites (BD1141A, BD1153 and BD2135) contain both clinopyroxene and orthopyroxene, but in order to use the preferred TA98 two pyroxene thermometer, these must be equilibrated. It was shown in Chapter 3 that the clinopyroxene and orthopyroxene in BD2135 are not equilibrated based on the Fe-Mg K_D. This disequilibrium is evident in the vast disparity in the temperature estimates using thermometers that are based on orthopyroxene against those reliant on clinopyroxene. When used alongside the MC74 barometer, the TA98 and NT00 clinopyroxene-based thermometers calculate temperatures of 770-790 °C at 21-22 kbar for BD2135, whereas the BKN90 Ca-in-orthopyroxene thermometer estimated temperatures of 905 °C and 29 kbar. The Wells77 thermometer estimated temperatures under 500 °C which is not plausible for the SCLM, and hence ruled out the use of this thermometer. The estimates produced by the single clinopyroxene and single orthopyroxene thermometers combined with the MC74 barometer for the remaining two garnet-absent peridotites (BD1141A, BD1153) are within 50°C and 3 kbar which implies that the two pyroxenes are equilibrated.

The second approach to account for pressure of the spinel peridotites is to calculate the temperatures using a single mineral thermometer (e.g. BK90 and NT00) and fitting this to the Kaapvaal geotherm. An approximation of the pressure as a function of temperature, between 800-1300 °C, was calculated from the Bultfontein lithospheric mantle geotherm of Mather *et al.* (2011). The approximate P-T relationship is: $P = 0.0425T - 3$. The equilibration temperatures calculated using the BK90 orthopyroxene thermometer and the NT00 clinopyroxene thermometer and fitted to the approximation of the geotherm are compared in Figure 4.3a. Where the two thermometers give the same temperature estimate, one can assume that the orthopyroxene and clinopyroxene are in equilibrium. This is the case for all of the clinopyroxene-bearing peridotites with the exception of BD2135 which has different orthopyroxene and clinopyroxene equilibration temperatures. This provides yet further evidence, on top of that discussed above, that in this spinel harzburgite the two phases have not equilibrated before the xenolith was carried to the surface by the Mothae kimberlite.

The equilibration *PT* conditions of the garnet peridotites estimated by fitting T to the geotherm are very similar to those calculated using the TA98-NG85 preferred geothermobarometer, however, when this method was used for the garnet-absent xenoliths it calculated high temperatures and pressures (930-996 °C and 36-39 kbar) that place them firmly within the garnet stability field (Figure 4.4b). This discrepancy leads to the third approach to estimate *PT* conditions for garnet-absent peridotites where the pressure is fixed at 20 kbar. Again, this method calculates very high equilibration temperatures (848 - 1042 °C; Table 4.1) for spinel peridotites that do not fit onto the Kaapvaal mantle geotherm.

There are three possible explanations for the discrepancy between the Al-phase present and the *PT* estimates: (i) the temperatures represent the elevated temperatures during metasomatism or ascent of the kimberlite; (ii) the clinopyroxene or orthopyroxene have been added during recent metasomatism and have not equilibrated (e.g. Brey *et al.* 1990; Simon *et al.* 2003); and (iii) the xenoliths originate in the garnet stability field but the garnet has decompressed to spinel during ascent which must be faster than clinopyroxene and orthopyroxene can equilibrate. The latter scenario would retain equilibration pressure and temperatures of the xenolith source in the garnet facies while the mineral assemblage reflects transport through the spinel stability field.

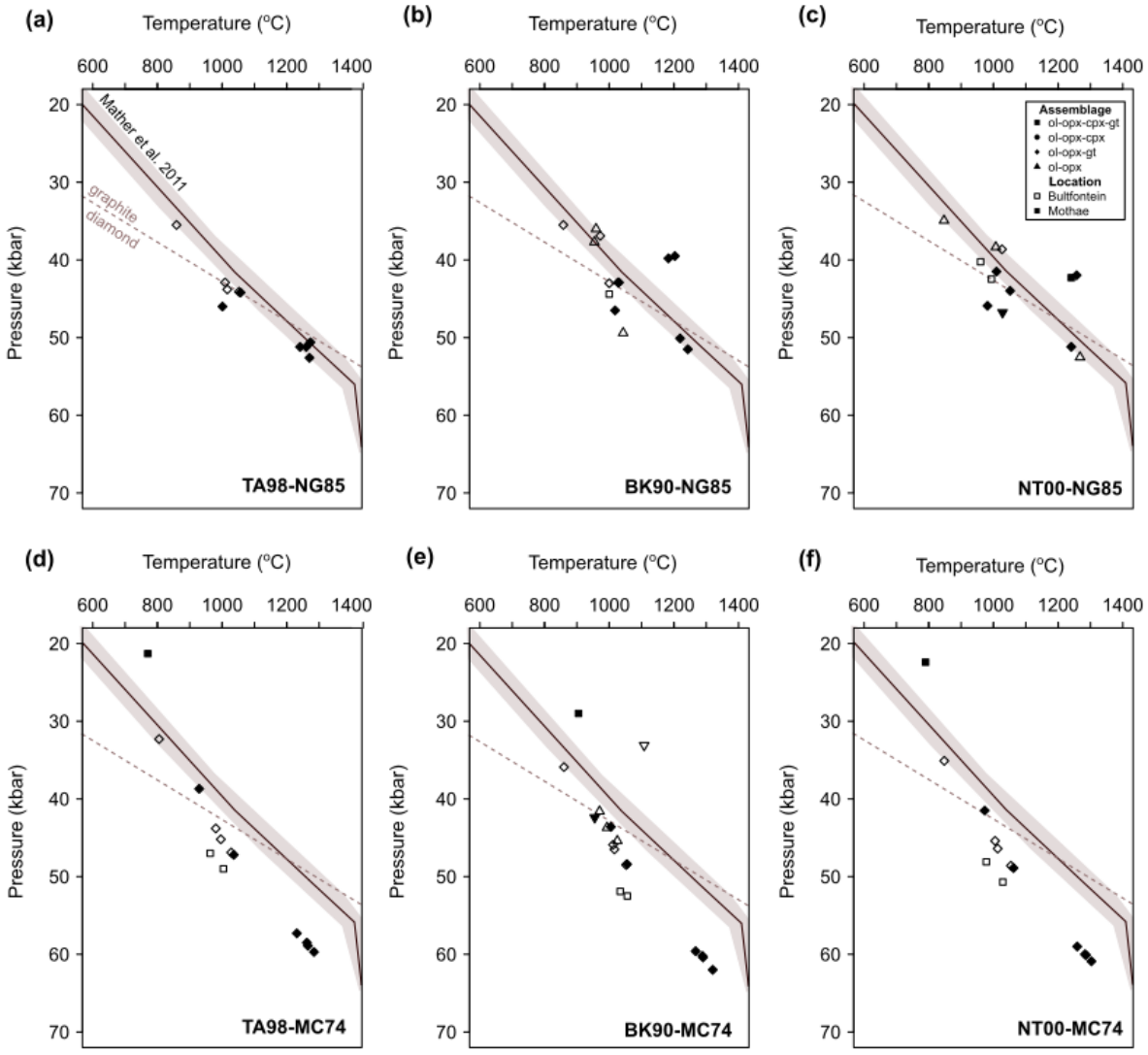

Figure 4.3 *The PT estimates of the Bultfontein and Mothae xenoliths using a range of geothermobarometers plotted against the Bultfontein geotherm constrained using coarse and porphyroclastic xenoliths by Mather* et al. *(2011) where: T_p = 1315 °C; and surface heat production = 43 mWm^{-2}. The range compare the geotherms produced using the two-pyroxene thermometer (TA98) and two single phase thermometers: Ca-in-orthopyroxene (BK90) and En-in-clinopyroxene (NT00) with the Orthopyroxene-Garnet Al-exchange barometer (NG85) and the Al-in-orthopyroxene barometer (MC74 - independent of garnet). (a) TA98-NG85; (b) BK90-NG85; (c) NT00-NG85; (d) TA98-MC74; (e) BK90-MC74; (f) NT00-MC74*

4.5 Perturbed conductive geotherm

Early studies of mantle xenoliths from northern Lesotho identified that there are a subset of sheared lherzolites that exhibit very high temperatures, of up to 200 °C above the steady state geotherm, at the base of the lithosphere (> 180 km; Boyd & Nixon 1973; Gurney *et al.* 1980; Mitchell 1984). The majority of these high-*T* lherzolites have been found in the Thaba Putsoa kimberlite, which also transports xenoliths from the greatest depths (200 km; Boyd & Nixon 1973) Original hypotheses proposed that the array of high-*T* sheared lherzolites represented an inflected geotherm (Boyd, 1973; Finnerty & Boyd, 1984, 1987; Gurney *et al.*, 1980). It was later agreed, however, that the inflected geotherm was not a steady state geotherm, just a perturbation to it (Mitchell, 1984). Multiple hypotheses were proposed to explain this

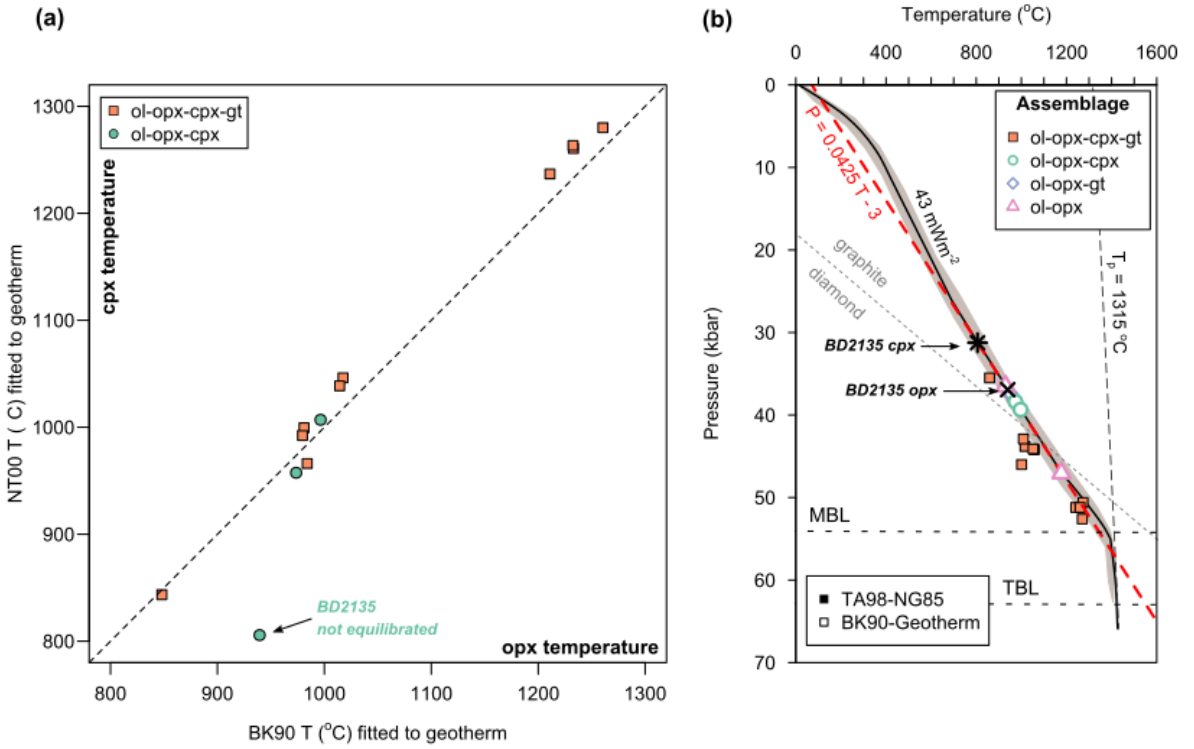

Figure 4.4 *(a) Comparison of the temperatures calculated using the BK90 Ca-in-orthopyroxene thermometer and the NT00 En-in-clinopyroxene thermometer. In all but one sample, the orthopyroxene and clinopyroxene give the same equilibration temperature. The orthopyroxene and clinopyroxene in BD2135 (spinel harzburgite, with exceptionally enriched clinopyroxene) are not in equilibrium. (b) Equilibration pressure and temperature of the Bultfontein and Mothae xenoliths, alongside the geotherm for the Kaapvaal fitted to a large array of coarse and porphyroclastic xenoliths by Mather* et al. *(2011). The solid squares represent the garnet and clinopyroxene-bearing peridotites that were applicable for the TA98-NG85 thermometer barometer combination. The temperatures of both the garnet-harzburgites and spinel-peridotites have been calculated using BK90 and fitted to an approximation of the geotherm between 800 - 1300 °C (P = 0.0425 T - 3). The different temperatures (and hence pressures) of the orthopyroxene and clinopyroxene are shown and labelled separately.*

perturbation including the slow upwelling of partially melted material (Boyd & Nixon, 1978) and the establishment of short-term horizontal temperature gradients around magmatic intrusions (Gurney *et al.*, 1980; Mitchell, 1984). Improvement of thermometers and barometers, specifically accounting for minor element behaviour, over the next two decades lead to the re-evaluation that the high-T sheared lherzolites do not represent an inflected geotherm but rather preserve localised thermal perturbations (Bell *et al.*, 2003b; Carswell & Gibb, 1980, 1987; Lazarov *et al.*, 2009; Nimis & Grütter, 2010). It was established that initial calculations over-estimated the *PT* conditions of the deformed xenoliths, but nevertheless a thermal anomaly is evident in a small subset of lherzolites from northern Lesotho regardless of the thermometer used. Bell *et al.* (2003b) attributed the high temperatures to a thermal disturbance in the Mesozoic, initiated at 180 Ma in the east, marked by the onset of Karoo magmatism, which then swept westward over the next 110 Ma. However, *PT* estimates of sheared xenoliths from other Lesotho kimberlites (Letseng, Mothae, Kao) suggest that there is no consistently perturbed geotherm beneath the whole Lesotho region, only localised perturbations (Lock & Dawson, 2013; Simon *et al.*, 2003). This could mean that a localised heating event associated with the thermal aureole of an intrusion or percolating proto-kimberlite melt could be responsible for the highly spatially variable thermal conditions towards the base of the lithosphere beneath the eastern edge of the Kaapvaal craton.

Despite the presence of high-*T* sheared lherzolites in the xenoliths from Mothae in this study, the equilibration *PT* conditions show that they represent mantle on the steady state geotherm rather than evidence of the localised thermal perturbation to higher temperatures. The sheared garnet lherzolites have equilibrated at 52 kbar (~ 165 km) which is potentially above the source of the thermal perturbation which has been identified at pressures greater than 60 kbar in xenoliths from other kimberlites in Lesotho.

4.6 Final *PT* estimates

A number of different barometer and thermometer combinations were used to estimate the equilibration pressure and temperature conditions for each of the Bultfontein and Mothae xenoliths. In this chapter the relative propriety of each geothermobarometer was assessed based on the state of equilibrium in the xenoliths (assessed in Chapter 3). The preferred *PT* estimates (Table 4.2) are those calculated using the two-pyroxene thermometer (TA98; Taylor 1998) and the Al in orthopyroxene and garnet barometer (NG85; Nickel & Green 1985). Where garnet and/or clinopyroxene are missing from the mineral assemblage or not in equilibrium with orthopyroxene, the single orthopyroxene (BKN90; Ca-in-orthopyroxene; Brey *et al.* 1990) and single clinopyroxene thermometer (NT00; En-in-clinopyroxene; Nimis & Taylor 2000) were chosen as an appropriate alternatives. The pressure was estimated by fitting the temperature to an approximation of the Kaapvaal geotherm (Mather *et al.*, 2011). The Bultfontein and Mothae xenoliths cover a pressure range of 30 - 52 kbar and temperature range of 800-1270 °C, with those from Mothae extending to the highest temperatures and pressures .

In the published literature, cratonic mantle xenoliths are often divided into two main populations based on their equilibration temperature and texture (Nixon, 1973). Low-*T* peridotites are generally coarse grained, exhibit low levels of deformation and equilibrated at $T < 1100$ °C. High-*T* peridotites, in comparison, are porphyroclastic, highly deformed and yield equilibration temperatures between 1100-1500 °C (Boyd & Nixon, 1973; Finnerty & Boyd, 1987; Harte, 1983; Nixon, 1973). In this study there are four xenoliths from Mothae that fall into the latter, high-*T* population, but the majority are low-*T* peridotite. There is, however, some overlap in the texture of the xenoliths, for example the low-*T* orthopyroxene-rich garnet harzburgite BD1672 has a slightly porphyroclastic texture and BD3021 is completely sheared.

The sample suite spans a large section of the Kaapvaal sub-cratonic lithospheric mantle through the spinel and garnet stability fields to depths close to the base of the lithosphere. As a result it is possible to identify any stratigraphic or temperature controls on volatile storage in the SCLM.

	Thermometer/ Barometer	TA98 (cpx-opx)	NG85 (Al-in-opx-gt)	BKN90 (Ca-in-opx)	Fitted to geotherm	NT00 (En-in-cpx)	Fitted to geotherm
Sample	**Mineral assemblage**	**T (°C)**	**P (kbar)**	**T (°C)**	**P (kbar)**	**T (°C)**	**P (kbar)**
Mothae							
Low-T							
BD2133	ol+opx			929	36.5		
BD2135	ol+opx+cpx			939	36.9	806	31.2
BD2122	ol+opx+cpx+gt	1001	46				
BD2125	ol+opx+cpx+gt	1057	44.2				
High-T							
BD2124	ol+opx+cpx+gt	1241	51.2				
BD2126	ol+opx+cpx+gt	1273	50.6				
BD2128	ol+opx+cpx+gt	1260	51.2				
BD2170	ol+opx+cpx+gt	1270	52.6				
Bultfontein							
BD3670	ol+opx			1177	47.0		
BD1141A	ol+opx+cpx			974	38.4	1007	39.8
BD1153	ol+opx+cpx			996	39.4	992	39.2
BD1140	ol+opx+cpx+gt	859	35.5				
BD1152	ol+opx+cpx+gt	1016	43.8				
BD1672	ol+opx+cpx+gt	1052	44.1				
BD1999	ol+opx+cpx+gt	1009	42.9				
BD3021	ol+opx+gt			998	39.4		
BD3028	ol+opx+gt			969	38.2		
BD3676	ol+opx+gt			953	37.5		

Table 4.2 *Preferred PT estimates for the Bultfontein and Mother xenoliths.*

Chapter 5

Xenolith history: melt depletion and metasomatism

5.1 Chapter outline

In Chapter 3, five distinct groups of clinopyroxene-bearing peridotites were identified on the basis of lithology, petrographic observations and mineral chemistry, with particular emphasis on the clinopyroxene and garnet trace-element signatures. In this chapter, each type of peridotite is investigated to identify the origin of the five different chemical fingerprints.

5.2 Introduction

The chemistry of mantle peridotite can change as a consequence of two main processes: partial melting and melt-rock interaction. Many studies have established that the peridotites from the Kaapvaal craton represent the mantle residue of 20-30% partial melting of the primitive mantle (e.g. Boyd & Mertzman 1987; Lazarov *et al.* 2009; Pearson *et al.* 1995a; Shu & Brey 2015; Shu *et al.* 2013; Walter 1998) but most exhibit evidence of later melt-rock reaction (e.g. Bell *et al.* 2005; Gibson *et al.* 2008; Kelemen *et al.* 1998; Simon *et al.* 2007; Stachel *et al.* 1998). In the sub-cratonic lithospheric mantle (SCLM), small-fraction melts and fluids have been metasomatising the peridotite for billions of years. These metasomatic agents can have a variety of compositions, the breadth of which is evident in the compositional array of inclusions in cratonic diamonds and extends between silicate, carbonatite and brine endmembers (Shirey *et al.*, 2013). The range of possible compositions of metasomatic agents, generates a corresponding range of metasomatic signatures in the lithospheric mantle. The level of metasomatic enrichment in mantle peridotite is intrinsically linked to the volume of the metasomatic agent because the initial melt fraction controls the absolute concentration of the most strongly incompatible trace-elements in the metasomatic agent and the melt:rock ratio controls the flux of trace-elements into the mantle wall-rock. Most metasomatic agents in the SCLM are low volume, which inherently results in a low melt:rock ratio. The local melt:rock ratio during metasomatism is considered to be high in a vein, and low where melt is percolating along grain boundaries and reacting with pre-existing minerals. There are three types of metasomatism that are underpinned by the different melt/fluid compositions and the volume of the metasomatic agent: modal metasomatism, cryptic metasomatism and stealth metasomatism.

1. **Modal Metasomatism**
   Modal metasomatism describes the process whereby new phases are added to the mineral assemblage (Dawson, 1984). These can crystallise directly from the metasomatic agent or form during the reaction of the melt/fluid with a pre-existing phase. Modal metasomatism may result in the

formation of volatile-rich phases such as phlogopite, amphibole, apatite and calcite. The proportion of metasomatic minerals depends on the melt fraction, and the mineral assemblage alludes to the composition of the metasomatic melt. There are two suites of xenoliths that describe the two most common (and well understood) metasomatic assemblages in the SCLM, these are the MARID suite (Mica-Amphibole-Rutile-Ilmenite-Diopside (Dawson & Smith, 1977; Fitzpayne *et al.*, 2018b; Konzett *et al.*, 1998; Kramers *et al.*, 1983; Sweeney *et al.*, 1993)) and the PIC suite (Phlogopite-Ilmenite-Clinopyroxene; Fitzpayne *et al.* 2018b; Grégoire *et al.* 2002).

2. **Cryptic Metasomatism**
   Cryptic metasomatism describes the process whereby melt-rock reaction only changes the chemistry of pre-existing mantle minerals (Dawson, 1984). This style of metasomatism is most apparent in the trace-element signature of mantle minerals, and particularly in clinopyroxene and garnet because the trace-elements (e.g. Rare Earth Elements; REE) are more compatible in clinopyroxene and garnet, than olivine and orthopyroxene. Metasomatism tends to enrich the minerals in the REEs, although the behaviour of the heavy rare-earth elements (HREE; e.g. Er, Yb, Lu) depends on whether garnet is present because the HREE are strongly compatible in garnet. If garnet is in equilibrium with the other minerals, they will exhibit a depletion in HREE and hence show strong fractionation trends between the light rare-earth elements (LREE; e.g. La, Ce) and the HREE. Specific elements can be very helpful in determining the nature of the metasomatic agent, for example the behaviour of the high-field-strength elements (HFSE; Zr, Hf, Nb, Ta, Ti) differ drastically and systematically depending on the composition of the metasomatic agent (Rudnick *et al.*, 1993).

3. **Stealth Metasomatism**
   Stealth metasomatism is a more recently defined process whereby garnet and/or clinopyroxene are the only new minerals that are added to the peridotite assemblage during melt-rock reaction (O'Reilly & Griffin, 2013). No indicative metasomatic minerals (e.g. amphibole, phlogopite, carbonate) are introduced during stealth metasomatism, therefore, the term 'stealth metasomatism' comes from the fact that the only minerals to crystallise during melt-rock are those that are already present in mantle lherzolite. Stealth metasomatism highlights the importance of mantle re-fertilisation by metasomatic agents.

Melts and fluids in the deep mantle can originate from many processes such as: plume-related partial melting in the asthenosphere; redox melting of carbonated peridotite; melting at the H_2O or CO_2- rich peridotite solidus or from subduction-related processes, e.g. melting of subducted sediments or basalt and release of fluids by dehydration (Brey *et al.*, 2009; Dasgupta, 2018; Fitzpayne *et al.*, 2019; Foley *et al.*, 2009; Hirschmann, 2000; Regier *et al.*, 2018). The present-day Kaapvaal craton stabilised at 2.6 Ga (De Wit *et al.*, 1992; Poujol *et al.*, 2003), following the closure of a subduction zone and continental collision of the Witswatersrand and Kimberley blocks at 2.9 Ga (Figure 1.7; Schmitz *et al.* 2004; Shirey *et al.* 2013 and references therein). A signature related to this subduction event, or any previous event, was therefore imparted a long time prior to incorporation of the xenoliths in Jurassic and Cretaceous kimberlites, such as the Bultfontein and Mothae kimberlites studied here. Sometimes the timing of metasomatism can be constrained if the xenolith contains a natural clock, for example metasomatic minerals with significant quantities of radiogenic isotopes whose decay can be dated (e.g. U-Pb, Lu-Hf, Sm-Nd and Rb-Sr in zircon/perovskite/titanite/sulfides; Giuliani *et al.* 2014b; Griffin *et al.* 2014b; Li *et al.*

2010; Pearson *et al.* 1995b; Woodhead *et al.* 2009, 2017; Zhang *et al.* 2005) or zoning in minerals that can be dated using diffusion modelling (e.g. Griffin *et al.* 1989; Jackson & Gibson 2018; Jollands *et al.* 2018). The ability to constrain the timing of metasomatism can help resolve the processes involved in generating the metasomatic agent, especially if the age coincides with a precursory magmatic or tectonic event, such as the eruption of the host kimberlite, a period of subduction or the eruption and emplacement of continental flood basalt.

This study is focused on metasomatism by small fraction melts/fluids in the sub-cratonic lithospheric mantle because they can (re)mobilise and (re)deposit volatile elements in new or existing phases. The age and tectonic quiescence of the Archaean sub-cratonic mantle make it the perfect place to study elemental storage and transport through time. In this chapter the chemical composition of the peridotite xenoliths from Bultfontein and Mothae is examined with the consideration that the different chemical signatures identified in Chapter 3 are the product of metasomatism by different agents.

5.3 Evidence for melt depletion

Peridotite xenoliths from the Kaapvaal craton represent mantle that initially formed as residues of melting (e.g. Boyd & Mertzman 1987; Gibson *et al.* 2008; Lazarov *et al.* 2009; Pearson *et al.* 1995a; Shu & Brey 2015; Shu *et al.* 2013; Simon *et al.* 2007). Melting depletes the mantle in the incompatible elements, and the extent of this is dependent on the degree of melting (i.e. the melt fraction). High Mg# alongside low Al_2O_3 and CaO concentrations in the Bultfontein and Mothae xenoliths is indicative of their origin as the residue of melting (Chapter 3), and the re-enrichment in some elements is a result of later metasomatism. The Kaapvaal craton has been the subject of many studies that have identified melt trends overprinted by later re-enrichment during metasomatism (e.g. Boyd 1989; Kelemen *et al.* 1992, 1998; Shu & Brey 2015; Simon *et al.* 2007; Walter 1998). The Mg# and modal mineral assemblage of the mantle residue after varying degrees of partial melting has been identified in a number of ways, for example using the composition of oceanic peridotites (Boyd, 1989), melting experiments on bulk peridotite (e.g. Walter 1998) and using ternary phase relationships (e.g. Kelemen *et al.* 1992). The oceanic trend of Boyd (1989) and the experimental results of Walter (1998) are shown in Figures 5.1 a and b, respectively. Boyd (1989) showed that both the abundance and Mg# of olivine increase in the mantle residue with increased degree of melting, and the same relationship was determined experimentally between the bulk Mg# and olivine abundance (Walter, 1998). The red arrows in Figure 5.1a highlight that low- and high-pressure melting of primitive mantle can have opposing effects on the modal abundance of olivine because the position of the eutectic in the ol-opx-cpx ternary is strongly pressure dependent. Kelemen *et al.* (1992) showed that low pressure melting can result in orthopyroxene crystallisation and hence inadvertently cause a slight decrease in the modal abundance of olivine. Their calculations indicate that the proportion of orthopyroxene cannot exceed a maximum of 23% due to melting processes alone, which has been backed by experimental results (e.g. Walter 1998).

Many high Mg# peridotite xenoliths from the Kaapvaal exhibit low modal proportions of olivine, and high abundances of orthopyroxene relative to the melting trend and oceanic peridotites (shaded region in Figure 5.1, e.g. Boyd 1989; Simon *et al.* 2003). The excess of orthopyroxene beyond 23% cannot be achieved by melting and therefore requires some kind of Si enrichment. The orthopyroxene-rich

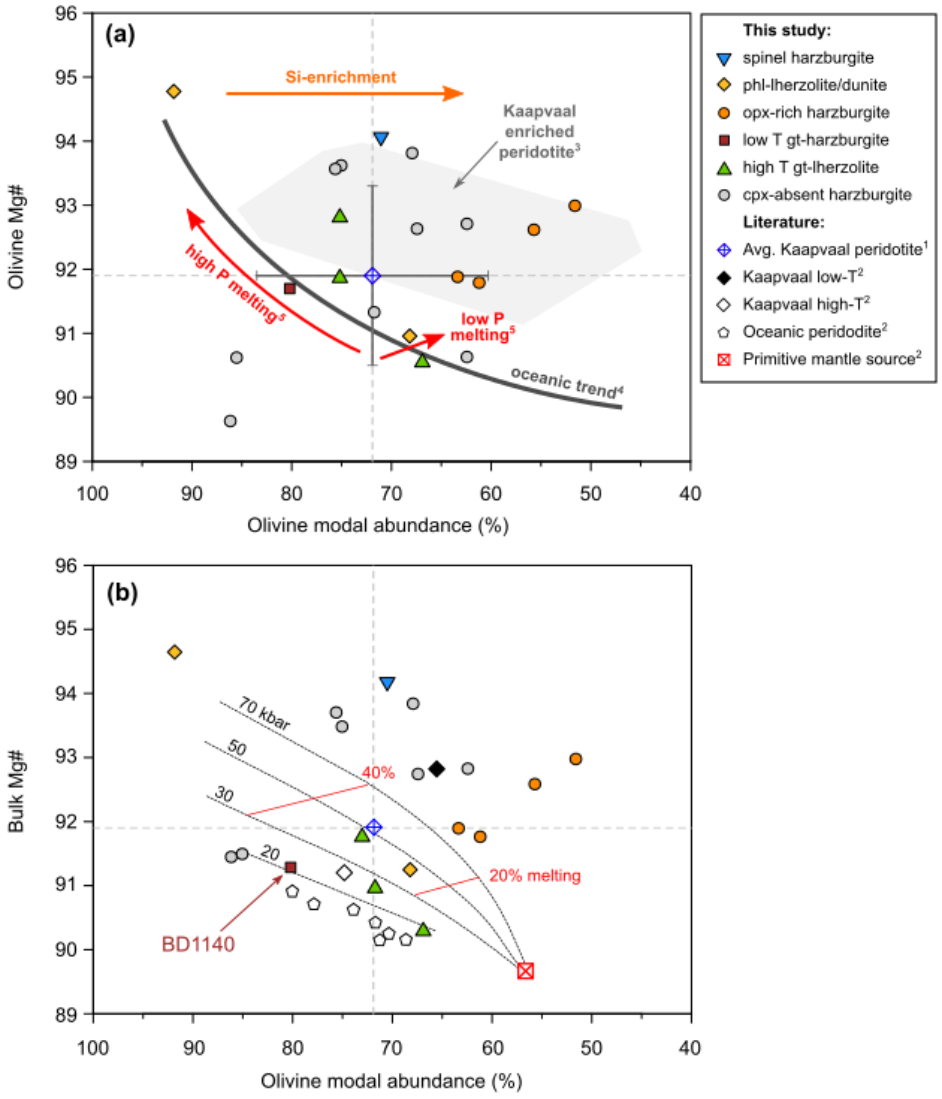

Figure 5.1 *(a) Olivine modal abundance vs. olivine Mg# (Boyd plot) showing the oceanic trend which reflects a depleted mantle residue and the region of Si-enriched Kaapvaal peridotites. (b) Olivine modal abundance vs. bulk rock Mg# with the experimentally derived mantle residue after partial melting of a primitive mantle source.* [1] *Pearson* et al. *(2003);* [2] *Walter (1998);* [3] *Simon* et al. *(2007);* [4] *Boyd (1989);* [5] *Kelemen* et al. *(1992)*

harzburgites recognised in Chapters 2 and 3 plot within this field along with a number of the clinopyroxene-absent xenoliths, but a number of the Bultfontein and Mothae xenoliths, however, plot along the melting trend. The isopleths in Figure 5.1b represent the evolution of composition of the mantle residue during melting of a bulk composition marked by the red square (Walter 1998). According to these experimental results, the average Kaapvaal peridotite composition (blue open diamond, Pearson *et al.* 2003) equates to 25-30% melting at 50 kbar. The orthopyroxene-poor garnet harzburgite (BD1140) and the garnet lherzolites plot within the range of the melting residues.

The composition of the mantle residue following partial melting can be modelled using the fractional and batch melting equations from Johnson *et al.* (1990). Equations 5.1 and 5.2 are used to calculate the concentration of a chosen element (i) of each mineral (C_i^{min}) in the mantle residue after F% melting during

fractional and batch melting, respectively, and the results are compared to the measured composition of the Bultfontein and Mothae xenoliths.

Fractional melting:

$$\frac{C_i^{min}}{C_i^0} = \left[1 - \frac{PF}{D_i^0}\right]^{\frac{1}{P}} \times \left[\frac{D_i^{min/melt}}{D_i^0 - PF}\right] \tag{5.1}$$

Batch melting:

$$\frac{C_i^{min}}{C_i^0} = \left[\frac{D_i^{min/melt}}{D_i^0 + F(1-P)}\right] \tag{5.2}$$

where :

C_i^0: Bulk mantle composition (Pyrolite, McDonough & Sun 1995)
$D_i^0 = \sum D_i^{min/melt}.X_i^{min}$: Bulk partition coefficient
X_i^{min}: Modal volume of each mineral
D_i^{min}: Mineral/melt partition coefficient
F: Melt fraction
$P = \sum D_i^{min/melt}.p^{min}$: weighted bulk partition coefficient
p^{min}: Melt mode - proportion of the mineral entering the melt

The behaviour of Ti and Zr relatively is well understood for all four mantle phases during partial melting. Figure 5.2 shows the calculated Ti and Zr concentrations in olivine, orthopyroxene, clinopyroxene and garnet in the mantle residue during fractional and batch melting of the primitive mantle source against the Ti and Zr concentrations in the Bultfontein and Mothae xenoliths. The olivine and orthopyroxene are extremely depleted in Zr relative to the primitive mantle source, and most are depleted in Ti. The phlogopite-lherzolite and dunite contain olivine and orthopyroxene that are enriched in Ti. All of the clinopyroxene in the Bultfontein and Mothae xenoliths are enriched in Zr relative to a melt depleted mantle residue, with the exception of the high-T garnet lherzolites. The orthopyroxene-rich harzburgites contain garnets enriched in Zr, while the garnet in the lherzolites are enriched in both Zr and Ti. The Ti and Zr concentrations in the olivine and orthopyroxene from the high-T garnet-lherzolites and the low-T garnet-harzburgite are consistent with an origin as a mantle residue of 25% partial melting, matching the observations from Mg# and olivine abundance (Figure 5.1)

The depletion in the Bultfontein and Mothae xenoliths is indicative of an initial melt extraction event but there is evidence for later re-enrichment in at least one phase in all xenoliths. Figures 5.1 and 5.2 suggest that the orthopyroxene-poor low-T garnet-harzburgite and the high-T garnet lherzolites could represent mantle residue with the metasomatic addition of clinopyroxene in low temperature samples, and of garnet in high temperature samples, but all other types display evidence of enrichment in major elements (e.g. Si) and trace-elements (e.g. Ti, Zr). Figure 5.3 compares the clinopyroxene and garnet compositions observed in the Bultfontein and Mothae xenoliths with the calculated composition of clinopyroxene and garnet in the mantle residue after 0-30% fractional melting calculated using Equation 5.1 and the

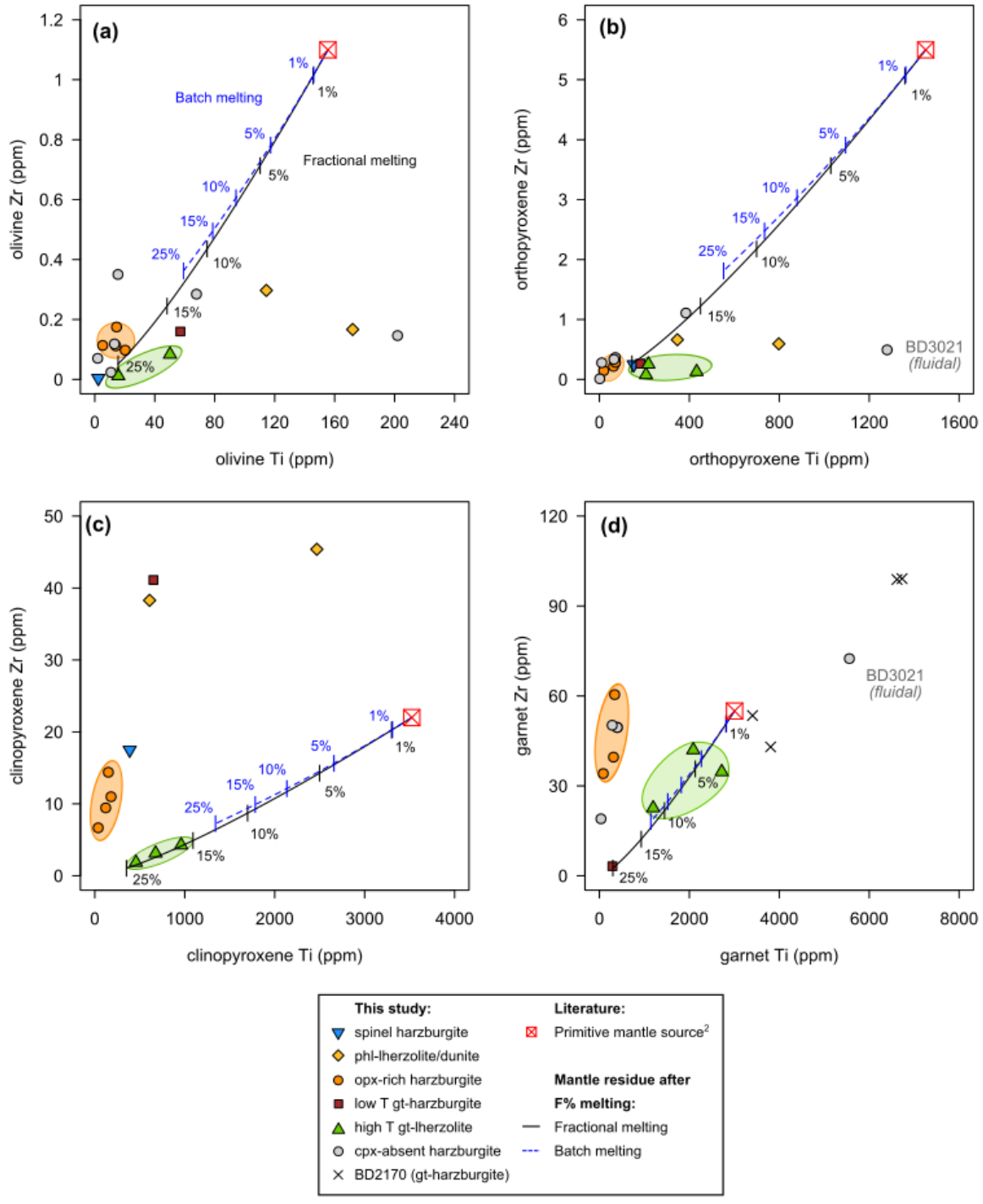

Figure 5.2 *Ti vs. Zr for (a) olivine; (b) orthopyroxene; (c) clinopyroxene and (d) garnet for the Bultfontein and Mothae xenoliths. The lines represent the composition of the mantle residue trends during fractional (solid line) and bulk (dashed line) melting of a primitive mantle source (McDonough & Sun, 1995). Tick marks represent the residue at 1, 5, 10, 15 and 25% melting. The mantle residue compositions is calculated using Equations 5.1 and 5.2 starting with bulk peridotite with the modal proportions of 55% ol; 20% opx; 15% cpx and 10% gt and the melting modes established by Walter (1998) for melting in the garnet stability field of 26% ol; 50% cpx and 24% gt.*

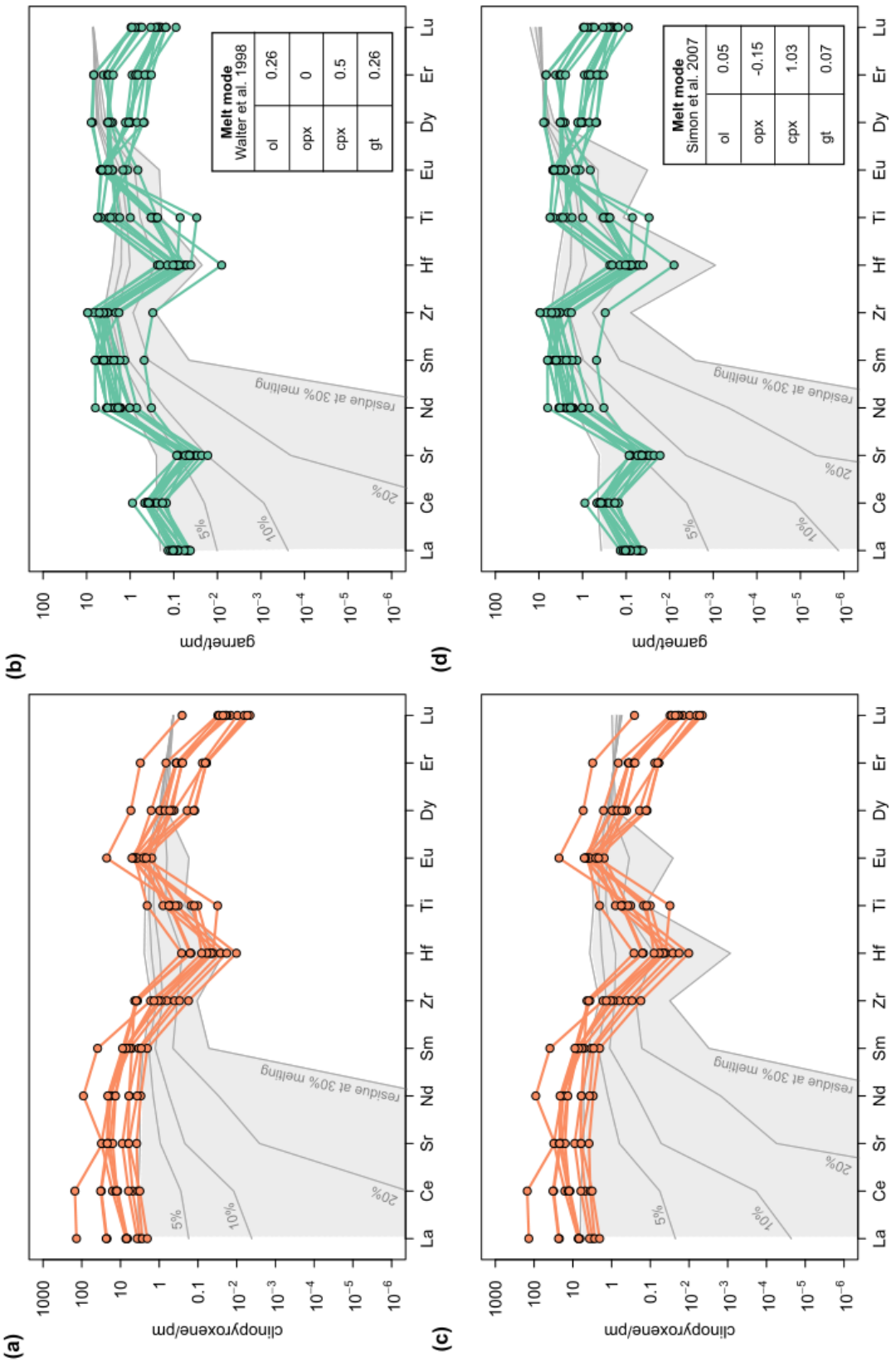

Figure 5.3 *(continues on next page)*

Mineral	Olivine	Orthopyroxene	Clinopyroxene	Garnet
Modal %	0.55	0.2	0.15	0.1
Melt Mode[1]	0.26	0	0.5	0.24
Melt Mode[2]	0.05	-0.15	1.03	0.07
$\mathbf{D}^{min/melt}$				
La	0.000007	0.0001	0.06	0.0035
Ce	0.00001	0.0009	0.07	0.005
Sr	0.0064	0.0034	0.124	0.0099
Nd	0.00007	0.009	0.178	0.052
Sm	0.0007	0.02	0.293	0.25
Zr*	0.01	0.05	0.2	0.5
Hf	0.0005	0.02	0.23	0.24
Ti	0.015	0.14	0.34	0.29
Eu	0.00095	0.03	0.32	0.4
Dy	0.004	0.06	0.38	2.2
Er	0.009	0.07	0.37	3.6
Lu	0.023	0.11	0.43	7

Table 5.1 *Parameters used in the melting equations. Melt mode*[1] *established by Walter (1998) in partial melting experiments at 7GPa; Melt mode*[2] *accounts for orthopyroxene addition during melting at lower pressure (Johnson* et al.*, 1990; Simon* et al.*, 2007).* $D^{min/melt}$ *values from Simon* et al. *(2007) and *Johnson* et al. *(1990) where marked with an asterisk.*

parameters given in Table 5.1. At the previously estimated 20-30% fractional melting of the primitive mantle source there is a significant depletion in the LREE concentration in the clinopyroxene and garnet in the mantle residue which is not observed in the Bultfontein and Mothae clinopyroxene and garnet. The LREE enrichment and HREE depletion in both clinopyroxene and garnet is, therefore, evidence for re-enrichment of the mantle by metasomatism; this changes the composition of pre-existing minerals or precipitates secondary clinopyroxene and garnet (e.g. Simon *et al.* 2007, 2003). The remainder of this chapter examines the composition of the metasomatic agent that has introduced clinopyroxene and garnet to the sub-cratonic lithospheric mantle in the Bultfontein and Mothae xenoliths.

5.4 Metasomatic agents in the sub-cratonic mantle

Clinopyroxene is a common metasomatic phase, and the fact that each type has a different trace-element signature implies that the clinopyroxenes have either crystallised from or reacted with different metasomatic agents. The chemistry of all five types of clinopyroxene-bearing peridotite in the Bultfontein and Mothae xenoliths shows some evidence of secondary enrichment relative to the calculated composition of the depleted mantle residue. The chemistry of clinopyroxenes in the Bultfontein and Mothae xenoliths is akin to those that formed as a result of metasomatism. When trying to assess the nature of the metasomatic

Figure 5.3 ***(previous page)*** *trace-element patterns for (a,c) clinopyroxene and (b,d) garnet in the Bultfontein and Mothae xenoliths. The grey field shows the calculated composition of the mantle residue after 0-30% fractional melting of a primitive mantle source. Two models are compared in (a,b) and (c,d) for melting at high pressure and low pressure, respectively. (a,b) Melt modes of Walter (1998) and modal abundances of 55% ol; 20% opx; 15% cpx and 10% gt (as in Figure 5.2); (c,d) Melt modes of Simon* et al. *(2007) that accounts for additional crystallisation of orthopyroxene during melting. The modal abundance used in (c,d) are taken from Simon* et al. *(2007) at 54% ol; 6% opx; 28% cpx and 12% garnet.*

agents, the most obvious first step is to calculate the composition of the melt or fluid in equilibrium with the clinopyroxene.

Diamond inclusions provide an insight into the possible range of composition of metasomatic agents in the cratonic mantle. Shirey *et al.* (2013) compiled the compositions of fluid inclusions in diamond, and showed that there is a continuous array between a saline endmember and carbonatite endmember, and another continuous array between the carbonatite endmember and a silicic endmember (Figure 5.4). Panel (b) in Figure 5.4 shows the corresponding range in trace-elements for different fluid compositions (Schrauder & Navon, 1994; Tomlinson *et al.*, 2009; Weiss *et al.*, 2011). Additionally, Nimis *et al.* (2016) present the first evidence of hydrous silicic fluid as films around solid inclusions in diamonds from the Siberian and Kaapvaal cratons.

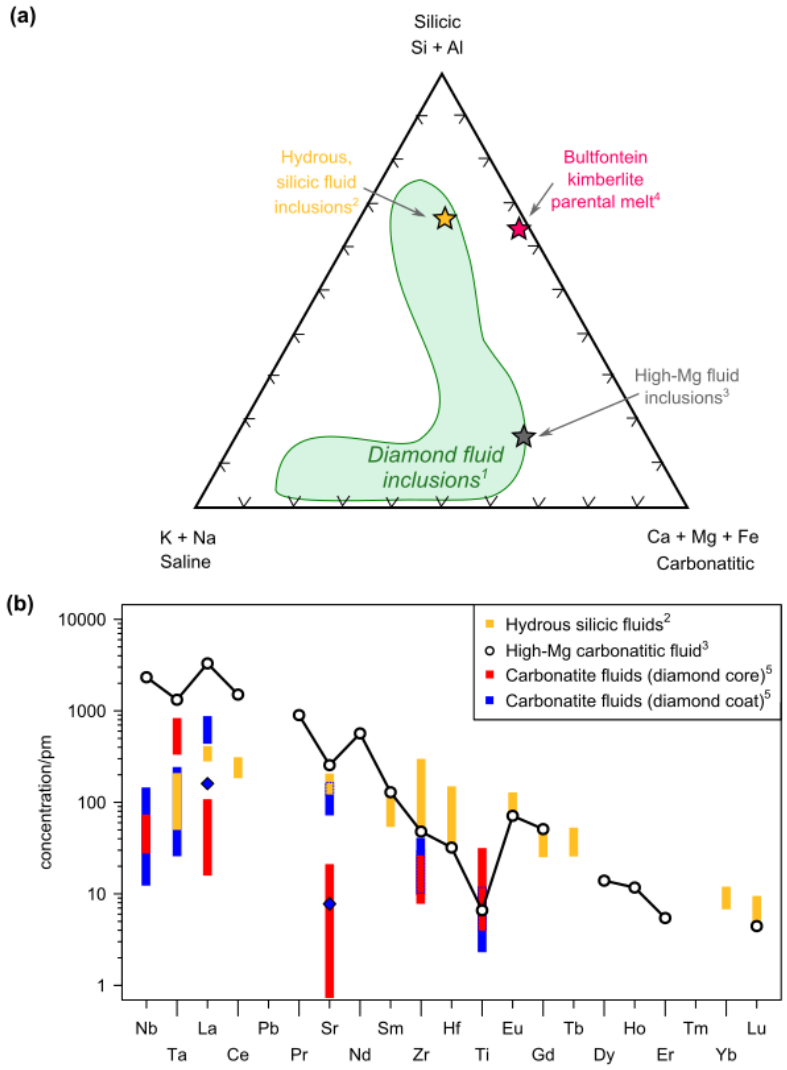

Figure 5.4 *The composition of fluid inclusions in cratonic diamonds. (a) The major element compositional array of fluid inclusions compiled by* [1]*Shirey* et al. *(2013) including data from Izraeli* et al. *(2004); Klein-BenDavid* et al. *(2004, 2007, 2009); Tomlinson* et al. *(2009). Individual compositions of hydrous silicic inclusions found in diamonds from Jwaneng, Botswana (*[2]*Schrauder & Navon 1994), high-Mg carbonatitic fluid inclusions from Udachnaya and Kankan, Siberia (*[3]*Weiss* et al. *2011) and the calculated parental melt composition of the Bultfontein kimberlite (*[4]*Soltys* et al. *2018) are plotted as stars. (b) The trace-element compositions of hydrous silica-rich fluids (Schrauder & Navon, 1994); high-Mg carbonatitic fluids (Weiss* et al.*, 2011) and carbonatitic fluid inclusions (Tomlinson* et al.*, 2005).*

There are two other important melt compositions in the sub-cratonic mantle that can be sampled at the surface: kimberlites and carbonatites. Soltys *et al.* (2018) have combined petrographic and chemical observations to model the predicted major element composition of the parental melt to the Bultfontein kimberlite. Their results suggest that this is a transitional silico-carbonatite melt (Figure 5.4a) which becomes progressively enriched during ascent, in agreement with the models of Brooker *et al.* (2011) and Keshav *et al.* (2005). The trace-element composition for the Bultfontein kimberlite has been measured from an aphanitic pipe by Roex *et al.* (2003) and is shown together with the composition of high-density fluid (HDF) inclusions from Udachnaya and Kankan diamonds (Weiss *et al.*, 2009, 2011) in Figure 5.5a. The similarities between the diamond fluid inclusions and kimberlite melts demonstrate the intrinsic relationship between metasomatic agents and the melts erupting at the surface.

The prevalence of carbonatitic fluids in diamond inclusions also requires the consideration of carbonatite melts as a metasomatic agent. Bizimis *et al.* (2003) measured the trace-element concentration of eleven global carbonatites. It can be seen from Figure 5.5b that globally erupted carbonatite melts are enriched in the MREE and HREE relative to kimberlite melts. This enrichment reflects the greater depth of source of kimberlite relative to carbonatite melts. The presence of garnet in the kimberlite melt source region produces a strong fractionation of the HREE, which is observed in the steeper gradient of the REE pattern. Nevertheless, the composition of surface carbonatite melts is a useful indicator of the fractionation of different elements during melt-rock reaction between a carbonatitic melt and mantle peridotite.

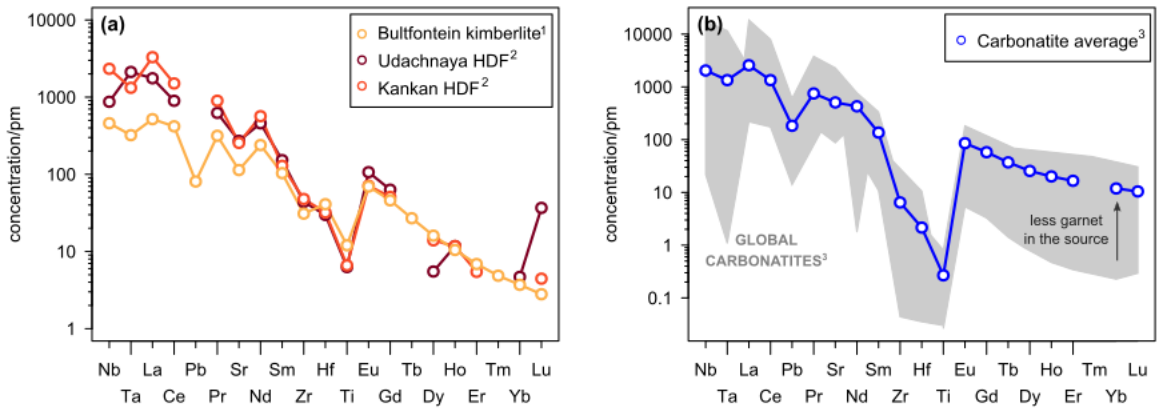

Figure 5.5 *(a) The composition of the Bultfontein kimberlite measured in an aphanitic pipe ([1]Roex* et al. *2003) compared to the high density fluid (HDF) high-Mg carbonatitic fluid inclusions from the Udachnaya and Kankan kimberlites ([2]Weiss* et al. *2011). (b) Average global carbonatite composition in blue, with the range of compositions measured in the grey region ([3]Bizimis* et al. *2003).*

5.5 Equilibrium melts

In this section, the composition of the melt in equilibrium with each clinopyroxene signature, identified in 3, are calculated according to Equation 5.3.

$$C_i^{melt} = \frac{C_i^{cpx}}{D_i^{cpx/melt}} \tag{5.3}$$

The calculated equilibrium melts are then compared to the array of potential metasomatic agents, such as the kimberlite and carbonatite melts as outlined above. The partition coefficients (D values) used to calculate the composition of the melt in equilibrium with clinopyroxene are compiled from the literature and also calculated using the lattice strain model (Blundy & Wood, 1994).

5.5.1 Published mineral-melt partition coefficients

Numerous sets of mantle $D^{cpx/melt}$ values are available in the published literature; most of these are determined from experimental run products but some are calculated from observations of elemental partitioning in fully equilibrated mantle peridotites. This study uses experimentally-determined sets of partition coefficients because the assessment of equilibrium of natural xenoliths is typically based upon major-element concentrations rather than the slow diffusing, large REE and other incompatible trace-elements. There are, however, limitations intrinsic to the experimentally-determined coefficients. Firstly, the pressure and temperature conditions do not match the range of conditions in this study. Although pressure does not have a large control on partitioning, mineral/melt partition coefficients are inversely correlated to temperature (Blundy & Wood, 1994). Therefore, using one set of partition coefficients (appropriate at a fixed pressure and temperature) to calculate equilibrium melts from clinopyroxene that have equilibrated over a pressure range of 3 GPa and temperature range of 400 °C introduces uncertainty to the calculated concentration and hence the perceived level of enrichment or depletion. The relative values of partition coefficients of different elements should be unaffected by temperature, therefore the shape of the primitive-mantle-normalised trace-element patterns can be used with confidence. The second limitation for consideration is the fact that the experiments are carried out in a closed system with a fixed bulk composition, this is an important limitation that must be considered when interpreting the results of equilibrium melt calculations. Each experiment considers the partitioning behaviour of elements between clinopyroxene and a specified melt composition, for example a carbonatite melt (e.g. Dasgupta *et al.* 2009; Klemme *et al.* 1995), a silicate melt (e.g. Hart & Dunn 1993; Suzuki *et al.* 2012) or a silico-carbonatite melt (e.g. Keshav *et al.* 2005). This creates a somewhat circular argument, for example if the cpx/melt partition coefficients are calculated for a carbonatite melt then the application of these coefficients to the measured clinopyroxene concentrations might also produce a carbonatitic melt composition. To try and account for this, sets of published partition coefficients for a range of melt compositions have been used (Table 5.2). A final limitation apparent in Table 5.2 is that each published study analyses a limited list of elements that is not always comprehensive nor complementary to this study.

5.5.2 Lattice strain model

An alternative set of partition coefficients has been calculated using the lattice strain model (Equation 5.4; Blundy & Wood 1994, 2003). The lattice strain model is underpinned by the theory that trace-element ions enter specific lattice sites in minerals and their partitioning is controlled by charge and size of the ion relative to the lattice site (Blundy & Wood, 2003; Goldschmidt, 1937). The model acts to minimise elastic surplus in the lattice produced by substituting different sized ions into to different lattice sites. Blundy & Wood (2003) summarise the model as follows: "The elastic strain energy is inversely correlated with the logarithm of the partition coefficient, which, for a specific lattice site, should vary near-parabolically

	Ht93	Km95		Ds09	Kv05	Gr92	Si07
T °C	1380	1100	1580	1265	1410	1240	var
P (GPa)	3	2	5	6.6	6	4	var
H_2O (wt. %)						15	
Melt comp.	alk-bas	carb	sil	carb	sil-carb	bas	var
Nb	0.0077	0.1	-	0.001	0.0052	0.0015	-
Ta	-	0.15	-	0.002	0.0035	0.014	-
La	0.0536	0.07	0.018	0.004	0.0123	0.044	0.048
Ce	0.0858	0.09	0.028	0.006	0.01	0.074	0.087
Pb	0.072	-	-	0.013	0.013	-	-
Pr	-	0.11	0.096	0.027	-	0.12	-
Sr	0.1283	0.08	0.048	-	0.05	0.2	0.125
Nd	0.1873	0.11	0.06	0.018	0.031	0.18	0.184
Sm	0.291	0.13	0.11	0.032	0.082	-	0.331
Zr	0.1234	0.48	0.04	0.059	0.016	0.065	0.12
Hf	0.256	0.16	0.074	0.18	0.035	0.15	0.25
Ti	0.384	1.42	0.18	0.21	0.15	-	0.36
Eu	-	0.22	0.11	0.039	0.1	0.29	0.386
Gd	-	0.26	0.14	0.048	-	0.24	-
Tb	-	-	0.16	-	-	0.26	-
Dy	0.442	0.29	0.2	0.07	-	0.32	0.519
Ho	-	-	0.21	-	-	0.31	-
Er	0.387	0.41	0.21	0.08	0.182	-	0.512
Tm	-	-	0.23	-	-	-	-
Yb	0.43	-	0.23	0.08	0.18	0.28	0.52
Lu	0.433	-	0.24	0.09	0.18	-	0.98

Table 5.2 *Clinopyroxene/melt partition coefficients compiled from the literature Ht93: Klemme* et al. *(1995); Km95: Klemme* et al. *(1995); Sz12: Suzuki* et al. *(2012); Ds09: Dasgupta* et al. *(2009); Kv05: Keshav* et al. *(2005); Gr92: Green* et al. *(1992); Si07: Simon* et al. *(2007). Melt composition: alk-bas: alkali basalt; carb: carbonatitic; sil: silicic; sil-carb: silico-carbonatite (kimberlite); bas: basaltic; var: variable (Si07 is a compilation from the literature).*

with ionic radius". The parabolic trend results from the fact that the elastic strain is symmetrical about an optimum ionic size (the peak of the parabola), which means that the energy penalty for accommodating an ion which is fractionally too large is the same as that for an ion too small by the same amount.

The lattice strain model provides a theoretical method to determine partition coefficients over a range of pressure and temperature conditions that are appropriate to the chemical composition of the system. A number of parameterisations for the lattice strain model are presented in the literature, in this study the parameterisations established by Liang *et al.* (2013) for REE partitioning between clinopyroxene and melt (Equations 5.5-5.7) are used to calculate the partition coefficients and corresponding equilibrium melt composition. This parameterisation was chosen because it was calibrated for mafic and ultra-mafic rocks and tested as a thermometer on well-equilibrated spinel lherzolite and harzburgite xenoliths from the continental lithosphere.

$$D_i^{pxn-melt} = D_0 exp\left\{\frac{-4\pi N_A E}{RT}\left[\frac{r_0}{2}(r_0 - r_i)^2 - \frac{1}{3}(r_0 - r_i)^3\right]\right\} \tag{5.4}$$

Clinopyroxene:

$$lnD_0 = -7.14 + 4.37X_{Al}^{T} + 1.98X_{Mg}^{M2} - 0.91X_{H_2O}^{melt} + \frac{7.19\times10^4}{RT} \tag{5.5}$$

$$r_0 = 1.066 - 0.104X_{Al}^{M1} - 0.212X_{Mg}^{M2} \tag{5.6}$$

$$E = (-2\times10^3) + (2.27\times10^3)r_0 \tag{5.7}$$

where:

T: Temperature in degrees K

N_A: Avogadro's number

R: gas constant

E: Young's modulus

r_0: optimum radius of the lattice site

r_i: radius of the substitute cation

$D_0(P,T,X)$: strain-free cation substitution (r_i=r_0)

	sp-harzburgite	**dunite**	**opx-rich gt-harzburgite**	**opx-poor gt-harzburgite**	**gt-lherzolite**
Sample	BD2135	BD1153	BD1999	BD1140	BD2124
X_{Al}^{T}	0.012	0.0086	0.012	0.0167	0.0015
X_{Mg}^{M2}	0.09	0.112	0.09	0.08	0.18
X_{Al}^{M1}	0.069	0.0795	0.069	0.0609	0.091
T °C	790	1030	1010	1240	860
La	0.423	0.126	0.051	0.293	0.06
Ce	0.726	0.197	0.08	0.488	0.088
Pr	1.15	0.29	0.119	0.756	0.122
Nd	1.679	0.402	0.164	1.087	0.164
Sm	2.65	0.615	0.247	1.704	0.245
Eu	2.96	0.694	0.276	1.912	0.278
Gd	3.129	0.753	0.295	2.043	0.307
Tb	3.128	0.784	0.302	2.074	0.329
Dy	2.952	0.783	0.295	1.998	0.341
Ho	2.655	0.753	0.278	1.841	0.344
Er	2.303	0.703	0.254	1.64	0.338
Tm	1.948	0.642	0.227	1.425	0.325
Yb	1.623	0.578	0.2	1.221	0.309
Lu	1.346	0.517	0.175	1.04	0.292

Table 5.3 *Clinopyroxene/melt partition coefficients calculated using the lattice strain model, with the parameters for each petrographic group represented by one sample.*

5.5.3 Melts in equilibrium with clinopyroxene

Using the partition coefficients compiled in the previous two sections, the composition of the melt in equilibrium with each type of clinopyroxene in the Bultfontein and Mothae xenoliths has been calculated according to Equation 5.3. The results are shown in Figures 5.6 and 5.7.

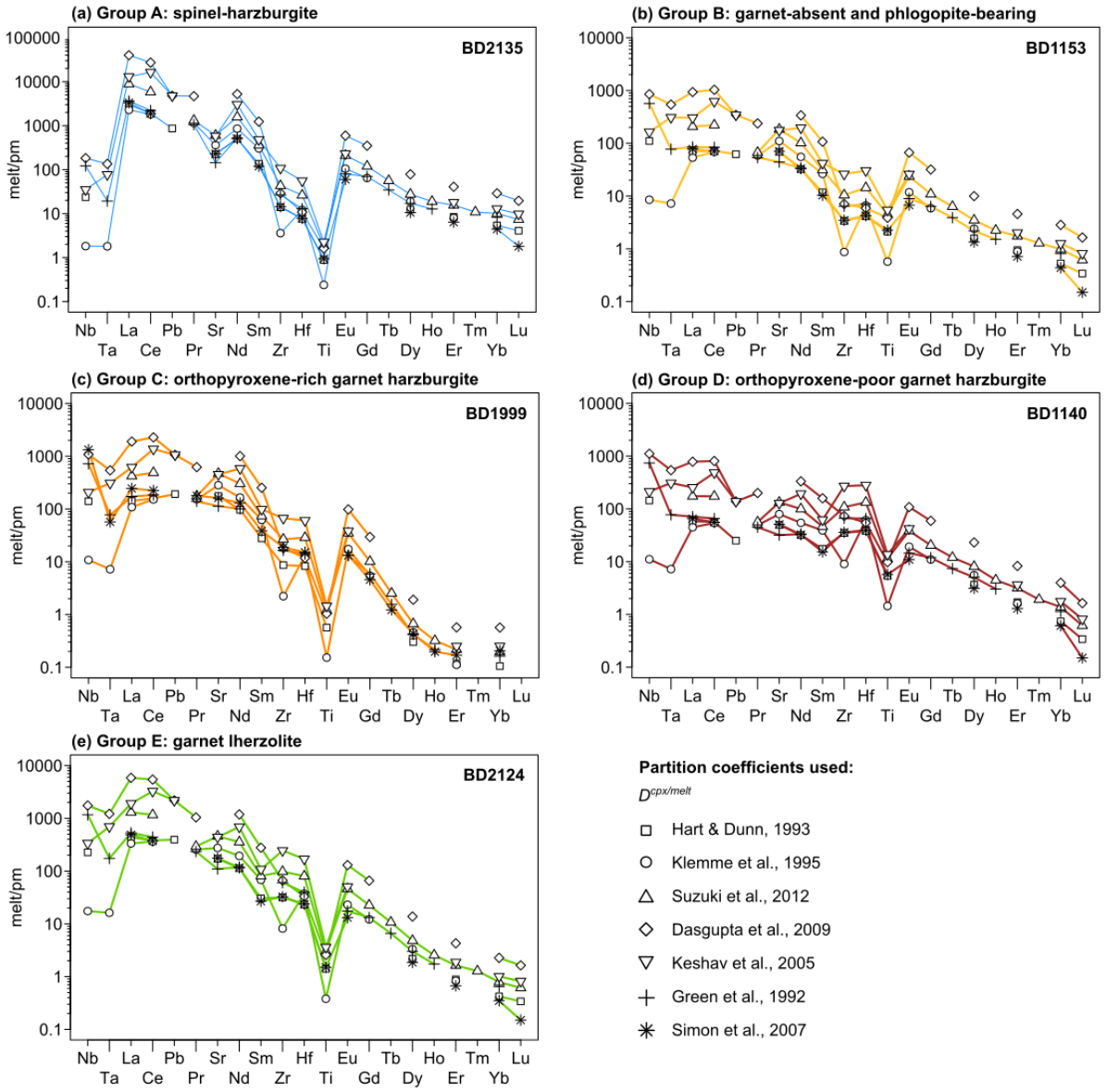

Figure 5.6 *Incompatible trace-element composition of melts in equilibrium with clinopyroxene calculated using the partition coefficients of Dasgupta* et al. *(2009); Green* et al. *(1992); Hart & Dunn (1993); Keshav* et al. *(2005); Klemme* et al. *(1995); Simon* et al. *(2007); Suzuki* et al. *(2012). The experimental conditions are detailed in Table 5.2*

The most interesting result is that the different sets of partition coefficients produce very similar results, especially in the shape of the REE pattern, although different levels of enrichment. This provides first order evidence that the relative partitioning of different elements is somewhat independent of the experimental melt composition. The main difference between the relative partition coefficients is between Zr and Hf. The $D_i^{cpx-melt}$ for a carbonatite melt, established by Klemme *et al.* (1995), fractionate Zr and Hf in the opposite sense to all other sets of partition coefficients. This confirms the use of Zr/Hf ratio

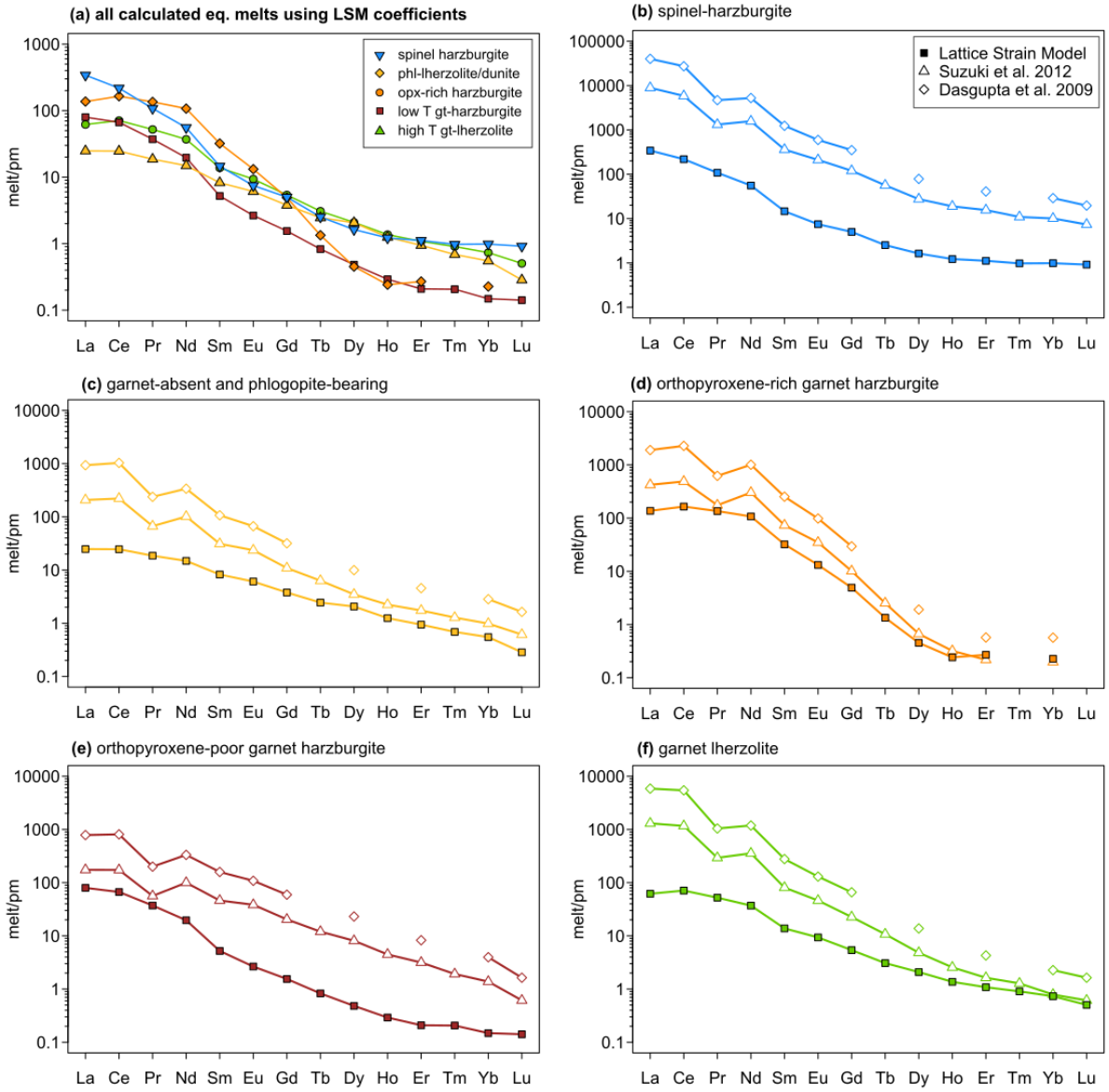

Figure 5.7 *Clinopyroxene equilibrium melt REE composition calculated using the partition coefficients calculated in this study using the Lattice Strain Model (LSM; Blundy & Wood 1994) and the parameterisations of Liang* et al. *(2013) as described by Equations 5.5:5.7. The same samples are used as in Figure 5.6. (a) Equilibrium melt REE composition using the lattice strain model. (b-f) Comparison of the lattice strain model calculated equilibrium melts with the equilibrium melt calculated using two experimentally determined partition coefficients of Suzuki* et al. *(2012) and Dasgupta* et al. *(2009).*

as an indicator for carbonatite metasomatism (Rudnick *et al.*, 1993). The equilibrium melt composition differs with the clinopyroxene type, based on all eight sets of partition coefficients. This implies the involvement of different metasomatic agents. There are some similarities between the equilibrium melts and the aforementioned metasomatic agents in the sub-cratonic mantle (e.g. Figure 5.5), for example the phlogopite-bearing, opx-poor harzburgites (BD1141A, BD1153 and BD3067) have equilibrium melts similar to a kimberlite melt, and the equilibrium melt for clinopyroxene in the spinel-harzburgite (BD2135) has similar composition to carbonatite melt.

5.6 Carbonatite melt metasomatism

There is convincing chemical and petrographic evidence for cryptic/stealth metasomatism by a very small-fraction carbonatite melt in spinel harzburgite BD2135 (Figure 5.6a). That being said, the major and trace-element signatures of the constituent mineral phases reflect rather contrasting histories. The olivine, orthopyroxene and clinopyroxene all have very high Mg# (94) which is typically thought to be representative of extreme depletion (Section 5.3) but, paradoxically the clinopyroxenes in this xenolith are the most enriched in incompatible trace-elements of all those in this study. It is safe to assume the involvement of a metasomatic agent to produce the extreme enrichment in the incompatible trace-elements, for example the REE which (except Ho) are an order of magnitude higher in the clinopyroxene from BD2135 than any other xenolith in this study, but in order to preserve a depleted major-element signature and harzburgitic mineral assemblage the melt volume must have been small, i.e. low melt:rock ratio.

The chemistry of the clinopyroxene in BD2135 provides more information about the composition of the small fraction metasomatic agent. The Ti/Eu ratio is very low (105) compared to the primitive mantle ratio (7800); this has long been used as an indicator of carbonatite metasomatism (Rudnick *et al.*, 1993). The primary evidence for carbonatite metasomatism, however, is derived from the primitive-mantle-normalised trace-element pattern and the composition of the melt in equilibrium with the clinopyroxene in BD2135. The clinopyroxene has the same trace-element pattern as that in the MARID suite of metasomatised xenoliths (Figure 5.8a). The source of the MARID suite minerals is debated, with both a magmatic and metasomatic origin suggested (Fitzpayne *et al.*, 2018a). Grégoire *et al.* (2002) proposed that there is a genetic link between the MARID suite and Group 2 kimberlites, and that the melt had a high carbonatitic component. The similarity of the clinopyroxene in BD2135 with the MARID diopside, but the lack of any other metasomatic phases corroborates the initial proposition that the xenolith represents the mantle wall-rock where a relatively small melt volume produces a cryptic metasomatic signature, elsewhere where the melt:rock ratio is high the same melt produces the MARID suite assemblage (i.e. in a vein).

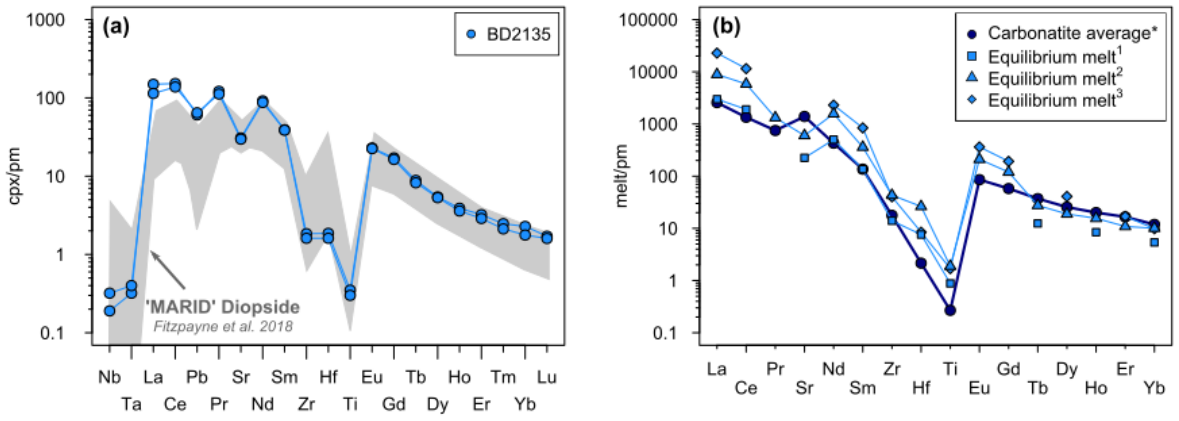

Figure 5.8 *(a) Clinopyroxene from spinel harzburgite BD2135 compared with clinopyroxene from the Mica-Amphibole-Rutile-Ilmenite-Diopside (MARID) suite of metasomatised xenoliths. MARID data from Fitzpayne* et al. *(2018a). (b) Comparison of the composition of the melt in equilibrium with BD2135 clinopyroxene and a global carbonatite average composition* (Bizimis* et al.*, 2003). Equilibrium melts plotted use the following sets of partition coefficients: [1]Hart & Dunn (1993); [2]Suzuki* et al. *(2012); [3]Dasgupta* et al. *(2009).*

The composition of the melt in equilibrium with the clinopyroxene in BD2135 has been calculated (Section 5.5.3) and supports the conclusion of Grégoire *et al.* (2002) that the melt has a high carbonatitic component. The melts calculated using the experimentally-determined partition coefficients (Dasgupta *et al.*, 2009; Hart & Dunn, 1993; Suzuki *et al.*, 2012) produce a very good match to the global average carbonatite composition published by Bizimis *et al.* (2003) (Figure 5.8b). The partition coefficients are determined at much higher temperatures (1100-1580 °C) than the equilibrium temperature of BD2135 (~ 800 °C; Table 5.2), however, the lattice strain model shows that the REE become more compatible in clinopyroxene with decreasing temperature. Therefore, the enrichment in both the clinopyroxene composition and the equilibrium melt composition relative to the global carbonatite average could be accounted for by the lower temperature conditions where BD2135 equilibrated.

As mentioned above, the major-element chemistry identifies the peridotite as a depleted harzburgite but the trace-element enrichment reveals cryptic metasomatism by a carbonatitic melt. The Mg-rich olivine and orthopyroxene can be explained if the rock is a residue of large amounts of partial melting, but there is, however, also evidence in diamond inclusions for high-Mg carbonatite fluids in the mantle (Weiss *et al.*, 2011). This discovery of high-Mg carbonatite fluids extends further the range of different metasomatic agents able to produce a similar trace-element metasomatic signature but maintain a high Mg#. Carbonatite melt is Si-under-saturated and reacts with orthopyroxene to form clinopyroxene at shallow depths (typically 20-25 kbar; Reaction 5.8; Green & Wallace 1988).

$$opx + melt^{carb} = cpx + ol + CO_2 \tag{5.8}$$

Nevertheless, the modal abundance of orthopyroxene in BD2135 is high (27%) and the proportion of clinopyroxene is extremely low (< 1%), which is not consistent with large scale carbonatite metasomatism. The clinopyroxene is present as small, isolated crystals and also as rims along orthopyroxene grain boundaries (Figure 2.5). The rims may demonstrate the occurrence of Reaction 5.8 occurring during melt percolation along grain boundaries. This textural relationship and the simultaneous occurrence of a carbonatite signature in clinopyroxene and high modal abundance of orthopyroxene is all evidence for limited melt-rock reaction by a small-fraction melt that was highly concentrated in the incompatible trace-elements but did not have the capacity to alter the major-element compositions or the modal mineral assemblage. As such, BD2135 represents the harzburgitic residue of partial melting that has been cryptically metasomatised by a small-fraction carbonatite melt.

5.7 Proto-kimberlite (silico-carbonatite melt) metasomatism

A phlogopite-bearing lherzolite (BD1141A), dunite (BD1153) and wehrlite (BD3067) show evidence of varying degrees of melt-rock reaction with a percolating proto-kimberlite (silico-carbonatite melt) melt. The degree of interaction is evident in the modal mineralogy of the three xenoliths: BD3067, shows the metasomatic-vein assemblage, i.e. a high melt:rock ratio, while BD1141A reflects a lower melt:rock ratio and BD1153 the cryptic interaction of the melt with the mantle wall-rock (Figure 5.9). All are united by their distinct clinopyroxene primitive-mantle-normalised trace-element signature (Section 3.2).

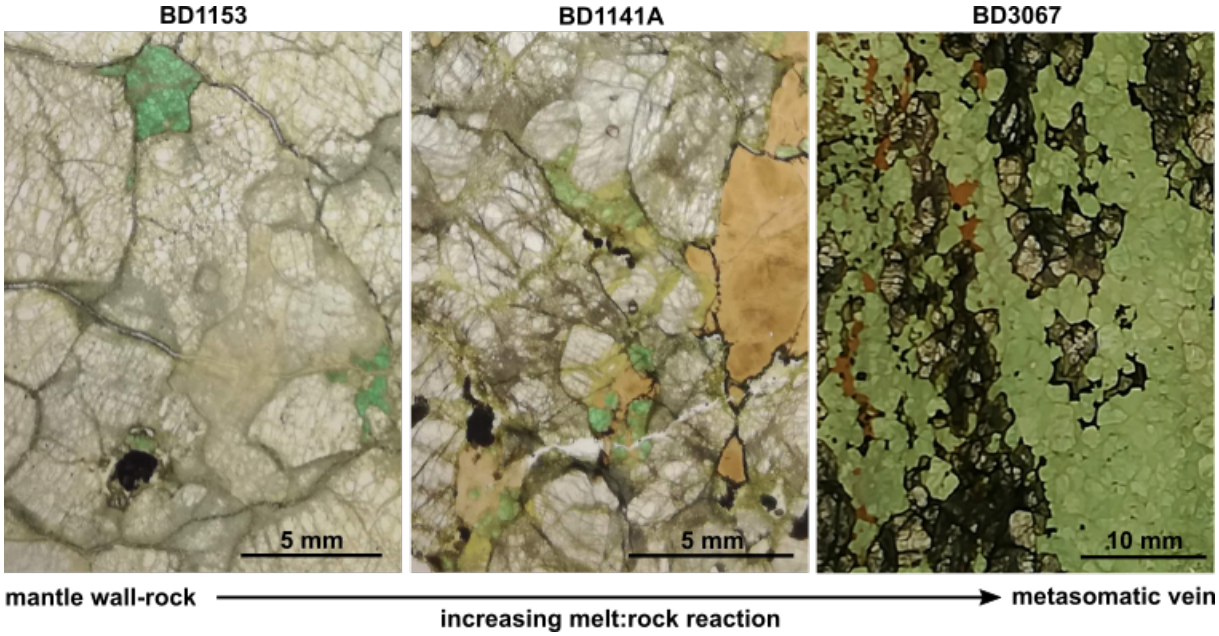

Figure 5.9 *Photographs of the thin sections of BD1153, BD1141A and BD3067 showing the range in mineral assemblage and modes. BD1153 represents limited kimberlite melt-rock reaction in the mantle wall-rock, while BD3067 contains the metasomatic vein assemblage produced when the melt volume is higher.*

Clinopyroxenes in BD1141A and BD1153 are emerald green due to high Cr (3-4 wt. %) contents (Figure 3.5). They have a characteristic primitive-mantle-normalised trace-element pattern that differs significantly to the other styles of metasomatism but is identical to the PIC (Phlogopite-Ilmenite-Clinopyroxene) metasomatic suite (Figure 5.10a; Fitzpayne *et al.* 2018a; Grégoire *et al.* 2002). The pattern is defined by a small negative Ti anomaly, lack of Zr anomaly, and a positive Hf anomaly that is greater than all of the REE and HFSE. These clinopyroxenes have the highest Hf and Zr contents of all xenoliths examined in this study which, when combined with the presence of zircon as a metasomatic phase (see Chapter 6), implies the involvement of a Hf- and Zr-rich melt. The REE pattern exhibits very little fractionation between the LREE and HREE ($[La/Yb]_n$ = 8-12; Figure 3.11). The similarities in trace-element composition of clinopyroxenes in BD1141A, BD1153 and BD3067 and PIC xenoliths attest to a genetic link. The PIC metasomatic suite is hypothesised to be the product of metasomatism of mantle peridotite by proto-kimberlite melts (Fitzpayne *et al.*, 2018a; Grégoire *et al.*, 2002; Jackson & Gibson, 2018). This is supported by the similarity in the composition of the melt in equilibrium with the clinopyroxene in BD1153 and BD3067 (Section 5.5.3) and the Bultfontein host kimberlite (Figure 5.10b).

The xenoliths that have undergone enrichment by proto-kimberlite melts are the only ones in this study with modal metasomatism, two of the three contain abundant phlogopite in addition to clinopyroxene, olivine and low abundances of orthopyroxene. The vein assemblage in BD3067 consists of clinopyroxene + phlogopite + ilmenite (+ sulfides + zircon), while the wall-rock is a dunite. Orthopyroxene is completely absent in BD3067. This metasomatic assemblage matches the PIC suite. Orthopyroxene is absent from kimberlites because the melt is Si-undersaturated, therefore the low modal abundance of orthopyroxene in all three samples is consistent with orthopyroxene dissolution during melt-rock reaction with a Si-undersaturated melt (e.g. Reaction 5.8; Gervasoni *et al.* 2017; Green & Wallace 1988; Russell *et al.* 2012).

Further evidence for interaction with a proto-kimberlite melt is found in the major- and minor-element composition of olivine in BD3067. The vein assemblage in BD3067 reflects the PIC suite and the presence of such a vein is indicative of a high volume of melt. In BD1153 where the melt volume was very low the olivines have high Mg# (94) and NiO (0.44 wt.%) contents, which represent the depleted mantle residue, this contrasts to BD3067 where the major-element composition of pre-existing mantle olivine has changed significantly. They have relatively low Mg# (88) and NiO contents (0.17-0.32 wt.%) and are comparable olivine phenocrysts in kimberlite (Figure 5.11). The porphyroclasts in BD3067 are zoned in Ni, Cr and Ti; these results are presented in Chapter 6 and discussed with respect to the implications for determining the timing of metasomatism. Olivine cores in kimberlites represent entrained lithospheric mantle olivine whereas the rims are thought to have crystallised from the kimberlite melt itself during ascent (Giuliani, 2018). In this study, the change in major-element composition instead reflects the equilibration of olivine porphyroclasts in the mantle with a proto-kimberlite melt prior to entrainment (see Chapter 6).

5.8 Hydrous siliceous fluid metasomatism

The orthopyroxene-rich garnet harzburgites (BD1152, BD1672, BD1999, BD2125) are interpreted to be the product of metasomatism by a hydrous siliceous fluid. All four samples equilibrated at the same conditions (approx. 43 kbar and 1000 °C) and are present in both Bultfontein and Mothae sample suites. The two defining features of the xenoliths are: (i) the sinusoidal nature of the clinopyroxene, garnet and bulk rock REE patterns; and (ii) the high modal abundance of orthopyroxene. These features are used to ascertain the complex metasomatic history of the xenoliths.

The modal abundance of orthopyroxene in the orthopyroxene-rich garnet harzburgites ranges from 30% to 39%. Large degrees of partial melting of primitive mantle lherzolite was originally thought to produce the orthopyroxene-rich harzburgitic residue (Nixon, 1973; Ringwood, 1958; Walker *et al.*, 1989), however, as already discussed in Section 5.3, Kelemen *et al.* (1992, 1998) showed that partial melting cannot produce a modal proportion of orthopyroxene greater than 23%. Orthopyroxene excess beyond

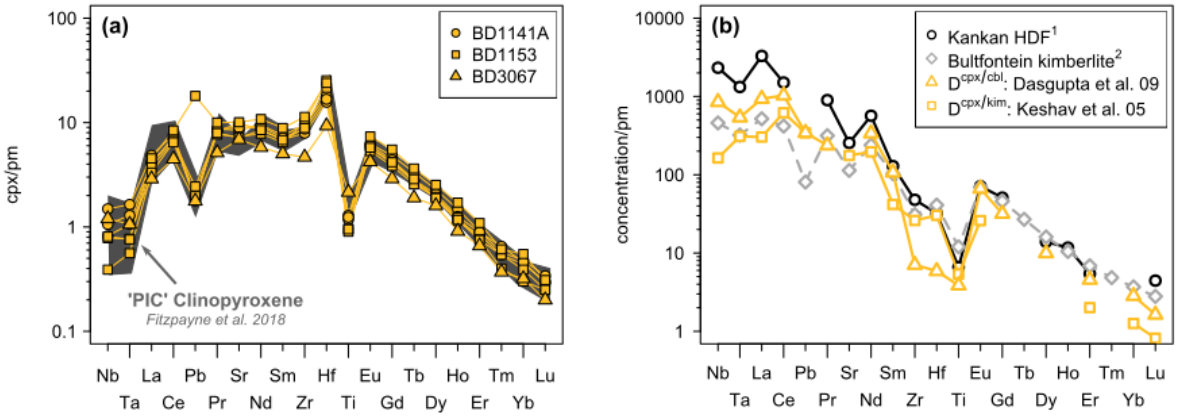

Figure 5.10 *(a) Clinopyroxene from kimberlite metasomatised xenoliths compared with Clinopyroxene from the Phlogopite-Ilmenite-Clinopyroxene (PIC) suite of metasomatised xenoliths. PIC data from Fitzpayne* et al. *(2018a). (b) Equilibrium melt for clinopyroxene in BD1153 using cpx/melt partition coefficients of Dasgupta* et al. *(2009) and Keshav* et al. *(2005). The host kimberlite composition (Roex* et al.*, 2003) and Kankan diamond HDF (Weiss* et al.*, 2009) are shown for comparison.*

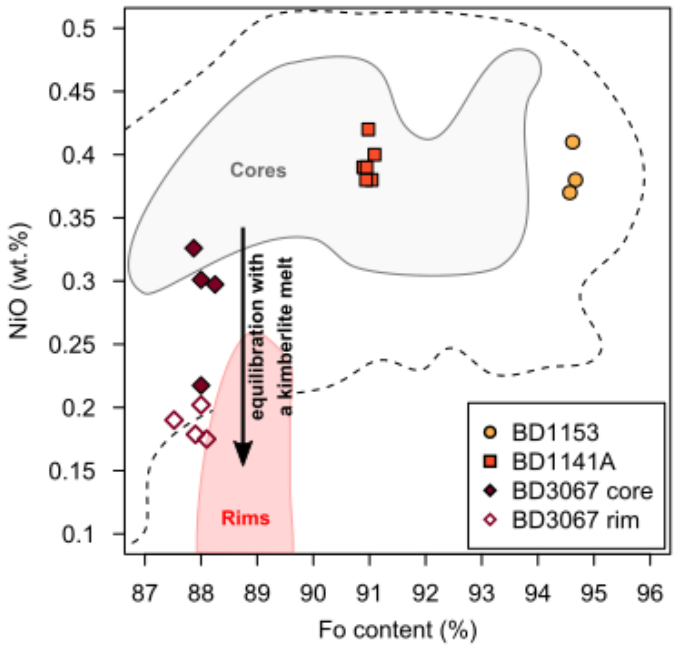

Figure 5.11 *Forsterite content vs. NiO content for olivine in three Bultfontein xenoliths metasomatised by a kimberlite melt. The fields of kimberlitic olivines from Giuliani (2018) are also plotted; the grey field shows the range of compositions of olivine cores in the Bultfontein kimberlite, and the red field is the corresponding rims. The black dashed line shows the range in the global compilation of olivine cores in kimberlite.*

this threshold is common in the Kaapvaal craton (Figure 5.1; Boyd 1989; Gibson *et al.* 2008; Stachel *et al.* 1998) and has been associated with silicate metasomatism (Kelemen *et al.*, 1992, 1998; Walter, 1998), where olivine and clinopyroxene react with a silicate melt or fluid to produce orthopyroxene. A multi-stage infiltration model has been proposed in a number of studies whereby partial melting by polybaric decompression melting produces a Mg-rich residue (Section 5.3) that is later enriched by the interaction with Si-rich metasomatic melts (Gibson *et al.*, 2008; Griffin *et al.*, 1999b; Kelemen *et al.*, 1992; Rudnick *et al.*, 1994; Zhang *et al.*, 2001). The composition of such Si-rich metasomatic agents is debated, Bell *et al.* (2005) draw parallels to metasomatism in the mantle wedge above subduction zones (Rapp *et al.*, 1999; Wunder & Melzer, 2003; Wyllie & Sekine, 1982; Wyllie *et al.*, 1989) to suggest that a hydrous siliceous fluid, rather than a silicate melt, reacts with olivine in the Kaapvaal peridotite via Reaction 5.9 to produce orthopyroxene, garnet and accessory phases.

$$ol + fluid = opx + gt + sulf + phl + carbonate \tag{5.9}$$

Bell *et al.* (2005) came to this conclusion using the relative abundances of melt soluble elements and fluid mobile or immobile elements. The high Mg#, low HREE, Ti and Ca contents and high incompatible element concentration rule out metasomatism by a mafic or ultramafic silicate melt. The high abundance of orthopyroxene suggests that there was a high volume of the metasomatic agent, if a melt of the same volume was involved one would expect a change in the major-element composition, particularly an increase

in Fe and Ti content (Gurney *et al.*, 1980), which is not observed. The lack of major element metasomatism in this case, therefore points towards a fluid metasomatic agent.

In this study the texture of orthopyroxene supports the hypothesis that they have formed during fluid-rock reaction. The orthopyroxenes are interconnected and in this section form a channel-like configuration (e.g. Figure 2.4). This texture is not observed in any other lithology, where orthopyroxenes are distributed randomly amongst olivine, clinopyroxene and garnet in the xenoliths. Additionally, there is a close relationship observed between the interconnected orthopyroxene and garnet, which supports a co-genetic origin as a secondary product of Reaction 5.9.

The garnet associated with excess orthopyroxene has a distinctive sinusoidal chondrite normalised REE pattern that is observed in many Kaapvaal peridotites (Bell *et al.*, 2005; Gibson *et al.*, 2008, 2013; Griffin *et al.*, 1999a,b; Lazarov *et al.*, 2012). The sinusoidal nature is produced by a depletion in the HREE as opposed to an enrichment in the LREE and MREE. Suggestions for the origin of this signature in the literature are summarised by Gibson *et al.* (2008) and repeated here as follows:

1. Disequilibrium due to slow diffusion of the HREE (Hoal *et al.*, 1994; Shimizu & Richardson, 1987). It is suggested that the harzburgitic garnets have not equilibrated with the metasomatic melt but the lherzolitic garnets have. The sinusoidal nature of the REE plot is a consequence of the decreasing diffusion rate with decreasing ionic radius in the HREE (Van Orman *et al.*, 2002).

2. Shu & Brey (2015) suggest that the interaction of depleted harzburgite with 0.3-3% carbonatite melt can produce the sinusoidal REE patterns.

3. An intrinisic relationship with the Ca content of the garnet. Low-Ca garnet have a reduced number of cation sites available for the LREE than high-Ca garnets. Griffin *et al.* (1999b) suggest this Ca control is produced by limited equilibration with a carbonatitic melt.

4. The sinusoidal garnets crystallise from a silicate melt that has already fractionated garnet at depth, and is therefore depleted in HREE (Burgess & Harte, 2004; Gibson *et al.*, 2008).

5. Spatial and temporal variations in the melt/rock ratio can control the equilibration of garnet. Wang *et al.* (2000) suggest that the garnet and metasomatic agent can only equilibrate if the melt/rock ratio is high and the system is open. They suggest sinusoidal garnets have not equilibrated.

6. Stachel *et al.* (1998) suggest a multi-stage tectono-magmatic process alters the ratios of the REEs and produces the sinusoidal garnet signature.

Combining the observations described above, with the findings of Bell *et al.* (2005), the origin of the sinusoidal signature in this study is suggested to be due to a fluid:peridotite reaction as follows:

7. The garnet either equilibrates with a fluid, is produced during fluid-rock reaction (e.g. Reaction 5.9) or exsolves from the newly formed orthopyroxene (Dawson, 2004; Gibson & Mills, 2017). The sinusoidal REE plot is related to the relative fluid-mobility of the elements. HREE are fluid immobile elements relative to the LREE which are fluid mobile, therefore the fluid is depleted in the HREE and enriched in the LREE. Garnets which crystallise from or fully equilibrate with this fluid will reflect this ratio. Likewise, orthopyroxene that forms through the fluid-rock reaction is depleted in the HREE and this signature is inherited in garnets that exsolve from the orthopyroxene

(Gibson & Mills, 2017). Modelling by Stachel *et al.* (2004) shows that the sinusoidal signature of harzburgitic garnet is best reproduced by reaction between peridotite and a CHO fluid.

The conclusion that the orthopyroxene-excess and garnet sinusoidal signature is a product of fluid-rock reaction is also supported using the method of classifying the origin of garnet first produced by Griffin *et al.* (1999a) using the Y and Zr concentrations. Their categorisation shows that high Y and Zr are produced by melt metasomatism, while low Y and moderate to high Zr are produced by fluid metasomatism (Figure 5.12). The garnets in the orthopyroxene-rich harzburgites plot with low Y and moderate Zr in the fluid metasomatism field.

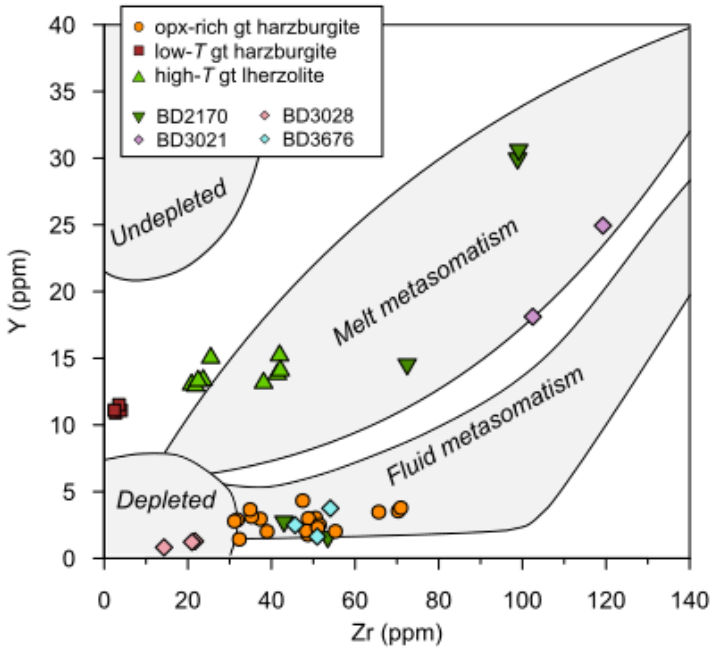

Figure 5.12 *Garnet Y vs. Zr with fields from Griffin* et al. *(1999a)*

The clinopyroxene in the orthopyroxene-rich garnet harzburgites has a similar composition to the clinopyroxene in the orthopyroxene-poor garnet harzburgite, BD1140 (Figure 5.13), but garnet in the latter show no evidence of melt or fluid metasomatism (Figure 5.12). The clinopyroxene in BD1140 was shown in Figure 5.2 to be a secondary phase added during metasomatism but the olivine and orthopyroxene compositions are consistent with an origin as the harzburgite residue of partial melting. The enrichment in LREE and depletion in HREE in the clinopyroxene ($[La/Yb]_n$ = 130) in BD1140 suggests that the clinopyroxene were the product of metasomatism by a small-fraction asthenospheric melt. The main difference between the clinopyroxenes in the fluid metasomatised xenoliths and BD1140, is in the behaviour of the middle rare earth elements (MREE) and the HREE. The REE pattern in the fluid metasomatised peridotite has a sinusoidal signature, similar to garnet but unusual in clinopyroxene, whereas in BD1140 the REE pattern is a conventional curve enriched in LREE and depleted in HREE uniformly according to ionic radius. Additionally, the fluid metasomatised clinopyroxenes are enriched in fluid mobile elements such as Sr, and depleted in fluid immobile elements such as Ti (Figure 5.13). Clinopyroxene is not a product of Reaction 5.9, between olivine and a siliceous fluid, therefore it is suggested that the the clinopyroxenes were introduced prior to fluid metasomatism by a small-fraction asthenospheric melt and initially had the same trace-element pattern as the clinopyroxene in the orthopyroxene-poor harzburgite.

As mentioned above, fluids are depleted in the HREE, and as a result the new garnets are also depleted in HREE which drives the diffusive subsolidus re-distribution of HREE into garnet.

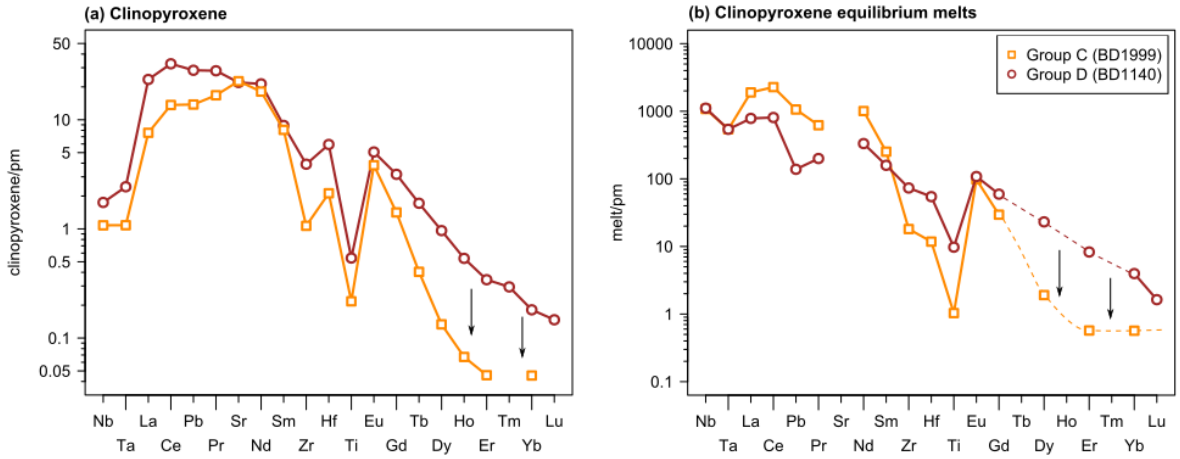

Figure 5.13 *(a) Comparison of Group C (fluid metasomatised) clinopyroxene and Group D (orthopyroxene-poor harzburgites) clinopyroxene, and (b) their corresponding equilibrium melts using the partition coefficients of Dasgupta* et al. *(2009)*

Kelemen *et al.* (1992), Zhang *et al.* (2001), Stachel *et al.* (1998) and Gibson *et al.* (2008) all propose that orthopyroxene-excess is produced during a multi-stage event starting with partial melting of lherzolite to produce a harzburgite residue which is succeeded by silicate metasomatism. In this study, the low fraction of clinopyroxene and ultra-high abundance of orthopyroxene (up to 40%) support this multi-stage hypothesis. Following a partial melting event, there is compelling evidence firstly for clinopyroxene addition by a percolating melt followed by metasomatism by a siliceous fluid that produces excess orthopyroxene and HREE-depleted garnet. Over time the HREE are re-distributed by sub-solidus diffusive re-equilibration. Two possibilities of the nature of such fluid metasomatism are discussed:

1. Metasomatism by a hydrous siliceous fluid only

2. Metasomatism by a silicate melt with an immiscible fluid phase

A Si-rich component is necessary to produce the orthopyroxene excess observed. Metasomatism by a hydrous siliceous fluid could involve Reaction 5.9 presented by Bell *et al.* (2005) to produce orthopyroxene and enrichment in fluid mobile elements (LREE, Sr, F) relative to immobile elements (HREE, Ti) to produce the ratios observed in the clinopyroxene and garnet. The presence of an immiscible fluid phase, has a greater ability to fractionate fluid mobile and immobile elements, while the silicate melt would be responsible for producing excess orthopyroxene. Klemme (2004) identified a F-rich immiscible liquid in mantle xenoliths from the South Island of New Zealand at similar *PT* conditions to the orthopyroxene-rich garnet harzburgites from Bultfontein and Mothae. Subduction was active beneath the South Island until 100 Ma (Weaver *et al.*, 1994) and the fluoride-silicate immiscibility occurred in the hydrous sub-arc environment directly amongst slab dehydration products. In the relatively dry Kaapvaal craton, metasomatism either occured prior to craton formation above the active subduction zone (e.g. Regier *et al.* 2018) or subduction-related fluids would have to originate from ancient recycled material. Subduction ceased in the region at 2.9 Ga when the Kaapvaal craton formed by the continental collision of the Kimberley block and the Witswatersrand block (Schmitz *et al.* 2004; Shirey *et al.* 2013 and references therein). If the

Si-rich fluids/melts, producing the orthopyroxene excess in the Kaapvaal harzburgites, are related to this period of subduction, e.g. generated by the partial melting of subducted metabasalts or metasediments (Kelemen *et al.*, 1992), then it has important implications for the preservation of a metasomatic signature over billions of years. Wasch *et al.* (2009) have dated a metasomatic orthopyroxene-rich vein from Kimberley at 2.97 ± 0.04 Ga and Sm-Nd and Lu-Hf ages of sub-calcic garnets from a number of diamond mines in the Kaapvaal (including Bultfontein) date back to the Archean and Proterozoic (Lazarov *et al.*, 2009, 2012; Shu & Brey, 2015; Shu *et al.*, 2013), all of which provide compelling support for the signature of subduction-related metasomatism persisting to the Cretaceous, at the point of xenolith entrainment.

5.9 Melt re-fertilisation

As mentioned in Section 5.3 the olivine and orthopyroxene composition in the orthopyroxene-poor low-T harzburgites and high-T garnet lherzolites are consistent with an origin as a mantle residue after >25% melting of a primitive mantle source, but the clinopyroxene and garnet signatures show LREE enrichment and HREE depletion that is not consistent with a mantle residue origin. This leads to the conclusion that the clinopyroxene and garnet are secondary phases that have been added during stealth metasomatism by small-fraction asthenospheric melts (e.g. Kobussen *et al.* 2009; O'Reilly & Griffin 2013; Simon *et al.* 2007, 2003).

The composition of the clinopyroxene in the garnet lherzolites can be recreated by calculating the composition of clinopyroxene in equilibrium with the primitive mantle composition using the partition coefficients of Dasgupta *et al.* (2009) and the modal abundances of the average Kaapvaal peridotite, according to Equation 5.10.

$$C_i^{cpx} = \frac{C_i^{PM}}{\frac{X^{opx}}{D_i^{cpx/opx}} + \frac{X^{ol}}{D_i^{cpx/ol}} + \frac{X^{gt}}{D_i^{cpx/gt}} + X^{cpx}} \tag{5.10}$$

Where X^{min} is the modal proportion of each mineral (min), and $D_i^{cpx/min}$ is the clinopyroxene/mineral partition coefficient for element i. The modal proportion of each mineral in the mantle is taken from Pearson *et al.* (2003), who compiled the modes of 210 cratonic peridotite xenoliths and calculated the mean average to be: 72% olivine, 20.8% orthopyroxene, 3.3% clinopyroxene and 6.2% garnet and 1.1% is spinel. The mineral/mineral partition coefficients (D values) were calculated from the mineral/melt partition coefficients published by Dasgupta *et al.* (2009) according to Equation 5.11. This set of experimental D values were chosen because the pressure (6 GPa) and temperature (1265°C) conditions of the experiments are most appropriate for the Mothae garnet lherzolites (5.2 GPa, 1270 °C), and the dataset is relatively complete; olivine/melt, orthopyroxene/melt, clinopyroxene/melt and garnet/melt partition coefficients allowed the full set of garnet-lherzolite clinopyroxene/mineral partition coefficients to be calculated.

$$D_i^{cpx/opx} = \frac{D_i^{cpx/melt}}{D_i^{opx/melt}} \tag{5.11}$$

Figure 5.14 compares the clinopyroxene trace-element pattern of the Mothae high-*T* garnet lherzolites with the calculated composition of the clinopyroxene in equilibrium with primitive mantle. The signatures are remarkably similar, the main differences being that the clinopyroxenes in the garnet lherzolite are more enriched in Sr and Nb and more depleted in Ti. In Section 5.3 the Ti and Zr concentrations in the garnet-lherzolite olivine, orthopyroxene and clinopyroxene were shown to reflect the mantle residue from 25% melting but the garnets are enriched in both Zr and Ti. Chapter 3 showed that the garnets in the garnet-lherzolites are enriched in HREE and depleted in LREE, as expected by the relative compatibility of the LREE:HREE in garnet. According to the the garnet classification diagram (Griffin *et al.*, 1999a) in Figure 5.12, the garnets in the lherzolites originate from melt metasomatism field, this conclusion supported by the trace-element pattern and Ti enrichment.

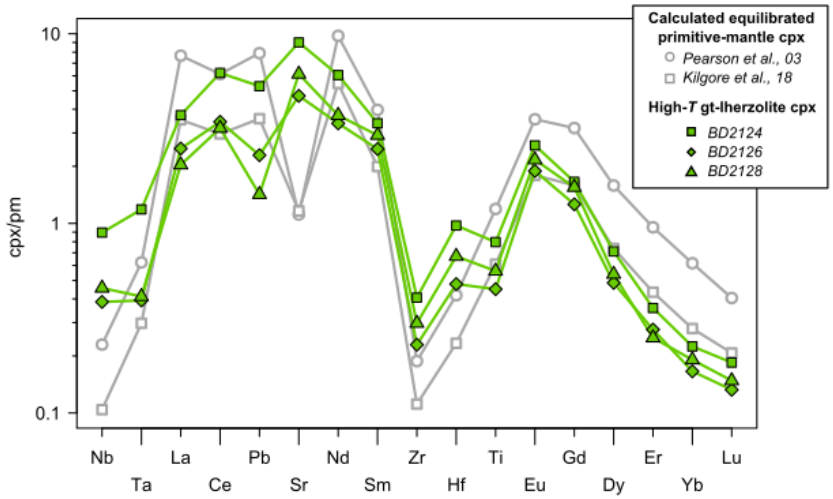

Figure 5.14 *primitive-mantle-normalised (pm) clinopyroxene composition of the Mothae garnet lherzolites, compared with the calculated composition of clinopyroxene in equilibrium with the primitive mantle source. The light grey show the calculated composition for two different modal proportions of olivine, orthopyroxene, clinopyroxene and garnet, using published estimates by Pearson* et al. *(2003) (circles: 72% ol; 20.8% opx; 3.3% cpx; 6.2% gt) and Kilgore* et al. *(2018) (squares: 55% ol; 20% opx; 15% cpx; 10% gt). Clinopyroxene from the three garnet-lherzolite samples are plotted in green (BD2124, BD2126; BD2128).*

Despite the metasomatic addition of garnet, and slight enrichment in some elements in clinopyroxene, the bulk-rock composition of the garnet-lherzolite has a flat signature on a primitive-mantle normalised spider diagram (Figure 3.14). The combination of the similarity between the clinopyroxene composition with equilibrated primitive mantle clinopyroxene (Figure 5.14) and flat bulk rock signature lead to the interpretation that the mineral assemblage in the garnet-lherzolites has fully re-equilibrated. The porphyroclastic nature of the xenoliths (i.e. small grain size of olivine) and high equilibration temperatures (1270 °C) are conducive to fast timescales of re-equilibration (see Chapter 7) such that metasomatic phases can re-equilibrate within a few million years. The garnet-lherzolites therefore represent the equilibrated high-temperature, re-fertilised residue of 25% partial melting of the primitive mantle source, while the orthopyroxene-poor harzburgite (BD1140) represents low-temperature, re-fertilised residue that has not fully re-equilibrated.

5.10 Kaapvaal database

In order to assess how representative the mantle xenoliths in this study are of metasomatism in the wider Kaapvaal craton, a database of peridotitic clinopyroxene compositions has been compiled (from Gibson *et al.* 2008; Grégoire *et al.* 2005; Hanger *et al.* 2015; Hin *et al.* 2009; Jacob *et al.* 2009; Lazarov *et al.* 2012; Peslier *et al.* 2012; Rehfeldt *et al.* 2008; Simon *et al.* 2007, 2003). The compilation reveals six categories of clinopyroxene in Kaapvaal xenoliths (Figure 5.15), five of those (a-e) are evident in the sample suite in this study. The sixth category is similar to the garnet lherzolites but with less REE enrichment (Figure 5.15f), therefore could reflect the equilibrated mantle residue without later enrichment. It should be noted that there are a few miscellaneous signatures that do not fit into any category.

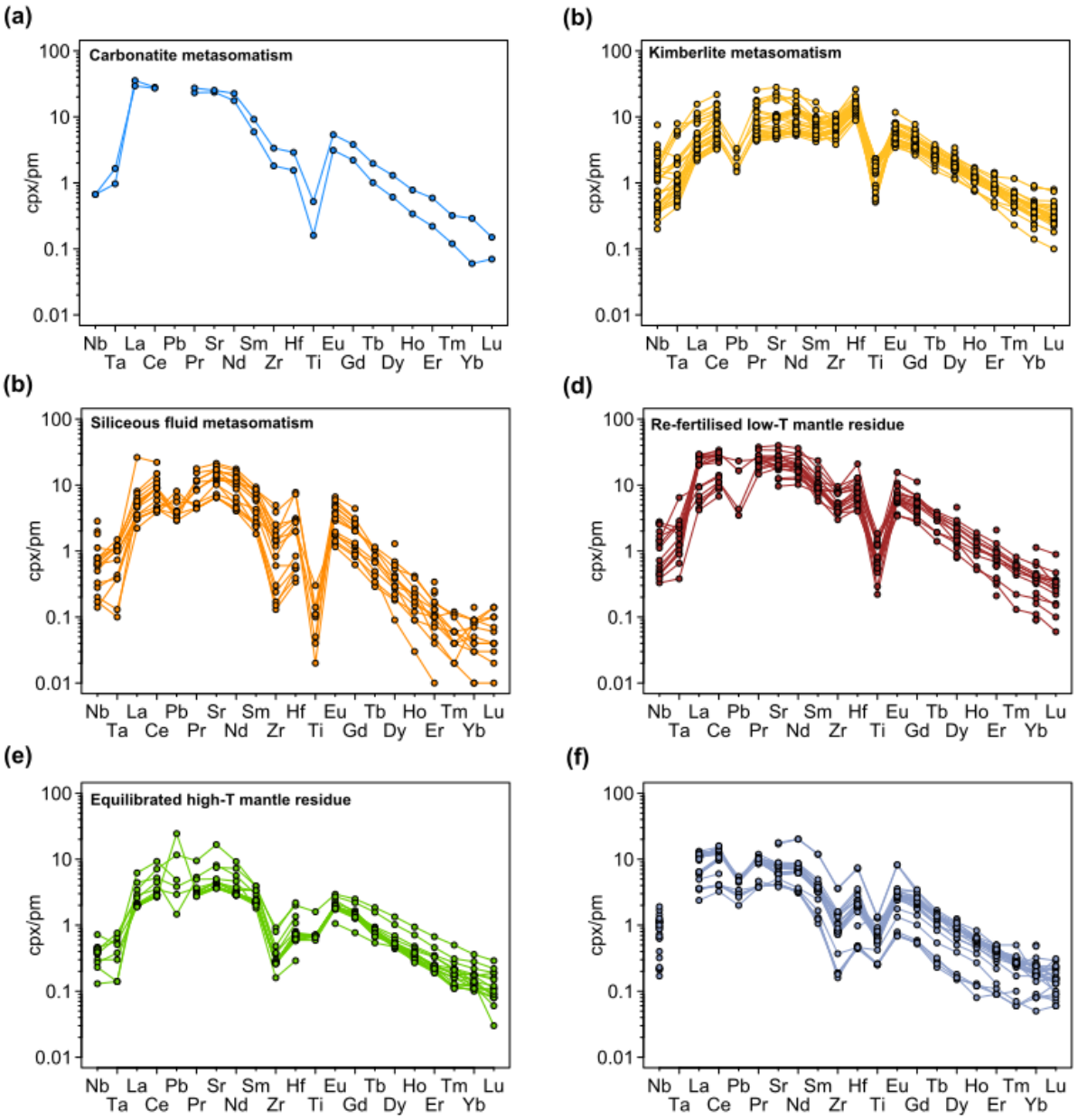

Figure 5.15 *Six distinct clinopyroxene trace-element patterns from the Kaapvaal craton identifiedin the published literature. The first five correspond to the groups in this study. The sixth group of clinopyroxene is evident in xenoliths from Finsch (Gibson* et al.*, 2008) and Mothae (Simon* et al.*, 2003).*

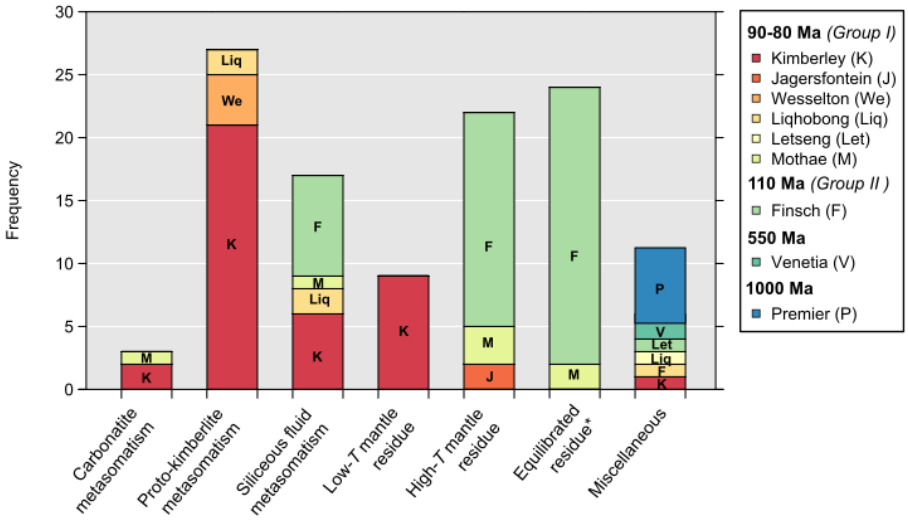

Figure 5.16 *Bar chart showing the grouping of clinopyroxene data from the literature according to the categories described in the text. The bars are split according to location. Data from Gibson* et al. *(2008); Grégoire* et al. *(2005); Hanger* et al. *(2015); Hin* et al. *(2009); Jacob* et al. *(2009); Lazarov* et al. *(2012); Peslier* et al. *(2012); Rehfeldt* et al. *(2008); Simon* et al. *(2003)*

Figure 5.16 presents a bar chart showing the frequency of each signature in the database. The garnet lherzolite signature is one of the most common supporting the conclusion that this is equilibrated mantle lherzolite. The kimberlite melt signature is the most common metasomatic signature observed in Kaapvaal clinopyroxenes, which is not unexpected considering that each xenolith is carried by a kimberlite. The question remains as to whether the metasomatism observed in the xenoliths was by the host kimberlite or a preceding proto-kimberlite magma? Carbonatite metasomatism is the least common, with only three samples showing this signature. This could be a sampling bias or reflect the low proportion of the mantle metasomatised in this way. Kimberley and Finsch exhibit a wider range of compositions but again this could be a sampling bias because Kimberley has a cluster of kimberlite pipes that have been extensively studied relative to the other locations and there are multiple studies with large datasets from the Finsch kimberlite pipe. The difference between the dominant clinopyroxene signature at Finsch and Kimberley may be related to their emplacement ages. Both the Finsch and Kimberley kimberlites erupted in the most recent period (50-130 Ma) of kimberlite magmatism in the Kaapvaal; Finsch erupted at the start of this period at 120 Ma, whereas the Kimberley cluster erupted at 90 Ma during the main peak of kimberlite activity in the Kaapvaal (90 ± 10 Ma; Griffin *et al.* 2014a; Woodhead *et al.* 2009). The dominant signatures at Finsch are the equilibrated signatures with low levels of enrichment and less fractionation, whereas at Kimberley the prevalence of kimberlite metasomatism is apparent (Figure 5.16). Many studies from Kimberley have highlighted the role of metasomatism by proto-kimberlite melts in the mantle prior to final kimberlite ascent (e.g. Giuliani *et al.* 2013a, 2016; Jackson & Gibson 2018), the occurrence of a period of kimberlite metasomatism in the craton interior beneath Kimberley from 130 Ma to the 'successful' eruptions at 90 Ma (e.g. Kobussen *et al.* 2009) is therefore evident in distribution of the different clinopyroxene patterns of the peridotite xenoliths. The earlier eruption of the Finsch kimberlites preceded this period of extensive mantle metasomatism and hence the xenoliths entrained reflect the mantle residue and the ancient metasomatism by a siliceous fluid that likely occurred prior to/during craton suturing at 2.9 Ga (see Chapter 10; Bell *et al.* 2005; Shu & Brey 2015; Wasch *et al.* 2009). Zhang *et al.*

(2001) suggest that silicate metasomatism could be far more widespread than is evident from the xenolith record because later deformation and subsequent metasomatism will have removed textures, obliterated or overprinted the Si metasomatic signature. This could be true for all metasomatic signatures; the one preserved is only the most recent and could hide a complex history of multiple metasomatic events.

This dataset is small (n = 102), and contains inherent sampling bias. It cannot tell us about the extent of metasomatism, but the comparison of all studies has shown the prevalent types of metasomatic agent and the metasomatic signatures that can be used to identify them.

5.11 Conclusions

This chapter presents a systematic investigation into the different varieties of peridotites from the Kaapvaal Craton based on modal mineralogy and chemical signatures. Using a combination of petrological observations and clinopyroxene, garnet and bulk rock chemistry three styles of metasomatism have been identified in the sample suite from Bultfontein and Mothae: (1) carbonatite melt metasomatism; (2) proto-kimberlite (silico-carbonatite) melt metasomatism; and (3) hydrous siliceous fluid metasomatism. A number of petrographic and chemical indicators are provided that can be used together to identify the nature of the metasomatic agent in a more robust manner than relying on isolated indicators such as the Ti/Eu ratio. Grégoire *et al.* (2002) identify two types of clinopyroxene in Kaapvaal xenoliths, this can now be expanded to six types that reflect the array of metasomatism and re-equilibration in the sub-cratonic mantle.

Metasomatism is pervasive in the Kaapvaal craton. Very few of the analysed xenoliths contain any evidence in the mineralogy, petrology or major element composition for extensive melt-rock reaction, however, the minor- and trace-element chemistry highlights the high degree of cryptic and stealth metasomatism in the mantle by small-fraction melts. This result highlights the necessity for combining all analyses in studies of mantle peridotite. Finally, trace-element analysis of all present phases is crucial to determine if there is any underlying cryptic metasomatism, especially in studies of what appears to be ‘un-metasomatised’ cratonic mantle peridotite.

Chapter 6

Constraining the timescales of proto-kimberlite metasomatism: a case study of BD3067

A version of this chapter was published in Lithos in October 2018 (Volumes 318–319, Pages 448-463; reviewers: Andrea Giuliani and Sonja Aulbach):

Preservation of systematic Ni and Cr heterogeneity in otherwise homogeneous mantle olivine: Implications for timescales of post-metasomatism re-equilibration

Charlotte G. Jackson and Sally A. Gibson

https://doi.org/10.1016/j.lithos.2018.08.026

6.1 Introduction

Numerous studies have attempted to date metasomatic events using radiometric dating techniques on metasomatic phases such as zircon and titanite. The highest precision ages are U-Pb dates on mantle zircons, and show that they precipitated from metasomatic melts within several million years prior to kimberlite emplacement at the surface. Some of these U-Pb zircon ages are coeval with the host kimberlite (Kinny & Dawson, 1992; Konzett *et al.*, 1998, 2000, 2013) while others are much older (Giuliani *et al.*, 2014b, 2015; Liati *et al.*, 2004; Woodhead *et al.*, 2017). The episodic versus continuous nature, timescales and extent over which metasomatic interactions occur in the sub-continental mantle are, however, poorly constrained. A limitation of radiometric dating techniques, however, is that their resolution is to an order of millions of years and so cannot be used to establish if a metasomatic event was related directly to the host kimberlite or not. Higher resolution inferences about the timing of metasomatic events in the mantle are reliant on mineral disequilibrium and diffusion timescales. In the deep lithosphere, the timescales of re-equilibration for minerals present in the refractory wall rocks of melt channels (e.g. garnet, olivine and orthopyroxene) are fast ($< 10^5$ years, e.g. Griffin *et al.* 1996) so that each crystal only records the most recent chemical perturbation. At shallower levels and lower temperatures, subsolidus cooling and re-equilibration timescales are longer, so the preservation of elemental zoning is more likely. Samples of mantle material entrained during this short re-equilibration time therefore potentially preserve diffusion profiles in minerals that can be used to estimate the timing of metasomatism prior to kimberlite emplacement.

In this chapter an in-depth case study of a veined mantle xenolith from Bultfontein (BD3067) is presented. The vein in BD3067 is the product of clinopyroxene and phlogopite crystallisation from a kimberlite melt percolating through the lithospheric mantle (see Chapter 5). Accessory ilmenite, zircon and sulfides are also identified in the metasomatic assemblage. The interaction between the metasomatic

agent and the pre-existing mantle olivine is preserved in Ni, Cr and Ti zoning within olivine porphyroclasts. Crystallographic controls and diffusion modelling of Ni in olivine are combined to quantify the timescales of equilibration of refractory wall rock following reactive percolation of proto-kimberlite melts through sub-cratonic lithospheric mantle.

6.2 Petrographic description

Mantle xenolith BD3067 from Bultfontein was described briefly in Chapter 2. This 13 cm diameter xenolith contains a spectacular, bright green, trichotomous branching, clinopyroxene-rich vein set in a matrix of olivine porphyroclasts and neoblasts (Figure 6.1a). Orthopyroxene is absent, and the vein host rock is a dunite. At its widest point, the clinopyroxene-rich vein measures 45 mm. Branch terminations and regions of more isolated clinopyroxene crystallisation are associated with small amounts of phlogopite. The large olivine porphyroclasts and clinopyroxenes (both 2-6 mm diameter) show significant internal deformation, exhibited in olivine subgrains, recrystallisation and complex fine structures (Figure 6.1c). Accessory phases include large anhedral zircons (up to 5mm diameter; Figure 6.1d) and very small amounts of Cr-spinel that have crystallised within the main vein. Away from this region we observe phlogopite, large (0.2-4 mm) Fe-Ni sulfides, interstitial amongst the small (<50 μm) olivine neoblasts, and ilmenite (Figure 6.1e).

6.3 Mineral chemistry

Multiple thin sections were made from xenolith BD3067, including across the main vein and regions further from it. The mineral chemistry presented for each phase here differentiates between those in close proximity to the main vein, and those distal to it (Figure 6.2).

6.3.1 Clinopyroxene

The clinopyroxenes in BD3067 have a high Mg number (Mg# = 89-93, average Mg# 91.1 ± 1.8 (2σ), n=45) and CaO content (22 ± 0.7 wt. %, n=45) and are diopsides (Table 1; Figure 2). They have low TiO_2 (0.20 ± 0.03 wt.%, n=45) and Na_2O (1.23 ± 0.37 wt.%, n=45), and very low Al_2O_3 contents (0.63 ± 0.15 wt.%, n=45). Diopsides in the main vein have lower Cr_2O_3 (0.74 ± 0.14 wt. %, n=15) and higher FeO (3.08 ± 0.25 wt.%, Mg# = 90.6 ± 0.75, n=15) than those further away (Cr_2O_3 = 0.98 ± 0.86 wt. %; FeO = 2.89 ± 0.58 wt.%; Mg# = 91.1 ± 1.78, n=10). There is also a subtle difference in Ni content with the distal diopsides having a higher Ni content and greater variability (243 ± 110 ppm, n=10) than those found in the vein (185 ± 23 ppm, n=15).

6.3.2 Olivine

The olivine neoblasts (nb) and porphyroclasts (pc) in BD3067 are characterised by uniform but moderate forsterite contents (nb Mg# = 88.0 ± 0.36, n=14; pc Mg# = 88.0 ± 0.22, n=12). Both generations also have moderate MnO (nb = 0.15 ± 0.04 wt.%, n=14; pc = 0.16 ± 0.03 wt.%, n=12) but low CaO («0.1 wt.

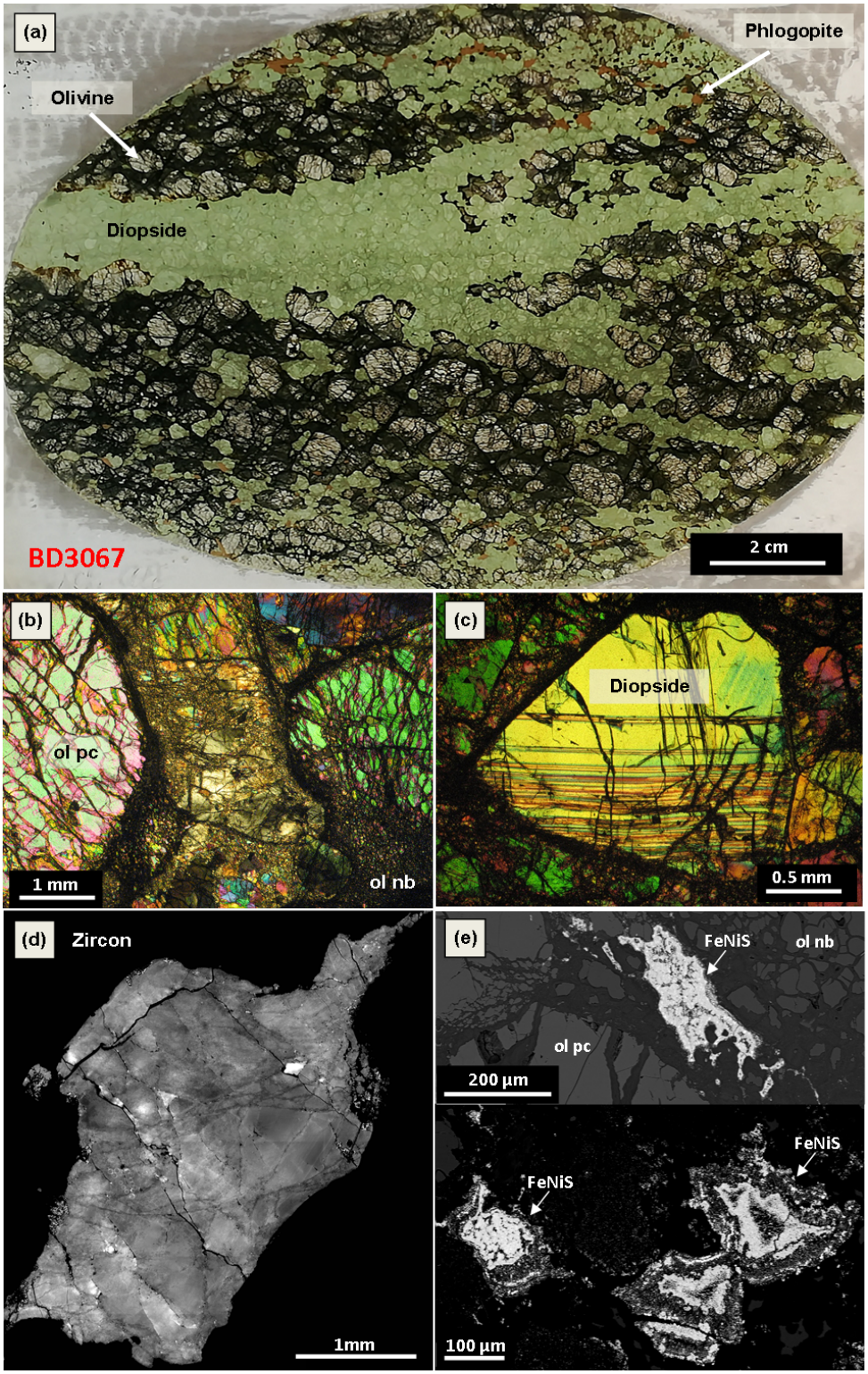

Figure 6.1 *Images of the veined xenolith BD3067. (a) Photograph of a large, 13 by 9 cm, thin section containing a trichotomously branching vein; (c) Photomicrographs of olivine porphyroclasts (ol pc) and neoblasts (ol nb) (cross polarised light); (d) Complex deformation in clinopyroxene (cross polarised light); (e) Cathodoluminescence image of large zircon crystal within the main vein. (e) Fe-Ni sulfides with complex breakdown and exsolution textures.*

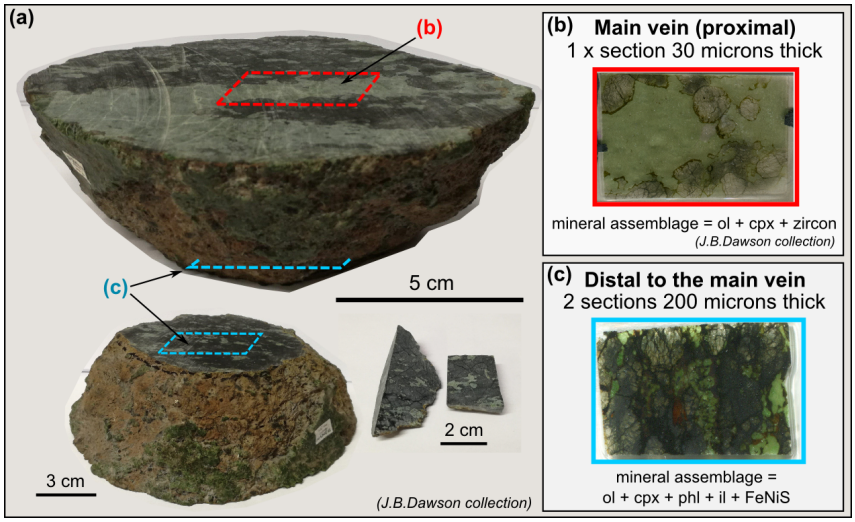

Figure 6.2 *The position of the proximal and distal sections relative to the main clinopyroxene vein in the hand specimen of BD3067.*

%) concentrations. Similar to the diopsides, all of the olivines have extremely low contents of Al (8 ± 5 ppm, n=12), and the neoblasts have low NiO (0.21 ± 0.05 wt.%, n=14).

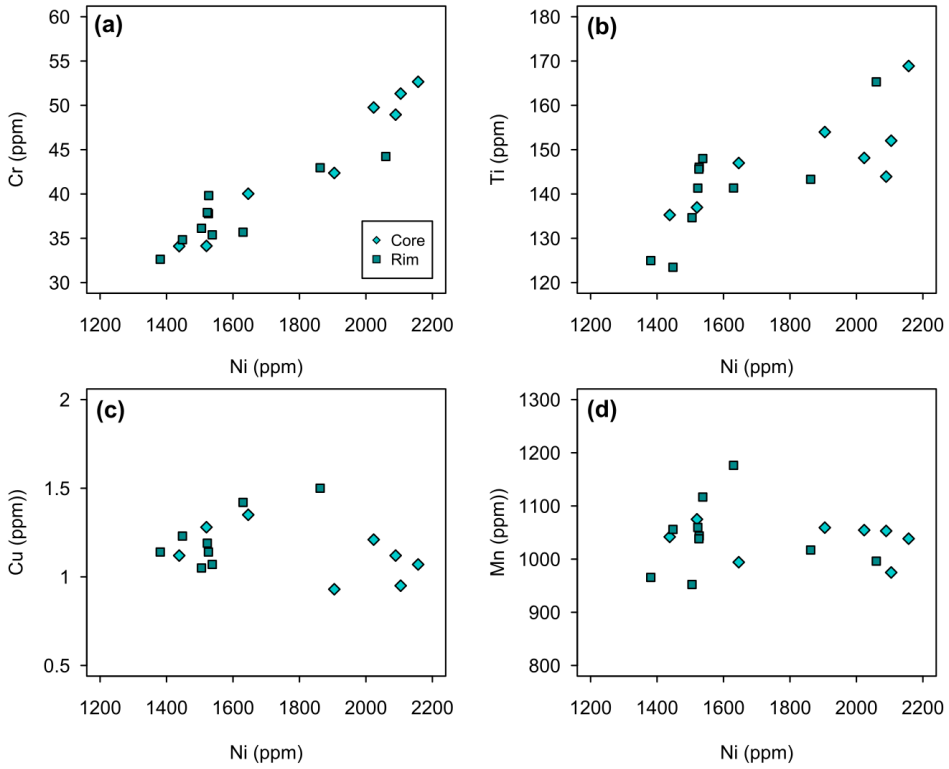

Figure 6.3 *Variation in minor and trace elements against Ni in the core and rim of distal olivine porphyroclasts. (a) Cr; (b) Ti; (c) Cu; (d) Mn*

The olivines in BD3067 have higher P (99 ± 35 ppm, n=9), Ti (150 ± 23 ppm, n=9) and Zn contents (105 ± 19 ppm, n=18) but similar concentrations of V (3.9 ± 0.7 ppm), Co (133 ± 11.4 ppm) and Cu (1.3 ± 0.6 ppm) to those found in previous studies of mantle olivines (e.g. Aulbach *et al.* 2017b; De Hoog *et al.* 2010). All of the olivine neoblasts are uniform in composition but a number of the large porphyroclasts

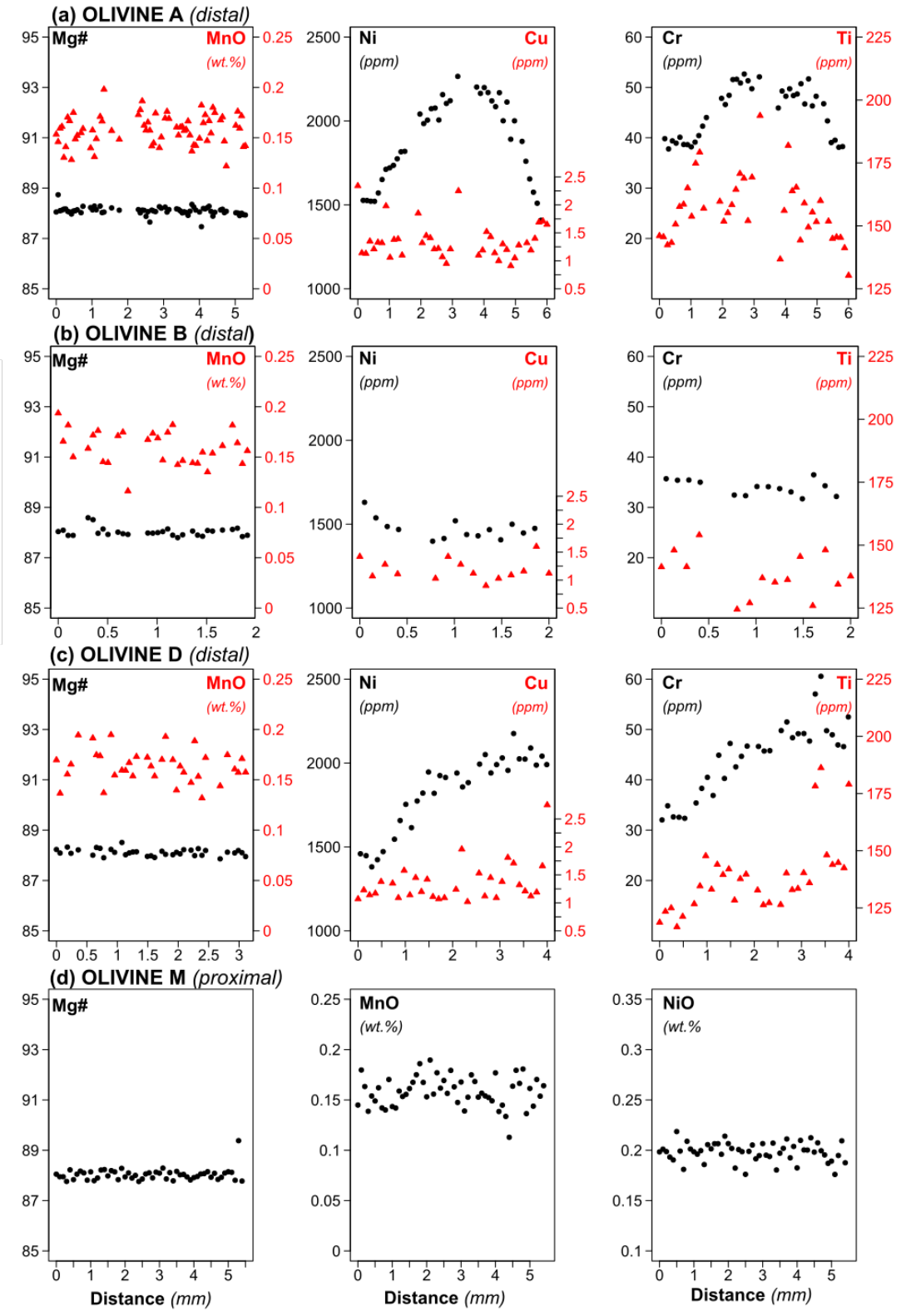

Figure 6.4 *Olivine profiles taken of rim to rim transects in four olivine crystals. Three distal olivines are shown (a) Olivine A; (b) Olivine B; (c) Olivine D, and one proximal olivine (d) Olivine M. The black circles represent the measurements for the y axis on the left-hand side (e.g. Mg# in column 1), and the red triangles are associated with the y axis on the right-hand side (e.g. MnO in column 1). Mg# (MgO/(MgO+FeO) mol) and MnO are measured using EPMA and Ni, Cu, Cr and Ti are LA-ICP-MS measurements. Olivines A and D show strong variation in Ni, Cr and Ti across the crystal whereas Olivines B and M are homogeneous.*

have Ni- and Cr-rich cores and Ni- and Cr-poor rims. These rims have the same composition as the neoblasts and the un-zoned porphyroclasts (NiO = 0.20 ± 0.02 wt.%, n=13; Cr = 37 ± 6 ppm, n=9). The cores of the zoned olivines show a range in Ni (0.20 – 0.33 wt.% NiO), Cr (32 – 63 ppm) and Ti (117 – 204 ppm) contents but are uniform for every other element and the same composition as the neoblasts and un-zoned olivine (e.g. Table 6.1 and Figure 6.3) . Profiles of major and minor element concentrations were measured across sixteen, large (2 to 6.3 mm), olivine porphyroclasts in BD3067. Six of these profiles are across olivines that border the main clinopyroxene vein (hereby referred to as proximal olivine). The remaining ten profiles are across porphyroclasts distal to the main vein (hereby referred to as distal olivine), where the proportion of clinopyroxene is lower and phlogopite and sulfides higher. Examples of

Grain	Olivine A	Olivine A	Olivine B	Olivine D	Olivine D	Olivine G	Olivine G
Proximal/distal	distal	distal	distal	distal	distal	distal	distal
Type (neoblast/porphyroclast)	porph	porph	porph	porph	porph	porph	porph
Core/rim	core	rim		core	rim	core	rim
SiO_2 (wt.%)	40.6	40.5	41.4	40.7	40.2	39.9	40.4
TiO_2	0.03	0.04	0.03	b.d.l	b.d.l	b.d.l	0.03
FeO	11.4	11.4	10.9	11.7	11.6	11.6	11.4
MnO	0.14	0.17	0.16	0.19	0.16	0.17	0.15
MgO	47.2	46.8	47.5	48.1	47.8	47.5	47.7
NiO	0.32	0.2	0.2	0.3	0.2	0.28	0.19
CaO	0.02	0.03	b.d.l	b.d.l	b.d.l	b.d.l	b.d.l
Fo (%)	88.1	88	88.6	88	88	87.9	88.1
Position	P1-25	P1-4	P1-8	P1-19	P1-1	P1-20	P1-4
Na (ppm)	80	60	59	57	57	67	60
Al	10.03	8.21	3.7	5.39	7.93	9.07	8.89
P	94	73	100	85	91	116	86
Ca	197	182	157	47	169	185	190
Sc	1.53	1.77	1.4	1.21	1.23	1.8	1.71
Ti	169	142	135	126	119	154	133
V	3.43	3.7	3.47	3.19	3.38	3.71	3.38
Cr	49.7	39.4	34.1	45.7	32	42.4	39.3
Mn	1014	1044	1042	1000	1011	1059	964
Co	127	130	129	121	125	137	130
Ni	2121	1522	1438	1857	1459	1905	1832
Cu	1.21	1.13	1.12	1.96	1.07	0.93	1.64
Zn	103	109	97	98	100	122	109
Zr	0.408	0.394	0.412	0.304	0.339	0.398	0.304
Nb	0.43	0.324	0.267	0.303	0.303	0.33	0.216

Grain	Olivine 1	Olivine 1	Olivine 2	Olivine M	Olivine N		
Proximal/distal	proximal	proximal	proximal	proximal	proximal	distal	proximal
Type (neoblast/porphyroclast)	porph	porph	porph	porph	porph	neo	neo
Core/rim	core	rim					
SiO_2 (wt.%)	40.9	40.6	40.8	40.7	40.4	40.6	40.2
TiO_2	b.d.l	b.d.l	b.d.l	0.03	0.03	0.03	b.d.l
FeO	11.7	11.5	11.6	11.9	11.4	11.9	11.7
MnO	0.18	0.16	0.16	0.14	0.17	0.15	0.16
MgO	47.9	47.5	47.8	48.0	47.8	47.3	47.5
NiO	0.19	0.21	0.21	0.2	0.21	0.21	0.19
CaO	0.03	0.05	0.04	0.03	b.d.l	0.03	0.03
Fo (%)	87.9	88	88	87.8	88.2	87.6	87.9

Table 6.1 *Composition at the core and rim of select distal and proximal olivine porphyroclasts and neoblasts from BD3067.*

representative profiles of elements across olivine porphyroclasts, determined by EPMA and LA-ICP-MS, in both the proximal and distal sections are shown in Figure 6.4, more analyses are presented in the data tables following the appendices.

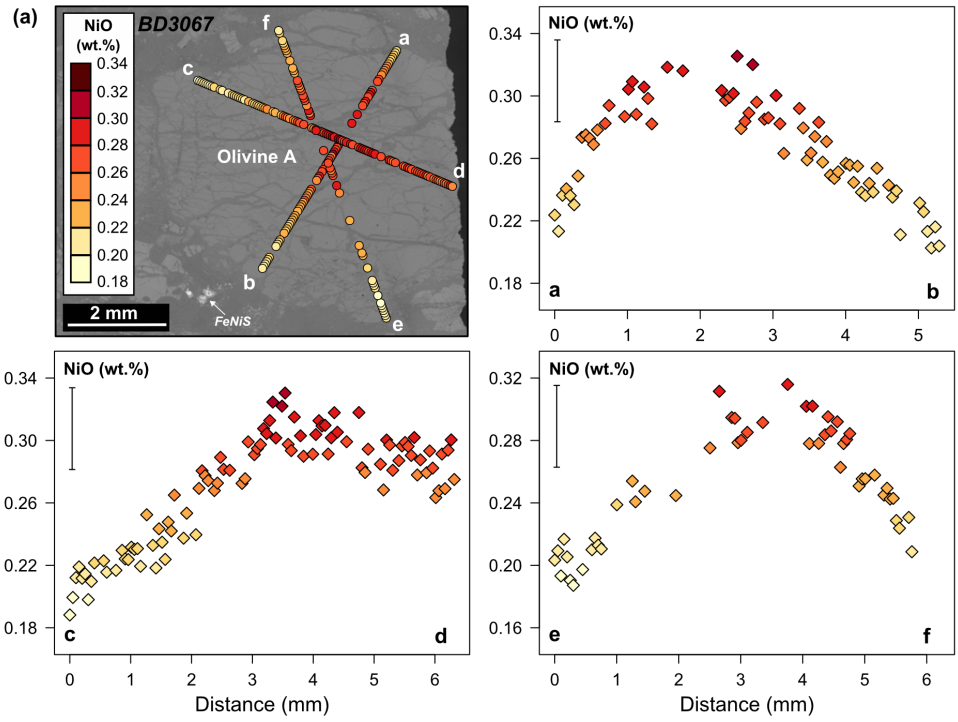

Figure 6.5 *Three profiles taken across Olivine A porphyroclast highlight the asymmetry in the profiles.*

An important finding arising from this systematic study of BD3067 is that olivine porphyroclasts which border the main vein have homogeneous major- and trace-element compositions (e.g. Figure 6.4, Olivine M) whereas those away from this region (e.g. Olivine A, D) exhibit a range in Ni, Cr and Ti but have constant Si, Mg, Fe and Mn, Co, V and Zn contents. Figure 6.3 show a positive correlation between Ni and Cr, and Ni and Ti, respectively, reflecting the corresponding zonation in each element. The Ni, Cr and Ti variation is not uniform across the olivine porphyroclasts: some show much stronger core-to-rim variation than others; some have parabolic zonation (e.g. Figure 6.5) and others more complex patterns. While the olivine crystals that exhibit zonation in Ni and Cr tend to be the largest, there are others of the same size that have homogeneous compositions. The gradient of the Ni and Cr profiles varies within and between crystals. Figure 6.4 shows profiles for two endmembers: Olivine A has the most strongly zoned core-to-rim profile and Olivine B has uniform concentrations of NiO (0.2 wt.%) and Cr (34 ppm) that are the same as those in the neoblasts. The core composition in the un-equilibrated profiles range from 0.28 - 0.32 wt.% NiO, and 50 – 63 ppm Cr. By contrast the rim composition of the zoned olivines are strikingly uniform with 0.18-0.2 wt.% NiO and 35-40 ppm Cr. The rims have the same chemical composition for all elements as the olivine neoblasts.

6.3.3 Sulfides

Several large, irregular, metasomatic Fe-Ni sulfides exist both in the main vein and distal to it in the thin sections of BD3067 (Figure 6.6). The shape, size and composition of these grains are extremely heterogeneous. Most of the sulfides have been heavily serpentinised to the low temperature assemblage of

magnetite, heazlewoodite and serpentine (Lorand & Grégoire, 2006), but some unaltered areas remain. The composition of the unaltered regions of the sulfides are shown in Table 6.2. The heterogeneity in composition is especially prevalent in Cu and Ni. Some regions have high Cu content but a low Cu concentration is more common in Kaapvaal peridotite mono-sulfide-solution, which demonstrates that they have re-equilibrated at a low temperature (Lorand & Grégoire, 2006). There are also Ni-rich exsolution lamellae in the sulfides (up to 44 wt. % NiS).

Section Sulfide/ Point	Tk5 45 / 1 .	Tk4 28 / 1 .	Tk4 32 / 1 .	Tk4 27 / 21 .	Tk4 27 / 25 .	Tk4 27 / 27 .
S (wt.%)	18.93	12.45	15.75	16.65	20.2	27.13
Ni	24.6	11.63	15.53	21.26	28.19	34.33
Fe	53.19	74.36	60.71	55.69	50.51	32.69
Si	2.46	0.94	4.07	5.95	0.43	5.15
Cu	0.12	0.38	3.67	0.09	0.22	0.1
Cr	0.71	0.23	0.28	0.36	0.45	0.6
NiS (%)	30.38	13.24	18.61	25.7	35.2	43.71
FeS (%)	66.34	85.2	73.37	67.9	63.7	42.08

Table 6.2 *Sulfide composition off heterogeneous sulfides in BD3067*

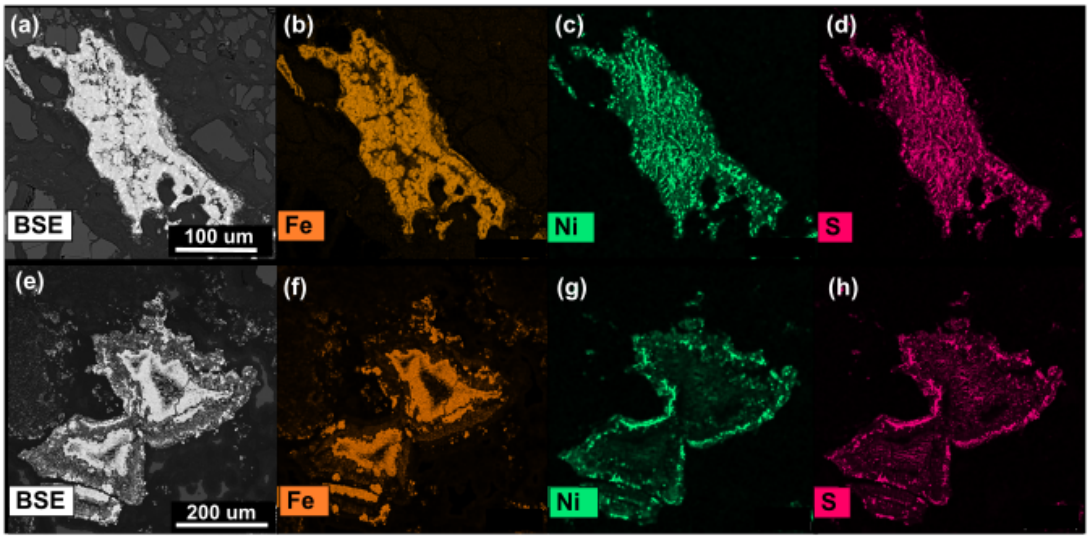

Figure 6.6 *Back-Scatter Electron (BSE) image (a, e) and EDS maps showing the Fe (b, f), Ni (c, g) and S (d, h) distribution in two selected sulfides from BD3067.*

6.3.4 Zircon

Energy Dispersive X-ray Spectroscopy (EDS) major-element mapping of the largest zircon, which is present in a bottlenecked region of the main vein and adjacent to olivine porphyroclasts, shows that it is un-zoned but regions of baddeleyite (ZrO_2) are present adjacent to cracks in the crystal.

6.4 Crystallographic orientation and Ni heterogeneity in olivine

Previous studies of element diffusivity in olivine have highlighted the importance of crystal orientation (e.g. Costa & Morgan 2010; Dohmen & Chakraborty 2007; Spandler & O'Neill 2010). The anisotropic

orthorhombic crystal structure of olivine results in anisotropy in the relative diffusion rate of major and minor elements along each crystallographic axis (Chakraborty, 2010; Dohmen & Chakraborty, 2007; Ito & Ganguly, 2006; Spandler & O'Neill, 2010). Diffusion in olivine is fastest along the [001] (c-axis), where there are parallel chains of octahedral sites (Dohmen & Chakraborty, 2007), and slower along the [100] and [010] axes (a-axis and b-axis, respectively). A FEI Quanta 650FEG SEM equipped with a Bruker e-Flash HR Electron Back-Scatter Diffraction (EBSD) detector in the Department of Earth Sciences at the University of Cambridge was used to make EBSD maps of variably equilibrated olivine porphyroclasts in veined xenolith BD3067, in regions parallel to the EPMA and LA-ICP-MS profiles.

The MTEX matlab toolkit (Bachmann *et al.*, 2010) was used to create inverse pole figures (IPF) such that the orientation of the crystallographic axes could be determined in reference to the plane of the crystal. Of particular interest is the orientation of the [001] axis in the olivine porphyroclasts with variable disequilibrium because diffusion is fastest along it. EBSD maps were made of eleven porphyroclasts in BD3067, five proximal to the main vein and six distal to it. All five proximal olivines are homogeneous regardless of the crystallographic orientation, however the six distal profiles provide a range in chemical zoning from completely homogeneous to asymmetric zoning and parabolic zoning that can be linked to the crystallographic orientation. In Figure 6.7, the NiO profile of the six distal olivines is plotted with the corresponding simplified IPF that shows the orientation of the three crystallographic axes relative to the cut plane of the olivine in question (the horizontal on the stereonet). The plunge and trend of the fast axis [001] is marked in red, and the plane normal to this axis, the (001) plane, contains both the [100] (blue) and [010] (green) axes where diffusion of Ni is slowest. The relationship between the extent of Ni disequilibrium and the crystallographic orientation is evident in Figure 6.8, where the range in NiO content correlates with the angle to the (001) plane. At 90° the (001) plane is perpendicular to the thin section which means the fast axes is within the crystal plane and re-equilibration of Ni is complete in this orientation. In contrast, at 0° the olivine in thin section is cut along the (001) plane containing both slow axes and hence exhibits the greatest heterogeneity.

6.5 Disequilibrium in olivine

Chemical disequilibrium is a common observation in mantle peridotites that have experienced metasomatism, but the decoupling of Ni and Cr disequilibrium from any other element in mantle olivine observed in BD3067 is a unique and puzzling finding. The olivine profiles reported here do, however, show a broad similarity to profiles observed in olivines from the Springwater pallasite (Leitch *et al.*, 1979; Zhou & Steele, 1993). In these meteoritic olivines, long wavelength diffusion profiles (mm scale) are observed in several elements, including Ni, Cr, Ca and Al, but flat profiles are observed in Fo content, Mn and V. In this case the outward diffusion of Ni and Cr is attributed to the decrease in the equilibrium concentration of the olivine with the adjacent metal phase, during cooling. The flat profiles are recognised as resulting from the lack of any other sink for these elements (e.g. V and Mn) outside of the olivine.

There has been no other study presenting decoupling of Ni and Cr from other elements in olivine. In BD3067 Ni and Cr are the only elements to show systematic core-to-rim variation although a few of the other minor elements show a degree of scatter. In some cases, for example Ti, this scatter weakly correlates with the Ni and Cr zoning (Figure 6.4 and 6.3). The core to rim multi-element decoupling, on

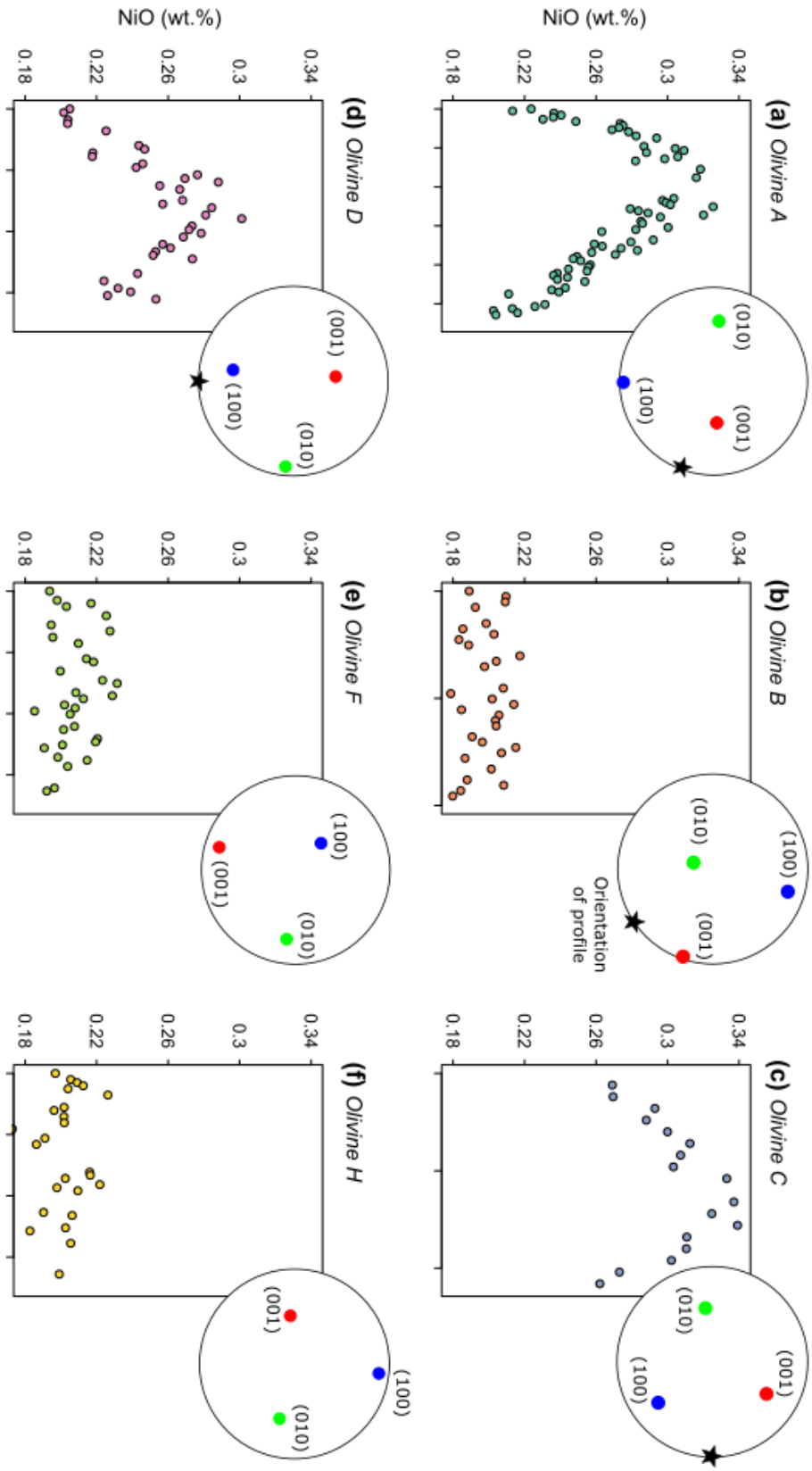

Figure 6.7 *NiO rim to rim profiles of distal olivines A, B, C, D, F and H and the corresponding stereonet showing the orientation of the three crystallographic axes relative to the thin section. The two slow diffusion axes are marked in blue, [100], and green, [010], and the fast diffusion axis is marked in red, [001]. The star marks the orientation of the profile. Each tick of the distance across the profile represents 1 mm.*

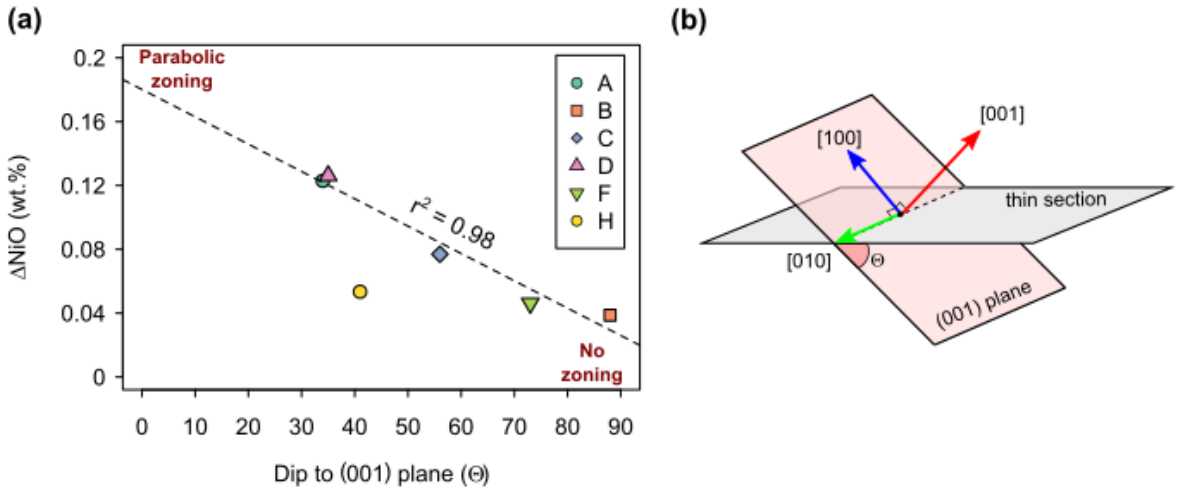

Figure 6.8 *(a)The range in NiO content (ΔNiO wt.%) in the profiles of olivines A, B, C, D, F and H against the dip of the (001) plane (Θ) relative to the thin section (i.e the plane of the crystal). Olivine H is homogeneous and not included in the regression. (b) The spatial relationship between the (001) plane, Θ, the three crystallographic axes and the thin section. The (001) plane contains the [100] and [010] axes which have the slowest diffusion rate for Ni in olivine. When Θ = 0, the maximum disequilibrium is observed, when Θ = 90 the profile is homogeneous because the plane contains the [001] fast axis.*

millimetre length scales, indicates that these variations are not caused by overgrowth of olivine formed by fractionation of a crystallising melt, as is observed in olivine xenocrysts in kimberlite magmas (e.g. Arndt *et al.* 2010; Bussweiler *et al.* 2015; Cordier *et al.* 2015; Giuliani *et al.* 2017; Pilbeam *et al.* 2013). It is unlikely that this is a growth effect due to the shape of the profile and the distance of the zoned olivines from the main vein, where the infiltrating melt would have facilitated growth. Instead, this is an effect of subsolidus re-equilibration.

No single factor can satisfactorily account for the observed decoupling of Ni and Cr in BD3067 olivines, rather several aspects have produced, and influenced the preservation of, the elemental patterns we see. These include: (i) mineral-melt and mineral-mineral concentration gradients during subsolidus re-equilibration; (ii) the presence of Ni/Cr stoichiometric phases; and (iii) anisotropy of diffusion in olivine. It is proposed that the observed profiles are caused by an evolving melt composition and locally changing concentration gradients as new phases crystallise and change the local equilibrium conditions. The profiles represent the re-distribution of elements during subsolidus re-equilibration (e.g. Figure 6.4; Cherniak & Liang 2012, 2014), but the fact that the profiles are only preserved in Ni and Cr, and to a lesser extent Ti, is influenced by the local mineral assemblage and the diffusion of these elements in olivine; Ni and Cr because they exhibit strong anisotropic diffusion in olivine, and Ti because it's high charge makes diffusion very slow in olivine.

6.5.1 Subsolidus re-equilibration of olivine and clinopyroxene

Re-equilibration during and after metasomatism is influenced by compositional differences and concentration gradients between: (i) the infiltrating melt; (ii) the pre-existing mantle phases; and (iii) the new metasomatic phases. In Chapter 5 it was established that the infiltrating melt was a silico-carbonatite kimberlite melt. The silico-carbonatite melt-rock reaction resorbed orthopyroxene and crystallised

clinopyroxene (Lim *et al.*, 2018; Simon *et al.*, 2003). This early pulse of volatile-rich proto-kimberlite melt introduced a suite of incompatible elements into the system, altering the equilibrium conditions of the local mantle peridotite. Following the melt infiltration event, the new mineral assemblage re-equilibrates by elemental re-distribution, which is apparent in the composition of the pre-existing mantle olivine porphyroclasts. The forsterite contents and other minor elements of the olivine in BD3067 have equilibrated with the infiltrating proto-kimberlite melt and new mineral assemblage, this can be observed in Figure 6.9a where the forsterite content and MnO concentration mirrors the rims of olivine macrocrysts in kimberlites from Kimberley (Giuliani, 2018). The rims of kimberlitic olivines are proposed to have crystallised from the kimberlite magma itself during ascent, while the cores represent disaggregated olivine from the mantle wall-rock assimilated during ascent (Arndt *et al.*, 2010; Bussweiler *et al.*, 2015; Cordier *et al.*, 2015; Giuliani, 2018; Pilbeam *et al.*, 2013). The MgO, FeO and MnO contents of BD3067 olivines match those in equilibrium with a kimberlite magma, but the case is not as straightforward for NiO. The proximal olivines and the rims of the distal olivines have a low NiO concentration (0.18-0.2 wt.%), equal to the rims of kimberlitic olivines, however the cores of the distal olivines have higher NiO concentrations representative of pre-existing mantle olivine. This observation leads to the conclusion that the proximal olivine in BD3067 have fully re-equilibrated with the kimberlite melt and local mineral assemblage but re-equilibration is incomplete in the distal olivines which preserves diffusion profiles, such as those observed in Ni, Cr and Ti (Figure 6.4).

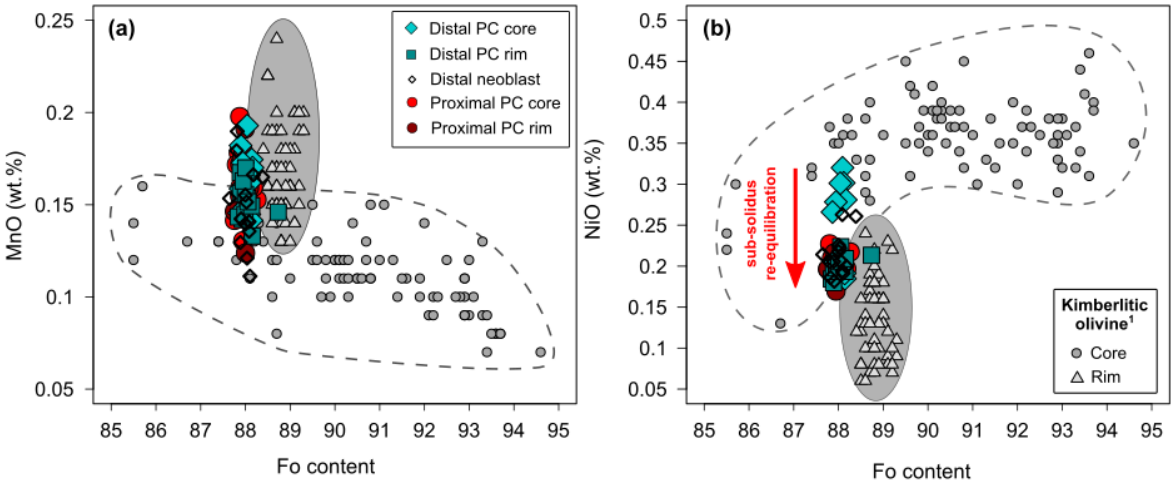

Figure 6.9 *Comparison of the forsterite, NiO and MnO contents of the distal and proximal olivine porphyroclasts and neoblasts in BD3067 against the olivine core and rim compositions from kimberlitic olivine xenocrysts from Kimberley ([1]Giuliani 2018). Kimberlitic olivine cores represent disaggregated mantle olivine and the rims are magmatic olivine in equilibrium with the kimberlite magma.*

In the main vein of BD3067 the olivine and clinopyroxene are homogeneous in all elements. Equilibrated coexisting mantle olivine and clinopyroxene have a K_D^{Fe-Mg} value close to 1 (Pearson *et al.*, 2003; Seckendorff & O'Neill, 1993). In the main vein of BD3067, the homogeneous clinopyroxene and bordering olivine have Mg# of 90.6 ± 0.75 (n=15) and 88.0 ± 0.21 (n=12), respectively, which is close to equilibrium whereas the distal olivine porphyroclasts and the clinopyroxene away from the main vein show a greater range in Mg# (cpx Mg# = 91.1 ± 1.78, n=30; olivine Mg# = 88.0 ± 0.36, n=14). As for Ni, based on a comparison with $D_{Ni}^{ol/cpx}$ of close to 0.13 for equilibrated mantle xenoliths (Gibson *et al.*,

2013; Stosch, 1981), the lower Ni, proximal clinopyroxenes (Ni = 185 ± 23 ppm) are close to equilibrium with: (i) un-zoned olivines; (ii) neoblasts; and (iii) porphyroclast rims (Ni = 1548 ± 271 ppm).

The clear differences between the levels of equilibration in mineral grains in the main vein and the regions distal to it in BD3067 highlight controls of: (i) local temperature; (ii) concentration gradients; and (iii) mineral assemblage. The olivine porphyroclasts bordering the main vein all have homogeneous compositions (e.g. Olivine M in Figure 6.4d). It is likely that the diffusivity of Ni and Cr in olivine and subsequent re-equilibration was increased near the vein due to the higher concentration gradients and temperatures associated with the larger volume of melt undergoing channelized flow (Griffin *et al.*, 1996).

6.5.2 Late-stage crystallisation of accessory phases

The major-element data suggest that the olivine content in BD3067 became buffered at Fo_{88}, perhaps due to the resorption of orthopyroxene (Bussweiler *et al.*, 2015; Giuliani *et al.*, 2017; Pilbeam *et al.*, 2013), but the Ni and Cr contents were still changing in response to the precipitation of late-stage minerals, such as sulfides and chrome-spinel, and a lag in diffusion. The infiltrating silico-carbonatite (kimberlite) melt is depleted in Ni (Roex *et al.*, 2003; Soltys *et al.*, 2018) and the Cr concentration is dependent on the abundance of garnet in the melt source. The clinopyroxenes are not particularly enriched in Cr (Figure 3.5) and Cr-spinel is only a minor phase in the vein assemblage, which implies that the melt was not significantly enriched in Cr.

A number of authors have suggested that an immiscible sulfide melt is produced at a late stage of kimberlite melt evolution (Giuliani *et al.*, 2013b; Lorand & Grégoire, 2006) and Aulbach *et al.* (2017b) attribute low Ni in mantle clinopyroxene from SW Greenland to concomitant sulfide saturation during metasomatism. For olivine to exchange Ni with sulfides, the latter must have initially been low in Ni. If the metasomatic agent was Ni-poor then it is possible that a Fe-Cu immiscible liquid separated from the melt and precipitated Fe-Cu base metal sulfides (BMS), as suggested by Lorand & Grégoire (2006) for the origin of Fe-Cu BMS in phlogopite (± ilmenite ± rutile) peridotites. In the case of BD3067, the introduction of sulfides, a phase for which Ni is a stoichiometric component, shifted the distribution coefficients for the evolving mineral assemblage. As a result local chemical gradients changed depending on the resorbing or crystallising phases (e.g. Giuliani *et al.* 2014a); the late-stage crystallisation of Ni-poor sulfides catalysed Ni re-distribution and drove the Ni concentration down in olivine (e.g. Barnes *et al.* 2013). The sulfides are associated with olivine porphyroclasts, but there is no systematic spatial relationship between the position of the sulfides and the specific zoned olivine porphyroclasts. The lack of a close spatial relationship between the olivine and the sulfides suggests that there has been migration of Ni to distant sulfides facilitated by open grain boundaries and cracks in the old crystals; this sluggish solid-state diffusion is able to produce long wavelength, near-symmetrical profiles like those observed in this study (e.g. Leitch *et al.* 1979). The same systematic variation in Fe and Cu (other stoichiometric components of sulfides) is not observed, this is likely because the melt was enriched in Fe and Cu relative to the olivine. It is also possible that the high concentrations of Fe in olivine, as a stoichiometric component, renders the effect of co-precipitating sulfides negligible compared to that on Ni where the relative change is much greater. If the sulfide melt was enriched in Cu (Lorand & Grégoire, 2006) there would be no concentration gradient to cause any Cu loss from olivine.

It is plausible that a similar mechanism has affected the redistribution of Cr and Ti. As aforementioned, it is expected that the melt was not particularly enriched in Cr, and that most of the Cr was partitioned into diopside, Cr-spinel and/or garnet during the early stages of crystallisation. The later stage melt, interacting with the distal olivine porphyroclasts, was therefore likely to be relatively Cr-poor. This reduced concentration gradient meant that re-equilibration was slower. Ti has also been affected by the crystallisation of diopside and ilmenite, with decreasing temperature (cooling post-metasomatism) Ti is preferentially partitioned from olivine to clinopyroxene (Witt-Eickschen & O'Neill, 2005) and during subsolidus re-equilibration Ti will diffuse out of olivine and into adjacent clinopyroxene (Cherniak & Liang, 2014). Ti diffuses very slowly in olivine due to its high charge, therefore explaining the sluggish re-equilibration (see Chapter 8).

6.5.3 Olivine diffusion anisotropy

The subsolidus re-equilibration of the metasomatic mineral assemblage in BD3067 has been achieved for many elements but the most systematic variation is observed in Ni and Cr. These elements have been slower to equilibrate than others, but only in some crystals (Figure 6.4). Part of this is due to the influence of late-stage crystallizing phases, e.g. sulfides, but the decoupled preservation is also influenced by the anisotropic diffusion of Ni and Cr in olivine.

Most studies that have quantified diffusion of Ni in olivine have used the parameterisation given by Chakraborty (2010), which combines the results of Holzapfel *et al.* (2007) and Petry *et al.* (2004). This parameterisation states that both Ni and Fe-Mg diffusion are six times faster along the [001] axis than the [100] and [010] axes. Since Ni diffuses faster along the [001] axis than Fe-Mg, this assumption implies that Ni diffusion should also be faster in the [100] and [010] axes. This relationship was investigated by Spandler & O'Neill (2010) who experimentally determined the relationship between diffusion rate and crystallographic orientation in San Carlos olivine equilibrating with a silicate melt. They published the diffusion coefficients of 19 elements in each of the three principle crystallographic axes. Spandler & O'Neill (2010) showed that there is a strong anisotropy in Ni and Cr diffusion compared to other elements. This is represented in Figure 6.10a by the higher gradient in logD for Ni and Cr relative to Fe-Mg and Mn. Ni and Cr diffuse faster along the [001] axis and slower along the [010] axis than Fe-Mg, which magnifies the order of anisotropy. Ito & Ganguly (2006) also found Cr to have anisotropic diffusion in olivine. The results of Spandler & O'Neill (2010) agree with the parameterisations in Chakraborty (2010) and Dohmen & Chakraborty (2007) for the [001] axis where Ni diffusion is 1.5 times faster than Fe-Mg, but they differ in the factor of anisotropy for Ni and Cr. The anisotropy observed by Spandler & O'Neill (2010) is as follows:

$$D^{Ni}_{[001]} = 9D^{Ni}_{[100]} = 11D^{Ni}_{[010]}$$

$$D^{Cr}_{[001]} = 6D^{Cr}_{[100]} = 17D^{Cr}_{[010]}$$

The observations of isolated Ni and Cr disequilibrium in the (001) plane of olivine porphyroclasts in BD3067 support the implication that their diffusion in olivine is faster in the [001] axis and slower in the [100] and [010] axes, than Fe-Mg, Mn, V, Sc etc. and highlight the importance of crystallographic orientation as a control on multi-element diffusion in olivine. The results here are consistent with other

studies in natural volcanic systems which have also inferred that Ni diffusion can be slower than Fe-Mg interdiffusion (e.g. Ruprecht & Plank 2013; Vinet & Higgins 2010).

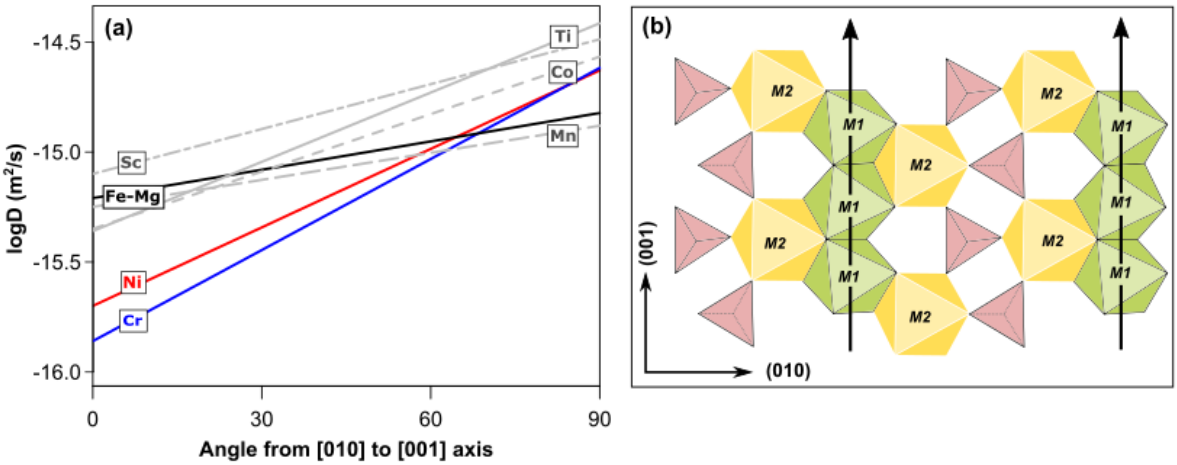

Figure 6.10 *(a) Diffusion coefficients for a selection of major, minor and trace elements in olivine, between the [010] axis (at 0°) and the [001] axis (at 90°) as determined by Spandler & O'Neill (2010). The elements are labelled on the diagram, including Fe-Mg interdiffusion. The level anisotropy is depicted in the gradient of the line for each element. (b) The olivine structure, showing the position of the M1 and M2 sites relative to the tetrahedra (pink triangle) in the (001) and (010) orientations. The M1 sites form chains parallel to (001), the preferred diffusion pathway for M1 ordered cations, such as Ni and Cr^{3+}, is along these chains.*

The greater anisotropy in Ni and Cr, relative to other elements, can be explained by their ordering in the olivine crystal structure. Ni is preferentially ordered into the M1 site in olivine, primarily due to its high electronegativity (Bish, 1981; Boström, 1989). The M1 sites form chains parallel to the [001] axis (Figure 6.10b) and the preferred diffusion pathway for Ni is along the M1 chains (Miyamoto & Takeda, 1983). As a result, Ni diffuses much faster along the [001] axis than the [100] and [010] axes. The diffusion mechanisms causing the enhanced anisotropy of Cr in olivine are poorly constrained (Ito & Ganguly, 2006) but it is understood that Cr^{3+} orders preferentially onto the M1 sites, and as a result has a stronger anisotropy. Cr^{2+} has an even distribution across M1 and M2 sites and therefore shows less anisotropy than Cr^{3+} (Jollands *et al.*, 2017). Jollands *et al.* (2017) find a similar level of anisotropy between Cr^{3+} and Ni^{2+}, hence the correlations observed in this study (Figure 6.3) could imply that the majority of Cr in the olivine porphyroclasts in BD3067 is Cr^{3+}.

The anisotropy of M1 ordered elements in olivine can be increased further by silica activity (Jollands *et al.*, 2017; Zhukova *et al.*, 2014). The silica activity (a_{SiO_2}) of the melt equilibrating with the olivine impacts the diffusion coefficients of M1 ordered cations because increased a_{SiO_2} creates more M1 vacancies, which increases the diffusion rates of M1 ordered cations along the [001] axis (Zhukova et al., 2014). Therefore, the low a_{SiO2} of kimberlite and carbonatite magmas is anticipated to decrease diffusion rates of Ni and Cr in olivine by an order of magnitude (Jollands *et al.*, 2017; Zhukova *et al.*, 2014).

In Section 6.4 a correlation was observed between the orientation of the crystallographic axes in the olivine porphyroclasts and the extent of Ni disequilibrium. Figure 6.8 showed that the closer the olivine plane was cut to the (001) plane, i.e. the greater the component of the two slow axes in the plane, the greater the core-rim range in NiO. This supports the conclusion that the anisotropic diffusion of Ni and

Cr in olivine has meant that these elements have been slow to re-equilibrate in the [100] and [010] (and intermediate) slow axes, whereas faster diffusion along the [001] axis has facilitated re-equilibration.

6.6 Timing of kimberlite metasomatism

Timescales of metasomatism are generally estimated by dating minerals or modelling diffusion profiles. The kimberlite metasomatism exhibited in BD3067 is dated using the U-Pb systematics of a large zircon in the vein assemblage and constrained further by modelling the Ni diffusion profiles in the olivine porphyroclasts.

6.6.1 Zircon dating

The large zircon present in the vein of BD3067 was dated using the ESI UP193UC laser inductively coupled to a Nexion 350D quadruple mass spectrometer (LA-ICP-MS) at the University of Cambridge. The data was processed using Ijolite©and the data reduction software, X-U-Pb-Geochron4. Three reference zircons of different ages were used as standards. Plesovice (Sláma *et al.*, 2008) was used as the primary standard with an age of 337 ± 1 Ma, and 91500 (1065 ± 1 Ma; Wiedenbeck *et al.* 1995, 2004) together with an in-house zircon KLDF (553 Ma; Dr. Richard Taylor) were used as secondary standards. The method reproduced the age of the secondary standards to within 10%.

Analysis of the same zircon over 3 days of testing and analysis produced a Pb^{206}/U^{238} age of 84 ± 11 Ma. The Pb^{207} concentrations were too low to obtain Pb^{207}/Pb^{206} or Pb^{207}/U^{235} ages. Nonetheless, the results of this preliminary investigation indicate that the metasomatism occurred concomitantly with the Late Cretaceous kimberlite activity in Kimberley (Figure 6.11), including the eruption of the host Bultfontein kimberlite (84 ± 0.9 Ma; Kramers *et al.* 1983).

6.6.2 Diffusion modelling

Diffusion modelling has been carried out to improve on the resolution of the age of metasomatism provided by U-Pb dating of zircon in BD3067. The preservation of Ni and Cr disequilibrium in the olivine porphyroclasts provides diffusion profiles that can be used to estimate the timing of metasomatism relative to the emplacement of the Bultfontein kimberlite. The subsolidus re-equilibration of Ni has been modelled as opposed to Cr because Ni diffusion in olivine is better understood than Cr diffusion. The calculations in this section estimate the timescales over which the large porphyroclasts (3-6 mm diameter) in BD3067 equilibrate with their local mineral assemblage following modal metasomatism by a kimberlite melt. The calculations assume that Ni diffusion in the xenolith ceased during kimberlite emplacement and cooling, hence the times represent the age of metasomatism prior to the emplacement of the Bultfontein kimberlite at 84 ± 0.9 Ma (Kramers *et al.*, 1983). A first order approximation can be made using the simplistic relationship that the diffusion time (t) is proportional to the distance (x) squared over diffusion rate (D): $t \propto \frac{x^2}{D}$; and a more thorough approach uses the one-dimensional diffusion equation of Crank (1956):

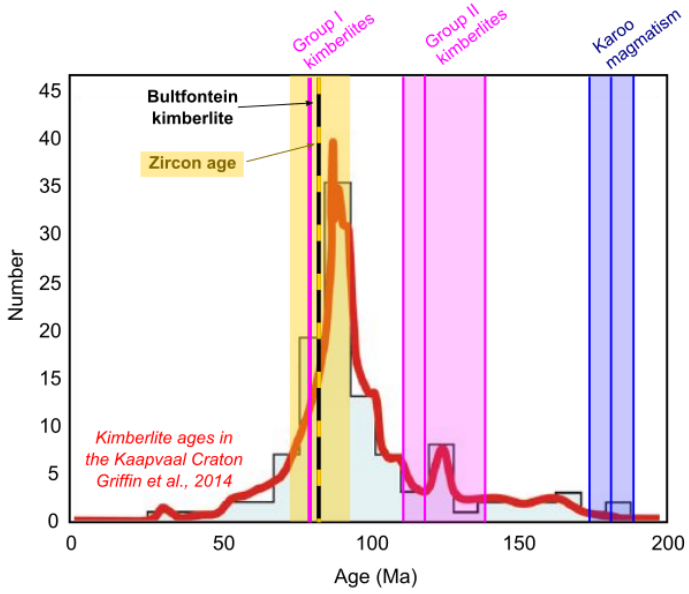

Figure 6.11 *Histogram from Griffin* et al. *(2014a) showing the age distribution of kimberlites emplaced during the past 200 Ma in the Kaapvaal Craton. The age of the Bultfontein kimberlite (Kramers* et al.*, 1983) is overlain alongside the age of metasomatic zircons associated with: (i) periods of Group I and II activity (Kinny & Dawson, 1992; Konzett* et al.*, 1998, 2000); (ii) Karoo magmatism (Giuliani* et al.*, 2014b); and (iii) the zircon dated in this study from veined xenolith BD3067.*

$$C = (C_0 - C_e)erf(\frac{x}{2\sqrt{Dt}}) + C_e \tag{6.1}$$

Where C_0 is the concentration at the core, C_e is the concentration of an element at the rim, x is the distance from the edge of the crystal, and C is the elements concentration at position x. In both cases the diffusion coefficient for Ni in the [001] axis was calculated using the parameterisation in Equation 6.2 (Chakraborty, 2010; Holzapfel *et al.*, 2007; Petry *et al.*, 2004)

$$D^{Ni}_{[001]} = 3.84\times10^{-9}\left(\frac{fO_2}{10^{-6}}\right)^{\frac{1}{4.25}} 10^{1.5(X_{Fe}-0.1)} exp\left(\frac{-220000+(P-10^5)(7\times10^{-6})}{RT}\right) \tag{6.2}$$

The anisotropy in diffusion rate was considered to be close to the factors established by Spandler and O'Neill (2010), i.e. 10 times slower in the [100] and [001] axes. The low silica activity of a kimberlite melt was also taken into consideration because diffusion rates are proposed to be slower during metasomatism by a low a_{SiO_2} melt (Zhukova *et al.*, 2014). There is no formal parameterisation to account for this difference with respect to kimberlite melts but based on the conclusions of Zhukova *et al.* (2014), the diffusion rates at low a_{SiO_2} are decreased by a factor of 10.

In Chapter 4, the *PT* conditions of BD3067 were not estimated because of the lack of either orthopyroxene or garnet in the mineral assemblage. Therefore, the timescales of re-equilibration are calculated at a range of temperature and pressure conditions appropriate to the Kaapvaal geotherm. The simple relationship of $t = \frac{x^2}{D}$ alone, demonstrates the several orders of magnitude change in equilibration

timescales for a 2 mm crystal over the temperature interval 900-1250 °C, where homogeneity can be achieved within 1 million years at 900 °C and as fast as 600 years at 1250°C, close to the base of the lithosphere.

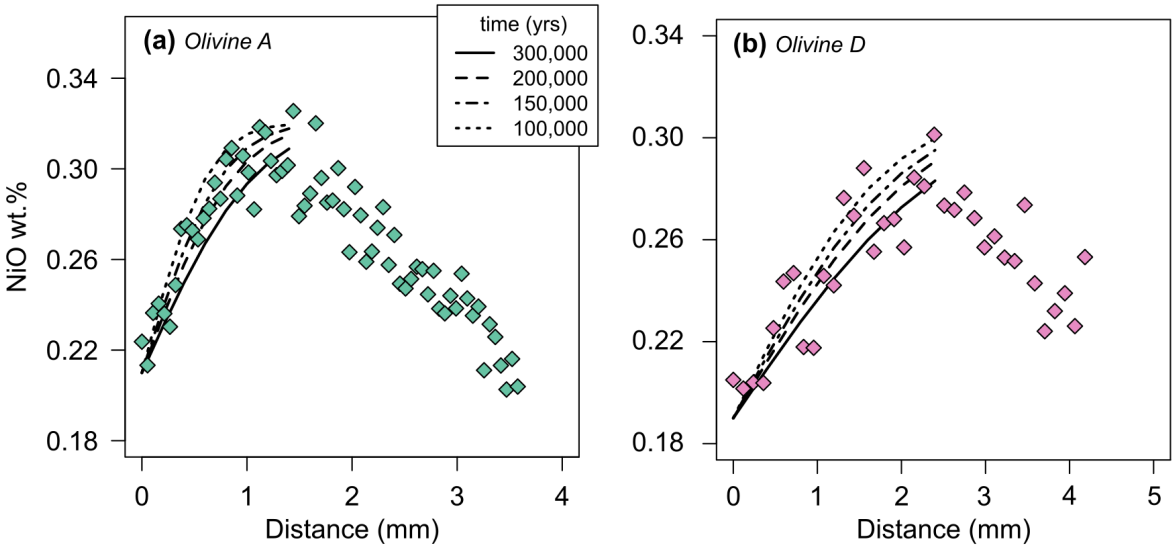

Figure 6.12 *NiO profiles from (a) Olivine A and (b) Olivine D with the calculated diffusion profile 100,000 to 300,000 years after chemical perturbation at 1000 °C.*

In order to further constrain the timescales of re-equilibration, the Ni profiles in the olivine porphyroclasts are fitted using Equation 6.1. The conditions that fit the profiles the best imply that at 1000 °C metasomatism occurred 200,000-300,000 years prior to kimberlite emplacement (Figure 6.12), and at 1200 °C this decreases to 10,000-20,000 years. Given the lack of garnet in the mineral assemblage, 1200 °C is most likely an overestimate of the temperature and 1000 °C or cooler is more realistic. Therefore the time estimate at 1000 °C can be treated as a minimum estimate because cooler temperatures will result in longer timescales of diffusion and hence subsolidus re-equilibration.

6.7 Xenolith history

The clinopyroxene vein in Bultfontein mantle xenolith BD3067 crystallized during reactive percolation of a very early pulse of proto-kimberlite melt that infiltrated and reacted with harzburgite wall rock. This involved assimilation of orthopyroxene (see Chapter 5) and diffusive exchange with the olivines in the mantle wall rock, together with fractionation of clinopyroxene and phlogopite from the melt (e.g. Aulbach *et al.* 2017b; Lim *et al.* 2018; Simon *et al.* 2003). If the clinopyroxene crystallised during an early stage of fractionation then the changing mineral assemblage created localised concentration gradients that initiated elemental re-distribution during subsolidus re-equilibration. At a later stage of fractionation, the residual melt became saturated in sulfur (e.g. Aulbach *et al.* 2017b; Giuliani *et al.* 2013b). As sulfides precipitated the equilibrium conditions changed again and the introduction of a phase with Ni as a stoichiometric component drove the equilibrating olivine Ni concentration even lower. The Cr concentration of the olivines was affected by the initial fractionation of clinopyroxene and Cr-spinel. Many elements experienced diffusive exchange during metasomatism, the subsolidus re-equilibration of

most elements is complete, but the lag in Ni and Cr diffusion, caused by anisotropic diffusion at low a_{SiO_2}, has limited subsolidus re-equilibration and hence diffusion profiles are preserved.

In this scenario, the newly formed mineral assemblage achieves local equilibrium over time, until another kimberlite pulse utilises the pathway generated by thousands of years of metasomatism to ascend to the surface (Giuliani *et al.*, 2014a, 2016). The rapid, violent ascent of the kimberlite fractures the wall-rock and the metasomatised mantle becomes entrained in the kimberlite. Figure 6.13 shows a summary of the metasomatic history of xenolith BD3067.

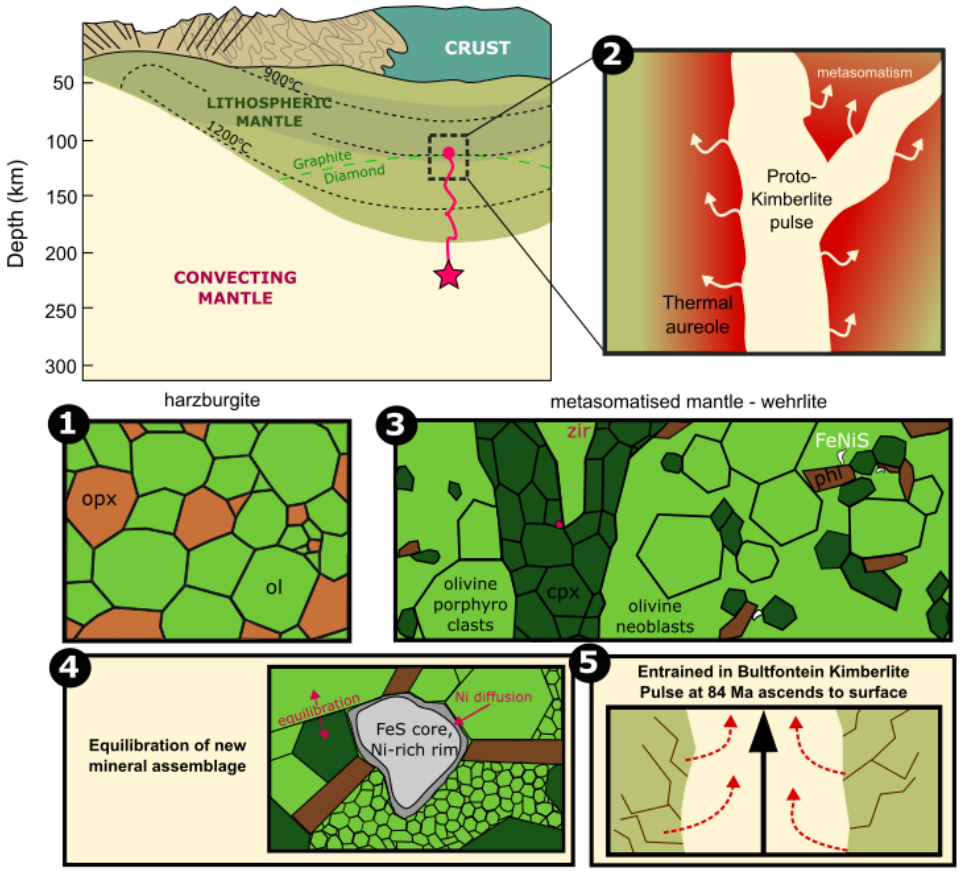

Figure 6.13 *Schematic diagram summarising the history of the veined xenolith from Bultfontein (BD3067). The emplacement of the Bultfontein kimberlite is preceded by a period of melt infiltration and metasomatism. The metasomatism changes the equilibrium conditions by altering the mineral assemblage. The subsequent re-equilibration takes place over a short timescale, 10^3-10^5 years, and the disequilibrium can be preserved if the xenolith is entrained before equilibration has been achieved.*

6.8 Metasomatism preceding kimberlite eruption

The sub-continental lithospheric mantle has a complex history and BD3067 represents an important period of metasomatism prior to eruption of the kimberlite at the surface. Kimberlite eruptions are enigmatic but it is generally agreed that they consist of pulses of magmatism (e.g. Dawson & Smith 1977; Field *et al.* 2009; Giuliani *et al.* 2014a, 2016; Mitchell 1991, 2008). Polymict breccias from Bultfontein are interpreted to represent 'failed' kimberlite melts that did not make it to the surface (Giuliani *et al.*, 2013b) and recently

Jollands *et al.* (2018) identified two stages of metasomatism preserved in garnet, the second of which was interpreted as reactive infiltration of a silico-carbonatite-rich melt, assumed to be a proto-kimberlite melt.

The ten to hundred thousand year timescales of equilibration estimated from Ni disequilibrium in the mantle olivine next to a kimberlite melt vein in BD3067 are comparable to, or slightly longer than, those derived from previous studies (Cordier *et al.*, 2015; Giuliani *et al.*, 2013a; Griffin *et al.*, 1996; Jollands *et al.*, 2018; Smith & Ehrenberg, 1984). The olivine disequilibrium related to crystallographic orientation observed in the detailed study of BD3067 has added an extra constraint to those studies using garnet zoning, which have a more uniform compositional zonation due to their isotropic structure. The range of timescales provided both here and in previous studies supports the hypothesis that a period of metasomatism by 'failed' kimberlite melts precedes the final kimberlite eruption, and that this period is necessary to provide a lubricated pathway for the 'successful' kimberlite to exploit (Bussweiler *et al.* 2016; Fitzpayne *et al.* 2018b; Giuliani *et al.* 2013b, 2014a, 2016; Soltys *et al.* 2018).

6.9 Conclusions

This chapter has investigated the processes associated with the infiltration of metasomatic kimberlite melts in the sub-cratonic lithospheric mantle, by focusing on a peridotite xenolith that represents a relatively rare, incomplete stage of melt-rock reaction. The xenolith (BD3067), which was brought to the surface by the Late Cretaceous Bultfontein kimberlite (South Africa), contains a spectacular metasomatic vein of diopside, sulfide, phlogopite, spinel and zircon set in a dunite host that is interpreted to be a relict melt channel.

Unique information on the variable rates of diffusion of major, minor and trace elements during sub-solidus re-equilibration that follows mantle metasomatism is preserved in relict olivine porphyroclasts (Fo88). These have homogeneous concentrations of Mg, Fe and Mn but exhibit significant core to rim decreases in both NiO (0.32 – 0.18 wt.%), and Cr (60 – 35 ppm). This heterogeneity is strongly influenced by concentration gradients in Ni and Cr away from the main melt channel and also the localised crystallisation of sulfides and spinel. EBSD mapping of the olivine porphyroclasts shows that Ni and Cr zoning is only evident in grains that contain large components of the [100] and [010] slow diffusion axes.

Diffusion models suggest the preservation of the observed core-to-rim variation of Ni in olivine requires that mantle metasomatism must have occurred within the order of 10^5 years prior to emplacement of the host Bultfontein kimberlite. This metasomatism may have been fundamental to the subsequent ascent and emplacement of the host kimberlite. This unique time constraint on preservation of core-to-rim variations in Ni and Cr combined with the crystallographic control on diffusion may explain why Ni and Cr heterogeneity in otherwise homogeneous mantle olivine has been so rarely encountered.

A broader implication of this study is that the magnitude of anisotropy in diffusion for Fe-Mg in olivine is different to highly-ordered elements such as Ni, which appear to diffuse much more slowly along the [100] and [010] axes. This is of significance to both mantle and magmatic olivines and highlights the importance for diffusion studies that combine chemical zonation with crystallographic information.

Chapter 7

Volatile storage in NVFMMs

7.1 Introduction

Despite the fact that volatile-rich minerals, such as amphibole and phlogopite, contain high contents of H_2O and the halogens, their volumetric insignificance diminishes their influence on the capacity of the SCLM to act as a reservoir for volatile elements. By comparison, nominally volatile-free mantle minerals (NVFMMs) are able to host small, although non-negligible, quantities of H_2O, F and Cl and their high modal abundance in the mantle makes them a potentially significant (but overlooked) host of volatiles in the SCLM. The H_2O contents in NVFMMs from the sub-cratonic mantle have been described in numerous studies (see Demouchy & Bolfan-Casanova 2016; Peslier 2010; Peslier *et al.* 2017 and references therein), but the halogens have been rather neglected thus far, despite experimental studies showing: (i) the high capacity of both olivine and the pyroxenes to host F (e.g. Beyer *et al.* 2012; Grützner *et al.* 2017; Joachim *et al.* 2015); and (ii) that the incorporation of F influences H, and vice versa (e.g. Guggino 2012; Urann *et al.* 2017). This is the first study of natural samples that quantifies the storage of F in NVFMMs in the sub-cratonic lithospheric mantle. This chapter presents the results of secondary ion mass spectrometry (SIMS) to measure the concentration of H_2O, F and Cl in olivine, orthopyroxene and clinopyroxene, and fourier transform infrared spectrometry (FTIR) to constrain the incorporation mechanisms of H_2O and F in olivine and orthopyroxene from Bultfontein and Mothae.

7.2 Secondary ion mass spectrometry: Concentration of H_2O, F and Cl in NVFMMs

Secondary ion mass spectrometry (SIMS) has become increasingly popular to measure H_2O, F and Cl in nominally volatile-free minerals. This is due to the characterisation of new standards and refinements to the analytical techniques that allow H_2O to be detected to the 0.5 ppmw level and F and Cl at even lower concentrations (Gibson *et al.*, 2020; Hauri *et al.*, 2006; Kumamoto *et al.*, 2017; Kurosawa *et al.*, 1997; Mosenfelder & Rossman, 2013a,b; Mosenfelder *et al.*, 2011; Peslier *et al.*, 2017; Rossman, 2006; Urann *et al.*, 2017). SIMS uses an ion beam to sputter ions from the sample, which are then directed to a mass spectrometer to be counted. The biggest challenge to using SIMS for hydrogen analysis is that the background concentrations are high (Rossman, 2006) nevertheless, methods of sample preparation, such as mounting in indium rather than epoxy and the use of a Cs^+ beam as opposed to a O^- beam, can be employed to reduce background H concentrations. SIMS analyses were performed on mineral separates over a period of three weeks in September 2018 and May 2019, on the Cameca 4f at the University of Edinburgh. The instrument can detect F and Cl down to ppb and H to ppm levels. San Carlos olivine was added to each mount and acted as a standard to test the background measurements; no measurement below

the analysed value for San Carlos is included in the results. The full sample preparation and analytical method can be found in Appendix 1. In most samples all three main constituent phases were analysed, but in four xenoliths from Bultfontein (BD1140, BD1999, BD3021 and BD3067) olivine was not analysed.

7.2.1 Olivine

The volatile concentrations of olivine in the Bultfontein and Mothae peridotite xenoliths is extremely variable (Figure 7.1). They reach up to 91 ppmw H_2O and 194 ppm F (see supplementary data tables) and are some of the highest concentrations recorded in natural mantle olivine to date. Occasionally during SIMS analyses fluid inclusions with F contents in excess of 3000 ppm were hit; this made it possible to distinguish between F hosted in the lattice and inclusions. Olivine in the spinel harzburgites (both clinopyroxene-absent and clinopyroxene-bearing) have the lowest F concentrations, with most having no F at all. The highest H_2O and F contents are measured in olivine found in peridotites that have interacted with a kimberlite melt (e.g. phlogopite-lherzolite and dunite) or a hydrous siliceous fluid (i.e. orthopyroxene-rich garnet-harzburgite). The F concentrations of 122-194 ppm in olivine from kimberlite melt metasomatised peridotite (BD1141A, BD1153) are the highest observed in sub-cratonic mantle xenoliths. Olivines in the garnet lherzolites contain a greater range in H_2O (avg. 6-103 ppmw) and F (avg. 8-63 ppm) than the kimberlite or fluid metasomatised peridotite (Table 7.1). Most samples exhibit uniform H_2O and F concentrations between different crystals, the exception to this is the high-*T* garnet lherzolite, BD2128 which contains olivine with H_2O contents that range from below detection to 90 ppmw. All Cl analyses of olivine were below the detection limit.

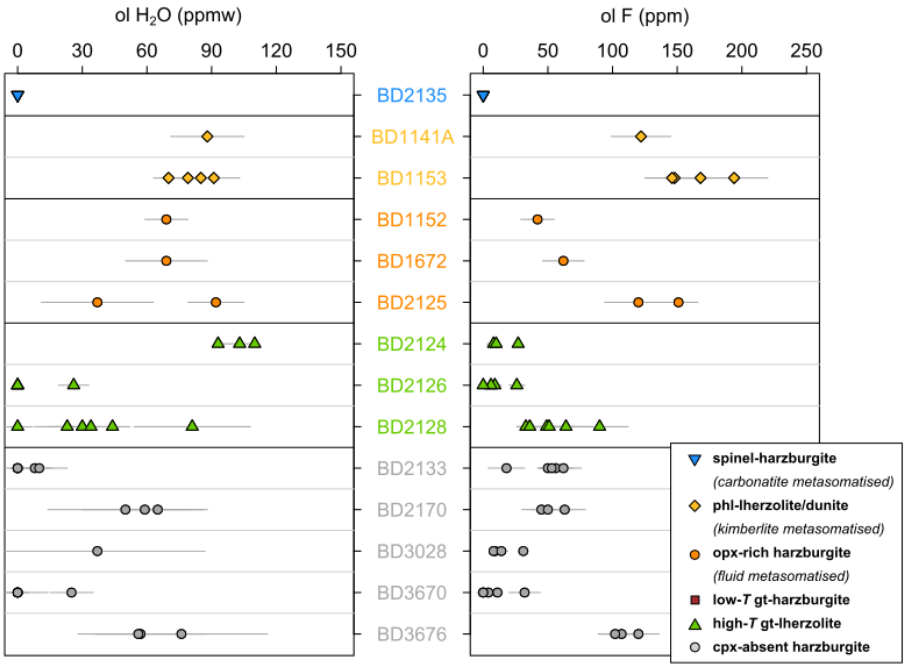

Figure 7.1 *SIMS analyses of the core of olivine separates, from each Bultfontein and Mothae xenolith. The results are grouped and colour coded according to the metasomatic groups identified in Chapters 3 and 5. Errors represent twice the sum of the standard deviation and instrument error. Each point plotted is the average of three point analyses per crystal.*

				Olivine		Orthopyroxene			Clinopyroxene			Bulk	
Sample	**Group**	**Location**	**Lithology**	**H_2O**	**F**	**H_2O**	**F**	**Cl**	**H_2O**	**F**	**Cl**	**H_2O**	**F**
BD2135	A	Mothae	sp-harz *(carb met)*	b.d.l	6	36	b.d.l	1.5	83	16	3	11	5
BD1141A	B	Bultfontein	phl-lherz *(kim met)*	88	122	159	20	b.d.l	300	20	5	99	87
BD1153	B	Bultfontein	dunite *(kim met)*	70	148	199	26	2.4	195	46	3	80	139
BD3067	B	Bultfontein	wehrlite *(kim met)*	-	-	-	-	-	97	25	13	-	-
BD1152	C	Bultfontein	opx-rich gt-harz *(fluid met)*	69	42	236	6	b.d.l	290	13	5	117	28
BD1672	C	Bultfontein	opx-rich gt-harz *(fluid met)*	69	62	254	13	b.d.l	285	22	7	126	43
BD1999	C	Bultfontein	opx-rich gt-harz *(fluid met)*	-	-	232	18	2.2	277	29	6	-	-
BD2125	C	Mothae	opx-rich gt-harz *(fluid met)*	55	130	164	23	1.7	109	26	5	92	76
BD1140	D	Bultfontein	low-*T* gt-harz	-	-	183	5	1.9	280	24	3	-	-
BD2124	E	Mothae	high-*T* gt-lherz	103	8	85	23	2.6	64	41	4	88	11
BD2126	E	Mothae	high-*T* gt-lherz	6	26	142	25	1.7	125	37	5	33	24
BD2128	E	Mothae	high-*T* gt-lherz	24	63	168	27	1.7	139	39	2	49	53
BD2170	E	Mothae	high-*T* gt-lherz	58	53	184	33	2.5	-	-	-	70	49
BD3028	O	Bultfontein	gt-harz	37	31	219	14	b.d.l	-	-	-	81	25
BD3670	O	Bultfontein	sp-harz	8	18	27		1.7	-	-	-	15	11
BD3676	O	Bultfontein	gt-harz	63	110	293	21	1.4	-	-	-	102	86
BD2133	O	Mothae	sp-harz	b.d.l	62	186	15	3.7	-	-	-	45	50

Table 7.1 *Average H_2O (ppmw), F (ppm) and Cl (ppm) concentration in olivine, orthopyroxene and clinopyroxene in each xenolith. The bulk H_2O and F concentrations were calculated using the modal abundances of each element in each xenoliths according to Table 2.1 (Chapter 2. b.d.l below detection limit; - not analysed; carb met: carbonatite metasomatism; kim met: kimberlite metasomatism; fluid met: siliceous fluid metasomatism. All analyses on individual grains are available in the supplementary data tables.*

For some olivine grains it was possible to carry out both core and rim analyses but there are limitations to the method of doing so. Mineral separates were used, and there is therefore the possibility that the true grain boundaries were lost during sample preparation. Additionally, much of the olivine has recrystallised in many of the xenoliths and so the rims of porphyroclasts may be lost. The lack of a systematic difference (either loss or gain) between the olivine core and rim could reflect this uncertainty. Nonetheless, the variation between the 'core' and 'rim' can be used to assess the heterogeneity of the H_2O and F contents in olivine. This is greater in H_2O (±68%) than F (±18%; Figure 7.2). 38% of the olivine analysed show a decrease in H_2O concentration at the rim by an average of -48%, 31% show an increase by an average of +85% and 31% exhibit no change. Of the olivines that show a change in F concentration between the core and rim, 50% have increased concentration of F at the rim by +21%, and 50% have decreased F by -15%. In order to improve the reliability of core-rim analysis, the sample preparation method would be altered to use polished rock fragments (i.e. thin sections) as opposed to mineral separates, which would increase the chance and certainty of mounting a whole crystal where the core and rim can be reliably identified.

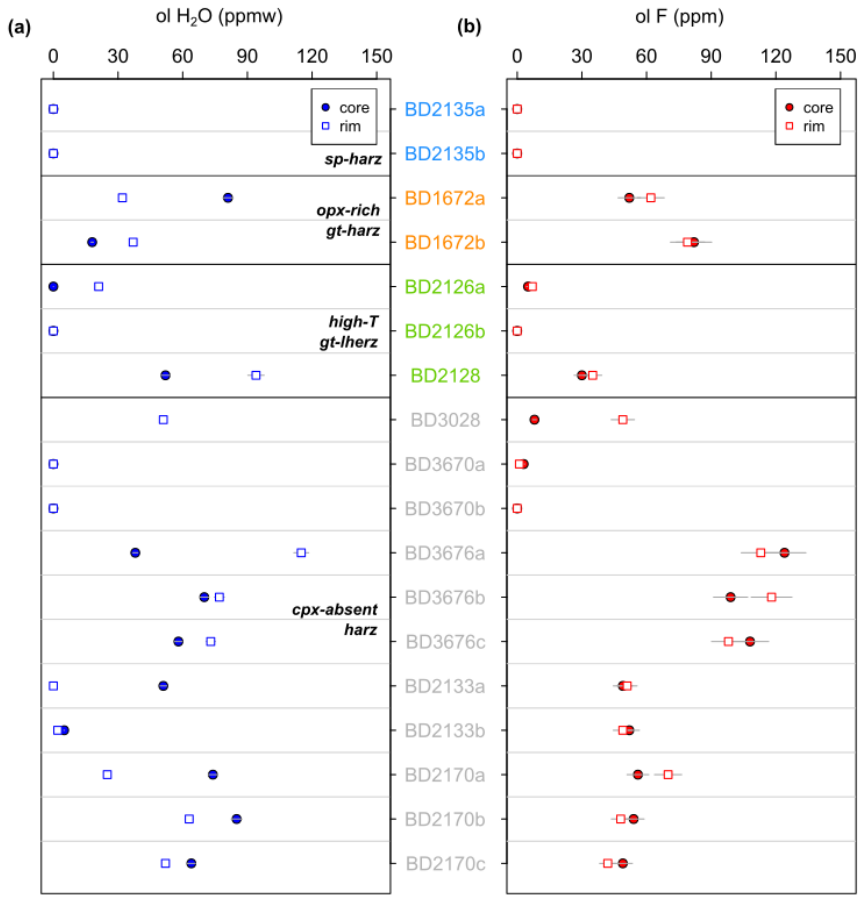

Figure 7.2 *Core and rim variations in select olivine crystals from the Bultfontein and Mothae xenoliths.*

7.2.2 Orthopyroxene

Orthopyroxenes in the Bultfontein and Mothae peridotite xenoliths contains the lowest F concentrations of the three nominally volatile-free mantle minerals analysed (Figure 7.3), while H_2O occupies a similar range of concentrations to the clinopyroxene (Table 7.1). Of the clinopyroxene-bearing peridotites,

the highest F contents in orthopyroxene are observed in the high-*T* garnet lherzolites (22-27 ppmw) while the orthopyroxene-rich harzburgites that have been metasomatised by a hydrous siliceous fluid (Chapter 5) have the highest H_2O contents (150-250 ppmw). Orthopyroxenes in the clinopyroxene-absent harzburgites exhibit a large range in H_2O and F concentrations and contain the highest H_2O contents (garnet-harzburgite BD3676; 308 ± 28 ppmw) and F contents (garnet-harzburgite BD2122; 37 ± 7 ppm). Chlorine concentrations are very low in all orthopyroxene crystals and do not exceed 3 ppm.

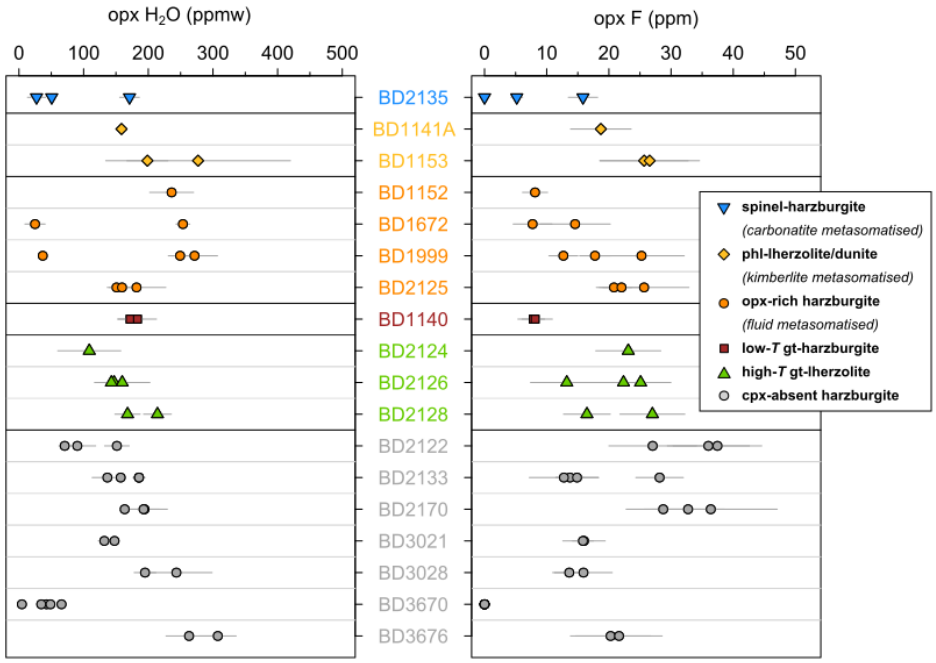

Figure 7.3 *SIMS analyses of orthopyroxene separates from each sample. The results are grouped and colour coded according to the metasomatic groups identified in Chapters 3 and 5. Errors represent twice the sum of the standard deviation and instrument error. Each point plotted is the average of three point analyses per crystal.*

Mineral separates from the same sample have relatively uniform volatile compositions. Core and rim analyses are compared for select orthopyroxene crystals in Figure 7.4. Of the 18 crystals, 50% had an increase in H_2O and F at the rim, with an average increase of +23% H_2O and +13% F. 44% exhibit a decrease at the rim, with an average decrease of -18% H_2O and -17% F. The same limitations and uncertainty in the reliability of assessment of the crystal rim described for olivine is also true for orthopyroxene.

7.2.3 Clinopyroxene

The H_2O content of clinopyroxene reaches 370 ppmw in the Bultfontein xenoliths and only 134 ppmw in the Mothae xenoliths. The F content reaches 26 ppm in xenoliths from Bultfontein and 39 ppm in those from Mothae. As was the case in orthopyroxene, the Bultfontein clinopyroxenes have higher H_2O and lower F concentrations than the Mothae clinopyroxenes (see Chapter 9).

There is very little intra-sample variation in clinopyroxene H_2O and F concentration but there is a great deal of variation between different xenoliths and across the different categories of peridotite (Figure 7.5). The greatest variation is observed in clinopyroxene from proto-kimberlite metasomatised xenoliths

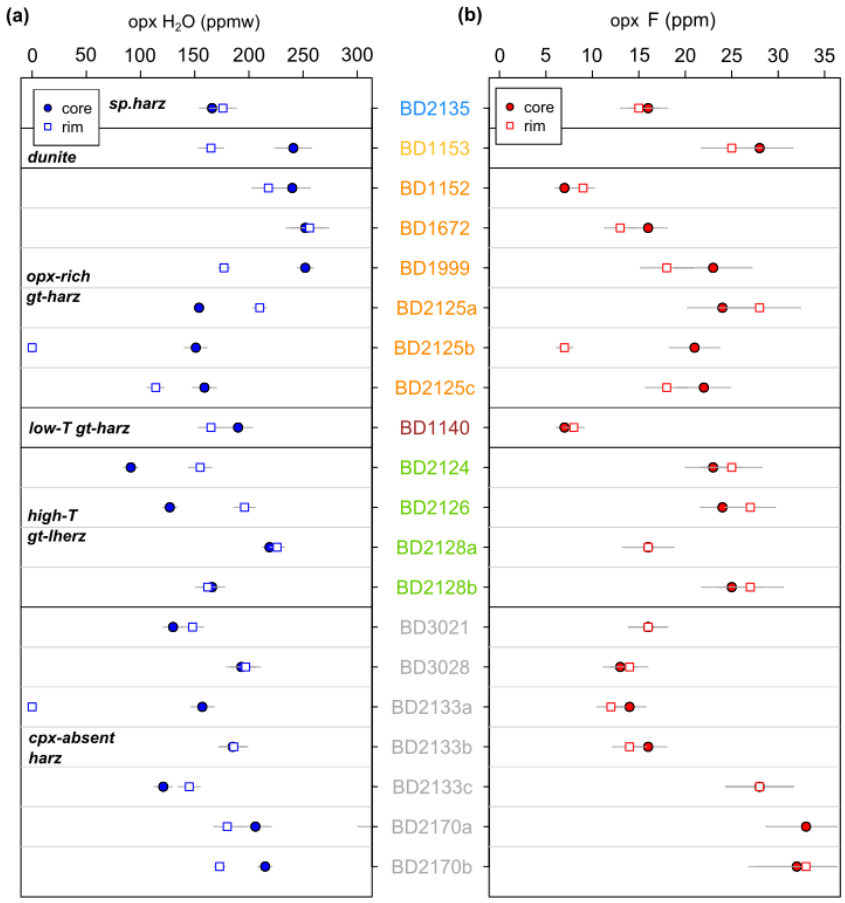

Figure 7.4 *Core and rim variations in select orthopyroxene crystals from the Bultfontein and Mothae xenoliths.*

(phlogopite-lherzolite/dunite/wehrlite), where the average concentration and standard deviation between the three xenoliths is as follows: H_2O = 157 ± 92 ppmw; F = 28 ± 11 ppm; Cl = 8 ± 5 ppm. The highest concentration of H_2O (195 ppmw) and F (46 ppm) is observed in the stealth metasomatised dunite BD1153 where the melt fraction was very low, and the highest concentration of Cl (17 ppm) is observed in the vein in BD3067, where the melt fraction was very high (see Chapter 9). Clinopyroxene volatile concentrations are the lowest in the carbonatite-metasomatised spinel harzburgite, but the sample size is very small (n=2). Clinopyroxene in the siliceous fluid metasomatised orthopyroxene-rich harzburgite also shows a large range in volatile concentrations, H_2O = 259 ± 75 ppmw; F = 24 ± 7 ppm; Cl = 6 ± 3 ppm. The H_2O content of the clinopyroxene in the siliceous fluid clinopyroxene is the highest in the sample suite. The clinopyroxene in the garnet lherzolites have the highest average F content (34 ± 6 ppm) but relatively low H_2O (121 ± 31 ppmw) and Cl (4 ± 2 ppm) concentrations.

Core and rim analyses are compared for select clinopyroxene crystals in Figure 7.6. There are fewer rim analyses for clinopyroxene because the mineral separates were extensively cracked and very fragile, as a result the true rim was often difficult to identify reliably. Most analyses were taken from the centre of the crystal and assumed to be close to the core. Of the few rim analyses, two have increased H_2O concentrations at the rim (+29%), and five exhibit increased F concentration (+15%). Five crystals have lower H_2O contents at the rim (-19%) and two have lower F concentrations at the rim (-21%).

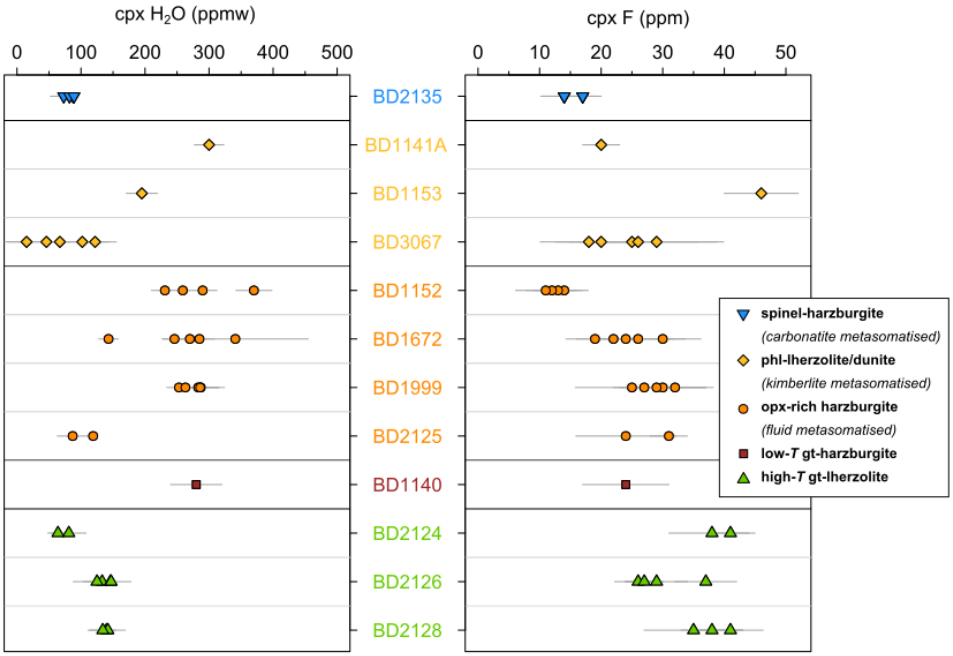

Figure 7.5 *SIMS analyses of clinopyroxene separates, from each sample. The results are grouped and colour coded according to the metasomatic groups identified in Chapters 3 and 5. Error bars represent twice the sum of the standard deviation and instrument error. Each point plotted is the average of three point analyses per crystal.*

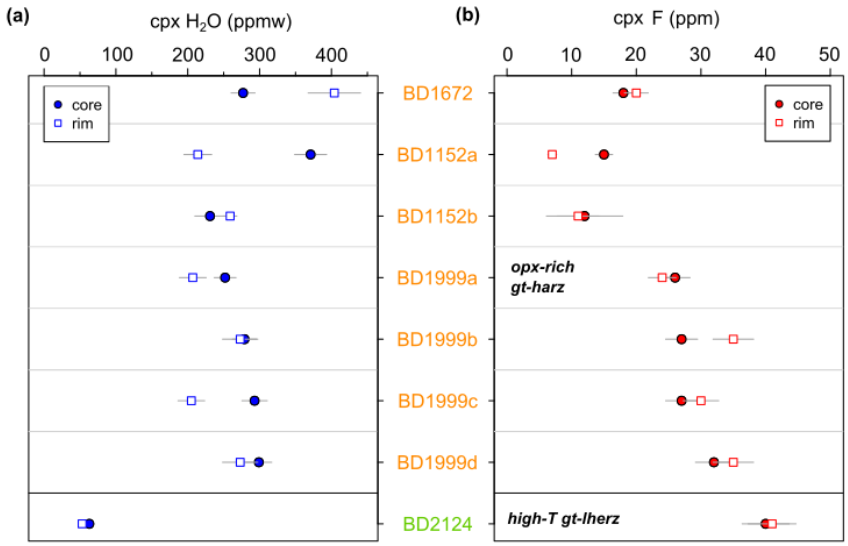

Figure 7.6 *Core and rim variation in select clinopyroxene crystals from the Bultfontein and Mothae xenoliths.*

7.2.4 Bulk rock

In most cases, the H_2O and F concentration of all of the main phases (ol + opx ± cpx) in each xenolith from Bultfontein and Mothae were analysed. The concentration of H_2O and F in garnet was assumed to be negligible based on the observations of Beyer *et al.* (2012) and confirmed by FTIR in this study, where the garnet spectra displayed no absorbance bands in the OH-stretching region. For the fourteen samples in which all of the main phases were analysed, the bulk H_2O and F content held in NVFMMs has been calculated using the average concentration (Table 7.1) and the modal abundance of each phase (Table 2.1)

according to Equation 7.1. This uses the same method that was used in Chapter 3 to calculate the bulk trace-element concentrations.

$$C^{bulk} = X^{ol}C^{ol} + X^{opx}C^{opx} + X^{cpx}C^{cpx}(+X^{gt}C^{gt}) \quad (7.1)$$

The bulk H_2O content in the Bultfontein and Mothae xenoliths exhibits a wide range (from 11 - 126 ppmw), which agrees with the estimated range for the sub-cratonic mantle of 24 - 100 ppmw by Peslier *et al.* (2017). The bulk estimate by Peslier *et al.* (2017) includes the presence of metasomatic phases that contains H as a stoichiometric component, whereas the results here indicate that the NVFMMs alone can host the H_2O budget for the sub-cratonic mantle. Nevertheless, overall the bulk sub-cratonic mantle composition is acknowledged to be towards the lower end of this scale with local enrichments related to metasomatism. The highest bulk H_2O contents (92-126 ppmw) are in the orthopyroxene-rich garnet-harzburgites, consistent with their being hydrated by siliceous fluids.

Six samples (BD2135, BD1152, BD2124, BD2126, BD3028 and BD3670) have low bulk F contents (5-25 ppm) that fall within the range of depleted mantle (11-17 ppm; Workman & Hart 2005) and the estimate for bulk anhydrous peridotite (1.4-31; Urann *et al.* 2017). In contrast, some of the other xenoliths are significantly enriched in F relative to these estimates, for example the Bultfontein dunite BD1153 has a bulk F concentration of 138 ppm. Figure 7.7b shows the relative contribution of each phase to the bulk F concentration. The most abundant phase, olivine, also has the highest F concentration in many of the samples. The olivine F concentration, therefore, has a strong control on the bulk concentration of F in the SCLM. As noted above, F is concentrated in olivine in the xenoliths that exhibit proto-kimberlite (silico-carbonate melt) and siliceous fluid metasomatism.

7.3 Fourier transform infrared spectroscopy: Position of absorbance bands in OH-stretching region

Fourier transform infrared spectroscopy (FTIR) has been used to investigate water storage in mantle silicates since the early nineteen eighties (Rossman, 2006) following the suggestion of Martin & Donnay (1972) that hydrogen might be stored in the deep Earth as OH-groups in minerals. FTIR is a vibrational spectroscopic technique which relies on the fact that OH bonds vibrate at a specific frequency that absorbs certain energies of light (Libowitzky & Beran, 2006). The absorbance can be related to the concentration and is a function of the thickness of the sample, and a calibration factor (Libowitzky & Rossman, 1997; Paterson, 1982; Rossman, 2006). The low mass of the H atom and the short nature, and hence high strength, of OH bonds results in high energy O-H vibrations and absorbance bands that can be identified between 3000-3800 cm^{-1}. This is known as the OH-stretching region, named after the stretching vibration of the OH bond, and was first identified in quartz by Kats *et al.* (1962). Within the OH-stretching region there can be many discrete absorbance bands, the wavenumber of these depends on the position of the OH bond in the crystal lattice and the variation in the strength of the OH bond (i.e. the bond length; Libowitzky & Beran 2006). Therefore, the position of absorbance bands in FTIR spectra is extremely site specific and can be used to investigate the incorporation of H in a mineral as well as quantify the

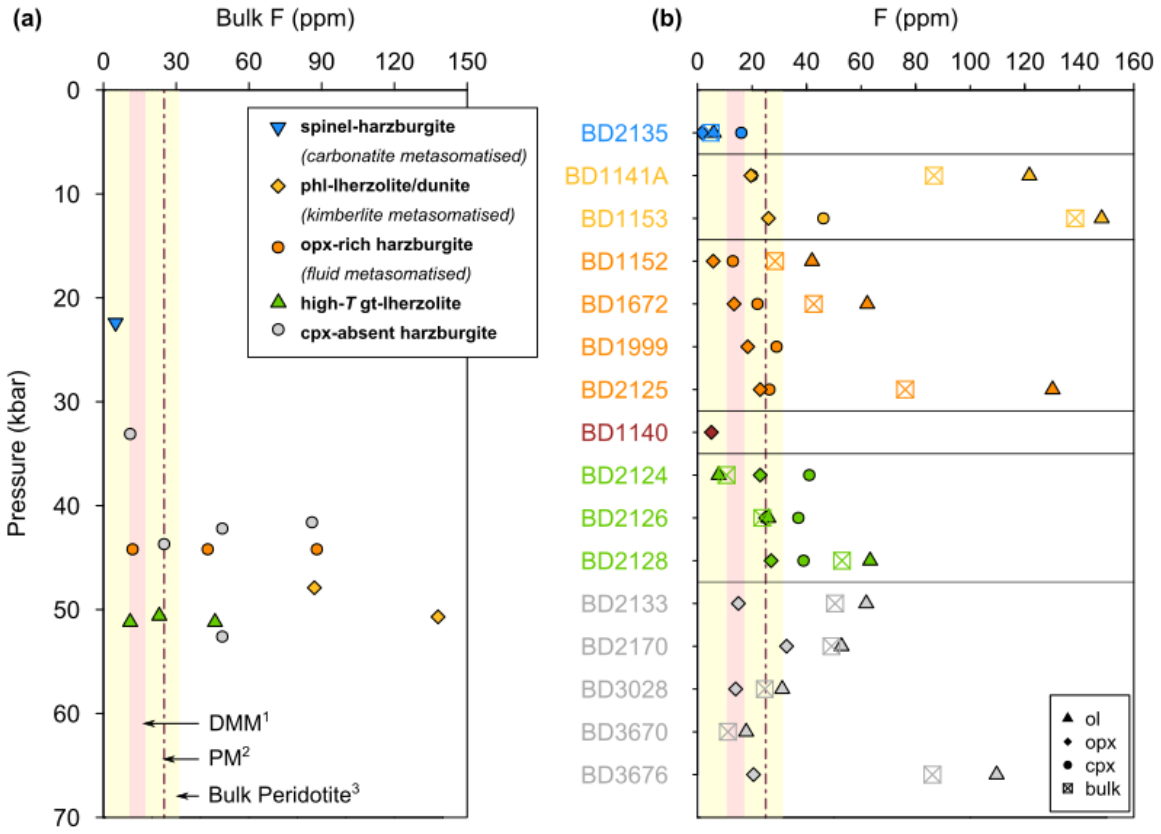

Figure 7.7 *(a) Bulk F concentration against depth; (b) Summary figure showing the average F concentration in olivine, clinopyroxene, orthopyroxene and the calculated bulk composition where all analyses of all phases were available. Samples are grouped and coloured according to the groupings identified in Chapter 5 and summarised in Table 3.6.* [1]*Depleted MORB Mantle (Workman & Hart, 2005),* [2]*Primitive Mantle (McDonough & Sun, 1995),* [3]*Bulk peridotite (***?***)*

concentration. The introduction of a positively charged H ion to the crystal lattice to form an OH group (2-) produces an excess negative charge (1-) that must be charge balanced. Incorporation mechanisms that can charge balance one or more OH groups include: (i) the creation of a cation vacancy; (ii) changing the charge of an adjacent heterovalent cation (e.g. Fe^{2+} to Fe^{3+}); or (iii) coupled substitutions of cations with different valance states (e.g. Si^{4+} - Al^{3+} exchange). Specific incorporation mechanisms can be identified by comparing the spectra to previous studies which have independently determined (usually through controlled experiments) the relationships (e.g. Bell & Rossman 1992; Berry *et al.* 2007a; Kovács *et al.* 2010; Stalder *et al.* 2015; Tollan *et al.* 2018; Walker *et al.* 2007).

FTIR spectra have three components: (i) at lower wavelengths the absorbance bands represent Si-O overtones which are used to identify the crystallographic orientation; (ii) between 2800-3650 cm^{-1} absorbance bands represent the OH-stretching region where O-H bonds associated with different point defects produce absorbance bands at a specific wavenumber; and (iii) absorbance bands between 3650-3700 cm^{-1} are produced by the presence of hydrous phases (i.e. serpentine). The total integrated absorbance in the OH-stretching region can be used to quantify H_2O concentrations using an absorption coefficient and parameters defined by experiments and independent calibration using SIMs (e.g. Aubaud *et al.* 2007; Koga *et al.* 2003; Libowitzky & Rossman 1997; Withers *et al.* 2012). In this study, FTIR was chosen as a

method to gain perspective on the incorporation mechanisms of both H and F in olivine and orthopyroxene rather than to supplement the concentration data acquired by SIMS.

FTIR was carried out at the University of Bern, Switzerland, in collaboration with Dr. P Tollan. The full analytical setup is described in Appendix 1. Unfortunately, the same mineral separates used for SIMS were not prepared for FTIR because their size limited the sample preparation methods. The thickness of the crystal was required to be at least 300-500 μm for FTIR which was not always possible on the very small crystals of olivine that had already been polished down to the core. Therefore, the major-, trace- and volatile-element concentrations were all analysed in the same mineral grain but the FTIR analysis was undertaken on freshly prepared, double polished fragments of the xenolith.

Double polished sections were prepared for the following xenoliths: BD1140, BD1141A, BD1152, BD1153, BD1672, BD1999, BD2125, BD2124, BD2126, BD2128. Where possible, both olivine and orthopyroxene were analysed using FTIR. The cracked and serpentinised nature of the xenoliths limited the acquisition, and in two samples (BD1141A and BD2124) it was not possible to obtain spectra of olivine or orthopyroxene. This was due to either serpentine or another hydrous phase producing a large peak at 3700 cm^{-1} (Khisina *et al.*, 2001; Post & Borer, 2000) which overlaps with the absorption bands produced by OH point defects in olivine and orthopyroxene. In all other samples, optically clear points were chosen for analysis. Another limitation was the sample preparation, small fragments were prepared in a limited time frame but in future it would be preferable to prepare larger sections so to include multiple crystals of each phase. The calculation of concentration from the absorbance is heavily dependent on the number of crystals used (Jackson *et al.*, 2018), because the absorption in each crystallographic axis differs considerably. To account for the different crystallographic axes, and the unknown orientation of the crystal to be analysed, a factor should be incorporated into the concentration calculations (e.g. Bell *et al.* 2003a; Koga *et al.* 2003; Kovács *et al.* 2010; Mosenfelder *et al.* 2011; Withers *et al.* 2012). Jackson *et al.* (2018) recommended that a minimum of 10 randomly oriented crystals are required to produce an accurate estimate of the true concentration. This was not possible from the samples prepared in this study and so FTIR concentrations of H are not considered further.

7.3.1 Olivine

The FTIR spectra of the three principal axes parallel to [100] (commonly referred to as A or α), [010] (B or β) and [001] (C or γ) in olivine are well established and have shown that absorbance in the OH-stretching region is highly anisotropic. The [100] axis has the highest absorbance, followed by the [001] axis and lastly the [010] axis which has very low OH absorbance. As a result, it is common place to acquire polarised FTIR spectra in olivine, particularly in studies such as this where the primary use for FTIR is to investigate incorporation mechanisms as opposed to measure concentrations. Polarised FTIR measurements were made using a Focal Plane Array (FPA) detector. An optically clear point on the olivine crystal was chosen and the polariser inserted. The angle of the polariser was adjusted until one of the three principal axes is found. The three axes were identified by the relative size of the absorbance bands in the wavenumber region 2200-1600 cm^{-1} and compared to reference spectra for mantle olivine (Asimow *et al.*, 2006). The second column in Figure 7.8 shows the shape of the spectra that identify the three principal crystallographic axes in olivine. In each crystal one of the principal axes was found, and the spectra was taken at this point before the polariser was turned 90° to acquire the second principal axis

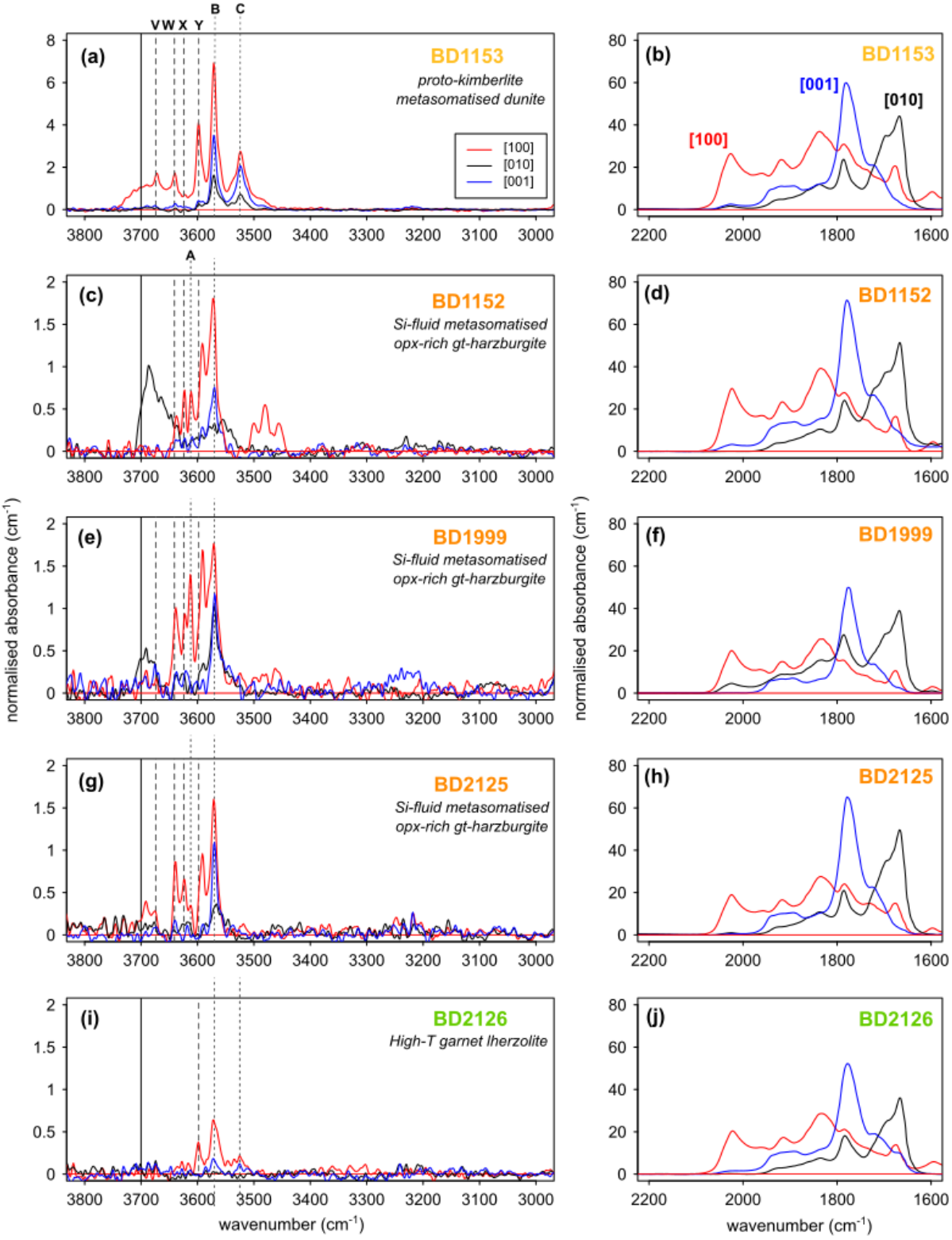

Figure 7.8 *Representative FTIR spectra showing the OH-stretching region in column 1 and the absorbance bands used to identify the three principal crystallographic axes in column 2. Five samples are shown representing (a,b) kimberlite metasomatism xenolith, BD1153; (c-h) siliceous fluid metasomatism, BD1152, BD1999 and BD2125; and (i,j) re-fertilised high-T garnet lherzolites, BD2126. Bands related to OH absorbance are marked A: 3612 cm^{-1}, B: 3570 cm^{-1} and C: 3525 cm^{-1}; and bands relating to F are marked as follows: V: 3674 cm^{-1}; W: 3641 cm^{-1}; X: 3624 cm^{-1}; and Y: 3598 cm^{-1}.*

in the crystal. Representative spectra for each axis in five samples are shown in Figure 7.8, with the first column showing the range of wavenumbers in the OH-stretching region (3800-3000 cm^{-1}). The spectra in Figure 7.8 clearly highlight the variation in absorbance across the three principal axes. Not only does the magnitude of absorbance vary, but also the number of absorbance bands in each axis. The spectra parallel to [100] has multiple absorbance bands in the OH-stretching region, whereas there are many fewer in the spectra parallel to [010] and [001]. Absorbance bands at 3612, 3572 and 3525 cm^{-1} are marked on each plot. The incorporation mechanisms of H represented by these three bands are well-established. The band at 3612 cm^{-1} represents the hydrogarnet substitution, [Si], where four H^+ ions substitute onto a tetrahedral vacancy (Braithwaite *et al.*, 2003; Matveev *et al.*, 2001, 2005; Tollan *et al.*, 2018) and the two bands at 3572 and 3525 cm^{-1} are indicative of a coupled Ti substitution, where two H^+ ions substitute onto a tetrahedral vacancy, charge balanced by Ti^{4+} in an octahedral site (Berry *et al.*, 2005, 2007b; Kovács *et al.*, 2010; Padrón-Navarta & Hermann, 2017; Shen *et al.*, 2014; Tollan *et al.*, 2018; Walker *et al.*, 2007). The absorbance band at 3612 cm^{-1} reflecting the hydrogarnet substitution is present in the [100] axis of olivine from BD1999 and BD2125, orthopyroxene-rich harzburgites (fluid metasomatism), but it is absent in the [010] and [001] axes and any axis in BD1153 (kimberlite metasomatised dunite) and BD2126 (high-*T* garnet-lherzolite). The absorbance band representing the [Ti] mechanism at 3572 cm^{-1} is present in all five xenoliths from Bultfontein and Mothae shown here and in all three crystallographic axes, with the exception of the [010] axis in BD2126 which has the lowest absorbance. The [Ti] band at 3525 cm^{-1} is present in all three axes in BD1153 (kimberlite metasomatised dunite) and in the [100] and [001] axis in BD2126. This band is absent in olivine from the fluid metasomatised orthopyroxene-rich harzburgites, which also have the lowest Ti concentrations.

Additional mechanisms for H incorporation in olivine include: (i) the [Mg] mechanism where two H^+ charge compensate a vacant octahedral site (bands at 3220 cm^{-1} and 3160 cm^{-1}); and (ii) the [triv] mechanism where one H^+ on a vacant octahedral site is charge balanced by a trivalent cation (bands between 3450 cm^{-1} and 3300 cm^{-1}; Jollands *et al.* 2016; Kovács *et al.* 2010; Padrón-Navarta *et al.* 2014; Tollan *et al.* 2017, 2018). These mechanisms are not present in the spectra of the olivine in the Bultfontein and Mothae xenoliths.

It is striking that there are many absorbance bands in the OH-stretching region of the [100] axis (Figure 7.8) which are not accounted for by these four well-established H incorporation mechanisms. The SIMS analyses show that some of the olivines from Bultfontein and Mothae have very high F concentrations. Two previous studies have identified absorbance bands associated with F in olivine: Fabbrizio *et al.* (2013a) investigated the partitioning of F between olivine, orthopyroxene and hydrous phases in high-pressure experiments, and Crépisson *et al.* (2014) published the spectra of forsterite synthesised in hydrous conditions with and without fluorine. Both these experimental approaches have highlighted the wavenumber of absorbance bands associated with F in the OH-stretching region of olivine. Furthermore, Crépisson *et al.* (2014) compare the spectra of their F-rich synthetic forsterite with natural F-rich Fe-bearing olivine from a crustal environment (which is not considered to be an hydrothermal olivine), the Pamir olivine (Pakistan; Libowitzky & Beran 1995), and find good agreement in the position of the F-related absorbance bands (Figure 7.9).

Figure 7.10 shows the FTIR spectra in the [100] axis for the five samples shown in Figure 7.8 and additionally BD1140 (low-*T* garnet harzburgite) and BD2128 (high-*T* garnet lherzolite). The four spectra

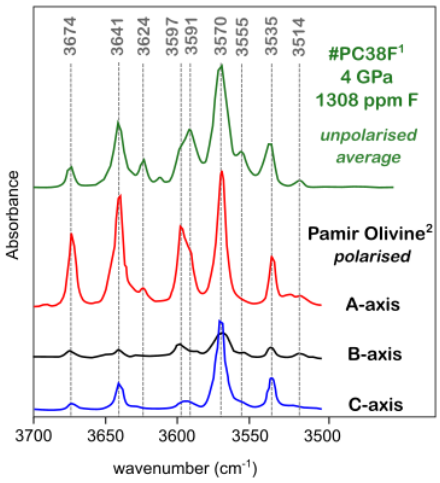

Figure 7.9 *The unpolarised FTIR spectra of an experimental forsterite, doped with 1308 ppm F ([1]Crépisson* et al. *2014), against the polarised spectra of the F-rich Pamir olivine ([2]Libowitzky & Beran 1995).*

from olivine in the orthopyroxene-rich garnet harzburgites (fluid metasomatism) are shown in the first column (a-d) to show the ubiquity of absorbance bands within the group. In contrast, the wavenumber of the different absorbance bands present differs significantly between four of the groups that have earlier been defined by the style of metasomatism (Chapter 5). Five of the F-related absorbance bands identified in Figure 7.9 (Crépisson *et al.*, 2014; Fabbrizio *et al.*, 2013a) are present to different extents in the spectra shown in Figure 7.10. In the orthopyroxene-rich harzburgites that have experienced siliceous fluid metasomatism (7.10a-d), the bands at 3641 (W), 3624 (X) and 3591 (Z) cm^{-1} are very prominent and in BD1999 and BD2125 there is an additional smaller band at 3674 cm^{-1}. The low-T garnet harzburgite, BD1140 (7.10e), has similar absorbance bands present to the orthopyroxene-rich harzburgites, but the absorbance is dominated by the OH-bands representing the [Si] and [Ti] H-incorporation mechanisms (3612, 3572 and 3525 cm^{-1}). The kimberlite metasomatised dunite, BD1153 (7.10f), contains a strong F-related absorbance band at 3598 cm^{-1}, which is also prominent in the high-T garnet lherzolites, BD2126 (7.10g) and BD2128 (7.10h). The absorbance in the high-T garnet lherzolites is low and dominated by two absorbance bands; a H band at 3572 cm^{-1} ([Ti]) and the aforementioned F band at 3598 cm^{-1}. The significance of the different absorbance bands that are apparent across the four metasomatic groups shown is discussed further in Chapter 9.

This study presents the first identification of multiple prominent F-related absorbance bands in olivine from the sub-cratonic lithospheric mantle. These bands are primarily present in the [100] axis of olivine. It is necessary to deconvolve the spectra into the individual peaks so that they can be assigned to the appropriate point defect associated with H and/or F. The spectra parallel to the [100] axis have been deconvolved into the individual peaks, an example is shown in Figure 7.11. The deconvolution method used is that of Tollan *et al.* (2015), that fits proportional gaussian/lorentzian curves to the bands and minimises the fit of the curve (determined by minimising $\sum(calculated - observed)^2$) using the SOLVER function in Microsoft Excel.

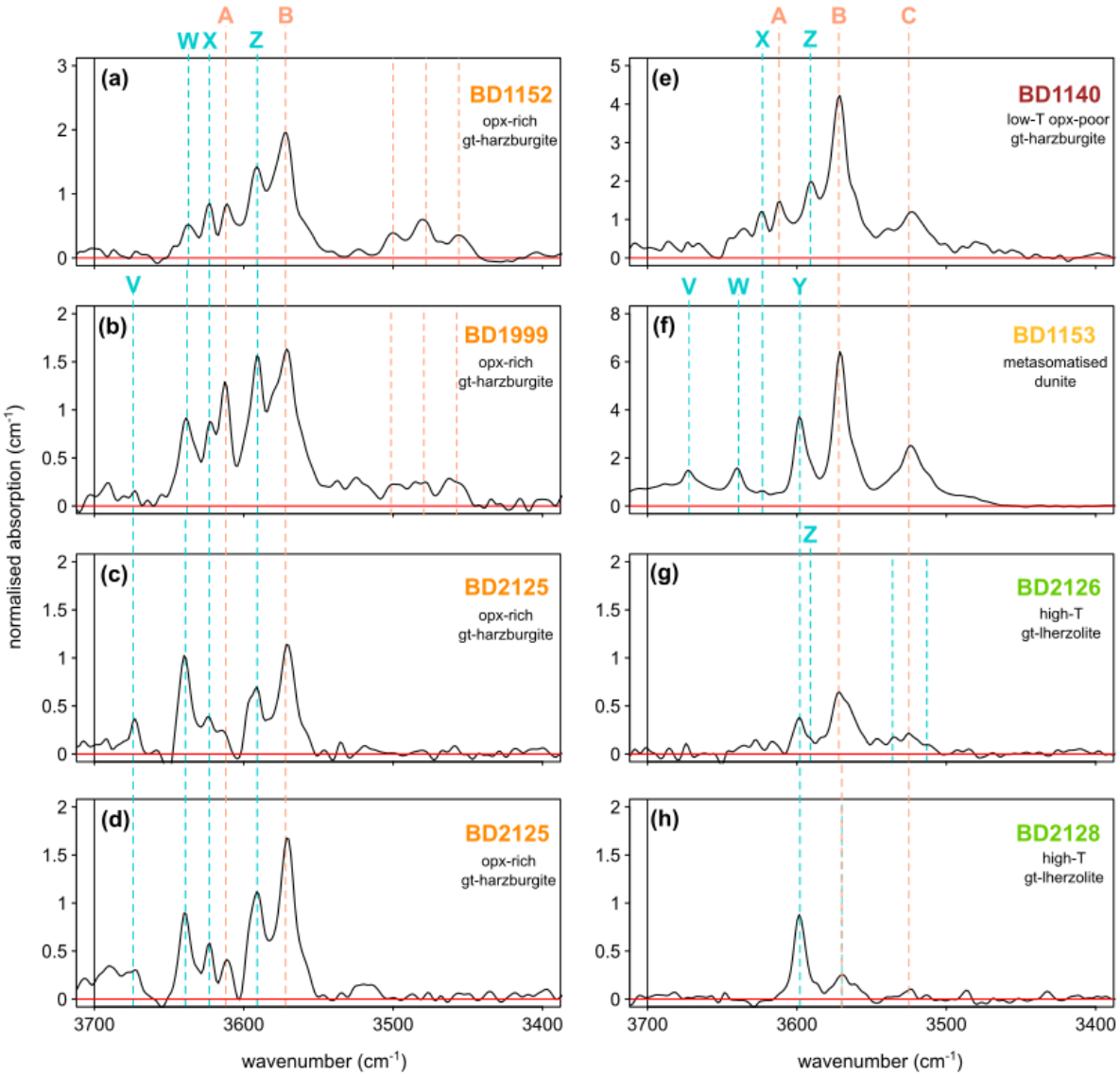

Figure 7.10 *A closer look at the olivine FTIR spectra of the [100] axis from Si-fluid metasomatised orthopyroxene-rich harzurgites: (a) BD1152; (b) BD1999; and (c,d) BD2125; low-T garnet harzburgite: (e) BD1140; kimberlite metasomatised dunite: (f) BD1153; and refertilised high-T garnet lherzolites: (g) BD2126; and (h) BD2128. The same H absorbance bands are marked A: 3612 cm^{-1}, B: 3570 cm^{-1} and C: 3525 cm^{-1}; and prominent F bands are marked as follows: V: 3674 cm^{-1}; W: 3641 cm^{-1}; X: 3624 cm^{-1}; Y: 3598 cm^{-1}; and Z: 3591 cm^{-1}*

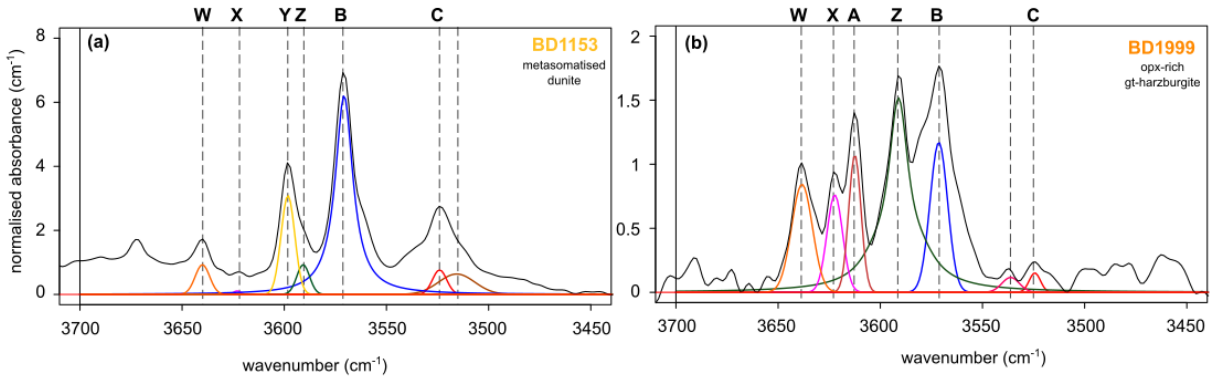

Figure 7.11 *The FTIR spectra parallel to the [100] axis of the OH-stretching region for olivine in (a) BD1153 and (b) BD1999 showing select individually deconvolved bands. Bands related to OH absorbance are marked A: 3612 cm^{-1}, B: 3570 cm^{-1} and C: 3525 cm^{-1}; and bands relating to F are marked as follows: V: 3674 cm^{-1}; W: 3641 cm^{-1}; X: 3624 cm^{-1}; Y: 3598 cm^{-1}; and Z: 3591 cm^{-1}*

7.3.2 Orthopyroxene

The identification of the three principal crystallographic axes in orthopyroxene is not as well established using FTIR as olivine. For this reason, during data acquisition only unpolarised measurements of orthopyroxene were acquired. The unpolarised measurements are nevertheless useful to identify the position of absorbance bands in the spectra of orthopyroxene from the Bultfontein and Mothae xenoliths. Any quantitative analysis must, however, take into consideration the variation in absorbance depending on the crystallographic orientation. Stalder *et al.* (2012) have shown that a single absorption coefficient is not appropriate for orthopyroxene, rather a function dependent on wavenumber is required to account for the different crystallographic axes in unpolarised measurements. Figure 7.12 shows the variation in absorption bands of five different crystals of orthopyroxene in sample BD1999, this was one of the only xenoliths where multiple points across different crystals could be analysed and showed any variation in crystallographic axes. The spectra in Figure 7.12 do not necessarily mark the A, B and C axes, rather just three different orientations to show a possible range. Nonetheless, all three orientations exhibit absorbance bands at the same wavenumbers in the OH-stretching region, with fairly similar ratios between absorbance bands, but the peak absorbance of individual bands and the total integrated area varies considerably. The difference in integrated absorbance and peak absorbance with orientation highlights the necessity to view unpolarised measurements with caution, especially in this study where not enough crystals were analysed to calculate concentrations with enough accuracy. This caution is corroborated by the results of Prechtel & Stalder (2012) who showed that the absorption, and the wavenumbers of bands present does vary with crystallographic orientation in pure enstatite.

Representative spectra for orthopyroxene in all eight xenoliths are presented in Figure 7.13. These were chosen because their spectra in the region 2400-1200 cm^{-1} are similar and because there is little to no influence of a hydrous phase at 3700 cm^{-1}. The following six absorbance bands are present to some extent in all eight samples: A: 3600 cm^{-1}; B: 3545 cm^{-1}; C: 3516 cm^{-1}; D: 3410 cm^{-1}; E: 3300 cm^{-1}; and F: 3060 cm^{-1}. The greatest variation is in the bands at 3600 cm^{-1} (A), 3545 cm^{-1} (B) and 3410 cm^{-1} (D). The bands at 3516 cm^{-1} (C) and 3060 cm^{-1} (F) are very prominent in all samples and show less variation across them. Interestingly, in olivine, the FTIR spectra was unique for each metasomatic signature but in orthopyroxene this is not the case. The most obvious difference is between samples from

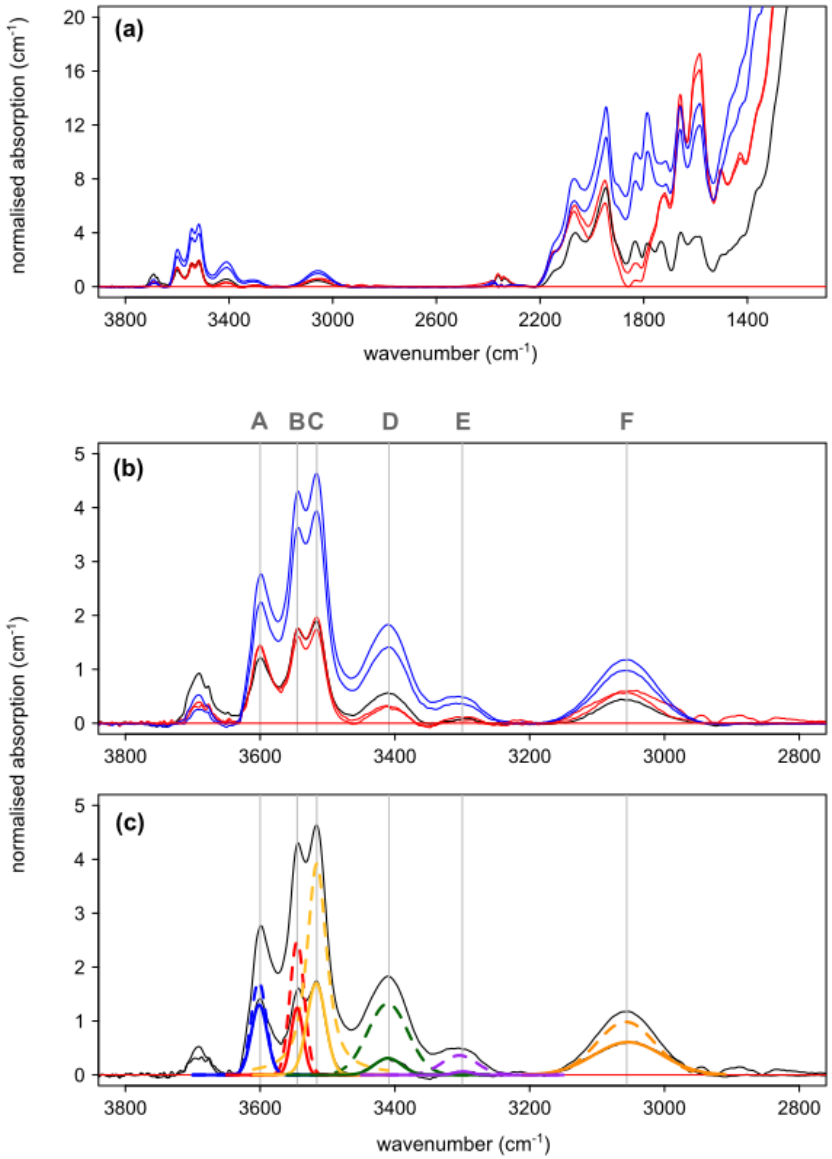

Figure 7.12 *(a) The full FTIR spectra of five points analysed in orthopyroxenes from sample BD1999 with different crystallographic orientations. (b) The OH-stretching region showing the variation in absorbance with crystallographic orientation. The individual bands are marked: A: 3600 cm^{-1}; B: 3545 cm^{-1}; C: 3516 cm^{-1}; D: 3410 cm^{-1}; E: 3300 cm^{-1}; and F: 3060 cm^{-1}. (c) The deconvolved solution to the spectra with the greatest absorbance and the lowest absorbance showing the individual bands A-F as dashed lines and solid lines, respectively.*

Bultfontein (Figure 7.13a-e) at the craton interior and Mothae (Figure 7.13f-h) at the craton margin. The orthopyroxenes in samples from Mothae (BD2125, BD2126 and BD2128) have much smaller bands at 3600 cm^{-1} (A) and 3545 cm^{-1} (B) than those from Bultfontein. The smaller band at 3545 cm^{-1} results in a significant difference in the ratio of the 3545:3516 cm^{-1} bands in the Bultfontein and Mothae orthopyroxene. The rest of the bands (C-F) are similar between locations at the craton interior and margin.

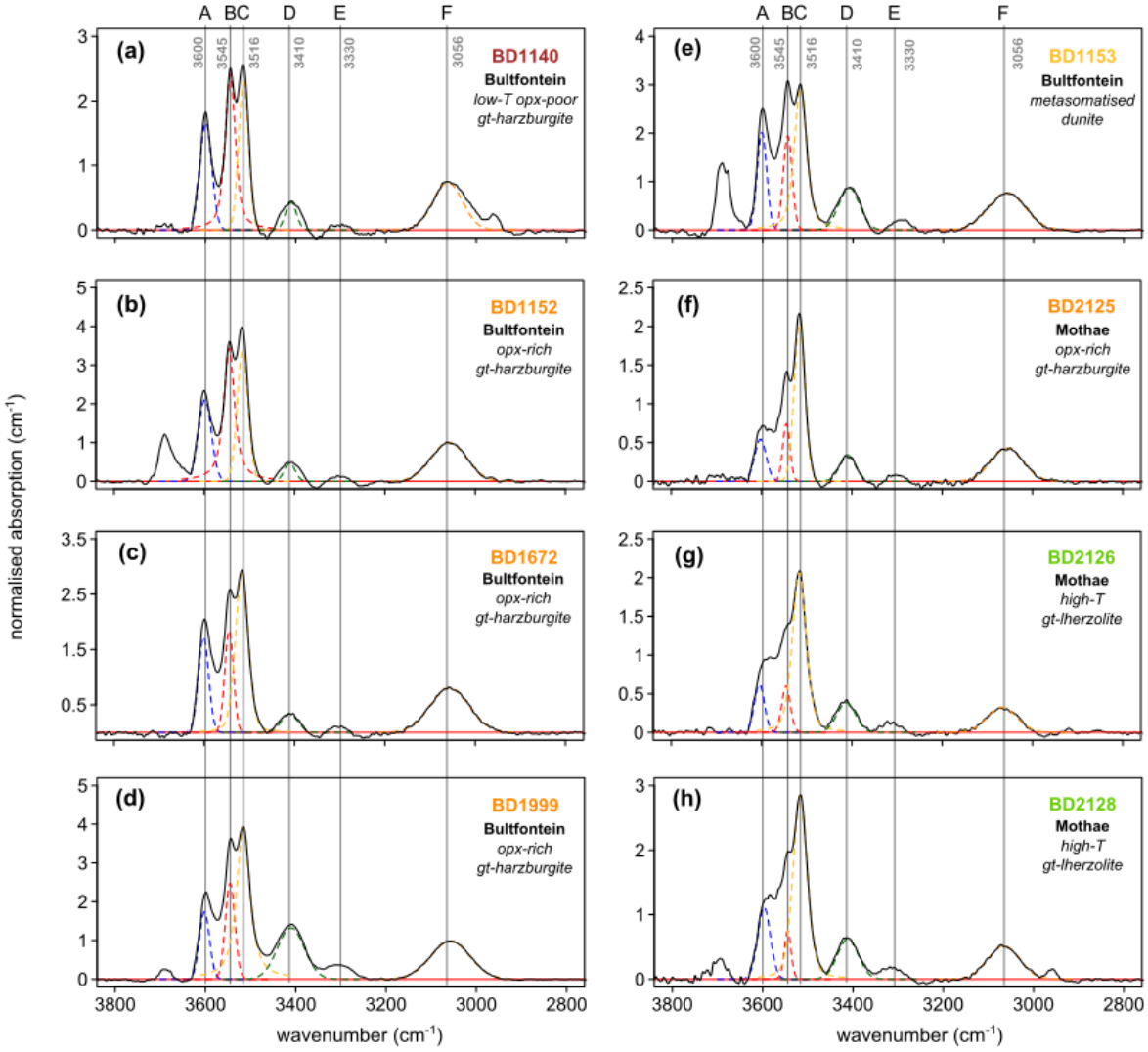

Figure 7.13 *The FTIR spectra confined to the OH-stretching region for xenoliths (a) BD1140; (b) BD1152; (c) BD1672; (d) BD1999; (e) BD1153; (f) BD2125; (g) BD2126; and (h) BD2128. with the same absorbance bands marked as A-F defined in Figure 7.12. The deconvolved solution to the spectra with the greatest absorbance and the lowest absorbance showing the individual bands A-F as dashed lines and solid lines, respectively.*

7.4 Summary

This chapter presents the results of SIMS and FTIR analyses on mantle olivine, orthopyroxene and clinopyroxene from the Kaapvaal craton. The results have shown that there is a large variation in H_2O and F concentrations between different NVFMMs and xenolith lithologies, in contrast Cl shows little variation and is low in all NVFMMs. F concentrations up to 196 ppm in olivine are the highest recorded in mantle olivine to date. These high concentrations are associated with xenoliths from Bultfontein that have been metasomatised by small-fraction silico-carbonate melts with affinities to kimberlites, and in xenoliths from both Bultfontein and Mothae that have interacted with silicic fluids. The highest H_2O concentrations are measured in orthopyroxenes and clinopyroxenes that have been hydrated by siliceous fluids, but these pyroxenes have some of the lowest F and Cl concentrations. The clinopyroxene from

high-T garnet lherzolites have high F concentrations but lower H_2O contents and the co-existing olivine and orthopyroxene are both H_2O- and F-poor.

The incorporation mechanisms of H and F in olivine also vary across the different xenolith lithologies. FTIR spectra identified two dominant mechanisms of H incorporation in most olivines from the Bultfontein and Mothae xenoliths: (i) hydrogarnet [Si] substitution; and (ii) Ti-clinohumite-like point defect [Ti]. Two absorbance bands are associated with the [Ti] mechanism, at 3572 and 3525 cm^{-1}. In contrast to the other xenolith types, the orthopyroxene-rich harzburgites lack the second absorbance band at 3525 cm^{-1}. These olivines have the lowest Ti concentrations, and instead there is a greater dominance of the hydrogarnet [Si] substitution for H incorporation. The FTIR spectra of the same olivines from the orthopyroxene-rich harzburgites also contain prominent absorbance bands at 3641, 3624 and 3591 cm^{-1}, which are all associated with F incorporation. This differs from the other lithologies which contain a dominant F-related absorbance band at 3598 cm^{-1}.

Contrary to olivine, the orthopyroxene FTIR spectra do not vary significantly between the different xenolith lithologies. Instead there is a systematic difference between the FTIR spectra of orthopyroxenes from Bultfontein at the craton interior and Mothae at the craton margin. The orthopyroxenes from Mothae have much smaller absorbance bands at 3600 and 3545 cm^{-1}. The spectra of orthopyroxenes from xenoliths at both locations are dominated by ubiquitous absorbance bands at 3516, 3410 and 3060 cm^{-1}.

Chapter 8

Incorporation of H_2O and F within and between NVFMMs

8.1 Introduction

In order to investigate the controls on volatile storage in NVFMMs in the sub-cratonic lithospheric mantle, it is important to first establish the dominant incorporation mechanisms of H_2O and F in NVFMMs, and their distribution within the mineral assemblage. The incorporation mechanisms and partitioning behaviour of H_2O in and between NVFMMs has been investigated in many studies, H incorporation in olivine is very well understood (e.g. Berry *et al.* 2005, 2007a; Demouchy & Mackwell 2006; Kovács *et al.* 2010; Tollan *et al.* 2018; Walker *et al.* 2007) whereas fewer studies have focused on orthopyroxene and clinopyroxene (e.g. Prechtel & Stalder 2012; Stalder 2004; Stalder *et al.* 2005, 2012, 2015). Numerous studies have investigated the partitioning of H_2O between NVFMMs in mantle xenoliths (Demouchy & Bolfan-Casanova, 2016; Gibson *et al.*, 2020; Kovács *et al.*, 2012; Novella *et al.*, 2014; Peslier *et al.*, 2015; Sundvall & Stalder, 2011; Warren & Hauri, 2014), including those from the sub-cratonic lithospheric mantle, however there is a great degree of variation within the published partition coefficients from experimental studies and those measured in mantle xenoliths, e.g. $D_{H_2O}^{cpx-opx}$ varies from 0.8-3.3. There is limited understanding of how F is incorporated in NVFMMs. The research to date uses theoretical models (Crépisson *et al.*, 2014) and correlations between F and other elements (Gibson *et al.*, 2020; Joachim *et al.*, 2015; Urann *et al.*, 2017). Most studies have investigated the partitioning behaviour of F between mantle minerals and melts, mostly in experiments (Beyer *et al.*, 2012, 2016; Fabbrizio *et al.*, 2013b; Hauri *et al.*, 2006; Joachim *et al.*, 2015; Rosenthal *et al.*, 2015), but a handful of studies have determined the partitioning of F between co-existing mantle minerals in natural xenoliths (Gibson *et al.*, 2020; Urann *et al.*, 2017).

In this chapter, the results of SIMS and FTIR analyses presented in Chapter 7 are combined to shed new light on the current understanding of both the incorporation and partitioning of H_2O and F in NVFMM from different xenolith lithologies in the Kaapvaal craton. The processes that control these volatile concentrations are investigated further in the knowledge of the extremely fast diffusion rates of hydrogen in olivine (e.g. Chakraborty 2010; Demouchy & Mackwell 2006; Kohlstedt & Mackwell 1998; Mackwell & Kohlstedt 1990). In Chapter 7 a number of systematic differences in H_2O and F concentrations and FTIR spectra were recognised between the different xenolith lithologies, following interaction with different metasomatic agents. Following this discovery, the chapter ends with a discussion of the timescales for subsolidus re-equilibration of volatiles following metasomatism and the implications for volatile storage in NVFMMs in the SCLM.

8.2 Incorporation mechanisms of H and F in NVFMMs

The FTIR spectra of olivine and orthopyroxene can be used to investigate the incorporation of H and F, by comparing the average major, trace and volatile concentrations for each xenolith with the integral and peak absorbance (normalised to 1 cm^{-1}) of the deconvolved bands (presented in supplementary data table 17).

8.2.1 Olivine

Water

As alluded to in Chapter 7, the H_2O in olivine in the Bultfontein and Mothae xenoliths is primarily hosted in tetrahedral vacancies in either: (i) the hydrogarnet substitution [Si] where the vacancy is charge balanced by four H^+ ([Si]=$(4\,H)^{\times}_{Si}$); or (ii) the [Ti] mechanism, also known as a Ti-clinohumite-like point defect (Berry *et al.*, 2005, 2007b), where Ti^{4+} in an octahedral site is charge balanced by the substitution of Si^{4+} by two H^+ in a neighbouring tetrahedral site ([Ti]=$(Ti^{4+})^{\bullet\bullet}_{Mg}(2\,H)''_{Si}$). These mechanisms use the Kröger-Vink notation where $(4\,H)^{\times}_{Si}$ represents 4 protons (H) in a Si vacancy (subscript) with neutral charge (superscript $\times$). The superscript $X^{\bullet}$ represents a single positive charge and X' represents a single negative charge.

The hydrogarnet substitution [Si] produces a prominent OH absorbance band at 3612 cm^{-1} (Kovács *et al.*, 2010; Walker *et al.*, 2007) and the clinohumite-like point defect [Ti] produces two bands at 3572 and 3525 cm^{-1} (Berry *et al.*, 2005, 2007a; Walker *et al.*, 2007). Importantly, the 3612 cm^{-1} OH-absorbance band is present in BD1153 (kimberlite melt metasomatism) and the orthopyroxene-rich harzburgites (siliceous fluid metasomatism) but not in the low-T orthopyroxene-poor harzburgite or high-T lherzolites. Even where it is present, this hydrogarnet band is always smaller than the Ti clinohumite-like point defect absorbance band at 3572 cm^{-1} which is the largest band in all samples. Importantly, the dominance of the two absorbance bands related to the [Ti] mechanism implies that a significant proportion of H is coupled to Ti in olivine in these xenoliths, in contrast the [Mg] and [triv] incorporation mechanisms are completely absent and the [Si] hydrogarnet substitution only constitutes a minor component of the total H-incorporation in four samples.

Fluorine

The incorporation mechanisms of F in olivine are very poorly constrained. Crépisson *et al.* (2014) modelled the incorporation of F^- on the oxygen sites in olivine (O1, O2 and O3, Figure 8.1) as clumped fluoride-hydroxyl groups that balance tetrahedral vacancies, i.e. one F^- replaces an OH^- group. They modelled a number of hypothetical configurations that could reproduce absorbance bands at the wavelengths observed in the synthetic forsterite.

This experimental and theoretical study by Crépisson *et al.* (2014) is one of a few to investigate F incorporation in olivine (Beyer *et al.*, 2012; Gibson *et al.*, 2020; Joachim *et al.*, 2015; Urann *et al.*, 2017). As shown above, the Bultfontein and Mothae xenoliths in this study have elevated F concentrations that occupy a large range and can be compared to mineral chemistry described in Chapter 3. The F-related absorbance bands identified from the FTIR spectra have been deconvolved (see supplementary data table

17) and the peak absorbance and integral of each band was compared to the average major-, minor- and trace-element concentrations in each xenolith. The advantage of the high F concentrations is that multiple bands are present and can be compared. The disadvantage of this sample set is its limited size, which is reduced further for each absorbance band because the individual bands are not ubiquitous across all samples. In some cases the absorbance band is only present in three samples which makes looking for a correlation difficult. Consequently, the results presented here are preliminary observations that provide a platform for future investigation.

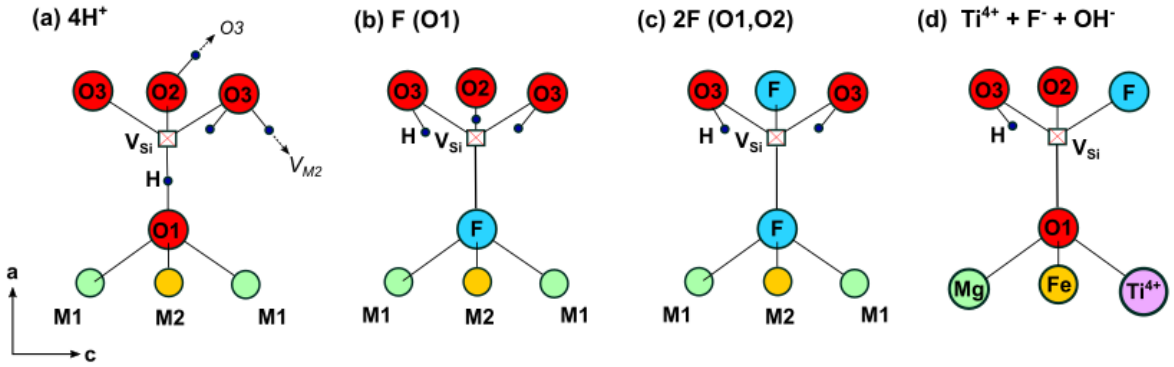

Figure 8.1 *Atomic configuration of olivine adapted from Beran & Libowitzky (2006).* ***(a)*** *The configuration of 4 protons around a Si vacancy in the hydrogarnet substitution.* ***(b)*** *The configuration where one F^- replaces an OH group in the O1 site, Crépisson* et al. *(2014) have shown can explain some component of the absorbance bands at 3641 and 3624 cm^{-1}.* ***(c)*** *The configuration where two F^- replace OH groups in the O1 and O2 sites, Crépisson* et al. *(2014) have shown can explain some component of the absorbance bands at 3598 and 3591 cm^{-1}.* ***d*** *A hypothetical configuration to explain the ratios between H_2O, F and Ti as described in the text, where one F and one OH-group charge balance Ti^{4+} in an octahedral site.*

The absorbance band at 3598 cm^{-1} is prominent in olivines from metasomatised dunite BD1153, high-*T* garnet lherzolites BD2126 and BD2128 and as a shoulder in orthopyroxene-rich garnet harzburgite BD2125. The integral of the deconvolved band at 3598 cm^{-1} correlates very well with F and Ti in these four xenoliths (Figure 8.2). The olivines in the remaining xenoliths that do not contain an absorbance band at 3598 cm^{-1} are the orthopyroxene-rich garnet harzburgites (BD1152, BD1999) which have very low Ti concentrations (due to their interaction with a Ti-poor fluid). These xenoliths have an absorbance band at 3591 cm^{-1}, the integral of which also correlates with F and Ti. It is possible that the bands at 3591 cm^{-1} and 3598 cm^{-1} both relate to a Ti coupled mechanism, and the wavenumber depends on some threshold of Ti and/or F. The xenoliths that have the absorbance band at 3591 cm^{-1} (BD1152, BD1999) also have multiple other absorbance bands in close succession between 3674 cm^{-1} and 3570 cm^{-1} compared to the four xenoliths with the 3598 cm^{-1} band (Figure 7.10).

The normalised integrated absorbance of the band at 3598 cm^{-1} correlates with both the F and Ti concentration in the olivine, and also with the Ti/F of clinopyroxene in the same xenolith. There are multiple lines of evidence to suggest that Ti and F are coupled in olivine and a possible mechanism is similar to the [Ti] mechanism for H incorporation in olivine. Rather than two H^+ in a tetrahedral vacancy charge balancing Ti^{4+} in one of the octahedral sites, F^- can charge balance Ti^{4+} by replacing one or two of the OH-groups. The results shown in Figure 8.2b demonstrate that the absolute concentrations of F and Ti in olivine fall on a 1:1 line while the absolute concentrations of H_2O and Ti sit on a 1:2 line. The concurrence of these two relationships suggests that Ti^{4+} cations in an octahedral site are charge balanced

by one F^- anion in an oxygen site and one OH-group around a Si-vacancy. An example of this hypothetical configuration is shown in Figure 8.1d, where Ti in one of the M1 sites is charge balanced by an OH-group at one of the O sites, and the replacement of oxygen in the O3 site by F. This can also be considered as a Ti-clinohumite-like point defect (Berry *et al.*, 2005) where F-bearing Ti-clinohumite has the stoichiometric formula: $[4(Mg,Fe)_2SiO_4(Mg_{1-X},Ti_X)O_{2X}(OH,F)_{2-X}]$; in which X is the Ti content (moles). While the configuration in Figure 8.1d is a hypothetical configuration, the placement of the F anion in the O3 site is based on the observation that almost all oxygen vacancies are in the O3 site (Brodholt & Refson, 2000) .

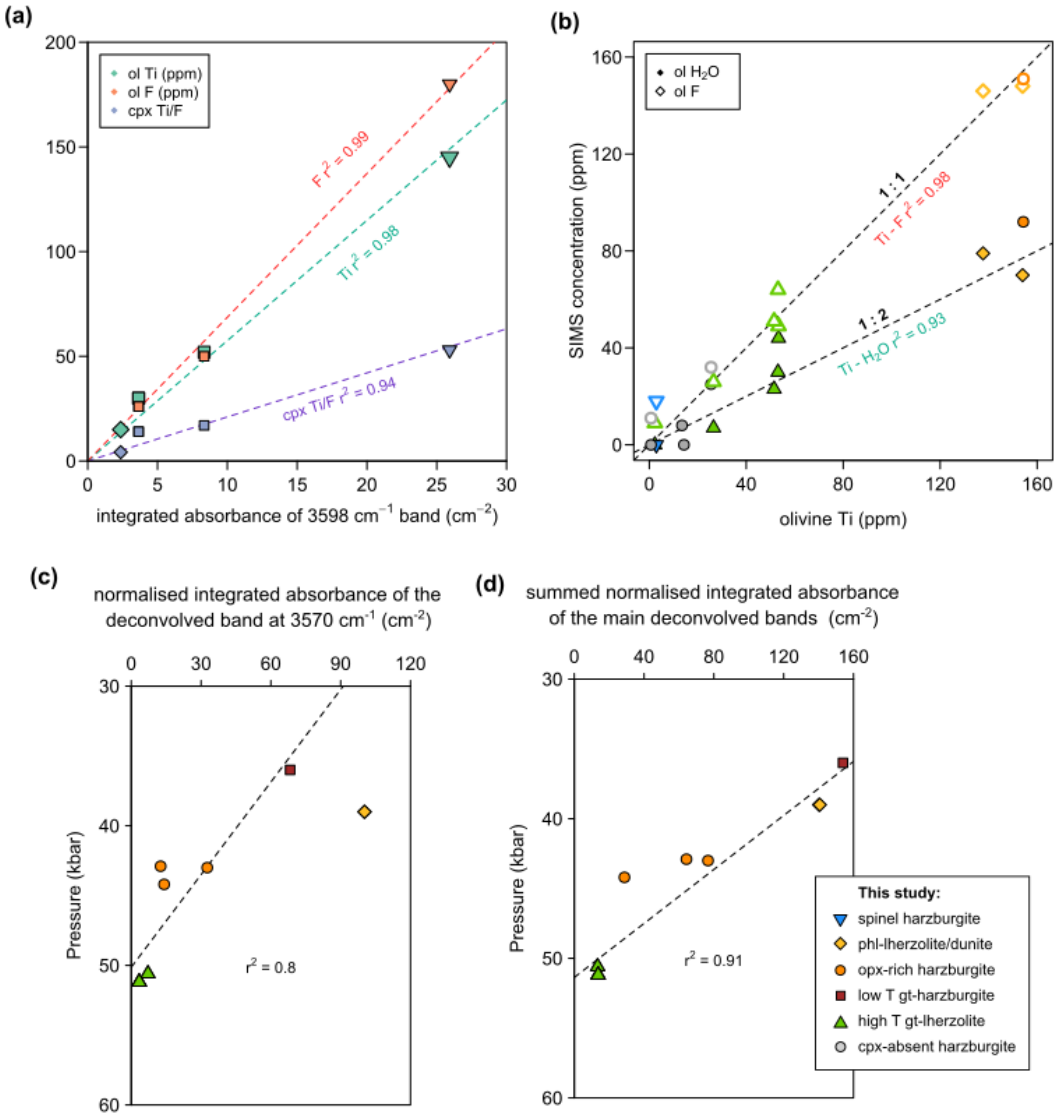

Figure 8.2 ***(a)*** *The normalised integral of the deconvolved absorbance band at 3598 cm^{-1} in the A axis of olivine plotted against olivine Ti concentration, olivine F concentration and the ratio of Ti/F of clinopyroxene in the same xenolith.* ***(b)*** *Absolute concentration of olivine Ti vs. the concentration of F and H_2O (SIMS). F:Ti plots on a 1:1 line whereas H_2O and Ti covary with the ratio 1:2.* ***c*** *The normalised integrated absorbance of the deconvolved absorbance band at 3570 cm^{-1} against pressure.* ***(d)*** *the sum of normalised integrated absorbance of the main deconvolved bands at 3624, 3612, 3598, 3591, 3570 and 3525 cm^{-1} against pressure.*

If F and H are preferentially incorporated together in such a manner, then there is less opportunity for H^+ to charge balance vacant tetrahedral sites by the hydrogarnet, [Si], substitution. In the Bultfontein and Mothae mantle olivines there is only one concurrence of the absorbance bands at 3612 cm^{-1} and

3598 cm^{-1}, and that is in BD2125 from Mothae where the band at 3598 cm^{-1} is a shoulder on the peak at 3591 cm^{-1}. The lack of simultaneous occurrence of absorbance bands at 3612 cm^{-1} and 3598 cm^{-1} supports the theory that where Ti content is low, tetrahedral vacancies are charge balanced by $4H^+$ forming OH-groups with the four oxygens, but where Ti content is high the excess charge of Ti^{4+} in the octahedral sites is charge balanced by the combination of H^+ forming OH-groups and F^- anions occupying oxygen sites. Alternatively there could be a control of pressure and/or water activity (see discussion in Chapter 9).

The integrated absorbance of the 3572/3570 cm^{-1} band and the sum of the main bands at 3624, 3612, 3598, 3591, 3570 and 3525 cm^{-1} for olivine are plotted against pressure in Figure 8.2. Some mechanisms appear to have a pressure or temperature control, for example the [Ti] mechanism at 3570. The relationship observed between the summed absorbance of six prominent bands implies that there is a decrease in olivine H_2O concentration with depth in the mantle; this has not been observed in other published literature from the Kaapvaal craton (e.g. Demouchy & Bolfan-Casanova 2016; Peslier *et al.* 2010).

The incorporation of F into olivine is complex because the multitude of different bands suggest that there could be multiple mechanisms, but the 1:1 relationship between F and Ti (Figure 8.2b) concentration implies a very strong chemical link. The different bands could be related to whether the F is hosted in oxygen vacancies or via an interstital mechanism and also then where the F anion and OH-groups are hosted in the lattice. Crépisson *et al.* (2014) showed that the relative positions of hydroxyl groups and fluorine in different oxygen sites in olivine can produce different absorbance bands in the FTIR spectra. A study using the same methods as Crépisson *et al.* (2014) to model the positioning of F and OH-groups coupled to Ti in the M1 or M2 sites would greatly improve the ability to assign absorbance bands to the specific incorporation mechanisms and configuration of volatile elements in olivine.

8.2.2 Orthopyroxene

Water

The limitations of using unpolarised FTIR spectra for quantitative analysis have been outlined previously in Chapter 7. All eight orthopyroxene spectra shown in Figure 7.13 contain the same absorbance bands, albeit with varying concentrations. The integrated and peak absorbance of each individual (deconvolved) absorbance band has been compared to the major- and trace-element concentrations of the corresponding orthopyroxenes. There are no strong correlations between any band and major-element composition. The only absorbance band that shows any kind of correlation with a trace-element is at 3060 cm^{-1}, which has a weak positive correlation with Nb and a slightly stronger negative correlation with Ga. Experimental studies have tied the absorbance band at 3600 cm^{-1} to the hydrogarnet, [Si], substitution (Stalder & Skogby, 2003; Tollan & Hermann, 2019) and bands at 3545, 3519 and 3323 cm^{-1} were identified by Prechtel & Stalder (2012) to be Al specific bands. In the same study they found bands at 3592, 3687 and 3067 cm^{-1} to be ubiquitous across all synthetic, doped enstatite analysed. Many authors have looked for a relationship with trivalent cations (e.g. Al^{3+}, Cr^{3+}, Fe^{3+}) because H^+ can charge balance the incorporation of a trivalent cation, or the oxidation of a heterovalent one (e.g Berry *et al.* 2007a; Grant *et al.* 2007; Stalder *et al.* 2005; Tollan *et al.* 2015). The problem with this approach is that trivalent cations have an increased tendency to form a Tschermaks substitution (e.g. Equation 8.1; Stalder *et al.* 2005).

$$Si_T^{4+} + Mg_{M1}^{4+} = Al_{IV}^{3+} + Cr_{M1}^{3+} \tag{8.1}$$

In orthopyroxene with high concentrations of Al^{3+}, Cr^{3+} and Fe^{3+}, the trivalent cations preferentially form a Tschermak substitution thus limiting H incorporation because it is not required to balance the excess charge. In the orthopyroxene in the Bultfontein and Mothae xenoliths there is a negative correlation between Al^{3+} in the tetrahedral site (Al^{IV}) and the H_2O concentration (Figure 8.3a). Low H_2O at high Al^{IV} could reflect the increased proportion of a Tschermak substitution in the orthopyroxene, and hence fewer tetrahedral vacancies for OH-groups and fewer trivalent cations to charge balance. There is a weak positive correlation between orthopyroxene Cr and Al^{IV} (Figure 8.3b) that supports this hypothesis. Other studies, including Peslier (2010), suggest the partitioning of water between clinopyroxene and orthopyroxene is somewhat dependent on the Al concentration of orthopyroxene. Figure 8.3c shows a negative correlation between orthopyroxene Al^{IV} and $D_{H_2O}^{cpx-opx}$ in the Bultfontein and Mothae xenoliths. The same relationship is not apparent with clinopyroxene Al^{IV}. O'Leary *et al.* (2010) find a strong dependence of $D_{H_2O}^{cpx-melt}$ on Al^{IV}, but that $D_{H_2O}^{opx-melt}$ is controlled by Al^{VI}. The concentrations of Al^{IV} in the Bultfontein and Mothae cratonic xenoliths is low (<0.08), and therefore does not have the same range as the data collected by O'Leary *et al.* (2010) to draw these conclusions. It is likely that there are many factors that control the partitioning of H_2O between mantle minerals, and the incorporation mechanism is a crucial component. Nonetheless, there is likely a complex relationship between H^+ incorporation (and hence partitioning) and the partitioning of trivalent cations between the two minerals, and the preference to form a Tschermak substitution. Stalder *et al.* (2015) note that the tendency to form a Tschermak substitution in orthopyroxene is reduced with increasing pressure, therefore at high pressure, trivalent cations and octahedral vacancies are increasingly charge balanced by H_2O incorporation (two H^+ charge compensating M1 vacancy; Prechtel & Stalder 2011). The decreased tendency for Al to form a Tschermak substitution at high pressure (and hence high temperature according to the mantle geotherm) is not evident in the Bultfontein and Mothae xenoliths.

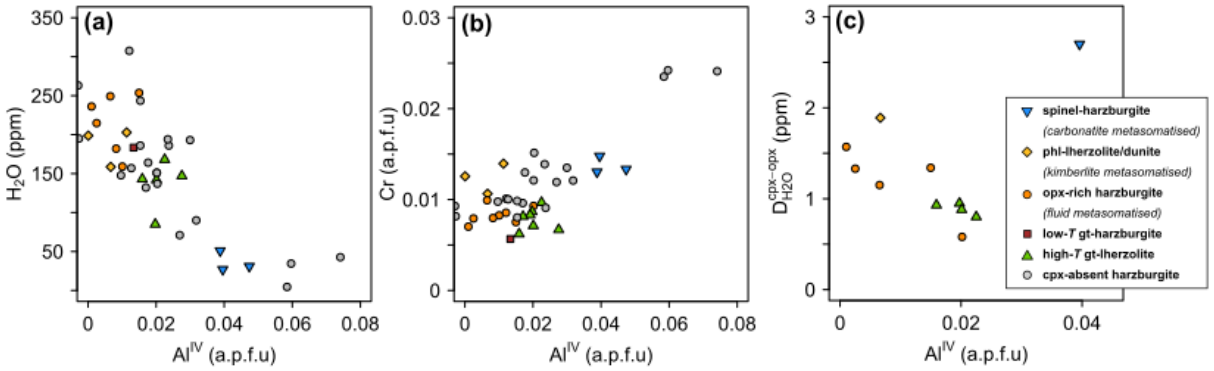

Figure 8.3 *Orthopyroxene Al^{IV} vs.* ***(a)*** *orthopyroxene H_2O;* ***(b)*** *orthopyroxene Cr; and* ***(c)*** $D_{H_2O}^{cpx-opx}$

The external influences of pressure, temperature and fO_2 add to the complicated nature of elemental incorporation and substitution in orthopyroxene. This makes it difficult to identify specific relationships, especially as there is a complete lack of any correlation between absorbance bands and specific elements

in all other studies of this nature. Consequently, there is very little consensus on the mechanisms by which H_2O is incorporated in orthopyroxene. It is, however, generally agreed that the trivalent cations do play a role, for example Tollan & Hermann (2019) identified a relationship between a number of orthopyroxene OH-absorbance bands and the fO_2 of the xenolith, calculated from Fe^{3+}/Fe^{2+} in spinel, supporting the hypothesis that H^+ forms OH-groups to balance the oxidation of Fe^{2+} to Fe^{3+}. The relationship of H_2O content and fO_2 is discussed further in Chapter 9.

Fluorine

The incorporation of F in orthopyroxene is very poorly constrained. Unlike in olivine, there are no extra absorbance bands in the FTIR spectra that can be attributed to F incorporation, and there have not been any experiments on F-doped enstatite to provide theoretical band positions. None of the deconvolved bands identified in the orthopyroxene spectra correlate with F, so the use of FTIR to identify incorporation mechanisms of F in orthopyroxene was ruled out for this study. Chapter 7 shows that the concentration of F in orthopyroxene is less than in co-existing olivine, and it is also much lower than the corresponding orthopyroxene H_2O concentration and this may explain why the absorbance bands are not observed.

While the FTIR results have been unable to identify any specific incorporation mechanisms, the elemental concentrations have all been acquired on the same crystals by SIMS and LA-ICP-MS and allow a comparison between different elements. The most notable relationship in orthopyroxene is between F and Na (Figure 8.4). There is a positive correlation between the two elements which is also observed in other studies (e.g. Peslier *et al.* 2017; Urann *et al.* 2017). The correlation is interpreted to represent the coupled, charge balanced substitution of F^- and Na^+ (Urann *et al.*, 2017).

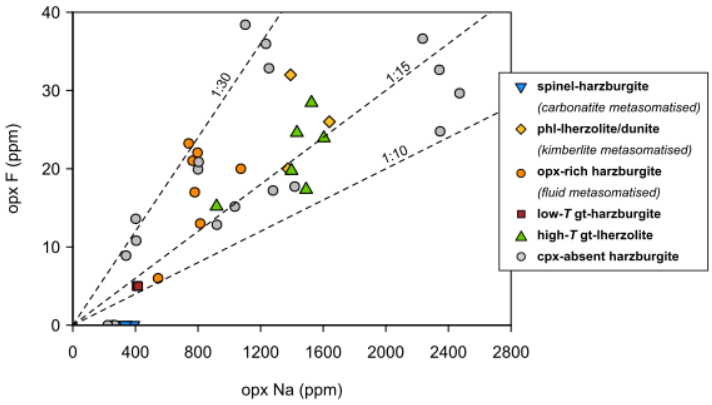

Figure 8.4 *Na vs. F in each orthopyroxene separate in the Bultfontein and Mothae xenoliths.*

8.3 Volatile partitioning

8.3.1 $D_{H_2O}^{cpx-opx}$

The partitioning of H_2O between clinopyroxene and orthopyroxene has been investigated in numerous studies over the last 30 years. Both experimental run products (e.g. Aubaud *et al.* 2004; Hauri *et al.* 2006; Kovács *et al.* 2012; Novella *et al.* 2014; Tenner *et al.* 2009) and co-existing pyroxenes in mantle xenoliths

(e.g. Bell & Rossman 1992; Bonadiman *et al.* 2009; Demouchy & Bolfan-Casanova 2016; Falus *et al.* 2008; Gibson *et al.* 2020; Grant *et al.* 2007; Li *et al.* 2008; Marshall *et al.* 2018; Peslier *et al.* 2002, 2017; Xia *et al.* 2010; Yang *et al.* 2008) have been analysed to try and establish $D_{H_2O}^{cpx-opx}$ in the sub-continental lithospheric mantle. These studies produce a range of values (Figure 8.5a and b), and there is no general consensus. The global dataset may be divided into five categories, the off-craton xenoliths, the North China Craton (thinned cratonic lithosphere, Fan *et al.* 2000; Menzies *et al.* 1993), the Siberian Craton and the interior and margin of the Kaapvaal Craton. The North China Craton and off-craton xenoliths have a wide range in partition coefficient that averages at 2.1. The xenoliths from the thick Siberian and Kaapvaal cratons (Priestley & McKenzie, 2002), typically have a lower $D_{H_2O}^{cpx-opx}$ ($\bar{x}$ = 1.56) than the off-craton samples. The xenoliths from Bultfontein and Mothae examined in this study all plot within the range of the Kaapvaal and Siberian Craton xenoliths from the Demouchy & Bolfan-Casanova (2016) compilation, suggesting that there could be a systematic difference in the partitioning behaviour in the mantle relating to the thickness of the lithosphere.

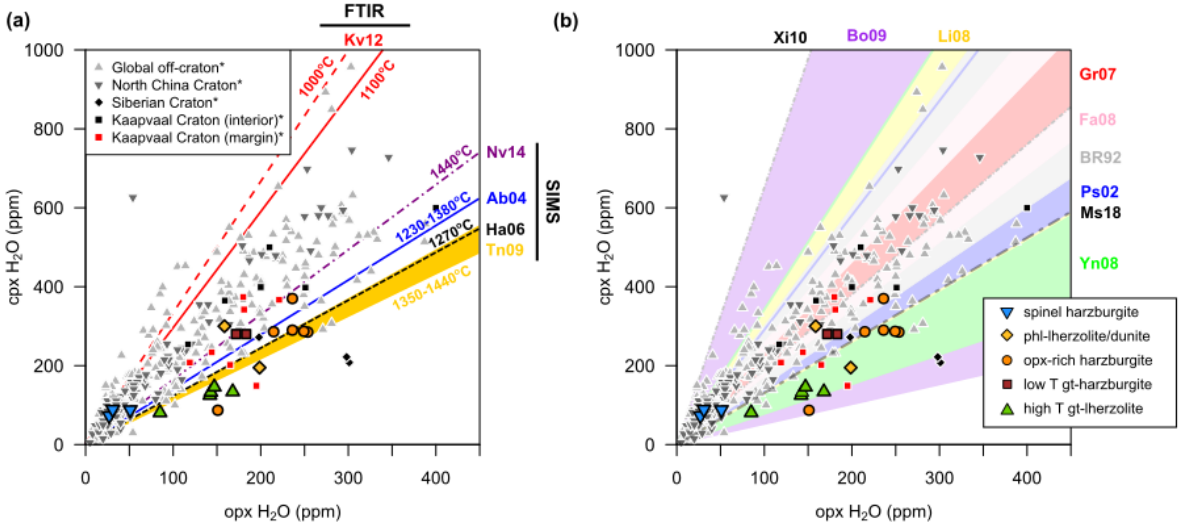

Figure 8.5 ***(a)*** *Water concentration of corresponding orthopyroxene and clinopyroxene in the Bultfontein and Mothae xenoliths alongside a global dataset of orthopyroxene and clinopyroxene water contents in continental peridotite (Demouchy & Bolfan-Casanova 2016 and references therein). The lines represent* $D_{H_2O}^{cpx-opx}$ *determined by experiment: red (FTIR), Kovács* et al. *(2012); purple (SIMS), Novella* et al. *2014 blue (SIMS), Aubaud* et al. *(2004); black (SIMS), Tenner* et al. *(2009); yellow (SIMS), Hauri* et al. *(2006).* ***(b)*** *The same dataset with the range of partition coefficients observed in mantle xenoliths from the continental lithosphere, compiled by Kovács* et al. *(2012), shaded in the backgroud. (Xi10 - Xia* et al. *2010; Bo09 - Bonadiman* et al. *2009; Li08 - Li* et al. *2008; Gr07 - Grant* et al. *2007; Fa08 - Falus* et al. *2008; BR92 - Bell & Rossman 1992; Ps02 - Peslier* et al. *2002; Ms18 - Marshall* et al. *2018; Yn08 - Yang* et al. *2008).*

Study	$D_{H_2O}^{cpx-opx}$	Temperature (°C)	Pressure (GPa)	Analysis
Kovács *et al.* (2012)	3.32	1000	2.5	FTIR
Kovács *et al.* (2012)	2.94	1100	4	FTIR
Novella *et al.* (2014)	1.65	1440	6	SIMS
Aubaud *et al.* (2004)	1.38	1230-1380	1-2	SIMS
Hauri *et al.* (2006)	1.21	1270	1-4	SIMS
Tenner *et al.* (2009)	1.07-1.23	1350-1440	3-5	SIMS

Table 8.1 *The conditions of the experiments in which the experimentally determined* $D_{H_2O}^{cpx-opx}$ *from Figure 8.5(a) were measured.*

In Figure 8.5a the partition coefficients of five experimental studies are plotted and labelled with the temperature at which the experiment was conducted. The lowest temperature experiments were conducted by Kovács *et al.* (2012), and produced the highest $D_{H_2O}^{cpx-opx}$ at 3.32 (1100 °C) and 2.94 (1000 °C). Interestingly, these are the only results that were measured using FTIR, the other experimental studies measured the H_2O contents of the pyroxenes using SIMS. The higher temperature experiments span a temperature range of 1230 - 1440 °C and the partition coefficients ($D_{H_2O}^{cpx-opx}$) vary from 1.65 (Novella *et al.*, 2014) to 1.07 (Tenner *et al.*, 2009). A similarly broad range in $D_{H_2O}^{cpx-opx}$ has been measured in mantle xenoliths from on- and off-craton settings (Figure 8.5b).

The lack of one consistent $D_{H_2O}^{cpx-opx}$ implies that the measured values have not equilibrated or there is another control on H_2O paritioning, such as temperature, pressure, diffusive loss/gain, pyroxene composition or the mineral assemblage. Given the fast diffusion rates of hydrogen in pyroxenes (Cherniak & Dimanov, 2010; Ingrin & Blanchard, 2006; Stalder & Skogby, 2003; Woods *et al.*, 2000), it is unlikely that the pyroxenes have not equilibrated in H_2O. The experimental conditions at which the partition coefficients in Figure 8.5a were determined are summarised in Table 8.2. There is a general trend towards a decrease in $D_{H_2O}^{cpx-opx}$ with increasing temperature but there is no apparent correlation between the partition coefficient and the pressure of the experiments (Gibson *et al.*, 2020).

In the Bultfontein and Mothae xenoliths, there is a negative correlation between $D_{H_2O}^{cpx-opx}$ and temperature (Figure 8.6a) with the partition coefficient approaching 1 at the highest temperatures in this study (1273 °C). BD2135 (carbonatite metasomatism) and BD2125 (siliceous fluid metasomatism) and two samples without a reliable temperature estimate (BD1141A and BD1153; kimberlite metasomatism) have anomalous $D_{H_2O}^{cpx-opx}$ values. Discounting these anomalies, the relationship can been quantified by fitting the linear regression in Equation 8.2 with $r^2 = 0.93$.

$$D_{H_2O}^{cpx/opx} = 2.99 - 0.001656T \tag{8.2}$$

The partition coefficients at 800°C, 1000°C and 1200°C, chosen to span the range in equilibration temperature of the Bultfontein and Mothae xenoliths, have been calculated using Equation 8.2 and are plotted as dashed lines in Figure 8.6c. This temperature control in the partitioning of H_2O between clinopyroxene and orthopyroxene in the Kaapvaal craton overprints any metasomatic signature. Therefore it is assumed that subsolidus re-equilibration of H_2O following metasomatism, facilitated by the fast diffusion rates of H in pyroxene, has been achieved. This same process can be observed in the relationship between partitioning of other elements between clinopyroxene and orthopyroxene and temperature, for example the equilibration of Na is also temperature dependent as seen in Figure 8.6b and d.

The relationship between $D_{H_2O}^{cpx-opx}$ and temperature observed in the Bultfontein and Mothae xenoliths has previously been observed in off-craton garnet peridotites (Gibson et al., 2020) but not in cratonic xenoliths, although prior to this study very few samples have analysed co-existing cratonic orthopyroxene and clinopyroxene H_2O contents. Peslier *et al.* (2012) observe a lack of temperature dependence on $D_{H_2O}^{cpx-opx}$ in the craton but find a great deal of scatter. The range in temperature of the Bultfontein and Mothae xenoliths is formed of clusters characterised by different styles of metasomatism (e.g. fluid metasomatism at 1000 °C and melt re-fertilisation at 1250 °C). The apparent temperature dependence

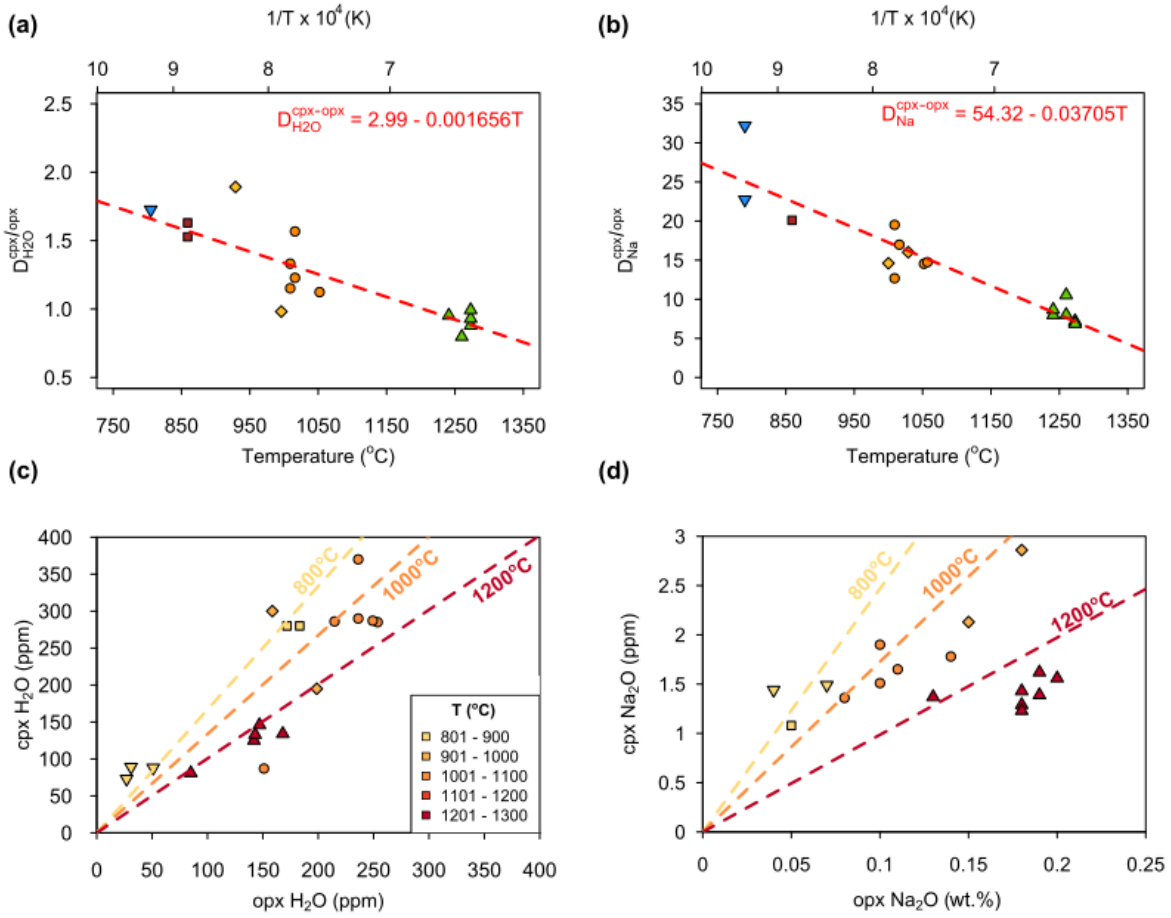

Figure 8.6 ***(a)*** *The relationship between the $D_{H_2O}^{cpx-opx}$ and xenolith equilibration temperature in the Bultfontein and Mothae xenoliths; showing a negative correlation with the relationship $D_{H_2O}^{cpx-opx} = 2.99 - 0.001656T$. Legend as in Figure 8.5.* ***(b)*** *$D_{Na}^{cpx-opx}$ vs. equilibration temperature for the Bultfontein and Mothae xenoliths.* ***(c)*** *The pyroxene water contents from the Bultfontein and Mothae xenoliths. The shapes reflect the groups shown in legend (a) but the colours are scaled according to equilibration temperature. Three partition coefficients according to the relationship in (a) are plotted as dashed lines: 800 °C ($D_{H_2O}^{cpx-opx} = 1.67$), 1000 °C ($D_{H_2O}^{cpx-opx} = 1.34$), 1200 °C ($D_{H_2O}^{cpx-opx} = 1.01$).* ***(d)*** *The pyroxene Na_2O contents from the Bultfontein and Mothae xenoliths. The symbols reflect the groups and the colours are scaled according to equilibration temperature, as in (a). Three partition coefficients according to the relationship in (c) are plotted as dashed lines: 800 °C ($D_{Na}^{cpx-opx} = 24.7$), 1000 °C ($D_{Na}^{cpx-opx} = 17.3$), 1200 °C ($D_{Na}^{cpx-opx} = 9.8$).*

could, therefore, be an artefact of a different metasomatic control or chemical control, for example oxygen fugacity, Ti concentration of the metasomatic agent or silica activity (e.g. Withers & Hirschmann 2008) that can influence the incorporation mechanism of H_2O (see Chapter 9).

8.3.2 $D_F^{cpx-opx}$

The partitioning of F between clinopyroxene and orthopyroxene has not been studied to the same extent as that of H_2O. The few studies that publish $D_F^{cpx-opx}$ values at mantle conditions include Hauri *et al.* (2006), Urann *et al.* (2017) and Gibson *et al.* (2020). Hauri *et al.* (2006) measure the $D_F^{cpx-opx}$ to equal 1.8 ± 0.34, while Urann *et al.* (2017) found $D_F^{cpx-opx}$ equal to 2.4 ($r^2 = 0.95$) and Gibson *et al.* (2020) found $D_F^{cpx-opx}$ to range from 0.25-4 in off-craton xenoliths. The results from the Bultfontein and Mothae

xenoliths analysed here significantly increases the global dataset for cratonic settings. The F concentration of clinopyroxene and orthopyroxene are plotted in Figure 8.7a. The garnet harzburgites with siliceous fluid metasomatism and high-T garnet lherzolites both exhibit very similar partitioning of F between the two pyroxenes close to the average and lower bound of the experimentally determined $D_F^{cpx-opx}$ by Hauri *et al.* (2006) equal to 1.8 ± 0.34. The two samples that have different $D_F^{cpx-opx}$ are spinel harzburgite BD2135 and low-T garnet harzburgite BD1140 in which the orthopyroxene F concentration is very low and close to the detection limit (<5 ppm).

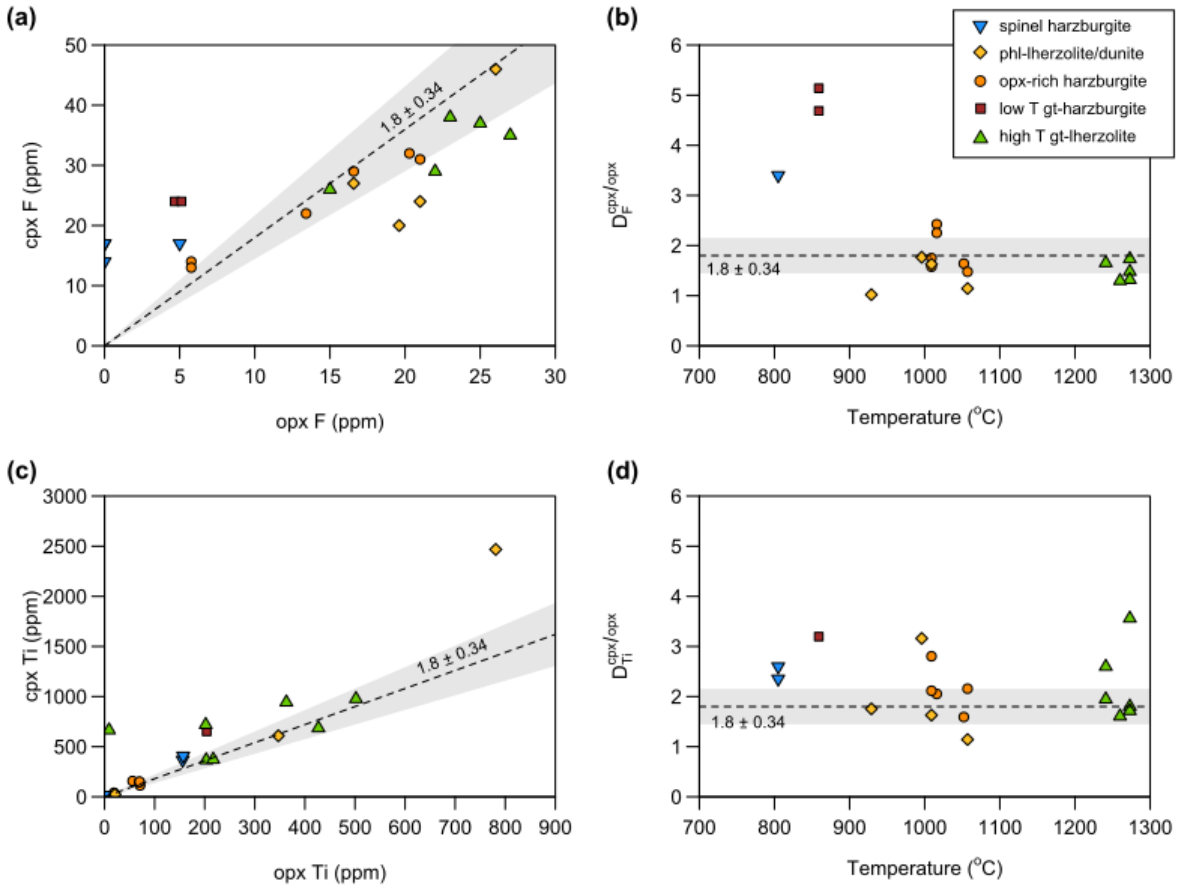

Figure 8.7 ***(a)*** *Orthopyroxene F concentration vs. clinopyroxene F concentration in the Bultfontein and Mothae xenoliths. In all four plots the dashed line marks* $D_F^{cpx-opx} = 1.8 \pm 0.34$ *determined by Hauri* et al. *(2006).* ***(b)*** $D_F^{cpx-opx}$ *vs. temperature.* ***(c)*** *Ti concentration in orthopyroxene against Ti in clinopyroxene. The line of* $D^{cpx-opx} = 1.8 \pm 0.34$ *is repeated on the Ti plots to show the similarity in the partitioning of F and Ti.* ***(d)*** $D_{Ti}^{cpx-opx}$ *vs. temperature.*

Unlike the partitioning of H_2O, there is no systematic relationship between $D_F^{cpx-opx}$ and temperature (Figure 8.7b) in the Bultfontein and Mothae cratonic xenoliths. The same is true for Ti. Figure 8.7c and d show the positive correlation between the Ti contents of orthopyroxene and clinopyroxene, reflecting a relatively uniform partition coefficient which matches that of F determined by Hauri *et al.* (2006) of 1.8 ± 0.34 (Figure 8.7d). Ti is a highly charged cation which diffuses slowly (Cherniak & Liang, 2012, 2014; Spandler & O'Neill, 2010). The lack of temperature control on Ti partitioning between clinopyroxene and orthopyroxene could imply that it has not re-equilibrated following metasomatism, and that the constant partition coefficient reflects the mineral/mineral distribution during metasomatism. If this is the case, the same could be said for F which is a large anion that potentially diffuses slowly through the pyroxene lattice.

To investigate this further the subsolidus re-equilibration timescales of Ti and H in the mantle are assessed in Section 8.4.

8.3.3 D_F^{ol-pxn}

Fluorine partitioning between olivine and the pyroxenes is even more poorly established. The F concentrations in olivine from the Bultfontein and Mothae xenoliths determined here provide a large concentration range to study the partitioning behaviour. The olivine F concentration correlates well with the orthopyroxene F concentration in the carbonatite, kimberlite and fluid metasomatised xenoliths and the clinopyroxene-absent xenoliths (Figure 8.8). The relationship produces an olivine/orthopyroxene partition coefficient of 5.1 (r^2 = 0.9). This is contrary to many experimental studies, which tend to find that orthopyroxene preferentially hosts F over olivine (Beyer *et al.*, 2012; Fabbrizio *et al.*, 2013a). Nevertheless, Crépisson *et al.* (2014) and Joachim *et al.* (2015) suggest that in the presence of H_2O the partitioning of F into olivine is increased. $D_F^{ol-melt}$ is also controlled by the degree of polymerisation of the melt while $D_F^{opx-melt}$ is unaffected (Guggino, 2012; Urann *et al.*, 2017). The greater D_F^{ol-opx} in the metasomatised samples could, therefore, be higher if their metasomatic agents were more polymerised. The high-T garnet lherzolites and BD2170 plot away from this trend, their average D_F^{ol-opx} is 1.3 ± 0.6. It is interesting that BD2170 is the only harzburgite to plot amongst the garnet lherzolites because this xenolith contains a very small modal proportion of clinopyroxene, associated with garnet rims, which has the same primitive-mantle-normalised trace-element pattern as the garnet lherzolites. Therefore, it can be assumed that the clinopyroxene in BD2170 has equilibrated in the same manner as the clinopyroxene in the garnet lherzolites (see Chapter 5). It is possible that this group represents the complete sub-solidus equilibration of F between olivine and orthopyroxene in the SCLM, whereas the orthopyroxene-rich and proto-kimberlite metasomatised samples have preserved the partitioning of F between phases during melt/rock reaction.

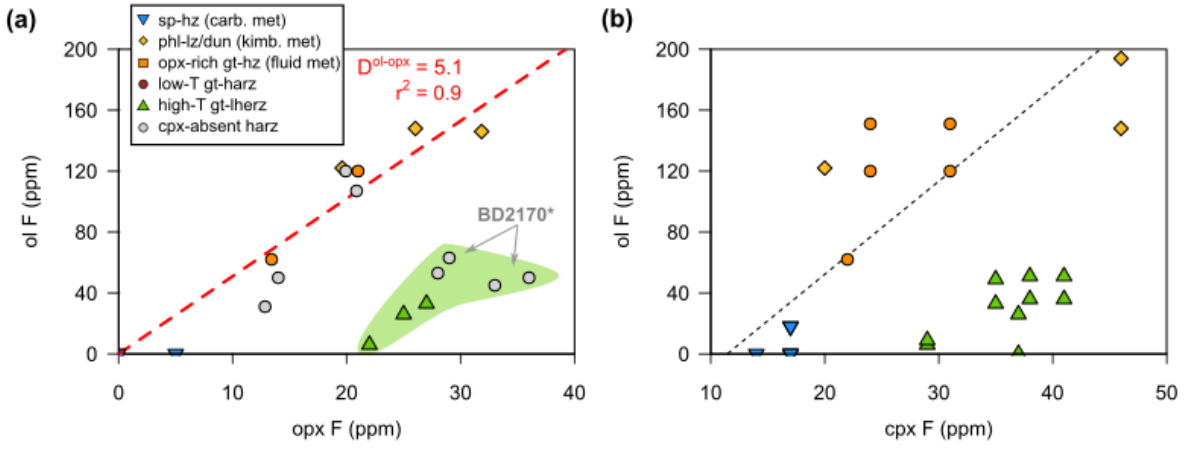

Figure 8.8 ***(a)*** *Olivine F concentration vs orthopyroxene F concentration in the Bultfontein and Mothae xenoliths. There is a trend amongst Group A, B, C and Other xenoliths, but the garnet lherzolites (Group E) and BD2170 fall off this trend. BD2170 contains very minor clinopyroxene with the same clinopyroxene composition as the garnet lherzolites, so it could be considered to be within Group E.* ***(b)*** *Olivine F concentration vs clinopyroxene F concentration.*

A similar distribution of the different groups is observed in the olivine and clinopyroxene F concentrations, with high-T garnet lherzolites having the lowest partition coefficient however, the same correlation in the metasomatised samples is not apparent.

8.4 Subsolidus re-equilibration in NVFMMs

Metasomatism introduces new elements into the local mantle assemblage and temporarily perturbs the system to higher temperatures than the geotherm. As a result, the distribution of elements established during metasomatism is not stable once the melt-rock reaction has finished and the system re-equilibrates back to the stable geotherm conditions. Following metasomatism, elements are re-distributed to establish the stable partitioning at the local PT conditions. At high temperatures the thermal perturbation during metasomatism is less than at low temperatures, and the diffusion rates are faster, which means less diffusive re-equilibration is required to stabilise the distribution of elements and it occurs much more quickly at high temperatures.

In Section 8.3 it was alluded to that the temperature dependence of $D_{H_2O}^{cpx-opx}$ indicates that the H_2O contents of the NVFMM have re-equilibrated following metasomatism, and that the lack of temperature dependence of $D_{F}^{cpx-opx}$ and $D_{Ti}^{cpx-opx}$ indicates that subsolidus re-equilibration of F and Ti is incomplete. The timescales of diffusive re-equilibration are controlled by: (i) the volume fraction of each mineral; (ii) grain size; (iii) the diffusion rate of the element of interest in each phase; and (iv) whether a melt phase is present (Liang, 2014). In this section the approximate solutions to diffusion equations obtained by Liang (2014) are used to calculate the timescale of re-equilibration for Ti and H in a bimineralic system and in a two-mineral-melt system for reference.

Equation 8.3 (Liang, 2014) can be used to calculate the timescales of diffusive re-equilibration, t_D, between two minerals (A and B) and a small fraction of melt (f):

$$\frac{t_D}{3} = \left(\frac{w_f^\infty + w_A^\infty}{R_B} + \frac{w_f^\infty + w_B^\infty}{R_A} \right) + \frac{1}{1 + \omega \phi_f} \tag{8.3}$$

$$w_j^\infty = \frac{\phi_j C_j^\infty}{\phi_f C_f^\infty + \phi_A C_A^\infty + \phi_B C_B^\infty} \quad , \quad j = f, A, B \tag{8.4}$$

$$R_A = \frac{3\beta D_A}{L_A^2} \quad \text{and} \quad R_B = \frac{3\beta D_B}{L_B^2} \tag{8.5}$$

$$\omega = \frac{R_A R_B (\phi_f + \phi_A k_A + \phi_B k_B)}{[R_A(\phi_f + \phi_A k_A) + R_B(\phi_f + \phi_B k_B)]^2} \tag{8.6}$$

where:

ϕ_j: volume fraction of component j

C_j^{∞}: equilibrium concentration of element in component j

$D_{A,B}$: diffusion coefficient of element in A,B

w_j^{∞}: equilibrium mass fraction of element in component j

R_j: diffusive exchange rate between A or B and the melt

β: a geometric factor to account for crystal shape. β = 4 (cylinder, radius L) or 5 (sphere, radius L).

$L_{A,B}$: average radius of A and B

$k_{A,B}$: mineral/melt partition coefficient

Equation 8.3 is adapted for a bimineralic system in the absence of melt by setting $\phi_f = 0$, to obtain Equation 8.7 (Liang, 2014).

$$\frac{t_D}{3} = \frac{w_B^{\infty}}{R_A} + \frac{w_A^{\infty}}{R_B} \tag{8.7}$$

The Arrhenius relations for diffusion of element, i, in mineral, j, are used according to Equation 8.8.

$$D^i = D_0^i exp\left(\frac{-Q}{RT}\right) \tag{8.8}$$

where:

D_0^i: material-dependent pre-exponential term

Q: activation energy in kJ mol^{-1}

T: temperature in K

R: gas constant

Element	D_0	Q	Reference
Forsterite			
H	$10^{-1.4}$	258	Demouchy & Mackwell (2006)
Mg-Fe	9.6 x 10^{-4}	400	Dohmen & Chakraborty (2007)
Dy	8 x 10^{-10}	289	Cherniak & Dimanov (2010)
Ti	5.97 x 10^{-14}	203	Cherniak & Liang (2014)
Enstatite			
H	1.37	295	Stalder & Skogby (2003)
Gd	2.55 x 10^{-9}	321	Cherniak & Liang (2007)
Ti	1.45 x 10^{-11}	270	Cherniak & Liang (2012)
Diopside			
H	$10^{-3.4}$	153	Woods *et al.* (2000)
Dy	4.9 x 10^{-4}	461	Van Orman *et al.* (2001)
Ti	8 x 10^{-11}	282	cherniak and liang 2012

Table 8.2 *The activation energy (Q) and material dependent pre-exponential term D_0 used in Equation 8.8 to calculate diffusion rates as a function of temperature.*

The diffusion parameters for elements of interest are given in Table 8.2 and the variation in diffusion rate is exhibited in Figure 8.9. The diffusive re-equilibration between olivine and orthopyroxene is the initial focus of this section, because these two phases constitute over 90% of the modal assemblage of most of

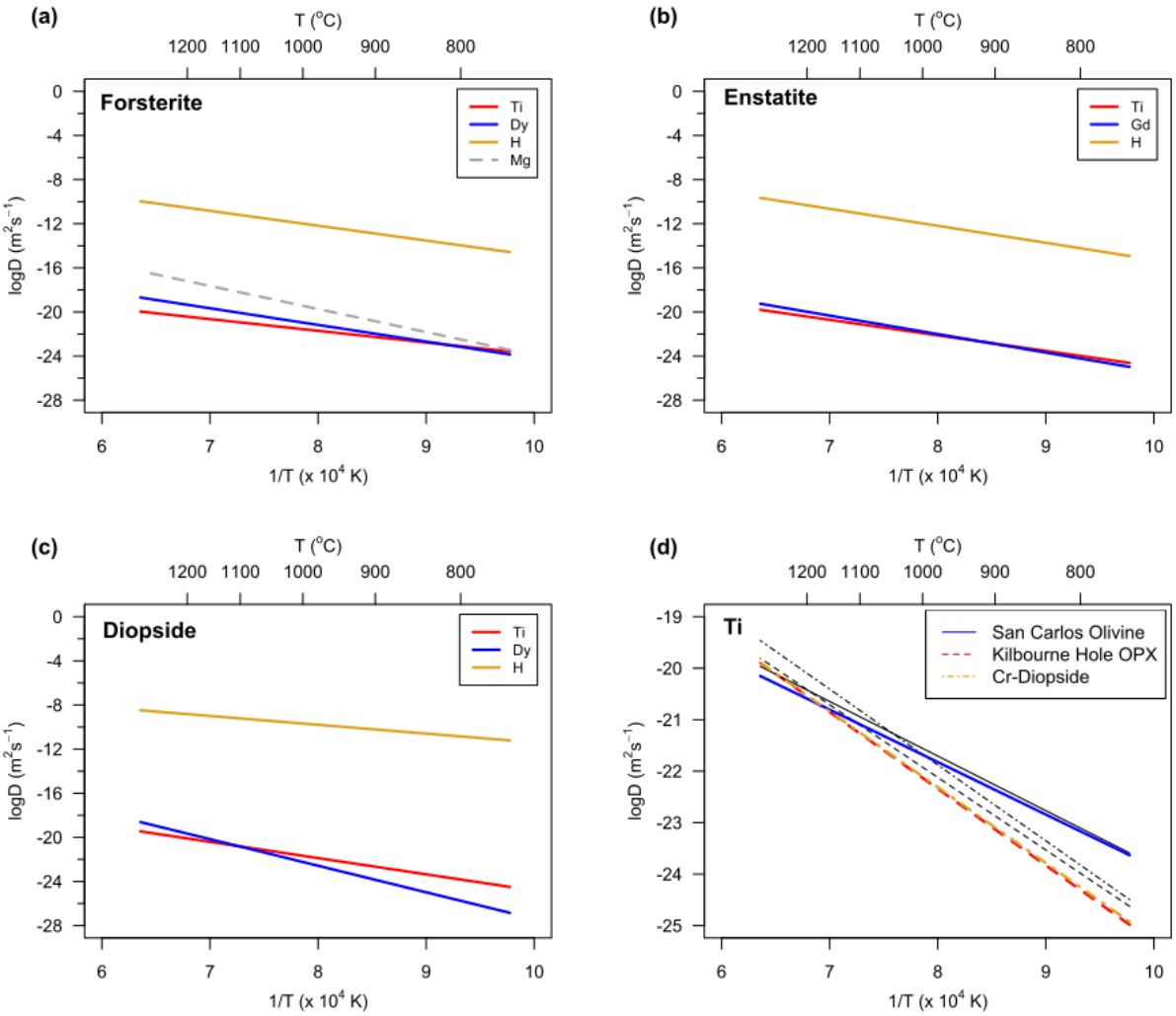

Figure 8.9 ***(a)*** *Diffusion rates of H, Mg, Dy and Ti in pure forsterite* ***(b)*** *Diffusion rates of Mg, Gd and Ti in pure enstatite.* ***(c)*** *Diffusion rates of H, Dy and Ti in pure diopside.* ***(d)*** *Diffusion rates of Ti in San Carlos olivine, Kilbourne Hole orthopyroxene and Chrome-Diopside (Cherniak & Liang, 2012, 2014). The diffusion rates for the pure phases are shown in black with the same line style.*

the studied xenoliths from Bultfontein and Mothae. Equations 8.3 and 8.7 show that the addition of melt into the system slows the re-equilibration time between the two minerals. In the Bultfontein and Mothae peridotite xenoliths the proportion of the infiltrating metasomatic melt fraction is assumed to have been very low (< 0.1%), so according to Equation 8.3 the presence of a small-fraction of melt increases the re-equilibration timescales by a factor less than 10.

Ti diffusion is slower than most other elements in both olivine and orthopyroxene (Figure 8.9, Cherniak & Liang 2012, 2014). The general solution in Figure 8.10a uses the primitive-mantle bulk Ti concentration, and the equilibrium Ti concentration for olivine and orthopyroxene to calculate the timescales of Ti subsolidus re-equilibration. Four scenarios were accounted for to reflect the range in mode and textures in the Bultfontein and Mothae xenoliths: (i) coarse grained orthopyroxene-rich assemblage; (ii) porphyroclastic orthopyroxene-rich assemblage; (iii) coarse grained orthopyroxene-poor assemblage; and (iv) porphyroclastic orthopyroxene-rich assemblage. The ratio of olivine:orthopyroxene was set to 65:35 in the orthopyroxene-rich assemblage, and 85:15 in the orthopyroxene-poor assemblage. In addition

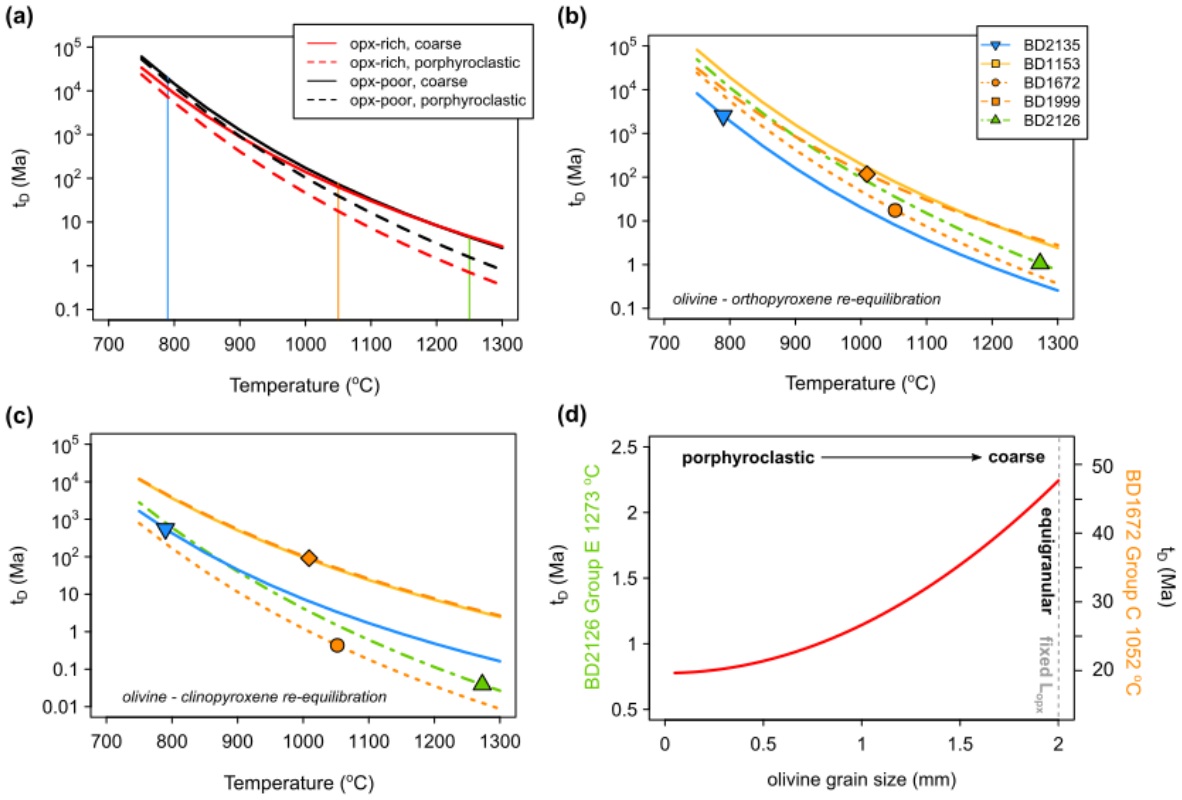

Figure 8.10 *Olivine-orthopyroxene diffusive re-equilibration of Ti.* ***(a)*** *General solution for the primitive-mantle - i.e. primitive-mantle composition - varying the proportion of opx from 15% to 35% and the texture from coarse to porphyroclastic.* ***(b)*** *Bulk Ti composition of xenoliths used to calculate the equilibrium concentrations of olivine and orthopyroxene based on the mineral-mineral partition coefficients obtained from Dasgupta* et al. *(2009). The same method was used as that in Chapter 5 to calculate the composition of mantle phases in equilibrium with primitive mantle.* ***(c)*** *Timescales of Ti re-equilibration between olivine and clinopyroxene in five of the Bultfontein and Mothae xenoliths.* ***(d)*** *The effects of changing grain size on olivine-opx diffusive re-equilibration*

to these generalised scenarios, the parameters for each type of xenolith in this study were used to calculate more specific timescale for diffusive re-equilibration in the Bultfontein and Mothae xenoliths (Figure 8.10b). Re-equilibration times are calculated for six xenoliths from Groups A-E that cover a range of temperatures, lithology and texture (Table 8.3).

Equation 8.7 requires the equilibrium concentration in each phase, but the Ti concentration in the natural xenoliths is not guaranteed to be in equilibrium; in fact it appears to be in dis-equilibrium by the vast difference between the calculated Ti composition of the melt in equilibrium with the olivine and orthopyroxene using the mineral/melt partition coefficients of Dasgupta *et al.* (2009). Therefore, the equilibrium concentration of Ti (i.e. the distribution after full sub-solidus re-equilibration) has been re-calculated assuming a closed system with a fixed bulk concentration of Ti in olivine, orthopyroxene, clinopyroxene and garnet. The bulk concentration of Ti was established in Chapter 3, and here the equilibrium concentrations of olivine, orthopyroxene and clinopyroxene are calculated using the same method that was used to estimate the concentrations of the minerals in equilibrium primitive mantle in Chapter 5 (Equation 5.10). The points marked on Figure 8.10b represent the timescale of diffusive re-equilibration at the temperature at which the corresponding xenolith equilibrated. The fastest re-equilibration time is at the highest temperature, i.e. 1273 °C in garnet lherzolite BD2126, where Ti is

Group	Lithology	Sample	Texture	Modal opx (%)	T (°C)	ol-opx Ti t_D (Ma)	ol-cpx Ti t_D (Ma)	ol-opx H t_D (yr)
Group A	sp-hz	BD2135	Pc	27.1	806	2536	549	0.6*
Group B	dunite	BD1153	C	6.1	992	230	109	0.035
Group C	opx-rich gt-hz	BD1672	Pc	31.5	1052	17	0.4	0.0034
Group C	opx-rich gt-hz	BD1999	C	36.8	1009	117	91	0.026
Group D	low-*T* gt-hz	BD1140	C	5.1	859	2990	896	0.75*
Group E	high-*T* gt-lhz	BD2126	Pc	13.6	1273	1	0.04	0.0001

Table 8.3 *Timescales of re-equilibration in a bimineralic system for Ti and H for six samples in all five of the clinopyroxene-bearing peridotites. The groups represent a range of temperatures (806-1273 °C), both coarse (C) and porphyroclastic textures (Pc) and a range in modal abundance of orthopyroxene (5 - 37%). Timescales for re-equilibration are givin in Ma for Ti and years for H. *denotes where weighted fraction (ω) of Ti distribution was used because H_2O concentrations were not analysed (BD1140) or below detection limit (BD2135).*

estimated to re-equilibrate in 1 Ma. The slowest re-equilibration time is for the shallowest and lowest-*T* xenolith (800 °C, spinel harzbugrite BD2135) which is estimated to take 2.5 Ga to re-equilibrate. The re-equilibration time for the orthopyroxene-rich garnet harzburgites BD1672 and BD1999, from 1052 °C and 1009 °C respectively, is estimated between 17 Ma and 117 Ma.

The calculated timescales of diffusive re-equilibration of Ti between olivine and clinopyroxene are shown in Figure 8.10c. In these calculations the proportion of clinopyroxene was as measured and the proportion of olivine was taken to constitute the rest of the xenolith. Clinopyroxene is only a minor phase within the xenoliths (1-8%) and therefore the re-equilibration times are faster than for olivine and orthopyroxene. Clinopyroxene re-equilibrates in 40,000 years in the high-*T* porphyroclastic garnet lherzolite (BD2126), while clinopyroxene and olivine in the low-*T* spinel-harzburgite (800 °C; BD2135) take 550 Ma to re-equilibrate, despite there only being 2% clinopyroxene. The coarse-grained xenoliths again have slower re-equilibration times, with a difference of two orders of magnitude between the two Group C xenoliths exhibiting coarse (BD1999) and porphyroclastic (BD1672) textures. The faster equilibration times of clinopyroxene and olivine convey the fact that re-equilibration of the whole peridotite assemblage is controlled by diffusive exchange between olivine and orthopyroxene.

The full effect of changing the relative grain size of olivine and orthopyroxene is shown in Figure 8.10d. The orthopyroxene grain size was fixed at a radius of 2mm so Figure 8.10d shows the effect of texture where: (i) the smallest olivine grain size of 50 μm represents a mosaic porphyroclastic texture in which all olivine is present as neoblasts; and (ii) the maximum grain size of 2mm represents a coarse granoblastic texture. The timescales calculated according to the parameters for the highest temperature garnet lherzolite xenoliths (Group E, BD2126), and those for slightly lower-temperature orthopyroxene-rich garnet harzburgite xenoliths (Group C, BD1672) are shown on the left- and right-hand side, respectively. In both cases there is a change in re-equilibration time by a factor between 2 and 3.

The difference in equilibration time of porphyroclastic and coarse xenoliths could explain the disequilibrium observed in some of the xenoliths in this study. In Chapter 3, a number of xenoliths were found to contain olivine, orthopyroxene and clinopyroxene that had not equilibrated in Mg-Fe (e.g. BD2135, BD1141A, BD2125, BD2128). Figure 8.11 compares the Mg-Fe equilibrium constant ($K_D^{opx/ol} = [MgO/FeO]_{opx}/[MgO/FeO]_{ol}$ mol) of the coarse xenoliths and porphyroclastic xenoliths. The majority of xenoliths that exhibit significant disequilibrium are coarse grained peridotites.

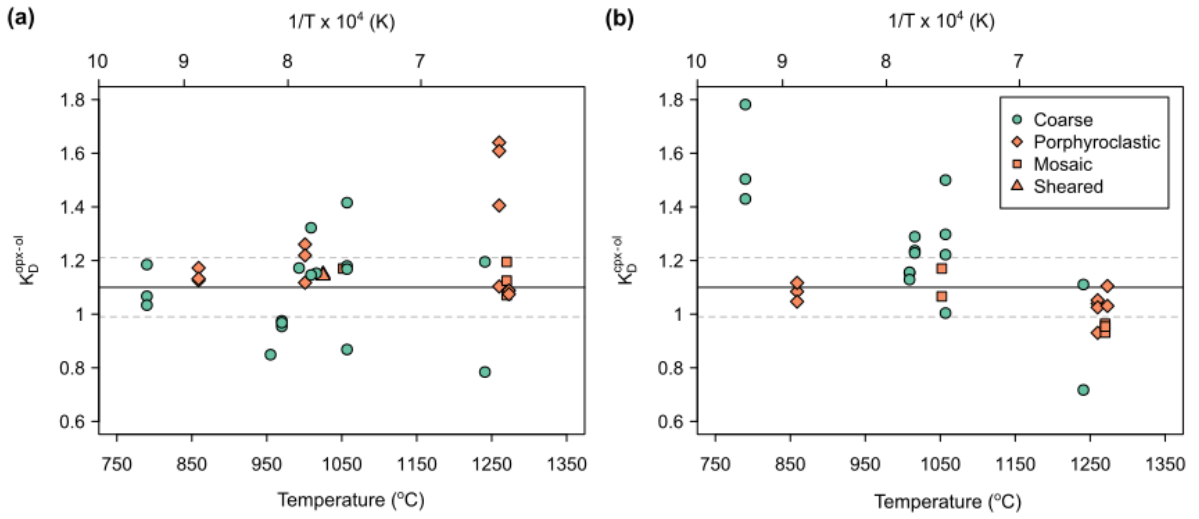

Figure 8.11 ***(a)****Kd [MgO/FeO]opx/[MgO/FeO]ol according to texture. In general the porphyroclastic samples have equilibrated but the coarse grained textures remain in disequilibrium. At high temperatures, especially in the coarse samples that have not re-equilibrated, this provides a short window for metasomatism.*

In contrast to the slow diffusing Ti, H diffuses extremely fast in olivine, orthopyroxene and clinopyroxene (Figure 8.9). The timescales for diffusive re-equilibration of Ti and H are compared in Figure 8.12 in which the vastly different re-equilibration timescales are evident in the two separate axes for Ti (left) and H (right). Specific re-equilibration timescales for the select xenoliths are marked as points. The fastest equilibration time for H between olivine and orthopyroxene is 50 minutes in BD2126, whereas that increases to 1 day in BD1672 and 9 days in BD1999.

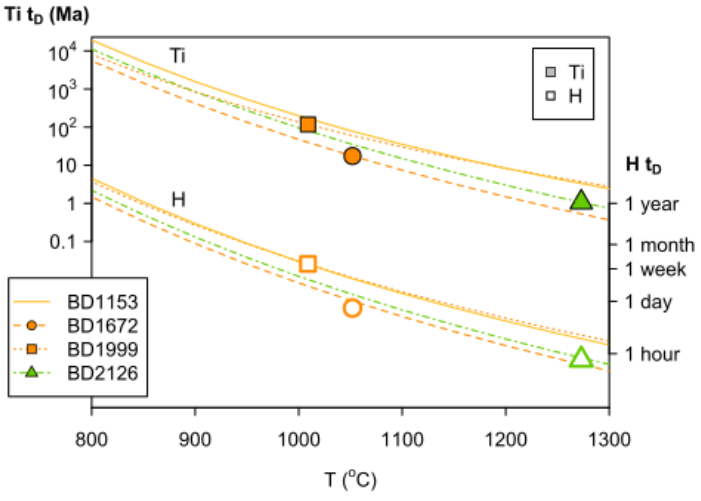

Figure 8.12 *Timescales of Ti (LHS) and H (RHS) subsolidus re-equilibration between olivine and orthopyroxene from 800-1300 °C in BD1153, BD1672, BD1999 and BD2126.*

These timescales highlight the disparity between different elements to re-equilibrate between two minerals. Slower diffusing elements such as Ti and the REE take a relatively long time to re-equilibrate. For example, in coarse peridotite BD1999 the signature of a metasomatic event that occurred over 100 Ma prior to entrainment can be preserved in the distribution of these slow diffusing elements. At lower temperatures, the timescale for diffusive re-equilibration is even greater so that carbonatite metasomatism

in spinel harzburgite (BD2135), which equilibrated to 800 °C, can preserve a Ti and REE metasomatic signature for billions of years. By contrast the H concentration should re-equilibrate instantaneously, which means that an inter-mineral distribution of H which is reflective of a metasomatic signature may only be preserved if the enrichment occurred by the host kimberlite itself during ascent. These results can explain the relationship between the partitioning of H and temperature (Figure 8.6), and the lack of such a relationship in the partitioning of Ti (Figure 8.7). The $D_{H_2O}^{cpx-opx}$-T relationship reflects complete subsolidus re-equilibration of H in the local mantle conditions, whereas the subsolidus re-equilibration of Ti is incomplete and the partitioning established between the minerals and the metasomatic agent is preserved. The preservation of disequilibrium can be used to help to estimate a minimum time of a metasomatic event in the mantle prior to the entrainment of the xenolith but high-resolution diffusion profiles are required to fully resolve the exact timing (e.g. Chapter 6).

8.5 Implications of Ti-H-F coupling to diffusion rates

The calculations in Section 8.4 show that diffusive re-equilibration of Ti can take millions of years, especially at low temperatures, while H re-equilibrates effectively instantaneously. Fluorine re-equilibration timescales were not calculated (due to the lack of published diffusion rate), however, there are at least three lines of evidence to suggest that F has not fully re-equilibrated in the Bultfontein and Mothae xenoliths: (i) F partitioning in this xenolith suite correlates well with Ti (Section 8.3), which implies that they behave similarly; (ii) both Ti and F partitioning are independent of temperature in the Bultfontein and Mothae xenoliths; and (iii) the F concentration in all NVFMMs analysed preserves correlations with metasomatic indicators, such as Ti/Eu ratio (see Chapter 9). As diffusion rate is the primary control of the time for complete subsolidus re-equilibration, the similarities between Ti and F suggest that they either have similar diffusion rates or diffusion is limited by coupling (e.g. Cherniak & Liang 2012). The re-equilibration timescales calculated above do not account for coupling of Ti with charge balancing species.

The lack of subsolidus re-equilibration in F, matching Ti, in this study could suggest that the diffusion of F in olivine, orthopyroxene and clinopyroxene is slow relative to H. F^- is a large anion (1.31 Å; Shannon 1976) which will slowly diffuse through the crystal lattice. If F^- is hosted in the oxygen sites, as suggested by Crépisson *et al.* (2014) and proposed in Figure 8.1, then the coupling of Ti-F could be stronger than that of Ti-H because a diffusion mechanism involving coupled Ti and F would have to also involve F being replaced by and moving between oxygen vacancies. Oxygen diffuses at a similar rate to the divalent cations, and slightly faster than Si which remains the slowest cation (Brady & Cherniak, 2010; Gérard & Jaoul, 1989; Houlier *et al.*, 1988; Ryerson *et al.*, 1989). The diffusion rate of oxygen is faster if this occurs via the interstitial mechanism as opposed to the vacancy mechanism (Walker *et al.*, 2003). Gérard & Jaoul (1989) infer that oxygen diffusion in San Carlos olivine occurs via the interstitial mechanism and that these defects carry one negative charge, which would match a F^- anion and could mean that the diffusion rate is similar if F is hosted interstitially. The diffusion mechanism depends on the oxygen fugacity, with the vacancy mechanism dominating at low fO_2 and interstital mechanism at high fO_2. If F is hosted in oxygen vacancies, as proposed, then the concentration and diffusion rates of F should be higher where the oxygen fugacity is low (i.e more reducing).

The diffusion rates of H are very well-understood in comparison to F, and are known to be very fast. As a result, the complete absence of any correlation between the H_2O concentration and metasomatic indicators, has been inferred to indicate the complete subsolidus re-equilibration or diffusive loss of H (e.g. Marshall *et al.* 2018). The timescales of subsolidus re-equilibration calculated for H in Section 8.4 are based on bulk H diffusion, and reflect the fastest diffusion rates for H in olivine (Demouchy & Mackwell, 2006). H diffusion in olivine is dependent on the point defect in which H is incorporated in the lattice (Demouchy & Mackwell, 2006; Jollands *et al.*, 2016; Padrón-Navarta *et al.*, 2014; Peslier *et al.*, 2015). The fastest diffusion mechanism for H is via M-site vacancies (Demouchy & Mackwell, 2006; Jollands *et al.*, 2016), therefore of the four common OH-substitutions in olivine the [Mg] and [triv] point defects are lost first during dehydroxylation of olivine (Padrón-Navarta *et al.*, 2014) because the H is already associated with a M-site vacancy and does not need to wait for a vacancy to appear to make a diffusive jump (Jollands *et al.*, 2016). This result could explain why there are no [Mg] or [triv] absorbance bands observed in the Bultfontein and Mothae mantle olivines, because the H associated with these mechanisms has preferentially been lost during ascent in the kimberlite. In contrast Padrón-Navarta *et al.* (2014) found that diffusion of H incorporated via the [Ti] mechanism is slower than the M-site vacancy mechanisms, especially when there are no [triv] point defects (Jollands *et al.*, 2016), and that the [Si] mechanism is able to retain water over long time periods at high temperatures. The interaction between [Ti] and [Si] point defects in olivine can lock H into the olivine structure, and hence preserve mantle water contents (Padrón-Navarta *et al.*, 2014).

It is important to remember that diffusion can only occur if mass balance, charge balance and site balance are all maintained. Using the results presented here it is proposed that there is a strong coupling not only between H and Ti, but also with F in cryptically metasomatised olivine. Therefore, the diffusion of any component must also involve the diffusion of the other two, while satisfying the aforementioned conditions. This complex mechanism could explain why there is a positive correlation between Ti and H_2O in the F-rich cryptically metasomatised olivines from Bultfontein and Mothae but not in the global dataset of mantle olivine.

8.6 Volatile enrichment in mantle olivines

This chapter has presented a number of observations that are unexpected or contrary to experimental results and other observations, one of these is the fact that olivine in the Bultfontein and Mothae xenoliths has significantly higher F concentrations than the co-existing pyroxenes. The clinopyroxene and orthopyroxene have very similar concentrations of both H_2O and F, whereas olivine has much higher F contents and lower H_2O concentrations. This trend suggests that H_2O preferentially partitions into the pyroxenes, and F appears to partition preferentially into olivine, which is contrary to most other observations and experimental results of fluorine partitioning between mantle minerals. Experimental studies suggest that F is preferentially incorporated into orthopyroxene over olivine (Beyer *et al.*, 2012; Dalou *et al.*, 2012; Hauri *et al.*, 2006; Joachim *et al.*, 2015).

In this chapter a number of mechanisms have been proposed as important processes that control the incorporation of H and F into olivine and orthopyroxene, these include the coupling of H, F and Ti, and the preference for minerals enriched in trivalent cations to form coupled Tschermak substitutions. These

mechanisms add to the complexity in observed partitioning behaviour in natural mantle xenoliths. During melt-rock reaction, Al^{3+} and Cr^{3+} are preferentially partitioned into clinopyroxene, then orthopyroxene and then olivine. The concentration of both Al and Cr are extremely low in olivine. The high concentration of these trivalent cations in clinopyroxene increases the Tschermak component of the mineral. In orthopyroxene the Tschermak component is smaller and there is, therefore, greater scope for trivalent cations to be charge balanced by OH-groups or F. Meanwhile, Ti^{4+} is incorporated into octahedral sites in clinopyroxene, orthopyroxene and olivine by the same order of preference. If the incorporation mechanism for H_2O and F both involve coupling with Ti, then this presents competition for space in the crystal lattice. Olivine should have the lowest concentrations of both H_2O and F if partitioning experiments are to be believed, but if H_2O is incorporated preferentially into the pyroxenes then, in a closed system, there is less remaining to be incorporated into olivine. Instead the results of SIMS and FTIR in olivine from Bultfontein and Mothae indicate that rather than being charge balanced by two H^+, as in the [Ti] mechanism, the Ti^{4+} in metasomatised olivine is charge balanced by one F^- anion replacing an oxygen and one H^+ forming an OH-group both around a neighbouring tetrahedral vacancy (Figures 8.1d and 8.2b). As a result, F is enriched in olivine relative to orthopyroxene and clinopyroxene, which instead accommodate a greater proportion of OH-groups in the lattice.

8.7 Summary

In this chapter the results of LA-ICP-MS, SIMS and FTIR analyses have been used to investigate the incorporation mechanisms and partitioning behaviour of H_2O and F in co-existing mantle minerals. While there are four common mechanisms for H incorporation in olivine, in the Bultfontein and Mothae xenoliths the most dominant mechanism is the Ti-clinohumite-like point defect. Another mechanism involving Ti, H and F is proposed here, whereby one Ti^{4+} in an octahedral site is charge balanced by one F anion in an oxygen site and the formation of an OH-group in a neighbouring tetrhedral vacancy. This can be considered as a clumped fluoride-hydroxyl group (i.e. Crépisson *et al.* 2014) coupled to a Ti cation. The recognition of this mechanism has important implications for the simultaneous incorporation of F and H during metasomatism, and the mechanics of diffusion of all three elements through the olivine lattice. The incorporation mechanisms of H_2O and F in orthopyroxene is difficult to determine without further experimental research into the defects that produce different FTIR absorbance bands. Despite this, a coupled charge balancing substitution of F^- and Na^+ is recognised, alongside the importance of trivalent cations and tschermak substitutions for both H and F incorporation in orthopyroxene.

In the published literature there is wide disagreement on the partitioning of H_2O between pyroxenes. In the Bultfontein and Mothae xenoliths there is a wide variation in $D_{H_2O}^{cpx-opx}$ from 0.8-2, which depends strongly on temperature so that $D_{H_2O}^{cpx-opx}$ decreases with increasing temperature. A temperature dependence on $D_{H_2O}^{cpx-opx}$ has only been rarely observed in other datasets (e.g. Gibson *et al.* 2020), however it must be acknowledged that the majority of analyses to date have been made on off-craton xenoliths that equilibrated over limited temperature and pressure ranges. Co-existing pyroxenes in cratonic xenoliths tend to have lower $D_{H_2O}^{cpx-opx}$ than the global average (predominantly off-craton) of 2.1 (Demouchy & Bolfan-Casanova, 2016), including the xenoliths from the Kaapvaal craton in this study. More studies are required to increase the available dataset of H_2O in cratonic NVFMM to fully investigate the controls on the partitioning of H_2O (see discussion in Chapter 9). Fluorine partitioning is independent of temperature

but is very similar to Ti partitioning. Both elements exhibit $D^{cpx-opx}$ close to the $D_F^{cpx-opx}$ = 1.8 ± 0.34 which was established experimentally by Hauri *et al.* (2006). The results indicate that both Ti and F partition similarly during melt-rock interaction, this could be due to a coupled incorporation in the pyroxenes as was established in olivine.

The similar behaviour of Ti and F with temperature lead to the interpretation that F diffuses at a similar rate to Ti. Ti is a slow diffusing element due to its high charge, the large size of the F anion could also limit diffusion. In contrast, H is the fastest diffusing species in NVFMM. The timescales of subsolidus re-equilibration are calculated for Ti and H, and while H re-equilibrates effectively instantaneously, Ti takes millions (high-T) to billions (low-T) of years to re-equilibrate following a chemical perturbation, e.g. melt-rock reaction. If the diffusion rate of F is assumed similar to Ti, then the implication is that F also takes this long to re-equilibrate. The observed correlations between Ti, H and F imply that their coupled incorporation (e.g. in olivine) limits diffusion, hence facilitating the preservation of such metasomatic signatures for millions-billions of years. This limited diffusion for specific point defects can also explain why the [Ti] mechanism is the dominant absorbance band in olivine FTIR spectra, if the H incorporated via other mechanisms has been lost due to faster, uninhibited diffusion pathways.

Chapter 9

Controls on volatile storage in the SCLM

9.1 Introduction

Melting in the convecting mantle removes volatiles from the peridotite residue and the resultant melts transfer these elements to the overlying lithospheric mantle via metasomatism (McKenzie, 1989). Metasomatic agents are, therefore, important carriers of volatile elements through the sub-cratonic lithospheric mantle and their variable interaction with the wall-rock peridotite can affect the overall volatile concentrations. Peslier *et al.* (2012), Doucet *et al.* (2014) and Hui *et al.* (2016) all recognise the role of metasomatism in adding water to nominally volatile-free mantle minerals (NVFMMs) in the mantle beneath the Kaapvaal, Siberian and Tanzanian cratons, respectively. In this chapter the role of metasomatism on the fluorine concentrations in NVFMM in sub-cratonic lithospheric mantle (SCLM) is investigated for the first time.

Only a few studies have analysed fluorine concentrations in NVFMMs, especially those from the sub-cratonic lithospheric mantle. These have focused on methodology of analysis (Mosenfelder & Rossman, 2013a,b; Urann *et al.*, 2017), partitioning behaviour (Bernini *et al.*, 2013; Beyer *et al.*, 2012, 2016; Bénard *et al.*, 2017; Dalou *et al.*, 2012; Gibson *et al.*, 2020; Joachim *et al.*, 2015; Rosenthal *et al.*, 2015) and incorporation mechanisms (Grützner *et al.*, 2017; Joachim *et al.*, 2015; Urann *et al.*, 2017). Urann *et al.* (2017) investigate the spatial variation of fluorine concentration in NVFMMs across different tectonic settings. Their dataset provides the first insight into the potential effects of mantle processes on fluorine concentration in the mantle but did not include any samples from the sub-cratonic lithospheric mantle. Recent work by Gibson *et al.* (2020) analysed F concentrations in NVFMMs from off-craton sub-continental lithospheric mantle (Pale Aike and the Antarctic Peninsula) which presents a complimentary case study to investigate the differences between off-craton and cratonic volatile storage. Chapters 3 and 7 presented the concentrations of major- and trace-elements, water, fluorine and chlorine analysed in the same mineral grains from nineteen xenoliths from the Kaapvaal craton. The large pressure and temperature range of the sample suite and the internally consistent geochemical dataset allow a comprehensive, systematic investigation into the external influences of fluorine and water concentrations in the NVFMMs that make up >95% of the sub-cratonic lithospheric mantle.

In Chapter 5, five chemically-distinct groups were identified in the Bultfontein and Mothae xenoliths on the basis of clinopyroxene and garnet trace-element compositions and petrographic observations. These groups represent different types of metasomatism including: (i) cryptic carbonatite melt metasomatism; (ii) cryptic and modal silico-carbonatite (proto-kimberlite) melt metasomatism; and (iii) metasomatism by hydrous siliceous fluids. The composition of the metasomatic agent strongly controls the incompatible trace-element composition (e.g. REE) of mineral phases, especially clinopyroxene, because they are highly concentrated in small-fraction melts. In Chapter 7 it was established that the diffusive re-equilibration of Ti and the REE are very slow, which means that a metasomatic signature involving Ti and REE can be

preserved for millions to billions of years. The diffusion of F in NVFMMs is also slow but H diffusion is very fast. In Chapter 7 it was proposed that strong coupling of F and H with Ti in mantle minerals inhibits their independent diffusion such that a metasomatic signature can also be preserved in the volatile concentrations beyond the expected timescales of re-equilibration for F or H alone. In the light of these findings, this chapter compares the volatile concentrations in olivine, orthopyroxene and clinopyroxene associated with the different styles of metasomatism to establish how the composition of the metasomatic agent and the style of metasomatism (cryptic, stealth or modal) influences the storage of fluorine, and to some extent water, in NVFMMs in the sub-cratonic lithospheric mantle.

9.2 Spatial controls on volatile concentration

The published dataset of water concentrations in olivine, orthopyroxene and clinopyroxene from the sub-cratonic mantle is limited, and very few analyses exist for fluorine. Peslier *et al.* (2012) showed that there is large variation in H_2O concentrations in the SCLM over very short length-scales. There is, however, no constraint to date on the spatial variation in F in sub-cratonic mantle. Figure 9.1b-d shows the H_2O concentration plotted against F concentration in mantle olivine and pyroxenes, separated by location. It can be seen from this that xenoliths from Bultfontein in the centre of the Kaapvaal craton show enrichment in H_2O relative to xenoliths from Mothae on the craton margin, in agreement with the findings of Peslier *et al.* (2010). This study shows for the first time that the reverse relationship, however, is true for F. This contrast is especially apparent in the orthopyroxene concentrations where those from Mothae are F-rich and H_2O-poor relative to those from Bultfontein. Moreover, a systematic difference is present in the shape of the orthopyroxene FTIR spectra in the OH-stretching region between the xenoliths from Bultfontein and Mothae (Chapter 7). The peak of the absorbance bands at 3600 and 3545 cm^{-1} is much lower in the orthopyroxene from Mothae than at Bultfontein and there is a significant difference in the ratio of absorbance between the 3545 and 3516 cm^{-1} bands. The smaller integrated absorbance in the OH-stretching region in the Mothae orthopyroxene reflects the lower water contents. This spatial variation exhibited in orthopyroxene FTIR spectra is contrary to the olivine crystals, which show systematic differences between different lithologies and styles of metasomatism, but no significant difference according to the location.

There is some constraint on the variation in water contents with depth in the cratonic mantle (see Demouchy & Bolfan-Casanova 2016; Peslier *et al.* 2010), however again the F concentrations presented here provide the first indication of the behaviour of F with depth in the craton. The water and fluorine concentrations of the olivine, orthopyroxene and clinopyroxene in the Bultfontein and Mothae xenoliths are plotted against pressure in Figures 9.2 and 9.3. The different lithologies and styles of metasomatism defined in Chapter 5 appear to define specific depth horizons in the craton, for example the high-*T* garnet lherzolites have all equilibrated towards the base of the lithosphere (~ 50 kbar, 1250 °C) whereas the orthopyroxene-rich garnet harzburgites that have undergone siliceous fluid metasomatism are from a horizon at ~42 kbar and 1000 °C. The phlogopite lherzolite, dunite and wehrlite xenoliths which exhibit proto-kimberlite metasomatism do not contain garnet and so while the thermobarometry estimates are treated with caution, they do suggest that the xenoliths are sourced from a similar depth in the mid-lithosphere.

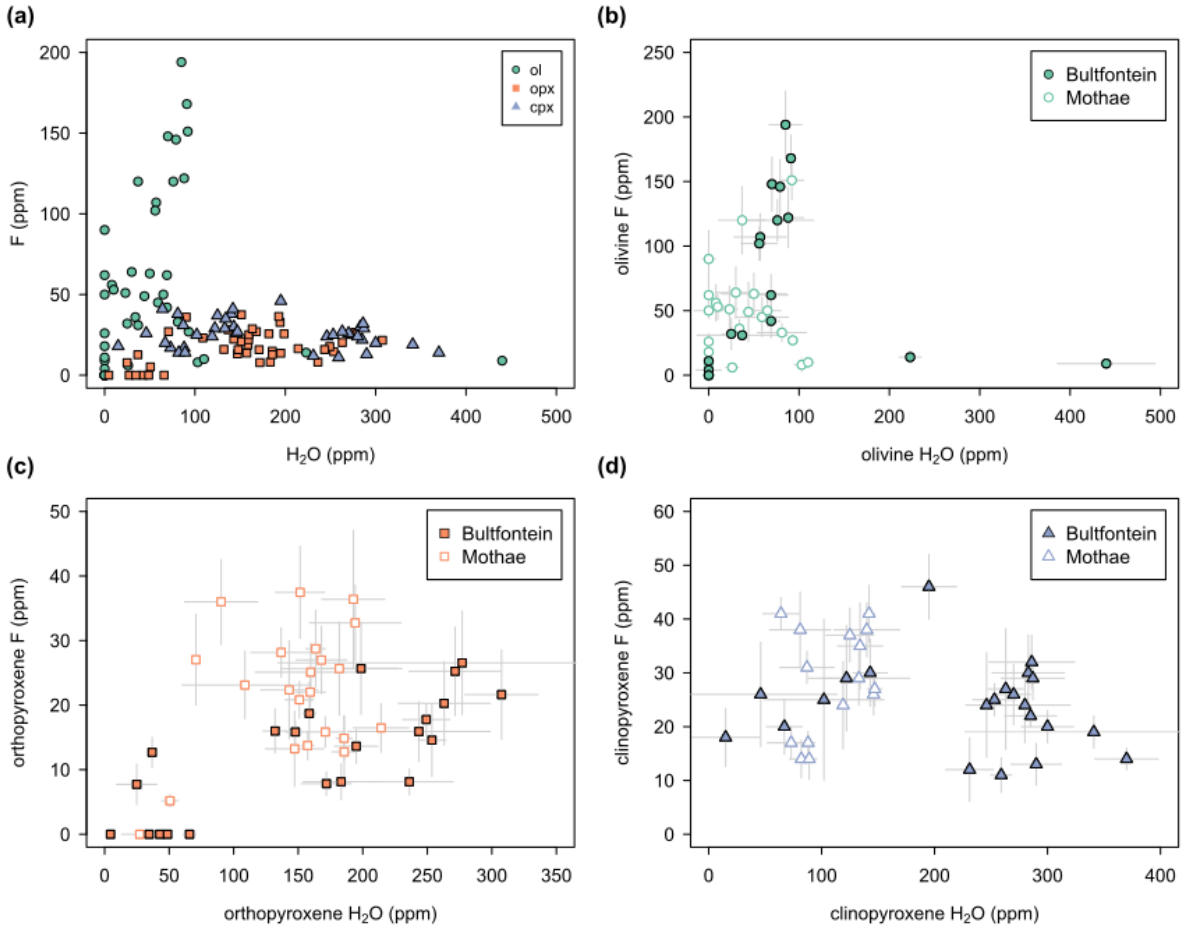

Figure 9.1 ***(a)*** *SIMS H_2O concentration vs F concentration in olivine, orthopyroxene and clinopyroxene in the Bultfontein and Mothae xenoliths.* ***(b)*** *Olivine H_2O concentration vs F concentration, filled symbols represent the xenoliths from Bultfontein and open symbols represent the xenoliths from Mothae.* ***(c)*** *Orthopyroxene H_2O concentration vs F concentration.* ***(d)*** *Clinopyroxene H_2O concentration vs F concentration. Error bars represent twice the sum of the standard deviation and instrument error.*

The water concentrations of all three minerals (olivine, orthopyroxene and clinopyroxene) show no systematic relationship with pressure (Figure 9.2). In Figure 9.2a the H_2O concentrations from the Bultfontein and Mothae xenoliths overlie the Kaapvaal and Siberian cratonic olivine, orthopyroxene and clinopyroxene concentrations compiled by Demouchy & Bolfan-Casanova (2016). Demouchy & Bolfan-Casanova (2016) note an increase in olivine H_2O concentration with depth and proposed that this is related to the increased partitioning of water into olivine at high pressures and temperatures. The water contents in the Bultfontein and Mothae xenoliths, however, show more variation according to the lithology and style of metasomatism than pressure. The deepest olivines, from the high-T garnet lherzolites, range up to the same high H_2O concentrations as those from shallower levels. This contrasts with their co-existing orthopyroxene and clinopyroxene, which have relatively low H_2O. This could reflect a change in H_2O partitioning behaviour between olivine and pyroxenes, as suggested by Demouchy & Bolfan-Casanova (2016). In the high-T garnet lherzolites $D_{H_2O}^{cpx-opx}$ is close to 1 and much lower than the mean off-craton partition coefficient of 2.1 (see Chapter 8). If the partitioning of H_2O into olivine increases with pressure and temperature then, in a closed system, the partitioning of H_2O into clinopyroxene and/or orthopyroxene will be reduced. The relationship observed in the high-T garnet lherzolites suggests that the

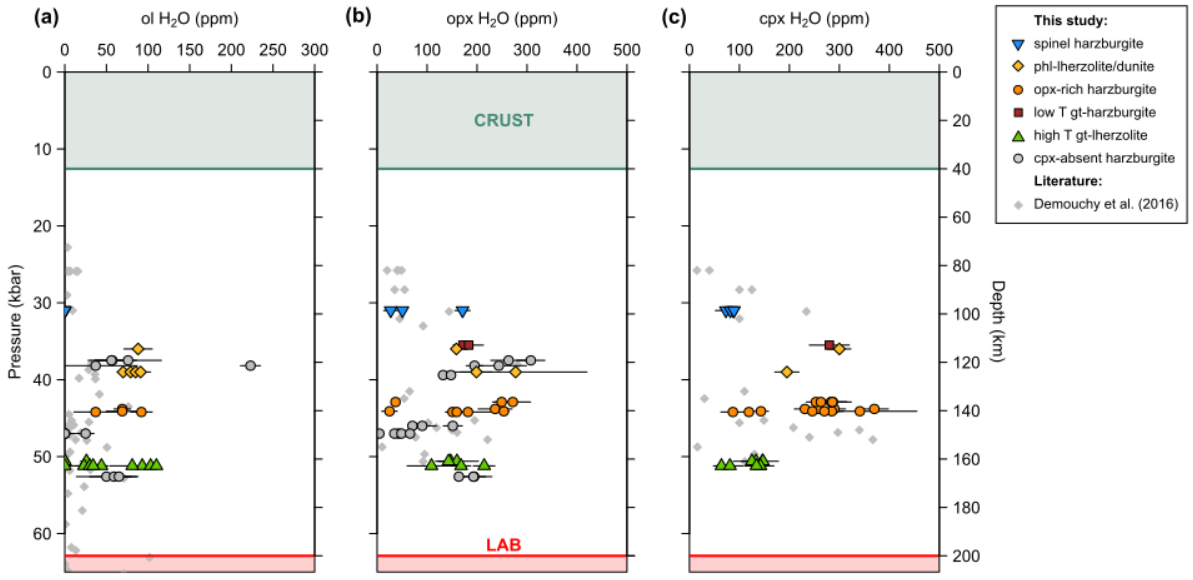

Figure 9.2 *Water concentration in (a) olivine, (b) orthopyroxene, (b) clinopyroxene with pressure in the Bultfontein and Mothae xenoliths. The data are plotted alongside the dataset from Demouchy & Bolfan-Casanova (2016)*

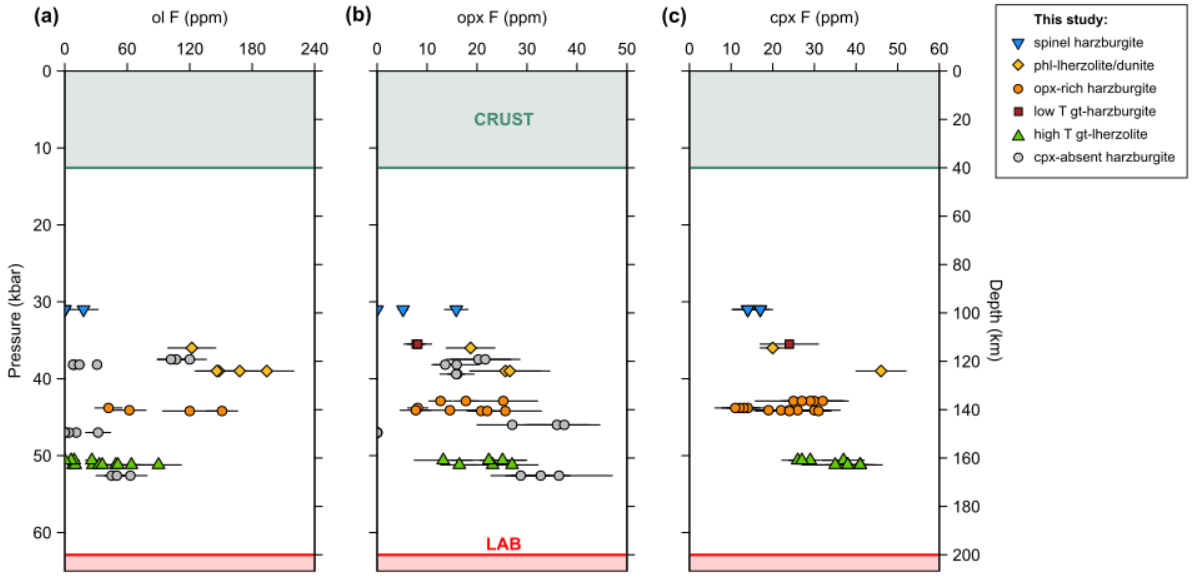

Figure 9.3 *Fluorine concentration in (a) olivine, (b) orthopyroxene, (b) clinopyroxene with pressure in the Bultfontein and Mothae xenoliths.*

partitioning of H_2O into clinopyroxene is reduced, while the orthopyroxene concentrations remain relatively unchanged. This results in the $D_{H_2O}^{cpx-opx}$ approaching a 1:1 ratio at high pressures and temperatures in the sub-cratonic lithosphere. The general lack of increased H_2O concentrations with depth in the Bultfontein and Mothae xenoliths could be a metasomatic overprint, the fluid metasomatism (opx-rich harzburgite) and silico-carbonatite melt metasomatised xenoliths (phlogopite-lherzolite, dunite, wehrlite) mostly show elevated H_2O contents relative to the Demouchy & Bolfan-Casanova (2016) cratonic dataset. Furthermore, all of the xenoliths in this study are from shallower than the depth (> 180 km) where Peslier *et al.* (2010) showed H_2O contents in olivine are reduced to below 10 ppmw and form an anhydrous, viscous barrier at the base of the lithosphere.

Figure 9.3 shows the relationship between fluorine concentration in NVFMMs and pressure. In the clinopyroxene and orthopyroxene there is a general increase in the maximum F concentration with depth. The olivine F contents reach a maximum in the mid-lithosphere, in the metasomatised silico-carbonatite xenoliths, before decreasing at greater depth. There are limited published $D_F^{min-melt}$ values at *PT* conditions appropriate to the cratonic mantle. Dalou *et al.* (2014) identified an increase in $D_F^{cpx-melt}$ and $D_F^{opx-melt}$ with increasing temperature from 1080 °C to 1310 °C, but unfortunately their experiments considered the combined effect of changing temperature and H_2O content so the true temperature control on F partitioning cannot be resolved.

The H_2O-rich and F-poor nature of the peridotite xenoliths at Bultfontein relative to those from Mothae is the only indication of any large scale spatial variation between the craton margin and craton interior. There appears to be a more dominant localised spatial variation according to the style of metasomatism in the SCLM. In all three mineral phases there is a zone of increased H_2O and F concentration and variability between 35 and 45 kbar. This corresponds with a zone of metasomatism (or a metasomatic 'front') observed at a similar level in cratons worldwide, e.g. at 45 kbar in the Slave Craton (Foley and Yaxley, Goldschmidt 2019). The data for the Bultfontein and Mothae peridotite xenoliths suggest that the metasomatic 'front' in the Kaapvaal occurs between 35 and 45 kbar and is also marked by an increase in heterogeneity and concentration of H_2O and F in the NVFMM.

9.3 Metasomatic controls on volatiles in NVFMM

9.3.1 Volatile contents in metasomatic agents

The incompatible nature of volatiles during melting of peridotite implies that small-fraction metasomatic melts ought to be enriched in H_2O, F, Cl and CO_2. This interpretation is supported by the variety of inclusions in diamonds, such as brine fluids with high concentrations of F and Cl while carbonatite melts have high CO_2 contents (e.g. Klein-BenDavid *et al.* 2009; Navon *et al.* 1988; Tomlinson *et al.* 2009; Weiss *et al.* 2011). While the true H_2O and F concentrations of metasomatic agents are very difficult to constrain, the concentration of these elements in similar melts at the surface can provide some insight.

Jago & Gittins (1991) established that carbonatite magmas become concentrated in fluorine very early in their magmatic evolution. As a result, carbonatite magmas contain F-rich phases such as apatite and pyrochlore, and there is also extensive substitution of OH for F in almost all micas and amphiboles in carbonatites (Gittins *et al.*, 1975; Jago & Gittins, 1993). Fluorite deposits associated with carbonatites tend to be much more REE and Sr enriched than crustal-derived fluorites (Bühn *et al.*, 2002), which makes carbonatite melts an important vehicle to transport these elements to Earth's surface. Small-fraction carbonatite melts in the SCLM are likely to also have high F contents, especially if they originate from immisciblity with a silicate melt. Brey *et al.* (2009) established that the partition coefficient of fluorine between immiscible carbonatite and silicate melts may be as high as 6 at temperatures below 1000 °C, reducing to 1-2 at 1250-1300 °C. Consequently, a carbonatite melt is expected to be significantly more enriched in F than a silicate melt in the pressure and temperature range of the Bultfontein and Mothae xenoliths.

It is well-established that kimberlite magmas are neccessarily H_2O and CO_2-rich to propel their ascent to the surface (Sparks *et al.*, 2006). The H_2O- and F-rich nature of kimberlites is also evident in the presence of phlogopite and apatite as crystallising phases. Attempts to quantify the magnitude of this enrichment have used these observations to reconstruct the volatile concentration of the parental kimberlite magma but they have produced a wide range of estimates. Soltys *et al.* (2018) estimate the H_2O and CO_2 concentration of the Bultfontein kimberlite to be 2.1 - 2.2 wt% and 22.9 - 25.4 wt.%, respectively, while Roex *et al.* (2003) estimates the H_2O and CO_2 concentrations of kimberlites in the same Kimberley cluster to be 7 and 8 wt.%, respectively. The latter agrees more closely with estimates of H_2O and CO_2 contents in kimberlites from other cratons (e.g. Lac de Gras kimberlite cluster, Slave Craton: Kjarsgaard *et al.* 2009; Kopylova *et al.* 2007). Kopylova *et al.* (2007) note that while the concentration of H_2O in this range (2-7 wt.%) is soluble in the Si-undersaturated kimberlite magma, the high CO_2 estimates are not soluble in kimberlite magmas. They infer the presence of a separate fluid phase during kimberlite ascent that is required to retain the estimated CO_2 concentrations in parental magma, it is possible that this fluid phase also carries the halogens.

The H_2O and CO_2 contents of the magma, and their ratio, likely play a strong role in halogen incorporation into NVFMMs. For example, the two volatile species have contrasting effects on the stability of olivine relative to pyroxenes and garnet, and also on the polymerisation on the melt. Both of which will influence F partitioning. Guggino (2012) and Urann *et al.* (2017) showed that $D_F^{ol-melt}$ increases with the degree of polymerisation of the melt; and H_2O depolymerises the aluminosilicate network whereas CO_2 does the opposite (Mysen *et al.*, 1982). An H_2O-rich melt expands the stability field of olivine relative to garnet and pyroxene, while the opposite is true for a CO_2-rich melt. Therefore, a CO_2-rich melt assimilates more olivine, which buffers the composition at a low Si content (Foley, 2011). The H_2O/CO_2 ratio of a metasomatic agent is, therefore, likely to have strong controls on the bulk F content of the rock because it controls the incorporation of F into olivine and the modal mineralogy. Brooker *et al.* (2011) suggest that the ratio of H_2O/CO_2 changes dramatically during kimberlite evolution. In their model the parental melt is a transitional silicate-carbonate melt which drives towards a more carbonatitic composition during melt evolution and fractionation of phases during ascent. The result of fractionation is to drive up the CO_2 content of the melt until it saturates and exsolves. If the melt freezes before this point, it is possible that high CO_2 concentrations are reached in the melt that interacts with the mantle wall-rock in the mid-lithosphere. This mechanism could explain the exceptionally high CO_2 contents predicted by Soltys *et al.* (2018).

There have been fewer attempts to reconstruct the halogen concentration of the primary kimberlite magma. A recent study by Abersteiner *et al.* (2018) recorded F concentrations of 2688 ppm in the Roger kimberlite (Ekati cluster, Canada) and identified bultfonteinite, $Ca_4(Si_2O_7)(F,OH)_2$, and fluorite as replacement products of olivine. Their reconstruction estimates that the host kimberlite melt contained 3460-4420 ppm F. The F concentration in some kimberlites from the Kaapvaal craton have only been published in one study (Paul *et al.*, 1976) that measured 750-3490 ppm F in kimberlite dykes from Monastery and Lesotho, and 70-250 ppm F in 'ultrabasic nodules' (here referred to as mantle xenoliths) from Bultfontein, Monastery and Lesotho.

Hydrous siliceous fluids derived by immiscibility with a silicate or carbonate melt (Brey *et al.*, 2009), are CO_2-rich and have been proposed as an effective carrier of the REE, Sr and halogens (Bühn *et al.*,

2002). Alternatively, if the fluids are derived from the melting of subducted-recylced oceanic crust, as proposed by Kelemen *et al.* (1992), then they are also likely to be enriched in F (especially relative to Cl), because very little F is recycled through the mantle wedge (Kendrick *et al.*, 2012; Ryan & Chauvel, 2014; Straub & Layne, 2003b).

9.3.2 Metasomatic indicators and volatiles

A number of petrographic and chemical observations have been used to establish the composition of the metasomatic agent, i.e. the style of metasomatism, associated with the trace-element signatures in the Bultfontein and Mothae xenoliths (Chapter 5). The high modal abundance of orthopyroxene, moderate Zr, low Y and a sinusoidal chondrite-normalised REE pattern in garnet are indicators of siliceous fluid metasomatism. Kimberlite (silico-carbonatite melt) metasomatism is identified from the trace-element composition of the clinopyroxene, low Ni contents in olivine and the presence of phlogopite, while carbonatite metasomatism is identified by the enriched clinopyroxene incompatible trace-element composition and the composition of the melt in equilibrium with the clinopyroxene. These metasomatic indicators can be compared to the volatile concentrations in the NVFMMs to establish if H_2O or F concentrations are affected by melt-rock reactions involving different metasomatic agents.

Marshall *et al.* (2018) showed that one should not expect to find any correlations between water concentration in NVFMM and metasomatic indicators due to the fast diffusion, and hence re-equilibration of H_2O. However it was noted, in Chapter 8, that although: (i) the diffusion of H is extremely fast; and (ii) subsolidus re-equilibration in a local mineral assemblage takes place effectively instantaneously for H incorporated in metal vacancies, a coupling between H, Ti and F can preserve the original H_2O concentration associated with [Ti] point defects. The low Ti concentration associated with the fluid metasomatised orthopyroxene-rich garnet harzburgites is reflected in the low H_2O concentration in olivine. The F concentration is also proposed to preserve the metasomatic signature due to the Ti-H-F coupling, and the inferred slow diffusion rates of F (Section 8.5, Chapter 7). Evidence for this is the correlation between F concentration and metasomatic indicators established during melt-rock reaction. Two interesting relationships that demonstrate this are shown in Figure 9.4, between F concentration, Ti/Eu ratio and the Sr concentration in clinopyroxene. Low Ti/Eu in clinopyroxene is an established indicator of carbonatite metasomatism (Rudnick *et al.*, 1993), where the Ti/Eu decreases with an increasing carbonatite component in the melt. Therefore a silicate-carbonate melt can also produce low Ti/Eu ratios. In clinopyroxene in the Bultfontein and Mothae xenoliths there is a positive correlation between Ti/Eu and F (Figure 9.4), thus suggesting that the extent of carbonatite metasomatism, or the fraction of the carbonate component in the metasomatic agent, correlates negatively with the F content in mantle clinopyroxene. Given the previous suggestion that carbonatite and silico-carbonatite (proto-kimberlite) melts are F-rich, this trend is unexpected and presents the proposition that melt-rock reaction can leech volatiles from NVFMM.

The relationship between Sr and F in clinopyroxene presents an additional complexity (Figure 9.4b). There is a general negative correlation between F and Sr across the whole dataset, however, if the garnet lherzolites are isolated they exhibit a strong positive correlation (r^2 = 0.9; opposing the general negative trend) between F and Sr. If Sr is introduced during metasomatism, then the general negative trend indicates a similar conclusion to the positive correlation between Ti/Eu and F. The opposing trend within a metasomatic subset of the xenoliths could highlight competing controls on each element that are controlled

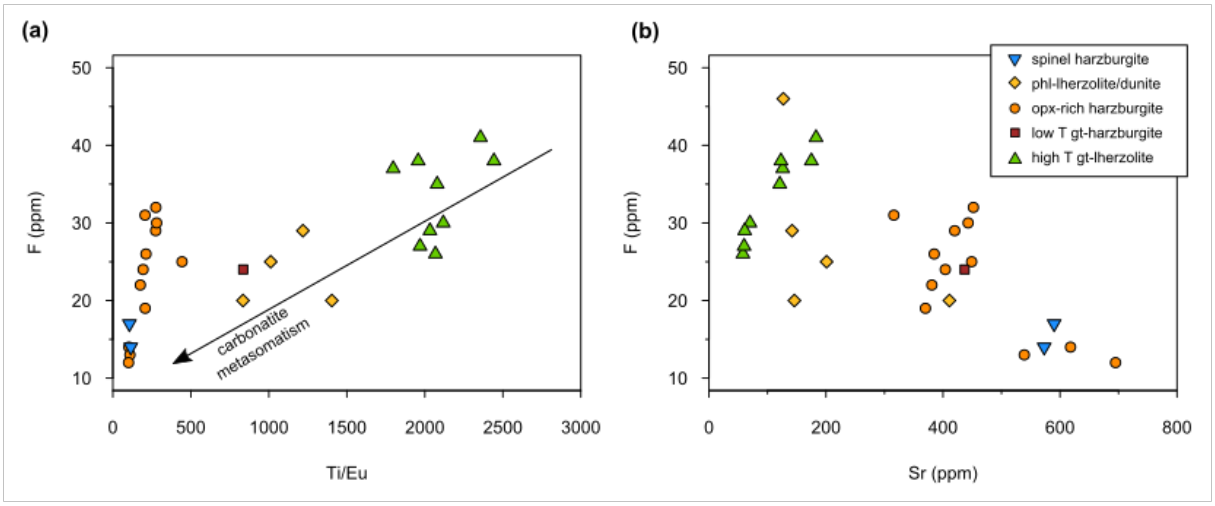

Figure 9.4 *Clinopyroxene F concentration against metasomatic indicators (a) Ti/Eu; (b) Sr.*

by the composition of the metasomatic agent; for example the positive correlation between F and Sr in high-T garnet lherzolites could indicate a similar partitioning behaviour or a shared incorporation mechanism, while the general negative trend reflects an influx of Sr during metasomatism combined with leeching of F.

Another important correlation exists between concentrations of Ti and F in the clinopyroxene from the Bultfontein and Mothae xenoliths. Within each metasomatic group there is a positive correlation between Ti and F (Figure 9.5a), i.e. a constant Ti/F ratio within the group. This is interesting because the clinopyroxenes are likely to be the product of metasomatism, especially in the wehrlite and phlogopite-lherzolite, and if Ti and F partition similarly (Chapter 8) then the Ti/F ratio should reflect that of the metasomatic agent. This interpretation is supported by the composition of the metasomatic agents. Clinopyroxene associated with a hydrous siliceous fluid (orthopyroxene-rich harzburgite) has the lowest Ti/F ratio which can be explained by the fluid immobile nature of Ti relative to F, whereas the clinopyroxene from proto-kimberlite melt metasomatised peridotite has a higher Ti/F ratio because Ti is more soluble in kimberlite melts. The Ti/F ratio varies between the groups, and this variation correlates with relative enrichment of the MREE (Figure 9.5b and c). Spinel harzburgite BD2135 has the lowest F concentration and is an anomaly to the general trend. In Chapter 5, it was established that BD2135 has experienced interaction with a very small fraction metasomatic melt and as a result it is exceptionally enriched in the REE relative to all of the other Bultfontein and Mothae xenoliths. There is a good correlation between the Ti/F and the MREE (Dy, Ho, Er) when BD2135 is excluded. It is possible that the relationship is underpinned by the size of the ions. Figure 9.5d shows the value of the correlation coefficient (r^2) between Ti/F and the REE from Lu to Gd against the ionic radius of the element (Shannon, 1976). There is a polynomial relationship between the strength of the correlation and the ionic radius, the best correlation (r^2 = 0.86) exists where the ionic radius is between 0.89 - 0.91 Å. Ionic radius is a key control in the mineral-melt partitioning behaviour of an element (Blundy & Wood, 1994, 2003; Goldschmidt, 1937), the relationship between Ti/F and the MREE could therefore reflect similar partitioning behaviour between these elements. A similar relationship is observed in off-craton peridotites (Gibson *et al.*, 2020).

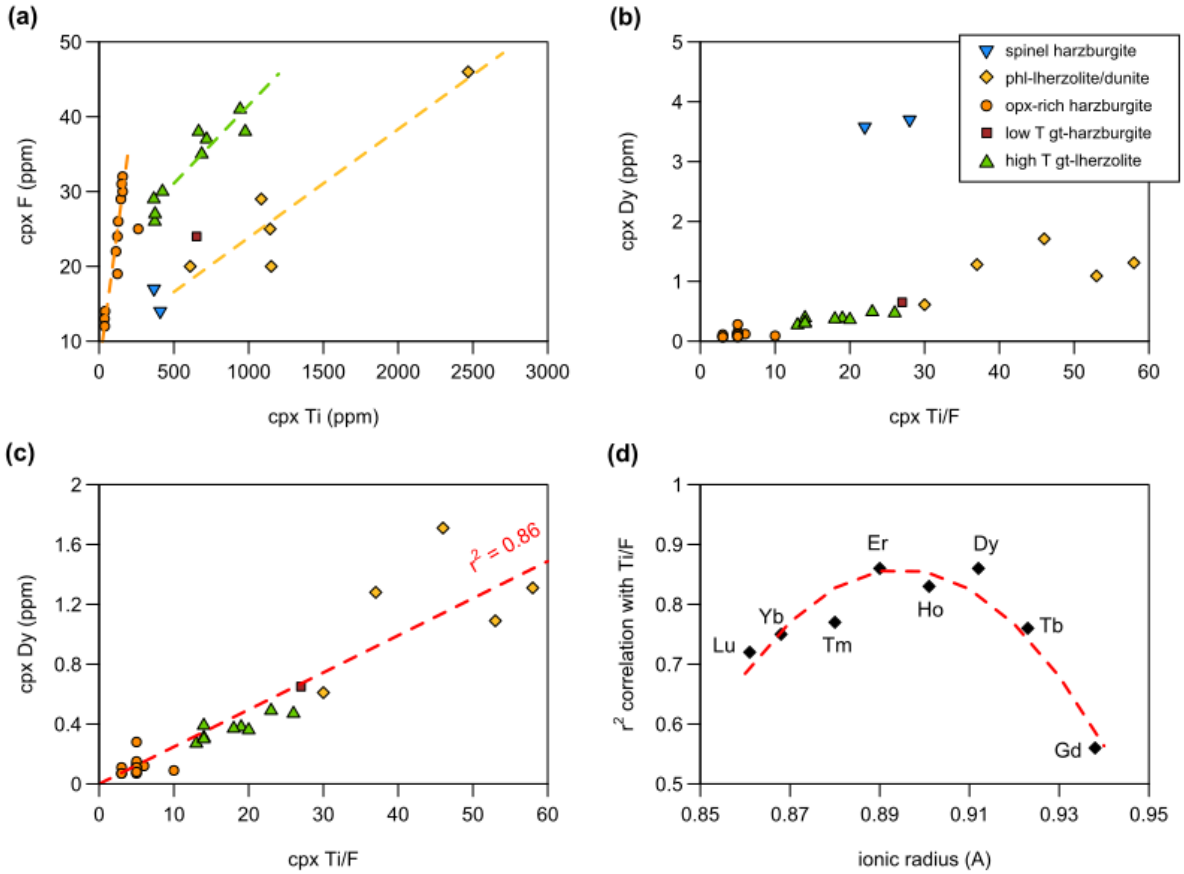

Figure 9.5 ***(a)*** *Ti vs. F concentration in clinopyroxene from Bultfontein and Mothae xenoliths, showing individual correlations within Groups B, C and E.* ***(b)*** *Clinopyroxene Ti/F ratio vs. Dy.* ***(c)*** *Linear relationship between Ti/F and Dy, excluding the Group A anomaly.* ***(d)*** *The correlation between Ti/F and various REE, plotted against the ionic radius of the REE in question. The ionic radii represent the VI-fold coordination of the trivalent cation from Shannon (1976).*

9.3.3 Volatile behaviour during melt-rock reaction by different metasomatic agents

In this section, the controls on volatile storage during melt-rock reaction are investigated with respect to the different styles of metasomatism that define the subdivisions of the Bultfontein and Mothae xenoliths.

1. Re-fertilisation of the depleted mantle residue ***(High-T garnet lherzolite and Low-T garnet harzburgite)***

Phase	F range (ppm)
Clinopyroxene	28-38
Orthopyroxene	15-27
Olivine	0-90
,	

Table 9.1 *F concentration in high-T garnet lherzolite*

The high-*T* garnet lherzolite and low-*T* garnet harzburgite xenoliths represent re-fertilised Kaapvaal mantle. The olivine and orthopyroxene compositions match the mantle residue following around 25% partial melting, while the composition of clinopyroxene and garnet indicate that these are secondary phases

that have been added during re-fertilisation of the base of the lithosphere by small-fraction asthenospheric melts (Chapter 5). In Chapter 8 it was established that subsolidus re-equilibration at the base of the lithosphere occurs quickly, and is complete in the high-*T* garnet lherzolites.

Following partial melting the mantle residue is depleted in H_2O and F. Experiments have shown that F partition coefficients are 2-3 times higher than those for H_2O (Beyer *et al.*, 2012; Hauri *et al.*, 2006), this means that the residue is more depleted in H_2O than F. The F composition of the mantle residue is difficult to estimate because the range of experimentally determined D_F for mantle minerals varies so widely: $D_F^{ol-melt}$: 0.0025 - 0.16 (Beyer *et al.*, 2012; Dalou *et al.*, 2012; Guggino, 2012; Hauri *et al.*, 2006; Joachim *et al.*, 2015); $D_F^{opx-melt}$: 0.02 - 0.25 (Beyer *et al.*, 2012; Dalou *et al.*, 2012, 2014; Hauri *et al.*, 2006; Joachim *et al.*, 2015; Rosenthal *et al.*, 2015); $D_F^{cpx-melt}$: 0.04 - 0.15 (Dalou *et al.*, 2012, 2014; Guggino, 2012; Hauri *et al.*, 2006; Rosenthal *et al.*, 2015). Dalou *et al.* (2014) find a strong dependence of temperature and water content on the partition coefficient, with $D_F^{opx-melt}$ and $D_F^{cpx-melt}$ increasing with increasing temperature and decreasing water content. At high water concentrations the partitioning of F is reduced which supports the theory of this work that F and H are competing for space in the crystal lattice of mantle minerals (Chapter 8). Additionally, as mentioned, Guggino (2012) and Urann *et al.* (2017) have shown that the polymerisation of the melt is an important control on the partitioning of F between olivine and melt. This relationship is exhibited by a negative correlation between the ratio of non-bridging oxygen atoms to tetrahedrally coordinated cations (NBO/T) in the melt and $D_F^{ol-melt}$, where NBO/T decreases with increasing degree of polymerization in the silicate melt (Mysen, 2007; Mysen & Cody, 2004). The dependence of $D_F^{ol-melt}$ on melt polymerisation means that the partitioning behaviour of F will differ during partial melting and later melt metasomatism. If the melt becomes more polymerised during increased melt-rock reaction and fractionation the $D_F^{ol-melt}$ will increase and more F is incorporated into the olivine structure. As the high-*T* garnet lherzolites are from near the base of the lithosphere, the melt is unlikely to have fractionated many phases and so may still be H_2O-rich and depolymerised.

Clinopyroxene in the high-*T* garnet lherzolites have high F concentrations but the orthopyroxene and olivine F contents are towards the lower end of the respective range for each mineral in the Bultfontein and Mothae xenoliths. Consequently, the bulk F concentration is relatively low and close to the estimates of bulk anhydrous peridotite (Urann *et al.*, 2017). The inference is that the mantle residue was depleted in F and then later interaction with small-fraction melts has re-enriched the bulk assemblage in F by crystallising high F clinopyroxene. BD2128 contains olivine with higher F concentrations than the other high-*T* garnet lherzolites, which could reflect a difference in the polymerisation of the metasomatic melt such that $D_F^{ol-melt}$ was higher, or metasomatism occurred more recently and F concentrations have not fully equilibrated in the local mineral assemblage.

The low-*T* garnet harzburgite BD1140, also exhibits secondary addition of clinopyroxene by melt metasomatism but in this case the lower temperature (859 °C) has slowed subsolidus re-equilibration. The H_2O and F concentrations of clinopyroxene and orthopyroxene in BD1140 are towards the lower end of the range in the high-*T* garnet lherzolites. If the mineral-melt partition coefficients of H_2O and F decrease with decreasing temperature (e.g. Dalou *et al.* 2014), then this can explain why the NVFMM in low-*T* garnet harzburgite are less enriched in volatile elements following re-fertilisation.

2. Cryptic carbonatite metasomatism *(Spinel harzburgite)*

Phase	F range (ppm)
Clinopyroxene	14-17
Orthopyroxene	< 5
Olivine	< 18

Table 9.2 *F concentration in NVFMMs from spinel harzburgite BD2135*

Cryptic metasomatism by a melt with a high carbonatitic component, in the shallow lithosphere, has produced the REE-enriched clinopyroxene in BD2135 (Chapter 5). Contrary to this enrichment in the incompatible REE, the clinopyroxene, orthopyroxene and olivine all have very low F concentrations and as a result the bulk rock F content is extremely low (<11 ppmw which is below the estimate for DMM or primitive mantle; Figure 7.7). The clinopyroxene in BD2135 was shown to have the same composition as the diopside in the MARID suite metasomatised xenoliths (Figure 5.8), and hence it is proposed that both originated from a carbonatite melt. The difference between BD2135 and MARID xenoliths is the metasomatic melt:rock ratio. The MARID suite represents a melt vein, where there was a large volume of melt relative to the wall-rock and the five phases (Mica, Amphibole, Rutile, Ilmenite and Diopside) crystallise into a vein assemblage. In contrast, BD2135 represents low volume melt-rock reaction in which a small amount of diopside precipitated along grain boundaries by reaction of the melt with orthopyroxene and in interstitial spaces. The major- and trace-element relationships indicate that this clinopyroxene has not re-equilibrated with the co-existing olivine and orthopyroxene (Chapter 3). This is not unexpected given the fact that timescales for diffusive re-equilibration between clinopyroxene and olivine in BD2135, at 800 °C, were estimated to be 550 Ma for Ti (and hence the REE; Chapter 8).

Section 9.3.1 identified that carbonatite melts should have high F concentrations and that the MARID suite vein assemblage contains F- and OH-rich amphibole and phlogopite. Therefore, the low F concentrations in the cryptically metasomatised mantle wall-rock suggests that there is a spatial and volumetric control on the behaviour of volatiles during carbonatite metasomatism, primarily related to proximity to the melt vein. Mica and amphibole are both very efficient at removing F from a melt (Foley *et al.*, 1986; Munoz & Eugster, 1969), so if these two phases have already started fractionating from the melt then the residue can become depleted in F very quickly. As a result a more evolved melt reacting with the mantle wall-rock is depleted in F to the extent that the concentration gradient required for F incorporation into the NVFMM is not established.

Additionally, the high CO_2 content of a carbonatite melt probably influences partitioning of F between clinopyroxene and the melt. Keshav *et al.* (2005) showed that the presence of CO_2 in the melt decreases the partition coefficients of the REE in clinopyroxene, i.e. making the REE more incompatible. In Section 9.3.2, the partitioning behaviour of F (and Ti) was presumed similar to the MREE, therefore if the REE partitioning decreases with melt CO_2 content, it could also be the case for F. A carbonatitic melt has a higher CO_2 content than silico-carbonatite or silicate melts and therefore it is possible that F is more incompatible during carbonatite metasomatism than silicate metasomatism.

Overall a carbonatite melt has a contrasting effect on the F concentration of the peridotite depending on the melt volume. If the melt volume is high, such that phlogopite and amphibole can fractionate, then F will partition into these minerals and the local mantle will be enriched in F. Where the melt volume is small the melt does not add F to nominally volatile-free minerals.

3. Proto-kimberlite (silico-carbonatite) melt metasomatism *(Phlogopite lherzolite, dunite, wehrlite)*

Phase	F range (ppm)
Clinopyroxene	15-46
Orthopyroxene	19-31
Olivine	122-194

Table 9.3 *The range in F concentration in the three xenoliths metasomatised by a proto-kimberlite melt.*

The fluorine concentration of the olivine, orthopyroxene and clinopyroxene in the xenoliths that have been metasomatised by a proto-kimberlite melt is highly variable. The additional presence of metasomatic phlogopite in the mineral assemblage of BD1141A and BD3067 increases the bulk F concentration further. Interestingly, of all nineteen Bultfontein and Mothae peridotite xenoliths the highest F concentrations in olivine and clinopyroxene are found in BD1153 (dunite) which has been cryptically metasomatised by a proto-kimberlite melt. The concurrent lack of phlogopite and high concentrations of F in NVFMMs in BD1153, compared the phlogopite-bearing xenoliths, highlights the influence of the local mineral assemblage on the distribution of F. Where phlogopite is present in the mineral assemblage, less F is incorporated into co-existing clinopyroxene and pre-existing mantle phases. There also appears to be a similar control by the crystallisation of phlogopite and amphibole during carbonatite metasomatism, but in this case the cryptic metasomatism produced a higher F concentration in NVFMM. This fundamental difference can be explained by considering the evolution of a proto-kimberlite melt as it ascends through the cratonic lithosphere (Figure 9.6). At early stages of melt evolution, the kimberlite melt is enriched in incompatible elements, including F. The interaction of the kimberlite melt with the mantle wall-rock results in a diffusive flux of F into the surrounding mantle peridotite driven by high concentration gradients. During ascent, the kimberlite melt evolves and more minerals appear on the liquidus, for example the familiar Phlogopite-Ilmenite-Clinopyroxene (PIC) metasomatic suite. As these minerals stabilise and start to precipitate in veins (such as that seen in BD3067, Figure 2.3), F is preferentially incorporated into phlogopite and Ti into ilmenite, as can be seen in the Bultfontein metasomatised dunite, lherzolite and wehrlite xenoliths. With increasing proportion of metasomatic phases (PIC) in the xenoliths, from BD1153 to BD1141A to BD3067, there is a decrease in F and Ti concentration in the NVFMMs, reflecting the sequestration of these elements by phlogopite and ilmenite. Additionally, if the kimberlite melt evolves towards a carbonatitic melt (e.g. Brooker *et al.* 2011) then the partitioning behaviour will also change and potentially F will become more incompatible (see above).

Proto-kimberlite (silico-carbonatite) melts have the capacity to increase the F concentration of NVFMM during early stages of their melt evolutions, but at later stages (i.e. at shallower depths and lower temperatures) the melt has less influence on the F concentration of NVFMM because F-bearing phases such as phlogopite and apatite fractionate F. Considering the suggestion that pervasive metasomatism is a pre-requisite for diamond-bearing kimberlites to ascend through the lithosphere (e.g. Drury & Roermund 1988; Giuliani *et al.* 2014a, 2016; Jackson & Gibson 2018), there is likely significant F-enrichment of the cratonic mantle by 'failed' kimberlite melts. F-enrichment is manifest in the pre-existing mantle phases during early stages of melt evolution and in metasomatic phases later on. Figure 9.6 presents a schematic illustration to show the changing F concentration in the mantle wall-rock and the metasomatic vein

assemblage as a kimberlite and carbonatite melt evolve during ascent through the sub-cratonic lithospheric mantle.

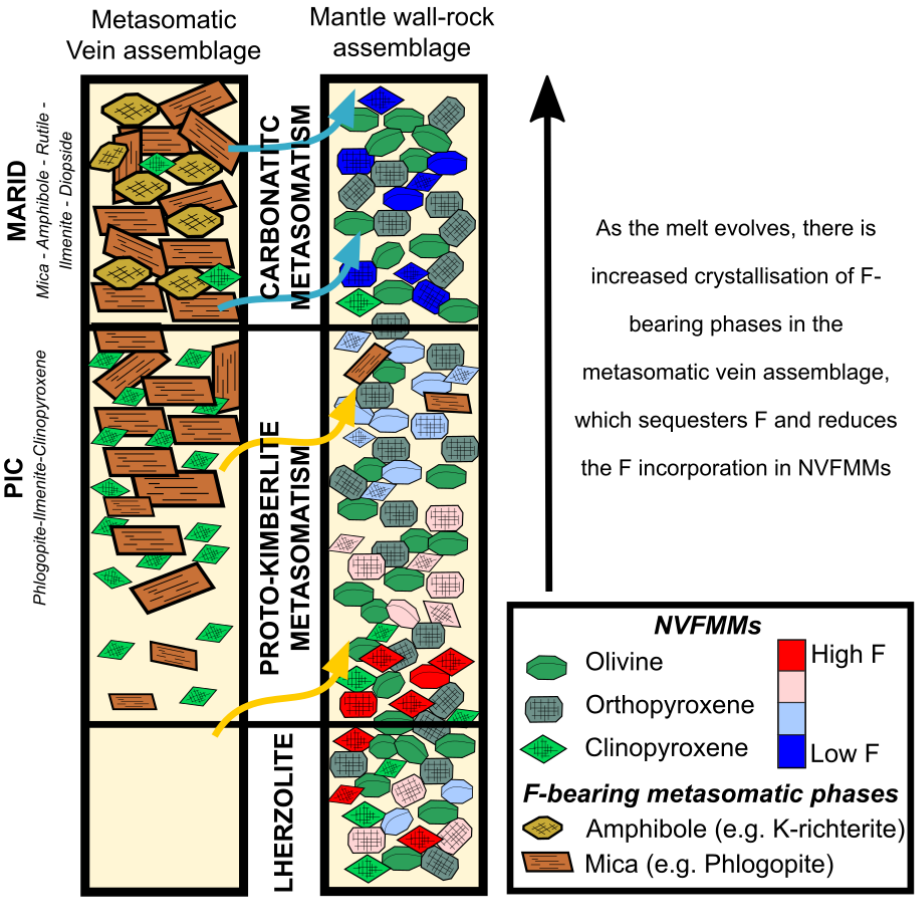

Figure 9.6 *Schematic illustration of the qualitative change in fluorine concentration in the mantle wall rock NVFMM, as F-bearing metasomatic assemblages crystallise in proximity. The PIC metasomatic assemblage is produced by proto-kimberlite melt metasomatism and the MARID metasomatic assemblage is produced by carbonatitic metasomatism, BD2135 represents the mantle wall-rock with minor infiltration of a carbonatitic melt.*

4. Siliceous fluid metasomatism *(Orthopyroxene-rich harzburgite)*

Phase	F range (ppm)
Clinopyroxene	12-31
Orthopyroxene	5-21
Olivine	91-120

Table 9.4 *The range in F concentration in the orthopyroxene-rich garnet harzburgites metasomatised by a hydrous siliceous fluid.*

In Chapter 5 it was established that the interaction of a metasomatic fluid and the depleted mantle residue likely produced the orthopyroxene-rich garnet harzburgites. Fluid mobility and melt solubility differ for most elements, including the halogens. Studies focused on slab-derived fluids in the mantle wedge at arc settings have established that F is less fluid mobile than Cl. As a consequence most Cl is recycled through the mantle wedge and most F is retained in the down-going slab and recycled through the

asthenosphere (Kendrick *et al.*, 2012; Ryan & Chauvel, 2014; Straub & Layne, 2003b). Although F may be less fluid mobile than Cl, it is more fluid mobile than Ti and the HREE, which are known to be very fluid immobile (e.g. Dorendorf *et al.* 2000; John *et al.* 2004). This can be observed in the relationships presented in Section 9.3.2. It was suggested that Ti and F partition similarly, therefore the Ti/F ratio in the clinopyroxene reflects the Ti/F ratio in the metasomatic agent. The orthopyroxene-rich harzburgites have the lowest Ti/F ratio, dominated by the low Ti concentrations and moderate F concentrations because the metasomatic agent was a fluid.

Two hypotheses were presented in Chapter 5 that could account for the fluid metasomatic signature in the orthopyroxene-rich xenoliths. Firstly, that a fluid alone was responsible and secondly, that a melt with an immiscible fluid phase metasomatised the mantle harzburgite. Both scenarios start with a mantle residue produced by partial melting of primitive mantle, followed by fluid metasomatism that re-enriched the harzburgite and produced excess orthopyroxene at the expense of olivine. The initial harzburgite residue will be depleted in volatile elements and composed primarily of high Mg# olivine and orthopyroxene. Partial melting will reduce the F concentration in the mantle residue and this is exemplified by Bultfontein harzburgite BD3670 in which F is below the detection limit. The same low concentrations are also observed in the olivine and orthopyroxene in BD2135 (spinel harzburgite), which represents a depleted harzburgite that has been cryptically metasomatised by a carbonatite melt. In the orthopyroxene-rich garnet harzburgites the subsequent re-enrichment by a fluid increased the modal abundance of orthopyroxene (beyond the realms capable of partial melting; Kelemen *et al.* 1992) and introduced F to the system by increased incorporation into olivine, orthopyroxene and clinopyroxene. This can be observed in the positive correlation between the modal abundance of orthopyroxene and the F concentration in olivine, orthopyroxene and clinopyroxene (Figure 9.7a). The modal abundance of orthopyroxene is chosen as a proxy for hydrous siliceous fluid metasomatism and the relationship with F concentration implies that fluid metasomatism enriches the NVFMMs in the lithospheric mantle in F. Phlogopite is also a minor product of the olivine-fluid reaction (Equation 5.9) and is present as a minor phase in the two xenoliths with the highest modal abundance of orthopyroxene, hence supporting the theory that the fluids are F-rich.

The positive correlation between orthopyroxene modal abundance and F concentration in olivine, orthopyroxene and clinopyroxene implies that with increased fraction of fluid, more F is deposited into the mantle wall-rock. The increase in F is matched by an increase in Ti with the modal abundance of orthopyroxene, which means the coincident behaviour could again reflect the coupling of these two elements. Ti is compatible and fluid immobile so will be preferentially incorporated into precipitating phases. The coupling of Ti and F to balance the excess charge involved in Ti incorporation into octahedral sites, produces the observed simultaneous increase in each element with modal abundance of orthopyroxene. Alternatively, an increased fluid volume will result in an increase in the extent of fluid-rock interaction, and the fluid:rock ratio. The larger volume of fluid percolating along grain boundaries could result in more grain boundary exchange of F with the mantle minerals.

The occurrence of the fluid signature in all samples with an orthopyroxene excess implies that either only a silicic fluid was involved or there was always an immiscible fluid coexisting with the silicate melt. It is suggested that the more plausible option of the two is that the metasomatic agent was a hydrous siliceous fluid rather than a silicate melt and an immiscible fluid phase for the following reasons:

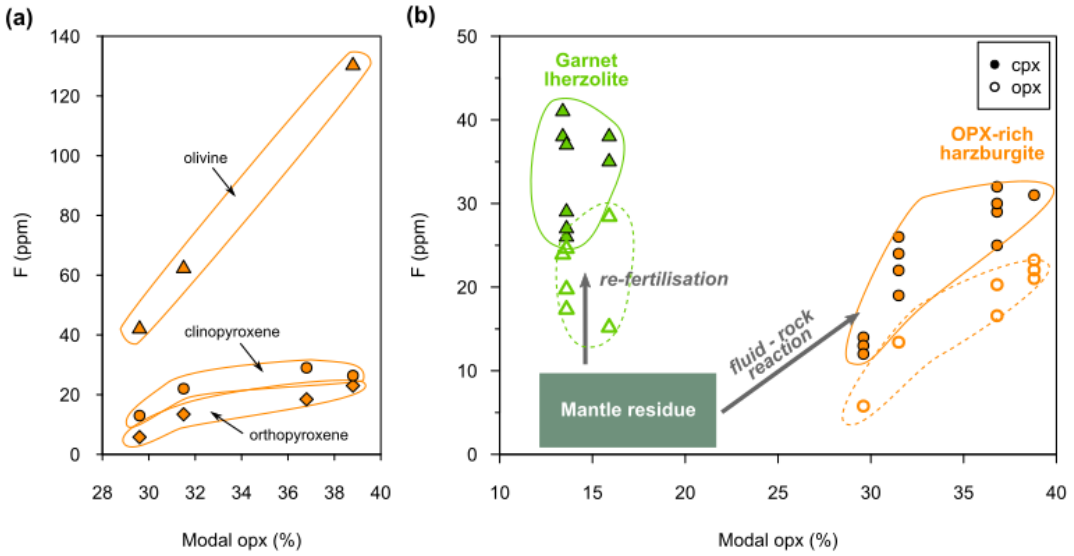

Figure 9.7 *(a) Modal abundance of orthopyroxene (%) vs. olivine, orthopyroxene and clinopyroxene F content in orthopyroxene-rich xenoliths. (b) Group A and C modal orthopyroxene abundance vs. clinopyroxene and orthopyroxene F content. Vectors are marked proposing the effect of partial melting and subsequent fluid metasomatism. The volume of fluid involved controls the magnitude of increase in the orthopyroxene excess and fluorine concentration. The same relationship is observed in olivine F contents.*

- All samples with orthopyroxene excess beyond 25% also have a fluid signature in the garnet and clinopyroxene incompatible trace-element patterns.
- There is a systematic correlation between the orthopyroxene excess and the fluorine concentration in all phases suggesting they are intrinsically linked.
- A significantly large volume of silicate melt is required to produce the volume of immiscible fluid that could increase the fluorine concentrations at such a scale.

The composition of the metasomatic agent has been shown to control the concentration of volatile elements in NVFMMs and also the incorporation mechanism of H and F in olivine and orthopyroxene. In Chapter 7 systematic differences between the FTIR spectra of olivine in the proto-kimberlite metasomatised peridotite, fluid metasomatised peridotite and the low-T garnet harzburgites and high-T garnet lherzolites were observed. The strong coupling between Ti, OH and F was identified in most samples by the dominance of the [Ti] point defect absorbance bands at 3572 and 3525 cm^{-1} and the strong correlation between Ti and F concentrations and the F absorbance bands at 3591 and 3598 cm^{-1}. The olivine from the fluid metasomatised harzburgites, however, exhibits only one of the two absorbance bands for the [Ti] mechanism and completely lacks the proposed Ti-F band at 3598 cm^{-1}. They are also the only olivines that display a clear absorbance band at 3612 cm^{-1}, which represents the hydrogarnet, [Si], mechanism for H incorporation. It is interesting that the orthopyroxene-rich peridotites are the only ones to exhibit the hydrogarnet substitution in olivine because this mechanism is depedent on the silica activity (a_{SiO_2}) of the system. At high a_{SiO_2} (i.e. high modal orthopyroxene) one would expect the [Si] mechanism to be less prominent than at low a_{SiO_2}, but the opposite is true here. Both the [Si] and [Ti] mechanisms involve tetrahedral vacancies, it seems that in the orthopyroxene-rich harzburgites xenoliths, where Ti concentration is low, tetrahedral vacancies are charge balanced by the hydrogarnet mechanism rather than any coupling with Ti in an octahedral site. In the relative absence of Ti-F and Ti-H coupling, both H and F

are incorporated in different ways into the olivine lattice. Although the exact mechanisms have not been identified in this small subset, the abundance of extra F and OH absorbance bands in the FTIR spectra indicates the involvement of different incorporation mechanisms for F in NVFMM.

One orthopyroxene-rich garnet harzburgite from Bultfontein, BD1672, contains a small number of clinopyroxenes with the same signature as the equilibrated high-T garnet lherzolites that have been re-fertilised by a melt rather than a fluid. These clinopyroxenes in BD1672 are likely to represent clinopyroxene produced during a different metasomatic event. The preservation of the two signatures in a single xenolith is evidence of incomplete subsolidus re-equilibration, and suggests that one stage of metasomatism occurred within 27 Ma (calculated in Chapter 8) prior to the entrainment of the xenolith by the Bultfontein kimberlite. Interestingly BD1672 is the only xenolith with excess orthopyroxene that also has a porphyroclastic texture, similar to the high-T garnet lherzolites, and has a lower proportion of orthopyroxene than the coarse orthopyroxene-rich harzburgites. High-T garnet harzburgite BD2170 also preserves the initial process of fluid metasomatism but this time within the garnet REE patterns. BD2170 has a minor proportion of clinopyroxene that contains the same metasomatic signature as that in the high-T garnet lherzolites, however there are two generations of garnet (Figure 3.12c). The first has a REE signature that is typical of the equilibrated lherzolites (low LREE, high HREE) and the second generation has a sinusoidal signature typical of the fluid metasomatism in the orthopyroxene-rich garnet harzburgites. The two xenoliths BD1672 and BD2170 therefore appear to represent a transition between garnet lherzolite and large scale fluid metasomatism.

9.4 The influence of metasomatism and oxygen fugacity

In addition to the controls on volatile composition in NVFMMs in the cratonic mantle imparted by the composition of the metasomatic agent, there are a few signs that the oxygen fugacity also influences the volatile concentrations in NVFMMs. In Chapter 8, trivalent cations were highlighted as an important mechanism by which hydrogen, and potentially fluorine, can be incorporated into olivine and orthopyroxene. This presents an intrinsic link to the oxidation state of the mantle or metasomatic agent. Both the reduction of Fe^{3+} or oxidation of Fe^{2+}, for example, can involve the incorporation of H_2 into the crystal lattice. The reduction of Fe^{3+} by the incorporation of H_2 is recognised by Peslier *et al.* (2002) and Demouchy & Bolfan-Casanova (2016) in the reaction:

$$Fe^{3+} + O^{2-} + \frac{1}{2}H_2 = Fe^{2+} + OH^- \tag{9.1}$$

This reaction is termed the proton-polaron effect. Polarons are localised electrons in the crystal structure that can transfer between adjacent Fe^{3+} and Fe^{2+}, and in the proton-polaron effect interstitial H (protons) counterbalance these polarons. In this mechanism, there is an negative correlation between the Fe^{3+}/Fe^{2+} ratio and the measured H_2O content of the mineral in question, i.e. water contents are higher in reducing conditions as opposed to oxidising conditions. This trend is observed by Peslier *et al.* (2002) in spinel-peridotite xenoliths from Mexico and North-West USA. By contrast, a positive correlation between orthopyroxene H_2O content and Fe^{3+}/Fe^{2+} ratio is observed by Tollan & Hermann (2019) in abyssal

peridotite recovered from the West Bismarck Island Arc. Tollan & Hermann (2019) suggest difference reflects the incorporation of H_2 or H_2O in a reducing or oxidising environment, respectively. They suggest that during metasomatism in the mantle wedge by oxidising melts or fluids, H_2O is incorporation involves the oxidation of Fe^{2+} to Fe^{3+} and an OH-group forming in a neighbouring octahedral vacancy. The greater proportion of H incorporated as H_2O by this oxidation mechanism simultaneously increases the Fe^{3+}/Fe^{2+} ratio and the H_2O content in the orthopyroxene. Tollan & Hermann (2019) suggest that both mechanisms are at play during slab-fluid percolation through the mantle wedge. The initial fluid is reducing such that H_2O dissociation in the melt drives the incorporation of H_2 into the mantle wall rock. As the melt evolves it becomes more oxidising, as a result of the H_2O dissociation, so at shallower levels H_2O can be incorporated into the mantle wall-rock (in addition to H_2). Therefore, the incorporation of H_2 at early stages (greater depths) maintains the reduced nature of the ambient mantle but at shallower depths, where the melt has evolved to a more oxidising state, metasomatism has the effect of oxidising the ambient mantle.

The cratonic mantle has been shown to exhibit a fO_2-depth trend, where the mantle becomes more reduced with increasing depth (Miller *et al.*, 2016; Stagno *et al.*, 2013). The Kaapvaal craton follows this trend in all locations with the exception of Kimberley (Creighton *et al.*, 2008; Woodland & Koch, 2003). The expected fO_2 trend is observed beneath northern Lesotho but at Kimberley fO_2 is extremely heterogeneous and increased to more oxidised conditions by up to 2 log bar units. This increase is attributed to oxidation by extensive metasomatism (Creighton *et al.*, 2008; Hanger *et al.*, 2015; McCammon *et al.*, 2001). MARID suite metasomatism (by carbonatitic melts) has been shown to increase the oxidation state of the mantle the most (Creighton *et al.*, 2008; Zhao *et al.*, 1999), but PIC metasomatism (proto-kimberlite melts) and fluids can also have an oxidising effect (Creighton *et al.*, 2008; Goncharov & Ionov, 2012).

Not all metasomatic agents, however, have an oxidising effect. Creighton *et al.* (2010) highlight the contrasting nature of metasomatic agents depending on their source. They identify metasomatism by oxidising fluids throughout the lithosphere in the Slave craton but also metasomatism by a reduced melt in the lower lithosphere. Goncharov & Ionov (2012) suggest that CH_4^--bearing asthenospheric melts reduce the base of the lithosphere but during ascent they evolve to more oxidised melts, for example through the chromatographic effects of percolation (Ionov *et al.*, 2002; Navon & Stolper, 1987). Therefore the oxidation state of the cratonic mantle can be locally perturbed by metasomatic agents in different ways, and again varying depending on the evolution of the melt. It is entirely plausible that some of the trends observed in the volatile concentrations of NVFMMs in the Bultfontein and Mothae xenoliths are related to oxygen fugacity.

The difference in oxidation state of the lithospheric mantle below Kimberley and northern Lesotho is proposed to be the underlying cause of the differing orthopyroxene FTIR spectra between the Bultfontein xenoliths and the Mothae xenoliths. The primary difference between the two spectra are observed in the height of the two absorbance bands at 3600 and 3545 cm^{-1} (Figure 7.13). Tollan & Hermann (2019) recognised a positive correlation between the absorbance band at 3545 cm^{-1} (amongst others) and the $Fe^{3+}/\sum Fe$, that they attributed to the, aforementioned, increased incorporation of H_2O in more oxidising conditions. The 3545 cm^{-1} band in the Bultfontein orthopyroxene is much large than in the Mothae orthopyroxene. The 3600 cm^{-1} band is proposed to represent the hydrogarnet mechanism in orthopyroxene, therefore, the smaller 3600 cm^{-1} absorbance band could reflect the lack of OH groups in the Si vacancy.

The H_2O concentrations in the Mothae xenoliths are generally lower than at Bultfontein (Figure 9.1) but the F concentrations are higher. No extra absorbance bands are observed that could be attributed to F incorporation, however this could be due to the higher H_2O concentrations in orthopyroxene relative to F. Crépisson *et al.* (2014) recognise that F absorbance bands may only be discernible in natural olivine when the H_2O concentration is less than 220 ppm, hence the higher H_2O concentrations in orthopyroxene and significantly lower F concentrations relative to olivine may mean that F absorbance bands are not detectable in orthopyroxene FTIR spectra.

The preferential incorporation of F at Mothae could be due to the more reduced nature of the mantle from which the xenoliths are sourced. This could be a coincidence because the xenoliths are from near the base of the lithosphere (high-T garnet lherzolites), where Creighton *et al.* (2010) and Goncharov & Ionov (2012) propose reducing melts metasomatise the lithosphere. One Mothae fluid metasomatised harzburgite (BD2125) also contains the lowest H_2O concentrations of the group. It has been proposed that F is incorporated into NVFMMs in oxygen sites due to the similar ionic radii of F, O and OH (Beyer *et al.*, 2012; Crépisson *et al.*, 2014; Urann *et al.*, 2017), and therefore it is possible that in reducing conditions the incorporation of F is preferred over the formation of OH groups.

The third observation that can be linked to oxygen fugacity is the variation in volatile concentrations in the NVFMMs that have interacted with a kimberlite melt. The oxygen fugacity of kimberlite melts is poorly constrained, Mitchell (1991) suggests that the initial proto-kimberlite melt is reducing compared to the ambient mantle, while Höfer *et al.* (2009) suggest that kimberlite melts end up highly oxidising relative to the ambient mantle. Hanger *et al.* (2015) propose that the carbonate content of a melt controls the oxidation state, with increased carbonate content resulting in a more oxidising melt. In the kimberlite metasomatised xenoliths from Bultfontein, there is a relationship between the evolution of the melt and the F concentration in the NVFMMs. If H_2O and F incorporation in NVFMMs is controlled, in part, by oxygen fugacity then the evolution of a kimberlite melt from reducing at early stages, to an oxidising melt through H_2O dissociation (e.g. Foley *et al.* 1986; Tollan & Hermann 2019) as the melt evolves and the carbonate component increases, could explain the trend between melt evolution and F contents in the proto-kimberlite metasomatised dunite, phlogopite-lherzolite and wehrlite xenoliths.

The high F concentration in metasomatised dunite BD1153 could be the product of enrichment by the early-stage reducing parental melt, whereas the modally metasomatised xenoliths (BD1141A and BD3067) have interacted with a more oxidised kimberlite melt and consequently have lower F concentrations. Support for the latter can be derived from the Cr profiles in BD3067 olivine. In Chapter 6 the preservation of Cr diffusion profiles in BD3067 olivine porphyroclasts were attributed to a high Cr^{3+} content because the diffusion of oxidised Cr^{3+} is more anisotropic than Cr^{2+} (Ito & Ganguly, 2006; Jollands *et al.*, 2017). Additionally, the change in oxygen fugacity of a kimberlite melt during ascent is supported by the observation that they both carry diamonds (reduced carbon) and crystallise carbonate (oxidised carbon) in the groundmass. The kimberlite melt composition must cross the EMOD (enstatite-magnesite-olivine-diamond) buffer but the ascent is fast enough to preserve metastable diamond. Late stage carbonate-rich metasomatic agents are shown to have a more oxidising fO_2 than the EMOD buffer (Zhao *et al.*, 1999), hence would destroy diamond. In contrast, during the early stages of evolution a proto-kimberlite melt is more reducing than the EMOD buffer and so diamond is preserved (McCammon *et al.*, 2001). This process is summarised in the schematic illustration in Figure 9.8.

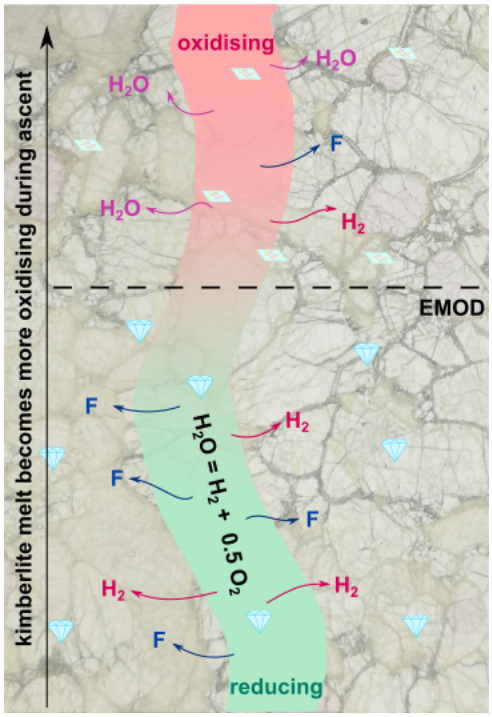

Figure 9.8 *Schematic illustration to show the evolution of the kimberlite melt from reducing conditions to oxidising conditions, and consequently crossing the EMOD (enstatite-magnesite-olivine-diamond) buffer. Diamond is stable in more reducing conditions than the EMOD buffer, and carbonate is more stable in more oxidising conditions. This would be true at depths below the diamond-graphite transition, at shallower depths the EMOD buffer is replaced by the EMOG buffer (enstatite-magnesite-olivine-graphite). The mechanism of water dissociation is shown as* $H_2O = H_2 + 0.5\ O_2$. *The volatile species that are preferentially incorporated in reducing conditions and oxidising conditions are shown.*

If F is incorporated preferentially into NVFMMs in reducing conditions then it could explain the general trend of increased F concentration with depth in the sub-cratonic lithospheric mantle. This is because (i) the ambient mantle is more reduced at greater depths and (ii) metasomatic agents are more reduced early on in their evolution and become more oxidised as they ascend through the lithosphere. Preliminary results of Fe-isotope systematics in a number of the Bultfontein xenoliths suggest that metasomatism by siliceous fluids and kimberlite melts are both associated with heavy Fe (Toby Brooks; MSci Thesis 2020); which can be directly related to the oxidation state of Fe, but in order to test the hypotheses presented in this section, the oxygen fugacity of the xenoliths should be assessed by measuring the Fe^{3+}/Fe^{2+} ratio using Mössbauer spectroscopy.

9.5 Implications

The xenoliths from Bultfontein and Mothae exhibit no systematic variation in the volatile concentrations of NVFMMs between the craton interior and margin, nor stratigraphically with depth at each location. Instead, the composition and nature (melt vs. fluid) of the metasomatic agent has a strong control on the H_2O and F composition of nominally volatile-free mantle minerals and also the bulk composition. While modal metasomatism can increase the bulk F content via storage of F in metasomatic phases, such as phlogopite and amphibole, cryptic metasomatism by fluids and proto-kimberlite melts at depth can significantly increase the F content of pre-existing mantle phases. The correlated variability in volatile

concentration in NVFMMs and the metasomatic melt:rock ratio indicates that the amount of H_2O or F incorporated into NVFMMs changes during melt evolution. Using xenoliths from Bultfontein, it has been shown that at early stages of proto-kimberlite melt evolution, significant amounts of F are incorporated into pre-existing mantle olivine and precipitating clinopyroxene. At later stages of melt evolution, more F is sequestered into metasomatic phases such as phlogopite and less into the mantle wall-rock. In contrast, during siliceous fluid-rock reaction the increased fluid:rock ratio facilitates the increased incorporation of F (and H_2O) into NVFMMs. This difference is most likely because phlogopite is only an accessory product during fluid-rock reaction.

This conclusion has important implications for the evolution of small-fraction melts that ascend to the surface and produce associated fluorite deposits. Brey *et al.* (2009) suggested that partial melting of phlogopite alone is not able to produce the F concentrations observed in kimberlite and carbonatite deposits at the surface. They invoke the contribution by melting of F-clinohumite in the mantle. The new dataset presented here suggests that olivine can host significant quantities of F in clinohumite-like point defects which can be re-mobilised during partial melting.

The large amount of metasomatism at Kimberley has potentially introduced a vast quantity of F into the mantle hosted in both NVFMMs and phlogopite. The high fluorine concentrations in olivine occurs within a specific depth range (35-45 kbar) and within an enriched 'metasomatic zone'. If the enrichment is pervasive throughout this zone then it provides a very large reservoir for fluorine in the Kaapvaal craton, which if later re-mobilised can contribute to the high F concentration in 'successful' kimberlite melts that reach the surface.

Chapter 10

History of metasomatic enrichment in the Kaapvaal craton

10.1 Metasomatic history of the craton

The volatile content of sub-cratonic lithospheric mantle (SCLM) is key to understanding kimberlite genesis and has important implications for long-term stability of the 'cores' of major continents. The different types of metasomatism, and the associated volatile enrichment, evident in the Bultfontein and Mothae mantle xenoliths studied here can be linked with specific events and time periods during the evolution of the Kaapvaal craton. A summary is provided in Figure 10.1 and discussed in detail below.

10.1.1 Craton formation: melt depletion and hydrous fluid metasomatism

Large degrees of partial melting (estimates range from 25-50%) are required to produce the depleted, buoyant peridotite in the sub-cratonic lithospheric mantle (SCLM). The large extent of partial melting required to form harzburgites that are characteristic of global SCLM can be achieved in sub-arc environments, spreading centres (mid-ocean ridges, MOR) or by plume-related activity. The model of craton formation involving accretion of residues formed in upwelling mantle plumes is the least favourable hypothesis due to the lack of evidence for the counterpart large-volume, mafic melts that would be associated with ultra-depleted cratonic roots (Pearson *et al.*, 2019). The more likely scenario is that mantle residues formed by low-pressure melting in sub-arc environments and spreading centres are responsible for the initial phase of depletion observed in the SCLM (Gibson *et al.*, 2008; Pearson & Wittig, 2008; Simon *et al.*, 2007). Convincing evidence for this is presented by Regier *et al.* (2018), who show that δ^{18}O of 93 peridotite xenoliths from five Archean cratons is remarkably uniform (olivine: 5.26 ± 0.22 ‰; orthopyroxene: 5.74 ± 0.27 ‰) and identical to the δ^{18}O of MORB (mid-ocean ridge basalt). Regier *et al.* (2018) proposed that the uniform δ^{18}O observed within otherwise chemically heterogeneous mantle peridotite can be achieved during melting processes at sub-arc and/or mid-ocean ridge settings and remains unaffected by later metasomatic events that produce the rest of the observed chemical heterogeneity.

Discounting the plume accretion model there are two mechanisms that can produce a thick sub-cratonic lithospheric keel from sub-arc and mid-ocean ridge residues, the first is subduction stacking (Helmstaedt & Schulze, 1989; Shirey *et al.*, 2004), where generations of slabs imbricate to produce a thick lithosphere, and the second is shortening during compressional collision followed by gravitational thickening (McKenzie & Priestley, 2016; Regier *et al.*, 2018). While subduction stacking can explain the decoupling of melt from the residue, and the presence of linear features and dipping reflectors (e.g. Zheng *et al.* 2009), Regier *et al.* (2018) have shown that a serpentinite source is inconsistent with the oxygen isotopes in cratonic peridotite. The theory of craton formation by shortening, accretion and subsequent thickening has been

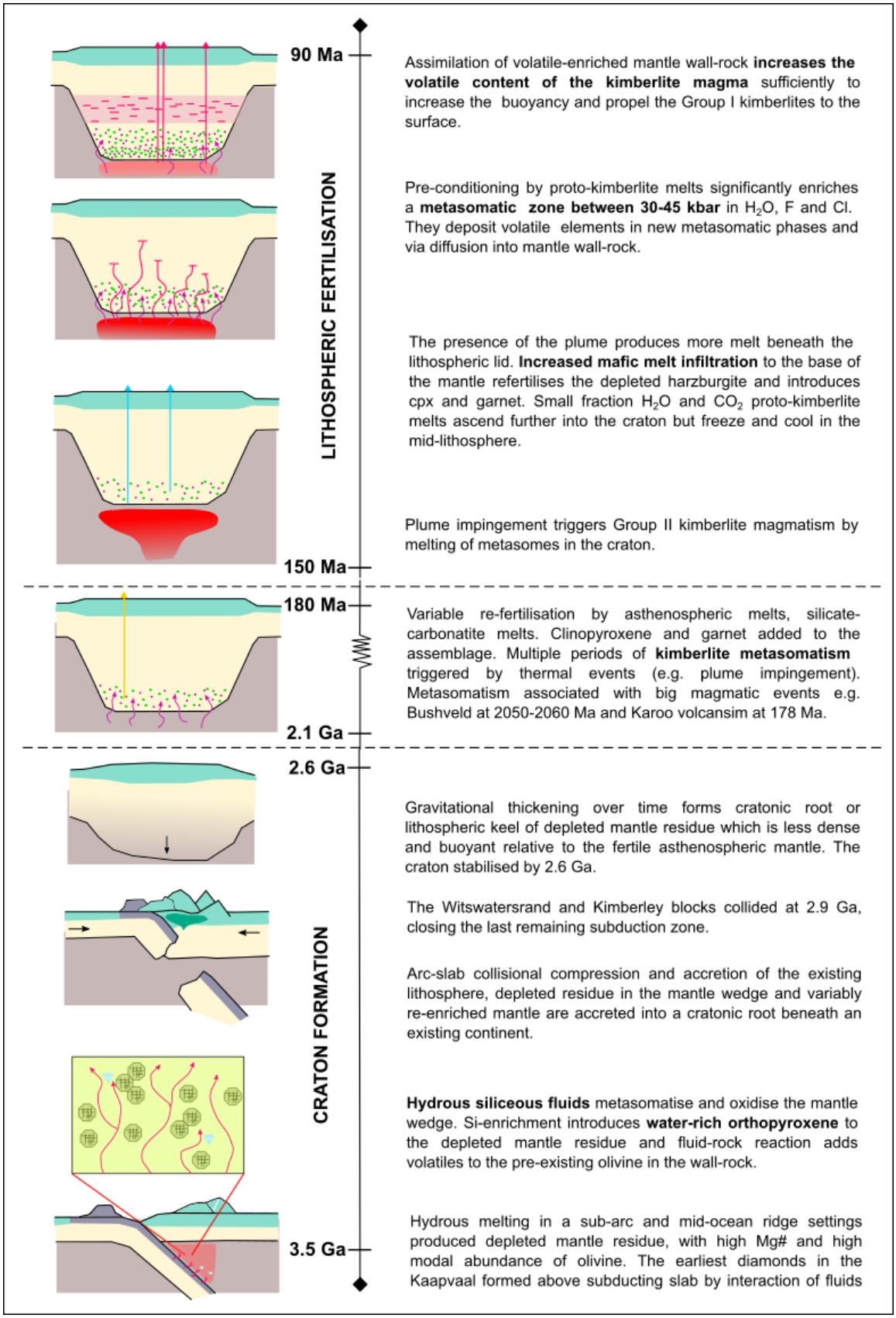

Figure 10.1 *Schematic showing the timing of different styles of metasomatism during the evolution of the Kaapvaal Craton.*

gaining support during the past few years, and can explain features such as the heterogeneous chemistry of cratonic peridotite and fabrics identified by olivine anisotropy in the lower lithosphere (Hwang *et al.*, 2011; McKenzie & Priestley, 2016). The Zealandia sub-continental lithospheric mantle is proposed to be a modern analogue where the stacking of arcs and lateral accretion of buoyant, depleted harzburgite fragments during shortening produced a continental lithospheric keel beneath Zealandia (Scott *et al.*, 2019).

The initial stages of Kaapvaal craton formation involved the building of the continental shield between 3.7 - 3.1 Ga, by the amalgamation of oceanic terranes, including arc-like complexes (De Wit *et al.*, 1992; Poujol *et al.*, 2003). De Wit *et al.* (1992) suggest that by 3.1 Ga the crust was already 40 km thick and the lithospheric keel extended to 170-350 km depth. The presence of a lithospheric keel by this point is supported by the occurrence of diamonds from the Kaapvaal dated between 3.5 and 3.1 Ga (Richardson *et al.*, 1984; Smart *et al.*, 2016). These early Archean diamonds and their inclusions provide an insight into the mantle conditions and dynamics at the time of crystallisation and entrapment. For example, the δ^{13}C and δ^{15}N ratios of inclusions from the Witswatersrand diamonds (3.5-3.1 Ga) preserve a signature of recycled crustal material, and the diamonds are thought to have formed by the interaction of slab fluids with mantle peridotite (or pyroxenite) above a low-angle subducting slab (Smart *et al.*, 2016). These results provide evidence for early Archean recycling and additional support for a sub-arc origin for at least some of the mantle residues in the Kaapvaal SCLM. Following stabilisation of the continental shield above a subduction zone, further accretion, and gravitational thickening, built up the extent and thickness of the craton, doubling the areal extent and consolidating the cratonic root (De Wit *et al.*, 1992; McKenzie & Priestley, 2016). At 2.9 Ga, the closure of last major subduction zone in the area coincided with the continental collision and suturing of the Witswatersrand and Kimberley blocks (Pearson *et al.*, 1995a; Schmitz *et al.*, 2004; Shirey *et al.*, 2013). Since 2.6 Ga the Kaapvaal craton has maintained long-term stability (De Wit *et al.*, 1992; Poujol *et al.*, 2003).

The amalgamation of low-density, harzburgite mantle residues formed at spreading centres and sub-arc environments produces only some of the heterogeneity manifested in the range of cratonic xenolith lithologies. Subsequent multi-phase metasomatism accounts for the rest. The widespread Si-enrichment observed in Kaapvaal mantle xenoliths has been associated with metasomatism by Si-rich melts or fluids (e.g. Bell *et al.* 2005; Gibson *et al.* 2008; Griffin *et al.* 1999b; Kelemen *et al.* 1998; Wasch *et al.* 2009). These have the capacity to increase modal abundance of orthopyroxene whilst rendering the bulk Mg# largely unaffected. A strong argument can be made to suggest that the Si-enrichment occurred either before or during craton formation by slab-related fluids. Prior to and during the collision of the Witswatersrand and Kimberley blocks fluids released from subducted slabs of oceanic lithosphere could flux through the residue that formed in the mantle wedge, a modern analogue occurs above the Chile-Argentina slab (Wagner *et al.*, 2008). Two studies present direct temporal evidence for fluid metasomatism at this time: (i) Bell *et al.* (2005) dated an orthopyroxene vein in a composite xenolith from Kimberley using Os isotopes and obtained a T_{RD} model age of 2.97 ± 0.04 Ga; and (ii) a later study by Wasch *et al.* (2009) of orthopyroxene-clots and orthopyroxene in harzburgites obtained T_{RD} ages of 2.8-2.9 Ga. Both studies implicate fluids from subducting oceanic lithosphere as the metasomatic agent that produced the widespread Si-enrichment in the Kaapvaal sub-cratonic mantle. In their study, Wasch *et al.* (2009) date other orthopyroxene veins at ~ 1.3 Ga, which implies that slab-related fluids from an active subduction zone may not be the only process that produces Si-enrichment in the craton.

In addition to the temporal evidence from orthopyroxene veins, the results of this study provide further support for the hypothesis that the hydrous siliceous fluid metasomatism occurred in a sub-arc environment. A key observation is the close association of the shape of the OH-stretching region in FTIR spectra in the cratonic orthopyroxene from Si-rich garnet harzburgites (Bultfontein; Figure 7.13) and sub-arc peridotitic orthopyroxene (e.g. West Bismarck Island Arc; Tollan & Hermann 2019). Tollan & Hermann (2019) identify prominent absorbance bands at 3600, 3544 and 3520 cm^{-1} in sub-arc orthopyroxene, the ratios of which are controlled by the interaction between oxidising metasomatic melts and orthopyroxene in the mantle wedge, where H_2 and H_2O is incorporated into orthopyroxene in the wall-rock (see Chapter 9). It is likely that the high Mg# orthopyroxenes in the Bultfontein harzburgites were produced by an analogous process in the Archean. The reaction of slab fluids with olivine in the mantle residue would form orthopyroxene (e.g. Wagner *et al.* 2008) enriched in volatile elements, especially H_2O, and poor in fluid immobile elements such as Ti and the HREE. The precipitation of volatile-rich orthopyroxene would be accompanied by fluid-rock reaction in the vicinity and the diffusive exchange of volatile elements between the fluid and pre-existing mantle minerals (i.e. NVFMMs). The oxidising nature of the fluid promotes the incorporation of H_2O into NVFMM as a coupled substitution with trivalent cations, e.g. Fe^{3+}. F incorporation is limited and depends on the F content of the subducted material, most F is retained by the slab but a small amount is fluxed through the mantle by fluids. This study has revealed that the Bultfontein xenoliths with fluid metasomatism have lower F concentrations than the orthopyroxene-rich harzburgites from Mothae. It is proposed that this may reflect different fluid sources if the peridotite beneath Lesotho, on the Witswatersrand block, is associated with a different slab or oceanic terrane to Bultfontein, on the Kimberley block.

10.1.2 Metasomatism and magmatism

The thick lithospheric lid of cratons prevents significant melting in the underlying asthenosphere because the geothermal gradient is below the dry peridotite solidus, and melting only occurs if the mantle is anomalously hot or volatile-rich, for example in oxidising carbonated (-hydrous) mantle (Dasgupta *et al.*, 2013; Rohrbach & Schmidt, 2011). In the model of craton formation that involves shortening and accretion, localised redox melting is more likely to occur where oxidised and reduced lithospheric blocks are juxtaposed against each other (Foley, 2011; Foley *et al.*, 2019; Yaxley *et al.*, 2017). During redox melting an increase in the oxidation state and presence of H_2O or CO_2 decreases the peridotite solidus so that it approaches the geotherm (Figure 10.2a). These conditions for melting would occur periodically throughout the history of the Kaapvaal craton and, incipient volatile-rich melts have metasomatised the lithospheric mantle over billions of years. Small-fraction asthenospheric mafic melts have infiltrated the base of the lithosphere and produced widespread re-fertilisation (by crystallising garnet and clinopyroxene) to the depleted harzburgite residue (Gibson *et al.*, 2008; O'Reilly & Griffin, 2010; Simon *et al.*, 2003). Volatile-rich silicate-carbonate melts, such as those produced by redox melting (Dasgupta *et al.*, 2013; Frost & McCammon, 2008; Rohrbach & Schmidt, 2011), have a relatively low viscosity and density. This enables them to migrate to shallower depths in the craton but their small fraction prevents them from transporting heat (McKenzie, 1989). As a result they freeze in the cool mid-lithosphere. Over time metasomes build up where carbonatite and silicate-carbonate melts have frozen in the lithosphere, for example the MARID- and PIC-suite xenoliths (Fitzpayne *et al.*, 2018a; Giuliani *et al.*, 2015; Grégoire

et al., 2002). Additionally, throughout the history of the craton (but prior to 180 Ma) there have been a number of specific magmatic events that can be linked to metasomatism, for example: (i) magmatism associated with the 2.05-2.06 Ga Bushveld complex; (ii) kimberlite magmatism at the surface has occurred at 1700, 1200, 500, 200 Ma (Griffin *et al.*, 2014a); and (iii) the Karoo volcanism affected large parts of the craton at 178 Ma. Metasomatism associated with the Karoo magmatism has been recognised by Giuliani *et al.* (2014b) by dating titanites in xenoliths from Bultfontein, Kimberley.

10.1.3 Cretaceous plume impingement: Group II kimberlite magmatism and fertilisation of the lithosphere

Most of the kimberlites in the Kaapvaal craton erupted in the Cretaceous within two periods of activity at 120-110 Ma (Group II kimberlites/olivine lamproites) and 90-80 Ma (Group I kimberlites). The latter group includes the two kimberlites that host the xenoliths in this study, i.e. Bultfontein and Mothae. The initiation of Group II kimberlite activity has been proposed by many authors to be due to the impingement of upwelling mantle on the base of the lithosphere (e.g. Becker & Roex 2006; Griffin *et al.* 2003; Jelsma *et al.* 2009; Kobussen *et al.* 2009). This event also triggered a change in the dominant style of metasomatism and increased the extent of melt infiltration to the base of the sub-cratonic lithospheric mantle (Kobussen *et al.*, 2008, 2009). During this period, significant volumes of clinopyroxene and garnet were added to the base of the lithosphere. A number of studies have shown that this 're-fertilisation' affected the lower 40 km of the Kaapvaal lithosphere and resulted in an increase in bulk FeO, Al_2O_3 and TiO_2 content (Griffin *et al.*, 2004; O'Reilly & Griffin, 2006, 2010). The addition of garnet also increases the bulk density. O'Reilly & Griffin (2010) outline a number of arguments for a 'chemical thinning' of the lithosphere, where extensive metasomatism fertilised the base of the lithosphere to such an extent that the Kaapvaal cratonic root lost 40 km of thickness (Griffin *et al.*, 2003, 2004; Kobussen *et al.*, 2008, 2009; O'Reilly & Griffin, 2006), and was only 160-170 km thick by the time of Group I kimberlite activity commencing at 90 Ma. This is a controversial argument, and the preferred interpretation in this study is that there was an upward migration of a metasomatic/fertilised front as opposed to thinning of the lithosphere. Nevertheless, there is clearly evidence for an increased amount of metasomatism in the Kaapvaal craton following the thermal event that triggered the Group II kimberlite activity and multiple studies have identified a minor increase in heat flow from 40 to 42 mW/m^2 between Group II and Group I activity (Lazarov *et al.*, 2009). The high-T sheared xenoliths from specific sites in Lesotho (see Chapter 4) provide further evidence for a thermal perturbation during this period (Bell *et al.*, 2003b; Boyd & Nixon, 1973; Griffin *et al.*, 2003; Lazarov *et al.*, 2009; Mitchell, 1984).

10.1.4 Lithospheric pre-conditioning: Group I kimberlite magmatism

During the 20-50 Ma period between Group II and Group I kimberlite activity phlogopite- and volatile-rich metasomatism occurred in the Kaapvaal craton (Kobussen *et al.*, 2009). This is recognised in multiple studies that have identified the occurrence of metasomatism by proto-kimberlite melts immediately preceding Group I kimberlite emplacement (e.g. Giuliani *et al.* 2014a, 2016; Jackson & Gibson 2018; Jollands *et al.* 2018). Sleep (2009) calculated that the rate of kimberlite melt production is enough to have sustained an eruption every 10 to 100 years for the past 2.5 Ga. The much lower frequency of

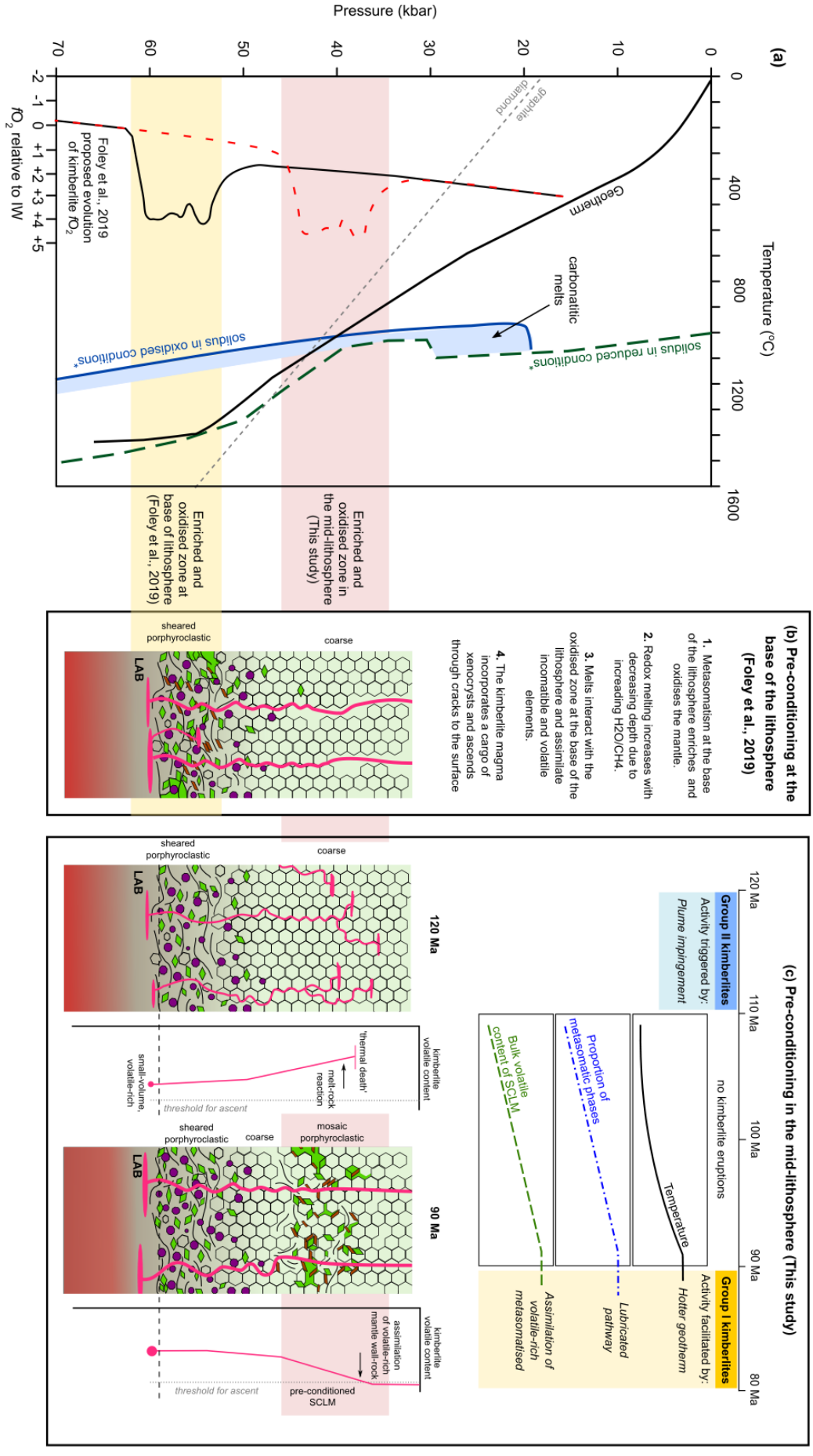

Figure 10.2 *(continues on next page)*

surface kimberlite emplacement, however, implies that the majority of kimberlite melts freeze in the mid-lithosphere (Aulbach *et al.*, 2016). This is exemplified by Bultfontein xenolith BD3067 which represents a proto-kimberlite melt frozen in the mid-lithosphere (see Chapter 6). Ni and Cr zoning in olivine from the mantle wall-rock requires that the timing of metasomatism was less than 0.5 Ma prior to emplacement of the host kimberlite. Thus, pre-conditioning of the lithospheric mantle by proto-kimberlite metasomatism appears to be an important process that precedes final kimberlite ascent by creating a lubricated pathway for later successful melts to exploit (e.g. Aulbach *et al.* 2016; Drury & Roermund 1988; Giuliani *et al.* 2014a, 2016; Jackson & Gibson 2018; O'Reilly & Griffin 2013; Yaxley *et al.* 2017). This model of pre-conditioning in the mid-lithosphere contrasts to the model of kimberlite evolution by Foley *et al.* (2019), in which a similar pre-conditioning of the mantle occurs at much higher pressures, i.e. at the base of the lithosphere. Figure 10.2 compares the two models for mantle pre-conditioning and their implications for kimberlite ascent. Foley *et al.* (2019) attribute the observed Ca, Na and CO_2 contents of kimberlites to assimilation of material from an enriched, oxidised zone between ~ 50-60 kbar, compared to the suggestion in this study that this metasomatised zone occurs between 35-45 kbar. Panel (a) in Figure 10.2 also highlights the impact of redox melting (by the low temperature of the oxidised solidus) in the oxidised lithosphere during kimberlite ascent which facilitates the assimilation of xenocrysts.

In Chapter 5 the styles of metasomatism in xenoliths hosted by different kimberlites in the Kaapvaal craton were divided into five distinct groups. A difference between the dominant styles of metasomatism was recognised between Finsch (Group II) and Kimberley (Group I), which can be extended to include the other Group I and Group II kimberlites (Figure 10.3). Melt re-fertilisation at the base of the Kaapvaal lithosphere is dominant in the xenoliths from Group II kimberlites, whereas the Group I kimberlites predominantly contain xenoliths that have been metasomatised by proto-kimberlite melts at shallower levels. Interestingly, none of the five styles of metasomatism identified from the Bultfontein and Mothae xenoliths are present in the xenoliths from the Venetia (520 Ma; Griffin *et al.* 2014a) or the Premier (1150 Ma; Griffin *et al.* 2014a) kimberlites. Figure 10.3 provides supplementary evidence to support the findings of Kobussen *et al.* (2009) that the dominant style of metasomatism changed between 110-90 Ma, and clearly shows that metasomatism by proto-kimberlite, silico-carbonatite melts became a dominant process during this period.

Figure 10.2 ***(previous page)*** *Schematic to illustrate metasomatic pre-conditioning prior to Group I kimberlite activity in the Kaapvaal craton as suggested by Foley* et al. *(2019) and in this study. (a) The position of the solidus in oxidised and reduced conditions, and the corresponding PT conditions where carbonatite melts form (Foley* et al.*, 2009). Regions of enriched, oxidised metasomatised mantle are proposed at 50-60 kbar by Foley* et al. *(2009) and at 35-45 kbar in this study. The evolution oxygen fugacity (fO_2) relative to the Iron-wüstite buffer(IW) of a kimberlite melt during ascent is shown schematically to the left of the geotherm: black solid line is according to the model of Foley* et al. *(2019); red dashed line according to this study. The interaction of the kimberlite magma with the metasomatised zone increases its fO_2. (b) Schematic illustration to illustrate the model of Foley* et al. *(2019) whereby pre-conditioning at the base of the lithosphere drives controls kimberlite composition and ascent by assimilation of Ca, Na and CO_2. (c) The suggested timeframe and process of mid-lithospheric conditioning according to this study: following plume impingement that triggered Group II kimberlite activity, extensive metasomatism refertilised the base of the lithosphere. Meanwhile small-fraction volatile-rich melts infiltrated to the mid-lithosphere but froze, depositing volatile-rich metasomatic phases and increasing the volatile concentration of NVFMM in the mantle wall-rock during melt-rock reaction. After 20 Ma of extensive metasomatic enrichment, kimberlite melts had a lubricated pathway and assimilation of mantle material sufficiently increased the volatile concentration to propel the ascent to the surface.*

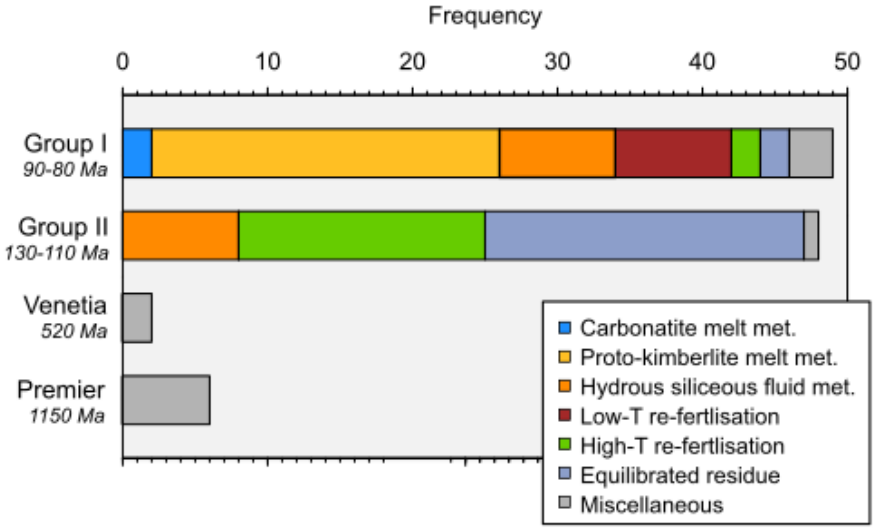

Figure 10.3 *The frequency of xenoliths showing evidence of the five styles of metasomatism identified in the Bultfontein and Mothae xenoliths, a sixth style probably related to silicate melt metasomatism (Chapter 5 and miscellaneous signatures in the Group I, Group II, Venetia and Premier kimberlites representing the time period from 80 to 1150 Ma.*

The results of this present study provide new constraints on the influx of volatiles during pre-conditioning of the lithospheric mantle. Proto-kimberlite (silico-carbonatite) melts have a great capacity to enrich the sub-cratonic lithospheric mantle in H_2O and F, via the crystallisation of hydrous minerals, such as phlogopite, and by diffusive exchange with the mantle wall-rock. Clinopyroxene crystallised from the kimberlite melt at early stages of the evolution of infiltrating metasomatic melts contains up to 46 ppm F and 195 ppmw H_2O, and olivine that has interacted with the same melt contains up to 196 ppm F and 70 ppmw H_2O. The results indicate that pre-conditioning of the mantle by proto-kimberlite melts significantly increases the bulk volatile concentrations such that assimilation of the mantle wall-rock by later kimberlite magmas can increase the volatile concentration of the kimberlite magma itself. The dissolution of orthopyroxene is considered an important process in kimberlite magma evolution, and is responsible driving the composition to more SiO_2-rich compositions and promoting the exsolution of CO_2 (Sharygin *et al.*, 2017; Stone & Luth, 2016). It is proposed that assimilation of F-rich olivine, orthopyroxene and clinopyroxene from the pre-conditioned mantle contributes to the F-rich nature of kimberlites (e.g. Kjarsgaard *et al.* 2009). The initiation of Group I kimberlite activity could represent the point in time where pre-conditioning has enriched the mid-lithosphere in volatiles to such an extent that the kimberlite magma no longer exchanges volatiles with the wall-rock but instead assimilates volatiles during ascent. This can decrease the buoyancy of the kimberlite enough to drive its ascent to the surface before freezing in the mid-lithosphere. The addition of volatiles to NVFMMs by metasomatism could, therefore, have important implications for diamond transport to the Earth's surface.

10.2 Seismic anomalies

A major anomaly in the seismic velocity structure of the cratonic mantle is referred to as the mid-lithospheric discontinuity (MLD); this has slow V_S relative to the otherwise fast, cold cratonic lithosphere (Aulbach

et al., 2016; Rader *et al.*, 2015; Selway *et al.*, 2015). The MLD is not continuous across cratons and different regions exhibit a velocity reduction of 2-7% within 10-20 km thick zones that are present between 60-160 km depth, but predominant in the mid-lithosphere at 80-100 km depth (Rader *et al.*, 2015). There is currently no consensus on the origin of the MLD (see Aulbach *et al.* 2016 for a review). It has been proposed that the accumulation of melt and the presence of hydrous metasomes produce the velocity reduction but this is problematic because the required volume of metasomatic hydrous minerals is inconsistent with the abundances observed in kimberlite-borne mantle xenoliths. A 2-7% velocity reduction over 10-20 km can be achieved by 5-10% phlogopite, 10-15% carbonates or >15% amphibole (Rader *et al.*, 2015), yet observations from mantle xenoliths suggest the abundance of hydrous minerals is closer to 2% (Aulbach *et al.*, 2016; Pearson *et al.*, 2003). It is possible that this discrepancy reflects a bias in kimberlite sampling or human sampling, but the results of this study invoke the additional influence of volatile-storage in NVFMMs around metasomes and it is suggested that these may contribute to the decrease in seismic velocity at MLDs. Silica-enriched, orthopyroxene-rich peridotite from the Kaapvaal craton has high V_S (Wagner *et al.*, 2008), and it is proposed that the orthopyroxene dissolution, hydrous mineral addition and NVFMM hydration by silicate-carbonate melts (Chapters 5 and 9) all result in decreasing V_S to produce the heterogeneous MLD observed in the Kaapvaal craton. The depth of the MLD corresponds to the region of metasomatism associated with proto-kimberlite and carbonatite metasomatism in this study, whereas the orthopyroxene-rich harzburgites originated from the lower extent of the dominant MLD (40 kbar, ~ 120 km; Figure 10.4).

10.3 Reservoir capacity, implications for craton stability

The measured H_2O and F concentrations in the Bultfontein and Mothae xenoliths provide important constraints on the capacity of NVFMMs in the Kaapvaal craton to act as a volatile reservoir for H_2O and F. Figure 10.4 shows that the Kaapvaal craton can be segmented into at least four stratigraphic units:

1. Volatile-enriched metasomatised zone in the mid-lithosphere (~ 1-20 km)
2. Si-enriched garnet harzburgite (~ 20 km)
3. Re-fertilised garnet lherzolite (~ 40-60 km)
4. Depleted mantle residue (harzburgite; ~ 56-95 km)

These units are based on the observations in this study but can be related to the widely-used groups defined by Griffin *et al.* (2002) who employed a statistical analysis of Cr-pyrope compositions to estimate the proportion of the mantle metasomatised by different agents. The orthopyroxene-rich (Si-enriched) garnet harzburgite corresponds with the sub-calcic garnet-bearing depleted harzburgite from Griffin *et al.* (2002) and the high-*T* re-fertilised garnet lherzolite corresponds to the fertile lherzolites and melt metasomatised peridotite with garnet enriched in Ti, Zr, Y and Ga and a sheared texture (Griffin *et al.*, 2003).

Many studies have applied the statistical garnet-based categorisation of Griffin *et al.* (2002) to different kimberlite xenolith suites to produce a stratigraphy that estimates how the proportion of each category changes with depth through the lithospheric mantle (Begg *et al.*, 2009; Griffin *et al.*, 2003, 2004, 2009;

O'Reilly & Griffin, 2006). A problem of using the categorisation of Griffin *et al.* (2002) is that it only uses the Cr-pyrope composition and this does not necessarily highlight the influence of earlier melt depletion if garnet is a secondary phase. The fertile lherzolites categorised by Griffin *et al.* (2002) are deemed to show no evidence of melt depletion, however by combining olivine, orthopyroxene and clinopyroxene it is evident that the fertile lherzolites from Mothae retain evidence of their origin as a depleted residue that has been re-fertilised by mafic asthenospheric melts (Chapter 5). Therefore, the four categories used for the estimates in this section combine petrographic observations and mineral chemistry of all four main phases. Pure carbonatite metasomatism has been discounted because it is believed to be a more rare form of metasomatism, relative to silicate-carbonate metasomatism (Chapter 5), that does not significantly enrich the NVFMM in volatile elements (Chapter 7 and 9)

	Group II	**Group I**	**Group I**[1]
Age (Ma)	120-110	90-80	90-80
Depth to LAB (km)	200	200	variable
t_c (km)	40	40	~ 40
t_l (km)	160	160	variable
Area[1] **(km^2)**	7.03×10^6	7.03×10^6	7.03×10^6
Volume (km^3)	1.12×10^9	1.12×10^9	9.02×10^8

Unit	**Bulk H_2O (ppmw)**	**Bulk F (ppm)**	**t (km)**	**t (km)**	**Proportion (%)**
Si-enriched peridotite	109 ±9	48 ±7	24 (15%)	24 (15%)	15
Kimberlite metasomatised	97 ±9	127 ±11	1 (0.6%)	20 (12.5%)	12.5
Melt refertilised	65 ±5	21 ±2	40 (25%)	60 (37.5%)	37.5
Depleted harzburgite	25 ±5	15 ±2	95 (59.4%)	56 (35%)	35
	Bulk H_2O (ppmw)		48 ±3	62 ±3	62 ±3
	Bulk F (ppm)		22 ±2	36 ±2	36 ±2

Table 10.1 *Capacity of NVFMM as a volatile reservoir in the Kaapvaal craton using the bulk average H_2O and F concentrations calculated in Chapter 7. The volume in the first two columns, Group II and Group I, has been calculated using the area of the Kaapvaal craton and assuming a constant thickness to the base of the lithosphere. In the third column, *Group I, the volume represents the volume of the mechanical boundary layer and is modelled using seismically detected lateral variations in crustal thickness and lithospheric thickness.* [1]*Gibson and McKenzie (in. prep); t: thickness; t_c: crustal thickness; t_l: thickness of the lithospheric mantle.*

A number of observations have been used to estimate the thickness and proportion of the SCLM that has been metasomatised by (i) silicious fluids and proto-kimberlite magmas in the mid-lithosphere and (ii) small-fraction asthenospheric melts at the base of the lithosphere during Group II (120-110 Ma) and Group I kimberlite activity (90-80 Ma). The proportion of the Si-enriched fluid metasomatised harzburgite is based on the proportion of clinopyroxene with the hydrous siliceous fluid signature in the Kaapvaal database compiled in Chapter 5 (~ 15%). This volume is predicted to stay constant between Group II and Group I because the majority of fluid metasomatism is assumed to pre-date craton formation (as above, Regier *et al.* 2018). The estimated stratigraphic thickness of fluid metasomatised peridotite (~ 20 km) is difficult to quantify and is likely an underestimate based on the documentation of Si-enrichment in the Kaapvaal craton. Based on Figure 10.3, re-fertilised xenoliths are predominant in Group II kimberlites, and there is a complete lack of xenoliths with a proto-kimberlite metasomatic signature. Kimberlite activity in the Kaapvaal craton has occurred over the last billion years (Griffin *et al.*, 2014a), and it is likely that some proportion of the mantle has been metasomatised by the parental melts. The degree of metasomatism

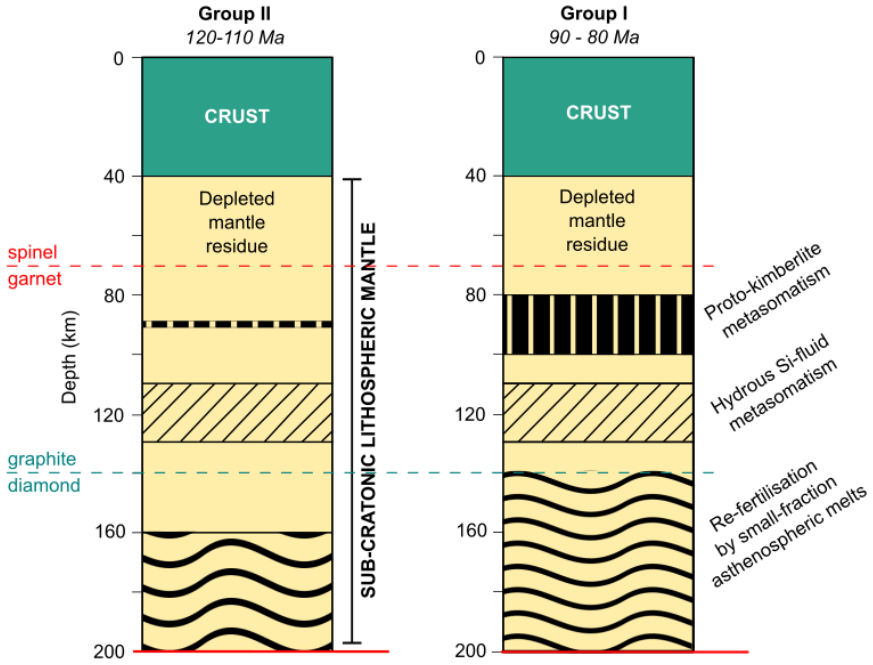

Figure 10.4 *Estimated thickness and proportions of different metasomatic units in the SCLM during Group II kimberlite activity, and 20 Ma later during Group I kimberlite activity.*

by proto-kimberlite melts is approximated as a 1 km thick layer (0.6%) in the SCLM during Group II magmatism. As discussed above, 20-40 Ma of extensive metasomatism accompanied by Early Cretaceous plume impingement on the base of the lithosphere and this was associated with a change in style of metasomatism to phlogopite-rich assemblages in the mid-lithosphere (Kobussen *et al.*, 2009; O'Reilly & Griffin, 2010). As a result, by the time of Group I kimberlite activity, there was an increased proportion of the mantle metasomatised by silico-carbonatite melts in the mid-lithosphere and also by less-evolved asthenospheric melts at the base of the lithosphere. The thickness of mid-lithsopheric discontinuities (Rader *et al.*, 2015) is used to set the zone of kimberlite metasomatism (including metasomes of MARID and PIC veins) at a 20 km thick layer by 90 Ma. The addition of clinopyroxene at the base of the lithosphere caused an upwards migration of the metasomatic front in the lower regions of the lithospheric keel (O'Reilly & Griffin, 2010), this heightened extent of metasomatism is reflected in the increased thickness of the re-fertilised layer from 40 to 60 km.

Using this estimated stratification of the mantle alongside the average bulk concentrations of each metasomatic unit (calculated in Chapter 7), it has been possible to calculate the approximate bulk H_2O and F concentrations for NVFMMs in the Kaapvaal craton before and after the period of extensive metasomatism between 110-90 Ma (Table 10.1, Figure 10.4). The results of these simple calculations suggest that a significant quantity of H_2O (48-62 ppmw) and F (22-36 ppm) can be hosted in NVFMMs alone in the craton, and that metasomatism can significantly increase the volatile contents of the SCLM in a short time frame. Between the Group II and Group I kimberlite activity it is estimated that the bulk H_2O and F concentrations in the Kaapvaal could have increased by 28% and 62%, respectively. The gain in both H_2O and F is dominated by the establishment of the mid-lithospheric 'proto-kimberlite' metasomatised zone (bulk H_2O: 97 ppmw; F: 127 ppm), where failed kimberlite magmas have frozen in

the lithosphere forming metasomes and adding volatile elements into the pre-existing wall-rock. These calculations only account for volatile storage in nominally volatile-free mantle minerals, therefore the inclusion of metasomatic hydrous phases (i.e. amphibole and phlogopite) would increase the bulk H_2O and F concentrations further.

The estimated bulk composition of F in the primitive mantle is 25 ppm (pyrolite; McDonough & Sun 1995). The measurements and calculations in this study have shown that this can be hosted within olivine, orthopyroxene and clinopyroxene alone. Moreover, this work has shown that metasomatic agents have significantly increased both the H_2O and F concentrations above the bulk composition of the mantle, thus confirming that the sub-cratonic lithospheric mantle is an important reservoir for volatile species including halogens. The temporal variation in this reservoir is evident in the critical role of metasomatic agents and their prevalence through time. The extent and style of metasomatism depends on various physical and chemical parameters including: (i) the redox state of the mantle; (ii) the presence of a thermal upwelling in the asthenosphere; and (iii) past metasomatic reactions in the lithosphere. The results here have profound implications for the stability of cratons because short time periods of extensive metasomatism have the ability to introduce significant volumes of volatiles to the SCLM. Higher water contents affect the rheology of the craton and increase instability, Liao *et al.* (2017) modelled how two stages of how hydration weakening could result in cratonic thinning. Fast lithospheric thinning occurs due to a convective instability followed by a slower process of convective thermal erosion, both processes are catalysed if metasomatism adds significant H_2O to olivine hence increasing both dislocation and diffusion creep. If sub-cratonic lithosphere is subject to multiple thermal heating events, or subduction is prominent nearby, then a large volume of volatiles can be accumulated during a short time period causing instability and potentially cratonic thinning, such as has occurred in the North China Craton (Menzies *et al.*, 2007).

10.4 Summary

Metasomatic introduction of volatiles into the sub-cratonic lithospheric mantle has important implications for the onset of kimberlite activity at Earth's surface and craton stability at depth. Metasomatism of the Kaapvaal lithosphere by hydrous siliceous fluids occurred in an early Archean sub-arc environment and was subsequently accreted into the Kaapvaal cratonic mantle. Over the next two billion years varying amounts of metasomatism involved silicate and more volatile-rich silicate-carbonate melts. Between the Group II and Group I kimberlite activity Kobussen *et al.* (2009) showed that the dominant style of metasomatism drastically changed and more phlogopite-bearing metasomatism occurred at mid-lithospheric depths in addition to the extensive melt metasomatism that re-fertilised the base of the lithosphere. This change resulted in a significant influx of H_2O and F to the SCLM, that are stored in both metasomatic phases and NVFMM. Pre-conditioning of the mid-lithosphere by kimberlite melts between 110-90 Ma provided preferential conditions (volatile-rich and a lubricated pathway) that triggered the large magnitude of Group I kimberlite magmatism at the surface. Assimilation of F-rich mantle wall-rock during ascent contributed to the final F-rich nature of the kimberlite.

The MLD is interpreted to represent the metasomatic zone in the mid-lithosphere that contains veins of amphibole and phlogopite and where, as has been shown in this study, the pre-existing mantle minerals (olivine and orthopyroxene) are significantly enriched in H_2O and F following melt-rock reaction. The

additional effect of mantle wall-rock hydration and F-enrichment associated with metasomes, and more widely where melts have percolated along grain boundaries (cryptic metasomatism), could decrease the required amount of phlogopite and amphibole for a 2-7% reduction in V_S to an closer to that observed in natural xenoliths.

Olivine, orthopyroxene and clinopyroxene are important hosts for both H_2O and F, and can accommodate the entire F budget of the upper mantle and additional F recycled into the mantle via subduction zones. It is apparent that the capacity of the SCLM as a volatile reservoir is transient and depends on the extent of metasomatism and magmatism, and consequently, on events such as plume impingement, rifting and subduction.

Chapter 11

Conclusions

The sub-cratonic lithospheric mantle has a complex history of melt depletion and metasomatic enrichment as is evident from the petrography and geochemistry of kimberlite-hosted mantle xenoliths. This study presents the first internally-consistent investigation into the variability of H_2O, F and Cl concentrations in nominally volatile-free mantle minerals (NVFMMs) in the sub-cratonic lithospheric mantle (SCLM). By examining variations in volatile storage associated with depth, spatial location and style of metasomatism in the Kaapvaal sub-cratonic mantle, it has been possible to produce, for the first time, a picture of: (i) how the craton has evolved as a volatile reservoir through time; and (ii) the capacity of the lithospheric keel to host H_2O and F. The EPMA, LA-ICP-MS, SIMS and FTIR analyses presented in Chapters 2, 3 and 7 provide a systematic dataset of the major-element, trace-element and volatile concentrations of olivine, orthopyroxene and clinopyroxene from the Kaapvaal craton. All analyses (with the exception of FTIR) were made on the same mineral separate which allows a comprehensive analysis of the controls on H_2O, F and Cl in the SCLM.

This study builds on the pioneering work by Anne Peslier who has published leading research into the storage of water in NVFMMs in the SCLM, especially in the Kaapvaal craton. Her work has also identified mechanisms by which cratons achieve long-term stability (e.g. Peslier *et al.* 2002, 2010, 2012, 2015). The work presented here compliments this previous work by including F and Cl analyses alongside H_2O. Additionally, the study of volatile concentrations of olivine, orthopyroxene and clinopyroxene from nineteen xenoliths, with different lithologies and equilibration conditions, from Bultfontein and Mothae significantly expands the existing dataset for H_2O and contributes new insight to the storage of F and Cl in NVFMM in the Kaapvaal SCLM. The systematic study of H_2O and F in the same mineral separate has highlighted important ways in which these two species interact in the crystal lattice of NVFMM. Previous studies have found that the storage of H_2O in olivine may be somewhat pressure dependent (Demouchy & Bolfan-Casanova, 2016; Peslier *et al.*, 2010), however no other systematic pressure or temperature relationships in orthopyroxene or clinopyroxene H_2O concentrations have been identified to date.

The petrography, major- and trace-element composition of the nineteen peridotites presented in Chapters 2 and 3 highlights systematic similarities between many of the xenoliths from Bultfontein at the craton interior and Mothae at the craton margin. Five different categories of clinopyroxene-bearing peridotite are identified (Chapter 3), each with a unique chemical composition and petrographic features, these are: (i) spinel-harzburgite with extremely enriched clinopyroxene; (ii) three different lithologies united by their emerald green clinopyroxene with an exclusive trace-element pattern and modal phlogopite; (iii) orthopyroxene-rich (30-40%) garnet harzburgite that all equilibrated at ~ 1000 °C and 42 kbar and contain garnet with a sinusoidal trace-element pattern; (iv) orthopyroxene-poor garnet harzburgite that equilibrated at relatively low pressure (~ 35 kbar); and (v) high temperature (1250 °C) garnet lherzolites with a porphyroclastic texture.

In Chapter 4 the equilibration pressure and temperature conditions of the Bultfontein and Mothae xenoliths were constrained using a number of geo-barometers and thermometers, the basis of which are underpinned by the pressure or temperature dependence of solid solution between different minerals or the solubility in a single phase. The preferred combination of the two-pyroxene thermometer calibrated by Taylor (1998) and the barometer based on Al exchange between orthopyroxene and garnet, calibrated by Nickel & Green (1985), were used for all four phase peridotites. Where either garnet or clinopyroxene were absent from the mineral assemblage two single phase thermometers were used: (i) Ca in orthopyroxene (Brey *et al.*, 1990); and (ii) the thermometer based on the enstatite (Mg) component in clinopyroxene (Nimis & Taylor, 2000). The temperature estimates were fitted to the geotherm of the Kaapvaal craton established from peridotite xenoliths by Mather *et al.* (2011). The nineteen xenoliths in this study span a pressure range of 30-52 kbar and a temperature range of 800-1270 °C, which permitted an investigation into whether the volatile concentrations of olivine, orthopyroxene or clinopyroxene are dependent on either *P* or *T*. Four xenoliths from Mothae are high-temperature sheared lherzolites, however, it must be noted that they do not exhibit the anomalously high temperatures which have been recognised in similar xenoliths from other kimberlites in northern Lesotho (e.g. Thaba Putsoa; Boyd & Nixon 1973; Gurney *et al.* 1980; Mitchell 1984).

The origin of the chemical signature preserved in each category of peridotite was identified in Chapter 5. All nineteen xenoliths from Bultfontein and Mothae exhibit evidence of melt depletion, as shown by modelling of the behaviour of trace-elements during partial melting of a primitive mantle source. Each category displayed varying levels of re-enrichment following partial melting, which is attributed to melt-rock reaction by different metasomatic agents. The evidence for carbonatite, silicate-carbonate and silicate melts in the mantle is drawn from diamond inclusions and the re-constructed compositions of parental melts of erupted kimberlites and carbonatites. Additionally, diamond inclusions host hydrous siliceous fluids and brines that expand the possible metasomatic agents further. The relative H_2O, CO_2 and halogen concentrations of each metasomatic agent was considered with respect to the effect on the mantle wall-rock during reactive infiltration.

In order to establish the composition of the metasomatic agents responsible for the different chemical signatures in the Bultfontein and Mothae xenoliths, the composition of the melt in equilibrium with each clinopyroxene was estimated using partition coefficients from: (i) the published literature; and (ii) calculated using the lattice strain model at the appropriate *PT* conditions for each xenolith. The trace-element composition of the equilibrium melts were combined with other petrographic and chemical observations to identify four different metasomatic agents in the sample suite from Bultfontein and Mothae.

1. **Carbonatite metasomatism** is identified in the spinel harzburgite BD2135 from Mothae. This harzburgite contains a very small volume of highly-enriched clinopyroxene, which is present along grain boundaries primarly around large orthopyroxene crystals. The primitive-mantle-normalised trace-element pattern of the clinopyroxene is identical to the diopside from MARID suite veins found in Kimberley (Dawson & Smith, 1977; Fitzpayne *et al.*, 2018a) and the melt in equilibrium with these clinopyroxene is very similar to the composition of erupted carbonatite melts (Bizimis *et al.*, 2003). The high abundance of orthopyroxene and the depleted nature (high Mg#) of both olivine and orthopyroxene in BD2135 are consistent with their formation as residues of a major partial melting event prior to craton formation. These preserved signatures alongside the interstitial texture of the

clinopyroxene indicate that the metasomatic agent was present as a very low volume. It is, therefore, concluded that xenolith BD2135 has undergone stealth metasomatism by a late-stage, small-fraction carbonatite melt which has percolated as an offshoot away from the main melt 'channel' where MARID veins form.

2. **Proto-kimberlite metasomatism** is responsible for the emerald green clinopyroxene and phlogopite present in three xenoliths from Bultfontein; the phlogopite-lherzolite (BD1141A), wehrlite (BD3067) and dunite (BD1153). The abundance of clinopyroxene and phlogopite in each reflects the melt:rock ratio metasomatism. The highest proportion is present in BD3067 which exhibits an entire metasomatic vein and the lowest is in BD1153 which has no phlogopite and only minor clinopyroxene. The clinopyroxene has the same composition as PIC suite clinopyroxene, and the calculated melt in equilibrium with both of these matches the composition of the host Bultfontein kimberlite. The proto-kimberlite melt is assumed to have a silico-carbonatite composition based on the work by Soltys *et al.* (2018) and Brooker *et al.* (2011).

3. **Hydrous siliceous fluid metasomatism** is present in four xenoliths from both Bultfontein and Mothae. These are the orthopyroxene-rich garnet harzburgites, that are characterised by a sinusoidal REE pattern in garnet, clinopyroxene and the bulk rock composition. Fluid metasomatism is responsible for the Si-excess observed by the exceptionally high orthopyroxene contents (up to 40%). It also causes HREE depletion in the phases that precipitate during fluid-rock reaction or the pre-existing phases which re-equilibrate with the fluid because the HREE are fluid immobile.

4. **Re-fertilisation** towards the base of the lithosphere is evident in the high-T garnet lherzolites from Mothae and the at shallower levels in the low-T garnet harzburgite from Bultfontein (BD1140). While both categories retain the bulk signature of the mantle residue following partial melting, they have, however, witnessed subsequent addition of clinopyroxene and garnet during melt-rock reaction. In the garnet lherzolites the high temperatures and porphyroclastic texture have accelerated subsolidus re-equilibration such that the original metasomatic signature is not preserved. This is shown by the trace-element equilibrium that has been achieved in clinopyroxene in the garnet lherzolites (shown to be in equilibrium with the bulk primitive mantle composition) and the flat bulk trace-element pattern. It is assumed that the re-fertilisation of the mantle occurred by small-fraction melts from the asthenosphere at early stages of melt percolation and evolution.

In Chapter 6 the timing of metasomatism by proto-kimberlite melts is investigated through a detailed case study of veined xenolith BD3067 from Bultfontein. Olivine porphyroclasts situated distal to the main metasomatic vein (assemblage: clinopyroxene + phlogopite + ilmente + sulfides + zircon) were found to display Ni and Cr zoning, implying the spatially-isolated disequilibrium of these elements where all other major and trace-elements were homogeneous. The de-coupling of Ni and Cr from other major and minor elements was shown to be associated with the crystallographic orientation and anisotropic diffusion in olivine. Consequently, it was concluded that the re-equilibration of Ni and Cr has been inhibited by the slow diffusion of these elements in the [100] and [010] axes of olivine, alongside the external pressures of co-precipitating sulfides and spinel on the local distribution coefficients. This discovery allowed the establishment of the timing of metasomatism by proto-kimberlite melts in the mid-lithosphere prior to entrainment by the host kimberlite. Diffusion modelling applied to the Ni profiles in olivine porphyroclasts shows that metasomatism by the proto-kimberlite melt occurred around 0.5 Ma prior to

the eruption of the Bultfontein kimberlite at 84 ± 0.9 Ma (Kramers *et al.*, 1983). These results show that there is a period of metasomatism that precedes 'successful' kimberlite emplacement which has important implications for theories of mantle pre-conditioning. If early melts/pulses metasomatise the mid-lithosphere by precipitating veins, such as that in BD3067, it can produce a lubricated pathway for future kimberlite magmas to exploit during their ascent to the surface (Jackson & Gibson, 2018).

In Chapter 7 the results of SIMS analyses on mineral separates of olivine, orthopyroxene and clinopyroxene are presented with respect to the different styles of metasomatism. The most important result from the SIMS work is that all three NVFMM analysed can host significant quantities of F: olivine in this study contains up to 196 ppm F, orthopyroxene up to 33 ppm F and clinopyroxene up to 46 ppm F. The H_2O concentrations align with previous studies with olivine H_2O ranging from 6-103 ppmw, orthopyroxene has 27-254 ppmw H_2O and clinopyroxene concentrations range from 64-300 ppmw. Chlorine concentrations in olivine were below detection limit, very low in orthopyroxene (1.5-3.7 ppm) and slightly higher in clinopyroxene (2-13 ppm). Variations exist between the styles of metasomatism. The xenoliths metasomatised by proto-kimberlite melts are highly enriched in F (46ppm F in clinopyroxene and 196 ppm F in olivine), and the highest Cl concentration in clinopyroxene (13 ppm). The carbonatite-metasomatised spinel harzburgite (and other spinel harzburgites) have the lowest concentrations of both H_2O, F and Cl, which are often below the detection limit. The hydrous siliceous fluid metasomatised orthopyroxene-rich harzburgites have the highest water concentrations (bulk H_2O 92-126 ppmw) and a range in F concentrations (bulk F 28-71 ppm).

This study shows for the first time that variation between different styles of metasomatism is not only limited to the water and halogen concentrations, but it is also reflected in the incorporation mechanisms of each species. FTIR spectra were presented in Chapter 7 and used in Chapter 8 to identify the point defects that host H and F in olivine and orthopyroxene. Titanium is identified as a key element to which both H and F are coupled for charge balance. Point defects involving Ti (e.g. clinohumite-like defect) are dominant in the FTIR spectra of all olivines, albeit with a lesser influence in the fluid metasomatised xenoliths because Ti is fluid immobile. A new mechanism for the incorporation of both H and F coupled to Ti in olivine is proposed whereby Ti^{4+} in an octahedral site is charge balanced by the formation of one OH-group and the replacement of an oxygen by a fluorine anion in a neighbouring tetrahedral vacancy. The presence of this coupled mechanism in metasomatised olivine has important implications for the preservation of mantle volatile concentrations associated with metasomatism. The strong coupling between H, F and Ti limits their independent diffusion. This is because diffusion must maintain charge and mass balance and in this coupled substitution, will limited by the slowest diffusing element, i.e. Ti. The timescales of independent diffusive re-equilibration of Ti and H between olivine and orthopyroxene are calculated in Chapter 8 and show that at the lowest temperatures in the spinel harzburgite (BD2135, 800 °C) Ti equilibrates in 2.5 Ga but H re-equilibration only takes months. In contrast, in the high-T garnet lherzolites (~ 1250 °C) Ti re-equilibration only takes 1 Ma, and H achieves re-equilibration in an hour. Evidence of this disparity is shown in the temperature dependence of Ti and H_2O partitioning between the two pyroxenes; $D_{H_2O}^{cpx-opx}$ varies with temperature following complete subsolidus re-equilibration but $D_{Ti}^{cpx-opx}$ is constant and reflects the partitoning behaviour during metasomatism. $D_{F}^{cpx-opx}$ also shows no apparent dependence on temperature, and F correlates very well with Ti in all three mineral phases. These observations are taken to show that: (i) Ti and F behave similarly during partitioning; and (ii) diffuse at similar rates. This

could be an artefact of their strong coupling in the crystal lattice, which affects incorporation (and hence partitioning) and diffusion.

Chapter 9 investigates the extrinsic controls on H_2O and F concentrations in NVFMMs, including pressure, temperature, metasomatism and oxygen fugacity. As mentioned above, Demouchy & Bolfan-Casanova (2016) and Peslier *et al.* (2010) identify a slight pressure dependence on H_2O concentration of olivine but not in orthopyroxene or clinopyroxene. In the Bultfontein and Mothae xenoliths there is a slight increase in clinopyroxene F concentration with depth but generally there is no systematic relationship with depth for H_2O or F concentration in any of the three phases. Instead, there appears to be a greater control by the composition of the metasomatic agent and an enriched zone is evident in the mid-lithosphere where the metasomatised xenoliths are concentrated. This metasomatic front in the mid-lithosphere has been identified in previous studies and the presence of metasomes of hydrous phases is known to increase the bulk H_2O and F concentrations. This study presents the first evidence that the pre-existing mantle minerals in this zone are also enriched in volatile elements.

Each metasomatic agent identified in Chapter 5 has a different control on the volatile concentrations. Carbonatite and proto-kimberlite metasomatism both have the ability to significantly enrich the mantle in volatiles by the precipitation of hydrous phases such as amphibole and phlogopite, however their effect on the NVFMMs varies according to the stage of melt evolution and the volume of the melt. Kimberlite metasomatism, by a silico-carbonatite melt, is shown to precipitate high F clinopyroxene (up to 46 ppm) as well as to significantly enrich pre-existing olivine and orthopyroxene during early stages of the evolution of the percolating melt. At this point the melt is still enriched in F, but, during later stages once phlogopite becomes stable, the equilibrium distribution of F changes and more F is incorporated into hydrous phases at the expense of the NVFMMs. An additional effect of the evolving melt composition is a change in the concentration of CO_2 in the melt. If CO_2 increases the incompatibility of F in a similar way to the REE then, as the kimberlite melt evolves and becomes more CO_2-rich, one would expect less F to be incorporated into the NVFMMs. This feature is observed in the clinopyroxene that precipitated as a result of carbonatite melt metasomatism, which has the lowest F and H_2O concentrations of all samples in this study. The shallow origin of the carbonatite metasomatised xenolith also increases the likelihood that the melt it interacted with had already fractionated abundant amphibole and phlogopite, which would have sequestered the H and F. The variable enrichment in NVFMMs from xenoliths that have been metasomatised by carbonatite and silico-carbonatite melts highlights the controls of melt evolution and local crystallising assemblage, but shows that proto-kimberlite metasomatism has the capacity to significantly enrich the SCLM in H_2O and F. Metasomes in the mid-lithosphere associated with kimberlite pre-conditioning of the mantle represent regions where volatiles are concentrated as stoichiometric components of hydrous phases and in addition, as this work has shown, in point defects in the crystal lattice of the pre-existing mantle minerals in and around metasomes.

Siliceous fluid metasomatism results in: (i) hydration of the mantle minerals; and (ii) the crystallisation of a small amount of phlogopite as a product of the reaction where fluid reacts with olivine to produce orthopyroxene. The modal abundance of orthopyroxene in the Si-enriched garnet harzburgites varies from 29 to 39% and is assumed to represent a proxy for the amount of fluid-rock reaction. The F concentration varies considerably within this style of metasomatism with a range of Δ20 ppm F in the pyroxenes and > Δ80 ppm in olivine. The F concentration in all three phases increases systematically with the modal

proportion of orthopyroxene, hence with the extent of fluid-rock reaction. The increased volume of fluid is presumed to be enriched in F and form a greater interconnected network within grain boundaries for diffusive exchange of F with pre-existing mantle minerals. Siliceous fluid metasomatism could be associated with slab fluids in the mantle wedge prior to craton formation, or from ancient recycled subducted material. Either scenario illustrates the longevity of a metasomatic signature in the volatile concentrations of the NVFMMs in addition to the more well-known trace-elements, for example a constant clinopyroxene Ti/F ratio exists within each category of peridotite. As established in Chapter 8, the diffusion and partitioning of Ti and F are very similar in the NVFMMs, and Ti has only equilibrated in a few of the high-T xenoliths. Therefore the constant Ti/F in clinopyroxene likely reflects the Ti/F of the metasomatic agent. The siliceous fluid metasomatised xenoliths have the lowest Ti/F ratio because Ti is immobile relative to F. The preservation of the fluid signatures, such as this, again exemplify the diffusion limiting nature of the coupling between Ti, F and H_2O.

Metasomatism can have another effect on volatile incorporation into olivine, orthopyroxene and clinopyroxene by altering the oxygen fugacity. Because both F and H are incorporated as charge balancing species in NVFMMs, there is a crucial role of coupled substitutions with trivalent and heterovalent cations. The oxidation of Fe^{2+} to Fe^{3+} in NVFMMs can be charge balanced by the incorporation of F or H_2O while the reverse reduction of Fe^{3+} to Fe^{2+} can be balanced by the incorporation of H_2. Oxidising fluids or melts are common metasomatic agents in the Kaapvaal mantle, especially in the Kimberley region (Creighton *et al.*, 2008), but reducing agents (e.g. CH_4) are expected to be more dominant towards the base of the lithosphere. In oxidising conditions it is expected that the incorporation of H_2O prevails over F, and vice versa in reducing conditions. The mantle is more reduced beneath northern Lesotho than Kimberley (Creighton *et al.*, 2008) and this could explain why the Mothae samples have higher F and lower H_2O concentrations than the Bultfontein xenoliths. The abundance of MARID and PIC xenoliths in the suites from Kimberley provide evidence for extensive metasomatism in the region by carbonatite and silico-carbonatite melts. The findings of this study suggest that the melt evolution during proto-kimberlite metasomatism and also its changing oxidation state control volatile incorporation. Kimberlites both preserve diamonds and precipitate carbonate which implies that the melt transitioned from reducing conditions into oxidising conditions during ascent. As the melt evolves, the incorporation of H_2O and F changes, at early (reduced) stages F is preferentially incorporated (e.g. enriched F in NVFMMs BD1153) and at later stages H_2O is preferentially incorporated (e.g. more hydrous minerals and lower F in BD3067).

The timing of metasomatism and volatile enrichment in the Kaapvaal sub-cratonic lithospheric mantle is tied together with the history of craton formation and evolution in Chapter 10 . The Kaapvaal craton formed between 3.5-2.6 Ga by the collision and accretion of oceanic terranes and continents. Melting beneath spreading centres and in sub-arc environments is proposed to have produced the low density residue that amalgamated and thickened over time to produce the thick lithospheric keel beneath the Kaapvaal craton. It is proposed that much of the fluid metasomatism that produced the Si-enrichment in Kaapvaal peridotites occurred in the mantle wedge, prior to the full construction of the craton. F-rich fluids were released from the slab, probably from serpentinite breakdown reactions, and reacted with the mantle wedge above. The Si-enrichment did not occur exclusively during this time, it is expected that fluid release from ancient recycled slabs occurred at later dates to further enrich the cratonic root in orthopyroxene, Si and volatiles.

An important period of volatile enrichment in the Kaapvaal craton occurred between Group II kimberlite magmatism between ~ 130-110 Ma and Group I kimberlite activity at 90-80 Ma. There is extensive evidence in the literature and also in this study (Chapters 5 and 10) that there was a change in the style and an increase in the extent of metasomatism between the phases of kimberlite activity. An increase in fertilisation (addition of clinopyroxene and garnet) at the base of the lithosphere was accompanied by pervasive metasomatism by more volatile-rich, silico-carbonatite melts in the mid-lithosphere. This produced a metasomatic zone between 35-45 kbar that became increasingly enriched in volatiles (hosted in hydrous phases and NVFMMs) over the 20-50 Ma year period sampled by the two generations of kimberlite. The addition of volatiles during this time has been estimated using the measured bulk H_2O and F concentrations associated with each metasomatic style, and the proportions of each in the mantle at the time of Group II and Group I activity (i.e. before and after extensive metasomatism). The results show that during Group II magmatism the SCLM had a bulk H_2O content of 48 ppmw and F of 22 ppm, and this increased to 62 ppmw and 36 ppm, respectively, by 90Ma. The increase in F storage is particularly high (+62%) because kimberlite metasomatism adds a significant amount of F to olivine and clinopyroxene. Chapter 10 presents an argument to suggest that this period of volatile-enrichment during kimberlite pre-conditioning was critical to feed the later 'successful' kimberlites with volatiles to aid their ascent. The modal metasomatism provides a lubricated pathway for later melts, while the increased H_2O and F concentrations in the mantle wall-rock lowers the solidus and enhances the assimilation of material and volatile elements into the ascending magma, all of which contribute to the fast, violent ascent of the host kimberlite.

The results from the calculations of the capacity of the SCLM as a reservoir in Chapter 10 provide a first approximation as to how metasomatism can introduce significant amounts of H_2O and F into the cratonic root over a relatively short time period. This has important implications for the long-term stability of the craton. Many studies have shown that hydration weakening of olivine increases the strain rate and the occurence of diffusion and dislocation creep. These rheological changes are also proposed to occur with the addition of halogens to the crystal lattice. Hydration of the SCLM, therefore, decreases its viscosity and stability and could lead to lithospheric thinning. According to this study, the majority of volatile enrichment appears to have occurred in the mid-lithosphere as opposed to the base of the lithosphere. Peslier *et al.* (2010) identify a dehydrated layer at the base of the lithosphere (> 180 km depth) where the olivine contain < 10 ppmw H_2O. They suggest that this layer provides a buffer to the rest of the lithospheric keel by establishing a substantial viscosity difference between the dry layer and the asthenosphere. The work in this study suggests that the storage of volatiles in the SCLM is highly temporally variable and hydration over a short time period following a thermal perturbation, for example, could increase the storage of H_2O and F in NVFMMs Thus would reduce the stability of the craton and potentially lead to lithospheric thinning.

11.1 Future Work

This thesis has presented the first analysis of halogen storage in the sub-cratonic lithospheric mantle and has highlighted a number of areas for future work:

1. FTIR was used on a small number of rock fragments. Preparation of larger sections of each fragment, which contain multiple whole mineral grains and can be pressed into indium for SIMS and double polished for FTIR, would improve core-rim analyses and investigations into partitioning behaviour. Additionally, it would allow for the cross-checking and calibration of FTIR and SIMS estimates of H_2O concentration by using both methods on the same grain. Additional FTIR analyses of more crystals are now required to provide a statistically robust dataset to further investigate the incorporation mechanisms.

2. Oxygen fugacity potentially exerts an important control on the H_2O and F concentrations of nominally volatile-free mantle minerals, and it would be very useful to assess the oxidation state of the Bultfontein and Mothae xenoliths, e.g. by analysing the Fe^{3+}/Fe^{2+} ratios using mössbauer spectroscopy.

3. The observations made from the database of xenoliths from the Kaapvaal has highlighted a change in metasomatism through time, which is associated with an increase in the bulk volatile concentration of the SCLM. It would be very interesting to analyse H_2O and F concentrations of xenoliths from older kimberlites to investigate the evolution of the mantle reservoir through time - e.g. Premier (1 Ga), Venetia (500 Ga), Group II (110 Ma). It would also be interesting to see if the same short length-scale variation in H_2O contents identified by Peslier *et al.* (2012) is also evident in the halogen contents. The initial observations from Mothae and Bultfontein in this study do imply that F concentrations vary spatially.

4. It is currently very difficult to identify the incorporation mechanisms of F in orthopyroxene using FTIR (in the same way is possible in olivine) due to a lack of experimental work in this field. It would therefore be useful for experiments to be conducted on F-doped orthopyroxene in FTIR to see whether there are any clumped hydroxyl-fluoride absorbance bands, such as those in olivine.

5. The diffusion of F in all NVFMM is completely unconstrained. This study suggests that F diffusion is slow, and limited by coupling with Ti and OH-groups. It would be interesting to conduct experiments to investigate this and constrain diffusion rates of F in NVFMM.

6. In order to investigate further the timing of metasomtic events, and their place in the evolution of the craton as a reservoir for volatiles, it would be beneficial to date metasomatic minerals in the Bultfontein and Mothae xenoliths - e.g. the orthopyroxene in the Si-fluid metasomatised xenoliths. This could be best achieved using radiogenic isotopes or by diffusion modelling if zoning is preserved in minerals.

References

Abersteiner, A., Kamenetsky, V. S., Kamenetsky, M., Goemann, K., Ehrig, K., & Rodemann, T., 2018. Significance of halogens (F, Cl) in kimberlite melts: Insights from mineralogy and melt inclusions in the Roger pipe (Ekati, Canada), *Chemical Geology*, **478**, 148–163.

Akaogi, M., 2007. Phase transitions of minerals in the transition zone and upper part of the lower mantle, *Special Papers-Geological Society Of America*, **421**, 1, Publisher: Boulder, Colo.; Geological Society of America; 1999.

Araujo, D. P., Gaspar, J. C., & Bizzi, L. A., 2001. Morphology and surface features of diamonds from the Juína Kimberlite province, Brazil, *Rev Bras Geo*, **31**(4), 605–615.

Arndt, N. T., Guitreau, M., Boullier, A.-M., Le Roex, A., Tommasi, A., Cordier, P., & Sobolev, A., 2010. Olivine, and the Origin of Kimberlite, *Journal of Petrology*, **51**(3), 573–602.

Asimow, P. D., Stein, L. C., Mosenfelder, J. L., & Rossman, G. R., 2006. Quantitative polarized infrared analysis of trace OH in populations of randomly oriented mineral grains, *American Mineralogist*, **91**(2-3), 278–284, Publisher: GeoScienceWorld.

Aubaud, C., Hauri, E. H., & Hirschmann, M. M., 2004. Hydrogen partition coefficients between nominally anhydrous minerals and basaltic melts, *Geophysical Research Letters*, **31**(20).

Aubaud, C., Withers, A. C., Hirschmann, M. M., Guan, Y., Leshin, L. A., Mackwell, S. J., & Bell, D. R., 2007. Intercalibration of FTIR and SIMS for hydrogen measurements in glasses and nominally anhydrous minerals, *American Mineralogist*, **92**(5-6), 811–828.

Aulbach, S., Mungall, J. E., & Pearson, D. G., 2016. Distribution and Processing of Highly Siderophile Elements in Cratonic Mantle Lithosphere, *Reviews in Mineralogy and Geochemistry*, **81**(1), 239–304.

Aulbach, S., Massuyeau, M., & Gaillard, F., 2017. Origins of cratonic mantle discontinuities: A view from petrology, geochemistry and thermodynamic models, *Lithos*, **268-271**, 364–382.

Aulbach, S., Sun, J., Tappe, S., Höfer, H. E., & Gerdes, A., 2017. Volatile-rich Metasomatism in the Cratonic Mantle beneath SW Greenland: Link to Kimberlites and Mid-lithospheric Discontinuities, *Journal of Petrology*, **58**(12), 2311–2338.

Bachmann, F., Hielscher, R., & Schaeben, H., 2010. Texture Analysis with MTEX – Free and Open Source Software Toolbox.

Ballentine, C. J. & Barfod, D. N., 2000. The origin of air-like noble gases in MORB and OIB, *Earth and Planetary Science Letters*, **180**(1), 39–48.

Ballentine, C. J. & Holland, G., 2008. What CO2 well gases tell us about the origin of noble gases in the mantle and their relationship to the atmosphere, *Philosophical Transactions of the Royal Society A: Mathematical, Physical and Engineering Sciences*, **366**(1883), 4183–4203, Publisher: Royal Society.

Banerjee, S., Kyser, T. K., & Mitchell, R. H., 2018. Oxygen and hydrogen isotopic composition of phlogopites and amphiboles in diamond-bearing kimberlite hosted MARID xenoliths: Constraints on fluid-rock interaction and recycled crustal material in the deep continental lithospheric mantle, *Chemical Geology*, **479**, 272–285.

Baptiste, V., Tommasi, A., & Demouchy, S., 2012. Deformation and hydration of the lithospheric mantle beneath the Kaapvaal craton, South Africa, *Lithos*, **149**, 31–50.

Barnes, S. J., Godel, B., Gürer, D., Brenan, J. M., Robertson, J., & Paterson, D., 2013. Sulfide-Olivine Fe-Ni Exchange and the Origin of Anomalously Ni Rich Magmatic Sulfides, *Economic Geology*, **108**(8), 1971–1982.

Bas, M. J. L. & Streckeisen, A. L., 1991. The IUGS systematics of igneous rocks, *Journal of the Geological Society*, **148**(5), 825–833.

Bebout, G. E., Ryan, J. G., Leeman, W. P., & Bebout, A. E., 1999. Fractionation of trace elements by subduction-zone metamorphism — effect of convergent-margin thermal evolution, *Earth and Planetary Science Letters*, **171**(1), 63–81.

Becker, M. & Roex, A. P. L., 2006. Geochemistry of South African On- and Off-craton, Group I and Group II Kimberlites: Petrogenesis and Source Region Evolution, *Journal of Petrology*, **47**(4), 673–703, Publisher: Oxford Academic.

Begg, G. C., Griffin, W. L., Natapov, L. M., O'Reilly, S. Y., Grand, S. P., O'Neill, C. J., Hronsky, J. M. A., Djomani, Y. P., Swain, C. J., Deen, T., & Bowden, P., 2009. The lithospheric architecture of Africa: Seismic tomography, mantle petrology, and tectonic evolutionThe lithospheric architecture of Africa, *Geosphere*, **5**(1), 23–50.

Bell, D. R. & Rossman, G. R., 1992. Water in Earth's Mantle: The Role of Nominally Anhydrous Minerals, *Science*, **255**(5050), 1391.

Bell, D. R., Rossman, G. R., Maldener, J., Endisch, D., & Rauch, F., 2003. Hydroxide in olivine: A quantitative determination of the absolute amount and calibration of the IR spectrum, *Journal of Geophysical Research: Solid Earth*, **108**(B2).

Bell, D. R., Schmitz, M. D., & Janney, P. E., 2003. Mesozoic thermal evolution of the southern African mantle lithosphere, *Lithos*, **71**(2), 273–287.

Bell, D. R., Rossman, G. R., & Moore, R. O., 2004. Abundance and Partitioning of OH in a High-pressure Magmatic System: Megacrysts from the Monastery Kimberlite, South Africa, *Journal of Petrology*, **45**(8), 1539–1564.

Bell, D. R., Grégoire, M., Grove, T. L., Chatterjee, N., Carlson, R. W., & Buseck, P. R., 2005. Silica and volatile-element metasomatism of Archean mantle: a xenolith-scale example from the Kaapvaal Craton, *Contributions to Mineralogy and Petrology*, **150**(3), 251.

Beran, A. & Libowitzky, E., 2006. Water in Natural Mantle Minerals II: Olivine, Garnet and Accessory Minerals, *Reviews in Mineralogy and Geochemistry*, **62**(1), 169–191.

Bernini, D., Wiedenbeck, M., Dolejš, D., & Keppler, H., 2013. Partitioning of halogens between mantle minerals and aqueous fluids: implications for the fluid flow regime in subduction zones, *Contributions to Mineralogy and Petrology*, **165**(1), 117–128.

Berry, A. J., Hermann, J., O'Neill, H. S. C., & Foran, G. J., 2005. Fingerprinting the water site in mantle olivine, *Geology*, **33**(11), 869–872.

Berry, A. J., O'Neill, H. S. C., Hermann, J., & Scott, D. R., 2007. The infrared signature of water associated with trivalent cations in olivine, *Earth and Planetary Science Letters*, **261**(1), 134–142.

Berry, A. J., Walker, A. M., Hermann, J., O'Neill, H. S. C., Foran, G. J., & Gale, J. D., 2007. Titanium substitution mechanisms in forsterite, *Chemical Geology*, **242**(1), 176–186.

Beyer, C., Klemme, S., Wiedenbeck, M., Stracke, A., & Vollmer, C., 2012. Fluorine in nominally fluorine-free mantle minerals: Experimental partitioning of F between olivine, orthopyroxene and silicate melts with implications for magmatic processes, *Earth and Planetary Science Letters*, **337-338**, 1–9.

Beyer, C., Klemme, S., Grützner, T., Ireland, T. R., Magee, C. W., & Frost, D. J., 2016. Fluorine partitioning between eclogitic garnet, clinopyroxene, and melt at upper mantle conditions, *Chemical Geology*, **437**, 88–97.

Bish, D. L., 1981. Cation ordering in synthetic and natural Ni-Mg olivine, *American Mineralogist*, **66**(7), 7.

Bizimis, M., Salters, V. J. M., & Dawson, J. B., 2003. The brevity of carbonatite sources in the mantle: evidence from Hf isotopes, *Contributions to Mineralogy and Petrology*, **145**(3), 281–300.

Blundy, J. & Wood, B., 1994. Prediction of crystal–melt partition coefficients from elastic moduli, *Nature*, **372**(6505), 452.

Blundy, J. & Wood, B., 2003. Partitioning of trace elements between crystals and melts, *Earth and Planetary Science Letters*, **210**(3-4), 383–397.

Bodnar, R. J., Azbej, T., Becker, S. P., Cannatelli, C., Fall, A., & Severs, M. J., 2013. Whole Earth geohydrologic cycle, from the clouds to the core: The distribution of water in the dynamic Earth system, *The Geological Society of America Special Paper*, **500**, 431–61.

Bonadiman, C., Hao, Y., Coltorti, M., Dallai, L., Faccini, B., Huang, Y., & Xia, Q., 2009. Water contents of pyroxenes in intraplate lithospheric mantle, *European Journal of Mineralogy*, **21**(3), 637–647.

Boström, D., 1989. Cation ordering at 1300 C in the (Ni, Mg)-olivine solid solution series, *Acta Chemica Scandinavica*, **43**, 116–120.

Boyd, F. R., 1973. A pyroxene geotherm, *Geochimica et Cosmochimica Acta*, **37**(12), 2533–2546.

Boyd, F. R., 1989. Compositional distinction between oceanic and cratonic lithosphere, *Earth and Planetary Science Letters*, **96**(1), 15–26.

Boyd, F. R. & Gurney, J. J., 1986. Diamonds and the African Lithosphere, *Science*, **232**(4749), 472–477, Publisher: American Association for the Advancement of Science Section: Articles.

Boyd, F. R. & Mertzman, S. A., 1987. Composition and structure of the Kaapvaal lithosphere, southern Africa, *Magmatic processes: physicochemical principles*, **1**, 3–12.

Boyd, F. R. & Nixon, P. H., 1973. Origin of the lherzolite nodules in the kimberlites of Northern Lesotho, in *International Kimberlite Conference: Extended Abstracts*, vol. 1, pp. 47–50.

Boyd, F. R. & Nixon, P. H., 1978. Ultramafic nodules from the Kimberley pipes, South Africa, *Geochimica et Cosmochimica Acta*, **42**, 1367.

Brady, J. B. & Cherniak, D. J., 2010. Diffusion in Minerals: An Overview of Published Experimental Diffusion Data, *Reviews in Mineralogy and Geochemistry*, **72**(1), 899–920.

Braithwaite, J. S., Wright, K., & Catlow, C. R. A., 2003. A theoretical study of the energetics and IR frequencies of hydroxyl defects in forsterite, *Journal of Geophysical Research: Solid Earth*, **108**(B6).

Brett, R. C., Russell, J. K., Andrews, G. D. M., & Jones, T. J., 2015. The ascent of kimberlite: Insights from olivine, *Earth and Planetary Science Letters*, **424**, 119–131.

Brey, G. P. & Köhler, T., 1990. Geothermobarometry in four-phase lherzolites II. New thermobarometers, and practical assessment of existing thermobarometers, *Journal of Petrology*, **31**(6), 1353–1378.

Brey, G. P., Köhler, T., & Nickel, K. G., 1990. Geothermobarometry in four-phase lherzolites I. Experimental results from 10 to 60 kb, *Journal of Petrology*, **31**(6), 1313–1352.

Brey, G. P., Bulatov, V. K., & Girnis, A. V., 2008. Geobarometry for Peridotites: Experiments in Simple and Natural Systems from 6 to 10 GPa, *Journal of Petrology*, **49**(1), 3–24, Publisher: Oxford Academic.

Brey, G. P., Bulatov, V. K., & Girnis, A. V., 2009. Influence of water and fluorine on melting of carbonated peridotite at 6 and 10 GPa, *Lithos*, **112, Supplement 1**, 249–259.

Broadley, M. W., Barry, P. H., Ballentine, C. J., Taylor, L. A., & Burgess, R., 2018. End-Permian extinction amplified by plume-induced release of recycled lithospheric volatiles, *Nature Geoscience*, **11**(9), 682–687, Number: 9 Publisher: Nature Publishing Group.

Brodholt, J. P. & Refson, K., 2000. An ab initio study of hydrogen in forsterite and a possible mechanism for hydrolytic weakening, *Journal of Geophysical Research: Solid Earth*, **105**(B8), 18977–18982.

Bromiley, D. W. & Kohn, S. C., 2007. Comparisons between fluoride and hydroxide incorporation in nominally anhydrous and fluorine-free mantle minerals, *Geochimica et Cosmochimica Acta*, **71**, A48–A138.

Brooker, R. A., Sparks, R. S. J., Kavanagh, J. L., & Field, M., 2011. The volatile content of hypabyssal kimberlite magmas: some constraints from experiments on natural rock compositions, *Bulletin of Volcanology*, **73**(8), 959–981.

Burgess, S. R. & Harte, B., 2004. Tracing lithosphere evolution through the analysis of heterogeneous G9–G10 garnets in peridotite xenoliths, II: REE chemistry, *Journal of Petrology*, **45**(3), 609–633.

Bussweiler, Y., Foley, S. F., Prelević, D., & Jacob, D. E., 2015. The olivine macrocryst problem: New insights from minor and trace element compositions of olivine from Lac de Gras kimberlites, Canada, *Lithos*, **220-223**(Supplement C), 238–252.

Bussweiler, Y., Stone, R. S., Pearson, D. G., Luth, R. W., Stachel, T., Kjarsgaard, B. A., & Menzies, A., 2016. The evolution of calcite-bearing kimberlites by melt-rock reaction: evidence from polymineralic inclusions within clinopyroxene and garnet megacrysts from Lac de Gras kimberlites, Canada, *Contributions to Mineralogy and Petrology*, **171**(7), 65.

Bussweiler, Y., Brey, G. P., Pearson, D. G., Stachel, T., Stern, R. A., Hardman, M. F., Kjarsgaard, B. A., & Jackson, S. E., 2017. The aluminum-in-olivine thermometer for mantle peridotites — Experimental versus empirical calibration and potential applications, *Lithos*, **272-273**, 301–314.

Bénard, A., Koga, K. T., Shimizu, N., Kendrick, M. A., Ionov, D. A., Nebel, O., & Arculus, R. J., 2017. Chlorine and fluorine partition coefficients and abundances in sub-arc mantle xenoliths (Kamchatka, Russia): Implications for melt generation and volatile recycling processes in subduction zones, *Geochimica et Cosmochimica Acta*, **199**, 324–350.

Bühn, B., Rankin, A. H., Schneider, J., & Dulski, P., 2002. The nature of orthomagmatic, carbonatitic fluids precipitating REE,Sr-rich fluorite: fluid-inclusion evidence from the Okorusu fluorite deposit, Namibia, *Chemical Geology*, **186**(1), 75–98.

Carswell, D. A., 1991. The garnet-orthopyroxene Al barometer: problematic application to natural garnet lherzolite assemblages, *Mineralogical Magazine*, **55**(378), 19–31, Publisher: Cambridge University Press.

Carswell, D. A. & Gibb, F. G. F., 1980. Geothermometry of garnet lherzolite nodules with special reference to those from the kimberlites of Northern Lesotho, *Contributions to Mineralogy and Petrology*, **74**(4), 403–416.

Carswell, D. A. & Gibb, F. G. F., 1987. Garnet lherzolite xenoliths in the kimberlites of northern Lesotho: revised P-T equilibration conditions and upper mantle Palaeogeotherm, *Contributions to Mineralogy and Petrology*, **97**(4), 473–487.

Chakraborty, S., 2010. Diffusion Coefficients in Olivine, Wadsleyite and Ringwoodite, *Reviews in Mineralogy and Geochemistry*, **72**(1), 603–639.

Cherniak, D. J. & Dimanov, A., 2010. Diffusion in Pyroxene, Mica and Amphibole, *Reviews in Mineralogy and Geochemistry*, **72**(1), 641–690.

Cherniak, D. J. & Liang, Y., 2007. Rare earth element diffusion in natural enstatite, *Geochimica et Cosmochimica Acta*, **71**(5), 1324–1340.

Cherniak, D. J. & Liang, Y., 2012. Ti diffusion in natural pyroxene, *Geochimica et Cosmochimica Acta*, **98**, 31–47.

Cherniak, D. J. & Liang, Y., 2014. Titanium diffusion in olivine, *Geochimica et Cosmochimica Acta*, **147**, 43–57.

Cordier, C., Sauzeat, L., Arndt, N. T., Boullier, A.-M., Batanova, V., & Barou, F., 2015. Metasomatism of the Lithospheric Mantle Immediately Precedes Kimberlite Eruption: New Evidence from Olivine Composition and Microstructures, *Journal of Petrology*, **56**(9), 1775–1796.

Costa, F. & Morgan, D., 2010. Time Constraints from Chemical Equilibration in Magmatic Crystals, in *Timescales of Magmatic Processes*, pp. 125–159, Wiley-Blackwell.

Crank, J., 1956. *The Mathematics of Diffusion*, Oxford University Press, Oxford.

Creighton, S., Stachel, T., Matveev, S., Höfer, H., McCammon, C., & Luth, R. W., 2008. Oxidation of the Kaapvaal lithospheric mantle driven by metasomatism, *Contributions to Mineralogy and Petrology*, **157**(4), 491.

Creighton, S., Stachel, T., Eichenberg, D., & Luth, R. W., 2010. Oxidation state of the lithospheric mantle beneath Diavik diamond mine, central Slave craton, NWT, Canada, *Contributions to Mineralogy and Petrology*, **159**(5), 645–657.

Crépisson, C., Blanchard, M., Bureau, H., Sanloup, C., Withers, A. C., Khodja, H., Surblé, S., Raepsaet, C., Béneut, K., Leroy, C., Giura, P., & Balan, E., 2014. Clumped fluoride-hydroxyl defects in forsterite: Implications for the upper-mantle, *Earth and Planetary Science Letters*, **390**, 287–295.

Dai, L. & Karato, S.-i., 2009. Electrical conductivity of pyrope-rich garnet at high temperature and high pressure, *Physics of the Earth and Planetary Interiors*, **176**(1), 83–88.

Dalou, C., Koga, K. T., Shimizu, N., Boulon, J., & Devidal, J.-L., 2012. Experimental determination of F and Cl partitioning between lherzolite and basaltic melt, *Contributions to Mineralogy and Petrology*, **163**(4), 591–609.

Dalou, C., Koga, K. T., Le Voyer, M., & Shimizu, N., 2014. Contrasting partition behavior of F and Cl during hydrous mantle melting: implications for Cl/F signature in arc magmas, *Progress in Earth and Planetary Science*, **1**(1), 26.

Dasgupta, R., 2018. Volatile-bearing partial melts beneath oceans and continents–Where, how much, and of what compositions?, *American Journal of Science*, **318**(1), 141–165.

Dasgupta, R. & Hirschmann, M. M., 2006. Melting in the Earth's deep upper mantle caused by carbon dioxide, *Nature*, **440**(7084), 659–662.

Dasgupta, R. & Hirschmann, M. M., 2010. The deep carbon cycle and melting in Earth's interior, *Earth and Planetary Science Letters*, **298**(1–2), 1–13.

Dasgupta, R., Hirschmann, M. M., McDonough, W. F., Spiegelman, M., & Withers, A. C., 2009. Trace element partitioning between garnet lherzolite and carbonatite at 6.6 and 8.6 GPa with applications to the geochemistry of the mantle and of mantle-derived melts, *Chemical Geology*, **262**(1), 57–77.

Dasgupta, R., Mallik, A., Tsuno, K., Withers, A. C., Hirth, G., & Hirschmann, M. M., 2013. Carbon-dioxide-rich silicate melt in the Earth's upper mantle, *Nature*, **493**(7431), 211–215.

Davis, G. L., 1977. The ages and uranium contents of zircons from kimberlites and associated rocks, in *International Kimberlite Conference: Extended Abstracts*, vol. 2, pp. 67–69.

Dawson, J., Hill, P., & Kinny, P., 2001. Mineral chemistry of a zircon-bearing, composite, veined and metasomatised upper-mantle peridotite xenolith from kimberlite, *Contributions to Mineralogy and Petrology*, **140**(6), 720–733.

Dawson, J. B., 1971. Advances in kimberlite geology, *Earth-Science Reviews*, **7**(4), 187–214.

Dawson, J. B., 1984. Contrasting types of upper mantle metasomatism., in *Kimberlites II: the mantle and crust-mantle relationships.*, Elsevier, Amsterdam.

Dawson, J. B., 2004. A fertile harzburgite–garnet lherzolite transition: possible inferences for the roles of strain and metasomatism in upper mantle peridotites, *Lithos*, **77**(1), 553–569.

Dawson, J. B., 2012. *Kimberlites and Their Xenoliths*, Springer Science & Business Media, Google-Books-ID: 6HYoBgAAQBAJ.

Dawson, J. B. & Smith, J. V., 1977. The MARID (mica-amphibole-rutile-ilmenite-diopside) suite of xenoliths in kimberlite, *Geochimica et Cosmochimica Acta*, **41**(2), 309–323.

Dawson, J. B. & Stephens, W. E., 1976. Statistical Classification of Garnets from Kimberlite and Associated Xenoliths: Addendum, *The Journal of Geology*, **84**(4), 495–496.

De Hoog, J. C. M., Gall, L., & Cornell, D. H., 2010. Trace-element geochemistry of mantle olivine and application to mantle petrogenesis and geothermobarometry, *Chemical Geology*, **270**(1), 196–215.

De Wit, M. J., de Ronde, C. E., Tredoux, M., Roering, C., Hart, R. J., Armstrong, R. A., Green, R. W., Peberdy, E., & Hart, R. A., 1992. Formation of an Archaean continent, *Nature*, **357**(6379), 553.

Debret, B., Nicollet, C., Andreani, M., Schwartz, S., & Godard, M., 2013. Three steps of serpentinization in an eclogitized oceanic serpentinization front (Lanzo Massif – Western Alps), *Journal of Metamorphic Geology*, **31**(2), 165–186, _eprint: https://onlinelibrary.wiley.com/doi/pdf/10.1111/jmg.12008.

Debret, B., Koga, K. T., Nicollet, C., Andreani, M., & Schwartz, S., 2014. F, Cl and S input via serpentinite in subduction zones: implications for the nature of the fluid released at depth, *Terra Nova*, **26**(2), 96–101.

Demouchy, S. & Bolfan-Casanova, N., 2016. Distribution and transport of hydrogen in the lithospheric mantle: A review, *Lithos*, **240-243**, 402–425.

Demouchy, S. & Mackwell, S., 2006. Mechanisms of hydrogen incorporation and diffusion in iron-bearing olivine, *Physics and Chemistry of Minerals*, **33**(5), 347–355.

Dohmen, R. & Chakraborty, S., 2007. Fe–Mg diffusion in olivine II: point defect chemistry, change of diffusion mechanisms and a model for calculation of diffusion coefficients in natural olivine, *Physics and Chemistry of Minerals*, **34**(6), 409–430.

Dorendorf, F., Wiechert, U., & Wörner, G., 2000. Hydrated sub-arc mantle: a source for the Kluchevskoy volcano, Kamchatka/Russia, *Earth and Planetary Science Letters*, **175**(1), 69–86.

Doucet, L. S., Peslier, A. H., Ionov, D. A., Brandon, A. D., Golovin, A. V., Goncharov, A. G., & Ashchepkov, I. V., 2014. High water contents in the Siberian cratonic mantle linked to metasomatism: An FTIR study of Udachnaya peridotite xenoliths, *Geochimica et Cosmochimica Acta*, **137**, 159–187.

Drury, M. R. & Roermund, H. L. M. v., 1988. Metasomatic origin for Fe-Ti-rich multiphase inclusions in olivine from kimberlite xenoliths, *Geology*, **16**(11), 1035–1038.

Eaton, D. W., Darbyshire, F., Evans, R. L., Grütter, H., Jones, A. G., & Yuan, X., 2009. The elusive lithosphere–asthenosphere boundary (LAB) beneath cratons, *Lithos*, **109**(1), 1–22.

Fabbrizio, A., Stalder, R., Hametner, K., & Günther, D., 2013. Experimental chlorine partitioning between forsterite, enstatite and aqueous fluid at upper mantle conditions, *Geochimica et Cosmochimica Acta*, **121**, 684–700.

Fabbrizio, A., Stalder, R., Hametner, K., Günther, D., & Marquardt, K., 2013. Experimental partitioning of halogens and other trace elements between olivine, pyroxenes, amphibole and aqueous fluid at 2 GPa and 900–1,300 °C, *Contributions to Mineralogy and Petrology*, **166**(2), 639–653.

Falus, G., Tommasi, A., Ingrin, J., & Szabó, C., 2008. Deformation and seismic anisotropy of the lithospheric mantle in the southeastern Carpathians inferred from the study of mantle xenoliths, *Earth and Planetary Science Letters*, **272**(1), 50–64.

Fan, W. M., Zhang, H. F., Baker, J., Jarvis, K. E., Mason, P. R. D., & Menzies, M. A., 2000. On and Off the North China Craton: Where is the Archaean Keel?, *Journal of Petrology*, **41**(7), 933–950.

Faure, S., 2010. *World Kimberlites CONSOREM Database*, Version.

Field, M., Gernon, T. M., Mock, A., Walters, A., Sparks, R. S. J., & Jerram, D. A., 2009. Variations of olivine abundance and grain size in the Snap Lake kimberlite intrusion, Northwest Territories, Canada: A possible proxy for diamonds, *Lithos*, **112**, 23–35.

Finnerty, A. A. & Boyd, F. R., 1984. Evaluation of thermobarometers for garnet peridotites, *Geochimica et Cosmochimica Acta*, **48**(1), 15–27.

Finnerty, A. A. & Boyd, F. R., 1987. Thermobarometry for garnet peridotites:basis for the determination of thermal and compositional structure of the upper mantle, *Mantle Xenolith*, pp. 403–412.

Fishwick, S., 2010. Surface wave tomography: Imaging of the lithosphere–asthenosphere boundary beneath central and southern Africa?, *Lithos*, **120**(1), 63–73.

Fitzpayne, A., Giuliani, A., Hergt, J., Phillips, D., & Janney, P., 2018. New geochemical constraints on the origins of MARID and PIC rocks: Implications for mantle metasomatism and mantle-derived potassic magmatism, *Lithos*, **318-319**, 478–493.

Fitzpayne, A., Giuliani, A., Phillips, D., Hergt, J., Woodhead, J. D., Farquhar, J., Fiorentini, M. L., Drysdale, R. N., & Wu, N., 2018. Kimberlite-related metasomatism recorded in MARID and PIC mantle xenoliths, *Mineralogy and Petrology*, pp. 1–14.

Fitzpayne, A., Giuliani, A., Maas, R., Hergt, J., Janney, P., & Phillips, D., 2019. Progressive metasomatism of the mantle by kimberlite melts: Sr–Nd–Hf–Pb isotope compositions of MARID and PIC minerals, *Earth and Planetary Science Letters*, **509**, 15–26.

Foley, S. F., 2011. A Reappraisal of Redox Melting in the Earth's Mantle as a Function of Tectonic Setting and Time, *Journal of Petrology*, **52**(7-8), 1363–1391.

Foley, S. F., Taylor, W. R., & Green, D. H., 1986. The role of fluorine and oxygen fugacity in the genesis of the ultrapotassic rocks, *Contributions to Mineralogy and Petrology*, **94**(2), 183–192.

Foley, S. F., Yaxley, G. M., Rosenthal, A., Buhre, S., Kiseeva, E. S., Rapp, R. P., & Jacob, D. E., 2009. The composition of near-solidus melts of peridotite in the presence of CO2 and H2O between 40 and 60 kbar, *Lithos*, **112, Supplement 1**, 274–283.

Foley, S. F., Yaxley, G. M., & Kjarsgaard, B. A., 2019. Kimberlites from Source to Surface: Insights from Experiments, *Elements*, **15**(6), 393–398.

Frost, D. J. & McCammon, C. A., 2008. The Redox State of Earth's Mantle, *Annual Review of Earth and Planetary Sciences*, **36**(1), 389–420.

Férot, A. & Bolfan-Casanova, N., 2012. Water storage capacity in olivine and pyroxene to 14GPa: Implications for the water content of the Earth's upper mantle and nature of seismic discontinuities, *Earth and Planetary Science Letters*, **349-350**, 218–230.

Förster, M. W., Foley, S. F., Marschall, H. R., Alard, O., & Buhre, S., 2019. Melting of sediments in the deep mantle produces saline fluid inclusions in diamonds, *Science Advances*, **5**(5), eaau2620, Publisher: American Association for the Advancement of Science Section: Research Article.

Gaetani, G. A. & Grove, T. L., 1998. The influence of water on melting of mantle peridotite, *Contributions to Mineralogy and Petrology*, **131**(4), 323–346.

Gao, S., Liu, X., Yuan, H., Hattendorf, B., Günther, D., Chen, L., & Hu, S., 2002. Determination of Forty Two Major and Trace Elements in USGS and NIST SRM Glasses by Laser Ablation-Inductively Coupled Plasma-Mass Spectrometry, *Geostandards Newsletter*, **26**(2), 181–196, _eprint: https://onlinelibrary.wiley.com/doi/pdf/10.1111/j.1751-908X.2002.tb00886.x.

Gervasoni, F., Klemme, S., Rohrbach, A., Grützner, T., & Berndt, J., 2017. Experimental constraints on the stability of baddeleyite and zircon in carbonate- and silicate-carbonate melts, *American Mineralogist*, **102**(4), 860–866.

Gibson, S. A. & Mills, S., 2017. On the nature and origin of garnet in highly-refractory Archean lithospheric mantle: constraints from garnet exsolved in Kaapvaal craton orthopyroxenes, *Mineralogical Magazine*, **81**(4), 781–809, Publisher: GeoScienceWorld.

Gibson, S. A., Malarkey, J., & Day, J. A., 2008. Melt Depletion and Enrichment beneath the Western Kaapvaal Craton: Evidence from Finsch Peridotite Xenoliths, *Journal of Petrology*, **49**(10), 1817–1852.

Gibson, S. A., McMahon, S. C., Day, J. A., & Dawson, J. B., 2013. Highly Refractory Lithospheric Mantle beneath the Tanzanian Craton: Evidence from Lashaine Pre-metasomatic Garnet-bearing Peridotites, *Journal of Petrology*, **54**(8), 1503–1546.

Gibson, S. A., Rooks, E. E., Day, J. A., Petrone, C. M., & Leat, P. T., 2020. The role of sub-continental mantle as both "sink" and "source" in deep Earth volatile cycles, *Geochimica et Cosmochimica Acta*, **275**, 140–162.

Gittins, J., Allen, C. R., & Cooper, A. F., 1975. Phlogopitization of pyroxenite; its bearing on the composition of carbonatite magmas, *Geological Magazine*, **112**(5), 503–507.

Giuliani, A., 2018. Insights into kimberlite petrogenesis and mantle metasomatism from a review of the compositional zoning of olivine in kimberlites worldwide, *Lithos*, **312-313**, 322–342.

Giuliani, A. & Pearson, D. G., 2019. Kimberlites: From Deep Earth to Diamond Mines, *Elements*, **15**(6), 377–380, Publisher: GeoScienceWorld.

Giuliani, A., Kamenetsky, V. S., Kendrick, M. A., Phillips, D., & Goemann, K., 2013. Nickel-rich metasomatism of the lithospheric mantle by pre-kimberlitic alkali-S–Cl-rich C–O–H fluids, *Contributions to Mineralogy and Petrology*, **165**(1), 155–171.

Giuliani, A., Kamenetsky, V. S., Kendrick, M. A., Phillips, D., Wyatt, B. A., & Maas, R., 2013. Oxide, sulphide and carbonate minerals in a mantle polymict breccia: Metasomatism by proto-kimberlite magmas, and relationship to the kimberlite megacrystic suite, *Chemical Geology*, **353**, 4–18.

Giuliani, A., Phillips, D., Kamenetsky, V. S., Kendrick, M. A., Wyatt, B. A., Goemann, K., & Hutchinson, G., 2014. Petrogenesis of Mantle Polymict Breccias: Insights into Mantle Processes Coeval with Kimberlite Magmatism, *Journal of Petrology*, **55**(4), 831–858.

Giuliani, A., Phillips, D., Maas, R., Woodhead, J. D., Kendrick, M. A., Greig, A., Armstrong, R. A., Chew, D., Kamenetsky, V. S., & Fiorentini, M. L., 2014. LIMA U–Pb ages link lithospheric mantle metasomatism to Karoo magmatism beneath the Kimberley region, South Africa, *Earth and Planetary Science Letters*, **401**(Supplement C), 132–147.

Giuliani, A., Phillips, D., Woodhead, J. D., Kamenetsky, V. S., Fiorentini, M. L., Maas, R., Soltys, A., & Armstrong, R. A., 2015. Did diamond-bearing orangeites originate from MARID-veined peridotites in the lithospheric mantle?, *Nature Communications*, **6**, 6837.

Giuliani, A., Phillips, D., Kamenetsky, V. S., & Goemann, K., 2016. Constraints on kimberlite ascent mechanisms revealed by phlogopite compositions in kimberlites and mantle xenoliths, *Lithos*, **240-243**, 189–201.

Giuliani, A., Soltys, A., Phillips, D., Kamenetsky, V. S., Maas, R., Goemann, K., Woodhead, J. D., Drysdale, R. N., & Griffin, W. L., 2017. The final stages of kimberlite petrogenesis: Petrography, mineral chemistry, melt inclusions and Sr-C-O isotope geochemistry of the Bultfontein kimberlite (Kimberley, South Africa), *Chemical Geology*, **455**, 342–356.

Goldschmidt, V. M., 1937. The principles of distribution of chemical elements in minerals and rocks. The seventh Hugo Müller Lecture, delivered before the Chemical Society on March 17th, 1937, *Journal of the Chemical Society (Resumed)*, (0), 655–673.

Golovin, A. V., Sharygin, I. S., Korsakov, A. V., Kamenetsky, V. S., & Abersteiner, A., 2019. Can primitive kimberlite melts be alkali-carbonate liquids: Composition of the melt snapshots preserved in deepest mantle xenoliths, *Journal of Raman Spectroscopy*, **n/a**(n/a), _eprint: https://onlinelibrary.wiley.com/doi/pdf/10.1002/jrs.5701.

Goncharov, A. G. & Ionov, D. A., 2012. Redox state of deep off-craton lithospheric mantle: new data from garnet and spinel peridotites from Vitim, southern Siberia, *Contributions to Mineralogy and Petrology*, **164**(5), 731–745.

Grant, K., Ingrin, J., Lorand, J. P., & Dumas, P., 2007. Water partitioning between mantle minerals from peridotite xenoliths, *Contributions to Mineralogy and Petrology*, **154**(1), 15–34.

Green, D. H., 1973. Experimental melting studies on a model upper mantle composition at high pressure under water-saturated and water-undersaturated conditions, *Earth and Planetary Science Letters*, **19**(1), 37–53.

Green, D. H. & Wallace, M. E., 1988. Mantle metasomatism by ephemeral carbonatite melts, *Nature*, **336**(6198), 459–462.

Green, D. H., Falloon, T. J., & Taylor, W. R., 1987. Mantle-derived magmas-roles of variable source peridotite and variable CHO fluid compositions.

Green, T. H., Adam, J., & Siel, S. H., 1992. Trace element partitioning between silicate minerals and carbonatite at 25 kbar and application to mantle metasomatism, *Mineralogy and Petrology*, **46**(3), 179–184.

Griffin, W. L., Smith, D., Boyd, F. R., Cousens, D. R., Ryan, C. G., Sie, S. H., & Suter, G. F., 1989. Trace-element zoning in garnets from sheared mantle xenoliths, *Geochimica et Cosmochimica Acta*, **53**(2), 561–567.

Griffin, W. L., Smith, D., Ryan, C. G., O'Reilly, S. Y., & Win, T. T., 1996. Trace-element zoning in mantle minerals; metasomatism and thermal events in the upper mantle, *The Canadian Mineralogist*, **34**(6), 1179–1193.

Griffin, W. L., Fisher, N. I., Friedman, J., Ryan, C. G., & O'Reilly, S. Y., 1999. Cr-Pyrope Garnets in the Lithospheric Mantle. I. Compositional Systematics and Relations to Tectonic Setting, *Journal of Petrology*, **40**(5), 679–704.

Griffin, W. L., Shee, S. R., Ryan, C. G., Win, T. T., & Wyatt, B. A., 1999. Harzburgite to lherzolite and back again: metasomatic processes in ultramafic xenoliths from the Wesselton kimberlite, Kimberley, South Africa, *Contributions to Mineralogy and Petrology*, **134**(2), 232–250.

Griffin, W. L., Fisher, N. I., Friedman, J. H., O'Reilly, S. Y., & Ryan, C. G., 2002. Cr-pyrope garnets in the lithospheric mantle 2. Compositional populations and their distribution in time and space, *Geochemistry, Geophysics, Geosystems*, **3**(12), 1–35.

Griffin, W. L., O'Reilly, S. Y., Natapov, L. M., & Ryan, C. G., 2003. The evolution of lithospheric mantle beneath the Kalahari Craton and its margins, *Lithos*, **71**(2), 215–241.

Griffin, W. L., Graham, S., O'Reilly, S. Y., & Pearson, N. J., 2004. Lithosphere evolution beneath the Kaapvaal Craton: Re–Os systematics of sulfides in mantle-derived peridotites, *Chemical Geology*, **208**(1), 89–118.

Griffin, W. L., O'Reilly, S. Y., Afonso, J. C., & Begg, G. C., 2009. The Composition and Evolution of Lithospheric Mantle: a Re-evaluation and its Tectonic Implications, *Journal of Petrology*, **50**(7), 1185–1204.

Griffin, W. L., Batumike, J. M., Greau, Y., Pearson, N. J., Shee, S. R., & O'Reilly, S. Y., 2014. Emplacement ages and sources of kimberlites and related rocks in southern Africa: U–Pb ages and Sr–Nd isotopes of groundmass perovskite, *Contributions to Mineralogy and Petrology*, **168**(1), 1032.

Griffin, W. L., Batumike, J. M., Greau, Y., Pearson, N. J., Shee, S. R., & O'Reilly, S. Y., 2014. Emplacement ages and sources of kimberlites and related rocks in southern Africa: U–Pb ages and Sr–Nd isotopes of groundmass perovskite, *Contributions to Mineralogy and Petrology*, **168**(1), 1032.

Grégoire, M., Bell, D., & Le Roex, A., 2002. Trace element geochemistry of phlogopite-rich mafic mantle xenoliths: their classification and their relationship to phlogopite-bearing peridotites and kimberlites revisited, *Contributions to Mineralogy and Petrology*, **142**(5), 603–625.

Grégoire, M., Tinguely, C., Bell, D. R., & le Roex, A. P., 2005. Spinel lherzolite xenoliths from the Premier kimberlite (Kaapvaal craton, South Africa): Nature and evolution of the shallow upper mantle beneath the Bushveld complex, *Lithos*, **84**(3), 185–205.

Grütter, H., Latti, D., & Menzies, A., 2006. Cr-Saturation Arrays in Concentrate Garnet Compositions from Kimberlite and their Use in Mantle Barometry, *Journal of Petrology*, **47**(4), 801–820.

Grütter, H. S., 2009. Pyroxene xenocryst geotherms: Techniques and application, *Lithos*, **112**, 1167–1178.

Grützner, T., Kohn, S. C., Bromiley, D. W., Rohrbach, A., Berndt, J., & Klemme, S., 2017. The storage capacity of fluorine in olivine and pyroxene under upper mantle conditions, *Geochimica et Cosmochimica Acta*, **208**, 160–170.

Gubanov, N., Zedgenizov, D., Sharygin, I., & Ragozin, A., 2019. Origin and Evolution of High-Mg Carbonatitic and Low-Mg Carbonatitic to Silicic High-Density Fluids in Coated Diamonds from Udachnaya Kimberlite Pipe, *Minerals*, **9**(12), 734, Number: 12 Publisher: Multidisciplinary Digital Publishing Institute.

Guggino, S., 2012. *Fluorine Partitioning Between Nominally Anhydrous Minerals (Olivine, Clinopyroxene, and Plagioclase) and Silicate Melt using Secondary Ion Mass Spectrometry and Newly Synthesized Basaltic Fluorine Microanalytical Glass Standards*, Ph.D., Arizona State University, United States – Arizona.

Gurney, J. J., Harte, B., Bailey, D. K., Tarney, J., & Dunham, K. C., 1980. Chemical variations in upper mantle nodules from southern African kimberlites, *Philosophical Transactions of the Royal Society of London. Series A, Mathematical and Physical Sciences*, **297**(1431), 273–293.

Gérard, O. & Jaoul, O., 1989. Oxygen diffusion in San Carlos olivine, *Journal of Geophysical Research: Solid Earth*, **94**(B4), 4119–4128.

Halliday, A. N., 2013. The origins of volatiles in the terrestrial planets, *Geochimica et Cosmochimica Acta*, **105**, 146–171.

Hanger, B. J., Yaxley, G. M., Berry, A. J., & Kamenetsky, V. S., 2015. Relationships between oxygen fugacity and metasomatism in the Kaapvaal subcratonic mantle, represented by garnet peridotite xenoliths in the Wesselton kimberlite, South Africa, *Lithos*, **212-215**, 443–452.

Hanyu, T. & Nakamura, E., 2000. Constraints on HIMU and EM by Sr and Nd isotopes re-examined, *Earth, Planets and Space*, **52**(1), 61–70.

Harley, S. L., 1984. An experimental study of the partitioning of Fe and Mg between garnet and orthopyroxene, *Contributions to Mineralogy and Petrology*, **86**(4), 359–373.

Hart, S. R. & Dunn, T., 1993. Experimental cpx/melt partitioning of 24 trace elements, *Contributions to Mineralogy and Petrology*, **113**(1), 1–8.

Hart, S. R. & Staudigel, H., 1989. Isotopic Characterization and Identification of Recycled Components, in *Crust/Mantle Recycling at Convergence Zones*, edited by S. R. Hart & L. Gülen, NATO ASI Series, pp. 15–28, Springer Netherlands, Dordrecht.

Harte, B., 1977. Rock Nomenclature with Particular Relation to Deformation and Recrystallisation Textures in Olivine-Bearing Xenoliths, *The Journal of Geology*, **85**(3), 279–288.

Harte, B., 1983. Mantle peridotites and processes: the kimberlite sample. In: Hawkesworth CJ, Norry MJ (eds) . Shiva, Nantwich, in *Continental basalts and their xenoliths*, Shiva, Nantwich.

Hauri, E. H., Gaetani, G. A., & Green, T. H., 2006. Partitioning of water during melting of the Earth's upper mantle at H2O-undersaturated conditions, *Earth and Planetary Science Letters*, **248**(3), 715–734.

Heaman, L. M., Phillips, D., & Pearson, G., 2019. Dating Kimberlites: Methods and Emplacement Patterns Through Time, *Elements*, **15**(6), 399–404.

Helmstaedt, H. & Schulze, D. J., 1989. Southern African kimberlites and their mantle sample: implications for Archean tectonics and lithosphere evolution, *Kimberlites and related rocks*, **1**, 358–368.

Hervig, R. L. & Bell, D. R., 2005. Fluorine and Hydrogen in Mantle Megacrysts, *AGU Fall Meeting Abstracts*, **41**, V41A–1426.

Hin, R. C., Morel, M. L. A., Nebel, O., Mason, P. R. D., van Westrenen, W., & Davies, G. R., 2009. Formation and temporal evolution of the Kalahari sub-cratonic lithospheric mantle: Constraints from Venetia xenoliths, South Africa, *Lithos*, **112**, 1069–1082.

Hirschmann, M. M., 2000. Mantle solidus: Experimental constraints and the effects of peridotite composition, *Geochemistry, Geophysics, Geosystems*.

Hirth, G. & Kohlstedf, D., 2003. Rheology of the upper mantle and the mantle wedge: A view from the experimentalists, *GEOPHYSICAL MONOGRAPH-AMERICAN GEOPHYSICAL UNION*, **138**, 83–106, Publisher: AGU AMERICAN GEOPHYSICAL UNION.

Hoal, K. E. O., Hoal, B. G., Erlank, A. J., & Shimizu, N., 1994. Metasomatism of the mantle lithosphere recorded by rare earth elements in garnets, *Earth and Planetary Science Letters*, **126**(4), 303–313.

Holzapfel, C., Chakraborty, S., Rubie, D. C., & Frost, D. J., 2007. Effect of pressure on Fe–Mg, Ni and Mn diffusion in (FexMg1x)2SiO4 olivine, *Physics of the Earth and Planetary Interiors*, **162**(3), 186–198.

Houlier, B., Jaoul, O., Abel, F., & Liebermann, R. C., 1988. Oxygen and silicon self-diffusion in natural olivine at T = 1300°C, *Physics of the Earth and Planetary Interiors*, **50**(3), 240–250.

Hui, H., Xu, Y., & Pan, M., 2016. On water in nominally anhydrous minerals from mantle peridotites and magmatic rocks, *Science China Earth Sciences*, **59**(6), 1157–1172.

Hwang, Y. K., Ritsema, J., & Goes, S., 2011. Global variation of body-wave attenuation in the upper mantle from teleseismic P wave and S wave spectra, *Geophysical Research Letters*, **38**(8), _eprint: https://agupubs.onlinelibrary.wiley.com/doi/pdf/10.1029/2011GL046812.

Höfer, H. E., Lazarov, M., Brey, G. P., & Woodland, A. B., 2009. Oxygen fugacity of the metasomatizing melt in a polymict peridotite from Kimberley, *Lithos*, **112**, 1150–1154.

Ingrin, J. & Blanchard, M., 2006. Diffusion of Hydrogen in Minerals, *Reviews in Mineralogy and Geochemistry*, **62**(1), 291–320.

Ingrin, J. & Grégoire, M., 2010. Water partitioning in spinel and garnet lherzolites xenoliths from the same kimberlite pipe (Premier Mine, Kaapvaal, South Africa)., **12**, 13028, Conference Name: EGU General Assembly Conference Abstracts.

Ionov, D. A., Bodinier, J.-L., Mukasa, S. B., & Zanetti, A., 2002. Mechanisms and Sources of Mantle Metasomatism: Major and Trace Element Compositions of Peridotite Xenoliths from Spitsbergen in the Context of Numerical Modelling, *Journal of Petrology*, **43**(12), 2219–2259.

Ito, E., Harris, D. M., & Anderson Jr, A. T., 1983. Alteration of oceanic crust and geologic cycling of chlorine and water, *Geochimica et Cosmochimica Acta*, **47**(9), 1613–1624, Publisher: Pergamon.

Ito, M. & Ganguly, J., 2006. Diffusion kinetics of Cr in olivine and 53Mn–53Cr thermochronology of early solar system objects, *Geochimica et Cosmochimica Acta*, **70**(3), 799–809.

Izraeli, E. S., Harris, J. W., & Navon, O., 2004. Fluid and mineral inclusions in cloudy diamonds from Koffiefontein, South Africa, *Geochimica et Cosmochimica Acta*, **68**(11), 2561–2575.

Jackson, A., Parker, R. L., Sambridge, M., Constable, C., & Wolf, A. S., 2018. The inverse problem of unpolarized infrared spectroscopy of geological materials: Estimation from noisy random sampling of a quadratic form, *American Mineralogist*, **103**(8), 1176–1184.

Jackson, C. G. & Gibson, S. A., 2018. Preservation of systematic Ni and Cr heterogeneity in otherwise homogeneous mantle olivine: Implications for timescales of post-metasomatism re-equilibration, *Lithos*, **318-319**, 448–463.

Jacob, D. E., Viljoen, K. S., & Grassineau, N. V., 2009. Eclogite xenoliths from Kimberley, South Africa — A case study of mantle metasomatism in eclogites, *Lithos*, **112**, 1002–1013.

Jago, B. C. & Gittins, J., 1991. The role of fluorine in carbonatite magma evolution, *Nature*, **349**(6304), 56–58.

Jago, J. & Gittins, B. C. ., 1993. Pyrochlore crystallization in carbonatites: the role of fluorine, *South African Journal of Geology*, **96**(3), 149–160.

Jelsma, H., Barnett, W., Richards, S., & Lister, G., 2009. Tectonic setting of kimberlites, *Lithos*, **112**, 155–165.

Joachim, B., Pawley, A., Lyon, I. C., Marquardt (neé Hartmann), K., Henkel, T., Clay, P. L., Ruzié, L., Burgess, R., & Ballentine, C. J., 2015. Experimental partitioning of F and Cl between olivine, orthopyroxene and silicate melt at Earth's mantle conditions, *Chemical Geology*, **416**, 65–78.

Jochum, K. P., Willbold, M., Raczek, I., Stoll, B., & Herwig, K., 2005. Chemical Characterisation of the USGS Reference Glasses GSA-1G, GSC-1G, GSD-1G, GSE-1G, BCR-2G, BHVO-2G and BIR-1G Using EPMA, ID-TIMS, ID-ICP-MS and LA-ICP-MS, *Geostandards and Geoanalytical Research*, **29**(3), 285–302, _eprint: https://onlinelibrary.wiley.com/doi/pdf/10.1111/j.1751-908X.2005.tb00901.x.

John, T., Scherer, E. E., Haase, K., & Schenk, V., 2004. Trace element fractionation during fluid-induced eclogitization in a subducting slab: trace element and Lu–Hf–Sm–Nd isotope systematics, *Earth and Planetary Science Letters*, **227**(3), 441–456.

John, T., Scambelluri, M., Frische, M., Barnes, J. D., & Bach, W., 2011. Dehydration of subducting serpentinite: Implications for halogen mobility in subduction zones and the deep halogen cycle, *Earth and Planetary Science Letters*, **308**(1), 65–76.

Johnson, K. T., Dick, H. J., & Shimizu, N., 1990. Melting in the oceanic upper mantle: an ion microprobe study of diopsides in abyssal peridotites, *Journal of Geophysical Research: Solid Earth*, **95**(B3), 2661–2678.

Jollands, M. C., Padrón-Navarta, J. A., Hermann, J., & O'Neill, H. S. C., 2016. Hydrogen diffusion in Ti-doped forsterite and the preservation of metastable point defects, *American Mineralogist*, **101**(7), 1571–1583.

Jollands, M. C., O'Neill, H. S. C., Van Orman, J., Berry, A. J., Hermann, J., Newville, M., & Lanzirotti, A., 2017. Substitution and diffusion of Cr2+ and Cr3+ in synthetic forsterite and natural olivine at 1200-1500 °C and 1 bar, *Geochimica et Cosmochimica Acta*.

Jollands, M. C., Hanger, B. J., Yaxley, G. M., Hermann, J., & Kilburn, M. R., 2018. Timescales between mantle metasomatism and kimberlite ascent indicated by diffusion profiles in garnet crystals from peridotite xenoliths, *Earth and Planetary Science Letters*, **481**, 143–153.

Jordan, T. H., 1975. The continental tectosphere, *Reviews of Geophysics*, **13**(3), 1–12.

Kamenetsky, M. B., Sobolev, A. V., Kamenetsky, V. S., Maas, R., Danyushevsky, L. V., Thomas, R., Pokhilenko, N. P., & Sobolev, N. V., 2004. Kimberlite melts rich in alkali chlorides and carbonates: A potent metasomatic agent in the mantle, *Geology*, **32**(10), 845–848, Publisher: GeoScienceWorld.

Kamenetsky, V. S. & Yaxley, G. M., 2015. Carbonate–silicate liquid immiscibility in the mantle propels kimberlite magma ascent, *Geochimica et Cosmochimica Acta*, **158**, 48–56.

Kamenetsky, V. S., Maas, R., Kamenetsky, M. B., Paton, C., Phillips, D., Golovin, A. V., & Gornova, M. A., 2009. Chlorine from the mantle: Magmatic halides in the Udachnaya-East kimberlite, Siberia, *Earth and Planetary Science Letters*, **285**(1), 96–104.

Kamenetsky, V. S., Kamenetsky, M. B., Golovin, A. V., Sharygin, V. V., & Maas, R., 2012. Ultrafresh salty kimberlite of the Udachnaya–East pipe (Yakutia, Russia): A petrological oddity or fortuitous discovery?, *Lithos*, **152**, 173–186.

Kamenetsky, V. S., Grütter, H., Kamenetsky, M. B., & Gömann, K., 2013. Parental carbonatitic melt of the Koala kimberlite (Canada): Constraints from melt inclusions in olivine and Cr-spinel, and groundmass carbonate, *Chemical Geology*, **353**, 96–111.

Kamenetsky, V. S., Golovin, A. V., Maas, R., Giuliani, A., Kamenetsky, M. B., & Weiss, Y., 2014. Towards a new model for kimberlite petrogenesis: Evidence from unaltered kimberlites and mantle minerals, *Earth-Science Reviews*, **139**, 145–167.

Karato, S., 1990. The role of hydrogen in the electrical conductivity of the upper mantle, *Nature*, **347**(6290), 272–273, Number: 6290 Publisher: Nature Publishing Group.

Katayama, I., Jung, H., & Karato, S.-i., 2004. New type of olivine fabric from deformation experiments at modest water content and low stress, *Geology*, **32**(12), 1045–1048, Publisher: GeoScienceWorld.

Kats, A., Haven, Y., & Stevels, J. M., 1962. Hydroxyl groups in -quartz, *Phys. Chem. Glasses*, **3**(3), 69–75.

Kelemen, P. B., Dick, H. J., & Quick, J. E., 1992. Formation of harzburgite by pervasive melt/rock reaction in the upper mantle, *Nature*, **358**(6388), 635.

Kelemen, P. B., Hart, S. R., & Bernstein, S., 1998. Silica enrichment in the continental upper mantle via melt/rock reaction, *Earth and Planetary Science Letters*, **164**(1), 387–406.

Kendrick, M. A., Woodhead, J. D., & Kamenetsky, V. S., 2012. Tracking halogens through the subduction cycle, *Geology*, **40**(12), 1075–1078.

Keshav, S., Corgne, A., Gudfinnsson, G. H., Bizimis, M., McDonough, W. F., & Fei, Y., 2005. Kimberlite petrogenesis: Insights from clinopyroxene-melt partitioning experiments at 6 GPa in the CaO-MgO-Al2O3-SiO2-CO2 system, *Geochimica et Cosmochimica Acta*, **69**(11), 2829–2845.

Khisina, N. R., Wirth, R., Andrut, M., & Ukhanov, A. V., 2001. Extrinsic and intrinsic mode of hydrogen occurrence in natural olivines: FTIR and TEM investigation, *Physics and Chemistry of Minerals*, **28**(5), 291–301.

Kilgore, M. L., Peslier, A. H., Brandon, A. D., & Lamb, W. M., 2018. Water and Oxygen Fugacity in the Lithospheric Mantle Wedge beneath the Northern Canadian Cordillera (Alligator Lake), *Geochemistry, Geophysics, Geosystems*, **19**(10), 3844–3869.

Kinny, P. D. & Dawson, J., 1992. A mantle metasomatic injection event linked to late Cretaceous kimberlite magmatism, *Nature*, **360**.

Kjarsgaard, B. A., Pearson, D. G., Tappe, S., Nowell, G. M., & Dowall, D. P., 2009. Geochemistry of hypabyssal kimberlites from Lac de Gras, Canada: Comparisons to a global database and applications to the parent magma problem, *Lithos*, **112**, 236–248.

Klein-BenDavid, O., Izraeli, E. S., Hauri, E., & Navon, O., 2004. Mantle fluid evolution—a tale of one diamond, *Lithos*, **77**(1-4), 243–253.

Klein-BenDavid, O., Izraeli, E. S., Hauri, E., & Navon, O., 2007. Fluid inclusions in diamonds from the Diavik mine, Canada and the evolution of diamond-forming fluids, *Geochimica et Cosmochimica Acta*, **71**(3), 723–744.

Klein-BenDavid, O., Logvinova, A. M., Schrauder, M., Spetius, Z. V., Weiss, Y., Hauri, E. H., Kaminsky, F. V., Sobolev, N. V., & Navon, O., 2009. High-Mg carbonatitic microinclusions in some Yakutian diamonds—a new type of diamond-forming fluid, *Lithos*, **112, Supplement 2**, 648–659.

Klemme, S., 2004. Evidence for fluoride melts in Earth's mantle formed by liquid immiscibility, *Geology*, **32**(5), 441–444.

Klemme, S., van der Laan, S. R., Foley, S. F., & Günther, D., 1995. Experimentally determined trace and minor element partitioning between clinopyroxene and carbonatite melt under upper mantle conditions, *Earth and Planetary Science Letters*, **133**(3), 439–448.

Kobussen, A. F., Griffin, W. L., O'Reilly, S. Y., & Shee, S. R., 2008. Ghosts of lithospheres past: Imaging an evolving lithospheric mantle in southern Africa, *Geology*, **36**(7), 515–518.

Kobussen, A. F., Griffin, W. L., & O'Reilly, S. Y., 2009. Cretaceous thermo-chemical modification of the Kaapvaal cratonic lithosphere, South Africa, *Lithos*, **112**, 886–895.

Koga, K., Hauri, E., Hirschmann, M., & Bell, D., 2003. Hydrogen concentration analyses using SIMS and FTIR: comparison and calibration for nominally anhydrous minerals, *Geochemistry, Geophysics, Geosystems*, **4**(2).

Kogiso, T., Tatsumi, Y., Shimoda, G., & Barsczus, H. G., 1997. High (HIMU) ocean island basalts in southern Polynesia: New evidence for whole mantle scale recycling of subducted oceanic crust, *Journal of Geophysical Research: Solid Earth*, **102**(B4), 8085–8103, _eprint: https://agupubs.onlinelibrary.wiley.com/doi/pdf/10.1029/96JB03892.

Kohlstedt, D. L., 2006. The Role of Water in High-Temperature Rock Deformation, *Reviews in Mineralogy and Geochemistry*, **62**(1), 377–396, Publisher: GeoScienceWorld.

Kohlstedt, D. L. & Mackwell, S. J., 1998. Diffusion of Hydrogen and Intrinsic Point Defects in Olivine, *Zeitschrift für Physikalische Chemie*, **207**(1-2), 147–162.

Konzett, J., Armstrong, R. A., Sweeney, R. J., & Compston, W., 1998. The timing of MARID metasomatism in the Kaapvaal mantle: An ion probe study of zircons from MARID xenoliths, *Earth and Planetary Science Letters*, **160**(1–2), 133–145.

Konzett, J., Armstrong, R. A., & Günther, D., 2000. Modal metasomatism in the Kaapvaal craton lithosphere: constraints on timing and genesis from U–Pb zircon dating of metasomatized peridotites and MARID-type xenoliths, *Contributions to Mineralogy and Petrology*, **139**(6), 704–719.

Konzett, J., Wirth, R., Hauzenberger, C., & Whitehouse, M., 2013. Two episodes of fluid migration in the Kaapvaal Craton lithospheric mantle associated with Cretaceous kimberlite activity: Evidence from a harzburgite containing a unique assemblage of metasomatic zirconium-phases, *Lithos*, **182-183**(Supplement C), 165–184.

Kopylova, M. G., Matveev, S., & Raudsepp, M., 2007. Searching for parental kimberlite melt, *Geochimica et Cosmochimica Acta*, **71**(14), 3616–3629.

Kovács, I., O'Neill, H. S. C., Hermann, J., & Hauri, E. H., 2010. Site-specific infrared O-H absorption coefficients for water substitution into olivine, *American Mineralogist*, **95**(2-3), 292–299.

Kovács, I., Green, D. H., Rosenthal, A., Hermann, J., O'neill, H. S. C., Hibberson, W. O., & Udvardi, B., 2012. An Experimental Study of Water in Nominally Anhydrous Minerals in the Upper Mantle near the Water-saturated Solidus, *Journal of Petrology*, **53**(10), 2067–2093.

Kramers, J. D., Roddick, J. C. M., & Dawson, J. B., 1983. Trace element and isotope studies on veined, metasomatic and "MARID" xenoliths from Bultfontein, South Africa., *Earth and Planetary Science Letters*, **65**(1), 90–106.

Kumamoto, K. M., Warren, J. M., & Hauri, E. H., 2017. New SIMS reference materials for measuring water in upper mantle minerals, *American Mineralogist*, **102**(3), 537–547, Publisher: GeoScienceWorld.

Kurosawa, M., Yurimoto, H., & Sueno, S., 1997. Patterns in the hydrogen and trace element compositions of mantle olivines, *Physics and Chemistry of Minerals*, **24**(6), 385–395.

Lazarov, M., Brey, G. P., & Weyer, S., 2009. Time steps of depletion and enrichment in the Kaapvaal craton as recorded by subcalcic garnets from Finsch (SA), *Earth and Planetary Science Letters*, **279**(1), 1–10.

Lazarov, M., Brey, G. P., & Weyer, S., 2012. Evolution of the South African mantle — A case study of garnet peridotites from the Finsch diamond mine (Kaapvaal craton); part 1: Inter-mineral trace element and isotopic equilibrium, *Lithos*, **154**, 193–209.

Le Maitre, R. W., Streckeisen, A., & Zanettin, B., 2004. *Igneous rocks: IUGS classification and glossary: recommendations of the International Union of Geological Sciences, Subcommission on the Systematics of Igneous Rock*, University of Cambridge.

Lee, H. Y. & Ganguly, J., 1988. Equilibrium Compositions of Coexisting Garnet and Orthopyroxene: Experimental Determinations in the System FeO-MgO-Al2O3-SiO2, and Applications, *Journal of Petrology*, **29**(1), 93–113.

Leitch, C., Steele, I., Hutcheon, I., & Smith, J. V., 1979. Minor Elements in Pallasites: Zoning in Springwater Olivine, *LUNAR AND PLANETARY SCIENCE X*, pp. 716–718.

Li, Q.-L., Li, X.-H., Liu, Y., Wu, F.-Y., Yang, J.-H., & Mitchell, R. H., 2010. Precise U–Pb and Th–Pb age determination of kimberlitic perovskites by secondary ion mass spectrometry, *Chemical Geology*, **269**(3), 396–405.

Li, Y., Yang, X., Yu, J.-H., & Cai, Y.-F., 2016. Unusually high electrical conductivity of phlogopite: the possible role of fluorine and geophysical implications, *Contributions to Mineralogy and Petrology*, **171**(4), 37.

Li, Y., Jiang, H., & Yang, X., 2017. Fluorine follows water: Effect on electrical conductivity of silicate minerals by experimental constraints from phlogopite, *Geochimica et Cosmochimica Acta*, **217**, 16–27.

Li, Z.-X. A., Lee, C.-T. A., Peslier, A. H., Lenardic, A., & Mackwell, S. J., 2008. Water contents in mantle xenoliths from the Colorado Plateau and vicinity: Implications for the mantle rheology and hydration-induced thinning of continental lithosphere, *Journal of Geophysical Research: Solid Earth*, **113**(B9).

Liang, Y., 2014. Time scales of diffusive re-equilibration in bi-mineralic systems with and without a fluid or melt phase, *Geochimica et Cosmochimica Acta*, **132**, 274–287.

Liang, Y., Sun, C., & Yao, L., 2013. A REE-in-two-pyroxene thermometer for mafic and ultramafic rocks, *Geochimica et Cosmochimica Acta*, **102**, 246–260.

Liao, J., Wang, Q., Gerya, T., & Ballmer, M. D., 2017. Modeling Craton Destruction by Hydration-Induced Weakening of the Upper Mantle, *Journal of Geophysical Research: Solid Earth*, **122**(9), 7449–7466, _eprint: https://agupubs.onlinelibrary.wiley.com/doi/pdf/10.1002/2017JB014157.

Liati, A., Franz, L., Gebauer, D., & Fanning, C. M., 2004. The timing of mantle and crustal events in South Namibia, as defined by SHRIMP-dating of zircon domains from a garnet peridotite xenolith of the Gibeon Kimberlite Province, *Journal of African Earth Sciences*, **39**(3), 147–157.

Libowitzky, E. & Beran, A., 1995. OH defects in forsterite, *Physics and Chemistry of Minerals*, **22**(6), 387–392.

Libowitzky, E. & Beran, A., 2006. The Structure of Hydrous Species in Nominally Anhydrous Minerals: Information from Polarized IR Spectroscopy, *Reviews in Mineralogy and Geochemistry*, **62**(1), 29–52, Publisher: GeoScienceWorld.

Libowitzky, E. & Rossman, G. R., 1997. An IR absorption calibration for water in minerals, *American Mineralogist*, **82**(11-12), 1111–1115, Publisher: Mineralogical Society of America.

Lim, E., Giuliani, A., Phillips, D., & Goemann, K., 2018. Origin of complex zoning in olivine from diverse, diamondiferous kimberlites and tectonic settings: Ekati (Canada), Alto Paranaiba (Brazil) and Kaalvallei (South Africa), *Mineralogy and Petrology*, pp. 1–16.

Lock, N. P. & Dawson, J. B., 2013. Contrasting Garnet Lherzolite Xenolith Suites from the Letšeng Kimberlite Pipes: Inferences for the Northern Lesotho Geotherm, in *Proceedings of 10th International Kimberlite Conference*, edited by D. G. Pearson, H. S. Grütter, J. W. Harris, B. A. Kjarsgaard, H. O'Brien, N. V. C. Rao, & S. Sparks, pp. 29–44, Springer India, New Delhi.

Lorand, J.-P. & Grégoire, M., 2006. Petrogenesis of base metal sulphide assemblages of some peridotites from the Kaapvaal craton (South Africa), *Contributions to Mineralogy and Petrology*, **151**(5), 521.

MacGregor, I. D., 1974. The System MgO-Ai2O3-Si02: Solubility of Ai2O3 in Enstatite for Spinel and Garnet Peridotite Compositions, *American Mineralogist*, **59**(1-2), 110–119.

Mackwell, S. J. & Kohlstedt, D. L., 1990. Diffusion of hydrogen in olivine: Implications for water in the mantle, *Journal of Geophysical Research: Solid Earth*, **95**(B4), 5079–5088.

Mackwell, S. J., Kohlstedt, D. L., & Paterson, M. S., 1985. The role of water in the deformation of olivine single crystals, *Journal of Geophysical Research: Solid Earth*, **90**(B13), 11319–11333, _eprint: https://agupubs.onlinelibrary.wiley.com/doi/pdf/10.1029/JB090iB13p11319.

Marshall, E. W., Lassiter, J. C., & Barnes, J. D., 2018. On the (mis)behavior of water in the mantle: Controls on nominally anhydrous mineral water content in mantle peridotites, *Earth and Planetary Science Letters*, **499**, 219–229.

Martin, R. F. & Donnay, G., 1972. Hydroxyl in the mantle, *American Mineralogist*, **57**(3-4_Part_1), 554–570, Publisher: GeoScienceWorld.

Mather, K. A., Pearson, D. G., McKenzie, D., Kjarsgaard, B. A., & Priestley, K., 2011. Constraints on the depth and thermal history of cratonic lithosphere from peridotite xenoliths, xenocrysts and seismology, *Lithos*, **125**(1), 729–742.

Matsumoto, T., Chen, Y., & Matsuda, J.-i., 2001. Concomitant occurrence of primordial and recycled noble gases in the Earth's mantle, *Earth and Planetary Science Letters*, **185**(1), 35–47.

Matveev, S., O'neill, H. S. C., Ballhaus, C., Taylor, W. R., & Green, D. H., 2001. Effect of Silica Activity on OH IR Spectra of Olivine: Implications for Low-aSiO2 Mantle Metasomatism, *Journal of Petrology*, **42**(4), 721–729.

Matveev, S., Portnyagin, M., Ballhaus, C., Brooker, R., & Geiger, C. A., 2005. FTIR Spectrum of Phenocryst Olivine as an Indicator of Silica Saturation in Magmas, *Journal of Petrology*, **46**(3), 603–614.

McCammon, C. A., Griffin, W. L., Shee, S. R., & O'Neill, H. S. C., 2001. Oxidation during metasomatism in ultramafic xenoliths from the Wesselton kimberlite, South Africa: implications for the survival of diamond, *Contributions to Mineralogy and Petrology*, **141**(3), 287.

McDonough, W. F. & Sun, S.-S., 1995. The composition of the Earth, *Chemical geology*, **120**(3-4), 223–253.

McKenzie, D., 1989. Some remarks on the movement of small melt fractions in the mantle, *Earth and Planetary Science Letters*, **95**(1), 53–72.

McKenzie, D. & Bickle, M. J., 1988. The Volume and Composition of Melt Generated by Extension of the Lithosphere, *Journal of Petrology*, **29**(3), 625–679, Publisher: Oxford Academic.

McKenzie, D. & Priestley, K., 2016. Speculations on the formation of cratons and cratonic basins, *Earth and Planetary Science Letters*, **435**, 94–104.

Menzies, M., Xu, Y., Zhang, H., & Fan, W., 2007. Integration of geology, geophysics and geochemistry: A key to understanding the North China Craton, *Lithos*, **96**(1), 1–21.

Menzies, M. A., Fan, W., & Zhang, M., 1993. Palaeozoic and Cenozoic lithoprobes and the loss of >120 km of Archaean lithosphere, Sino-Korean craton, China, *Geological Society, London, Special Publications*, **76**(1), 71–81.

Miller, W. G. R., Holland, T. J. B., & Gibson, S. A., 2016. Garnet and Spinel Oxybarometers: New Internally Consistent Multi-equilibria Models with Applications to the Oxidation State of the Lithospheric Mantle, *Journal of Petrology*, **57**(6), 1199–1222.

Mitchell, R. H., 1984. Garnet lherzolites from the Hanaus-I and Louwrensia kimberlites of Namibia, *Contributions to Mineralogy and Petrology*, **86**(2), 178–188.

Mitchell, R. H., 1991. Kimberlites and lamproites: Primary sources of diamond., *Geoscience Canada*, **18**.

Mitchell, R. H., 2008. Peridotite Xenoliths and the Dynamics of Kimberlite Intrusion - The Mantle Sample: Inclusion in Kimberlites and Other Volcanics - Mercier - Wiley Online Library, *Journal of Volcanology and Geothermal Research*, **174**.

Miyamoto, M. & Takeda, H., 1983. Atomic diffusion coefficients calculated for transition metals in olivine, *Nature*, **303**(5918), 602–603.

Mosenfelder, J. L. & Rossman, G. R., 2013. Analysis of hydrogen and fluorine in pyroxenes: I. Orthopyroxene, *American Mineralogist*, **98**(5-6), 1026–1041.

Mosenfelder, J. L. & Rossman, G. R., 2013. Analysis of hydrogen and fluorine in pyroxenes: II. Clinopyroxene, *American Mineralogist*, **98**(5-6), 1042–1054.

Mosenfelder, J. L., Voyer, M. L., Rossman, G. R., Guan, Y., Bell, D. R., Asimow, P. D., & Eiler, J. M., 2011. Analysis of hydrogen in olivine by SIMS: Evaluation of standards and protocol, *American Mineralogist*, **96**(11-12), 1725–1741.

Munoz, J. L. & Eugster, H. P., 1969. Experimental control of fluorine reactions in hydrothermal systems, *American Mineralogist*, **54**(5-6), 943–959.

Mysen, B. O., 2007. The solution behavior of H2O in peralkaline aluminosilicate melts at high pressure with implications for properties of hydrous melts, *Geochimica et Cosmochimica Acta*, **71**(7), 1820–1834.

Mysen, B. O. & Cody, G. D., 2004. Solubility and solution mechanism of H2O in alkali silicate melts and glasses at high pressure and temperature, *Geochimica et Cosmochimica Acta*, **68**(24), 5113–5126.

Mysen, B. O., Virgo, D., & Seifert, F. A., 1982. The structure of silicate melts: Implications for chemical and physical properties of natural magma, *Reviews of Geophysics*, **20**(3), 353–383, _eprint: https://agupubs.onlinelibrary.wiley.com/doi/pdf/10.1029/RG020i003p00353.

Navon, O. & Stolper, E., 1987. Geochemical Consequences of Melt Percolation: The Upper Mantle as a Chromatographic Column, *The Journal of Geology*, **95**(3), 285–307.

Navon, O., Hutcheon, I. D., Rossman, G. R., & Wasserburg, G. J., 1988. Mantle-derived fluids in diamond micro-inclusions, *Nature*, **335**(6193), 784–789.

Nestola, F. & Smyth, J. R., 2016. Diamonds and water in the deep Earth: a new scenario, *International Geology Review*, **58**(3), 263–276, Publisher: Taylor & Francis _eprint: https://doi.org/10.1080/00206814.2015.1056758.

Nickel, K. G. & Green, D. H., 1985. Empirical geothermobarometry for garnet peridotites and implications for the nature of the lithosphere, kimberlites and diamonds, *Earth and Planetary Science Letters*, **73**(1), 158–170.

Nimis, P. & Grütter, H., 2010. Internally consistent geothermometers for garnet peridotites and pyroxenites, *Contributions to Mineralogy and Petrology*, **159**(3), 411–427.

Nimis, P. & Taylor, W. R., 2000. Single clinopyroxene thermobarometry for garnet peridotites. Part I. Calibration and testing of a Cr-in-Cpx barometer and an enstatite-in-Cpx thermometer, *Contributions to Mineralogy and Petrology*, **139**(5), 541–554.

Nimis, P., Alvaro, M., Nestola, F., Angel, R. J., Marquardt, K., Rustioni, G., Harris, J. W., & Marone, F., 2016. First evidence of hydrous silicic fluid films around solid inclusions in gem-quality diamonds, *Lithos*, **260**, 384–389.

Nixon, P. H., 1973. Petrogenesis of the granular and sheared ultrabasic nodule suite in Kimberlites, *Lesotho Kimberlites*, pp. 48–56.

Novella, D., Frost, D. J., Hauri, E. H., Bureau, H., Raepsaet, C., & Roberge, M., 2014. The distribution of H2O between silicate melt and nominally anhydrous peridotite and the onset of hydrous melting in the deep upper mantle, *Earth and Planetary Science Letters*, **400**, 1–13.

Nowell, G. M., Pearson, D. G., Bell, D. R., Carlson, R. W., Smith, C. B., Kempton, P. D., & Noble, S. R., 2004. Hf Isotope Systematics of Kimberlites and their Megacrysts: New Constraints on their Source Regions, *Journal of Petrology*, **45**(8), 1583–1612.

Nyblade, A. A. & Pollack, H. N., 1993. A global analysis of heat flow from Precambrian terrains: Implications for the thermal structure of Archean and Proterozoic lithosphere, *Journal of Geophysical Research: Solid Earth*, **98**(B7), 12207–12218, _eprint: https://agupubs.onlinelibrary.wiley.com/doi/pdf/10.1029/93JB00521.

O'Leary, J. A., Gaetani, G. A., & Hauri, E. H., 2010. The effect of tetrahedral Al3+ on the partitioning of water between clinopyroxene and silicate melt, *Earth and Planetary Science Letters*, **297**(1-2), 111–120, Publisher: Elsevier.

O'Neill, C. J., Lenardic, A., Griffin, W. L., & O'Reilly, S. Y., 2008. Dynamics of cratons in an evolving mantle, *Lithos*, **102**(1), 12–24.

O'Reilly, S. Y. & Griffin, W. L., 2006. Imaging global chemical and thermal heterogeneity in the subcontinental lithospheric mantle with garnets and xenoliths: Geophysical implications, *Tectonophysics*, **416**(1–4), 289–309.

O'Reilly, S. Y. & Griffin, W. L., 2010. The continental lithosphere–asthenosphere boundary: Can we sample it?, *Lithos*, **120**(1), 1–13.

O'Reilly, S. Y. & Griffin, W. L., 2013. Mantle metasomatism, in *Metasomatism and the chemical transformation of rock*, pp. 471–533, Springer.

Padrón-Navarta, J. A., Hermann, J., & O'Neill, H. S. C., 2014. Site-specific hydrogen diffusion rates in forsterite, *Earth and Planetary Science Letters*, **392**, 100–112.

Padrón-Navarta, J. A. & Hermann, J., 2017. A Subsolidus Olivine Water Solubility Equation for the Earth's Upper Mantle, *Journal of Geophysical Research: Solid Earth*, **122**(12), 9862–9880.

Parsons, B. & Sclater, J. G., 1977. An analysis of the variation of ocean floor bathymetry and heat flow with age, *Journal of Geophysical Research (1896-1977)*, **82**(5), 803–827, _eprint: https://agupubs.onlinelibrary.wiley.com/doi/pdf/10.1029/JB082i005p00803.

Paterson, M., 1982. The determination of hydroxyl by infrared absorption in quartz, silicate glasses and similar materials, *Bulletin de Minéralogie*, **105**(1), 20–29, Publisher: Persée - Portail des revues scientifiques en SHS.

Paul, D. K., Buckley, F., & Nixon, P. H., 1976. Fluorine and chlorine geochemistry of kimberlites, *Chemical Geology*, **17**, 125–133.

Pearson, D. G. & Wittig, N., 2008. Formation of Archaean continental lithosphere and its diamonds: the root of the problem, *Journal of the Geological Society*, **165**(5), 895–914.

Pearson, D. G. & Wittig, N., 2014. The formation and evolution of cratonic mantle lithosphere–evidence from mantle xenoliths, Publisher: Elsevier.

Pearson, D. G., Carlson, R. W., Shirey, S. B., Boyd, F. R., & Nixon, P. H., 1995. Stabilisation of Archaean lithospheric mantle: A ReOs isotope study of peridotite xenoliths from the Kaapvaal craton, *Earth and Planetary Science Letters*, **134**(3), 341–357.

Pearson, D. G., Shirey, S. B., Carlson, R. W., Boyd, F. R., Pokhilenko, N. P., & Shimizu, N., 1995. Re-Os, Sm-Nd, and Rb-Sr isotope evidence for thick Archaean lithospheric mantle beneath the Siberian craton modified by multistage metasomatism, *Geochimica et Cosmochimica Acta*, **59**(5), 959–977.

Pearson, D. G., Canil, D., & Shirey, S. B., 2003. Mantle Samples Included in Volcanic Rocks: Xenoliths and Diamonds, *Treatise on Geochemistry*, **2**, 568.

Pearson, D. G., Woodhead, J., & Janney, P. E., 2019. Kimberlites as Geochemical Probes of Earth's Mantle, *Elements*, **15**(6), 387–392.

Peslier, A. H., 2010. A review of water contents of nominally anhydrous natural minerals in the mantles of Earth, Mars and the Moon, *Journal of Volcanology and Geothermal Research*, **197**(1), 239–258.

Peslier, A. H., Luhr, J. F., & Post, J., 2002. Low water contents in pyroxenes from spinel-peridotites of the oxidized, sub-arc mantle wedge, *Earth and Planetary Science Letters*, **201**(1), 69–86.

Peslier, A. H., Woodland, A. B., Bell, D. R., & Lazarov, M., 2010. Olivine water contents in the continental lithosphere and the longevity of cratons, *Nature*, **467**(7311), 78–81.

Peslier, A. H., Woodland, A. B., Bell, D. R., Lazarov, M., & Lapen, T. J., 2012. Metasomatic control of water contents in the Kaapvaal cratonic mantle, *Geochimica et Cosmochimica Acta*, **97**, 213–246.

Peslier, A. H., Bizimis, M., & Matney, M., 2015. Water disequilibrium in olivines from Hawaiian peridotites: Recent metasomatism, H diffusion and magma ascent rates, *Geochimica et Cosmochimica Acta*, **154**, 98–117.

Peslier, A. H., Schönbächler, M., Busemann, H., & Karato, S.-I., 2017. Water in the Earth's Interior: Distribution and Origin, *Space Science Reviews*, **212**(1), 743–810.

Petry, C., Chakraborty, S., & Palme, H., 2004. Experimental determination of Ni diffusion coefficients in olivine and their dependence on temperature, composition, oxygen fugacity, and crystallographic orientation, *Geochimica et Cosmochimica Acta*, **68**(20), 4179–4188.

Pilbeam, L. H., Nielsen, T. F. D., & Waight, T. E., 2013. Digestion Fractional Crystallization (DFC): an Important Process in the Genesis of Kimberlites. Evidence from Olivine in the Majuagaa Kimberlite, Southern West Greenland, *Journal of Petrology*, **54**(7), 1399–1425.

Pilet, S., Baker, M. B., Müntener, O., & Stolper, E. M., 2011. Monte Carlo Simulations of Metasomatic Enrichment in the Lithosphere and Implications for the Source of Alkaline Basalts, *Journal of Petrology*, **52**(7-8), 1415–1442.

Plank, T. & Kelley, K., 2001. Contrasting Sediment Input and Output at the Izu and Mariana Subduction Factories, *AGU Fall Meeting Abstracts*, **22**, T22D–10.

Poe, B. T., Romano, C., Nestola, F., & Smyth, J. R., 2010. Electrical conductivity anisotropy of dry and hydrous olivine at 8GPa, *Physics of the Earth and Planetary Interiors*, **181**(3), 103–111.

Pollack, H. N. & Chapman, D. S., 1977. On the regional variation of heat flow, geotherms, and lithospheric thickness, *Tectonophysics*, **38**(3-4), 279–296.

Post, J. L. & Borer, L., 2000. High-resolution infrared spectra, physical properties, and micromorphology of serpentines, *Applied Clay Science*, **16**(1), 73–85.

Poujol, M., Robb, L. J., Anhaeusser, C. R., & Gericke, B., 2003. A review of the geochronological constraints on the evolution of the Kaapvaal Craton, South Africa, *Precambrian Research*, **127**(1), 181–213.

Prechtel, F. & Stalder, R., 2011. The potential use of OH-defects in enstatite as geobarometer, *Contributions to Mineralogy and Petrology*, **162**(3), 615–623.

Prechtel, F. & Stalder, R., 2012. OH-defects in Al- and Cr- doped synthetic enstatites and defect geobarometry on natural orthopyroxenes from the Earth's mantle, *European Journal of Mineralogy*, **24**(3), 471–481.

Priestley, K. & McKenzie, D., 2002. The structure of the upper mantle beneath southern Africa, *Geological Society, London, Special Publications*, **199**(1), 45–64.

Priestley, K. & McKenzie, D., 2013. The relationship between shear wave velocity, temperature, attenuation and viscosity in the shallow part of the mantle, *Earth and Planetary Science Letters*, **381**, 78–91.

Priestley, K., McKenzie, D., & Debayle, E., 2006. The state of the upper mantle beneath southern Africa, *Tectonophysics*, **416**(1), 101–112.

Rader, E., Emry, E., Schmerr, N., Frost, D., Cheng, C., Menard, J., Yu, C.-Q., & Geist, D., 2015. Characterization and Petrological Constraints of the Midlithospheric Discontinuity, *Geochemistry, Geophysics, Geosystems*, **16**(10), 3484–3504.

Rapp, R. P., Shimizu, N., Norman, M. D., & Applegate, G. S., 1999. Reaction between slab-derived melts and peridotite in the mantle wedge: experimental constraints at 3.8 GPa, *Chemical Geology*, **160**(4), 335–356.

Rapp, R. P., Irifune, T., Shimizu, N., Nishiyama, N., Norman, M. D., & Inoue, T., 2008. Subduction recycling of continental sediments and the origin of geochemically enriched reservoirs in the deep mantle, *Earth and Planetary Science Letters*, **271**(1), 14–23.

Regier, M., Mišković, A., Ickert, R., Pearson, D., Stachel, T., Stern, R., & Kopylova, M., 2018. An oxygen isotope test for the origin of Archean mantle roots, *Geochemical Perspectives Letters*, pp. 6–10.

Rehfeldt, T., Foley, S. F., Jacob, D. E., Carlson, R. W., & Lowry, D., 2008. Contrasting types of metasomatism in dunite, wehrlite and websterite xenoliths from Kimberley, South Africa, *Geochimica et Cosmochimica Acta*, **72**(23), 5722–5756.

Richardson, S. H., Gurney, J. J., Erlank, A. J., & Harris, J., 1984. Origin of diamonds in old enriched mantle, *Nature*, **310**(5974), 198–202, Publisher: Springer.

Ringwood, A. E., 1958. The constitution of the mantle—III Consequences of the olivine-spinel transition, *Geochimica et Cosmochimica Acta*, **15**(3), 195–212.

Roex, A. P. L., Bell, D. R., & Davis, P., 2003. Petrogenesis of Group I Kimberlites from Kimberley, South Africa: Evidence from Bulk-rock Geochemistry, *Journal of Petrology*, **44**(12), 2261–2286.

Rohrbach, A. & Schmidt, M. W., 2011. Redox freezing and melting in the Earth's deep mantle resulting from carbon–iron redox coupling, *Nature*, **472**(7342), 209–212.

Rosenthal, A., Hauri, E. H., & Hirschmann, M. M., 2015. Experimental determination of C, F, and H partitioning between mantle minerals and carbonated basalt, CO2/Ba and CO2/Nb systematics of partial melting, and the CO2 contents of basaltic source regions, *Earth and Planetary Science Letters*, **412**, 77–87.

Rossman, G. R., 2006. Analytical Methods for Measuring Water in Nominally Anhydrous Minerals, *Reviews in Mineralogy and Geochemistry*, **62**(1), 1–28, Publisher: GeoScienceWorld.

Rudnick, R. L., McDonough, W. F., & Chappell, B. W., 1993. Carbonatite metasomatism in the northern Tanzanian mantle: Petrographic and geochemical characteristics, *Earth and Planetary Science Letters*, **114**(4), 463–475.

Rudnick, R. L., McDonough, W. F., & Orpin, A., 1994. Northern Tanzanian peridotite xenoliths: A comparison with Kaapvaal peridotites and inferences on metasomatic interactions., in *Kimberlites, Related Rocks and Mantle Xenoliths (ed. H. O. A. Meyer and O. Leonardos)*, vol. 1, pp. 336–353.

Ruprecht, P. & Plank, T., 2013. Feeding andesitic eruptions with a high-speed connection from the mantle, *Nature*, **500**(7460), 68–72.

Russell, J. K., Porritt, L. A., Lavallée, Y., & Dingwell, D. B., 2012. Kimberlite ascent by assimilation-fuelled buoyancy, *Nature*, **481**(7381), 352–356.

Ryan, J. & Chauvel, C., 2014. The Subduction-Zone Filter and the Impact of Recycled Materials on the Evolution of the Mantle, *Treatise on Geochemistry (Second Edition)*, **3**, 479–508.

Ryerson, F. J., Durham, W. B., Cherniak, D. J., & Lanford, W. A., 1989. Oxygen diffusion in olivine: Effect of oxygen fugacity and implications for creep, *Journal of Geophysical Research: Solid Earth*, **94**(B4), 4105–4118.

Sarda, P., Moreira, M., & Staudacher, T., 1999. Argon-Lead Isotopic Correlation in Mid-Atlantic Ridge Basalts, *Science*, **283**(5402), 666–668, Publisher: American Association for the Advancement of Science Section: Report.

Schilling, J.-G., Unni, C. K., & Bender, M. L., 1978. Origin of chlorine and bromine in the oceans, *Nature*, **273**(5664), 631–636, Publisher: Springer.

Schmitz, M. D., Bowring, S. A., de Wit, M. J., & Gartz, V., 2004. Subduction and terrane collision stabilize the western Kaapvaal craton tectosphere 2.9 billion years ago, *Earth and Planetary Science Letters*, **222**(2), 363–376.

Schmädicke, E., Gose, J., Witt-Eickschen, G., & Brätz, H., 2013. Olivine from spinel peridotite xenoliths: Hydroxyl incorporation and mineral composition, *American Mineralogist*, **98**(10), 1870–1880.

Schrauder, M. & Navon, O., 1994. Hydrous and carbonatitic mantle fluids in fibrous diamonds from Jwaneng, Botswana, *Geochimica et Cosmochimica Acta*, **58**(2), 761–771.

Scott, J. M., Liu, J., Pearson, D. G., Harris, G. A., Czertowicz, T. A., Woodland, S. J., Riches, A. J. V., & Luth, R. W., 2019. Continent stabilisation by lateral accretion of subduction zone-processed depleted mantle residues; insights from Zealandia, *Earth and Planetary Science Letters*, **507**, 175–186.

Seckendorff, V. v. & O'Neill, H. S. C., 1993. An experimental study of Fe-Mg partitioning between olivine and orthopyroxene at 1173, 1273 and 1423 K and 1.6 GPa, *Contributions to Mineralogy and Petrology*, **113**(2), 196–207.

Selway, K., Ford, H., & Kelemen, P., 2015. The seismic mid-lithosphere discontinuity, *Earth and Planetary Science Letters*, **414**, 45–57.

Seyfried Jr, W. E. & Ding, K., 1995. Phase equilibria in subseafloor hydrothermal systems: A review of the role of redox, temperature, pH and dissolved Cl on the chemistry of hot spring fluids at mid-ocean ridges, *Seafloor Hydrothermal Systems: Physical, Chemical, Biological, and Geological Interactions*, **91**, 248–272, Publisher: Wiley Online Library.

Shannon, R. D., 1976. Revised effective ionic radii and systematic studies of interatomic distances in halides and chalcogenides, *Acta Crystallographica Section A: Crystal Physics, Diffraction, Theoretical and General Crystallography*, **32**(5), 751–767.

Sharygin, I. S., Litasov, K. D., Shatskiy, A., Safonov, O. G., Golovin, A. V., Ohtani, E., & Pokhilenko, N. P., 2017. Experimental constraints on orthopyroxene dissolution in alkali-carbonate melts in the lithospheric mantle: Implications for kimberlite melt composition and magma ascent, *Chemical Geology*, **455**, 44–56.

Shen, T., Hermann, J., Zhang, L., Padrón-Navarta, J. A., & Chen, J., 2014. FTIR spectroscopy of Ti-chondrodite, Ti-clinohumite, and olivine in deeply subducted serpentinites and implications for the deep water cycle, *Contributions to Mineralogy and Petrology*, **167**(4), 992.

Shimizu, N. & Richardson, S. H., 1987. Trace element abundance patterns of garnet inclusions in peridotite-suite diamonds, *Geochimica et Cosmochimica Acta*, **51**(3), 755–758.

Shirey, S. B., Richardson, S. H., & Harris, J. W., 2004. Integrated models of diamond formation and craton evolution, *Lithos*, **77**(1), 923–944.

Shirey, S. B., Cartigny, P., Frost, D. J., Keshav, S., Nestola, F., Nimis, P., Pearson, D. G., Sobolev, N. V., & Walter, M. J., 2013. Diamonds and the geology of mantle carbon, *Reviews in Mineralogy and Geochemistry*, **75**(1), 355–421.

Shu, Q. & Brey, G. P., 2015. Ancient mantle metasomatism recorded in subcalcic garnet xenocrysts: Temporal links between mantle metasomatism, diamond growth and crustal tectonomagmatism, *Earth and Planetary Science Letters*, **418**, 27–39.

Shu, Q., Brey, G. P., Gerdes, A., & Hoefer, H. E., 2013. Geochronological and geochemical constraints on the formation and evolution of the mantle underneath the Kaapvaal craton: Lu–Hf and Sm–Nd systematics of subcalcic garnets from highly depleted peridotites, *Geochimica et Cosmochimica Acta*, **113**, 1–20.

Simon, N. S., Carlson, R. W., Pearson, D. G., & Davies, G. R., 2007. The origin and evolution of the Kaapvaal cratonic lithospheric mantle, *Journal of Petrology*, **48**(3), 589–625.

Simon, N. S. C., Irvine, G. J., Davies, G. R., Pearson, D. G., & Carlson, R. W., 2003. The origin of garnet and clinopyroxene in "depleted" Kaapvaal peridotites, *Lithos*, **71**(2), 289–322.

Skogby, H., 2006. Water in Natural Mantle Minerals I: Pyroxenes, *Reviews in Mineralogy and Geochemistry*, **62**(1), 155–167.

Sleep, N. H., 2003. Simple features of mantle-wide convection and the interpretation of lower-mantle tomograms, *Comptes Rendus Geoscience*, **335**(1), 9–22.

Sleep, N. H., 2009. Stagnant lid convection and carbonate metasomatism of the deep continental lithosphere, *Geochemistry, Geophysics, Geosystems*, **10**(11).

Sláma, J., Košler, J., Condon, D. J., Crowley, J. L., Gerdes, A., Hanchar, J. M., Horstwood, M. S. A., Morris, G. A., Nasdala, L., Norberg, N., Schaltegger, U., Schoene, B., Tubrett, M. N., & Whitehouse, M. J., 2008. Plešovice zircon — A new natural reference material for U–Pb and Hf isotopic microanalysis, *Chemical Geology*, **249**(1), 1–35.

Smart, K. A., Tappe, S., Stern, R. A., Webb, S. J., & Ashwal, L. D., 2016. Early Archaean tectonics and mantle redox recorded in Witwatersrand diamonds, *Nature Geoscience*, **9**(3), 255–259, Number: 3 Publisher: Nature Publishing Group.

Smith, C. B., 1983. Rubidium-strontium, uranium-lead and samarium-neodymium isotopic studies of kimberlite and selected mantle-derived xenoliths.

Smith, D. & Ehrenberg, S. N., 1984. Zoned minerals in garnet peridotite nodules from the Colorado Plateau: implications for mantle metasomatism and kinetics, *Contributions to Mineralogy and Petrology*, **86**(3), 274–285.

Soltys, A., Giuliani, A., & Phillips, D., 2018. A new approach to reconstructing the composition and evolution of kimberlite melts: A case study of the archetypal Bultfontein kimberlite (Kimberley, South Africa), *Lithos*, **304-307**, 1–15.

Spandler, C. & O'Neill, H. S. C., 2010. Diffusion and partition coefficients of minor and trace elements in San Carlos olivine at 1,300°C with some geochemical implications, *Contributions to Mineralogy and Petrology*, **159**(6), 791–818.

Sparks, R. S. J., Baker, L., Brown, R. J., Field, M., Schumacher, J., Stripp, G., & Walters, A., 2006. Dynamical constraints on kimberlite volcanism, *Journal of Volcanology and Geothermal Research*, **155**(1), 18–48.

Stachel, T., Viljoen, K. S., Brey, G., & Harris, J. W., 1998. Metasomatic processes in lherzolitic and harzburgitic domains of diamondiferous lithospheric mantle: REE in garnets from xenoliths and inclusions in diamonds, *Earth and Planetary Science Letters*, **159**(1), 1–12.

Stachel, T., Aulbach, S., Brey, G. P., Harris, J. W., Leost, I., Tappert, R., & Viljoen, K. S. F., 2004. The trace element composition of silicate inclusions in diamonds: a review, *Lithos*, **77**(1), 1–19.

Stagno, V., Ojwang, D. O., McCammon, C. A., & Frost, D. J., 2013. The oxidation state of the mantle and the extraction of carbon from Earth's interior, *Nature*, **493**(7430), 84–88, Number: 7430 Publisher: Nature Publishing Group.

Stalder, R., 2004. Influence of Fe, Cr and Al on hydrogen incorporation in orthopyroxene, *European Journal of Mineralogy*, **16**(5), 703–711.

Stalder, R. & Skogby, H., 2003. Hydrogen diffusion in natural and synthetic orthopyroxene, *Physics and Chemistry of Minerals*, **30**(1), 12–19.

Stalder, R., Klemme, S., Ludwig, T., & Skogby, H., 2005. Hydrogen incorporation in orthopyroxene: interaction of different trivalent cations, *Contributions to Mineralogy and Petrology*, **150**(5), 473–485.

Stalder, R., Prechtel, F., & Ludwig, T., 2012. No site-specific infrared absorption coefficients for OH-defects in pure enstatite, *European Journal of Mineralogy*, **24**(3), 465–470.

Stalder, R., Karimova, A., & Konzett, J., 2015. OH-defects in multiple-doped orthoenstatite at 4–8 GPa: filling the gap between pure and natural systems, *Contributions to Mineralogy and Petrology*, **169**(4), 38.

Staudacher, T. & Allègre, C. J., 1988. Recycling of oceanic crust and sediments: the noble gas subduction barrier, *Earth and Planetary Science Letters*, **89**(2), 173–183.

Stephens, W. E. & Dawson, J. B., 1977. Statistical Comparison between Pyroxenes from Kimberlites and Their Associated Xenoliths, *The Journal of Geology*, **85**(4), 433–449.

Stone, R. S. & Luth, R. W., 2016. Orthopyroxene survival in deep carbonatite melts: implications for kimberlites, *Contributions to Mineralogy and Petrology*, **171**(7), 63.

Stosch, H.-G., 1981. Sc, Cr, Co and Ni partitioning between minerals from spinel peridotite xenoliths, *Contributions to Mineralogy and Petrology*, **78**(2), 166–174.

Stracke, A., Hofmann, A. W., & Hart, S. R., 2005. FOZO, HIMU, and the rest of the mantle zoo, *Geochemistry, Geophysics, Geosystems*, **6**(5), _eprint: https://agupubs.onlinelibrary.wiley.com/doi/pdf/10.1029/2004GC000824.

Straub, S. M. & Layne, G. D., 2003. Decoupling of fluids and fluid-mobile elements during shallow subduction: Evidence from halogen-rich andesite melt inclusions from the Izu arc volcanic front, *Geochemistry, Geophysics, Geosystems*, **4**(7).

Straub, S. M. & Layne, G. D., 2003. The systematics of chlorine, fluorine, and water in Izu arc front volcanic rocks: Implications for volatile recycling in subduction zones, *Geochimica et Cosmochimica Acta*, **67**(21), 4179–4203.

Sundvall, R. & Stalder, R., 2011. Water in upper mantle pyroxene megacrysts and xenocrysts: A survey study, *American Mineralogist*, **96**(8-9), 1215–1227.

Suzuki, T., Hirata, T., Yokoyama, T. D., Imai, T., & Takahashi, E., 2012. Pressure effect on element partitioning between minerals and silicate melt: Melting experiments on basalt up to 20 GPa, *Physics of the Earth and Planetary Interiors*, **208–209**, 59–73.

Sweeney, R. J., Thompson, A. B., & Ulmer, P., 1993. Phase relations of a natural MARID composition and implications for MARID genesis, lithospheric melting and mantle metasomatism, *Contributions to Mineralogy and Petrology*, **115**(2), 225–241.

Tappe, S., Smart, K. A., Pearson, D. G., Steenfelt, A., & Simonetti, A., 2011. Craton formation in Late Archean subduction zones revealed by first Greenland eclogites, *Geology*, **39**(12), 1103–1106, Publisher: GeoScienceWorld.

Tappe, S., Graham Pearson, D., Kjarsgaard, B. A., Nowell, G., & Dowall, D., 2013. Mantle transition zone input to kimberlite magmatism near a subduction zone: Origin of anomalous Nd–Hf isotope systematics at Lac de Gras, Canada, *Earth and Planetary Science Letters*, **371-372**, 235–251.

Tappe, S., Smart, K., Torsvik, T., Massuyeau, M., & de Wit, M., 2018. Geodynamics of kimberlites on a cooling Earth: Clues to plate tectonic evolution and deep volatile cycles, *Earth and Planetary Science Letters*, **484**, 1–14.

Taylor, W. R., 1985. *The role of COH fluids in upper mantle processes: a theoretical, experimental and spectroscopic study*, PhD Thesis, University of Tasmania.

Taylor, W. R., 1998. An experimental test of some geothermometer and geobaro-meter formulations for upper mantle peridotites with application to the ther-mobarometry of fertile lherzolite and garnet websterite, *Neues Jahrbuch für Mineralogie - Abhandlungen*, pp. 381–408.

Taylor, W. R. & Green, D. H., 1988. Measurement of reduced peridotite-COH solidus and implications for redox melting of the mantle, *Nature*, **332**(6162), 349–352, Publisher: Springer.

Tenner, T. J., Hirschmann, M. M., Withers, A. C., & Hervig, R. L., 2009. Hydrogen partitioning between nominally anhydrous upper mantle minerals and melt between 3 and 5 GPa and applications to hydrous peridotite partial melting, *Chemical Geology*, **262**(1), 42–56.

Tollan, P. & Hermann, J., 2019. Arc magmas oxidized by water dissociation and hydrogen incorporation in orthopyroxene, *Nature Geoscience*, **12**(8), 667–671.

Tollan, P. M. E., O'Neill, H. S. C., Hermann, J., Benedictus, A., & Arculus, R. J., 2015. Frozen melt–rock reaction in a peridotite xenolith from sub-arc mantle recorded by diffusion of trace elements and water in olivine, *Earth and Planetary Science Letters*, **422**, 169–181.

Tollan, P. M. E., Smith, R., O'Neill, H. S., & Hermann, J., 2017. The responses of the four main substitution mechanisms of H in olivine to H2O activity at 1050 °C and 3 GPa, *Progress in Earth and Planetary Science*, **4**(1), 14.

Tollan, P. M. E., O'Neill, H. S. C., & Hermann, J., 2018. The role of trace elements in controlling H incorporation in San Carlos olivine, *Contributions to Mineralogy and Petrology*, **173**(11), 89.

Tomlinson, E., De Schrijver, I., De Corte, K., Jones, A. P., Moens, L., & Vanhaecke, F., 2005. Trace element compositions of submicroscopic inclusions in coated diamond: A tool for understanding diamond petrogenesis, *Geochimica et Cosmochimica Acta*, **69**(19), 4719–4732.

Tomlinson, E. L., Jones, A. P., & Harris, J. W., 2006. Co-existing fluid and silicate inclusions in mantle diamond, *Earth and Planetary Science Letters*, **250**(3), 581–595.

Tomlinson, E. L., Müller, W., & EIMF, 2009. A snapshot of mantle metasomatism: Trace element analysis of coexisting fluid (LA-ICP-MS) and silicate (SIMS) inclusions in fibrous diamonds, *Earth and Planetary Science Letters*, **279**(3–4), 362–372.

Urann, B. M., Roux, V. L., Hammond, K., Marschall, H. R., Lee, C.-T. A., & Monteleone, B. D., 2017. Fluorine and chlorine in mantle minerals and the halogen budget of the Earth's mantle, *Contributions to Mineralogy and Petrology*, **172**(7), 51.

Van Orman, J. A., Grove, T. L., & Shimizu, N., 2001. Rare earth element diffusion in diopside: influence of temperature, pressure, and ionic radius, and an elastic model for diffusion in silicates, *Contributions to Mineralogy and Petrology*, **141**(6), 687–703.

Van Orman, J. A., Grove, T. L., Shimizu, N., & Layne, G. D., 2002. Rare earth element diffusion in a natural pyrope single crystal at 2.8 GPa, *Contributions to Mineralogy and Petrology*, **142**(4), 416–424.

Vinet, N. & Higgins, M. D., 2010. Magma Solidification Processes beneath Kilauea Volcano, Hawaii: a Quantitative Textural and Geochemical Study of the 1969–1974 Mauna Ulu Lavas, *Journal of Petrology*, **51**(6), 1297–1332.

Wagner, L. S., Anderson, M. L., Jackson, J. M., Beck, S. L., & Zandt, G., 2008. Seismic evidence for orthopyroxene enrichment in the continental lithosphere, *Geology*, **36**(12), 935–938.

Wagner, P. A., 1914. *The Diamond Fields of Southern Africa.*, Johannesburg: Transvaal Leader.

Walker, A. M., Wright, K., & Slater, B., 2003. A computational study of oxygen diffusion in olivine, *Physics and Chemistry of Minerals*, **30**(9), 536–545.

Walker, A. M., Hermann, J., Berry, A. J., & O'Neill, H. S. C., 2007. Three water sites in upper mantle olivine and the role of titanium in the water weakening mechanism, *Journal of Geophysical Research: Solid Earth*, **112**(B5).

Walker, R. J., Carlson, R. W., Shirey, S. B., & F.r, B., 1989. Os, Sr, Nd, and Pb isotope systematics of southern African peridotite xenoliths: Implications for the chemical evolution of subcontinental mantle, *Geochimica et Cosmochimica Acta*, **53**(7), 1583–1595.

Wallace, M. E. & Green, D. H., 1988. An experimental determination of primary carbonatite magma composition, *Nature*, **335**(6188), 343–346.

Walter, M. J., 1998. Melting of Garnet Peridotite and the Origin of Komatiite and Depleted Lithosphere, *Journal of Petrology*, **39**(1), 29–60.

Wang, W., Sueno, S., Takahashi, E., Yurimoto, H., & Gasparik, T., 2000. Enrichment processes at the base of the Archean lithospheric mantle: observations from trace element characteristics of pyropic garnet inclusions in diamonds, *Contributions to Mineralogy and Petrology*, **139**(6), 720–733.

Warren, J. M., 2016. Global variations in abyssal peridotite compositions, *Lithos*, **248-251**, 193–219.

Warren, J. M. & Hauri, E. H., 2014. Pyroxenes as tracers of mantle water variations, *Journal of Geophysical Research: Solid Earth*, **119**(3), 1851–1881.

Wasch, L. J., van der Zwan, F. M., Nebel, O., Morel, M. L. A., Hellebrand, E. W. G., Pearson, D. G., & Davies, G. R., 2009. An alternative model for silica enrichment in the Kaapvaal subcontinental lithospheric mantle, *Geochimica et Cosmochimica Acta*, **73**(22), 6894–6917.

Weaver, S. D., Storey, B. C., Pankhurst, R. J., Mukasa, S. B., DiVenere, V. J., & Bradshaw, J. D., 1994. Antarctica-New Zealand rifting and Marie Byrd Land lithospheric magmatism linked to ridge subduction and mantle plume activity, *Geology*, **22**(9), 811–814.

Weiss, Y., Kessel, R., Griffin, W. L., Kiflawi, I., Klein-BenDavid, O., Bell, D. R., Harris, J. W., & Navon, O., 2009. A new model for the evolution of diamond-forming fluids: Evidence from microinclusion-bearing diamonds from Kankan, Guinea, *Lithos*, **112**, 660–674.

Weiss, Y., Griffin, W. L., Bell, D. R., & Navon, O., 2011. High-Mg carbonatitic melts in diamonds, kimberlites and the sub-continental lithosphere, *Earth and Planetary Science Letters*, **309**(3–4), 337–347.

Wells, P. R., 1977. Pyroxene thermometry in simple and complex systems, *Contributions to mineralogy and Petrology*, **62**(2), 129–139.

Wiedenbeck, M., Allé, P., Corfu, F., Griffin, W. L., Meier, M., Oberli, F., Quadt, A. V., Roddick, J. C., & Spiegel, W., 1995. Three Natural Zircon Standards for U-Th-Pb, Lu-Hf, Trace Element and Ree Analyses, *Geostandards Newsletter*, **19**(1), 1–23.

Wiedenbeck, M., Hanchar, J. M., Peck, W. H., Sylvester, P., Valley, J., Whitehouse, M., Kronz, A., Morishita, Y., Nasdala, L., Fiebig, J., Franchi, I., Girard, J.-P., Greenwood, R. C., Hinton, R., Kita, N., Mason, P. R. D., Norman, M., Ogasawara, M., Piccoli, P. M., Rhede, D., Satoh, H., Schulz-Dobrick, B., Skår, O., Spicuzza, M., Terada, K., Tindle, A., Togashi, S., Vennemann, T., Xie, Q., & Zheng, Y.-F., 2004. Further Characterisation of the 91500 Zircon Crystal, *Geostandards and Geoanalytical Research*, **28**(1), 9–39.

Withers, A. C. & Hirschmann, M. M., 2008. Influence of temperature, composition, silica activity and oxygen fugacity on the H2O storage capacity of olivine at 8 GPa, *Contributions to Mineralogy and Petrology*, **156**(5), 595–605.

Withers, A. C., Bureau, H., Raepsaet, C., & Hirschmann, M. M., 2012. Calibration of infrared spectroscopy by elastic recoil detection analysis of H in synthetic olivine, *Chemical Geology*, **334**, 92–98.

Witt-Eickschen, G. & O'Neill, H. S. C., 2005. The effect of temperature on the equilibrium distribution of trace elements between clinopyroxene, orthopyroxene, olivine and spinel in upper mantle peridotite, *Chemical Geology*, **221**(1), 65–101.

Witt-Eickschen, G. & Seck, H. A., 1991. Solubility of Ca and Al in orthopyroxene from spinel peridotite: an improved version of an empirical geothermometer, *Contributions to Mineralogy and Petrology*, **106**(4), 431–439.

Woodhead, J., Hergt, J., Phillips, D., & Paton, C., 2009. African kimberlites revisited: In situ Sr-isotope analysis of groundmass perovskite, *Lithos*, **112**, 311–317.

Woodhead, J., Hergt, J., Giuliani, A., Phillips, D., & Maas, R., 2017. Tracking continental-scale modification of the Earth's mantle using zircon megacrysts, *Geochemical Perspectives Letters*, pp. 1–6.

Woodhead, J., Hergt, J., Giuliani, A., Maas, R., Phillips, D., Pearson, D. G., & Nowell, G., 2019. Kimberlites reveal 2.5-billion-year evolution of a deep, isolated mantle reservoir, *Nature*, **573**(7775), 578–581, Number: 7775 Publisher: Nature Publishing Group.

Woodland, A. B. & Koch, M., 2003. Variation in oxygen fugacity with depth in the upper mantle beneath the Kaapvaal craton, Southern Africa, *Earth and Planetary Science Letters*, **214**(1), 295–310.

Woods, S. C., Mackwell, S., & Dyar, D., 2000. Hydrogen in diopside: Diffusion profiles, *American Mineralogist*, **85**(3-4), 480–487.

Workman, R. K. & Hart, S. R., 2005. Major and trace element composition of the depleted MORB mantle (DMM), *Earth and Planetary Science Letters*, **231**(1), 53–72.

Workman, R. K., Hart, S. R., Jackson, M., Regelous, M., Farley, K. A., Blusztajn, J., Kurz, M., & Staudigel, H., 2004. Recycled metasomatized lithosphere as the origin of the Enriched Mantle II (EM2) endmember: Evidence from the Samoan Volcanic Chain, *Geochemistry, Geophysics, Geosystems*, **5**(4), _eprint: https://agupubs.onlinelibrary.wiley.com/doi/pdf/10.1029/2003GC000623.

Wunder, B. & Melzer, S., 2003. Experimental evidence on phlogopitic mantle metasomatism induced by phengite dehydration, *European Journal of Mineralogy*, **15**(4), 641–647.

Wunder, B. & Schreyer, W., 1997. Antigorite: High-pressure stability in the system MgOSiO2H2O (MSH), *Lithos*, **41**(1), 213–227.

Wyllie, P. J. & Sekine, T., 1982. The formation of mantle phlogopite in subduction zone hybridization, *Contributions to Mineralogy and Petrology*, **79**(4), 375–380.

Wyllie, P. J., Carroll, M. R., Johnston, A. D., Rutter, M. J., Sekine, T., & Van der Laan, S. R., 1989. Interactions among magmas and rocks in subduction zone regions: experimental studies from slab to mantle to crust, *European Journal of Mineralogy*, **1**(2), 165–179.

Wyman, D. A. & Kerrich, R., 2002. Formation of Archean continental lithospheric roots: The role of mantle plumes, *Geology*, **30**(6), 543–546, Publisher: GeoScienceWorld.

Xia, Q.-K., Hao, Y., Li, P., Deloule, E., Coltorti, M., Dallai, L., Yang, X., & Feng, M., 2010. Low water content of the Cenozoic lithospheric mantle beneath the eastern part of the North China Craton, *Journal of Geophysical Research: Solid Earth*, **115**(B7).

Yang, X., Keppler, H., & Li, Y., 2016. Molecular hydrogen in mantle minerals, *Geochem Perspect Lett*, **2**, 160–168.

Yang, X.-Z., Xia, Q.-K., Deloule, E., Dallai, L., Fan, Q.-C., & Feng, M., 2008. Water in minerals of the continental lithospheric mantle and overlying lower crust: A comparative study of peridotite and granulite xenoliths from the North China Craton, *Chemical Geology*, **256**(1), 33–45.

Yaxley, G. M., Berry, A. J., Rosenthal, A., Woodland, A. B., & Paterson, D., 2017. Redox preconditioning deep cratonic lithosphere for kimberlite genesis – evidence from the central Slave Craton, *Scientific Reports*, **7**(1), 1–10.

Zhang, B., Yoshino, T., Wu, X., Matsuzaki, T., Shan, S., & Katsura, T., 2012. Electrical conductivity of enstatite as a function of water content: Implications for the electrical structure in the upper mantle, *Earth and Planetary Science Letters*, **357-358**, 11–20.

Zhang, H., Menzies, M. A., Gurney, J. J., & Zhou, X., 2001. Cratonic peridotites and silica-rich melts: diopside-enstatite relationships in polymict xenoliths, Kaapvaal, South Africa, *Geochimica et Cosmochimica Acta*, **65**(19), 3365–3377.

Zhang, R. Y., Yang, J. S., Wooden, J. L., Liou, J. G., & Li, T. F., 2005. U–Pb SHRIMP geochronology of zircon in garnet peridotite from the Sulu UHP terrane, China: Implications for mantle metasomatism and subduction-zone UHP metamorphism, *Earth and Planetary Science Letters*, **237**(3), 729–743.

Zhao, D., Essene, E. J., & Zhang, Y., 1999. An oxygen barometer for rutile–ilmenite assemblages: oxidation state of metasomatic agents in the mantle, *Earth and Planetary Science Letters*, **166**(3), 127–137.

Zheng, T., Zhao, L., & Zhu, R., 2009. New evidence from seismic imaging for subduction during assembly of the North China craton, *Geology*, **37**(5), 395–398, Publisher: GeoScienceWorld.

Zhou, Y. & Steele, I., 1993. Chemical zoning and diffusion of Ca, Al, Mn, and CR in olivine of springwater pallasite, in *Lunar and Planetary Inst., Twenty-Fourth Lunar and Planetary Science Conference. Part 3*.

Zhukova, I., O'Neill, H. S., Cambell, I. H., & Kilburn, M. R., 2014. The effect of silica activity on the diffusion of Ni and Co in olivine, *Contributions to Mineralogy and Petrology*, **168**(2), 1029.

Zindler, A. & Hart, S., 1986. Chemical geodynamics, *Annual review of earth and planetary sciences*, **14**(1), 493–571, Publisher: Annual Reviews 4139 El Camino Way, PO Box 10139, Palo Alto, CA 94303-0139, USA.

Analytical Techniques

A Scanning Electron Microscopy

A Quanta-650F Scanning Electron Microscope (SEM) was used to map crystals in BD3067 (Chapter 6) using Energy Dispersive Spectroscopy (EDS) and Electron Back Scatter Diffraction (EBSD) methods. The former mapped out the concentration of elements and was used for sulfide and zircon analysis. EBSD was used on olivine porphyroclasts in BD3067 to establish the crystallographic orientation of the grains. EBSD data were collected on a FEI Quanta 650FEG SEM equipped with a Bruker e- Flash HR detector, operating at 20 kV and with a beam size of 5.0. The following settings were used: detector resolution 320 x 240 pixels; working distance 30-37 mm; sample to detector distance 12-15mm. The data collection and indexing was perfomed with Bruker QUANTAX CrystAlign software[1], using a Hough transform resolution of 60. Data were analysed using MTEX V4.0[2], a freeware toolset for the commercial software package MATLAB[3].

B Electron Microprobe Analysis

Major and minor element analysis of olivine, orthopyroxene, clinopyroxene, garnet, phlogopite and sulfides were made using the Cameca SX-100 Electron Probe Micro-Analyser (EPMA) in the Department of Earth Sciences at the University of Cambridge. An accelerating voltage of 15 kV together with a 5 μm beam and a current of 20 nA was used for all analyses of olivine, orthopyroxene, clinopyroxene and garnet, except the olivine/clinopyroxene profiles in BD3067 where a beam size of 1 μm was used. A higher accelerating voltage of 20 kV was used with a lower current of 10 nA for phlogopite analyses. Counting times varied from 10 s for the alkali elements Na and K, 20-30 s for major elements and up to 140s for minor elements where more counts were desired to reduce error. A high current (20 nA) was chosen to reduce the detection limits by increasing the number of x-rays exposed to the detector. The phases used for calibration are shown in Table 1 with the instrument error and detection limits for each phase. Secondary standards of San Carlos olivine, augite, diopside, basaltic glass, rhyolite glass and hornblende (where appropriate) were run before, during and after each set of analyses, the standard reproducibilty and precision are presented in the subsequent data tables. In the olivine profiles in Chapter 6, the distance between successive EPMA measurements (1 µm spot size) was either 50 or 100 µm.

C Laser Ablation - ICP-MS

Trace element analysis of olivine and clinopyroxene in 200 µm thick sections, was carried out using an ESI UP193UC laser system coupled to a Perkin Elmer Nexion 350D Inductively Coupled Plasma Mass

[1]QUANTAX CrystAlign. Bruker Nano GmbH, Berlin, Germany, 2010.

[2]Bachmann, F., Ralf Hielscher, and Helmut Schaeben. "Texture analysis with MTEX–free and open source software toolbox." Solid State Phenomena. Vol. 160. Trans Tech Publications, 2010

[3]MATLAB 2016a, The MathWorks, Natick, 2016

Table 1 *EPMA calibration, instrument errors and detection limits. *denotes beam size for olivine and clinopyroxene profiles in BD3067*

	Mineral	**Olivine**		**Clinopyroxene**		**Orthopyroxene**		**Garnet**		**Phlogopite**	
	Hv (kV)	15		15		15		15		20	
	I (nA)	20		20		20		20		10	
	Beam size (μm)	5 (1*)		5 (1*)		5		5		5	
Element	**Calibration Standard**	st.dev (wt.%)	det.lim (ppm)	st.dev (wt.%)	det.lim (ppm)	st.dev (wt.%)	det.lim (ppm)	st.dev (wt.%)	det.lim (ppm)	st.dev (wt.%)	det.lim (ppm)
Si	Diopside	0.47	400	0.65	400	0.46	620	0.37	580	0.45	700
Cr	Cr	0.02	250	0.05	280	0.03	250	0.07	360	0.06	500
Fe	Fayalite	0.34	620	0.13	500	0.17	520	0.23	580	0.14	500
Mn	Mn-Metal	0.04	440	0.04	450	0.04	430	0.05	460	0.04	500
Mg	St. Johns Olivine	1.25	450	0.46	330	0.33	470	0.11	250	0.51	540
Ni	NiO	0.03	330	0.03	350	0.03	330	0.03	340		
Ca	Diopside	0.01	150	0.36	280	0.02	150	0.08	230	0.04	380
Na	Jadeite	0.03	290	0.09	340	0.03	270	0.03	300	0.04	300
Al	Corundum	0.01	58	0.01	57	0.01	70	0.28	360	0.20	320
Ti	Rutile	0.02	200	0.02	210	0.02	220	0.02	205	0.04	215
K	K-Feldspar					0.03	360	0.03	320	0.18	220
F	LiF									0.28	2700
Cl	Halite									0.01	125

Spectrometer (LA-ICP-MS) in the Department of Earth Sciences at the University of Cambridge. During the analysis we used a 100 µm diameter laser beam, a laser repetition rate of 10 Hz for clinopyroxene and garnet and 20 Hz for olivine and orthopyroxene and laser fluence of 8 J cm^{-2} set at 50% power. This is the optimum for signal intensity while minimising down hole fractionation on the instrument. Space is not a limiting factor in these large crystals so the spot size was chosen to maximise the volume of ablated material and hence the signal. The LA-ICP-MS data acquisition settings were 1 sweep per reading, 80 readings, 1 replicate, and total data acquisition lasted 60 seconds (approximately 1 data point for each element per second). The laser was programmed to run for 40 seconds on clinopyroxene and 35 seconds on olivine, with a laser warm-up time of 20 seconds for each spot analysis in both instances. The ICP-MS dwell time for each mass was dependent on the isotope and concentration of the element in the samples, but was typically 20 milliseconds (ms) for most trace elements in clinopyroxene and this was increased up to 100 ms for some low concentration elements in olivine. NIST 612 was used to calibrate element concentrations for all analyses with the exception of Ti in clinopyroxene. NIST 610 was used to calibrate Ti in clinopyroxene due to the very low concentrations of Ti in NIST 612. In order to improve olivine analyses using LA-ICP-MS, a new San Carlos in house standard (BD4074) was characterised using both laser and solution mode. Eight crystals were mounted and their homogeneity assessed by making multiple profiles across each crystal. Two crystals were chosen as reference material for their homogeneity and uniform composition. During all analysis calibration accuracy was verified by analysing combinations of NIST 610, NIST 614, BCR-2G, BIR-1G and BHVO-2G. Recoveries were typically 90 to 110% of the values found on the GEOREM database. Repeated analysis of BIR-2G, BHVO-2G, an in house clinopyroxene standard (BD3735b) and in house San Carlos olivine standard (BD4074) are shown in the supplementary tables, with better than 10% reproducibility for most REE and trace elements. LA-ICP-MS raw intensity drift during an analytical session of 8 hours is typically less than 10% based on raw counts for NIST standards. This drift is compensated for by the internal standard calculations in the Glitter Software (GEMOC, Australia); no other drift corrections are used. Glitter Software was used to process the raw data files from the Nexion software containing the signal intensity versus time. The SiO_2 content of standards and samples (determined by EPMA) was used for internal standard normalization of

the trace-element signals in olivine and orthopyroxene, and CaO was used for clinopyroxene and garnet. Replicate LA-ICP-MS results from three or more spots in the same area were averaged where possible, and chosen carefully to avoid contamination and ensure laser sampling from the target material only. The profiles across olivine grains used a spot size of 100 µm at intervals of 20 µm.

D Secondary Ion Mass Spectrometry

Sample preparation

Sample preparation for volatile analysis using SIMS is designed specifically to reduce the background volatile concentrations by avoiding materials that degas, in particular epoxy. Small sections of the xenolith hand specimen were cut, these were taken as close to the core of the xenolith as possible, to avoid the weathered edges of the nodule, whilst still trying to preserve the specimen. The off-cuts were crushed and sieved to separate the material. For each xenolith, olivine, orthopyroxene and clinopyroxene were picked from the aggregate. As far as possible large, well-formed crystals were chosen for each sample however in some cases there had been extensive re-crystallisation which made finding appropriate olivine crystals difficult. Each crystal was mounted in crystal bond before being ground down to the core and polished down to 1 μ m diamond polish. The polished crystals were removed from their temporary crystal bond mount, cleaned using acetone and mounted into indium, set within aluminium disks. Indium is the preferred mounting medium for volatile analyses in nominally anhydrous minerals because it improves the stability of the vacuum and reduces the background H concentration. Epoxy mounts degas and increase the background, which is not suitable when analysing such low concentrations oh H_2O and halogens in mantle minerals. The indium mounts were cleaned again before being gold-coated at the University of Edinburgh prior to SIMS analysis. Six mounts were made, hosting olivine, orthopyroxene and clinopyroxene from most xenoliths.

Analytical technique

Secondary ion mass spectrometry was completed on the Cameca IMS 4f at the NERC ion microprobe facility at the University of Edinburgh, under the supervision of Dr. Cristina Talavera Rodrigues. SIMS analyses were made over two periods from 17-28 September 2018 and 28-31 May 2019. The mounts were loaded into the vacuum chamber on the instrument over 48 hours (often in excess of 60 hours) before the first analysis. A Cs^+ primary beam was used with a 10 kV primary accelerating voltage and 7-8 nA current. An energy offset of 75 was chosen to reduce the interference without losing signal. Prior to each analysis an area of 50 μm was chosen to raster for 4 minutes. During this time the peaks for Si, Mg, Ca, Li, B, H, F and Cl were aligned. Si was used as the reference and in ratios to calculate other concentrations. Mg and Ca were analysed for cross referencing. At the start of each day, background values were measured by analysing the anhydrous olivine standards OL DC212, OL116610-5, Ol-Koh and Ol-Fo. Clinopyroxene and orthopyroxene standards with known H_2O and F concentrations were used for the calibration (CPX-SC-J1, CPX-KH03-4, CPX-SMC31139, CPX SMC31011, OPX KH03-4, OPX 116610-10). Olivine H_2O and F concentrations were first calculated using a basaltic glass standard (ALV519-4-1) and then also using orthopyroxene standards because the matrix effect is established to be minimal (C.J. De Hoog, pers. comm). A San Carlos olivine was added to each mount to check for drift. The acquisition itself went through 10 acquisition cycles but only the last 5 are used. The raw data was initially processed by Dr. C Talavera Rodrigues using the JCION5 software, followed by manual

background correction on Microsoft Excel. Two different apertures were used for olivine analysis and orthopyroxene and clinopyroxene analysis. Olivine is expected to have much lower concentrations of H_2O than the pyroxenes and therefore a smaller aperture was used, this decreases the background by lowering the number of counts but therefore increases the uncertainty. Nonetheless a smaller aperture is better at resolving low concentrations.

Standard	H2O (ppmw)	F (ppm)
AVL-519-4-15	1700	95
OPX-KH03-4-3	216	25
OPX-116610-3	128	17.4
CPX-KH03-4-1	427	64.8
CPX-SC-J1-1	62	26
CPX-SMC31139-1	5	0.5

Table 2 *H_2O and F composition of the standards used for SIMS (Kumamoto* et al.*, 2017).*

H_2O and F concentrations of the mineral separates were calculated from a calibration line of the ratio of H/Si counts for standards with known H_2O and F concentration. The error for all H_2O, F and chlorine concentrations are calculated by summing the instrument error and the standard deviation in point analyses averaged for each crystal. The instrument error is calculated by taking the square root of the sum of the square of the % count error in H and Si, or F and Si.

$$\%instrumenterror = \sqrt{(\%error_{Si})^2 + (\%error_H)^2} \tag{1}$$

Chlorine concentrations were not known for any pyroxene or olivine standards. The raw data was reprocessed through JCION5 using another basaltic glass, ST8-1A9, with known Cl concentration (2025 ppm). The counts were then normalised to the Si concentrations from prior EPMA and Cl concentrations calculated using the ST8-1A9 composition and the conversion factor established using Si counts.

E Fourier Transform Infrared Spectroscopy

Sample preparation

Samples must be double polished for Fourier transform infrared spectrometry. The priority for FTIR in this study was olivine, however the mineral separates used for SIMS were not large enough to double polish. The thickness of the material for analysis controls the absorbance of infrared, if the sample is too thin then the absorbance is not high enough to detect low H_2O concentrations. In order to achieve the appropriate double polish with a suitable thickness, new fragments from each sample were picked from the largest material from the original crushed aggregate. This method had the advantage of preparing all mineral phases, rather than just olivine. The fragments all contained olivine and orthopyroxene, and some also contained garnet and clinopyroxene.

Double polish was achieved by mounting the fragments onto metal mounts using crystal bond, which has the advantage that the fragment could be removed. After the first polish, the crystal bond was heated

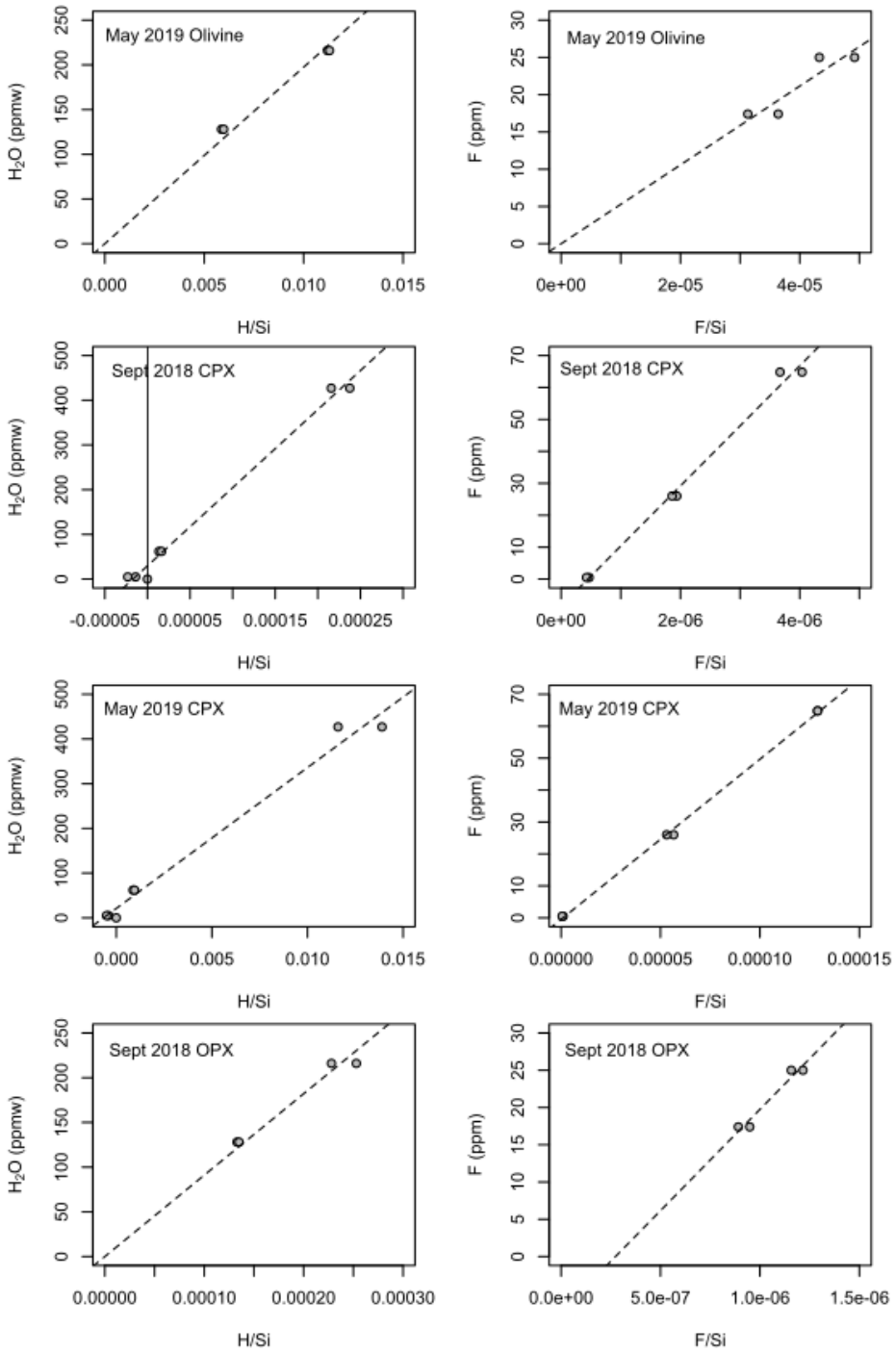

Figure 1 *Example calibration lines for olivine, orthopyroxene and clinopyroxene SIMS analyses.*

and the fragment was flipped to expose the unpolished side. The second side was polished down to 500 μm initially, which had to be reduced to ~300 μm during analysis at Universität Bern.

Analytical technique

Fourier transform infrared spectrometry was carried out at the Institut für Geologie, Universität Bern, Switzerland in collaboration with Dr. Peter Tollan. Measurements were conducted in transmission mode and under unpolarized light, using a Bruker Tensor II spectrometer with a Globar infrared source and a KBr beamsplitter, coupled to a Bruker Hyperion 3000 microscope with a dry air-purged sample chamber. The cores of each crystal were measured using a liquid nitrogen-cooled mercury cadmium telluride (MCT) detector, employing a ~50 μm × 50 μm square spot, 64 scans and 4 cm^{-1} resolution. Unpolarised measurements were made on olivine, orthopyroxene, clinopyroxene and garnet. Polarised measurements were made on olivine. Background absorbance was analysed every 5 analyses. All data was processed using the OPUS software provided by Bruker. Data were corrected for atmospheric contamination using the algorithm built into OPUS, and then baseline-corrected using the 'concave rubberband' algorithm (three iterations and 64 baseline points). Spectra were chosen that were not contaminated by hydrous phases (e.g. serpentine) at ~3700 cm^{-1}. In order to try and avoid such contamination each analysis was made on regions that were optically clean (determined by focusing through the crystal).

The absorbance is a function of the thickness of the crystal, so all spectra were normalised to a thickness of 1 cm^{-1}. Thicknesses of the fragments were measured using a digital micrometer with a precision of ~3 μm, the thickness at six points across the fragment were analysed to assess uniformity. Where the thickness varied beyond the precision of the micrometer, the variation was accounted for in the normalisation by measuring the thickness of the specific crystal analysed.

Data Tables

3. EPMA standard recovery and precision
4. LA-ICP-MS standard recovery and precision
5. Olivine separates - all analyses
6. Orthopyroxene separates - all analyses
7. Clinopyroxene separates - all analyses
8. Bultfontein garnet - all analyses
9. Mothae garnet - all analyses
10. Phlogopite - all analyses
11. BD3067 distal olivine major and trace element composition
12. BD3067 olivine major element profiles
13. BD3067 olivine trace element profiles
14. BD3067 clinopyroxene major and trace element composition
15. Olivine, orthopyroxene and clinopyroxene SIMS analyses
16. Calculated bulk NVFMM volatile concentrations
17. Olivine and orthopyroxene FTIR integrated absorbance of key absorbance bands

Table 3 *EPMA Standard recovery and precision using in-house standards at the University of Cambridge.*

Standard		Na_2O	SiO_2	MgO	Al_2O_3	CaO	TiO_2	FeO	Cr_2O_3	MnO	NiO	K_2O	F	Cl
Augite1	Ref.	0.83	50.98	17.24	7.27	17.36	0.48	4.79		0.14				
	avg.	0.84	50.89	17.20	7.14	17.13	0.48	4.75	0.92	0.10	0.05			
	st.dev	0.02	0.23	0.18	0.09	0.04	0.01	0.07	0.02	0.05	0.01			
	% rsd	0.03	0.00	0.01	0.01	0.00	0.01	0.01	0.02	0.50	0.21			
	% rep	1.01	1.00	1.00	0.98	0.99	1.00	0.99		0.73				
Augite2	Ref.	0.86	50.74	17.13	7.49	17.34	0.49	4.79		0.14				
	avg.	0.86	50.38	16.11	7.38	17.22	0.50	4.78	0.90	0.15	0.06			
	st.dev	0.00	0.00	1.20	0.00	0.00	0.00		0.00	0.00	0.00			
	% rsd	0.00	0.00	0.07	0.00	0.00	0.00	0.00	0.00	0.00	0.00			
	% rep	1.00	0.99	0.94	0.99	0.99	1.01	1.00		1.07				
Diopside1	Ref.	0.13	55.68	18.23	0.15	25.93	0.01	0.23		0.03				
	avg.	0.21	55.53	17.87	0.29	25.43	0.02	0.25		0.02				
	st.dev	0.03	0.29	0.23	0.04	0.07	0.00	0.03		0.01				
	% rsd	0.14	0.01	0.01	0.14	0.00	0.18	0.11		0.64				
	% rep	1.11	0.99	0.99	1.12	0.98	1.09	1.04		0.60				
SanCarlos Olivine1	Ref.		41.23	49.10	0.04	0.13		9.93	0.01	0.15	0.38			
	avg.	0.00	41.10	48.89	0.03	0.11	0.00	9.75	0.02	0.14	0.38			
	st.dev	0.00	0.11	0.38	0.00	0.00	0.00	0.05	0.00	0.00	0.01			
	% rsd	1.23	0.00	0.01	0.03	0.02	0.72	0.01	0.12	0.03	0.02			
	% rep		1.00	1.00	0.83	0.82		0.98	2.29	0.94	0.99			
San Carlos Olivine2	Ref.		40.96	49.03	0.04	0.11		9.94	0.02	0.15	0.38			
	avg.	0.01	41.19	48.72	0.03	0.11		9.62	0.02	0.10	0.38			
	st.dev	0.01	0.27	1.21	0.00	0.00		0.09	0.01	0.07	0.01			
	% rsd	0.88	0.01	0.02	0.08	0.04		0.01	0.40	0.63	0.03			
	% rep		1.01	0.99	0.87	0.98		0.97	0.97	0.69	1.00			
San Carlos Olivine3	Ref.		41.22	48.81	0.04	0.11		9.80	0.01	0.15	0.36			
	avg.	0.01	41.10	48.82	0.03	0.10	0.01	9.70	0.01	0.08	0.37			
	st.dev	0.01	0.25	0.50	0.00	0.00	0.00	0.09	0.00	0.08	0.01			
	% rsd	0.81	0.01	0.01	0.04	0.04	0.60	0.01	0.21	1.09	0.03			
	% rep		1.00	1.00	0.83	0.95		0.99	1.43	0.51	1.04			
Rhyolite	Ref.	3.65	77.23	0.02	12.12	0.42	0.07	1.02	0.00	0.01		5.04	0.24	0.11
	avg.	3.73	77.22	0.04	11.91	0.44	0.08	1.12				5.11	0.21	0.11
	st.dev	0.09	0.86	0.01	0.20	0.03	0.01	0.05				0.07	0.08	0.01
	% rsd	0.02	0.01	0.39	0.02	0.07	0.17	0.04				0.01	0.37	0.08
	% rep	1.02	1.00	1.58	0.98	1.04	1.06	1.10				1.01	0.89	0.94
Basalt	Ref.	2.64	50.99	7.91	14.88	11.17	1.36	9.12	0.06	0.20		0.09	0.02	0.00
	avg.	2.83	51.01	7.98	14.26	11.04	1.33	9.11	0.03	0.18		0.08		
	st.dev	0.06	0.56	0.09	0.22	0.13	0.02	0.12	0.02	0.03		0.01		
	% rsd	1.97	1.09	1.08	1.53	1.22	1.40	1.34	59.13	15.90		9.25		
	% rep	1.07	1.00	1.01	0.96	0.99	0.98	1.00	0.54	0.89		0.87		
Hornblende	Ref.	2.60	40.37	12.80	14.90	10.30	4.73	11.25		0.09		2.05		
	avg.	2.79	39.98	12.47	13.61	10.07	4.86	10.65	0.01	0.09		2.14	0.20	0.02
	st.dev	0.13	0.43	0.19	0.25	0.14	0.06	0.12	0.02	0.02		0.04	0.07	0.00
	% rsd	0.04	0.01	0.01	0.02	0.01	0.01	0.01	2.06	0.24		0.02	0.37	0.18
	% rep	1.07	0.99	0.97	0.91	0.98	1.03	0.95		0.98		1.04		

Table 4 *LA-ICP-MS Standard recovery and precision. Standard values from Jochum* et al. *(2005) unless denoted * which are from Gao* et al. *(2002)*

Standard	BIR-1G					BHVO-2G					In-house SC Olivine (BD4074)		
	Lit.	n=21 Avg.	Stdev.	% rsd	% rep	Lit.	n=9 Avg.	Stdev.	% rsd	% rep	n=28 Avg.	Stdev.	% rsd
Li7*	3.6	3.26	0.24	0.07	0.91	5	4.49	0.15	0.03	0.90	1.82	0.57	0.31
Na23	14132	14337	802	0.06	1.01	17672	17206	420	0.02	0.97	42.92	3.69	0.09
Al27		109864	13370	0.12			98897	6709	0.07		92.68	20.80	0.22
P31		88.99	10.25	0.12			808.85	195.52	0.24		36.46	5.44	0.15
Ca43		97929.81	8283.31	0.08			80496.19	4472.67	0.06		487.91	73.56	0.15
Sc45*	41	43.80	3.61	0.08	1.07	31	30.64	1.64	0.05	0.99	3.78	0.25	0.07
Ti47*	5532	6471.26	466.21	0.07	1.17	15621	17435.03	662.57	0.04	1.12	15.81	1.52	0.10
V51*	338	350.96	25.33	0.07	1.04	329	318.91	12.01	0.04	0.97	3.42	0.32	0.09
Cr53*	403	432.68	31.74	0.07	1.07	285	300.01	9.84	0.03	1.05	134.46	8.87	0.07
Mn55*	1417	1335.61	110.43	0.08	0.94	1345	1216.51	63.70	0.05	0.90	1076.29	99.44	0.09
Fe57		79315.84	10601.41	0.13			77909.12	3517.12	0.05		76943.00	8115.28	0.11
Co59*	52.5	55.86	3.83	0.07	1.06	43	44.45	1.75	0.04	1.03	151.51	11.56	0.08
Ni60	179	182.56	12.17	0.07	1.02	112	117.81	5.88	0.05	1.05	2906.47	215.07	0.07
Cu65	121	124.44	9.25	0.07	1.03	120	118.70	7.32	0.06	0.99	3.44	0.74	0.21
Zn66*	86	98.80	8.72	0.09	1.15	107	129.24	10.44	0.08	1.21	77.21	5.37	0.07
Ga69	14	15.55	1.12	0.07	1.11	20.3	23.40	2.18	0.09	1.15	0.10	0.04	0.45
Ge72	1.21	1.18	0.35	0.30	0.97	1.6	1.50	0.30	0.20	0.94	0.70	0.14	0.20
Y89	15.8	13.75	1.35	0.10	0.87	27.2	21.39	1.61	0.08	0.79	0.02	0.01	0.29
Zr90	12.9	12.91	1.40	0.11	1.00	160	140.45	12.88	0.09	0.88	0.01	0.01	0.53
Nb93	0.564	0.53	0.05	0.10	0.94	18.1	16.91	1.33	0.08	0.93	0.01	0.01	0.93
Sn120	3.27	1.38	0.26	0.19	0.42	5.86	2.14	0.14	0.07	0.36	0.65	0.40	0.62
Ce140	1.93	1.88	0.04	0.02	0.97	36	36.28	1.29	0.04	1.01	0.01	0.02	1.88
Pb208	3.9	3.62	0.41	0.11	0.93	1.75	1.68	0.16	0.10	0.96	0.04	0.05	1.27

Table 4 ***(continued)*** *LA-ICP-MS Standard recovery and precision. Standard values from Jochum* et al. *(2005) unless denoted * which are from Gao* et al. *(2002)*

Standard	BCR-2G					BIR-1G					BHVO-2G					In-house Clinopyroxene (BD3575)		
	Lit.	n=18 Avg.	Stdev.	% rsd	% rep	Lit.	n=12 Avg.	Stdev.	% rsd	% rep	Lit.	n=12 Avg.	Stdev.	% rsd	% rep	n=21 Avg.	Stdev.	% rsd
Al27		85806	7050	0.08			96265	6594	0.07			85736	5909	0.07		19135	1632	0.09
Si29		274507	34919	0.13			233558	34250	0.15			238137	37251	0.16		278756	17021	0.06
K39		17761	2026	0.11			182	13	0.07	1.06		3843	78	0.02		209	14	0.07
Ca43		7.12	0.00	0.00			95055	0.01	0.00	1.48		81476	0.01	0.00		67303	48739	0.72
Sc45	32	34.81	1.79	0.05	1.09	41	43.36	2.30	0.05	1.05	31	32.29	1.75	0.05	1.04	4830	22049	4.56
Ti47*	13005	19228	3270	0.17	1.48	5532	8191	1756	0.21		15621	22593	4715	0.21	1.45	2942	811	0.28
V51*	425	469.13	45.48	0.10	1.10	338	354	33	0.09	1.08	329	330	29	0.09	1.00	433	539	1.24
Cr53*	17	14.50	2.45	0.17	0.85	403					285	227.03	4.72	0.02	0.80			
Fe57		91207	13212	0.14			58195	5838	0.10	1.05		59920	5728	0.10		37485	6204	0.17
Co59*	35.5	41.27	3.05	0.07	1.16	52.5	56.74	5.67	0.10	0.96	43	45.64	3.72	0.08	1.06	38.51	2.19	0.06
Ni60	10.9	13.36	1.36	0.10	1.23	179	188.32	22.21	0.12	0.84	112	122.51	11.88	0.10	1.09	392.31	22.12	0.06
Sr88	332	339.71	22.76	0.07	1.02	112	107.84	5.94	0.06	0.93	389	374.77	15.12	0.04	0.96	83.97	4.37	0.05
Y89	36.9	32.34	2.20	0.07	0.88	15.8	13.27	0.94	0.07	0.99	27.2	22.90	2.01	0.09	0.84	4.34	0.28	0.06
Zr90*	167	167.77	9.73	0.06	1.00	12.9	12.03	0.75	0.06	0.97	160	147.78	12.60	0.09	0.92	13.97	0.95	0.07
Nb93	12.3	12.80	0.72	0.06	1.04	0.564	0.56	0.05	0.09	0.94	18.1	17.87	0.93	0.05	0.99	0.14	0.03	0.20
Ba137	650	670.13	36.89	0.06	1.03	6.6	6.37	0.58	0.09	0.98	127	125.31	5.37	0.04	0.99	0.17	0.04	0.23
La139	25.5	25.29	1.70	0.07	0.99	0.623	0.59	0.03	0.05	0.93	15.8	14.96	0.95	0.06	0.95	1.10	0.08	0.07
Ce140	50.4	54.16	3.29	0.06	1.07	1.93	1.90	0.19	0.10	0.93	36	37.19	1.67	0.04	1.03	4.55	0.24	0.05
Pr141	6.59	6.69	0.46	0.07	1.01	0.381	0.36	0.03	0.10	0.98	5.16	5.06	0.24	0.05	0.98	0.82	0.04	0.05
Nd143	28.5	29.27	1.33	0.05	1.03	2.49	2.31	0.14	0.06	0.91	24.3	24.46	1.80	0.07	1.01	4.65	0.40	0.09
Sm147	6.58	6.49	0.37	0.06	0.99	1.14	1.12	0.08	0.07	0.86	6.07	5.90	0.36	0.06	0.97	1.38	0.14	0.10
Eu153	1.95	1.94	0.15	0.08	0.99	0.537	0.49	0.04	0.09	0.85	2.1	1.96	0.11	0.06	0.93	0.48	0.04	0.08
Gd157	6.74	6.45	0.42	0.06	0.96	1.91	1.64	0.17	0.11	0.83	6.35	5.69	0.53	0.09	0.90	1.44	0.15	0.11
Tb159	1.07	0.98	0.07	0.07	0.91	0.369	0.31	0.03	0.10	0.83	0.959	0.84	0.08	0.09	0.88	0.20	0.02	0.09
Dy163	6.59	6.23	0.37	0.06	0.95	2.73	2.26	0.12	0.05	0.81	5.47	4.85	0.40	0.08	0.89	1.08	0.11	0.10
Ho165	1.34	1.21	0.07	0.06	0.90	0.599	0.50	0.03	0.06	0.87	1.03	0.92	0.10	0.11	0.89	0.18	0.02	0.13
Er166	3.76	3.40	0.31	0.09	0.90	1.79	1.44	0.12	0.08	0.87	2.56	2.34	0.18	0.08	0.91	0.41	0.04	0.11
Tm169	0.532	0.50	0.03	0.07	0.93	0.26	0.23	0.01	0.06	0.80	0.339	0.32	0.04	0.12	0.93	0.04	0.01	0.16
Yb172	3.59	3.49	0.25	0.07	0.97	1.79	1.57	0.09	0.06	0.79	2.13	1.90	0.09	0.05	0.89	0.26	0.04	0.15
Lu175	0.531	0.48	0.05	0.11	0.91	0.27	0.22	0.03	0.12	1.02	0.293	0.27	0.05	0.17	0.93	0.03	0.01	0.23
Hf178	5.07	4.38	0.35	0.08	0.86	0.609	0.48	0.06	0.13	0.97	4.6	3.80	0.19	0.05	0.83	0.83	0.07	0.08
Ta181	0.761	0.78	0.06	0.08	1.02	0.038	0.04	0.01	0.17	1.04	1.15	1.10	0.05	0.05	0.96	0.01	0.00	0.35
Pb208	10.6	12.23	1.15	0.09	1.15	3.9	3.79	0.56	0.15	0.84	1.75	2.03	0.12	0.06	1.16	0.18	0.08	0.41
Th232	6.12	5.77	0.36	0.06	0.94	0.03	0.03	0.01	0.17		1.27	1.21	0.07	0.06	0.95	0.01	0.00	0.30
U238	1.67	1.84	0.15	0.08	1.10	0.016	0.01	0.00	0.17		0.414	0.43	0.04	0.09	1.04	0.00	0.00	0.31

Table 5 ***(continues on next page)*** *Major and trace element composition of olivine mineral separates*

Olivine separate	BD1141A		BD1153A		BD1153B		BD1672A		BD3028B		BD3670A		BD3670B	
Lithology	phl-lz		dun		dun		gt-hz		gt-hz		sp-hz		sp-hz	
	avg	st.dev	avg	st.dev	avg	st.dev	avg	st.dev	avg	st.dev	avg	st.dev	avg	st.dev
EPMA														
SiO_2	40.77	0.09	41.59	0.02	41.60	0.05	41.00	0.28	41.39	0.15	40.75	0.15	41.44	0.07
TiO_2	0.02	0.00	0.03	0.00	0.03	0.00								
Al_2O_3	0.01	0.00	0.02	0.00	0.01	0.00	0.01	0.00	0.02	0.00	0.02	0.00	0.01	0.00
Cr_2O_3			0.04	0.01	0.05	0.02					0.05	0.02		
FeO	8.75	0.11	5.20	0.07	5.21	0.11	8.01	0.11	6.13	0.07	9.09	0.08	7.20	0.16
MnO	0.12	0.01	0.11	0.02	0.09	0.02	0.11	0.03	0.09	0.01	0.11	0.01	0.11	0.02
MgO	49.36	0.24	52.97	0.31	52.90	0.15	50.24	0.05	52.18	0.15	49.32	0.27	51.36	0.39
NiO	0.39	0.00	0.35	0.03	0.36	0.02	0.44	0.02	0.37	0.01	0.41	0.01	0.36	0.01
CaO	0.02	0.00	0.03	0.01	0.04	0.00	0.03	0.00	0.02	0.00	0.08	0.01	0.02	0.01
forsterite	91.0	0.4	94.8	0.3	94.8	0.2	91.8	0.3	93.8	0.2	90.6	0.4	92.7	0.6
LA-ICP-MS														
Li7	2.61	0.09	2.27	0.17	2.29	0.06	1.58	0.05	0.88	0.02	2.26	0.07	0.47	0.04
B11	1.5	0.08	1.51	0.00	1.25	0.06	1.33	0.08	1.54	0.23	1.33	0.14	1.34	0.10
Na23	90	8	112	1	116	2	64	2	86	4	132	3	2	0
Al27	26	11	37	7	35	1	40	2	48	6	134	3	24	5
Si29	192819	0	196979	0	196979	0	194268	0	195764	0	195156	0	195623	0
P31	73	2	64	4	56	3	62	7	96	7	43	2	33	3
Ca44	227	12	237	2	261	3	242	4	232	14	402	8	174	5
Sc45	1.71	0.03	1.71	0.01	1.71	0.04	1.62	0.07	1.46	0.03	2.05	0.08	2.28	0.06
V51	3.21	0.19	3.71	0.01	3.65	0.06	5.55	0.15	5.51	0.14	9.24	0.25	2.51	0.01
Mn55	956	16	676	13	691	6	799	22	606	5	915	13	802	10
Fe57	69564	1406	43333	1430	44550	163	68095	1745	48368	497	71461	387	52047	681
Co59	146	3	119	4	122	2	155	2	127	4	156	3	144	3
Ni60	3126	51	2966	112	2939	25	3629	86	3035	52	3220	44	3100	28
Cu65	2.94	0.10	3.76	0.30	3.61	0.10	3.57	0.32	2.99	0.26	7.33	0.10	1.8	0.07
Zn66	81	1	48	1	48	1	68	1	50	2	84	4	57	1
Ga69	0.12	0.03	0.13	0.01	0.13	0.01	0.1	0.02	0.09	0.01	0.25	0.02	0.06	0.01
Y89	0.01	0.00					0.01	0.00			0.01	0.00		0.00
Zr90	0.3	0.06	0.18	0.01	0.16	0.01	0.11	0.01	0.07	0.01	0.02	0.01		
Nb93	0.36	0.03	0.15	0.00	0.07	0.00	0.18	0.01	0.49	0.03	0.02	0.01		
Sn120	0.4	0.02	0.41	0.00	0.34	0.00	0.42	0.01	0.38	0.01	0.37	0.02	0.36	0.02
Pb208	0.01	0.02	0.01	0.00	0.01	0.00	0	0.00	0.01	0.01	0.04	0.06	0.01	0.00
Ti (610)	97	4.05	154	4.50	137.7	3.13	11.6	0.79	1.6	0.34	25.5	0.95	0.7	0.05
Cr (610)	136.5	5.93	304.9	5.61	322.3	2.08	150.8	5.65	163	2.52	238.6	7.13	42.5	3.94
SIMS														
H	88.32	15.17	85.41	15.81	91		68.66	17.12	36.97	49.16	b.d.l	13.90	b.d.l	5.16
F	121.7	13.55	193.88	14.76	167.63	7.79	62.25	9.71	31.15	0.45	3.61	2.34	b.d.l	3.65

Table 5 ***(continued)*** *Major and trace element composition of olivine mineral separates*

Olivine separate	BD3670C		BD3676B		BD3676A		BD3676B		BD3676C		BD2125		BD2126A	
Lithology	sp-hz		gt-hz		gt-hz		gt-hz		gt-hz		gt-hz		gt-lz	
	avg	st.dev	avg	st.dev	avg	st.dev	avg	st.dev	avg	st.dev	avg	st.dev	avg	st.dev
EPMA														
SiO_2	41.21	0.20			41.44	0.11	41.46	0.17	41.32	0.06	41.49	0.19	41.84	0.17
TiO_2					0.01						0.03	0.01		
Al_2O_3	0.01	0.00			0.01	0.01	0.01	0.00	0.01	0.00	0.01	0.00		
Cr_2O_3					0.05	0.01					0.05			
FeO	7.19	0.10			6.28	0.08	6.29	0.21	6.34	0.04	5.22	0.15	5.78	0.07
MnO	0.11	0.00			0.07	0.01	0.05	0.01	0.08	0.01	0.09	0.02	0.08	0.00
MgO	51.41	0.15			51.68	0.08	51.83	0.06	51.82	0.12	52.66	0.15	52.43	0.14
NiO	0.40	0.03			0.38	0.02	0.38	0.02	0.40	0.00	0.37	0.03	0.43	0.02
CaO	0.03	0.01			0.02	0.00	0.02	0.00	0.02	0.00	0.04	0.01	0.02	0.01
forsterite	92.7	0.4			93.6	0.2	93.6	0.4	93.6	0.1	94.7	0.5	94.2	0.3
LA-ICP-MS														
Li7	0.48	0.03	1.18	0.08	1.16	0.07	1.15	0.07	1.16	0.03	2.14	0.14	2.25	0.03
B11	2.99	0.32	1.33	0.06	1.46	0.11	1.45	0.04	1.41	0.07	1.27	0.07	3.63	0.08
Na23	1.47	0.34	80.24	0.88	76.66	1.77	75.48	2.18	82.55	1.83	114.35	6.00	139.86	3.88
Al27	38.66	3.10	58.05	1.18	41.14	7.08	57.26	1.51	50.42	2.73	37.14	4.02	145.47	12.42
Si29			195623.45	0.01	195623.4	0.01	195623.39	0.00	195623.39	0.00	194267.87	0.01	193192.7	0.00
P31	34.3	3.76	64.27	6.00	62.55	3.57	63.55	1.41	61.74	0.64	66.23	3.82	42.78	3.83
Ca44	210	16	234	16	224	1	224	16	232	15	236	19	404	10
Sc45	2.93	0.27	1.4	0.01	1.44	0.07	1.45	0.01	1.51	0.04	1.67	0.06	2.51	0.04
V51	2.91	0.03	6.26	0.39	5.76	0.31	5.83	0.02	6.19	0.10	3.69	0.12	9.09	0.09
Mn55	787	39	601	30	595	20	603	7	611	5	666	20	868	12
Fe57	51871	3249	47898	2050	51512	2259	52445	394	53089	1011	39965	1021	84511	4238
Co59	142	5	136	4	129	6	133	2	135	1	122	5	149	2
Ni60	2939	160	3083	119	3047	133	3074	72	3164	49	2957	140	3034	16
Cu65	2.05	0.02	2.09	0.18	2.16	0.39	1.84	0.11	2.15	0.16	3.98	0.22	7.21	0.53
Zn66	55	4	64	3	54	0	52	1	55	1	54	3	90	1
Ga69	0.1	0.01	0.11	0.01	0.09	0.00	0.13	0.00	0.1	0.01	0.12	0.02	0.25	0.02
Y89												0.00	0.01	0.00
Zr90			0.13	0.01	0.12	0.00	0.11	0.01	0.11	0.01	0.21	0.01	0.02	0.01
Nb93			0.35	0.02	0.29	0.01	0.32	0.00	0.32	0.02	0.08	0.01	0.02	0.00
Sn120	0.45	0.06	0.39	0.01	0.39	0.04	0.37	0.04	0.38	0.02	0.4	0.04	0.42	0.01
Pb208			0	0.00	0.03	0.04			0	0.00	0	0.00	0.01	0.00
Ti (610)	0.7	0.22			10.2	0.37	10.7	0.49	11	1.26	154.3	11.33	26.5	0.94
Cr (610)	57.7	2.82			168.8	2.48	169.8	0.87	172.7	3.37	302.7	6.61	235.8	6.05
SIMS														
H	b.d.l	1.96			76.17	38.52	57.45	27.75	56.01	18.39		2	b.d.l	0.98
F	b.d.l	4.76			120.05	6.13	107.3	9.65	101.74	5.34	7	2	b.d.l	0.94

Table 5 ***(continued)*** *Major and trace element composition of olivine mineral separates*

Olivine separate	BD2126B		BD2128A		BD2128B		BD2128C		BD2128D		BD2170A		BD2170B	
Lithology	gt-lz		gt-hz		gt-hz		gt-hz		gt-hz		gt-hz		gt-hz	
	avg	st.dev	avg	st.dev	avg	st.dev	avg	st.dev	avg	st.dev	avg	st.dev	avg	st.dev
EPMA														
SiO_2			40.94	0.11	41.05	0.11	41.37	0.15	40.10	2.25	40.99	0.11	41.00	0.03
TiO_2			0.01		0.01	0.00	0.01	0.00			0.04	0.01	0.04	0.00
Al_2O_3			0.02	0.01	0.03	0.00	0.03	0.01	0.02	0.01	0.03	0.01	0.03	0.01
Cr_2O_3			0.06	0.02	0.04	0.00	0.04	0.01	0.04		0.07	0.01	0.08	0.01
FeO			7.99	0.07	8.12	0.09	7.99	0.12	6.82	0.39	8.45	0.07	8.38	0.04
MnO			0.10	0.02	0.09	0.02	0.10	0.02	0.08	0.02	0.11	0.01	0.10	0.02
MgO			50.63	0.14	50.36	0.11	50.56	0.13	49.36	3.39	49.95	0.05	50.20	0.21
NiO			0.40	0.02	0.40	0.01	0.40	0.02	0.41	0.02	0.40	0.02	0.39	0.01
CaO			0.06	0.00	0.06	0.00	0.06	0.01	0.06	0.04	0.06	0.00	0.07	0.01
forsterite			91.86	0.07	91.71	0.14	91.85	0.37	92.81	6.04	91.33	0.20	91.44	0.21
LA-ICP-MS														
Li7	1.07	0.00	1.78	0.02	1.81	0.20	1.96	0.29	1.3	0.05	2.36	0.04	2.34	0.09
B11	1.39	0.06	1.86	0.16	1.82	0.15	1.67	0.14	1.42	0.10	2.03	0.02	1.89	0.21
Na23	11	0.34	144.44	1.72	145.81	9.42	252.46	180.91	59.88	0.99	230.18	9.75	273.23	85.44
Al27	5	1	121	10	122	6	138	6	47	3	138	2	136	4
Si29	193193	0	196091	0	196091	0	196091	0	196091	0	194502	0	194502	0
P31	74	2	48	2	48	1	45	4	54	3	57	1	34	3
Ca44	160	8	402	5	376	19	396	5	258	3	375	13	383	9
Sc45	1.87	0.06	2.24	0.14	2.16	0.15	2.24	0.02	1.5	0.06	2.72	0.13	2.72	0.09
V51	0.55	0.03	9.28	0.25	9.12	0.15	9.42	0.22	3.79	0.04	11.34	0.25	11.29	0.17
Mn55	628	8	853	20	817	4	859	17	699	8	883	14	888	22
Fe57	42470	164	61487	270	59729	489	62831	1862	53459	460	60216	1054	60639	1381
Co59	126	1	149	3	142	1	150	2	144	2	146	3	146	3
Ni60	3209	25	3226	69	3083	61	3263	80	3464	29	3137	74	3093	54
Cu65	2.04	0.18	7.33	0.32	6.85	0.42	7.25	0.50	2.97	0.40	7.27	0.39	6.87	0.05
Zn66	39	0	75	1	70	0	74	1	62	1	77	1	75	1
Ga69	0.08	0.01	0.22	0.02	0.21	0.02	0.21	0.01	0.08	0.01	0.26	0.02	0.29	0.04
Y89			0.01	0.00	0.01	0.00		0.00			0.01	0.01	0.01	0.00
Zr90			0.06	0.01	0.06	0.02	0.06	0.01	0.15	0.01	0.15	0.02	0.15	0.02
Nb93			0.03	0.00	0.02	0.00	0.03	0.01	0.28	0.02	0.03	0.00	0.03	0.00
Sn120	0.4	0.02	0.41	0.03	0.37	0.06	0.41	0.02	0.39	0.01	0.39	0.01	0.41	0.04
Pb208			0.04	0.07	0	0.00	0.01	0.01	0.01	0.00	0	0.00	0.03	0.00
Ti (610)	2.3	0.24	53.3	1.35	51.5	4.17	53.1	2.10	13.3	0.56	179.2	7.99	170	1.81
Cr (610)	11	0.07	341.5	2.25	333.4	1.12	341.6	13.60	191.2	2.69	535	15.35	541.6	12.23
SIMS														
H	25.8	6.27	81	24.98	34	4.29			b.d.l	7.00	49.7	34.72	59.2	27.30
F	6	1.25	33.4	2.88	35.8	2.38			90	11.64	63.1	9.98	45.5	10.43

Table 5 ***(continued)*** *Major and trace element composition of olivine mineral separates*

Olivine separate	BD2133B		BD2133A		BD2135A		BD2135B		BD2135C	
Lithology	sp-hz		sp-hz		sp-hz		sp-hz		sp-hz	
	avg	st.dev	avg	st.dev	avg	st.dev	avg	st.dev	avg	st.dev
EPMA										
SiO_2	41.46	0.11	41.52	0.04	41.60	0.19	41.66	0.13	41.54	0.14
TiO_2							0.01			
Al_2O_3	0.01	0.00	0.01	0.00	0.01	0.00			0.01	0.00
Cr_2O_3	0.04									
FeO	6.38	0.11	6.46	0.14	5.85	0.09	5.72	0.09	5.66	0.18
MnO	0.08	0.01	0.11	0.01	0.07	0.02	0.08	0.04	0.07	0.01
MgO	52.06	0.15	52.00	0.07	52.03	0.25	52.52	0.05	52.43	0.12
NiO	0.42	0.01	0.41	0.02	0.40	0.03	0.42	0.02	0.42	0.02
CaO	0.04	0.00	0.03	0.00	0.02	0.01	0.02	0.00	0.01	
forsterite	93.6	0.1	93.5	0.2	94.1	0.5	94.2	0.1	94.3	0.2
LA-ICP-MS										
Li7	1.07	0.01	1.14	0.05	1.08	0.02	1.15	0.02	1.08	0.00
B11	2.67	0.17	2.52	0.14	2.2	0.01	2.21	0.12	1.64	0.06
Na23	40.34	0.64	43.77	2.34	10.63	1.09	10.38	0.41	9.99	0.06
Al27	32.84	1.61	31.42	1.70	4.83	0.45	4.05	0.18	3.6	1.85
Si29	196091		194829	0	195997	0	195997	0	195997	0
P31	52.37	2.44	71.27	7.77	69.19	4.96	66.62	2.73	60.38	4.24
Ca44	235.15	12.74	258.4	30.63	169.39	2.72	163.77	4.25	170.02	7.90
Sc45	2.14	0.08	2.02	0.07	2.16	0.13	2.06	0.09	1.96	0.03
V51	3.55	0.03	3.42	0.06	0.64	0.03	0.53	0.01	0.58	0.02
Mn55	673	19	655	5	604	8	599	23	588	15
Fe57	45638	859	44778	1188	41478	434	40595	957	42532	324
Co59	135	1	134	2	125	0	121	2	124	3
Ni60	3274	68	3184	106	3194	34	3108	43	3243	44
Cu65	3.44	0.18	3.6	0.19	2.1	0.25	1.99	0.15	2.06	0.16
Zn66	55.82	2.22	53.63	0.44	35.02	0.27	34.95	1.30	34.46	0.78
Ga69	0.08	0.01	0.08	0.01	0.08	0.01	0.07	0.01	0.08	0.02
Y89			0.01	0.00	0.01	0.00		0.00	0.01	0.00
Zr90	0.36	0.02	0.34	0.01	0.01	0.00				
Nb93	0.79	0.00	0.78	0.00						
Sn120	0.42	0.03	0.44	0.02	0.42	0.03	0.39	0.02	0.38	0.00
Pb208	0.01	0.01					0.01	0.01	0.01	0.00
Ti (610)	14.3	0.39	13.5	0.42	2.9	0.32	1.7	0.27	1.7	0.24
Cr (610)	150.9	5.26	148.7	4.20	10.6	1.48	9.7	0.07	10.7	0.24
SIMS										
H	10.3	12.45	b.d.l	16.32	b.d.l	4.79	b.d.l	20.14	b.d.l	23.11
F	53.3	5.41	49.8	1.43	b.d.l	3.93	b.d.l	1.24	b.d.l	1.20

Table 6 ***(continues on next page)*** *Major and trace element composition of orthopyroxene mineral separates*

Opx separate	BD1140B	M3	BD1140A	M3	BD1141A	M2	BD1152	M3	BD1153	M3	BD1153	M2	BD1672	M2	BD1999A	M3
Lithology	gt-hz		gt-hz		phl-lz		gt-hz		dun		dun		gt-hz		gt-hz	
	avg.	st.dev	avg.	st.dev	avg.	st.dev	avg.	st.dev	avg.	st.dev	avg.	st.dev	avg.	st.dev	avg.	st.dev
EPMA																SiO_2
58.07	0.08	57.77	0.12	57.80	0.12	58.21	0.29	58.77	0.09	58.43	0.11	57.84	0.06	58.73	0.07	
TiO_2	0.04	0.00	0.03	0.00	0.06	0.00			0.16	0.01	0.14	0.01	0.01	0.00		
Al_2O_3	0.73	0.00	0.68	0.01	0.45	0.01	0.70	0.01	0.53	0.00	0.49	0.00	0.72	0.00	0.82	0.00
Cr_2O_3	0.23	0.01	0.21	0.06	0.39	0.04	0.26	0.00	0.47	0.00	0.52	0.03	0.28	0.01	0.29	0.02
FeO	4.90	0.13	4.94	0.13	5.23	0.15	4.81	0.17	3.34	0.04	3.28	0.05	4.81	0.02	3.94	0.05
MnO	0.02	0.01	0.02	0.01	0.15	0.02	0.02	0.00	0.02	0.00	0.11	0.01	0.13	0.02	0.02	0.00
MgO	35.60	0.28	35.54	0.12	34.86	0.03	35.20	0.32	36.17	0.06	36.40	0.05	35.31	0.08	35.96	0.07
NiO	0.08	0.02	0.07	0.01	0.12	0.01	0.11	0.01	0.11	0.01	0.10	0.01	0.12	0.01	0.09	0.01
CaO	0.24	0.01	0.24	0.01	0.43	0.00	0.45	0.00	0.47	0.01	0.48	0.00	0.51	0.00	0.40	0.01
Na_2O	0.05	0.01	0.06	0.03	0.15	0.03	0.08	0.01	0.18	0.00	0.16	0.01	0.11	0.01	0.14	0.01
Total	99.97	0.50	99.56	0.29	99.62	0.17	99.84	0.76	100.20	0.16	100.11	0.08	99.85	0.10	100.39	0.08
LA-ICP-MS																
Li7	0.86	0.01	0.89	0.02	1.49	0.03	0.68	0.01	1.03	0.00	1.00	0.07	0.78	0.02	0.58	0.02
B11	1.42	0.10	1.55	0.08	2.29	0.54	1.40	0.06	2.03	0.11	2.12	0.06	1.90	0.06	2.61	1.29
Na23	417	10	408	11	1374	46	545	3	1639	35	1391	38	814	27	1074	19
Al27	3823	176	3557	92	2361	139	3584	153	2431	135	2856	136	4340	55	3995	189
Si29	272985	0	272985	0	273312	0	274854	0	277191	0	277098	0	274013	0	275322	0
P31	28.69	2.35	27.34	0.66	33.57	1.38	27.81	4.56	32.36	5.13	37.45	2.28	43.12	2.67	31.19	0.85
Ca44	1495	19	1474	10	2072	71	2620	43	2528	136	2246	36	2500	55	2264	95
Sc45	2.11	0.14	1.99	0.07	3.06	0.03	2.12	0.10	2.44	0.28	2.89	0.02	2.76	0.09	2.15	0.10
Ti47	203.72	4.02	160.26	1.41	346.85	56.07	19.34	0.46	781.15	39.29	814.69	23.08	70.62	3.40	56.36	3.22
V51	36.21	0.45	34.00	0.46	25.39	1.04	41.90	0.11	23.13	0.07	21.92	0.68	43.87	0.34	44.63	1.57
Cr53	1420	42	1407	11	2744	43	1810	26	3241	30	3513	180	2141	60	1941	45
Mn55	730	5	734	10	1050	37	812	10	701	7	707	27	858	22	649	24
Fe57	35375	301	35090	447	41659	1476	34107	543	22915	489	23068	818	35705	887	27851	811
Co59	54.51	0.57	54.85	0.44	58.11	0.57	60.47	0.37	46.51	0.80	47.05	1.02	63.09	1.33	52.96	1.80
Ni60	726	9	732	4	827	23	915	15	769	11	771	23	975	22	839	34
Cu65	1.54	0.19	1.79	0.04	2.24	0.27	1.45	0.13	2.29	0.00	2.57	0.14	2.21	0.31	1.36	0.22
Zn66	50.47	1.26	49.76	0.59	47.19	2.02	42.42	0.41	28.85	0.98	29.76	0.98	49.00	1.61	34.63	1.26
Ga69	2.12	0.03	2.11	0.06	0.91	0.05	1.28	0.04	1.82	0.14	1.72	0.05	1.60	0.03	1.05	0.05
Y89	0.03	0.00	0.03	0.00	0.08	0.02	0.01	0.00	0.08	0.00	0.06	0.02	0.02	0.01	0.01	0.00
Zr90	0.27	0.02	0.26	0.04	0.66	0.19	0.15	0.00	0.72	0.05	0.47	0.30	0.28	0.03	0.26	0.03
Nb93	0.12	0.01	0.12	0.00	0.15	0.10	0.17	0.01	0.27	0.11	0.11	0.11	0.09	0.01	0.15	0.02
Sn120	0.43	0.04	0.45	0.03	0.38	0.01	0.40	0.03	0.36	0.00	0.41	0.03	0.43	0.03	0.38	0.06
Pb208	0.01	0.00	0.00	0.00	0.01	0.01	0.00	0.00	0.04	0.06	0.01	0.00	0.01	0.01	0.02	0.02
SIMS																
H	172	14.3	183	20.8	159	4.8	236	24.0	199	26.3	277	134.4	254	8.3	272	28.5
F	8	1.3	8	2.0	19	4.9	8	1.4	26	5.1	27	7.0	15	4.3	25	5.0

Table 6 ***(continued)*** *Major and trace element composition of orthopyroxene mineral separates*

Opx separate	BD1999C	M3	BD3021A	M1	BD3021B	M1	BD3028	M3	BD3028	M2	BD3670A	M1	BD3670B	M1	BD3670C	M1
Lithology	gt-hz		gt-hz		gt-hz		gt-hz		gt-hz		sp-hz		sp-hz		sp-hz	
	avg.	st.dev	avg.	st.dev	avg.	st.dev	avg.	st.dev	avg.	st.dev	avg.	st.dev	avg.	st.dev	avg.	st.dev
EPMA																
SiO_2	58.37	0.12	57.95	0.23	58.34	0.13	58.87	0.11	58.45	0.06	56.50	0.12	56.38	0.12	55.95	0.07
TiO_2	0.02	0.00	0.07	0.00	0.06	0.00			0.01	0.01						
Al_2O_3	0.73	0.01	0.75	0.02	0.74	0.00	0.77	0.00	0.76	0.01	2.66	0.00	2.80	0.01	2.75	0.06
Cr_2O_3	0.37	0.02	0.36	0.02	0.36	0.02	0.30	0.02	0.30	0.02	0.87	0.04	0.89	0.03	0.89	0.02
FeO	4.44	0.11	4.39	0.05	4.46	0.05	3.62	0.08	3.69	0.09	4.28	0.08	4.38	0.04	4.39	0.13
MnO	0.02	0.00	0.13	0.01	0.11	0.01	0.02	0.00	0.08	0.02	0.12	0.02	0.10	0.03	0.12	0.00
MgO	35.61	0.02	35.59	0.06	35.59	0.05	36.10	0.18	36.46	0.16	34.37	0.09	34.25	0.00	34.49	0.13
NiO	0.12	0.03	0.13	0.02	0.11	0.02	0.10	0.01	0.12	0.01	0.10	0.02	0.08	0.00	0.07	0.02
CaO	0.44	0.01	0.53	0.02	0.46	0.01	0.35	0.01	0.37	0.01	1.01	0.01	0.85	0.05	0.96	0.15
Na_2O	0.10	0.01	0.12	0.02	0.13	0.01	0.12	0.01	0.12	0.01			0.03	0.00	0.03	0.01
Total	100.22	0.20	100.01	0.29	100.36	0.23	100.26	0.36	100.35	0.20	99.93	0.22	99.76	0.12	99.64	0.17
LA-ICP-MS																
Li7	0.69	0.04	0.69	0.08	0.84	0.10	0.45	0.11	0.52	0.05	2.39	1.02	2.19	0.14	1.81	0.37
B11	2.62	1.77	3.34	0.08	3.49	0.13	1.57	0.17	2.18	0.07	3.79	0.16	3.07	0.08	2.86	0.32
Na23	779	26	1279	54	1418	131	920	24	1035	19	253	21	269	16	223	5
Al27	3724	35	3819	191	4624	507	3914	109	4487	83	13456	359	12398	49	12913	703
Si29	275322	0	274854	0	274854	0	274854	0	274854	0	265739	0	265506	0	265739	0
P31	28.79	4.56	36.13	2.02	50.36	5.17	31.18	1.64	45.95	2.98	32.93	1.80	29.41	3.90	30.21	3.39
Ca44	2562	21	2603	108	3502	148	2159	90	1850	32	6043	151	5710	340	5933	159
Sc45	2.40	0.05	3.36	0.06	3.79	0.40	2.05	0.09	2.51	0.04	12.88	0.21	11.64	0.05	12.52	0.47
Ti47	69.26	3.00	336.30	7.54	433.33	32.26	8.23	0.20	12.86	1.81	1.88	0.37	1.53	0.25	1.75	0.17
V51	37.97	1.14	41.92	0.20	46.43	2.62	42.63	0.81	44.19	0.58	69.53	1.00	66.03	2.42	69.79	2.23
Cr53	2469	46	2567	41	2728	204	1955	38	2226	14	6392	181	6221	141	6253	225
Mn55	773	22	739	8	767	22	666	22	679	8	817	27	788	19	800	25
Fe57	32135	856	31530	233	32341	175	26103	428	27151	158	34058	1356	32524	528	32257	916
Co59	58.41	1.89	57.44	0.71	58.48	1.98	51.75	0.90	53.35	1.39	55.87	1.21	55.39	0.46	54.42	2.46
Ni60	916	26	898	12	926	12	837	20	838	20	710	20	691	13	661	23
Cu65	2.98	0.02	1.92	0.11	1.98	0.18	1.89	0.38	2.04	0.06	1.22	0.15	1.15	0.17	1.08	0.07
Zn66	39.39	1.43	35.92	0.85	39.61	1.10	33.17	0.40	35.75	0.93	40.01	2.84	38.32	1.12	37.55	1.16
Ga69	1.44	0.05	1.03	0.10	1.27	0.05	1.20	0.02	1.20	0.02	0.94	0.06	0.89	0.04	0.91	0.05
Y89	0.01	0.00	0.06	0.01	0.14	0.03	0.01	0.00	0.01	0.01	0.01	0.00	0.00	0.00	0.00	0.00
Zr90	0.17	0.01	0.61	0.14	1.61	0.08	0.21	0.02	0.35	0.10	0.01	0.00	0.01	0.00	0.01	0.00
Nb93	0.20	0.01	0.18	0.09	0.77	0.30	0.39	0.03	0.50	0.03	0.02	0.00	0.02	0.00	0.02	0.00
Sn120	0.38	0.01	0.40	0.01	0.43	0.02	0.38	0.01	0.41	0.01	0.46	0.01	0.44	0.01	0.41	0.04
Pb208	0.01	0.01	0.01	0.01	0.08	0.00	0.00	0.00	0.07	0.06	0.01	0.01	0.00	0.00	0.00	0.00
SIMS																
H	249	18.2	132	7.1	148	7.4	195	14.4	243	48.2	5	1.1	35	2.7	43	2.2
F	18	2.5	16	2.4	16	1.7	14	2.1	16	4.3	0	0.0	0	0.0	0	0.0

Table 6 ***(continued)*** *Major and trace element composition of orthopyroxene mineral separates*

Opx separate	BD3676A	M3	BD3676B	M3	BD2122A	M4	BD2122B	M4	BD2122C	M4	BD2124	M1	BD2125A	M1	BD2125B	M1
Lithology	gt-hz		gt-hz		gt-hz		gt-hz		gt-hz		gt-lz		gt-hz		gt-hz	
	avg.	st.dev	avg.	st.dev	avg.	st.dev	avg.	st.dev	avg.	st.dev	avg.	st.dev	avg.	st.dev	avg.	st.dev
EPMA																
SiO_2	58.37	0.21	58.29	0.18	57.98	0.20	57.83	0.03	57.72	0.17	57.82	0.09	58.14	0.10	58.34	0.26
TiO_2	0.02	0.00	0.02	0.00	0.15	0.00	0.15	0.01	0.15	0.00	0.09	0.00	0.01	0.00	0.02	0.00
Al_2O_3	0.70	0.00	0.72	0.00	0.83	0.00	0.83	0.01	0.79	0.02	0.87	0.01	0.74	0.01	0.74	0.01
Cr_2O_3	0.34	0.01	0.37	0.01	0.45	0.01	0.45	0.02	0.44	0.02	0.32	0.01	0.35	0.02	0.32	0.01
FeO	4.39	0.04	4.52	0.07	5.16	0.02	5.37	0.06	5.78	0.09	5.03	0.06	4.11	0.13	4.13	0.10
MnO	0.02	0.00	0.02	0.01							0.13	0.01	0.08	0.02	0.09	0.01
MgO	35.30	0.02	35.77	0.09	35.25	0.07	35.49	0.17	35.01	0.08	34.77	0.06	36.09	0.17	35.91	0.03
NiO	0.12	0.03	0.11	0.02	0.11	0.01	0.11	0.01	0.11	0.01	0.11	0.04	0.13	0.01	0.12	0.02
CaO	0.45	0.00	0.44	0.00	0.45	0.01	0.46	0.01	0.47	0.01	0.93	0.01	0.52	0.01	0.52	0.00
Na_2O	0.10	0.02	0.09	0.01	0.15	0.01	0.15	0.01	0.15	0.01	0.20	0.00	0.10	0.01	0.10	0.02
Total	99.81	0.24	100.35	0.29	100.55	0.14	100.85	0.19	100.64	0.21	100.27	0.17	100.27	0.37	100.28	0.34
LA-ICP-MS																
Li7	0.69	0.02	0.69	0.07	0.98	0.24	1.02	0.21	0.86	0.14	0.96	0.07	0.63	0.01	0.66	0.03
B11	1.66	0.11	2.28	0.56	1.66	0.09	1.41	0.11	1.35	0.06	1.94	0.09	2.13	0.14	2.29	0.26
Na23	800	61	804	17	1102	21	1234	13	1253	39	1604	67	765	27	886	151
Al27	3671	52	3840	189	3959	81	3951	40	3924	56	4640	318	3736	196	4102	219
Si29	274854	0	274854	0	270647	0	270647	0	270647	0	269245	0	272985	0	272985	0
P31	30.58	4.02	33.38	2.83	27.64	1.73	29.30	4.67	31.05	2.93	31.20	5.03	30.48	4.79	34.27	5.09
Ca44	2585	66	2710	37	2475	148	2568	72	2788	52	5334	395	2864	64	3043	116
Sc45	2.37	0.04	2.43	0.06	3.80	0.14	4.09	0.19	4.40	0.07	3.55	0.31	2.48	0.05	2.56	0.09
Ti47	69.95	1.66	72.55	1.66	712	23	749	12	779	17	502	31	70	2	76	3
V51	37.73	0.26	39.57	1.31	46.62	2.45	46.04	1.25	45.59	0.91	48.85	1.76	27.29	0.36	27.97	0.31
Cr53	2398	22	2499	65	2944	149	2970	84	2876	39	2175	108	2244	25	2322	39
Mn55	761	4	788	22	881	68	918	32	981	15	849	44	732	14	730	10
Fe57	32035	757	32521	944	35055	2346	36554	690	41660	465	35928	1426	30118	598	29175	142
Co59	57.44	0.99	59.54	2.80	56.09	1.76	56.49	1.41	61.88	1.75	61.44	2.97	56.79	0.24	56.67	0.51
Ni60	916	16	938	29	842	36	849	21	886	24	942	45	910	16	912	10
Cu65	3.23	0.29	3.43	0.21	2.29	0.17	2.39	0.07	2.31	0.30	4.59	0.17	1.90	0.26	1.96	0.23
Zn66	39.77	0.83	39.76	2.58	46.01	2.43	49.81	1.36	55.28	0.64	42.85	2.04	36.24	0.70	37.24	0.33
Ga69	1.44	0.05	1.50	0.03	1.90	0.12	1.89	0.03	2.03	0.08	2.38	0.10	0.77	0.06	0.91	0.03
Y89	0.01	0.00	0.01	0.01	0.09	0.01	0.13	0.02	0.14	0.01	0.07	0.01	0.01	0.00	0.01	0.00
Zr90	0.35	0.12	0.38	0.15	0.87	0.14	1.27	0.24	1.37	0.31	0.14	0.02	0.23	0.03	0.29	0.02
Nb93	0.45	0.23	0.52	0.25	0.18	*	0.23	0.08	0.28	0.16	0.07	0.00	0.11	0.02	0.13	0.00
Sn120	0.40	0.01	0.39	0.03	0.34	0.01	0.37	0.01	0.36	0.03	0.37	0.03	0.39	0.02	0.41	0.01
Pb208	0.01	0.01	0.03	0.02	0.01	0.00	0.01	0.01	0.01	0.00	0.00	0.00	0.00	0.00	0.06	0.07
SIMS																
H	263	25.2	308	23.2	151	15.1	90	25.8	71	2.3	109	41.5	151	11.0		
F	20	4.6	22	5.0	37	6.4	36	5.9	27	7.0	23	3.8	21	2.8		

Table 6 ***(continued)*** *Major and trace element composition of orthopyroxene mineral separates*

Opx separate	BD2125C	M1	BD2125A	M4	BD2126A	M4	BD2126B	M4	BD2126	M1	BD2128	M1	BD2128	M4	BD2133A	M1
Lithology	gt-hz		gt-hz		gt-lz		gt-lz		gt-lz		gt-lz		gt-lz		sp-hz	
	avg.	st.dev	avg.	st.dev	avg.	st.dev	avg.	st.dev	avg.	st.dev	avg.	st.dev	avg.	st.dev	avg.	st.dev
EPMA																
SiO_2	58.33	0.11	58.86	0.09	58.01	0.07	58.05	0.05	57.45	0.19	57.78	0.10	58.69	0.13	57.38	0.14
TiO_2	0.02		0.02		0.04	0.01	0.04	0.00	0.04	0.00	0.07	0.00			0.23	0.01
Al_2O_3	0.70	0.00	0.74	0.00	0.94	0.00	0.94	0.01	0.92	0.00	0.89	0.00	0.80	0.01	0.90	0.01
Cr_2O_3	0.31	0.00	0.30	0.02	0.26	0.02	0.23	0.01	0.25	0.01	0.36	0.03	0.30	0.01	0.56	0.01
FeO	4.16	0.01	4.18	0.03	5.59	0.08	5.48	0.08	5.41	0.09	4.98	0.10	3.61	0.07	4.99	0.08
MnO	0.11	0.02							0.14	0.01	0.15	0.02			0.11	0.02
MgO	35.87	0.04	36.15	0.13	34.59	0.13	34.51	0.15	34.55	0.13	34.80	0.05	36.73	0.03	34.12	0.09
NiO	0.11	0.02	0.13	0.01	0.12	0.01	0.12	0.01	0.12	0.01	0.12	0.02	0.10	0.01	0.13	0.01
CaO	0.51	0.01	0.51	0.01	1.07	0.00	1.08	0.01	1.08	0.01	1.01	0.01	0.38	0.00	1.02	0.01
Na_2O	0.09	0.00	0.09	0.01	0.18	0.02	0.19	0.02	0.18	0.01	0.18	0.01	0.13	0.01	0.28	0.02
Total	100.19	0.13	100.99	0.15	100.84	0.29	100.68	0.25	100.13	0.19	100.35	0.19	100.77	0.11	99.72	0.23
LA-ICP-MS																
Li7	0.64	0.02	0.66	0.08	1.17	0.11	1.13	0.06	1.27	0.02	0.97	0.18	0.37	0.02	1.28	0.04
B11	2.04	0.12	1.12	0.14	1.41	0.09	1.44	0.16	2.01	0.04	2.58	0.81	1.03	0.11	2.66	0.09
Na23	797	32	740	18	1432	67	1397	5	1491	34	1525	62	918	27	2471	47
Al27	4001	172	3639	153	4699	124	4666	139	4829	169	5012	262	3789	72	4809	94
Si29	272985	0	272985	0	271582	0	271582	0	271582	0	273919	0	273919	0	271115	0
P31	31.47	3.19	24.35	4.20	28.40	2.01	26.78	3.35	33.50	2.68	35.44	1.64	34.10	8.91	32.28	0.90
Ca44	3063	124	2874	76	5746	318	6011	271	6099	156	5888	306	2156	114	5744	154
Sc45	2.49	0.17	2.02	0.08	3.01	0.13	3.13	0.13	3.36	0.19	3.62	0.19	1.89	0.08	4.86	0.17
Ti47	74	2	67	2	202	7	203	13	217	7	427	24	9	1	1273	25
V51	27.63	0.43	26.96	0.55	48.13	1.35	47.93	1.52	49.95	1.42	50.31	1.72	41.21	0.69	62.30	1.11
Cr53	2374	37	2018	64	1593	55	1640	62	1819	67	2595	62	1914	38	4155	72
Mn55	731	16	747	20	888	45	912	22	908	24	839	25	635	10	907	14
Fe57	29657	605	28992	908	37510	1330	38611	756	38706	1408	34844	1439	25439	102	36540	513
Co59	55.71	0.19	55.83	1.45	62.70	2.05	64.77	1.76	64.29	1.77	61.29	2.06	50.32	0.44	62.04	1.56
Ni60	907	26	912	23	965	26	994	31	975	24	990	35	808	9	981	14
Cu65	1.90	0.16	1.71	0.18	4.52	0.40	4.51	0.23	4.63	0.09	4.42	0.17	1.87	0.11	4.49	0.06
Zn66	37.85	1.35	37.69	1.83	50.59	1.11	50.93	2.32	48.98	2.03	41.43	1.61	31.84	1.50	42.21	1.44
Ga69	0.83	0.03	0.83	0.05	2.73	0.10	2.82	0.08	2.82	0.08	2.24	0.13	1.16	0.11	3.29	0.03
Y89	0.01	0.01	0.01	0.00	0.05	0.01	0.06	0.01	0.06	0.00	0.06	0.01	0.01	0.01	0.13	0.02
Zr90	0.27	0.03	0.35	0.10	0.08	0.02	0.08	0.01	0.07	0.01	0.18	0.01	0.32	0.19	0.44	0.01
Nb93	0.13	0.01	0.23	0.11	0.07	0.02	0.06	0.01	0.06	0.00	0.08	0.02	0.82	0.80	0.06	0.01
Sn120	0.39	0.01	0.32	0.01	0.35	0.04	0.36	0.04	0.41	0.01	0.40	0.01	0.34	0.05	0.41	0.04
Pb208	0.01	0.00	0.01	0.01	0.00	0.00	0.00	0.00			0.03	0.04	0.03	0.03	0.00	0.00
SIMS																
H	159	11.6	182	40.1	142	31.8	143	18.2	147	16.9	168	14.2	214	16.3	137	16.8
F	22	3.0	26	5.2	25	3.2	22	5.4	15	5.2	27	3.9	16	3.0	28	3.7

Table 6 ***(continued)*** *Major and trace element composition of orthopyroxene mineral separates*

Opx separate	BD2133C	M4	BD2133B	M4	BD2133	M2	BD2135B	M1	BD2135A	M1	BD2135B	M4	BD2170	M1	BD2170B	M4	BD2170A	M4
Lithology	sp-hz		sp-hz		sp-hz		sp-hz		sp-hz		sp-hz		gt-hz		gt-hz		gt-hz	
	avg.	st.dev	avg.	st.dev	avg.	st.dev	avg.	st.dev	avg.	st.dev	avg.	st.dev	avg.	st.dev	avg.	st.dev	avg.	st.dev
EPMA																		
SiO_2	58.57	0.21	58.67	0.12	57.96	0.07	57.57	0.08	57.37	0.13	58.05	0.07	57.56	0.15	58.13	0.08	57.83	0.40
TiO_2	0.01	0.00	0.01	0.00	0.01	0.00	0.03	0.00	0.03	0.00	0.02	0.00	0.22	0.00	0.22	0.00	0.22	0.01
Al_2O_3	0.72	0.00	0.70	0.00	0.69	0.01	1.65	0.01	1.62	0.03	1.65	0.00	0.85	0.00	0.90	0.00	0.89	0.00
Cr_2O_3	0.37	0.00	0.37	0.04	0.34	0.02	0.55	0.02	0.50	0.01	0.49	0.02	0.48	0.01	0.52	0.01	0.50	0.01
FeO	3.94	0.10	3.96	0.02	3.92	0.02	3.72	0.06	3.77	0.04	3.75	0.10	5.04	0.07	5.11	0.02	5.21	0.04
MnO					0.12	0.01	0.09	0.01	0.10	0.03			0.12	0.00				
MgO	36.37	0.02	36.61	0.20	36.40	0.23	36.11	0.02	36.15	0.12	36.51	0.03	34.28	0.17	34.83	0.13	34.81	0.10
NiO	0.08	0.01	0.11	0.02	0.11	0.01	0.09	0.00	0.07	0.01	0.09	0.01	0.13	0.01	0.13	0.01	0.12	0.01
CaO	0.42	0.06	0.36	0.02	0.37	0.05	0.30	0.02	0.47	0.16	0.29	0.02	0.94	0.01	0.96	0.01	1.00	0.01
Na_2O	0.07	0.03	0.04	0.01	0.06	0.01	0.04	0.01	0.07	0.02	0.03	0.01	0.26	0.02	0.27	0.01	0.29	0.02
Total	100.58	0.16	100.86	0.33	100.00	0.19	100.15	0.12	100.14	0.07	100.90	0.04	99.87	0.19	101.12	0.16	100.90	0.37
LA-ICP-MS																		
Li7	0.47	0.03	0.49	0.03	0.54	0.02	0.40	0.08	0.48	0.07	0.39	0.05	1.19	0.05	1.22	0.05	1.14	0.02
B11	1.13	0.06	0.82	0.14	2.47	0.37	1.74	0.11	1.95	0.21	1.37	0.04	2.66	0.03	1.29	0.01	1.16	0.16
Na23	405	5	402	0	340	9	328	70	387	59	335	59	2347	55	2342	49	2236	54
Al27	3515	85	3542	69	3685	239	7969	72	7945	415	7672	185	4928	113	4795	353	4789	351
Si29	271115	0	271115	0	271115	0	271115	0	271115	0	271115	0	272798	0	272985	0	272985	0
P31	23.33	1.15	24.16	2.22	31.07	5.83	32.95	2.98	33.36	1.74	28.25	2.41	28.00	1.99	23.50	0.95	20.29	2.66
Ca44	2013	80	1970	17	1577	87	1953	225	2310	360	1906	293	5680	118	5843	319	5838	402
Sc45	2.85	0.10	2.84	0.06	3.40	0.09	8.68	0.24	9.18	0.60	8.35	0.41	4.92	0.05	4.54	0.31	4.54	0.30
Ti47	63	3	65	2	66	3	156	3	157	6	149	5	1276	19	1284	57	1279	118
V51	33.96	0.55	34.03	0.21	31.81	1.50	52.21	1.09	55.23	2.26	55.11	1.22	60.51	1.63	62.29	1.35	61.78	1.49
Cr53	2468	5	2448	29	2500	87	3473	238	3581	212	3376	88	4002	162	3713	24	3497	95
Mn55	738	16	752	10	716	23	671	24	686	27	697	26	908	17	946	27	969	24
Fe57	27760	249	28423	549	27230	787	26096	431	26875	1067	26859	447	36641	1075	36456	899	37861	810
Co59	52.21	0.97	52.77	1.20	50.65	2.20	42.20	0.82	44.00	1.43	44.77	0.80	62.29	0.53	61.94	0.60	63.59	2.05
Ni60	812	7	822	5	784	39	600	5	624	17	650	15	984	19	990	15	1018	33
Cu65	2.46	0.10	2.41	0.10	2.38	0.16	1.38	0.13	1.42	0.12	1.33	0.07	4.26	0.11	4.49	0.46	4.51	0.36
Zn66	31.89	0.75	32.14	1.31	27.72	3.70	22.89	0.91	25.33	1.40	25.67	0.57	41.64	1.95	43.86	1.90	44.44	2.03
Ga69	0.53	0.03	0.53	0.05	0.51	0.03	1.21	0.04	1.20	0.02	1.21	0.03	3.28	0.05	3.27	0.08	3.35	0.08
Y89	0.02	0.01	0.01	0.01	0.01	0.00	0.30	0.01	0.35	0.05	0.32	0.04	0.13	0.01	0.16	0.03	0.17	0.02
Zr90	0.40	0.07	0.34	0.02	0.27	0.03	0.20	0.02	0.25	0.04	0.25	0.05	0.44	0.01	0.51	0.04	0.53	0.08
Nb93	0.30	0.00	0.31	0.02	0.26	0.02	0.07	0.11	0.01	0.01	0.01	0.00	0.05	0.00	0.05	0.01	0.05	0.02
Sn120	0.34	0.02	0.38	0.02	0.39	0.01	0.40	0.03	0.39	0.03	0.37	0.06	0.41	0.02	0.37	0.04	0.39	0.05
Pb208	0.01	0.00	0.02		0.01	0.01	0.03	0.03	0.04	0.05	0.01	0.01	0.00		0.00	0.00	0.02	0.02
SIMS																		
H	157	4.7	186	5.6	186	6.8	27	12.6	171	10.8	51	5.0	164	5.5	194	30.1	193	19.4
F	14	2.2	15	2.7	13	4.0	0	0.0	16	1.8	5	0.8	29	4.8	33	5.3	36	7.6

Table 7 ***(continues on next page)*** *Major and trace element composition of clinopyroxene mineral separates*

Clinopyroxene separates	BD1140		BD1141A		BD1152		BD1672B		BD1672A		BD1999D	
	avg.	st.dev	avg.	st.dev	avg.	st.dev	avg.	st.dev	avg.	st.dev	avg.	st.dev
EPMA												
SiO_2	54.18		54.79	0.14	54.89	0.15	54.86	0.19	54.72	0.21	54.85	0.13
TiO_2	0.14		0.11	0.01			0.02		0.03		0.03	0.00
Al_2O_3	1.80		2.52	0.02	1.59	0.01	1.93	0.02	1.91	0.06	1.85	0.01
Cr_2O_3	1.54		1.78	0.01	1.45	0.05	1.57	0.12	1.53	0.05	2.13	0.04
FeO	2.50		2.38	0.14	2.11	0.07	2.29	0.10	2.27	0.09	1.96	0.01
MnO			0.09	0.01			0.10	0.01	0.10			
MgO	16.30		15.37	0.14	16.73	0.13	16.68	0.16	16.47	0.12	16.26	0.04
NiO									0.10			
CaO	21.62		20.29	0.05	20.80	0.01	19.88	0.04	19.94	0.04	19.92	0.10
Na_2O	1.08		2.13	0.05	1.36	0.06	1.65	0.05	1.66	0.12	1.78	0.04
Total	99.30		99.47	0.24	99.03	0.39	98.99	0.16	98.68	0.45	98.88	0.13
LA-ICP-MS												
Al27	13290	231	12745	366	8533	92	11159	1108	10467	89	9812	257
Sc45	23.1	0.5	21.5	0.5	13.2	0.4	15.9	0.4	16.0	0.3	15.4	0.7
Ti47	652	73	609	112	39	3	113	9	122	16	157	16
V51	377	5	351	9	269	9	309	11	290	6	311	14
Cr53	11491	246	11223	209	9704	321	9667	184	9505	376	11442	373
Fe57	11333	666	10944	770	10327	367	12273	358	12161	206	11976	483
Co59	17.15	0.60	16.03	0.72	21.69	0.88	24.20	0.97	23.12	0.49	24.31	0.78
Ni60	320	2	297	11	437	19	480	22	462	15	471	18
Sr88	437	12	411	17	618	26	381	6	370	8	452	19
Y89	1.95	0.10	1.80	0.04	0.27	0.01	0.34	0.07	0.36	0.06	0.27	0.02
Zr90	41.12	1.45	38.29	1.86	6.88	0.14	8.85	0.38	9.62	0.08	10.44	0.51
Nb93	1.15	0.02	0.74	0.42	0.64	0.11	0.51	0.13	0.42	0.11	0.50	0.05
Ba137	3.99	3.36	1.92	2.18	1.57	0.49	0.85	0.57	0.47	0.24	0.40	0.19
La139	15.16	0.37	14.45	0.32	4.97	0.28	4.39	0.10	3.81	0.14	4.53	0.25
Ce140	54.55	1.19	52.51	1.15	27.53	1.84	21.01	0.59	17.94	0.44	23.30	0.23
Pr141	7.14	0.10	6.83	0.05	5.55	0.34	3.59	0.06	3.21	0.12	4.23	0.14
Nd143	26.66	0.50	25.61	1.72	24.55	1.37	17.84	0.09	16.49	0.60	22.13	0.62
Sm147	3.60	0.24	3.22	0.10	2.48	0.10	3.14	0.19	3.11	0.29	3.23	0.15
Eu153	0.78	0.01	0.73	0.03	0.38	0.04	0.64	0.06	0.59	0.05	0.57	0.05
Gd157	1.72	0.03	1.66	0.06	0.65	0.06	1.06	0.09	0.98	0.08	0.70	0.03
Tb159	0.17	0.01	0.16	0.02	0.03	0.02	0.06	0.00	0.06	0.01	0.04	0.01
Dy163	0.65	0.08	0.61	0.09	0.11	0.04	0.13	0.02	0.12	0.03	0.07	0.03
Ho165	0.08	0.02	0.08	0.01	0.01	0.00	0.01	0.01	0.01	0.00	0.01	0.00
Er166	0.15	0.02	0.16	0.00	0.03	0.00	0.03	0.01	0.03	0.01	0.03	0.01
Tm169	0.02	0.00	0.02	0.01	0.00	0.00	0.00	0.00	0.01	0.00	0.00	0.00
Yb172	0.08	0.02	0.08	0.01	0.02	0.01	0.02	0.01	0.02	0.01	0.02	0.00
Lu175	0.01	0.01	0.01	0.00	0.00	0.00	0.01	0.00	0.00	0.00	0.00	0.00
Hf178	1.68	0.15	1.58	0.02	0.46	0.06	0.48	0.10	0.49	0.08	0.62	0.02
Ta181	0.09	0.01	0.07	0.02	0.04	0.01	0.05	0.01	0.04	0.02	0.04	0.01
Pb208	4.26	1.93	3.06	0.42	1.62	1.22	1.10	0.52	0.96	0.68	0.69	0.06
Ti (610 cal)	535	26	499	47	33	3	96	7	114	5	130	16
Cr (610 cal)	11155	197	10565	340	8829	567	10456	286	9953	238	14248	956
SIMS												
H	280	28.6	300	21.0	318	92.4	285	20.2	341	93.3	286	27.2
F	24	5.1	20	2.1	12	4.0	22	1.9	19	2.4	32	3.4

Table 7 ***(continued)*** *Major and trace element composition of clinopyroxene mineral separates*

Clinopyroxene separates	BD1999C		BD1999B		BD1999A		BD3067C		BD3067B		BD3067A	
	avg.	st.dev	avg.	st.dev	avg.	st.dev	avg.	st.dev	avg.	st.dev	avg.	st.dev
EPMA												
SiO_2	54.59	0.16	54.91	0.12	55.41	0.10	55.00	0.16	55.05	0.15	55.24	0.22
TiO_2	0.02	0.01	0.03	0.01	0.03		0.23	0.01			0.21	0.01
Al_2O_3	1.90	0.01	1.88	0.01	1.83	0.01	0.65	0.04	0.62	0.01	0.57	0.02
Cr_2O_3	2.22	0.04	2.16	0.05	2.07	0.05	1.06	0.11	0.79	0.11	0.95	0.25
FeO	2.15	0.10	2.04	0.05	2.11	0.03	2.82	0.32	2.97	0.10	2.88	0.11
MnO			0.10	0.03	0.11		0.07	0.03			0.09	0.01
MgO	16.37	0.13	16.27	0.05	16.47	0.13	16.34	0.32	16.54	0.14	16.49	0.32
NiO	0.09											
CaO	19.87	0.03	19.85	0.06	19.69	0.16	21.96	0.20	22.11	0.17	21.97	0.21
Na_2O	1.90	0.09	1.84	0.03	1.84	0.13	1.25	0.10	1.12	0.02	1.18	0.07
Total	99.12	0.42	99.13	0.24	99.58	0.08	99.42	0.34	99.52	0.25	99.58	0.33
LA-ICP-MS												
Al27	10034	263	10233	215	10206	549	2929	112	3032	109	2650	66
Sc45	15.6	0.3	15.9	0.3	16.1	0.7	53.6	3.5	52.5	2.1	37.2	1.2
Ti47	146	15	157	25	262	172	1151	65	1084	52	1143	24
V51	292	4	297	17	288	5	394	17	404	23	255	11
Cr53	11546	338	11823	545	11937	293	13530	1922	12036	820	21549	2855
Fe57	10629	99	10720	538	11135	211	14469	1367	14701	601	12464	748
Co59	22.38	1.13	22.02	1.08	21.66	0.88	19.41	0.33	19.10	0.54	17.36	0.45
Ni60	442	7	443	17	435	10	244	37	201	11	239	21
Sr88	420	4	443	3	449	10	146	7	142	5	201	9
Y89	0.26	0.03	0.28	0.01	0.28	0.04	3.89	0.38	3.78	0.18	5.30	0.29
Zr90	10.93	0.43	11.38	0.24	11.20	0.29	104.68	12.64	92.88	9.49	118.91	7.62
Nb93	0.56	0.02	0.61	0.07	0.71	0.17	0.51	0.18	0.26	0.10	0.53	0.18
Ba137	0.33	0.08	1.72	1.39	1.04	1.05	2.27	1.61	0.36	0.17	4.22	0.94
La139	4.16	0.10	4.59	0.19	4.92	0.18	2.43	0.57	2.15	0.10	2.94	0.14
Ce140	20.52	0.37	21.98	0.56	22.87	0.46	11.16	2.33	10.81	0.32	14.09	0.63
Pr141	3.75	0.03	4.10	0.24	4.26	0.05	1.95	0.36	2.02	0.08	2.54	0.09
Nd143	21.08	0.37	22.19	0.52	22.64	0.64	9.77	1.60	10.59	0.73	13.50	0.56
Sm147	3.22	0.13	3.14	0.34	3.28	0.20	2.62	0.46	2.76	0.18	3.60	0.38
Eu153	0.53	0.03	0.56	0.01	0.59	0.01	0.82	0.12	0.89	0.08	1.13	0.11
Gd157	0.98	0.13	0.73	0.21	0.77	0.20	2.09	0.34	2.27	0.11	3.00	0.18
Tb159	0.05	0.01	0.04	0.01	0.04	0.01	0.25	0.03	0.28	0.04	0.36	0.03
Dy163	0.11	0.02	0.08	0.03	0.09	0.04	1.31	0.10	1.28	0.13	1.71	0.10
Ho165	0.01	0.01	0.01	0.01	0.01	0.01	0.18	0.01	0.18	0.02	0.25	0.02
Er166	0.02	0.01	0.03	0.01	0.02	0.01	0.34	0.03	0.33	0.02	0.48	0.03
Tm169	0.00	0.00	0.00	0.00	0.00	0.00	0.03	0.00	0.04	0.01	0.04	0.01
Yb172	0.02	0.01	0.03	0.01	0.02	0.01	0.13	0.03	0.17	0.01	0.24	0.02
Lu175	0.00	0.00	0.01	0.00	0.00	0.00	0.02	0.00	0.02	0.01	0.02	0.00
Hf178	0.66	0.02	0.61	0.03	0.60	0.04	7.19	0.99	6.11	0.76	6.79	0.33
Ta181	0.04	0.00	0.04	0.02	0.04	0.01	0.03	0.01	0.02	0.00	0.03	0.01
Pb208	0.68	0.09	1.72	1.86	2.07	2.37	0.37	0.09	0.30	0.09	2.70	2.48
Ti (610 cal)	121	13	125	17	133	12	1108	66	1052	50	1119	21
Cr (610 cal)	14054	565	13829	381	13901	871	6468	738	5192	250	8288	1246
SIMS												
H	287	22	283	23	253	18					102	46
F	29	3	30	5	25	2	26	5	18	3	25	10

Table 7 ***(continued)*** *Major and trace element composition of clinopyroxene mineral separates*

Clinopyroxene	BD2124B		BD2124A		BD2125		BD2126B		BD2126A		BD2128B		BD2128A		BD2135	
separates	avg.	st.dev	avg.	st.dev	avg.	st.dev	avg.	st.dev	avg.	st.dev	avg.	st.dev	avg.	st.dev	avg.	st.dev
EPMA																
SiO_2	55.49	0.13	54.63	0.07	54.89	0.07	54.78	0.26	54.84	0.05	55.27	0.09	55.19	0.30	54.39	0.27
TiO_2	0.16	0.01	0.16	0.01	0.03	0.01	0.06	0.01	0.12	0.02	0.12	0.01	0.11	0.01	0.07	0.01
Al_2O_3	2.16	0.02	2.16	0.02	1.83	0.00	1.91	0.02	1.82	0.01	1.85	0.00	1.81	0.02	2.60	0.02
Cr_2O_3	1.18	0.03	1.22	0.08	1.62	0.04	0.82	0.07	1.20	0.06	1.23	0.07	1.24	0.08	1.65	0.12
FeO	2.83	0.10	2.86	0.07	1.84	0.03	3.15	0.07	2.82	0.10	2.81	0.07	2.83	0.06	1.22	0.04
MnO	0.10	0.03	0.11	0.01	0.08		0.12	0.03	0.11	0.01	0.10	0.01	0.12	0.02		
MgO	18.18	0.27	17.69	0.14	16.86	0.12	18.46	0.08	18.26	0.13	18.50	0.30	18.47	0.20	15.87	0.14
NiO	0.09	0.00					0.12	0.02			0.11	0.02				
CaO	17.80	0.03	17.81	0.05	20.30	0.01	17.72	0.04	18.03	0.00	18.02	0.04	17.98	0.04	21.73	0.29
Na_2O	1.56	0.02	1.62	0.03	1.51	0.02	1.29	0.04	1.39	0.03	1.43	0.03	1.37	0.02	1.44	0.10
Total	99.53	0.38	98.30	0.32	99.00	0.19	98.42	0.07	98.63	0.22	99.39	0.39	99.20	0.54	99.04	0.54
LA-ICP-MS																
Al27	11412	44	11428	349	10147	137	10117	607	10407	180	9781	491	10002	532	12870	896
Sc45	15.5	0.2	15.6	0.2	13.2	0.4	13.8	0.6	11.7	0.4	12.9	0.8	12.8	0.6	49.4	3.4
Ti47	977	35	943	13	151	13	719	15	366	15	686	55	665	43	367	34
V51	238	5	243	11	190	2	202	12	192	3	196	10	196	6	203	21
Cr53	9954	49	10694	550	13088	488	11405	421	9438	374	11941	357	12983	676	20349	2684
Fe57	14023	256	14326	110	9041	294	14142	1028	15488	159	13904	1398	13276	608	6303	739
Co59	28.71	0.17	29.37	1.26	23.04	0.17	29.89	1.31	32.54	1.42	28.43	1.09	28.77	1.11	14.67	1.28
Ni60	527	15	536	37	477	10	551	33	567	25	538	25	533	13	263	22
Sr88	175	1	183	6	316	12	126	9	61	3	121	9	123	4	590	59
Y89	1.68	0.05	1.76	0.11	0.43	0.04	1.23	0.07	1.25	0.03	1.16	0.17	1.21	0.10	13.93	0.99
Zr90	4.38	0.05	4.14	0.13	14.39	0.90	3.48	0.15	1.33	0.11	3.27	0.14	2.98	0.26	16.89	0.73
Nb93	0.56	0.09	0.62	0.15	0.39	0.08	0.20	0.06	0.31	0.08	0.37	0.16	0.23	0.05	0.21	0.07
Ba137	0.69	0.08	1.76	1.40	0.64	0.38	0.51	0.38	1.16	1.12	1.94	1.85	0.21	0.06	2.06	1.77
La139	2.42	0.11	2.41	0.05	4.55	0.18	1.39	0.06	1.83	0.09	1.38	0.16	1.26	0.07	73.89	3.45
Ce140	10.37	0.15	10.45	0.19	20.85	0.36	5.50	0.42	6.00	0.35	5.51	0.60	5.13	0.17	230.76	20.22
Pr141	1.627	0.068	1.617	0.040	3.630	0.191	0.915	0.065	0.774	0.048	0.884	0.065	0.899	0.023	28.427	2.712
Nd143	7.600	0.443	7.540	0.509	16.830	0.293	5.047	0.247	3.370	0.123	4.757	0.538	4.527	0.291	109.293	10.695
Sm147	1.390	0.131	1.350	0.159	2.860	0.137	1.393	0.074	0.610	0.095	1.170	0.070	1.197	0.162	15.700	1.883
Eu153	0.398	0.023	0.396	0.021	0.726	0.035	0.402	0.002	0.180	0.023	0.327	0.050	0.341	0.052	3.463	0.337
Gd157	0.833	0.116	0.970	0.080	1.255	0.172	0.873	0.096	0.498	0.064	0.797	0.047	0.890	0.075	8.890	1.309
Tb159	0.099	0.020	0.098	0.014	0.094	0.006	0.091	0.009	0.057	0.012	0.078	0.007	0.080	0.014	0.814	0.022
Dy163	0.472	0.046	0.487	0.070	0.278	0.024	0.381	0.086	0.274	0.016	0.359	0.016	0.368	0.057	3.580	0.445
Ho165	0.070	0.008	0.075	0.008	0.023	0.004	0.054	0.001	0.061	0.016	0.047	0.007	0.046	0.010	0.535	0.017
Er166	0.165	0.032	0.149	0.026	0.029	0.008	0.119	0.022	0.122	0.015	0.106	0.008	0.113	0.029	1.263	0.150
Tm169	0.024	0.002	0.020	0.008	0.006	0.003	0.007	0.002	0.015	0.001	0.012	0.004	0.009	0.001	0.144	0.031
Yb172	0.104	0.035	0.094	0.026	0.024	0.009	0.065	0.027	0.081	0.020	0.087	0.035	0.081	0.029	0.780	0.046
Lu175	0.011	0.004	0.014	0.008	0.002	0.002	0.009	0.004	0.009	0.002	0.014	0.006	0.006	0.002	0.108	0.014
Hf178	0.300	0.007	0.251	0.032	0.844	0.064	0.211	0.043	0.060	0.027	0.169	0.031	0.211	0.052	0.454	0.034
Ta181	0.039	0.009	0.049	0.009	0.040	0.012	0.012	0.003	0.018	0.010	0.015	0.019	0.015	0.002	0.015	0.011
Pb208	0.673	0.135	0.913	0.346	0.720	0.047	0.240	0.105	0.446	0.314	0.216	0.004	0.210	0.072	9.677	1.520
Ti (610 cal)	889	11	850	34	130	11	662	12	343	10	637	49	625	42	332	6
Cr (610 cal)	8050	346	7904	528	11051	250	8146	455	5340	87	7971	414	8009	187	9901	110
SIMS																
H	81	22.0	64	14.3	87	19.4	125	14.6	133	38.0	134	14.4	140	21.0	73	16.8
F	38	4.9	41	3.4	31	2.5	37	3.8	29	3.1	35	6.0	38	3.8	17	1.9

Table 8 ***(continues on next page)*** *Major and trace element compositions of Bultfontein garnet*

Sample	BD1140		BD1140		BD1140		BD1140		BD1152		BD1152		BD1152		BD1152		BD1152	
Grain	A		B		C		D		A		B		C		D		E	
Lithology	gt-hz		gt-hz		gt-hz		gt-hz		gt-hz		gt-hz		gt-hz		gt-hz		gt-hz	
	avg.	st. dev	avg.	st. dev	avg.	st. dev	avg.	st. dev	avg.	st. dev	avg.	st. dev	avg.	st. dev	avg.	st. dev	avg.	st. dev
EPMA																		
SiO_2 (wt.%)	42.32	0.37	42.03	0.37	42.20	0.37	42.56	0.37	42.00	0.37	42.63	0.37	42.20	0.37	42.20	0.37	42.20	0.37
TiO_2	0.03	0.02	0.04	0.02	0.05	0.02	0.05	0.02	-		-		-		-		-	
Al_2O_3	21.91	0.28	22.00	0.28	21.79	0.28	21.78	0.28	20.50	0.27	20.51	0.27	20.37	0.27	20.37	0.27	20.37	0.27
Cr_2O_3	2.32	0.07	2.25	0.07	2.31	0.07	2.16	0.07	4.17	0.1	4.21	0.1	4.19	0.1	4.19	0.1	4.19	0.1
FeO	8.14	0.23	8.36	0.23	8.43	0.23	8.32	0.23	7.26	0.21	7.27	0.21	7.25	0.21	7.25	0.21	7.25	0.21
MnO	0.44	0.05	0.43	0.05	0.41	0.05	0.40	0.05	0.35	0.05	0.33	0.05	0.35	0.05	0.35	0.05	0.35	0.05
MgO	20.61	0.11	20.61	0.11	20.67	0.11	20.83	0.11	20.79	0.11	20.94	0.11	20.94	0.11	20.94	0.11	20.94	0.11
CaO	4.68	0.08	4.57	0.08	4.70	0.08	4.70	0.08	5.29	0.09	5.39	0.09	5.38	0.09	5.38	0.09	5.38	0.09
Total	100.50		100.29		100.58		100.81		100.40		101.31		100.71		100.71		100.71	
LA-ICP-MS																		
Sc45 (ppm)	85	2.9	90	5.4	86	6.2	88	5.0	102	5.3	104	7.0	104	4.4	102	6.5	96	6.5
Ti47	246	30.3	310	35.1	324	17.1	280	40.9	91	3.1	85	15.0	87	12.3	94	8.2	74	11.6
V51	128	1.8	106	21.4	165	11.1	120	24.2	222	2.9	224	21.3	230	11.5	219	15.8	214	13.2
Ni60	19	0.5	24	1.5	22	0.9	21	2.4	48	2.1	49	2.9	47	0.4	46	3.4	48	4.4
Rb85	-	-	-	-	-	-	-	-	-	-	-	-	-	-	0.88	-	-	-
Sr88	0.960	0.834	-	-	-	-	-	-	0.680	0.270	1.060	0.566			0.765	0.106	0.910	0.390
Y89	10.91	0.23	11.09	0.52	11.51	0.74	11.10	0.74	2.95	0.06	2.89	0.12	3.12	0.17	3.65	0.87	2.78	0.21
Zr90	2.72	1.62	4.01	1.11	3.55	0.74	2.42	0.07	37.32	3.00	31.84	3.48	35.23	1.44	34.90	2.87	31.17	3.46
Nb93	0.182	0.082	0.132	0.019	0.128	0.033	0.220	0.001	0.457	0.055	0.437	0.057	0.437	0.055	0.410	0.036	0.423	0.060
Ba137	0.277	0.077	-	-	-	-	0.100	0.018	0.017	-	0.032	-	-	-	-	-	-	-
La139	0.112	0.021	0.030	0.000	0.029	0.001	0.019	0.001	0.032	0.016	0.030	0.006	0.031	0.009	0.047	0.013	0.033	0.011
Ce140	0.405	0.076	0.218	0.003	0.183	0.007	0.184	0.013	0.757	0.015	0.710	0.053	0.843	0.068	0.807	0.025	0.687	0.006
Pr141	0.068	0.002	0.073	0.011	0.048	0.007	0.059	0.001	0.400	0.008	0.375	0.007	0.412	0.028	0.369	0.028	0.377	0.024
Nd143	0.42	0.02	0.54	0.05	0.32	0.03	0.34	0.15	4.26	0.06	4.29	0.36	4.74	0.12	4.51	0.36	4.14	0.64
Sm147	0.178	0.026	0.265	0.051	0.141	0.034	0.193	0.021	1.660	0.061	1.697	0.229	1.830	0.200	1.873	0.170	1.787	0.162
Eu153	0.076	0.001	0.144	0.029	0.086	0.026	0.105	0.001	0.498	0.014	0.537	0.014	0.513	0.044	0.534	0.047	0.508	0.039
Gd157	0.432	0.127	0.503	0.064	0.444	0.013	0.625	0.035	1.240	0.066	1.337	0.065	1.287	0.125	1.517	0.240	1.303	0.032
Tb159	0.149	0.006	0.199	0.010	0.155	0.009	0.148	0.002	0.156	0.010	0.155	0.007	0.150	0.030	0.197	0.029	0.147	0.025
Dy163	1.660	0.099	1.767	0.055	1.720	0.151	1.650	0.042	0.747	0.081	0.787	0.064	0.770	0.079	1.077	0.306	0.767	0.047
Ho165	0.551	0.013	0.498	0.058	0.540	0.034	0.448	0.032	0.137	0.006	0.154	0.004	0.131	0.011	0.188	0.065	0.119	0.011
Er166	1.765	0.134	1.757	0.131	1.933	0.169	1.795	0.177	0.371	0.039	0.365	0.044	0.401	0.024	0.493	0.158	0.352	0.018
Tm169	0.358	0.004	0.296	0.074	0.356	0.048	0.284	0.013	0.057	0.005	0.072	0.007	0.069	0.008	0.073	0.012	0.058	0.004
Yb172	2.775	0.078	2.333	0.123	2.770	0.221	2.290	0.566	0.527	0.061	0.593	0.024	0.520	0.067	0.700	0.095	0.475	0.091
Lu175	0.437	0.023	0.352	0.025	0.487	0.013	0.412	0.084	0.102	0.007	0.099	0.008	0.104	0.023	0.123	0.016	0.088	0.005
Hf178	0.079	0.040	0.076	0.017	0.112	0.016	0.067	0.011	0.880	0.092	0.987	0.105	0.807	0.100	0.873	0.085	0.843	0.090
Ta181	0.008	0.004	0.003	0.001	0.004	0.002	0.004	0.001	0.029	0.005	0.031	0.007	0.028	0.006	0.026	0.003	0.030	0.005
Pb208	-	-	0.049	0.003	-	-	0.096	0.070	0.032	-	-	-	-	-	0.090	0.008	-	-
Th232	0.021	0.013	0.013	0.007	0.014	0.006	0.010	0.005	0.008	0.002	0.007	0.004	0.004	0.002	0.008	0.003	0.004	0.001
U238	0.053	0.001	0.048	0.015	0.056	0.018	0.054	0.003	0.035	0.011	0.539	0.884	0.035	0.004	0.033	0.004	0.031	0.002

Table 8 ***(continued)*** *Major and trace element compositions of Bultfontein garnet*

Sample	BD1672		BD1672		BD1672		BD1999		BD1999		BD1999		BD3021		BD3021		BD3028	
Grain	A		B		C		A		B		C		A		B		A	
Lithology	gt-hz		gt-hz		gt-hz		gt-hz		gt-hz		gt-hz		gt-hz		gt-hz		gt-hz	
	avg.	st. dev	avg.	st. dev	avg.	st. dev	avg.	st. dev	avg.	st. dev	avg.	st. dev	avg.	st. dev	avg.	st. dev	avg.	st. dev
EPMA																		
SiO_2	42.51	0.37	42.25	0.37	42.11	0.37	42.18	0.37	42.01	0.37	42.01	0.37	42.30	0.37	42.68	0.37	43.16	0.38
TiO_2	0.04	0.02	0.04	0.02	0.04	0.02	0.07	0.02	0.05	0.02	0.05	0.02	0.22	0.02	0.21	0.02		0.02
Al_2O_3	20.21	0.26	20.19	0.26	20.43	0.26	19.23	0.25	18.96	0.25	18.96	0.25	19.39	0.25	19.48	0.25	21.12	0.27
Cr_2O_3	4.44	0.1	4.48	0.1	4.22	0.1	5.83	0.12	5.92	0.12	5.92	0.12	5.50	0.11	5.21	0.11	3.87	0.09
FeO	7.26	0.21	7.38	0.21	7.44	0.21	6.80	0.2	6.75	0.2	6.75	0.2	6.58	0.2	6.80	0.2	5.53	0.18
MnO	0.41	0.05	0.36	0.05	0.35	0.05	0.33	0.05	0.35	0.05	0.35	0.05	0.30	0.05	0.32	0.05	0.26	0.05
MgO	20.93	0.11	21.01	0.11	21.03	0.11	20.81	0.11	20.81	0.11	20.81	0.11	21.37	0.11	21.48	0.11	23.68	0.12
CaO	5.06	0.09	5.06	0.09	5.10	0.09	5.52	0.09	5.54	0.09	5.54	0.09	5.15	0.08	4.94	0.08	3.32	0.07
Total	100.93		100.79		100.74		100.75		100.41		100.41		100.87		101.22		100.94	
LA-ICP-MS																		
Sc45	104	4.1	103	4.8	117	7.5	114	9.1	113	2.6	115	7.2	102	0.6	111.9	7.5	85	10.1
Ti47	311	21.3	266	8.0	364	43.2	400	34.4	399	29.2	396	57.0	1617	153.9	1710.3	63.7	38	12.8
V51	215	8.0	224	5.9	240	15.0	237	12.3	222	21.1	237	20.3	220	5.6	210.5	8.7	190	14.7
Ni60	57	4.6	56	1.8	64	0.9	57	7.9	51	4.1	59	1.9	55	2.3	60.5	3.0	53	6.1
Rb85	-	-	-	-	-	-	-	-	-	-	-	-	1.370	0.820	3.283	2.618	-	-
Sr88			0.960	0.130			0.905	0.205	0.823	0.124	1.090	0.540	4.240	2.135	13.935	1.266	1.847	0.651
Y89	2.01	0.19	1.43	0.15	4.32	0.26	2.73	0.40	3.02	0.12	2.99	0.20	18.11	0.91	24.94	2.50	0.82	0.19
Zr90	38.95	0.38	32.32	2.07	47.47	3.63	49.08	5.85	50.55	7.43	48.83	9.49	102.49	1.07	119.26	17.63	14.31	1.57
Nb93	0.440	0.030	0.463	0.076	0.593	0.031	0.690	0.070	0.783	0.127	0.633	0.050	0.545	0.318	0.910	0.614	1.510	0.017
Ba137	0.068	0.011	-	-	-	-	0.298	0.058	0.214	0.158	-	-	1.465	0.813	4.782	4.285	-	-
La139	0.023	0.004	0.031	0.007	0.031	0.001	0.056	0.025	0.067	0.017	0.033	0.009	0.365	0.262	0.549	0.537	0.151	0.022
Ce140	0.447	0.025	0.443	0.045	0.497	0.146	0.707	0.060	0.773	0.102	0.683	0.035	1.020	0.495	1.511	1.197	2.200	0.131
Pr141	0.215	0.011	0.192	0.001	0.227	0.049	0.308	0.020	0.321	0.020	0.330	0.036	0.136	0.058	0.236	0.129	1.057	0.057
Nd143	2.52	0.17	2.47	0.21	2.67	0.11	4.09	0.26	4.02	0.11	4.27	0.52	1.71	0.04	1.77	0.30	9.85	0.80
Sm147	1.837	0.040	1.777	0.199	1.987	0.185	2.400	0.137	2.510	0.191	2.547	0.232	1.855	0.007	1.780	0.154	2.820	0.478
Eu153	0.610	0.036	0.600	0.044	0.757	0.023	0.727	0.051	0.697	0.199	0.800	0.026	0.970	0.028	0.977	0.059	0.607	0.081
Gd157	1.660	0.044	1.410	0.256	1.967	0.083	1.630	0.175	1.723	0.093	1.743	0.140	3.160	0.000	3.653	0.057	1.230	0.161
Tb159	0.140	0.005	0.107	0.025	0.219	0.023	0.148	0.012	0.174	0.026	0.165	0.016	0.605	0.007	0.703	0.074	0.068	0.004
Dy163	0.537	0.085	0.356	0.035	1.130	0.053	0.580	0.066	0.680	0.056	0.697	0.064	3.900	0.057	5.173	0.537	0.166	0.022
Ho165	0.076	0.014	0.051	0.010	0.177	0.016	0.094	0.015	0.107	0.012	0.119	0.004	0.740	0.042	0.967	0.093	0.030	0.009
Er166	0.186	0.043	0.181	0.026	0.470	0.036	0.306	0.020	0.333	0.031	0.344	0.020	1.625	0.092	2.377	0.310	0.173	0.015
Tm169	0.038	0.011	0.031	0.006	0.068	0.005	0.050	0.003	0.061	0.007	0.061	0.005	0.180	0.001	0.292	0.033	0.043	0.009
Yb172	0.422	0.112	0.344	0.017	0.590	0.017	0.453	0.036	0.517	0.055	0.520	0.115	1.040	0.014	1.723	0.110	0.495	0.082
Lu175	0.075	0.003	0.074	0.007	0.106	0.017	0.090	0.011	0.092	0.005	0.097	0.010	0.139	0.015	0.229	0.041	0.106	0.005
Hf178	0.553	0.021	0.460	0.108	0.783	0.049	0.813	0.097	0.833	0.047	0.873	0.051	1.845	0.064	1.840	0.078	0.283	0.025
Ta181	0.039	0.010	0.031	0.011	0.032	0.002	0.051	0.008	0.044	0.013	0.040	0.007	0.032	0.006	0.045	0.026	0.112	0.023
Pb208	-	-	-	-	-	-	-	-	-	-	0.038	0.007	-	-	0.094	0.045	-	-
Th232	0.005	0.002	0.010	0.003	0.015	0.010	0.010	0.005	0.015	0.003	0.006	0.001	0.040	0.013	0.078	0.078	0.039	0.005
U238	0.033	0.009	0.042	0.003	0.055	0.013	0.039	0.006	0.035	0.010	0.033	0.003	0.032	0.014	0.035	0.025	0.146	0.014

Table 8 ***(continued)*** *Major and trace element compositions of Bultfontein garnet*

Sample	BD3028		BD3028		BD3676		BD3676		BD3676	
Grain	B		C		A		B		C	
Lithology	gt-hz		gt-hz		gt-hz		gt-hz		gt-hz	
	avg.	st. dev	avg.	st. dev	avg.	st. dev	avg.	st. dev	avg.	st. dev
EPMA										
SiO_2	43.09	0.38	43.09	0.38	42.71	0.38	43.04	0.38	42.86	0.38
TiO_2					0.04	0.02	0.04	0.02	0.04	0.02
Al_2O_3	21.43	0.27	21.43	0.27	21.41	0.27	21.33	0.27	21.30	0.27
Cr_2O_3	3.66	0.09	3.66	0.09	3.49	0.09	3.42	0.09	3.59	0.09
FeO	5.59	0.18	5.59	0.18	5.65	0.19	5.72	0.19	5.88	0.19
MnO	0.30	0.05	0.30	0.05	0.27	0.05	0.25	0.05	0.26	0.05
MgO	23.79	0.12	23.79	0.12	23.19	0.12	23.43	0.12	23.38	0.12
CaO	3.38	0.07	3.38	0.07	3.50	0.07	3.51	0.07	3.50	0.07
Total	101.25		101.25		100.32		100.76		100.80	
LA-ICP-MS										
Sc45	74	2.4	77	3.4	85	3.1	80	6.2	79	1.9
Ti47	33	2.7	36	14.7	290	23.4	279	27.5	286	23.6
V51	169	4.3	172	10.0	192	6.3	191	18.7	185	4.1
Ni60	48	1.9	49	2.2	54	3.0	52	5.9	49	0.5
Rb85	-	-	-	-	-	-	-	-	-	-
Sr88	1.480	0.693	1.250	0.099	1.100	0.297	-	-	0.890	0.057
Y89	1.28	0.14	1.22	0.11	1.63	0.09	2.49	0.21	3.75	0.20
Zr90	21.72	1.74	20.97	1.34	50.93	7.48	45.65	2.41	54.08	5.67
Nb93	1.187	0.126	1.187	0.193	0.513	0.023	0.563	0.111	0.530	0.026
Ba137	-	-	-	-	-	-	-	-	-	-
La139	0.043	0.015	0.069	0.025	0.035	0.005	0.039	0.003	0.038	0.007
Ce140	1.003	0.075	1.243	0.409	0.607	0.058	0.560	0.066	0.597	0.035
Pr141	0.569	0.098	0.667	0.168	0.263	0.020	0.222	0.023	0.241	0.006
Nd143	6.44	0.60	7.31	1.11	2.81	0.04	2.78	0.05	2.80	0.13
Sm147	2.460	0.246	2.480	0.406	1.473	0.205	1.377	0.117	1.447	0.127
Eu153	0.740	0.040	0.747	0.015	0.519	0.059	0.524	0.061	0.553	0.049
Gd157	1.560	0.026	1.617	0.067	1.240	0.165	1.323	0.212	1.533	0.118
Tb159	0.127	0.015	0.135	0.008	0.151	0.012	0.166	0.014	0.220	0.031
Dy163	0.380	0.053	0.410	0.049	0.471	0.043	0.673	0.035	1.033	0.047
Ho165	0.050	0.011	0.040	0.009	0.060	0.005	0.094	0.016	0.141	0.020
Er166	0.167	0.017	0.168	0.019	0.213	0.019	0.240	0.035	0.415	0.035
Tm169	0.038	0.003	0.045	0.006	0.049	0.007	0.056	0.009	0.070	0.008
Yb172	0.447	0.052	0.472	0.027	0.580	0.017	0.562	0.103	0.670	0.066
Lu175	0.104	0.011	0.109	0.013	0.107	0.008	0.115	0.011	0.131	0.017
Hf178	0.500	0.036	0.497	0.060	0.743	0.050	0.823	0.093	1.090	0.030
Ta181	0.096	0.015	0.091	0.004	0.047	0.013	0.049	0.011	0.056	0.009
Pb208	-	-	-	-	-	-	-	-	-	-
Th232	0.014	0.004	0.018	0.009	0.007	0.003	0.009	0.002	0.013	0.001
U238	0.084	0.013	0.087	0.021	0.024	0.004	0.021	0.001	0.026	0.007

Table 9 ***(continues on next page)*** *Mothae garnet trace element compositions, analysed by Lydia Gibson as part of MSci thesis at University of Cambridge*

Sample	BD2124		BD2124		BD2124		BD2124		BD2125		BD2125		BD2125		BD2125		BD2125	
Lithology	gt-lz		gt-lz		gt-lz		gt-lz		gt-hz		gt-hz		gt-hz		gt-hz		gt-hz	
Grain	2		2		1		1		1		1		2		2		4	
Core/rim	rim		core		rim		core		rim		core		core		rim		core	
	conc.	err.	conc.	err.	conc.	err.	conc.	err.	conc.	err.	conc.	err.	conc.	err.	conc.	err.	conc.	err.
Li7 (ppm)	0.159	0.065	-		0.089	0.045	0.101	0.061	0.043	0.043	0.041	0.041	-		0.049	0.049	0.044	0.044
Be9	-		0.190	0.19	-		-		-		-		-		-		0.280	0.28
P31	108	11.7	122	13.38	120	12.39	104	11.04	75	12.28	69	11.13	83	12.67	99	14.79	110	16.29
K39	-		-		-		-		-		-		-		-		-	1.81
Sc45	87	3.39	84	3.36	85	3.28	83	3.18	79	2.96	77	2.88	79	2.93	82	3.13	84	3.14
Ti47	2664	444.87	2613	437.61	2739	456.52	3041	506.25	310	48.15	382	56.82	342	50.92	362	55.3	280	43.55
V51	226	8.15	219	8.02	240	8.56	248	8.83	160	7.55	179	8.41	145	6.79	148	7.06	150	7.1
Mn55	1965	96.56	1913	94.75	1856	90.72	1864	91.06	2110	135.67	2137	137.18	2006	128.55	2128	137.21	2110	135.76
Co59	35.3	1.67	34.3	1.66	32.4	1.52	32.9	1.54	29.6	1.26	30.6	1.29	29.1	1.22	31.7	1.37	29.9	1.28
Ni60	73.0	3.32	72.1	3.42	72.1	3.2	69.5	3.09	41.1	3.06	39.1	2.9	37.1	2.73	41.5	3.14	44.4	3.29
Rb85	-		-		0.008	0.0059	0.023	0.012	-		-		-		-		-	
Sr88	0.27	0.15	0.70	0.22	0.43	0.14	0.65	0.18	0.63	0.3	0.70	0.24	0.36	0.16	0.56	0.23	-	
Y89	13.69	0.6	13.78	0.63	14.03	0.59	13.18	0.56	2.72	0.22	1.77	0.17	3.55	0.25	3.74	0.28	3.78	0.27
Zr90	35.8	1.79	34.6	1.8	35.7	1.75	33.8	1.66	64.3	3.32	48.7	2.57	70.3	3.54	68.0	3.54	70.9	3.64
Nb93	0.660	0.048	0.587	0.048	0.680	0.046	0.705	0.047	0.759	0.06	0.642	0.054	0.628	0.051	0.721	0.062	0.607	0.054
Ba137	0.018	0.01	-		0.020	0.011	-		0.265	0.045	1.008	0.089	0.583	0.063	-		-	
La139	0.024	0.0046	0.023	0.0051	0.032	0.0053	0.037	0.0051	0.036	0.0076	0.058	0.0086	0.056	0.0076	0.052	0.009	0.029	0.0082
Ce140	0.405	0.02	0.391	0.021	0.423	0.02	0.442	0.02	0.655	0.035	0.704	0.037	0.627	0.033	0.689	0.038	0.623	0.035
Pr141	0.140	0.0095	0.158	0.011	0.148	0.0093	0.143	0.009	0.324	0.019	0.357	0.02	0.316	0.018	0.358	0.021	0.348	0.021
Nd143	1.31	0.089	1.35	0.099	1.27	0.082	1.21	0.079	3.10	0.19	3.21	0.19	3.35	0.19	3.62	0.22	3.35	0.2
Sm147	0.84	0.062	0.97	0.075	0.92	0.062	0.90	0.06	1.59	0.11	1.27	0.096	1.78	0.11	1.86	0.13	1.81	0.12
Eu153	0.377	0.022	0.379	0.023	0.365	0.02	0.413	0.022	0.501	0.028	0.430	0.025	0.582	0.03	0.544	0.031	0.554	0.03
Gd158	1.39	0.078	1.48	0.088	1.37	0.073	1.34	0.072	1.64	0.11	1.52	0.099	2.02	0.12	2.10	0.13	1.94	0.12
Tb159	0.276	0.016	0.285	0.018	0.292	0.016	0.276	0.015	0.208	0.017	0.172	0.014	0.246	0.018	0.222	0.018	0.246	0.019
Dy163	2.110	0.11	2.070	0.11	2.050	0.1	2.070	0.1	0.840	0.065	0.687	0.055	1.071	0.071	0.886	0.071	1.023	0.074
Ho165	0.476	0.028	0.467	0.028	0.476	0.027	0.505	0.028	0.104	0.011	0.083	0.0096	0.143	0.013	0.116	0.012	0.135	0.013
Er166	1.490	0.085	1.490	0.089	1.518	0.083	1.515	0.082	0.204	0.025	0.180	0.024	0.227	0.026	0.206	0.027	0.194	0.026
Tm169	0.210	0.015	0.260	0.018	0.225	0.015	0.234	0.015	0.028	0.0059	0.024	0.0053	0.027	0.005	0.041	0.0071	0.027	0.0059
Yb172	1.733 0.094	1.530	0.092	1.801	0.092	1.579	0.083	0.156	0.029	0.152	0.028	0.206	0.03	0.175	0.03	0.174	0.029	
Lu175	0.271	0.017	0.261	0.017	0.245	0.015	0.268	0.016	0.028	0.0055	0.031	0.006	0.040	0.0063	0.045	0.0078	0.039	0.0066
Hf178	0.812	0.07	0.834	0.078	0.702	0.061	0.682	0.059	1.098	0.096	0.861	0.081	1.052	0.089	1.003	0.099	0.964	0.091
Ta181	0.063	0.011	0.071	0.013	0.092	0.013	0.089	0.012	0.040	0.012	0.048	0.012	0.039	0.011	0.061	0.013	0.050	0.012
Pb208	0.124	0.031	0.065	0.026	-		-		-		0.055	0.024	0.055	0.025	0.161	0.036	-	
Th232	0.015	0.0045	0.015	0.005	0.011	0.0036	0.017	0.0043	0.016	0.0072	0.025	0.008	0.057	0.01	0.035	0.0093	0.018	0.006
U238	0.016	0.0038	0.015	0.0036	0.017	0.0035	0.026	0.0041	0.057	0.0082	0.055	0.0076	0.047	0.0067	0.051	0.0078	0.041	0.007

Table 9 ***(continued)*** *Mothae garnet trace element compositions, analysed by Lydia Gibson as part of MSci thesis at University of Cambridge*

Sample	BD2126		BD2126		BD2126		BD2126		BD2126		BD2126		BD2128		BD2128		BD2128	
Lithology	gt-lz		gt-lz		gt-lz		gt-lz		gt-lz		gt-lz		gt-lz		gt-lz		gt-lz	
Grain	1		1		3		4		4		5		2		2		3	
Core/rim	core		rim		core		core		rim		core		core		rim		core	
	conc.	err.	conc.	err.	conc.	err.	conc.	err.	conc.	err.	conc.	err.	conc.	err.	conc.	err.	conc.	err.
Li7 (ppm)	0.260	0.14	-		-		-		0.048	0.048	0.130	0.075	-		-		0.175	0.088
Be9	-		-		-		-		0.310	0.31	-		-		0.300	0.31	-	
P31	87	14.13	105	16.03	74	12.1	74	12.56	98	15.2	88	13.55	92	14	113	16.81	104	15.63
K39	-		-		-		-		-		-		-		-		-	
Sc45	83	3.24	81	3.15	82	3.1	78	3.03	80	3.08	75	2.86	85	3.16	86	3.26	84	3.15
Ti47	1182	165.17	1131	157.58	1188	163.77	1141	158.48	1154	159.92	1338	183.36	2068	278.98	2235	302.79	2188	295.63
V51	227	10.88	215	10.28	208	9.88	220	10.49	219	10.43	225	10.65	232	10.91	231	10.94	224	10.57
Mn55	1927	125.33	1932	125.34	1778	114.89	2023	131.05	2000	129.43	1974	127.35	1843	118.51	1868	120.77	1799	116
Co59	35.1	1.53	33.0	1.44	31.6	1.35	34.7	1.5	35.8	1.53	33.7	1.43	32.5	1.36	32.1	1.38	31.2	1.33
Ni60	75.0	5.36	76.5	5.41	65.5	4.63	76.0	5.36	72.3	5.12	76.8	5.33	70.0	4.85	75.9	5.33	66.9	4.71
Rb85	-		-		-		-		-		0.007	0.0072	0.013	0.0092	-		0.022	0.013
Sr88	-		0.48	0.26	-		-		-		0.33	0.17	-		-		-	
Y89	15.03	0.75	13.32	0.68	13.36	0.65	13.03	0.66	14.17	0.7	12.93	0.63	13.15	0.62	14.96	0.73	15.21	0.72
Zr90	25.5	1.56	23.8	1.46	23.7	1.42	20.9	1.31	21.2	1.32	21.9	1.32	38.1	2.06	41.2	2.27	41.9	2.27
Nb93	0.513	0.052	0.628	0.059	0.445	0.045	0.510	0.051	0.556	0.053	0.554	0.051	0.361	0.038	0.380	0.044	0.411	0.043
Ba137	-		-		0.040	0.018	-		-		0.049	0.022	0.068	0.03	-		-	
La139	0.027	0.0081	0.033	0.0082	0.037	0.0071	0.026	0.0074	0.031	0.0062	0.034	0.0062	0.030	0.0063	0.037	0.0074	0.032	0.0067
Ce140	0.281	0.022	0.300	0.022	0.314	0.021	0.346	0.023	0.329	0.022	0.315	0.021	0.306	0.02	0.307	0.021	0.295	0.02
Pr141	0.102	0.011	0.104	0.01	0.098	0.0093	0.091	0.0094	0.101	0.0097	0.082	0.0083	0.100	0.0088	0.116	0.011	0.101	0.0095
Nd143	0.82	0.095	0.94	0.096	0.91	0.09	1.04	0.1	0.86	0.091	0.74	0.08	1.20	0.099	1.23	0.11	1.41	0.11
Sm147	0.51	0.065	0.47	0.06	0.55	0.061	0.55	0.065	0.49	0.06	0.52	0.058	1.09	0.084	1.06	0.091	1.30	0.099
Eu153	0.195	0.017	0.218	0.018	0.198	0.016	0.187	0.016	0.212	0.017	0.188	0.015	0.379	0.023	0.415	0.026	0.371	0.023
Gd158	1.10	0.089	1.15	0.09	1.20	0.087	0.98	0.081	1.08	0.083	1.09	0.081	1.52	0.097	1.93	0.12	1.95	0.12
Tb159	0.217	0.019	0.243	0.02	0.213	0.017	0.245	0.02	0.233	0.019	0.243	0.018	0.293	0.02	0.327	0.023	0.332	0.023
Dy163	2.070	0.13	2.050	0.12	2.000	0.12	1.790	0.11	1.830	0.11	1.810	0.11	2.060	0.11	2.120	0.12	2.250	0.12
Ho165	0.467	0.03	0.423	0.028	0.472	0.028	0.449	0.028	0.498	0.03	0.421	0.026	0.472	0.027	0.461	0.029	0.441	0.027
Er166	1.498	0.096	1.515	0.096	1.449	0.088	1.423	0.09	1.459	0.091	1.261	0.079	1.342	0.08	1.351	0.086	1.254	0.079
Tm169	0.255	0.02	0.241	0.019	0.231	0.018	0.245	0.019	0.262	0.019	0.230	0.017	0.212	0.016	0.218	0.017	0.212	0.017
Yb172	1.880	0.12	1.770	0.12	1.730	0.11	1.890	0.12	1.710	0.11	1.780	0.11	1.447	0.093	1.470	0.1	1.461	0.096
Lu175	0.316	0.023	0.296	0.022	0.301	0.021	0.268	0.02	0.281	0.021	0.242	0.018	0.229	0.017	0.217	0.018	0.227	0.017
Hf178	0.501	0.066	0.535	0.071	0.518	0.063	0.513	0.069	0.621	0.073	0.418	0.056	0.831	0.078	0.842	0.087	1.040	0.093
Ta181	0.052	0.014	0.055	0.013	0.057	0.013	0.034	0.011	0.048	0.012	0.054	0.012	0.027	0.0089	0.028	0.009	0.036	0.0098
Pb208	-		-		0.068	0.025	-		-		-		-		-		0.039	0.022
Th232	0.019	0.0075	0.007	0.004	0.034	0.0082	0.011	0.0049	-		-		0.008	0.0048	-		0.015	0.0063
U238	0.023	0.0055	0.019	0.0053	0.027	0.0053	0.025	0.0056	0.012	0.0036	0.022	0.0047	0.007	0.0028	0.010	0.0035	0.014	0.004

Table 9 ***(continued)*** *Mothae garnet trace element compositions, analysed by Lydia Gibson as part of MSci thesis at University of Cambridge*

Sample	BD2128		BD2128		BD2128		BD2170		BD2170		BD2170		BD2170		BD2170	
Lithology	gt-lz		gt-lz		gt-lz		gt-hz		gt-hz		gt-hz		gt-hz		gt-hz	
Grain	3		1		1		1		1		3		2		7	
Core/rim	rim		core		rim											
	conc.	err.	conc.	err.	conc.	err.	conc.	err.	conc.	err.	conc.	err.	conc.	err.	conc.	err.
Li7 (ppm)	0.220	0.11	-	0.069	0.160	0.093	-		0.169	0.085	0.270	0.1	0.270	0.1	0.250	0.11
Be9	-		-	0.32	-		-		-		0.240	0.25	-		-	
P31	96	15.15	79	12.92	120	17.93	80	12.98	63	10.67	127	17.96	147	20.43	92	14.46
K39	-		-	0.82	-		-		-		-		3.540	0.8	-	
Sc45	83	3.23	86	3.26	83	3.21	101	3.76	119	4.34	101	3.66	96	3.5	141	5.19
Ti47	2193	298.53	2037	276.31	1996	272.06	5560	740.33	3807	508.41	6618	877.57	6731	892.67	3405	457.32
V51	227	10.87	232	11	221	10.52	292	13.73	318	14.84	293	13.64	304	14.15	360	16.93
Mn55	1776	115.43	1799	116.19	1813	117.58	2084	134.07	2094	134.3	2228	142.56	2244	143.64	2123	136.77
Co59	31.1	1.38	32.0	1.37	31.2	1.37	30.4	1.3	30.9	1.3	30.7	1.28	32.0	1.32	30.8	1.33
Ni60	72.0	5.18	69.0	4.88	71.1	5.09	80.7	5.6	72.9	5.05	93.0	6.27	87.6	5.95	77.2	5.43
Rb85	0.009	0.0093	0.008	0.0078	0.044	0.02	0.023	0.013	-	0.011	0.036	0.021	-		0.092	0.028
Sr88	-		0.45	0.24	0.21	0.15	1.65	0.55	1.08	0.39	1.70	0.36	-		0.87	0.33
Y89	14.05	0.72	13.81	0.68	14.57	0.73	14.54	0.7	2.76	0.23	29.97	1.21	30.62	1.24	1.59	0.21
Zr90	46.5	2.59	41.5	2.28	42.7	2.39	72.5	3.72	43.0	2.31	98.9	4.87	99.1	4.88	53.5	2.87
Nb93	0.322	0.042	0.391	0.044	0.339	0.042	0.428	0.047	0.449	0.044	0.453	0.043	0.431	0.042	0.438	0.048
Ba137	-		-		0.078	0.024	-		0.485	0.059	13.950	0.66	0.733	0.072	2.210	0.16
La139	0.023	0.0067	0.018	0.0061	0.033	0.0073	0.052	0.0095	0.077	0.0096	0.069	0.0087	0.064	0.0097	0.067	0.01
Ce140	0.274	0.021	0.304	0.021	0.312	0.022	0.692	0.037	0.780	0.04	0.622	0.033	0.677	0.036	0.631	0.036
Pr141	0.115	0.011	0.116	0.01	0.107	0.01	0.213	0.015	0.265	0.016	0.207	0.014	0.230	0.015	0.234	0.016
Nd143	1.24	0.12	1.10	0.1	1.28	0.12	2.03	0.15	2.15	0.15	2.42	0.15	2.20	0.15	2.36	0.17
Sm147	1.04	0.097	1.17	0.096	0.98	0.092	1.31	0.1	0.70	0.067	1.61	0.11	1.64	0.11	0.96	0.086
Eu153	0.378	0.026	0.414	0.026	0.434	0.028	0.497	0.029	0.176	0.015	0.724	0.035	0.690	0.034	0.226	0.018
Gd158	1.90	0.13	1.77	0.11	2.05	0.13	1.89	0.12	0.47	0.049	3.26	0.17	3.53	0.18	0.78	0.07
Tb159	0.314	0.024	0.356	0.025	0.410	0.028	0.386	0.026	0.087	0.01	0.704	0.039	0.741	0.041	0.068	0.01
Dy163	2.160	0.13	2.260	0.13	2.300	0.13	2.180	0.12	0.472	0.048	4.900	0.22	5.280	0.23	0.333	0.045
Ho165	0.453	0.03	0.461	0.028	0.466	0.03	0.443	0.028	0.097	0.011	1.122	0.052	1.107	0.051	0.066	0.01
Er166	1.429	0.095	1.318	0.084	1.344	0.088	1.074	0.073	0.203	0.027	3.030	0.15	3.000	0.15	0.143	0.026
Tm169	0.213	0.018	0.238	0.018	0.209	0.018	0.165	0.015	0.039	0.0062	0.409	0.024	0.446	0.026	0.027	0.0071
Yb172	1.630	0.11	1.620	0.11	1.480	0.1	1.008	0.078	0.330	0.039	2.800	0.15	2.790	0.15	0.300	0.043
Lu175	0.271	0.021	0.217	0.017	0.243	0.019	0.149	0.014	0.067	0.0088	0.343	0.022	0.402	0.024	0.067	0.0097
Hf178	0.905	0.098	0.866	0.088	0.990	0.099	1.470	0.12	0.796	0.08	2.480	0.16	2.200	0.14	1.090	0.1
Ta181	0.033	0.012	0.039	0.011	0.032	0.01	0.044	0.012	-		0.036	0.0092	0.011	0.0063	0.021	0.008
Pb208	-		-		0.050	0.024	-		0.026	0.013	-		0.041	0.019	-	
Th232	0.013	0.0056	-		0.012	0.0053	0.019	0.0063	0.016	0.0075	0.029	0.0076	0.014	0.0049	-	
U238	0.016	0.0045	0.017	0.0051	0.013	0.0043	0.017	0.0046	0.014	0.0045	0.024	0.0049	0.022	0.0047	0.017	0.0047

Table 10 *Major element compositions of phlogopite*

Sample	BD1141		BD1141		BD1141		BD1141		BD1141		BD1141		BD1141		BD1141		BD1141	
Crystal	A		B		C		C-rim		D		E		F		G		H	
n	5		5		4		5		3		3		5		2		5	
(wt.%)	avg.	st.dev	avg.	st.dev	avg.	st.dev	avg.	st.dev	avg.	st.dev	avg.	st.dev	avg.	st.dev	avg.	st.dev	avg.	st.dev
SiO_2	41.17	0.22	41.44	0.30	41.78	0.39	41.90	0.48	42.23	0.58	41.89	0.48	41.87	0.79	41.40	0.06	41.42	0.24
TiO_2	0.99	0.02	0.98	0.02	0.97	0.01	1.01	0.02	1.01	0.03	0.99	0.05	1.00	0.02	1.01	0.02	0.98	0.04
Al_2O_3	11.09	0.26	11.20	0.13	11.16	0.16	11.27	0.13	11.57	0.15	11.38	0.23	11.34	0.27	11.61	0.09	11.44	0.48
Cr_2O_3	0.46	0.02	0.48	0.02	0.49	0.02	0.47	0.02	0.47	0.06	0.49	0.05	0.49	0.02	0.52	0.01	0.47	0.02
FeO	3.09	0.11	3.12	0.03	3.13	0.06	3.18	0.07	3.22	0.07	3.26	0.03	3.24	0.09	3.21	0.01	3.21	0.07
MnO	0.02	0.01	0.02	0.01	0.02	0.02	0.01	0.03	0.02	0.02			0.01	0.03	0.02	0.01	0.03	0.02
MgO	24.20	0.11	24.70	0.11	24.72	0.24	24.86	0.29	25.02	0.28	24.93	0.37	24.89	0.33	24.72	0.19	24.95	0.44
CaO	0.05	0.01			0.13	0.22	0.02	0.01	0.00	0.02	0.03	0.02	0.04	0.01	0.08	0.05	0.05	0.06
Na_2O	0.22	0.02	0.19	0.03	0.19	0.03	0.19	0.03	0.21	0.03	0.24	0.05	0.22	0.03	0.22	0.03	0.20	0.02
K_2O	10.61	0.09	10.76	0.12	10.77	0.07	10.85	0.11	11.03	0.13	10.90	0.17	10.88	0.17	10.69	0.03	10.59	0.42
F	0.47	0.13	0.46	0.08	0.47	0.03	0.50	0.07	0.44	0.09	0.51	0.15	0.47	0.02	0.47	0.10	0.44	0.12
Cl	0.04	0.01	0.04	0.01	0.04	0.00	0.04	0.01	0.04	0.00	0.05	0.00	0.05	0.00	0.04	0.00	0.04	0.01
Total	92.40		93.41		93.88		94.31		95.26		94.65		94.41		93.98		93.82	

Sample	BD2125		BD3067	BD3067	BD3067	BD3067	BD3067	BD3067	BD3067	BD3067	BD3067	BD3067	BD3067	BD3067	BD3067		BD3067	
Crystal			A	B	C	D	E	F	G	H	I	J	K	L	Group 1		Group2	
Group			1	1	2	2	2	2	2	2	2	2	2	2				
n	6		1	1	1	1	1	1	1	1	1	1	1	1	2		10	
(wt.%)	avg.	st.dev													avg.	st.dev	avg.	st.dev
SiO_2	41.69	0.18	41.90	42.40	41.47	41.70	42.23	42.23	41.96	41.62	41.86	42.39	41.99	41.86	42.15	0.36	41.93	0.29
TiO_2	0.12	0.01	0.49	0.47	0.85	0.80	0.76	0.79	0.80	0.84	0.73	0.82	0.81	0.80	0.48	0.01	0.80	0.04
Al_2O_3	12.51	0.09	7.83	7.31	12.25	12.04	11.63	12.02	12.09	12.02	11.48	12.06	11.98	11.97	7.57	0.37	11.95	0.23
Cr_2O_3	0.84	0.02	0.08	0.11	0.21	0.15	0.14	0.12	0.18	0.35	0.15	0.18	0.16	0.18	0.10	0.02	0.18	0.07
FeO	2.44	0.03	2.87	2.42	4.14	4.08	4.00	4.25	4.25	3.86	4.11	4.25	4.18	4.42	2.65	0.32	4.15	0.15
MnO	bdl		0.07	0.07	0.06										0.07	0.00	0.06	
MgO	25.20	0.21	30.84	32.07	25.40	24.94	25.76	25.07	24.94	24.84	25.46	24.70	25.19	25.01	31.46	0.87	25.13	0.32
NiO	na		0.07	0.05	0.09	0.12	0.08	0.11	0.12	0.14	0.08		0.11	0.12	0.06	0.01	0.11	0.02
CaO	0.06	0.05	0.08	0.12	0.04	0.08	0.03			0.04					0.10	0.03	0.05	0.03
Na_2O	0.07	0.02	0.12	0.17	0.17	0.15	0.13	0.11	0.12	0.19	0.13	0.11	0.11	0.11	0.14	0.03	0.13	0.03
K_2O	10.79	0.14	6.81	6.00	9.71	10.70	10.46	10.91	11.05	10.73	10.21	11.18	11.11	10.82	6.40	0.57	10.69	0.45
F	0.49	0.08	0.29	0.35	0.48	0.73	0.64	0.41	0.66	0.59	0.66	0.62	0.63	0.60	0.32	0.04	0.60	0.09
Cl	0.17	0.01	bdl	bdl	bdl	bdl	bdl	bdl	bdl	bdl	bdl	bdl	bdl	bdl	bdl	-	0.05	0.01
Total	94.42		91.46	91.53	94.88	95.49	95.85	96.03	96.17	95.23	94.87	96.32	96.28		91.50		95.85	

Table 11 *Composition of the distal olivine composition in wehrlite BD3067 (Chapter 6)*

Grain **Core/rim**	neoblast average	1 sd	porhyroclast rim average	1 sd	porphyroclast core average	1 sd
EPMA						
n	14		13		12	
SiO_2 (wt.%)	40.55	0.25	40.75	0.83	40.57	0.43
MgO	47.44	0.14	47.71	0.78	47.52	0.34
CaO			0.04	0.03	0.05	0.03
NiO	0.21	0.02	0.20	0.01	0.24	0.05
MnO	0.15	0.02	0.15	0.01	0.16	0.02
FeO	11.54	0.18	11.54	0.13	11.53	0.14
Mg#	88.00	0.18	88.05	0.23	88.02	0.11
LA-ICP-MS						
n			9		9	
Na23 (ppm)			65.09	13.97	74.03	13.31
Al27			6.86	1.21	7.75	2.71
P31			95.31	22.96	102.62	10.83
Sc45			1.62	0.20	1.49	0.16
Ti47			138.75	9.09	150.42	11.84
V51			3.99	0.35	3.74	0.29
Cr53			37.02	3.04	44.88	7.38
Mn55			1047.27	69.29	1038.85	32.87
Co59			133.98	7.39	131.89	3.41
Ni60			1548.86	135.49	1944.53	367.21
Cu65			1.34	0.40	1.16	0.17
Zn66			105.37	10.87	106.08	8.56
Ga69			0.19	0.24	0.20	0.21
Y89			0.02	0.01	0.04	0.02
Zr90			0.43	0.09	0.55	0.22
Nb93			0.32	0.08	0.44	0.16
Sn120			0.72	0.09	0.75	0.15
Pb208			0.05	0.08	0.37	0.79

Table 12 ***(continues on next page)*** *Select olivine major element profiles from wehrlite BD3067*

Olivine A (Distal)					Olivine B (Distal)					Olivine D (Distal)				
x (μm)	MgO	NiO	MnO	FeO	x (μm)	MgO	NiO	MnO	FeO	x (μm)	MgO	NiO	MnO	FeO
0	47.63	0.22	0.15	11.52	0	47.25	0.19	0.19	11.44	0	47.88	0.20	0.14	11.65
53	50.00	0.21	0.15	11.31	50	46.96	0.21	0.17	11.31	26	47.82	0.20	0.16	11.62
107	47.61	0.24	0.16	11.46	101	47.10	0.21	0.18	11.57	53	47.99	0.20	0.17	11.38
160	47.62	0.24	0.16	11.44	151	46.79	0.19	0.15	11.50	79	47.88	0.20	0.18	11.45
214	47.71	0.24	0.13	11.42	302	47.47	0.20	0.16	10.90	105	47.93	0.19	0.17	11.49
267	47.30	0.23	0.14	11.31	352	48.17	0.19	0.17	11.14	132	47.91	0.22	0.17	11.61
320	47.71	0.25	0.17	11.51	403	47.08	0.20	0.18	11.47	158	47.63	0.19	0.16	11.64
374	47.54	0.27	0.17	11.50	453	46.79	0.18	0.15	11.22	184	47.95	0.18	0.15	11.56
427	46.85	0.28	0.13	11.42	503	46.81	0.19	0.14	11.46	211	47.95	0.20	0.16	11.28
480	47.39	0.27	0.18	11.42	604	47.02	0.22	0.17	11.41	237	47.73	0.19	0.14	11.48
534	47.37	0.27	0.15	11.40	654	46.84	0.20	0.17	11.43	290	47.99	0.20	0.17	11.53
587	47.15	0.28	0.15	11.31	704	46.75	0.20	0.12	11.44	316	47.49	0.23	0.16	11.39
694	47.14	0.28	0.15	11.43	906	46.97	0.21	0.17	11.44	342	47.89	0.20	0.13	11.42
747	48.51	0.29	0.16	11.48	956	47.34	0.18	0.17	11.53	369	47.77	0.20	0.18	11.43
961	47.45	0.29	0.14	11.28	1006	47.38	0.20	0.17	11.52	395	47.68	0.20	0.14	11.61
1014	47.45	0.30	0.16	11.39	1057	47.47	0.21	0.15	11.50	421	47.83	0.18	0.17	11.46
1068	47.51	0.31	0.13	11.24	1107	47.27	0.18	0.17	11.33	448	47.59	0.22	0.16	11.16
1121	47.05	0.29	0.15	11.29	1157	47.12	0.21	0.18	11.57	474	47.64	0.21	0.15	11.33
1228	47.82	0.31	0.17	11.31	1208	46.64	0.20	0.14	11.55	500	47.62	0.21	0.13	11.49
1281	47.16	0.30	0.17	11.43	1258	47.02	0.20	0.15	11.52	527	47.03	0.20	0.17	11.31
1335	47.08	0.28	0.20	11.39	1359	46.34	0.19	0.14	11.20	553	47.51	0.19	0.16	11.35
1548	47.34	0.32	0.16	11.27	1409	47.18	0.20	0.14	11.58	579	46.86	0.24	0.18	11.47
1762	46.84	0.32	0.15	11.25	1459	46.66	0.22	0.15	11.50	790	47.46	0.24	0.16	11.22
2295	47.48	0.30	0.17	11.38	1510	47.44	0.21	0.14	11.44	816	48.13	0.21	0.17	11.59
2349	45.96	0.30	0.18	11.16	1560	46.67	0.19	0.15	11.28	842	46.65	0.22	0.15	11.45
2402	47.26	0.30	0.19	11.35	1660	47.52	0.20	0.16	11.44	869	47.79	0.22	0.16	11.54
2456	47.11	0.30	0.16	11.33	1761	47.72	0.19	0.18	11.46	895	47.38	0.20	0.18	11.60
2509	46.71	0.33	0.16	11.49	1811	47.21	0.21	0.16	11.29	921	47.56	0.22	0.19	11.31
2562	47.14	0.28	0.17	11.39	1862	47.27	0.18	0.14	11.66	974	47.84	0.25	0.18	11.43
2616	45.99	0.28	0.16	11.55	1912	47.26	0.18	0.16	11.61	1000	47.70	0.24	0.16	11.36
2669	47.40	0.29	0.14	11.39						1027	47.66	0.24	0.17	11.38
2722	47.16	0.32	0.14	11.36						1053	47.52	0.20	0.16	11.52
2776	47.32	0.30	0.17	11.43						1079	47.56	0.24	0.16	11.39
2883	47.56	0.29	0.14	11.27						1106	47.88	0.23	0.14	11.17
2936	46.83	0.29	0.15	11.16	Olivine R (Distal)					1132	48.01	0.22	0.14	11.40
3043	47.50	0.30	0.17	11.28	x (μm)	MgO	NiO	MnO	FeO	1158	47.45	0.23	0.14	11.33
3096	47.44	0.28	0.18	11.48	0	47.62	0.22	0.16	11.68	1185	47.67	0.27	0.15	11.75
3150	47.77	0.26	0.17	11.45	50	47.42	0.20	0.17	11.45	1211	47.25	0.25	0.15	11.48
3363	47.42	0.29	0.16	11.34	100	47.46	0.19	0.15	11.64	1237	47.45	0.24	0.16	11.58
3416	47.16	0.28	0.15	11.30	150	47.66	0.21	0.14	11.62	1369	47.79	0.24	0.20	11.39
3470	47.31	0.26	0.16	11.40	201	47.28	0.19	0.15	11.81	0	47.52	0.21	0.17	11.30
3523	47.25	0.26	0.16	11.47	251	47.12	0.21	0.17	11.27	60	47.54	0.20	0.14	11.46
3577	47.21	0.27	0.16	11.41	301	47.67	0.21	0.16	11.72	179	47.76	0.20	0.16	11.25
3630	47.15	0.28	0.16	11.43	351	47.84	0.20	0.15	11.64	239	48.09	0.20	0.17	11.60
3683	46.47	0.26	0.17	11.38	401	47.31	0.21	0.14	11.91	359	48.02	0.23	0.19	11.43
3737	47.07	0.27	0.15	11.35	602	47.48	0.19	0.16	11.42	598	47.73	0.24	0.19	11.59
3843	47.52	0.25	0.14	11.28	702	47.05	0.18	0.16	11.49	657	48.29	0.25	0.17	11.39
3897	47.01	0.25	0.14	11.29	752	47.48	0.20	0.15	11.63	717	46.08	0.22	0.17	10.91
4004	47.13	0.26	0.15	11.40	802	47.09	0.20	0.15	11.47	777	47.40	0.22	0.14	11.63
4057	46.44	0.26	0.18	11.86	852	47.46	0.19	0.15	11.21	837	45.21	0.22	0.13	10.44
4110	47.28	0.24	0.16	11.28	1003	47.30	0.20	0.14	11.76	896	47.50	0.25	0.19	11.29
4164	47.14	0.26	0.17	11.27	1103	47.54	0.18	0.13	11.62	956	47.61	0.24	0.15	11.44
4217	47.40	0.24	0.15	11.28	1153	47.51	0.20	0.15	11.76	1076	47.29	0.28	0.16	10.94
4271	48.12	0.24	0.17	11.39	1253	47.67	0.20	0.17	11.70	1135	47.93	0.27	0.16	11.63
4324	47.07	0.24	0.15	11.36	1504	46.76	0.20	0.16	11.71	1195	47.87	0.29	0.17	11.53
4377	47.26	0.24	0.18	11.61	1554	47.77	0.19	0.15	11.45	1255	47.95	0.26	0.15	11.51
4431	47.25	0.25	0.17	11.44	1755	47.70	0.20	0.17	11.75	1315	47.93	0.27	0.17	11.50
4591	47.60	0.24	0.17	11.43	1805	46.93	0.19	0.13	11.62	1494	46.26	0.27	0.17	11.29
4644	47.43	0.24	0.17	11.35	1855	48.43	0.19	0.16	11.41	1554	47.12	0.26	0.16	11.47
4698	47.13	0.24	0.15	11.43	1905	47.89	0.21	0.12	11.62	1613	47.11	0.28	0.15	11.54
4751	47.39	0.21	0.12	11.43	1955	47.64	0.21	0.17	11.63	1733	47.71	0.28	0.17	11.42
5018	46.95	0.23	0.16	11.39	2005	47.67	0.20	0.16	11.91	1793	48.11	0.30	0.19	11.65
5071	47.12	0.23	0.18	11.44	2256	47.72	0.21	0.18	11.73	1912	47.18	0.27	0.17	11.44
5125	46.90	0.21	0.16	11.50						1972	47.39	0.27	0.14	11.39
5178	46.78	0.20	0.17	11.37						2032	47.78	0.28	0.16	11.55
5231	46.80	0.22	0.14	11.44						2091	47.25	0.27	0.16	11.24
5285	46.53	0.20	0.14	11.38						2211	47.01	0.26	0.15	11.21
										2271	47.85	0.26	0.19	11.64
										2330	48.25	0.25	0.15	11.43
										2390	47.43	0.25	0.13	11.53
										2450	47.39	0.27	0.17	11.31
										2689	47.04	0.24	0.14	11.58
										2808	47.53	0.22	0.17	11.42
										2928	47.53	0.23	0.16	11.45
										2988	47.69	0.24	0.16	11.38
										3047	47.61	0.23	0.17	11.46
										3107	48.16	0.25	0.16	11.76

Table 12 ***(continued)*** *Select olivine major element profiles from wehrlite BD3067*

Olivine G (Distal)					Olivine H (Distal)					Olivine 1 (Proximal)				
x (μm)	MgO	NiO	MnO	FeO	x (μm)	MgO	NiO	MnO	FeO	x (μm)	MgO	NiO	MnO	FeO
0	47.68	0.19	0.15	11.43	0	47.79	0.20	0.14	11.44	0	47.92	0.19	0.18	11.74
50	47.46	0.21	0.15	11.47	101	47.88	0.21	0.17	11.63	75	47.45	0.20	0.16	11.43
100	47.28	0.21	0.17	11.61	151	47.58	0.21	0.13	11.40	225	47.69	0.20	0.15	11.57
150	47.43	0.21	0.19	11.58	202	47.39	0.21	0.17	11.41	376	47.69	0.21	0.18	11.63
201	47.41	0.20	0.15	11.56	252	47.82	0.20	0.18	11.72	451	47.65	0.21	0.16	11.37
301	47.23	0.21	0.16	11.57	353	47.48	0.23	0.16	11.79	526	47.68	0.20	0.19	11.65
401	47.10	0.21	0.17	11.55	555	47.80	0.20	0.15	11.64	826	47.45	0.19	0.16	11.51
451	47.10	0.22	0.14	11.48	605	47.44	0.20	0.16	11.52	902	47.96	0.20	0.17	11.60
502	46.89	0.22	0.16	11.62	706	46.67	0.20	0.14	11.67	977	46.93	0.20	0.17	11.25
602	47.54	0.24	0.18	11.57	807	47.58	0.20	0.15	11.24	1052	47.79	0.20	0.15	11.37
652	47.57	0.24	0.17	11.49	908	47.90	0.17	0.16	11.39	1127	47.63	0.19	0.16	11.43
702	46.93	0.23	0.14	11.28	1059	47.94	0.19	0.14	11.50	1277	47.37	0.21	0.16	11.54
752	47.39	0.25	0.16	11.52	1160	47.63	0.19	0.16	11.70	1352	47.37	0.20	0.15	11.45
803	47.42	0.25	0.17	11.51	1614	47.70	0.22	0.17	11.38	1428	47.81	0.19	0.15	11.41
853	47.23	0.25	0.16	11.43	1665	47.18	0.22	0.15	11.44	1503	47.66	0.22	0.14	11.82
953	47.28	0.26	0.17	11.66	1715	47.66	0.20	0.13	11.30	1578	47.64	0.21	0.16	11.24
1003	45.50	0.24	0.17	11.56	1816	47.76	0.22	0.14	11.44	1653	47.34	0.21	0.15	11.44
1053	47.10	0.27	0.14	11.46	1867	46.42	0.20	0.15	11.30	1728	47.74	0.21	0.19	11.46
1104	47.47	0.30	0.16	11.66	1917	47.75	0.21	0.16	11.47	1953	47.95	0.19	0.17	11.71
1254	46.72	0.25	0.13	11.09	2270	48.05	0.19	0.17	11.61	2254	47.70	0.21	0.16	11.88
1304	47.26	0.26	0.15	11.37	2321	48.52	0.21	0.16	11.45	2329	47.70	0.21	0.18	11.79
1354	47.00	0.25	0.16	11.46	2523	47.60	0.20	0.14	11.25	2404	47.91	0.20	0.16	11.64
1404	46.97	0.26	0.12	11.49	2573	47.48	0.18	0.17	11.48	2479	47.61	0.20	0.17	11.46
1455	47.03	0.25	0.14	11.44	2775	47.31	0.21	0.15	11.41	2555	47.56	0.20	0.15	11.32
1505	46.83	0.26	0.16	11.50	3279	47.85	0.20	0.17	11.45	2630	47.58	0.20	0.19	11.78
1605	47.80	0.26	0.18	11.39						2705	47.47	0.20	0.12	11.74
1655	47.55	0.27	0.14	11.46						2855	47.79	0.21	0.16	11.89
1705	47.14	0.27	0.17	11.52						2930	47.69	0.23	0.17	11.47
1756	47.05	0.28	0.17	11.53	Olivine H (Distal) - Profile 2					3005	47.90	0.21	0.19	11.28
1856	47.45	0.28	0.17	11.60	0	47.99	0.21	0.14	11.49	3080	47.59	0.22	0.16	11.64
1906	47.32	0.27	0.15	11.65	201	48.16	0.19	0.16	11.36	3156	47.64	0.21	0.16	11.60
1956	47.14	0.25	0.14	11.58	251	47.72	0.20	0.16	11.66	3306	47.90	0.20	0.20	11.78
2006	47.15	0.26	0.15	11.56	401	47.57	0.19	0.17	11.73	3381	47.52	0.21	0.16	11.54
2057	46.97	0.23	0.14	11.67	451	47.52	0.19	0.18	11.63	3456	46.75	0.21	0.15	11.46
2157	47.34	0.25	0.13	11.49	602	47.46	0.19	0.18	11.76	3606	47.95	0.21	0.18	11.62
2207	47.17	0.24	0.15	11.60	652	47.96	0.23	0.17	11.64	3832	47.65	0.21	0.16	11.86
2257	46.94	0.23	0.16	11.58	702	47.48	0.19	0.15	11.63	3907	48.05	0.23	0.14	11.65
2307	47.18	0.24	0.16	11.59	752	48.14	0.21	0.16	11.48	3982	47.62	0.21	0.16	11.81
2358	46.97	0.23	0.15	11.38	802	48.41	0.20	0.18	11.59	4132	46.96	0.20	0.16	11.53
2408	47.04	0.23	0.16	11.52	852	48.02	0.20	0.12	11.32	4208	47.51	0.23	0.18	11.32
2458	47.19	0.24	0.13	11.46	903	47.61	0.22	0.17	11.60	4433	47.57	0.22	0.16	11.34
2508	47.21	0.24	0.19	11.54	1003	47.88	0.20	0.16	11.25	4508	47.36	0.22	0.18	11.34
2608	47.00	0.27	0.17	11.76	1053	47.67	0.22	0.16	11.53	4583	47.56	0.21	0.16	11.60
2658	47.01	0.24	0.15	11.57	1103	47.44	0.21	0.16	11.40	4658	47.63	0.21	0.18	11.49
2709	47.52	0.23	0.14	11.39	1153	47.95	0.20	0.18	11.51	4809	47.79	0.21	0.16	11.35
2809	47.20	0.24	0.15	11.37	1203	46.65	0.22	0.17	11.49	4884	47.64	0.21	0.16	11.59
2859	46.95	0.25	0.15	11.60	1254	48.29	0.19	0.16	11.52	4959	47.80	0.20	0.16	11.42
3010	48.11	0.23	0.14	11.57	1554	48.06	0.20	0.15	11.74	5034	47.68	0.19	0.17	11.48
3110	47.36	0.22	0.18	11.48	1655	47.50	0.21	0.18	11.48	5109	47.74	0.22	0.15	11.60
3160	47.37	0.23	0.17	11.60	1755	47.39	0.21	0.17	11.46	5184	47.98	0.21	0.14	11.50
3210	47.15	0.23	0.20	11.56	2407	47.76	0.19	0.13	11.55	5560	47.64	0.20	0.17	11.75
3260	47.17	0.23	0.18	11.50	2507	47.39	0.20	0.18	11.73	5860	47.16	0.20	0.17	11.24
3311	47.24	0.23	0.15	11.62	2657	47.45	0.19	0.16	11.47	5936	47.61	0.20	0.15	11.40
3461	46.90	0.24	0.17	11.50	2758	47.57	0.21	0.16	11.60	6161	47.86	0.18	0.15	11.67
3511	47.31	0.24	0.13	11.49	2808	47.20	0.18	0.13	11.62	6386	47.40	0.21	0.16	11.52
3561	45.15	0.22	0.16	11.11	2908	47.62	0.20	0.16	11.55	6462	48.03	0.20	0.17	11.48
3662	47.49	0.24	0.18	11.51	2958	47.74	0.20	0.19	11.67	6612	48.00	0.19	0.14	11.45
4063	47.44	0.24	0.18	11.52	3008	47.74	0.20	0.16	11.95					
4113	47.34	0.24	0.15	11.62	3059	47.12	0.18	0.12	11.36					

Table 13 ***(continues on next page)*** *Olivine trace element profiles from wehrlite BD3067*

OLIVINE A-P1	x (μm)	Na23	Al27	Sc45	Ti47	V51	Cr53	Mn55	Co59	Ni60	Cu65	Zn66	Zr90	Nb93	Sn120
BD3067OlA-P1-2	170	57.48	7.23	1.811	146	3.72	39.82	1044	136.82	1527	2.34	111.29	0.407	0.277	0.752
BD3067OlA-P1-3	290	56.28	7.87	1.682	146	3.81	37.78	1038	136.34	1526	1.14	105.3	0.288	0.289	0.737
BD3067OlA-P1-4	410	60	8.21	1.767	142	3.7	39.38	1044	130.28	1522	1.13	108.91	0.394	0.324	0.812
BD3067OlA-P1-5	530	57.84	7.38	1.628	143	3.43	38.93	966	123.72	1521	1.35	99.16	0.346	0.336	0.726
BD3067OlA-P1-6	650	86.76	8.27	1.613	151	3.66	40.1	979	127.44	1571	1.21	100.62	0.523	0.461	0.672
BD3067OlA-P1-7	770	148.96	10.76	1.725	158	3.74	38.66	979	129.36	1651	1.33	106.09	1.315	0.843	0.679
BD3067OlA-P1-8	890	89.75	8.5	1.725	159	3.97	38.63	1004	130.69	1712	1.32	102.05	0.949	0.753	0.677
BD3067OlA-P1-9	1010	79.81		1.708	165	4.06	38.2	936	125.94	1721	1.98	84.33	1.85	0.826	0.685
BD3067OlA-P1-10	1130	109.99	7.97	1.473	154	3.76	39.13	1018	126.36	1735	1.06	104.09	0.644	0.51	0.684
BD3067OlA-P1-11	1250	95.29	12.91	1.621	175	4.04	40.43	968	127.72	1775	1.38	99.99	1.98	0.814	0.744
BD3067OlA-P1-12	1370	107.93	12.02	1.65	179	3.97	42.3	994	130.66	1816	1.39	102.83	1.99	0.885	0.758
BD3067OlA-P1-13	1490	98.73	6.65	1.548	157	3.75	44.02	1006	127.82	1819	1.1	102.78	0.912	0.651	0.701
BD3067OlA-P1-17	1970	64.19	12.66	1.651	160	3.87	47.83	921	119.01	2041	1.85	84.03	0.674	0.506	0.702
BD3067OlA-P1-18	2090	114.53	8.78	1.554	152	3.56	46.6	1022	124.52	1984	1.32	101.86	0.812	0.494	0.711
BD3067OlA-P1-19	2210	119.51	8.84	1.59	155	3.71	48.43	1009	127.09	2005	1.45	104.3	0.821	0.587	0.712
BD3067OlA-P1-20	2330	109.11	7.1	1.642	158	3.98	51.56	1007	130.17	2073	1.41	102.78	0.74	0.609	0.764
BD3067OlA-P1-21	2450	112.49	8.14	1.59	164	4.13	51.62	1009	127.74	2077	1.21	100.41	1.276	0.767	0.687
BD3067OlA-P1-22	2570	131.93	12.41	1.577	171	3.8	50.88	977	122.94	2006	1.22	95.63	1.64	0.871	0.719
BD3067OlA-P1-23	2690	88.63	7.99	1.554	169	3.72	52.66	1038	129.6	2157	1.07	104.06	0.592	0.521	0.74
BD3067OlA-P1-24	2810	70.53	6.16	1.451	152	3.52	51.33	975	126.66	2105	0.95	98.03	0.37	0.351	0.765
BD3067OlA-P1-25	2930	80.2	10.03	1.529	169	3.43	49.74	1014	127.37	2121	1.21	102.79	0.408	0.43	0.796
BD3067OlA-P1-26	3050	82.83	8.83	1.546	478	4.33	63.38	973	125.24	2140	1.07	108.48	0.736	1.669	0.905
BD3067OlA-P1-27	3170	113.82	13.09	1.659	194	3.85	52.1	993	127.17	2266	2.25	98.1	0.87	0.596	0.804
BD3067OlA-P1-32	3770	128.52	9.87	1.486	137	3.36	45.92	996	125.55	2202	1.1	108.81	0.584	0.502	0.702
BD3067OlA-P1-33	3890	83.38	10.85	1.492	156	3.43	49.28	979	124.33	2164	1.19	101.88	0.499	0.448	0.791
BD3067OlA-P1-34	4010	95.38		1.655	182	4.59	48.25	936	126.65	2199	1.52	88.94	2	1.138	0.842
BD3067OlA-P1-35	4130	81.36	6.6	1.705	164	3.62	49.73	1021	125.58	2170	1.43	104.75	0.448	0.42	0.949
BD3067OlA-P1-36	4250	83.61	2.02	1.58	165	3.51	48.38	998	125.4	2120	1.14	98.89	0.7	0.468	0.591
BD3067OlA-P1-37	4370	77.37	6.85	1.475	144	3.47	48.69	989	124.2	2085	1	101.47	0.448	0.381	0.688
BD3067OlA-P1-38	4490	144.46	7.68	1.593	159	3.79	50.73	1054	131.28	2169	1.3	104.51	0.876	0.572	0.643
BD3067OlA-P1-39	4610	57.69	5.24	1.382	149	3.45	46.71	937	123.79	2001	1.2	90.21	0.268	0.372	0.733
BD3067OlA-P1-40	4730	64.89	7.3	1.674	155	3.78	51.69	1072	132.68	2113	0.91	106.62	0.286	0.328	0.741
BD3067OlA-P1-41	4850	60.08	7.66	1.545	152	3.47	46.32	994	122	1891	1.05	97.7	0.332	0.34	0.641
BD3067OlA-P1-42	4970	67.38	4.88	1.634	160	3.76	48.24	1047	132.88	2001	1.28	107.57	0.369	0.356	0.74
BD3067OlA-P1-44	5210	55.43		1.614	152	3.54	46.76	963	110.86	1878	1.32	87.03	0.336	0.315	0.727
BD3067OlA-P1-45	5330	62.21	11.26	1.746	145	3.84	43.35	1012	128.88	1760	1.19	97.95	1.214	0.469	0.681
BD3067OlA-P1-46	5450	57.18	9.61	1.609	146	3.68	39.05	997	125.48	1655	1.4	97.72	0.436	0.345	0.677
BD3067OlA-P1-47	5570	53.81	15.21	1.582	145	3.82	39.51	988	123.26	1575	1.69	97.09	0.43	0.354	0.685
BD3067OlA-P1-48	5690	50.64	26.39	1.8	141	4.69	38.11	990	121.4	1510	1.71	94.61	2.2	0.672	0.755
BD3067OlA-P1-49	5810	44.01	21.5	1.524	130	3.61	38.25	914	115.1	1408	1.65	87.09	0.446	0.246	0.65

OLIVINE A-P2	x (μm)	Na23	Al27	Sc45	Ti47	V51	Cr53	Mn55	Co59	Ni60	Cu65	Zn66	Zr90	Nb93	Sn120
BD3067-OlA-P2-2	170	59.36	3.78	1.474	150	3.15	42.75	950	124.24	1894	1.44	97.3	0.344	0.336	0.736
BD3067-OlA-P2-4	410	56.35	8.63	1.475	148	3.32	43.86	963	125.53	1926	1.33	96.43	0.276	0.308	0.678
BD3067-OlA-P2-5	530	66.74	7.25	1.382	150	3.6	46.21	996	126.16	2010	1.1	103.84	0.278	0.273	0.667
BD3067-OlA-P2-6	650	68.45	9.62	1.386	147	3.47	48.12	1026	127.73	2044	1.14	99.53	0.29	0.341	0.77
BD3067-OlA-P2-7	770	65.78	8.16	1.453	153	3.52	47.21	1048	129.02	2073	1.16	100.51	0.257	0.38	0.713
BD3067-OlA-P2-8	890	65.16	6.61	1.47	155	3.61	46.16	1012	131.83	2074	1.49	96.91	0.271	0.337	0.83
BD3067-OlA-P2-9	1010	68.23	5.16	1.327	144	3.35	43.93	979	122.11	1980	1.27	97.78	0.27	0.351	0.655
BD3067-OlA-P2-10	1130	65.04	4.85	1.351	152	3.39	43.82	1007	122.9	2020	1.19	99.66	0.273	0.346	0.655
BD3067-OlA-P2-11	1250	86.8	5.3	1.483	153	3.56	46.23	1027	128.98	2100	1.08	99.82	0.33	0.425	0.649
BD3067-OlA-P2-12	1370	151.82	13.44	1.347	162	3.95	42.96	1001	126.5	2082	1.07	97.46	2.41	1.165	1.82
BD3067-OlA-P2-13	1490	115.19	6.55	1.515	155	3.65	45.44	1007	129.37	2093	1.07	98.47	1.045	0.636	0.678
BD3067-OlA-P2-14	1610	64.85	19.23	1.407	156	3.97	45.97	1001	127.23	2123	1.7	93.92	0.357	0.467	0.735
BD3067-OlA-P2-25	2930	81.55	5.63	1.456	231	3.5	53.27	993	125.44	2095	1.22	92.24	0.586	0.756	0.636
BD3067-OlA-P2-26	3050	93.11	11.89	1.527	183	3.5	53.6	1052	130.82	2228	1.38	101.31	0.626	0.599	0.695
BD3067-OlA-P2-27	3170	65.56	8.56	1.3	176	3.5	50.9	978	124.9	2085	1.11	92.04	0.314	0.504	0.611
BD3067-OlA-P2-28	3290	68.75	5.89	1.367	150	3.38	50.72	998	129.5	2174	1.29	96.56	0.303	0.31	0.675
BD3067-OlA-P2-29	3410	111.72	11.05	1.485	150	3.81	50.22	1034	126.82	2209	1.78	98.12	0.495	0.467	0.598
BD3067-OlA-P2-31	3650	67.16	5.94	1.239	136	3.27	44.94	951	121.36	1998	0.96	86.25	0.229	0.303	0.601
BD3067-OlA-P2-33	3890	60.44	12.85	1.354	144	3.6	45.56	960	122.61	2063	1.39	88.55	0.249	0.333	0.651
BD3067-OlA-P2-35	4130	64.99	8.81	1.354	144	3.53	43.46	1005	128.41	1965	1.47	97.96	0.241	0.36	0.671
BD3067-OlA-P2-36	4250	57.59	8.11	1.482	155	3.66	43.81	1009	128.35	1971	1.16	99.42	0.28	0.334	0.696
BD3067-OlA-P2-37	4370	71.26	5.23	1.5	157	3.82	44.98	1113	137.42	2057	1.24	110.31	0.312	0.468	0.729
BD3067-OlA-P2-39	4610	86.58	11.3	1.57	154	8.15	42.25	1036	126.39	1839	1.64	98.49	2.16	1.39	0.654
BD3067-OlA-P2-41	4850	61.09	4.87	1.282	130	3.52	37.81	1004	127.22	1757	1.22	95.83	0.369	0.3	0.628
BD3067-OlA-P2-43	5090	152.74	11.01	1.421	141	6.71	40.36	1042	132.2	1692	1.61	102.03	1.08	1.41	0.645
BD3067-OlA-P2-44	5210	73.14	6.03	1.509	142	4.8	39.45	1005	129.29	1699	2.35	91.3	0.579	1.106	0.635
BD3067-OlA-P2-45	5330	111.72	8.63	1.431	145	3.79	38.5	992	128.25	1656	1.2	92.14	0.75	0.536	0.653
BD3067-OlA-P2-46	5450	128.44	10.6	1.357	147	4.05	41.35	991	123.15	1588	1.2	89.58	1.52	0.878	0.499
BD3067-OlA-P2-50	5930	75.8	41.35	2.33	142	7.72	43.33	959	132.95	1554	2.27	83.32	2.37	1.3	0.658
BD3067-OlA-P2-51	6050	56.44	6.65	1.423	124	3.35	43.16	985	122.21	1521	0.98	89.81	0.386	0.306	0.577
BD3067-OlA-P2-52	6170	60.67	6.36	1.332	125	3.68	41.24	1013	128.96	1500	1.36	97.34	0.4	0.276	0.625
BD3067-OlA-P2-53	6290	81.8	7.02	1.398	126	3.62	38.59	996	127.63	1498	1.12	95.5	0.546	0.33	0.602
BD3067-OlA-P2-54	6410	69.02	18.71	1.448	128	3.94	40.05	1024	121.92	1489	1.51	97.02	0.705	0.459	0.603

Table 13 ***(continued)*** *Olivine trace element profiles from wehrlite BD3067*

OLIVINE D	x (μm)	Na23	Al27	Sc45	Ti47	V51	Cr53	Mn55	Co59	Ni60	Cu65	Zn66	Zr90	Nb93	Sn120
BD3067OlD-P3	290	65.1	6.35	1.279	125	3.51	32.63	966	119.98	1381	1.14	91.13	0.345	0.298	0.627
BD3067OlD-P4	410	54.95	3.33	1.28	117	3.5	32.56	943	122.87	1424	1.17	86.78	0.301	0.332	0.627
BD3067OlD-P5	530	59.19	4.92	1.296	121	3.49	32.35	1009	125.71	1472	1.38	95.27	0.351	0.316	0.601
BD3067OlD-P6	650	53.03	22.38	1.43	128	3.82	35.28	978	129.83	1497	1.62	93.49	0.436	0.343	0.673
BD3067OlD-P7	770	60.04	5.34	1.337	127	3.64	35.4	1023	129.59	1546	1.35	99.21	0.349	0.262	0.63
BD3067OlD-P8	890	60.58	7.3	1.4	135	3.48	38.3	1070	131.61	1657	1.09	101.08	0.352	0.329	0.639
BD3067OlD-P9	1010	62.42	13.1	1.55	148	3.76	40.49	1081	133.87	1754	1.58	104.59	0.414	0.413	0.727
BD3067OlD-P10	1130	55.61	14.43	1.4	133	3.23	36.89	911	122.61	1615	1.14	87.69	0.392	0.363	0.578
BD3067OlD-P11	1250	61.06	11.6	1.59	144	4.2	44.89	1057	135.51	1774	1.45	105.43	0.35	1.038	2.12
BD3067OlD-P12	1370	52.18	3.51	1.3	140	3.44	40.27	981	128.44	1821	1.2	94.24	0.347	0.327	0.762
BD3067OlD-P13	1490	60.06	7.16	1.34	142	3.62	47.22	1053	137.38	1946	1.42	104.27	0.456	0.374	0.706
BD3067OlD-P14	1610	63.53	6.45	1.28	128	3.48	42.57	1031	129.06	1820	1.11	104.27	0.312	0.369	0.626
BD3067OlD-P16	1850	62.66	9.24	1.33	140	3.48	46.69	1090	131.57	1914	1.09	110.38	0.431	0.368	0.618
BD3067OlD-P18	2090	61.21	5.54	1.2	133	3.43	46.63	1061	129.06	1940	1.24	102.74	0.314	0.321	0.656
BD3067OlD-P19	2210	57.42	5.39	1.208	126	3.19	45.72	1000	121.19	1857	1.96	98.08	0.304	0.303	0.614
BD3067OlD-P20	2330	56.53	5.17	1.26	127	3.25	45.79	974	121.11	1883	1.02	94.1	0.285	0.302	0.542
BD3067OlD-P22	2570	67.49	6.75	1.29	126	3.2	49.78	1054	128.3	1994	1.53	101.72	0.347	0.319	0.6
BD3067OlD-P23	2690	74.49	5.33	1.32	140	3.43	51.49	1056	132.78	2050	1.12	103.96	0.356	0.424	0.607
BD3067OlD-P24	2810	64	6.03	1.193	133	3.18	48.36	1004	123.17	1941	1.45	97.49	0.329	0.375	0.582
BD3067OlD-P26	3050	89.43	4.79	1.33	140	3.32	49.19	985	126.74	2030	1.38	95.77	0.714	0.575	0.656
BD3067OlD-P27	3170	87.39	9.05	1.27	136	3.38	47.7	980	121.35	1956	1.81	93.47	1.022	0.665	0.573
BD3067OlD-P30	3530	97.04	7.99	1.36	148	3.64	49.76	1055	129.47	2023	1.21	102.89	1.042	0.758	0.578
BD3067OlD-P31	3650	85.15	10.54	1.31	144	3.44	48.95	1053	133.66	2089	1.12	102.52	0.549	0.584	0.577
BD3067OlD-P32	3770	98.7	10.37	1.3	145	3.56	46.93	1015	128.49	1988	1.19	102.74	0.725	0.645	0.636
BD3067OlD-P33	3890	101.53	12.16	1.36	143	4.33	46.6	1007	128.89	2041	1.66	90.5	1.001	0.743	0.59
BD3067OlD-P34		131.28	21	1.62	179	4.84	52.49	1002	129.2	1991	2.75	90.23	2.76	1.24	0.611

OLIVINE B	x (μm)	Na23	Al27	Sc45	Ti47	V51	Cr53	Mn55	Co59	Ni60	Cu65	Zn66	Zr90	Nb93	Sn120
BD3067OlB-1	50	82	4.77	1.55	141	4.02	35.69	1176	145.34	1630	1.42	116.18	0.471	0.447	0.784
BD3067OlB-2	170	89.31	7	1.54	148	3.67	35.39	1117	140.01	1538	1.07	109.2	0.629	0.442	0.834
BD3067OlB-3	290	66.04	8.55	1.51	141	3.85	35.43	1064	134.59	1486	1.28	102.65	0.542	0.431	0.664
BD3067OlB-4	410	96.8	5.55	1.47	154	3.96	35	1063	132.58	1468	1.11	104.69	1.24	0.67	0.694
BD3067OlB-7	770	88.44	6.31	1.24	124	3.61	32.45	1005	126.83	1398	1.03	96.57	0.426	0.302	0.561
BD3067OlB-8	890	90.36	6.42	1.35	127	3.62	32.32	1010	126.92	1415	1.42	95.56	0.495	0.347	0.572
BD3067OlB-9	1010	59.15	3.83	1.38	137	3.82	34.14	1075	133.18	1520	1.28	106.32	0.447	0.275	0.691
BD3067OlB-10	1130	58.53	3.7	1.4	135	3.47	34.11	1042	128.58	1438	1.12	96.76	0.412	0.267	0.642
BD3067OlB-11	1250	78.35	6.45	1.35	136	3.57	33.72	1046	131.71	1431	0.9	96.59	0.652	0.353	0.57
BD3067OlB-12	1370	71.33	10.21	1.46	145	3.98	33.07	970	128.23	1467	1.03	79.02	1.34	0.808	0.616
BD3067OlB-13	1490	88.84	5.29	1.29	126	3.49	31.71	984	124.93	1407	1.09	91.6	0.94	0.567	0.596
BD3067OlB-14	1610	89.33	12.08	1.41	148	4.06	36.47	1054	133.35	1500	1.16	96.72	1.61	0.894	0.664
BD3067OlB-15	1730	152.18	10.15	1.39	134	3.83	34.29	1023	128.25	1447	1.6	95.52	1.63	1.015	0.569
BD3067OlB-16	1850	153.31	8.96	1.41	138	3.84	32.16	1062	133.81	1475	1.12	103.28	1.11	0.653	0.598

OLIVINE G	x (μm)	Na23	Al27	Sc45	Ti47	V51	Cr53	Mn55	Co59	Ni60	Cu65	Zn66	Zr90	Nb93	Sn120
BD3067-OlG-P3	290	65.65	5.73	1.84	143	4.57	42.96	1017	135.61	1862	1.5	118.3	0.403	0.225	0.731
BD3067-OlG-P4	410	59.88	8.89	1.71	133	3.38	39.32	964	129.5	1832	1.64	109	0.304	0.216	0.751
BD3067-OlG-P5	530	63.55	4.01	1.66	138	3.53	39.89	1009	128.88	1822	1.29	112.4	0.336	0.227	0.737
BD3067-OlG-P6	650	60.58	9.97	1.66	144	3.65	38.82	972	126.73	1790	0.92	112.47	0.385	0.201	0.646
BD3067-OlG-P7	770	97.54	10.18	1.71	155	3.66	37.79	1004	129.85	1806	1.08	112.95	0.812	0.454	0.766
BD3067-OlG-P8	890	76.53	5.77	1.6	148	3.65	38.21	924	127.29	1765	1.13	103.19	0.674	0.422	0.755
BD3067-OlG-P9	1010	167.57	17.51	1.93	155	4.01	44.74	977	133.74	1831	1.58	107.13	1.93	1.007	0.689
BD3067-OlG-P10	1130	237.95	37.21	1.86	165	4.98	44.92	981	127.36	1756	1.48	107.78	3.3	1.421	0.823
BD3067-OlG-P12	1370	119.99	17.11	1.83	189	4.82	44.56	998	132.75	1842	1.49	109.6	2.79	1.266	0.877
BD3067-OlG-P13	1490	134.9	10.92	1.8	147	3.82	40.22	995	132.35	1824	1.2	109.57	0.87	0.622	2.41
BD3067-OlG-P14	1610	129.26	4.2	1.67	148	3.79	40.01	1017	130.31	1818	1.06	112.29	0.639	0.433	0.735
BD3067-OlG-P15	1730	67.57	8.01	1.64	138	3.33	37.28	978	126.06	1733	0.93	108.51	0.412	0.352	0.743
BD3067-OlG-P16	1850	77.62	5.74	1.66	148	3.65	41.34	1031	131.93	1840	1.46	116.26	0.387	0.327	1.019
BD3067-OlG-P17	1970	68.78	8.86	1.64	139	3.77	40.29	938	123.68	1816	1.29	104.25	0.416	0.38	0.674
BD3067-OlG-P18	2090	66.74	9.47	1.56	143	3.51	38.99	946	123.96	1709	0.99	104.04	0.437	0.305	0.767
BD3067-OlG-P19	2210	77.04	6.89	1.79	152	3.88	40.65	1034	136.22	1894	1.3	119.65	0.507	0.372	0.837
BD3067-OlG-P20	2330	67.4	9.07	1.8	154	3.71	42.37	1059	136.87	1905	0.93	122.21	0.398	0.33	0.979
BD3067-OlG-P21	2450	61.06	1.04	1.57	135	3.56	40.21	998	130.3	1805	1.05	111.48	0.344	0.295	0.932
BD3067-OlG-P22	2570	64.73	4.89	1.73	145	3.76	41.73	1099	139.12	1944	1.21	116.81	0.365	0.288	0.758
BD3067-OlG-P23	2690	62.59	11.22	1.388	132	3.56	38.49	1004	127.74	1842	1.18	108.51	0.354	0.245	0.637
BD3067-OlG-P24	2810	69.54	9.71	1.69	155	3.88	41.51	1095	141.01	2003	1.06	120.91	0.355	0.282	0.795
BD3067-OlG-P25	2930	123.81	4.4	1.53	137	3.51	39.76	986	129.09	1850	1.37	103.83	0.654	0.403	0.719
BD3067-OlG-P26	3050	84.8	7.85	1.51	142	3.81	38.74	1004	128.39	1868	1.22	110.19	0.556	0.338	0.732
BD3067-OlG-P27	3170	121.71	11.47	1.66	161	3.9	39.97	956	127.24	1910	1.33	105.57	1.73	0.774	0.745
BD3067-OlG-P31	3650	63.61	3.23	1.46	150	3.67	41.5	1000	131.82	1877	1.27	107.29	0.367	0.329	0.786
BD3067-OlG-P32	3770	62.12	4.1	1.6	143	3.32	37.92	984	125.2	1777	1.22	106.56	0.357	0.35	0.733
BD3067-OlG-P33	3890	62.98	6.28	1.59	147	3.71	40.56	1048	133.77	1884	1.09	112.32	0.378	0.335	0.665
BD3067-OlG-P35	4130	58.1		1.1	138	3.32	36.44	949	124.46	1664	2.21	97.71	1.009	0.413	0.675
BD3067-OlG-P36	4250	48.8		1.53	135	3.5	39.47	980	127.89	1601	1.33	99.68	0.337	0.22	0.756
BD3067-OlG-P38	4490	57	8.19	1.77	144	3.85	39.79	1065	136.94	1629	1.61	113.24	0.381	0.292	0.85
BD3067-OlG-P39	4610	49.49	4.61	1.81	130	3.85	38.33	1025	132.18	1513	0.82	106.73	0.367	0.269	0.619
BD3067-OlG-P40	4730	47.54	7.71	1.83	141	4.09	37.91	1060	134.64	1523	1.19	112.49	0.466	0.257	0.766

OLIVINE E	x (μm)	Na23	Al27	Sc45	Ti47	V51	Cr53	Mn55	Co59	Ni60	Cu65	Zn66	Zr90	Nb93	Sn120
BD3067-OlE-P6	650	55.78	7.16	1.64	143	3.91	39.69	1077	135.55	1685	1.16	106.5	0.439	0.277	0.644
BD3067-OlE-P7	770	56.35	10.13	1.53	131	3.48	36.92	966	131.03	1619	1.09	107.08	0.359	0.331	0.635
BD3067-OlE-P8	890	55.38	7.1	1.6	135	3.55	38.24	1005	132.48	1648	1.64	99.67	0.396	0.249	0.643
BD3067-OlE-P9	1010	69.78	11.35	1.65	147	4.33	40.03	994	134.04	1646	1.35	103.86	0.764	0.459	0.801
BD3067-OlE-P11	1250	48.92	29.9	1.85	139	4.25	38.39	934	128.16	1632	1.68	88.58	0.679	0.369	0.671
BD3067-OlE-P12	1370	49.1		1.63	146	4.35	39.53	925	130.54	1612	1.54	89.68	4.07	0.308	0.616
BD3067-OlE-P13	1490	43.75	12.96	1.54	136	4.03	36.91	979	131.44	1658	1.34	100.18	0.478	0.287	0.613
BD3067-OlE-P14	1610	48.57	12.12	1.63	132	3.91	38.86	974	130.03	1641	1.8	93.3	0.33	0.266	0.651
BD3067-OlE-P15	1730	60.6	16.55	1.56	130	4.46	37.97	950	125.21	1573	1.33	92.98	0.361	0.31	0.617
BD3067-OlE-P16	1850	56.81	4.51	1.5	132	3.43	36.92	955	126.02	1578	1.07	101.34	0.292	0.327	0.589
BD3067-OlE-P17	1970	56.26	15.14	1.52	135	3.49	38.76	959	126.28	1567	1.13	98.54	0.274	0.27	0.592
BD3067-OlE-P18	2090	50.85	6.28	1.66	135	4.03	36.13	952	128.43	1505	1.05	89.93	0.437	0.336	0.569

Table 13 ***(continued)*** *Olivine trace element profiles from wehrlite BD3067*

OLIVINE C	x (μm)	Na23	Al27	Sc45	Ti47	V51	Cr53	Mn55	Co59	Ni60	Cu65	Zn66	Zr90	Nb93	Sn120
BD3067-Tk4-OlC-L6	50	145.26	14.03	1.834	175	4.07	46.15	1103	142.33	2115	1.57	119.95	1.857	1.063	0.999
BD3067-Tk4-OlC-L7	170	59.03	11.19	1.659	134	3.84	45.55	1031	137.26	2118	1.34	106.67	0.607	0.214	0.91
BD3067-Tk4-OlC-L8	290	65.8	6.92	1.539	164	3.53	47.84	1120	140.03	2302	1.34	126.44	0.481	0.327	1.039
BD3067-Tk4-OlC-L9	410	55.62	6.96	1.289	170	3.67	46.18	1005	132.87	2264	1.54	113.78	0.513	0.329	1.005
BD3067-Tk4-OlC-L10	530	54.3	7.87	1.594	162	3.55	50.22	1029	131.81	2357	1.42	110.12	0.53	0.387	1.002
BD3067-Tk4-OlC-L11	650	55.99	11.19	1.492	171	3.54	48.3	964	138.55	2456	1.39	96.58	0.52	0.467	0.798
BD3067-Tk4-OlC-L12	770	58.36	10.1	1.296	160	3.5	48.72	989	126.92	2415	1.68	97.15	0.383	0.342	0.903
BD3067-Tk4-OlC-L13	890	64.62	4.01	1.39	158	3.34	46.25	999	124.67	2383	1.16	112.23	0.335	0.311	0.942
BD3067-Tk4-OlC-L14	1010	70.04	9.16	1.507	168	4.01	50.59	1059	134.96	2618	1.42	118.04	0.396	0.446	0.975
BD3067-Tk4-OlC-L16	1250	75.28	12.67	1.384	179	5.7	49.63	1037	135.19	2649	9.68	109.28	0.545	0.548	0.92
BD3067-Tk4-OlC-L17	1370	126.43	<12.44	1.473	174	4.09	51.16	1019	137.07	2552	1.74	110.95	1.458	1.036	1.033
BD3067-Tk4-OlC-L18	1490	100.18	7.4	1.542	177	3.86	53.26	1074	139.03	2665	1.36	120.69	0.82	0.614	1.089
BD3067-Tk4-OlC-L19	1610	80.91	5.28	1.543	171	3.7	51.04	1016	134.36	2442	1.3	112.89	0.698	0.568	0.901
BD3067-Tk4-OlC-L20	1730	74.25	8.28	1.544	170	3.9	49.2	1103	139.69	2440	1.23	121.7	0.477	0.38	0.915
BD3067-Tk4-OlC-L21	1850	84.36	8.11	1.536	162	3.69	49.17	1040	139.01	2375	1.17	114.52	0.824	0.58	0.91
BD3067-Tk4-OlC-L22	1970	90.81	11.79	1.653	165	3.93	45.4	1052	132.86	2146	1.42	106.48	1.467	0.836	0.818
BD3067-Tk4-OlC-L23	2090	72.48	76.19	1.622	165	5.46	44.23	996	137.52	2060	4.07	92.42	1.457	0.936	0.829

Table 14 *Distal and proximal clinopyroxene composition from wehrlite BD3067 (Chapter 6)*

Position	Distal average	1 sd	Proximal average	1 sd	All average	1 sd
EPMA						
n	30		15		45	
SiO_2 (wt.%)	54.68	0.51	54.47	0.25	54.61	0.44
TiO_2	0.20	0.01	0.20	0.01	0.20	0.01
Al_2O_3	0.63	0.08	0.63	0.05	0.63	0.08
Cr_2O_3	0.98	0.43	0.74	0.07	0.98	0.43
FeO	2.89	0.29	3.08	0.12	2.89	0.29
MnO	0.07	0.01			0.07	0.01
MgO	16.60	0.34	16.67	0.13	16.60	0.34
NiO	0.03	0.01	0.02	0.00	0.03	0.01
CaO	22.03	0.35	21.99	0.22	22.03	0.35
Na_2O	1.23	0.18	1.17	0.09	1.23	0.18
Mg#	91.10	0.89	90.60	0.38	91.10	0.89
LA-ICP-MS						
n	10		15		25	
Al27	3342	425	3485	162	3397.05	350.56
K39	110	92	88	49	101.74	78.02
Sc45	50.1	8.6	55.7	3.7	52.26	7.55
Ti47	1046	75	1306	66	1146.17	146.62
V51	378	89	377	24	377.70	70.11
Co59	19.9	1.6	18.9	0.8	19.51	1.45
Ni60	243	55	185	11	220.87	51.87
Sr88	181	33	157	10	171.77	28.91
Y89	4.43	0.98	4.12	0.23	4.31	0.79
Zr90	114	20	98	10	107.99	18.79
Nb93	0.543	0.417	0.447	0.480	0.51	0.44
La139	3.02	0.85	2.52	0.43	2.83	0.75
Ce140	14.05	3.39	11.12	1.20	12.92	3.09
Pr141	2.48	0.58	2.11	0.18	2.34	0.49
Nd143	12.80	2.95	11.52	0.95	12.31	2.44
Sm147	3.20	0.71	2.97	0.19	3.11	0.57
Eu153	1.013	0.245	0.914	0.032	0.97	0.20
Gd157	2.57	0.60	2.45	0.11	2.52	0.47
Tb159	0.313	0.077	0.293	0.017	0.31	0.06
Dy163	1.528	0.312	1.375	0.049	1.47	0.26
Ho165	0.202	0.042	0.193	0.017	0.20	0.03
Er166	0.386	0.099	0.355	0.024	0.37	0.08
Tm169	0.038	0.007	0.034	0.003	0.04	0.01
Yb172	0.167	0.037	0.160	0.016	0.16	0.03
Lu175	0.017	0.005	0.017	0.006	0.02	0.01
Hf178	6.93	1.68	6.16	0.73	6.63	1.42
Ta181	0.029	0.020	0.022	0.016	0.03	0.02
Pb208	0.362	0.075	0.305	0.035	0.34	0.07
Th232	0.069	0.068	0.035	0.035	0.06	0.06
U238	0.016	0.016	0.011	0.009	0.01	0.01

Table 15 *Olivine, Orthopyroxene and Clinopyroxene SIMS analyses.*

Phase	Orthopyroxene (September)					Clinopyroxene (September)					Clinopyroxene (May)					Olivine (September)					Olivine (May)				
		H_2O		F			H_2O		F			H_2O		F			H_2O		F			H_2O		F	
Sample	**n**	avg	s.d	avg	s.d	**n**	avg	s.d	avg	s.d	**n**	avg	s.d	avg	s.d	**n**	avg	s.d	avg	s.d	**n**	avg	s.d	avg	s.d
Bultfontein																									
BD1140	**2**	178	*13*	8	*1*	**1**	280	*29*	24	*5*	**1**	280	*40*	24	*7*										
BD1141A	**1**	159	*5*	19	*5*	**1**	300	*21*	20	*2*	**1**	300	*23*	20	*3*	**1**	88	*17*	122	*23*					
BD1152	**1**	236	*24*	8	*1*	**1**	318	*92*	12	*4*	**4**	287	*11*	12	*2*	**1**	69	*10*	42	*13*					
BD1153	**2**	238	*68*	26	*4*						**1**	195	*24*	46	*6*	**2**	88	*9*	181	*16*	**2**	75	*4*	147	*15*
BD1672	**1**	254	*8*	15	*4*	**2**	313	*48*	21	*2*	**5**	257	*24*	24	*3*	**1**	69	*19*	62	*16*					
BD1999	**2**	260	*17*	22	*3*	**4**	277	*11*	29	*2*	**5**	274	*12*	29	*4*										
BD3021	**2**	140	*5*	16	*1*																				
BD3028	**2**	219	*25*	15	*2*											**3**	357	*144*	16	*2*	**1**	223	*12*	14	*5*
BD3067						**3**	54	*32*	23	*4*	**5**	70	19	24	*4*										
BD3670	**3**	27	*1*	0	*0*											**3**	0	*5*	1	*2*	**2**	15	*11*	21	*6*
BD3676	**2**	285	*17*	21	*3*											**3**	63	*18*	110	*9*					
Mothae																									
BD2122	**2**	104	*15*	33	*6*																				
BD2124	**1**	109	*42*	23	*4*	**2**	73	*13*	39	*3*	**2**	73	*16*	40	*4*	**2**	106	*4*	9	*3*	**1**	93	*2*	27	*3*
BD2125	**3**	164	*14*	23	*2*	**1**	87	*19*	31	*3*	**2**	103	*12*	28	*4*	**1**	37	*26*	120	*26*	**1**	92	*13*	151	*15*
BD2126	**3**	144	*13*	21	*3*	**2**	129	*20*	33	*2*	**4**	138	*13*	30	*2*	**2**	13	*4*	3	*1*	**2**	0	*8*	18	*4*
BD2128	**2**	191	*11*	22	*2*	**2**	137	*13*	37	*4*	**3**	139	*12*	38	*4*	**3**	38	*10*	53	*8*	**3**	33	*8*	54	*12*
BD2133	**3**	160	*6*	19	*2*											**2**	5	*10*	52	*6*	**2**	3	*2*	59	*10*
BD2135	**3**	83	*6*	7	*1*	**1**	73	*17*	17	*2*	**4**	83	*6*	16	*2*	**3**	0	*10*	0	*1*	**1**	0	*7*	18	*14*
BD2170	**2**	183	*18*	33	*5*											**3**	58	*16*	53	*8*					

Table 16 *Bulk NVFMM Volatile Concentrations*

	H_2O (ppmw)				F (ppm)			
Analyses	September		May		September		May	
Sample	avg	s.d	avg	s.d	avg	s.d	avg	s.d
Bultfontein								
BD1140								
BD1141A	99	*13*	99	*13*	87	*17*	87	*17*
BD1152	117	*14*	117	*13*	29	*9*	29	*9*
BD1153	96	*12*	87	*13*	168	*15*	138	*14*
BD1672	126	*15*	125	*14*	43	*11*		
BD1999								
BD3021								
BD3028	298	*104*	207	*104*	15	*2*	13	*2*
BD3067								
BD3670	10	*4*	20	*4*	1	*1*	13	*4*
BD3676	100	*17*			86	*8*		
Mothae								
BD2122								
BD2124	95	*9*	85	*9*	11	*3*	25	*3*
BD2125	83	*19*	111	*19*	71	*14*	87	*8*
BD2126	39	*6*	31	*5*	7	*1*	17	*3*
BD2128	63	*9*	59	*9*	44	*7*	45	*9*
BD2133	43	*9*	41	*9*	44	*5*	49	*8*
BD2135	23	*9*	24	*9*	2	*1*	15	*10*
BD2170								

Table 17 *Olivine and Orthopyroxene FTIR: Integrated absorbance normalised to 1 cm^{-1} of selected deconvolved bands in the polarised A-axis olivine spectra and unpolarised orthopyroxene FTIR spectra.*

Sample	**BD1153**	**BD1152**	**BD1672**	**BD1999**	**BD2125**	**BD1140**	**BD2126**	**BD2128**
Lithology	dunite *(kim met.)*	opx-rich gt-harz *(fluid met)*	opx-rich gt-harz *(fluid met)*	opx-rich gt-harz *(fluid met)*	opx-rich gt-harz *(fluid met)*	low-*T* gt-harz	high-*T* gt-lherz	high-*T* gt-lherz
Olivine								
3525 cm^{-1}	6.6			0.7		14.9	2.0	1.0
3570 cm^{-1}	100.3	32.7		12.6	14.1	68.3	7.2	3.4
3591 cm^{-1}	7.4	31.2		35.6	4.7	49.5	0.5	
3598 cm^{-1}	25.9				2.4		3.6	8.3
3612 cm^{-1}		5.2		8.1	1.7	10.8		
3623 cm^{-1}	0.5	5.7		7.3	4.5	7.3		
Orthopyroxene								
3600 cm^{-1}	53.5	75.6	49.2	48.6	17.3	55.0	17.4	39.2
3545 cm^{-1}	48.2	122.9	44.5	66.0	14.8	79.4	14.6	14.3
3516 cm^{-1}	97.2	90.5	93.3	140.4	55.4	57.5	72.0	101.1
3410 cm^{-1}	50.0	13.9	15.5	98.9	14.6	12.8	20.1	36.1
3300 cm^{-1}	8.7		3.8	23.7	2.9		4.8	9.9
3060 cm^{-1}	78.1	97.5	86.7	106.0	37.8	60.3	26.5	44.9